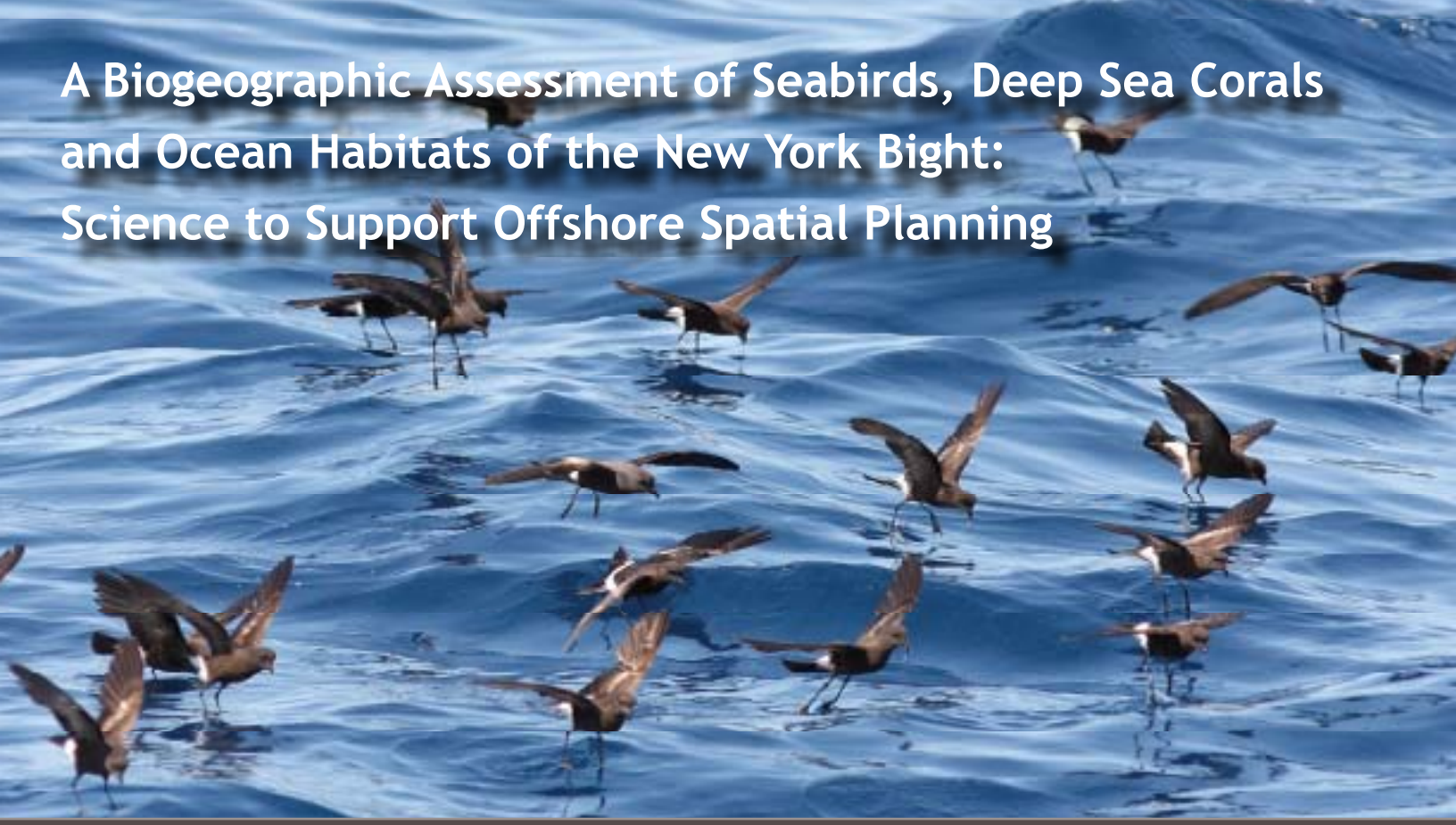


A Biogeographic Assessment of Seabirds, Deep Sea Corals and Ocean Habitats of the New York Bight: Science to Support Offshore Spatial Planning



Charles Menza

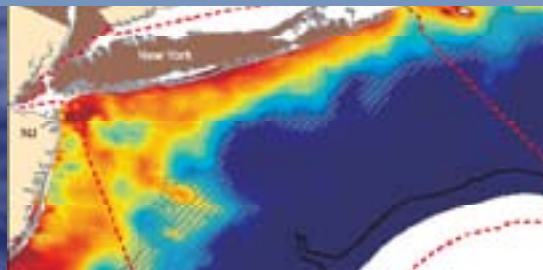
Brian P. Kinlan

Dan S. Dorfman

Matthew Poti

Chris Caldow

NOAA National Centers for Coastal Ocean Science



April 2012

NOAA TECHNICAL MEMORANDUM NOS NCCOS 141



NOAA NCCOS Center for Coastal Monitoring and Assessment

Citation

Full report citation:

Menza, C., B.P. Kinlan, D.S. Dorfman, M. Poti and C. Caldow (eds.). 2012. A Biogeographic Assessment of Seabirds, Deep Sea Corals and Ocean Habitats of the New York Bight: Science to Support Offshore Spatial Planning. NOAA Technical Memorandum NOS NCCOS 141. Silver Spring, MD. 224 pp.

Citations for individual chapters (example Chapter 6):

Kinlan, B.P., C. Menza, and F. Huettmann. 2012. Chapter 6: Predictive Modeling of Seabird Distribution Patterns in the New York Bight. pp. 87-148. In: C. Menza, B.P. Kinlan, D.S. Dorfman, M. Poti and C. Caldow (eds.). A Biogeographic Assessment of Seabirds, Deep Sea Corals and Ocean Habitats of the New York Bight: Science to Support Offshore Spatial Planning. NOAA Technical Memorandum NOS NCCOS 141. Silver Spring, MD. 224 pp.

Acknowledgments

This work would not have been possible without the numerous contributors who shared their data, time and expertise. Many people are acknowledged among the individual chapters of this report, but we must also thank Jamie Higgins for organizing and formatting the content of this report, as well as Kevin McMahon, Sarah Hile, Tom McGrath and Moe Nelson for preparing this report for publication.

Contract support was provided by Consolidated Safety Service, Inc. under NOAA Contract No. DG133C07NC0616.

Cover and Back

Seabird photos on the front and back cover were provided by D. Pereksta (BOEM); the wind turbine photo on the front cover was provided by A. Meskens (Wikimedia Commons); the coral *Madrepora oculata* on the front cover was provided by Islands in the Sea 2002, NOAA/OAR; the large photo of the coral *Paragorgia hirez* on the back cover was provided by MBRI/NOAA and the small photo of the sponge by Mountains in the Sea Research Team, IFE/NOAA; and the gray seafloor map was provided by US Geological Survey.

Mention of trade names or commercial products does not constitute endorsement or recommendation for their use by the United States government.

A Biogeographic Assessment of Seabirds, Deep Sea Corals and Ocean Habitats of the New York Bight: Science to Support Offshore Spatial Planning

Prepared by the
Biogeography Branch (BB)
Center for Coastal Monitoring and Assessment (CCMA)
National Centers for Coastal Ocean Science (NCCOS)
National Oceanic and Atmospheric Administration National Ocean Service (NOAA)
1305 East West Highway (SSMC-IV, N/SCI-1)
Silver Spring, MD 20910
USA

April 2012

Editors

Charles Menza
NOAA Center for Coastal Monitoring and Assessment
Biogeography Branch

Brian P. Kinlan
NOAA Center for Coastal Monitoring and Assessment, Biogeography Branch and
Consolidated Safety Services, Inc.

Dan S. Dorfman
NOAA Center for Coastal Monitoring and Assessment, Biogeography Branch and
Consolidated Safety Services, Inc.

Matthew Poti
NOAA Center for Coastal Monitoring and Assessment, Biogeography Branch and
Consolidated Safety Services, Inc.

Chris Caldow
NOAA Center for Coastal Monitoring and Assessment
Biogeography Branch

NOAA Technical Memorandum NOS NCCOS 141



United States
Department of Commerce

National Oceanic and
Atmospheric Administration

National Ocean Service

John Bryson
Secretary

Jane Lubchenco
Administrator

David Kennedy
Assistant Administrator

This page intentionally left blank.

About this document

This report provides a compilation of maps and spatial assessments of bathymetry, surficial sediments, oceanographic habitat variables, deep sea corals, and seabirds for offshore waters of New York. The information was compiled to support an offshore spatial plan being developed by the New York Department of State's Ocean and Great Lakes Program (OGLP). The report is a product of collaboration started in 2009 between scientists at the National Oceanic and Atmospheric Administration's National Centers for Coastal Ocean Science (NCCOS) and coastal managers at OGLP. NCCOS and OGLP worked closely to identify priority scientific needs, plan the analytical approach, assess existing data, and compile findings into this report. The targeted users of this report are coastal managers at OGLP, but other State and federal decision-makers, offshore renewable energy development interests and environmental advocates will also find the information useful.

The presented data and maps are the most accurate and up-to-date ecological information available for the study area. The diverse ecological themes which are treated here represent priority data gaps and were requested by OGLP to better understand and balance ocean uses and environmental conservation. The data will feed into a larger project led by OGLP to compile and assess existing data for offshore spatial planning.

NCCOS is a recognized scientific leader in developing biogeographic assessments. These assessments are organized around the development of geospatial data layers for ecological parameters, integrated analyses, and specific quantitative products to aid in resource management. The spatial analyses in this report build on and advance existing biogeographic techniques developed by NCCOS for other coastal and marine areas, including the Gulf of Maine, North and Central California, and the Northwestern Hawaiian Islands. This report, along with similar biogeographic products from around the nation, is also available online. For more information please visit NCCOS' webpage (<http://coastalscience.noaa.gov/>) or direct questions and comments to:

Chris Caldwell
Biogeography Branch Chief
National Oceanic and Atmospheric Administration /National Ocean Service/National Centers for Coastal Ocean Science/Center for Coastal Monitoring and Assessment/Biogeography Branch
Phone: (301) 713-3028 x164
E-mail: Chris.Caldow@noaa.gov

Or

Jeff Herter
Offshore Spatial Planning Research and Development Manager
Ocean and Great Lakes Program
New York Department of State
Phone: (518) 408 - 4799
E-mail: jeff.herter@dos.state.ny.us

Table of Contents

Executive Summary

Chapter 1: Introduction

Charles Menza, Chris Caldwell, Jeff Herter, and Greg Capobianco

1.1. A Call for Spatial Planning Offshore of New York	1
1.2. Data to Support Offshore Spatial Planning	2
1.3. An Analytical Approach Useful to Spatial Planning	3
1.4. Description of the Study Area	5
1.5. References	7

Chapter 2: Bathymetry

Matthew Poti, Brian Kinlan, and Charles Menza

2.1. Summary	9
2.2. Background	9
2.3. Methods	11
2.3.1. General Modeling Approach	11
2.3.2. Data Acquisition and Preparation	13
2.3.3. Development of the Bathymetric Model	14
2.3.4. Model Validation and Accuracy Assessment	17
2.4. Results and Discussion	17
2.4.1. Bathymetry Model Predictions	17
2.4.2. Bathymetry Model Uncertainty	18
2.4.3. Cross-validation of the Training Dataset	21
2.4.4. Independent Accuracy Assessment	25
2.5. Limitations to Interpretation and Future Directions	26
2.5.1. Data Quality	26
2.5.2. Resolution	27
2.5.3. Model Assumptions	28
2.6. Acknowledgments	29
2.7. References	30

Chapter 3: Surficial Sediments

Matthew Poti, Brian Kinlan, and Charles Menza

3.1. Summary	33
3.2. Background	33
3.3. Methods	34
3.3.1. Study Region and Grid	34
3.3.2. Mean Grain Size	35
3.3.3. Sediment Composition	36
3.3.4. Hard Bottom Occurrence	37
3.3.5. Model Validation	39
3.4. Results and Discussion	39
3.4.1. Mean Grain Size	39
3.4.2. Sediment Composition	43
3.4.3. Hard Bottom Occurrence	48
3.5. Limitations to Interpretation	52
3.6. Acknowledgments	55
3.7. References	56

Chapter 4: Oceanographic Setting

Brian Kinlan, Matthew Poti, and Charles Menza

4.1. Summary	59
4.2. Background	59
4.3. Methods	60
4.4. Acknowledgments	66
4.4. References	67

Chapter 5: Deep Sea Corals

Dave Packer and Dan Dorfman

5.1. Summary	69
5.2. Introduction	69
5.2.1. Studies of Deep Sea Corals in the Northeast Region	70
5.2.2. The Role of Deep Sea Corals as Habitat	72
5.3. Objectives	72
5.4. Methods	73
5.5. Results	73
5.6. Discussion	82
5.7. References	84

Chapter 6: Predictive Modeling of Seabird Distribution Patterns in the New York Bight

Brian P. Kinlan, Charles Menza, and Falk Huettmann

6.1. Summary	87
6.2. Definition of Seabirds	87
6.3. Seabird Ecology in the New York Bight	88
6.4. Threats to Seabirds	89
6.5. Management and Conservation Status	90
6.6. Challenges of Understanding Seabird Distribution and Abundance	91
6.7. Summary of Previous Studies Relevant to the Study Region	92
6.8. Methods	95
6.8.1. Study region and grid	95
6.8.2. Seabird survey data	95
6.8.3. Processing of quantitative seabird data for analysis	104
6.8.4. Grouping and selection of species for modeling	105
6.8.5. Potential environmental predictors	105
6.8.6. Seasonal predictive modeling	106
6.8.7. Generation of annual maps	107
6.8.8. Hotspot analysis	108
6.9. Results	109
6.9.1. Species notes	116
6.9.2. Group notes	119
6.9.3. Non-modeled species groups	121
6.9.4. 'No birds sighted'	122
6.9.5. Hotspots	122
6.9.6. Point maps of seabirds of concern	122
6.9.7. Maps and tables for species, groups and hotspots	123
6.10. Discussion	140
6.11. Acknowledgments	143
6.12. References	144

Chapter 6: Appendices

149

Appendix 6.A. Statistical Methods	149
6.A.1. Model overview	149
6.A.2. Transformation of potential predictor variables for normality and linearity	151
6.A.3. Selection of training and validation subsets for cross-validation	151
6.A.4. Stage I trend model	152
6.A.5. Stage I residual model	152
6.A.6. Final Stage I model	153
6.A.7. Stage II trend model	153
6.A.8. Stage II residual model	155
6.A.9. Final Stage II model	155
6.A.10. Final Stage I x II model	155
6.A.11. Relative uncertainty calculations	155
6.A.11.1. Stage I	156
6.A.11.2. Stage II	157
6.A.11.3. Stage IxII	157
6.A.12. Model evaluation and uncertainty calibration	157
6.A.13. Combination of seasonal climatological maps to produce annual climatological maps	157
6.A.14. Summary and implications of model assumptions	158
Appendix 6.B. Environmental Predictor Variables	161
6.B.1. Overview	161
6.B.2. Bathymetry and coastline (BATH, SLOPE, SLPSLP, DIST, SSDIST)	161
6.B.3. Benthic surficial sediments (PHIM)	164
6.B.4. Pelagic environmental variables (STRT, SST, TUR, CHL, ZOO)	164
Appendix 6.C. Species and Group Seasonal Profiles	169
<i>List of species</i>	169
6.C.1. Profile interpretation guide	170
6.C.2. A note on error masking	170
Appendix 6.D. Hotspot Predictive Model Profiles	221
6.D.1. Overview	221

Chapter 6: Online Supplements

Online Supplements can be found by going to <http://oceanservice.noaa.gov/programs/nccos/welcome.html> and searching on the keywords: *New York Spatial Plan*

Online Supplement 6.1: Predictor variable transformation details

This document provides additional detail on the statistical preparation of potential predictor variables for analysis.

Online Supplement 6.2: Species and group seasonal models, full diagnostic reports

This Online Supplement is presented in the form of an HTML document providing links to full diagnostic reports from each of the seasonal species/group predictive models.

List of Tables

Table 2.1. Depths used to stratify hydrographic soundings and the corresponding number of soundings within each stratum.	14
Table 2.2. Semivariogram parameters for each depth stratum.	16
Table 2.3. Search neighborhood parameters by depth stratum.	16
Table 2.4. Cross-validation statistics for the geostatistical model built from the training dataset.	21
Table 2.5. Performance of theoretical 68% and 95% confidence intervals.	25
Table 2.6. Results from an accuracy assessment of the geostatistical model and the coastal relief model (CRM).	25
Table 3.1. Semivariogram parameters for the mean grain size model.	36
Table 3.2. Semivariogram parameters for the sediment composition models.	37
Table 3.3. Total area and percent area of predicted mean grain size classes in the study area.	41
Table 3.4. Cross-validation statistics for the mean grain size model.	45
Table 3.5. Total area and percent area of predicted sediment texture classes in the study area.	47
Table 3.6. Cross-validation statistics for the sediment composition models.	47
Table 3.7. Relative contributions of predictor variables to the MaxEnt model for hard bottom occurrence.	50
Table 6.1. Birds of conservation concern.	90
Table 6.2. Species recorded by MBO CSAP quantitative surveys (1980-1988) in the study region, and groupings used for analysis.	98
Table 6.3. Definition of seasons.	100
Table 6.4. Summary of numbers of identifiable species, unidentified types, and contributions to species richness of each mapped species and group.	100
Table 6.5. Numbers of unique shipboard survey locations in which each species or species group was seen, overall and by season.	101
Table 6.6. Summary of seasons chosen for predictive modeling.	102
Table 6.7. Summary of cross-validation diagnostic statistics for annual models.	113
Tables 6.9. - 6.11. Data, predictor, and diagnostic tables for Black-legged Kittiwake (<i>Rissa tridactyla</i>).	123
Tables 6.12. - 6.14. Data, predictor, and diagnostic tables for Common Loon (<i>Gavia immer</i>).	123
Tables 6.15. - 6.17. Data, predictor, and diagnostic tables for Common Tern (<i>Sterna hirundo</i>).	124
Tables 6.18. - 6.20. Data, predictor, and diagnostic tables for Cory's Shearwater (<i>Calonectris diomedea</i>).	124
Tables 6.21. - 6.23. Data, predictor, and diagnostic tables for Dovekie (<i>Alle alle</i>).	125
Tables 6.24. - 6.26. Data, predictor, and diagnostic tables for Great Black-backed Gull (<i>Larus marinus</i>).	125
Tables 6.27. - 6.29. Data, predictor, and diagnostic tables for Great Shearwater (<i>Puffinus gravis</i>).	126
Tables 6.30. - 6.32. Data, predictor, and diagnostic tables for Herring Gull (<i>Larus argentatus smithsonianus</i>).	126
Tables 6.33. - 6.35. Data, predictor, and diagnostic tables for Laughing Gull (<i>Leucophaeus atricilla</i>).	127
Tables 6.36. - 6.38. Data, predictor, and diagnostic tables for Northern Fulmar (<i>Fulmarus glacialis</i>).	127
Tables 6.39. - 6.41. Data, predictor, and diagnostic tables for Northern Gannet (<i>Morus bassanus</i>).	128
Tables 6.42. - 6.44. Data, predictor, and diagnostic tables for Pomarine Jaeger (<i>Stercorarius pomarinus</i>).	128
Tables 6.45. - 6.47. Data, predictor, and diagnostic tables for Sooty Shearwater (<i>Puffinus griseus</i>).	129
Tables 6.48. - 6.50. Data, predictor, and diagnostic tables for Wilson's Storm-Petrel (<i>Oceanites oceanicus</i>).	129
Tables 6.51. - 6.53. Data, predictor, and diagnostic tables for Alcids, less common (4 species).	130
Tables 6.54. - 6.56. Data, predictor, and diagnostic tables for Coastal Waterfowl (7 species).	130
Tables 6.57. - 6.59. Data, predictor, and diagnostic tables for Jaegers (2 species).	131
Tables 6.60. - 6.62. Data, predictor, and diagnostic tables for Phalaropes (2 species).	131
Tables 6.63. - 6.65. Data, predictor, and diagnostic tables for Shearwaters, less common (2 species).	132

List of Tables cont.

Tables 6.66. - 6.68. Data, predictor, and diagnostic tables for Small Gulls, less common (2 species).	132
Tables 6.69. - 6.71. Data, predictor, and diagnostic tables for Storm-Petrels, less common (3 species).	133
Tables 6.72. - 6.74. Data, predictor, and diagnostic tables for Terns, less common (7 species).	133
Tables 6.75. - 6.77. Data, predictor, and diagnostic tables for Unidentified Gulls (0 species).	134
Tables 6.78. Data tables for Cormorants (2 species).	134
Tables 6.79. Data tables for Rare Visitors (10 species).	135
Tables 6.80. Data tables for Skuas, less common (1 species).	135
Tables 6.81 - 6.83. Data, predictor, and diagnostic tables for 'No birds sighted'.	136

List of Figures

Figure 1.1	These four panels show the general analytical approach used in this report to develop continuous distribution maps, assess certainty, and make easily understood products from typical survey data.	4
Figure 1.2	A map of the study area used in this report. Map produced by New York State Department of State.	6
Figure 2.1	Spatial extent of selected multibeam and sidescan sonar surveys in the study area.	10
Figure 2.2	Most recent survey year for soundings within 1 km rectangular neighborhoods.	11
Figure 2.3	General workflow describing the geostatistical approach used to develop the predictive model for bathymetry.	12
Figure 2.4	Estimated semivariograms of residuals and fitted semivariogram models for each depth stratum.	15
Figure 2.5	Bathymetric surface developed from the geostatistical model, draped over separate hillshade layers derived for the continental shelf (0-200 m) and the shelf slope (>200 m).	18
Figure 2.6	Estimated error of predictions (standard error) from the bathymetric model.	19
Figure 2.7	Spatial condition number from the LOESS trend model.	20
Figure 2.8	Locations of transects used to depict theoretical 95% confidence intervals of the geostatistical model predictions as a function of distance from score and local geomorphology.	21
Figure 2.9	Predicted depth with theoretical 95% confidence intervals along Transect 1.	22
Figure 2.10	Predicted depth with theoretical 95% confidence intervals along Transect 2.	23
Figure 2.11	Depth contours derived from the predicted bathymetric surface and from the upper and lower limits of the theoretical 95% confidence intervals ($\pm 1.96 \times$ standard error) overlaid on the predicted bathymetric surface and theoretical potential wind farm areas for New York.	24
Figure 2.12	Mean estimated vertical measurement error for soundings within 1 km rectangular neighborhoods.	27
Figure 3.1	Predicted mean grain size of surficial sediments from kriging interpolation of mean grain size data in the Mid-Atlantic Bight.	40
Figure 3.2	Distribution of predicted surficial sediment mean grain size classes, derived from kriging interpolation of mean grain size data in the Mid-Atlantic Bight.	41
Figure 3.3	Surficial sediment mean grain size prediction standard error from kriging interpolation of the mean grain size data in the Mid-Atlantic Bight.	42
Figure 3.4	Maps of the probability that surficial sediment mean grain size is less than threshold values.	43
Figure 3.5	Same as Figure 3.4, with probability values standardized by maximum probability of each corresponding threshold map.	43
Figure 3.6	Comparison of overlapping portions of the (a) USGS acoustic backscatter data and (b) surficial sediment mean grain size prediction.	44
Figure 3.7	Locations of usSEABED sediment survey data in the study area.	45
Figure 3.8	Surficial sediment composition maps from kriging interpolations of usSEABED sediment composition data in the Mid-Atlantic Bight.	46
Figure 3.9	Standard error maps for (a) predicted mud percentage, (b) predicted sand percentage, and (c) predicted gravel percentage of surficial sediments from kriging interpolations of usSEABED sediment composition data in the Mid-Atlantic Bight.	48
Figure 3.10	Comparison of overlapping portions of the (a) USGS acoustic backscatter data and (b) the predicted gravel percentage in surficial sediments.	49
Figure 3.11	MaxEnt model of hard bottom occurrence. Map depicts the predicted relative likelihood of hard bottom occurrence from the maximum entropy model.	50
Figure 3.12	Jackknife test of predictor variable importance for the MaxEnt model of hard bottom occurrence.	51
Figure 3.13	Receiver operating characteristic-like (ROC-like) curve for the MaxEnt model of hard bottom occurrence.	51
Figure 3.14	Comparison of overlapping portions of the (a) USGS acoustic backscatter data and (b) the predicted hard bottom occurrence likelihood index.	53

List of Figures cont.

Figure 4.1	Seasonal stratification climatology maps for spring, summer, fall, and winter.	61
Figure 4.2	Seasonal sea surface temperature climatology maps for spring, summer, fall, and winter.	62
Figure 4.3	Seasonal chlorophyll a climatology maps for spring, summer, fall, and winter.	63
Figure 4.4	Seasonal turbidity climatology maps for spring, summer, fall, and winter.	64
Figure 4.5	Seasonal zooplankton climatology maps for spring, summer, fall, and winter.	65
Figure 5.1	White sea pens (<i>Stylatula elegans</i>) on muddy sand from 119 m on the outer continental shelf near Hudson Canyon. Solitary hard coral (<i>Dasmosmilia lymani</i>) on shelly sand from 108 m on the rim of Hudson Canyon.	69
Figure 5.2	Deep sea coral taxonomy for those species found in the northeastern U.S. from Maine to Cape Hatteras including four seamounts (Bear, Physalia, Mytilus, and Retriever) off of Georges Bank that lie within the Exclusive Economic Zone (EEZ).	70
Figure 5.3	Observed Pennatulacea locations.	74
Figure 5.4	Observed Scleractinea locations.	75
Figure 5.5	Observed Alcyonacea locations.	76
Figure 5.6	Observed Gorgonacea locations.	77
Figure 5.7	Distribution and approximate densities (polyps per square meter) of the solitary stony coral <i>Dasmosmilia lymani</i> in samples from the Mid-Atlantic shelf around Hudson Canyon.	78
Figure 5.8	Observed deep sea sponge locations.	79
Figure 5.9	Observed deep sea coral and sponge locations.	80
Figure 5.10	Known deep sea coral locations for the Northeast Region.	81
Figure 6.1	Locations (centroids) of all unique MBO CSAP seabird survey transects sampled between April 1980 and October 1988 in Spring, Summer, Fall, and Winter.	95
Figure 6.2	Flowchart of seasonal predictive mapping process for seabirds.	96
Figure 6.3	Example geospatial information from each step of the seasonal predictive modeling process.	97
Figure 6.4	Potential environmental predictor variables considered for each predictive model.	103
Figure 6.5	Summary of environmental predictor variable importance in the seasonal predictive models.	110
Figure 6.6	Summary of variance partitioning in model fits among the trend component, spatial component and white noise component for Stage I and Stage II.	111
Figure 6.7	Summary of annual cross-validation model diagnostic statistics.	112
Figure 6.8	Predicted annual average relative index of abundance for Black-legged Kittiwake, with certainty classes overlaid.	123
Figure 6.9	Predicted annual average relative index of abundance for Common Loon, with certainty classes overlaid.	123
Figure 6.10	Predicted annual average relative index of abundance for Common Tern, with certainty classes overlaid.	124
Figure 6.11	Predicted annual average relative index of abundance for Cory's Shearwater, with certainty classes overlaid.	124
Figure 6.12	Predicted annual average relative index of abundance for Dovekie, with certainty classes overlaid.	125
Figure 6.13	Predicted annual average relative index of abundance for Great Black-backed Gull, with certainty classes overlaid.	125
Figure 6.14	Predicted annual average relative index of abundance for Great Shearwater, with certainty classes overlaid.	126
Figure 6.15	Predicted annual average relative index of abundance for Herring Gull, with certainty classes overlaid.	126
Figure 6.16	Predicted annual average relative index of abundance for Laughing Gull, with certainty classes overlaid.	127

List of Figures cont.

Figure 6.17	Predicted annual average relative index of abundance for Northern Fulmar, with certainty classes overlaid.	127
Figure 6.18	Predicted annual average relative index of abundance for Northern Gannet, with certainty classes overlaid.	128
Figure 6.19	Predicted annual average relative index of abundance for Pomarine Jaeger, with certainty classes overlaid.	128
Figure 6.20	Predicted annual average relative index of abundance for Sooty Shearwater, with certainty classes overlaid.	129
Figure 6.21	Predicted annual average relative index of abundance for Wilson's Storm-Petrel, with certainty classes overlaid.	129
Figure 6.22	Predicted annual average relative index of abundance for Less Common Alcids, with certainty classes overlaid.	130
Figure 6.23	Predicted annual average relative index of abundance for Coastal Waterfowl, with certainty classes overlaid.	130
Figure 6.24	Predicted annual average relative index of abundance for Jaegers, with certainty classes overlaid.	131
Figure 6.25	Predicted annual average relative index of abundance for Phalaropes, with certainty classes overlaid.	131
Figure 6.26	Predicted annual average relative index of abundance for Less Common Shearwaters, with certainty classes overlaid.	132
Figure 6.27	Predicted annual average relative index of abundance for Less Common Small Gulls, with certainty classes overlaid.	132
Figure 6.28	Predicted annual average relative index of abundance for Less Common Storm-Petrels, with certainty classes overlaid.	133
Figure 6.29	Predicted annual average relative index of abundance for Less Common Terns, with certainty classes overlaid.	133
Figure 6.30	Predicted annual average relative index of abundance for Unidentified Gulls, with certainty classes overlaid.	134
Figure 6.31	Point observations of the relative abundance index for Cormorants.	134
Figure 6.32	Point observations of the relative abundance index for Rare Visitors.	135
Figure 6.33	Point observations of the relative abundance index for Less Common Skuas.	135
Figure 6.34A	Predicted annual average relative index of survey effort resulting in 'No birds sighted' observations, with error class overlay.	136
Figure 6.34B	Predicted annual integrated probability of a 'No birds sighted' observation.	136
Figure 6.35	Predicted seabird abundance hotspot map.	137
Figure 6.36	Predicted species richness hotspot map.	138
Figure 6.37	Predicted Shannon species diversity index hotspot map.	138
Figure 6.38	Point map of raw sightings data for species of concern.	139

This page intentionally left blank.

Executive Summary

This report provides a compilation of new maps and spatial assessments for seabirds, bathymetry, surficial sediments, deep sea corals, and oceanographic habitats in support of offshore spatial planning led by the New York Department of State Ocean and Great Lakes Program. These diverse ecological themes represent priority information gaps left by past assessments and were requested by New York to better understand and balance ocean uses and environmental conservation in the Atlantic. The main goal of this report is to translate raw ecological, geomorphological and oceanographic data into maps and assessments that can be easily used and understood by coastal managers involved in offshore spatial planning.



Image 0.1. Roseate Tern (Sterna dougallii) in flight. This species is endangered in the Mid-Atlantic. Photo credit: David Pereksta, BOEM.

New York plans to integrate information in this report with other ecological, geophysical and human use data to obtain a broad perspective on the ocean environment, human uses and their interactions.

New York will then use this information in an ecosystem-based framework to coordinate and support decisions balancing competing demands in their offshore environment, and ultimately develop a series of amendments to New York's federally approved Coastal Management Program.

The targeted users of this report and the compiled spatial information are New York coastal managers, but other State and federal decision-makers, offshore renewable energy development interests and environmental advocates will also find the information useful. In addition, the data and approaches will be useful to regional spatial planning initiatives set up by the Mid-Atlantic Regional Council on the Ocean (MARCO) and federal regional planning bodies for coastal and marine spatial planning.

This report represents a synthesis of existing information rather than a new data collection effort. Given the short time frame over which management decisions frequently need to be made and the high cost of new natural resource surveys, this approach may be one other coastal zone managers will want to consider. The data and maps were developed by employing a spatial analytical approach which applies predictive modeling and geostatistics to interpolate among data, identify important spatial patterns and develop continuous distribution maps of species and physical resources at fine spatial resolutions required to support spatial management decisions. This analytical approach also allows for a quantitative description of prediction certainty a useful parameter for spatial planning. For example, maps of prediction reliability can be used to target efforts to collect new survey data to fill information gaps, or to incorporate measures of certainty into risk assessments.

In Chapter 2, a new bathymetric model with spatially-explicit certainty estimates is presented which builds on previous predictive bathymetric modeling approaches in the region. The new model provides a continuous gridded bathymetric surface for the study area, and allows users to view and explore spatial variation in the vertical accuracy of depth predictions. The new model is similar to the National Oceanic and Atmospheric Administration's Coastal Relief Model but provides estimates of prediction certainty, which can be used to prioritize locations for new bathymetric surveys and better understand the reliability of depth predictions and derived spatial layers (e.g., benthic habitats, positions of depth contours).

Predictive models of mean grain size, sediment composition, and hard bottom occurrence were developed to map the distribution of surficial sediments and habitats on the seafloor. These new models presented in

Chapter 3 build upon the data compilations and analytical frameworks laid out by existing work in the area. For mean grain size and sediment composition (e.g., mud, sand, gravel) the models provide continuous, gridded spatially-explicit prediction surfaces and corresponding certainty estimates. A hard bottom occurrence model also provides a continuous gridded prediction surface representing the likelihood of hard bottom habitats.

In Chapter 5, the locations of deep sea coral and sponge records within NOAA's Deep Sea Coral Research and Technology Program's geodatabase are examined within the New York Bight. Predictive models were not developed for deep sea corals or sponges because of limitations on the quantity and type of data available within the New York Study area. Instead, we focused on mapping known locations of deep sea corals and sponges, discussing their role as important habitat for other marine organisms, and discussing and summarizing past studies in the region.

In Chapter 6, new maps of the seasonal and annual distributions of seabird species and seabird ecological groups are provided. These distributions were predicted based on statistical models fit to visual shipboard seabird observational data collected as part of a standardized survey program from 1980-1988. Species and group distributional models were then combined to produce "hotspot" maps depicting multi-species abundance and diversity patterns. Spatial predictors included long-term archival satellite, oceanographic, hydrographic, and biological datasets. Seabird distributional maps for seasonal and annual relative indices of occurrence and abundance were produced, accompanied by maps depicting metrics of certainty. The resolution of predictions is approximately 400 times finer than previous 10 arc-minute maps of seabird distribution in this region. These high-resolution, contiguous predictive maps of seabird distribution are expected to be useful contributions to offshore spatial planning, particularly of activities that may affect seabirds or their habitats.

Introduction

Charles Menza¹, Chris Caldwell¹, Jeff Herter², and Greg Capobianco²

1.1. A CALL FOR SPATIAL PLANNING OFFSHORE OF NEW YORK

New York depends on healthy coastal and marine ecosystems for its thriving economy and vibrant communities. These ecosystems support critical habitats for wildlife and a growing number of significant and often competing ocean uses and activities, such as fishing, commercial transportation, recreational boating and energy production. Planners, policy makers and resource managers are being challenged to sustainably balance ocean uses and environmental conservation in a finite space and with limited information. Solutions to these challenges are complicated by emerging industries, climate change, and a growing coastal population with shifting needs.



*Image 1.1. Offshore wind farm.
Photo credit: A. Meskens (Wikimedia Commons)*

New York is addressing competition and evolving threats to coastal and marine resources and services by compiling spatial information and applying ecosystem-based management to spatial planning. In 2006, the New York Oceans and Great Lakes Ecosystem Conservation Act created the New York Oceans and Great Lakes Ecosystem Conservation Council and charged the New York Department of State (DOS) with developing amendments to its federally-

approved Coastal Management Program to better manage human activities that impact coastal and marine ecosystems.

The Coastal Management Program within DOS has broad authority to guide human uses and can use the consistency determination process, outlined in the Coastal Zone Management Act of 1972 (Public Law 92-583, 16 U.S.C. 1451-1456), to affect decisions made in both federal and state waters. Ultimately amendments will be integrated into state and federal permitting processes related to siting ocean uses and regional ocean planning programs. A state with an approved Coastal Management Program has the authority to approve or deny a proposed federal action if it may affect the state's coastal resources.

DOS is taking a phased approach for developing amendments by focusing on the most pressing issues first. New York's first amendment will apply to the Atlantic waters off New York out to the continental shelf and will focus on guiding decisions for new clean, renewable energy production and transmission, while addressing conflicts with other human activities and protecting critical habitats. Future amendments will include Long Island Sound and the Great Lakes.

New York has joined a growing number of states and federal agencies thinking about offshore spatial planning. For instance, Massachusetts and Rhode Island have recently completed ocean management plans, and New Jersey, Oregon and California are in the process of developing plans or collecting information necessary for planning purposes. In addition to state-level planning initiatives, multi-state partnerships and the federal government are undertaking spatial planning and have adopted a regional approach. The regional approach was chosen to allow for the variability of economic, environmental, and social aspects among different areas, provide an ecosystem-based perspective, and match existing regional governance structures.

¹ Center for Coastal Monitoring and Assessment, National Centers for Coastal Ocean Science, National Ocean Service, National Oceanic and Atmospheric Administration

² Ocean and Great Lakes Program, New York Department of State

In 2009, the governors of New York, New Jersey, Delaware, Maryland and Virginia committed to a comprehensive regional approach to address challenges faced in the ocean waters of the Mid-Atlantic, and created the Mid-Atlantic Regional Council on the Ocean (MARCO). The council has since developed action teams to protect critical habitats, improve water quality, support sustainable development of renewable energy, prepare for climate change, and build capacity for effective spatial planning in the region. Many of the data and analytical approaches used in this report will likely be useful to the entire mid-Atlantic region.

The MARCO initiative fits in well with the first ever National Ocean Policy signed by President Obama in 2010 (Executive Order 13547, 2010). The policy seeks to improve stewardship of the oceans, coasts, and Great Lakes by way of: adopting ecosystem-based management; obtaining, advancing, using, and sharing the best science and data; promoting efficiency and collaboration; and strengthening regional efforts. The order established the National Ocean Council to guide implementation of the policy, and identified nine national priority objectives, one of which is to implement coastal and marine spatial planning (CMSP). The Council outlined a flexible framework for spatial planning that is regional in scope, developed cooperatively among federal, state, tribal, and local authorities, and includes substantial stakeholder, scientific, and public input (NOC, 2012).

1.2. DATA TO SUPPORT OFFSHORE SPATIAL PLANNING

New York requires accurate, accessible and integrated ecological and human use data in order to base spatial planning on sound science. Whenever possible, these data are needed at spatial and temporal scales that are in line with management decisions, and need to provide continuous information over the whole management domain. With these requirements in mind, over the past year New York has compiled diverse ecological and human use datasets, including: biogeographic data from The Nature Conservancy's Northwest Atlantic Marine EcoRegional Assessment (NAMERA); distributions of marine fishes, marine mammals and sea turtles from Stone Environmental Inc., the University of Rhode Island, the New England Aquarium, and the National Marine Fisheries Services' Northeast Fisheries Science Center; infrastructure data, chiefly from the NOAA electronic navigation charts; jurisdictional information downloaded from the Multi-purpose Marine Cadastre (MMC), a tool developed in collaboration between NOAA Coastal Services Center (CSC) and DOI's Bureau of Ocean Energy Management (BOEM – formerly the Bureau of Ocean Energy Management, Regulation and Enforcement, BOEMRE), and; offshore human use information collected through participatory geographic information system workshops developed and carried out in partnership between the New York State Coastal Management Program and CSC.

This report supplements other datasets and reports compiled by OMAFRA's Great Lakes Program (OGLP), and provides data identified by OGLP as a priority to satisfy the needs of a Coastal Management Program amendment in the Atlantic. Specifically, this report examines the spatial distribution of: seabirds, bathymetry, surficial sediments, deep sea corals, and dynamic oceanographic habitats. We developed new geospatial synthesis products with the objective of providing:

- The most accurate and up-to-date information available,
- Continuous information over the management domain and at the finest spatial scale raw data would support,
- Estimates of synthesis product reliability (certainty) and assessments of data quality,
- Data products in digital formats that allow easy integration with other datasets in a geographic information system, and
- Maps, assessments and interpretations that are easily understood and used by coastal managers to support spatial management decisions.

According to U.S. Executive Order 13547, CMSP is a “comprehensive, adaptive, integrated, ecosystem-based, and transparent spatial planning process, based on sound science, for analyzing current and anticipated uses....[CMSP] identifies areas most suitable for various types or classes of activities in order to reduce conflicts among uses, reduce environmental impacts, facilitate compatible uses, and preserve critical ecosystem services to meet economic, environmental, security, and social objectives.”

All data and assessments in this report represent a synthesis of existing information rather than a new data collection effort. Given the short time frame over which management decisions frequently need to be made and omnipresent budget constraints, this approach of interest to be one other coastal zone managers.

1.3. AN ANALYTICAL APPROACH USEFUL TO SPATIAL PLANNING

The ocean area offshore of New York has a significant amount of raw data, ranging from sediment samples to bird observations to ocean temperature profiles. But many of these datasets are spatially and temporally limited or exist only as scattered points. As such, they are difficult to use for spatial planning, especially when decisions must be made in locations that are in-between surveys, have few surveys, have widely varying measurements or require a regional context. Where possible, we overcame these challenges by using a spatial analytical approach which applied statistical modeling to generalize from scattered sets of data points to regional maps of important patterns and processes.

Not all data can support this type of spatial analytical approach, especially datasets with few observations and/or with unknown sampling effort. For instance, predictive coral and sponge distribution models could not be developed in this report (Chapter 5) due to these data limitations. In this case, the goal was not to make spatial predictions, but rather to compile the most up-to-date observations and develop maps providing the best available information to make management decisions.

In the remaining chapters, datasets for bathymetry (Chapter 2), surficial sediments (Chapter 3), dynamic oceanographic habitats (Chapter 4), and seabirds (Chapter 6) included sufficient information to develop reliable spatial models. In-depth discussions of the statistical methods used to convert observation point data into continuous surfaces are available in corresponding chapters. A generalized representation of the approach using actual data (common loon sightings) is presented in Figure 1.1.

The spatial analytical approach follows Cressie (1993) and Hengl et al. (2007), where the variables of interest are modeled as a linear combination of components representing a deterministic mean trend, a spatially structured random process, and non-spatially structured error. The deterministic mean trend is estimated using a suitable broad spatial-scale function (generalized linear model for seabirds, or a smoothing function for bathymetry and surficial sediments) and the spatially structured random process and error term are estimated by geostatistical analysis of the residuals. There is no loss of information in this approach since the residuals contain all of the information removed from the trend surface.

The result is a spatially-explicit distribution of predicted outcomes, whether the outcomes are of abundance or the likelihood of occurrence. This predicted distribution of outcomes has two uses. First, the average taken from of the distribution can be mapped and used to represent the most likely outcome for a given location. Second, the distribution provides an estimate of certainty for the mapped outcome. That is, the mapped prediction for an area with a narrow distribution (outcomes are similar) has greater certainty, than the prediction for an area with a wide distribution (outcomes are dissimilar). Knowledge of a prediction's certainty is a useful measure in spatial planning, because it allows planners to use the best available data to make decisions with an understanding of limitations on generalizations that can be made from the available data. We use the terms reliability, certainty and uncertainty throughout this report.

The applied spatial predictive methods involve a number of statistical assumptions, and it is important to note that the accuracy of model predictions and estimates of certainty depend to varying degrees on these assumptions being met. A complete discourse on all statistical assumptions is beyond the scope of this report (for detailed discussions see the methodological citations in each of the individual analytical chapters of this report), but several general assumptions are:

- *Spatial patterns and sampling effort are constant over the analyzed timeframe*
To compile sufficient data to make predictions we integrated data over several years. This approach provides information on the long-term average state of the system, but ignores long-term trends or cycles.

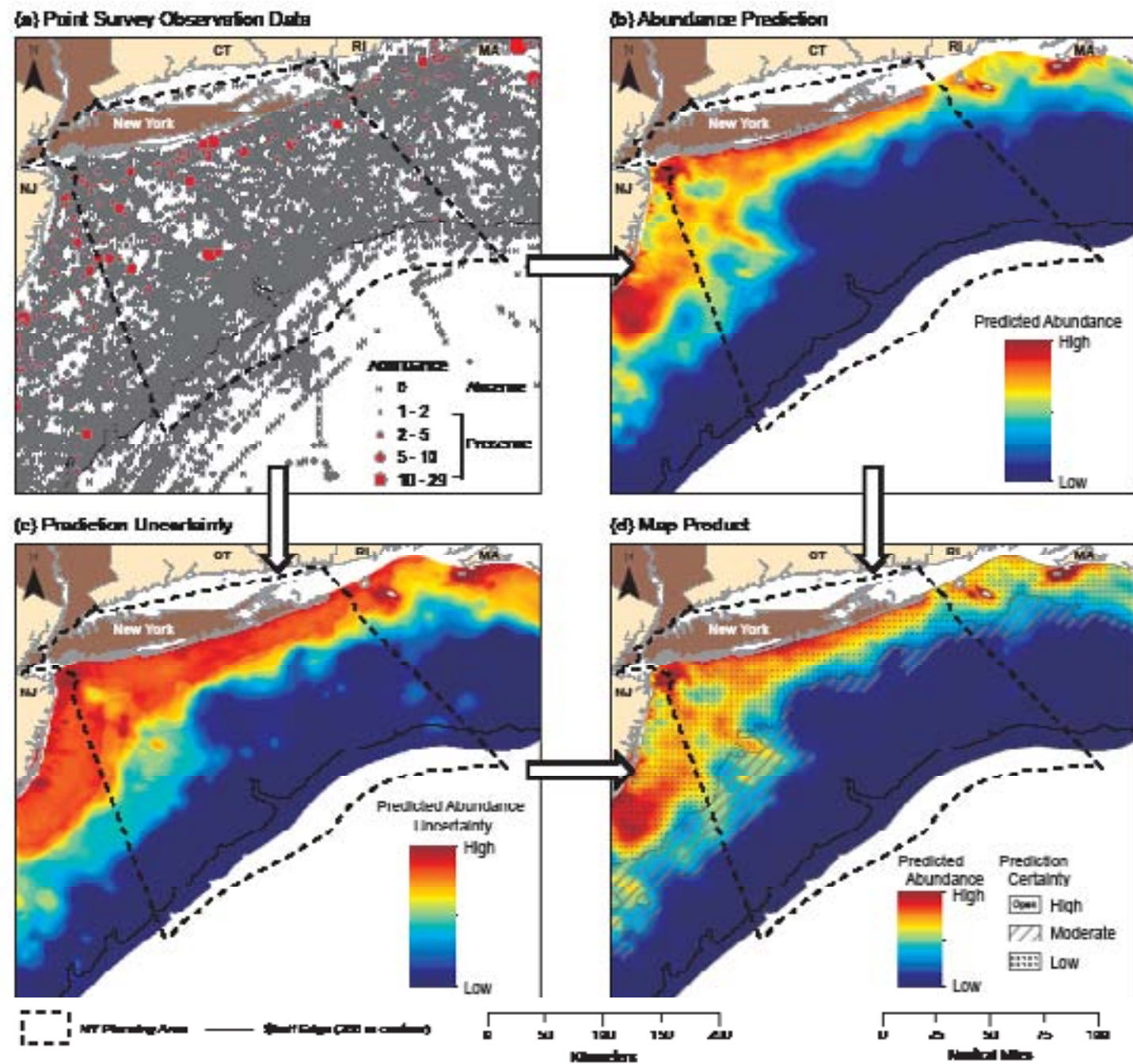


Figure 1.1: These four panels show the general analytical approach used in this report to develop continuous distribution maps, assess certainty, and make easily understood products from typical survey data. This example uses data from the Manomet Bird Observatory Seabird and Cetacean Assessment Program database. Panel A shows common loon sightings distributed across the study area. A clear spatial pattern is difficult to discern, since sampling effort is irregular and observed presences are dispersed among observed absences. This is a typical ecological pattern since seabirds move around, detection is not perfect and sampling effort is irregular. Panel B shows the continuous output from a predictive model which has linked observations of the common loon to environmental predictors such as sea surface temperature, depth and oceanographic productivity. The model displays the average likelihood of observing a common loon given these environmental linkages and fills in gaps where survey data is missing. Panel C displays the uncertainty related to the predictive model, where areas of most uncertainty indicate the greatest range in possible predicted outcomes. Model uncertainty is commonly greatest where the resource of interest is most variable or where few data are available. Panel D shows a map where certainty (the inverse of uncertainty) is draped over predicted relative abundance. This type of map was requested by coastal resource managers in OGLP, because it was easy to understand and use for spatial management decisions.

- Resources and species are precisely detected and measured

Species or resources are seldom perfectly detectable, meaning corresponding occurrence and abundance estimates will be biased compared to true abundance and occurrence values. When sampling effort is known and heterogeneous, values can be standardized by effort to allow relative comparisons, but difficulties still arise in assessing areas where little sampling effort was devoted.

- There exists a constant relationship between sampling effort, relative indices of occurrence and abundance, and true values of occurrence and abundance

Not only are species and resources unlikely to be perfectly detectable, the relationship between relative indices of occurrence and abundance and the true values of occurrence and abundance could vary in time and space, depending on differences in observers, weather conditions, animal behavior, etc. Such variation introduces an unaccounted for source of measurement error into data, and it is not possible to correct for all such sources of variation.

In addition to the assumptions inherent in modeling techniques, maps and assessments are a reflection of data quality and we assume that the data quality is suitable for spatial modeling and are representative of the ecosystem's true state. The key challenges of using existing data are that it was collected for a specific purpose, which may not be congruent with spatial analysis, and by definition it was collected in the past. It is important to understand potential limitations inherent to each dataset, and in each chapter we have identified and assessed key data quality issues.

We understand that statistical and data quality assumptions may not be completely met, thus model validation is an important part of the modeling approach. Validation is usually done by cross-validation, a process in which some data are left out of model fitting and model predictions are tested against those data. Model predictions can also be tested against high-precision "ground-truth" datasets where such datasets are available. We use both methods to validate predictions and maps in this report.

1.4. DESCRIPTION OF THE STUDY AREA

This report focuses on a study area in ocean waters off the coast of New York. The area covers a portion of the Mid-Atlantic Bight and much of the area characterized as the New York Bight. The study boundaries extend from the southern shores of Long Island to the edge of the continental shelf and from Nantucket Shoals to the shores of New Jersey (Figure 1.2). Both state and federal waters are included.

The study area covers a "spatial planning area" chosen by the OGLP in which they will focus their planning efforts, as well as ocean waters immediately adjacent to the planning area. The spatial planning area includes New York's territorial sea and Federal waters where natural phenomena and human activities can affect services and resources within the territorial sea.

The majority of the study area is characterized by a broad continental shelf approximately 150-200 km wide. At its outer edge, the shelf meets the continental slope, an area 40-60 km wide with very steep slopes and that extend to depths greater than 2 km. The most prominent topographic features in the study are the Hudson shelf valley, which crosses the entire shelf, and several shelf edge incisions made by submarine canyons. These topographic features alter the broad-scale hydrography of the region, are important to cross-shelf water movement and provide important benthic habitats which differ from the surrounding seascape (Cooper, 1987; Steimle et al., 1999).

The seafloor on the shelf is composed of mostly sand which grades to silt and clay in deeper areas (Poppe et al., 2005). The relatively homogenous seafloor has sporadic relic sand and gravel ridges; exposed sandstone and bedrock, dumping sites, dredge disposal sites and artificial reefs (i.e., shipwrecks, lost cargo, submerged pipelines). Bottom sediments play critical roles as habitats for benthic organisms such as demersal fish, clams and corals, and in storage and processing of settling organic matter.

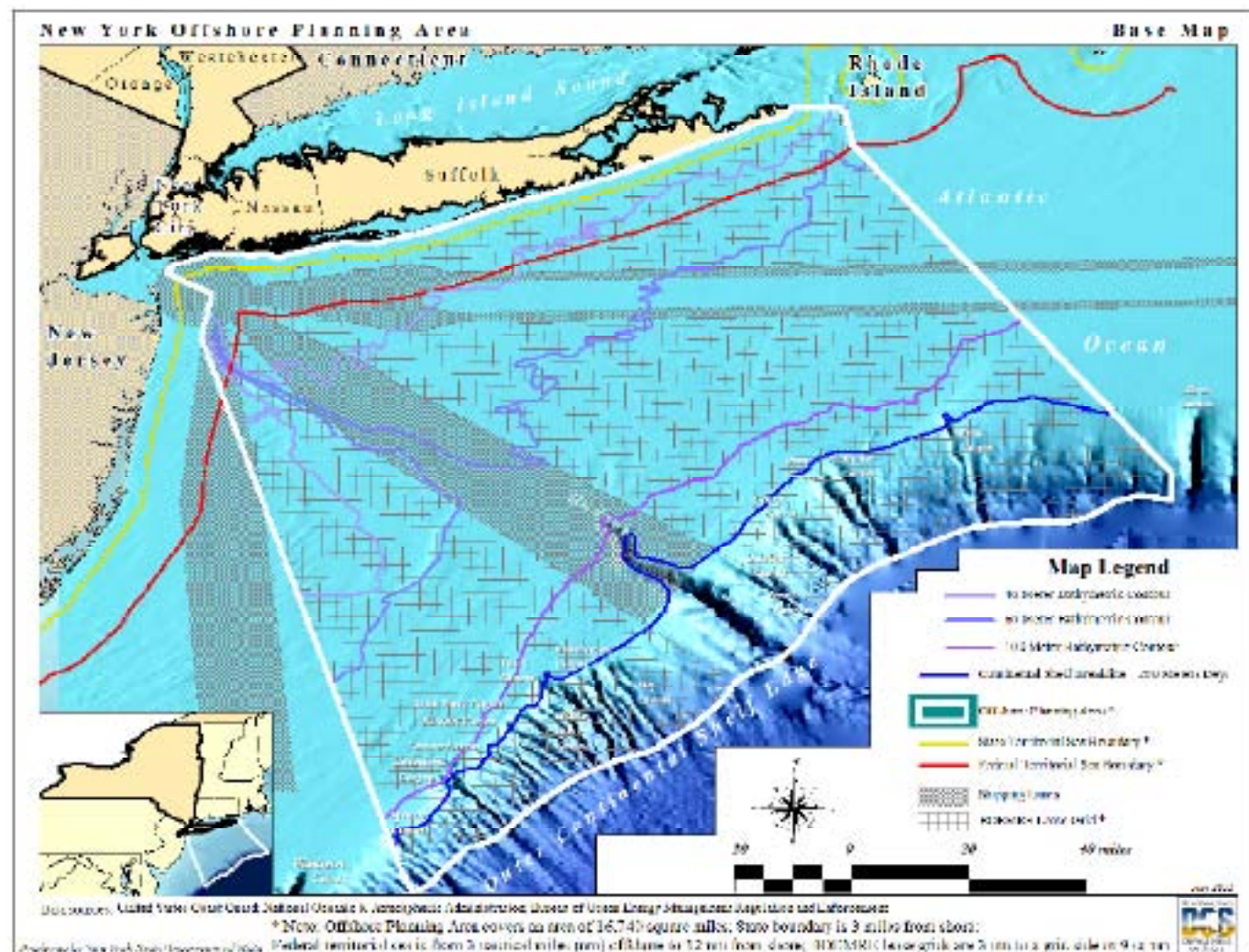


Figure 1.2: A map of the study area used in this report. Map produced by New York State Department of State. Note that, effective October 1, 2001, the Bureau of Ocean Energy Management, Regulation and Enforcement (BOEMRE) was renamed to the Bureau of Ocean Energy Management (BOEM).

The hydrography of the study area is characterized by a strong seasonal cycle, considerable freshwater input from rivers, storm dominated sediment transport and interactions among large distinct water masses which extend across the Northwest Atlantic (Townsend et al., 2006). These hydrographic characteristics, along with characteristics of the seafloor and geomorphological setting produce patterns across multiple spatial and temporal scales in resources (e.g., fish, sand, renewable energy) and ecosystem services (e.g., coastal protection, tourism and transportation).

1.5. REFERENCES

Cooper, R.A., P. Valentine, J.R. Uzzmann, and R.A. Slater. 1987. Submarine canyons. In R.H. Backus and D.W. Bourne. eds. *Georges Bank*. p. 52-65. MIT Press, Cambridge, MA.

Cressie, N.A.C. 1993. *Statistics for spatial data* (revised ed.). New York: John Wiley & Sons, Inc.

Executive Order 13547. 2010. *Stewardship of the ocean, our coasts, and the great lakes*. President Barack Obama, Office of the Press Secretary. July 19, 2010.

Hengl, T., G.M.B. Heuvelink, and D.G. Rossiter. 2007. About regression-kriging: from equations to case studies. *Computers and Geosciences*, 33(10):1301-1315.

NOC (National Ocean Council). 2012. *Draft National Ocean Policy Implementation Plan*. <http://www.whitehouse.gov/administration/eop/oceans/implementationplan>. Plan released January 12, 2012. Website accessed February 20, 2012.

Poppe, L.J., S.J. Williams, and V.F. Paskevich. 2005. *U.S. Geological Survey East-Coast Sediment Analysis: Procedures, Database, and GIS Data: Open-File Report 2005-1001*, U.S. Geological Survey, Coastal and Marine Geology Program, Woods Hole Science Center, Woods Hole, MA.

Steimle, F.W. C.A. Zetlin, P.L. Berrien, D.L. Johnson, and S. Chang. 1999. *Tilefish (*Lopholatilus chamaeleonticeps*) life history and habitat characteristics*. U.S. Department of Commerce, NOAA Technical Memorandum NMFS-NE-152, 30 p.

Townsend, D.W., A.C. Thomas, L.M. Mayer, M. Thomas, and J. Quinlan. 2006. *Oceanography of the Northwest Atlantic Continental Shelf*. pp. 119-168. In: Robinson, A.R. and K.H. Brink (eds). *The Sea, Volume 14*, Harvard University Press.

This page intentionally left blank.

Bathymetry

Matthew Poti^{1,2}, Brian Kinlan^{1,2,3}, and Charles Menza¹

2.1 SUMMARY

A new bathymetric model with spatially-explicit uncertainty estimates was developed for the New York study area (Figure 1.1). The model builds on previous predictive bathymetric modeling approaches in the region (e.g., Calder, 2006), provides a continuous gridded bathymetric surface for the study area, and allows users to view and explore spatial variation in the vertical accuracy of depth predictions. The spatial resolution of the model is identical to the National Oceanic and Atmospheric Administration's (NOAA) Coastal Relief Model (CRM; horizontal resolution approximately 83.8 m) in the study area and was built from the same database of hydrographic survey points. Unlike the CRM, the new geostatistical model provides estimates of prediction certainty, which can be used to prioritize locations for new bathymetric surveys and better understand the reliability of depth predictions and derived spatial layers (e.g., benthic habitats, positions of depth contours).

2.2 BACKGROUND

Bathymetry (also called seafloor topography) is an important base environmental layer for spatial planning since it influences both planning of human activities (e.g., construction, shipping) and many physical, chemical and ecological processes. For instance, reliable bathymetric information can simultaneously improve habitat conservation and energy development by supporting the identification of:

- Unique or vulnerable benthic habitats
- Distributions of rare or endangered species
- Efficient corridors for transmission lines
- Suitable sites for turbine platforms, and
- Potential construction hazards



Image 2.1. An example of a bathymetric surface in the New York Bight, showing the change in depth with distance from shore and the complexity of the seafloor across the shelf. The Hudson Shelf Valley is prominently visible in the center of the model as the area of darker blue extending from New York harbor (top left) towards the shelf edge (bottom right). Coastal managers and engineers use bathymetric surfaces to assess shipping lanes, identify fish habitats, lay undersea cables and find sand and gravel resources. The bathymetric surface shown here is the the NOAA Coastal Relief Model (CRM), draped over a derived hillshade layer to highlight bathymetric variation. Terrestrial imagery is the ArcGIS Online World User Imagery layer (ESRI Online).

Bathymetry can be measured by a range of instruments, which determine the precision, spatial resolution, extent and cost of bathymetric information and nautical charts. Until the latter half of the 20th century, lead lines dropped from a ship were used to estimate depths (Calder, 2006) and were compiled on charts to give a coarse-scale representation of the seafloor and identify navigation hazards. Lead lines were eventually replaced by more accurate vertical beam echosounders (VBES) and subsequently by multibeam echosounders (MBES). Modern MBES can collect millions of precise soundings efficiently and quickly, making possible high-resolution bathymetric maps that reveal fine-scale features of the seafloor (Calder, 2006). Horizontal positioning technologies have also advanced over the years from sextant-based navigation to modern GPS.

When combined with backscatter information and validation samples, MBES data offers an unprecedented view of the composition and morphology of the seafloor at multiple spatial scales (Kostylev et al., 2001; Gardner et al., 2003). The States of Oregon and California recently collected new data to take advantage of insights

¹ Center for Coastal Monitoring and Assessment, National Centers for Coastal Ocean Science, National Ocean Service, National Oceanic and Atmospheric Administration

² Consolidated Safety Services, Inc.

³ Corresponding author: Brian.Kinlan@noaa.gov

provided by MBES and these data have been integrated into state spatial planning initiatives, specifically the Oregon Territorial Sea Plan and California Marine Life Protection Act Initiative. On the East Coast, fewer states have comprehensive MBES coverage; this may be a reflection of the increased costs involved in surveying comparatively wide, shallow continental shelves.

About 20% of the New York planning area is covered by MBES surveys (Figure 2.1) which have been collected by the United States Geological Survey (USGS), NOAA and the Woods Hole Oceanographic Institution (Schwab et al., 1997a and 1997b; Butman et al., 1998; Goff et al., 1999; Butman et al., 2006). The corresponding data have helped researchers map benthic habitats and identify physical features on the seafloor within the footprints of surveys.

Unfortunately, the incomplete distribution of multibeam surveys limits their usefulness for understanding the relative distribution of habitats, features, processes and species over the entire planning area, a critical component of integrated marine spatial planning. The U.S. Coastal Relief Model developed by the National Geophysical Data Center (NGDC; <http://www.ngdc.noaa.gov/mgg/coastal/model.html>) offers a 3-arc second continuous bathymetric model that covers the majority of the study area (including all of the continental shelf and slope). The CRM is derived from the largest single compilation of bathymetric soundings for US coastal waters and has been used effectively to inform spatial planning on the East Coast as part of the Massachusetts

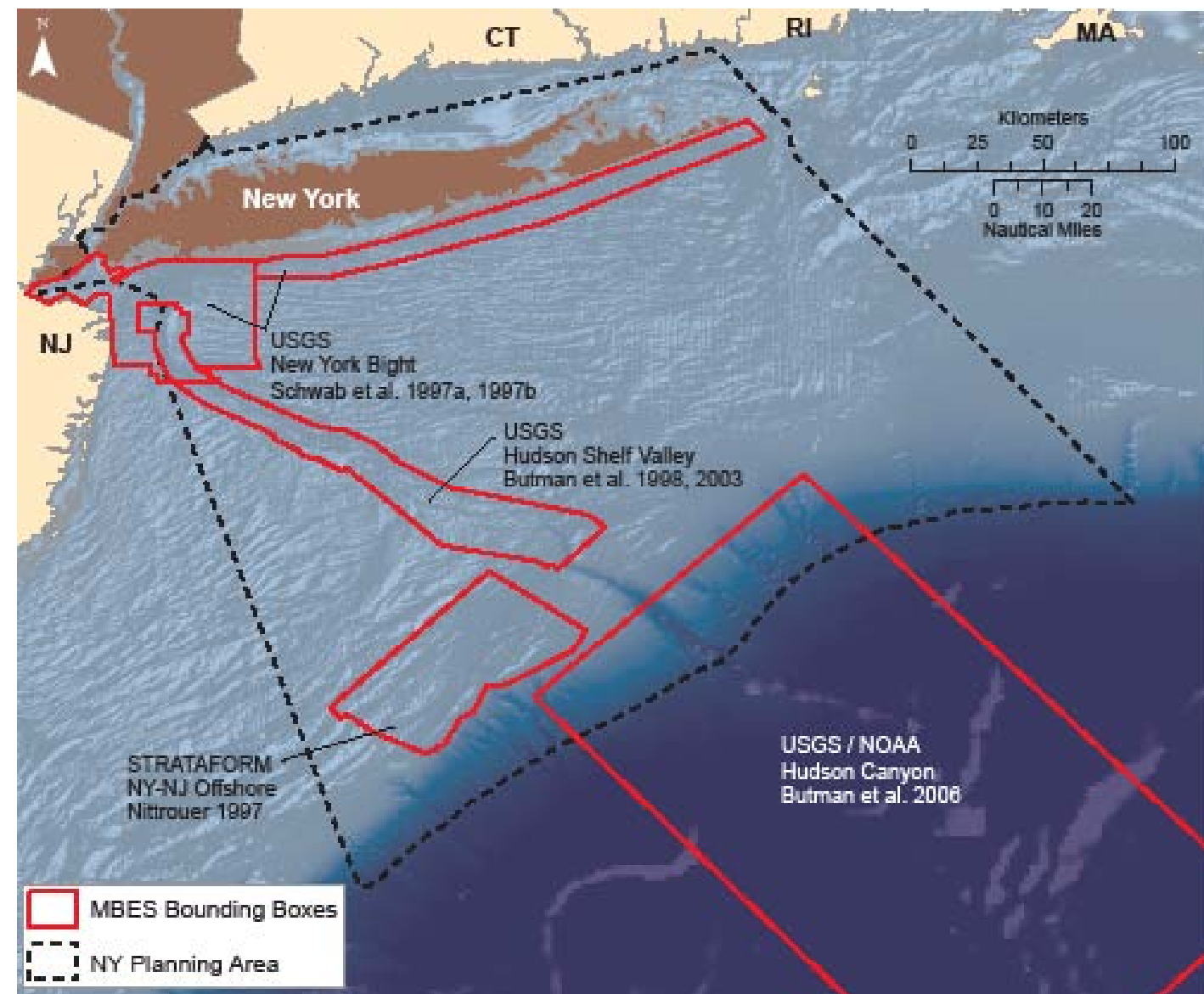


Figure 2.1. Spatial extent of selected multibeam and sidescan sonar surveys in the study area. Survey boundaries are overlaid on bathymetry data from the Coastal Relief Model blended with the ETOPO1 Global Relief Model (Amante and Eakins 2009).

Ocean Plan and Rhode Island Special Area Management Plan. Although coarser than multibeam data, the ~84 m horizontal resolution of the CRM is still sufficient to resolve general features of interest for marine spatial planning (e.g., canyons, ridges, sand waves, bathymetric contours).

The portion of the CRM that overlaps the New York planning area was produced in 1999 and is a compilation of historical hydrographic surveys, collected using VBES and MBES from various data sources, including NOAA, USGS, the U.S. Army Corps of Engineers, and various academic institutions. Although compiled surveys are brought together under a common spatial framework, they possess different spatial footprints and resolutions, and were collected using different instruments. Newer surveys commonly overlap, adjoin and supersede older surveys.

Generally, the CRM is used in resource management applications assuming the depth measurements and predictions to be accurate, but significant uncertainty in model depth estimates arises from measurement error in hydrographic surveys, methods used to interpolate between survey points and data processing (discussed in detail in Calder, 2006 and references therein). These errors are variable over the study area (Figure 2.2) due to various factors, including survey age, processing guidelines, and distances amongst soundings. Since bathymetric errors in the CRM are not quantified, users cannot know whether depth predictions at a given location are likely to deviate from the true value by a few centimeters or hundreds of meters. Disregarding uncertainty might be acceptable for some analyses conducted at coarse spatial resolutions, but is problematic for finer resolution analyses and when precise measurements are needed. Knowing where bathymetric predictions are precise and where they are not provides managers with information to define and manage risk associated with decisions relying on bathymetry or derived products (e.g., defining benthic habitats, estimating construction costs, placing shipping lanes).

2.3 METHODS

2.3.1 General Modeling Approach

A geostatistical modeling approach was used to predict a continuous, gridded bathymetric surface from scattered sounding points and to generate corresponding spatially-explicit uncertainty estimates. Geostatistical methods are based on the premise that neighboring samples are more similar than samples farther away (Tobler, 1970), a phenomenon known as spatial autocorrelation. Spatial autocorrelation can be detected, quantified and modeled by semivariogram analysis, and used to make predictions at locations that have not been measured

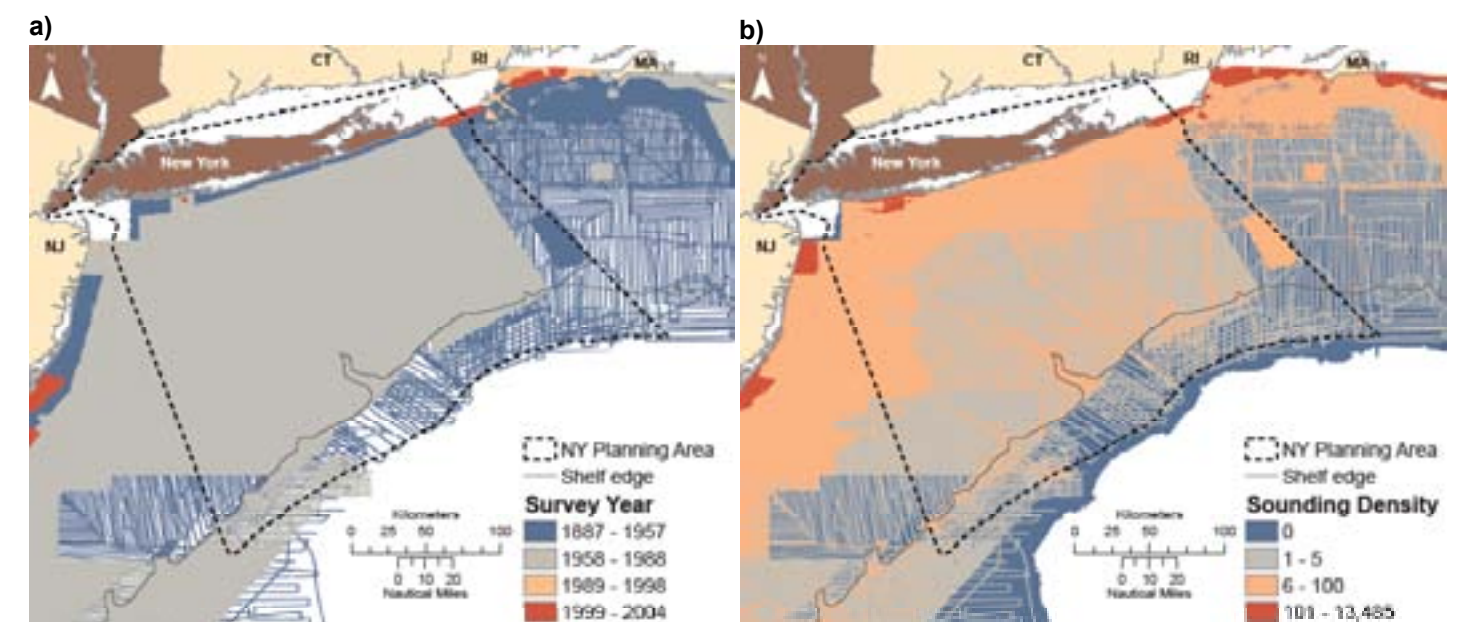


Figure 2.2. (a) Most recent survey year for soundings within 1 km rectangular neighborhoods. Survey year classes generally correspond with the evolution of horizontal positioning and vertical sounding technologies. More recent soundings tend to be more precise. (b) The number of bathymetric soundings per square kilometer. The shelf edge corresponds to the 200 m depth contour.

(Cressie, 1993; Chiles and Delfiner, 1999). In addition, the same spatial model used to develop predictions can be used to model uncertainty (i.e., expected precision) of predictions.

The geostatistical modeling approach used here follows Cressie (1993), where estimates of depth for a given location, $Z(x,y)$, are modeled as a linear combination (sum) of components representing a deterministic mean trend, $\mu(x,y)$, a spatially structured random process, $\delta(x,y)$, and non-spatially structured error, ϵ .

$$Z(x,y) = \mu(x,y) + \delta(x,y) + \epsilon \quad (\text{Equation 2.1})$$

Equation 2.1 defines the workflow used to arrive at $Z(x,y)$. The deterministic mean trend and spatially structured random process with error term are modeled separately and then combined by summation (see Figure 2.3 for schematic representation of work flow). The deterministic mean trend, $\mu(x,y)$, is estimated using a suitable smoothing function and residuals of original data from this smoothing function are computed at the data positions by subtracting the trend prediction from the observed data value. The spatially structured random process, $\delta(x,y)$, and error term, ϵ , are then estimated by fitting a suitable semivariogram model to the empirical semivariogram of the residuals. The error term is defined by the semivariogram nugget and represents error that is not spatially correlated, which includes both measurement error and variability occurring at spatial scales shorter than the sampling resolution (Cressie, 1993).

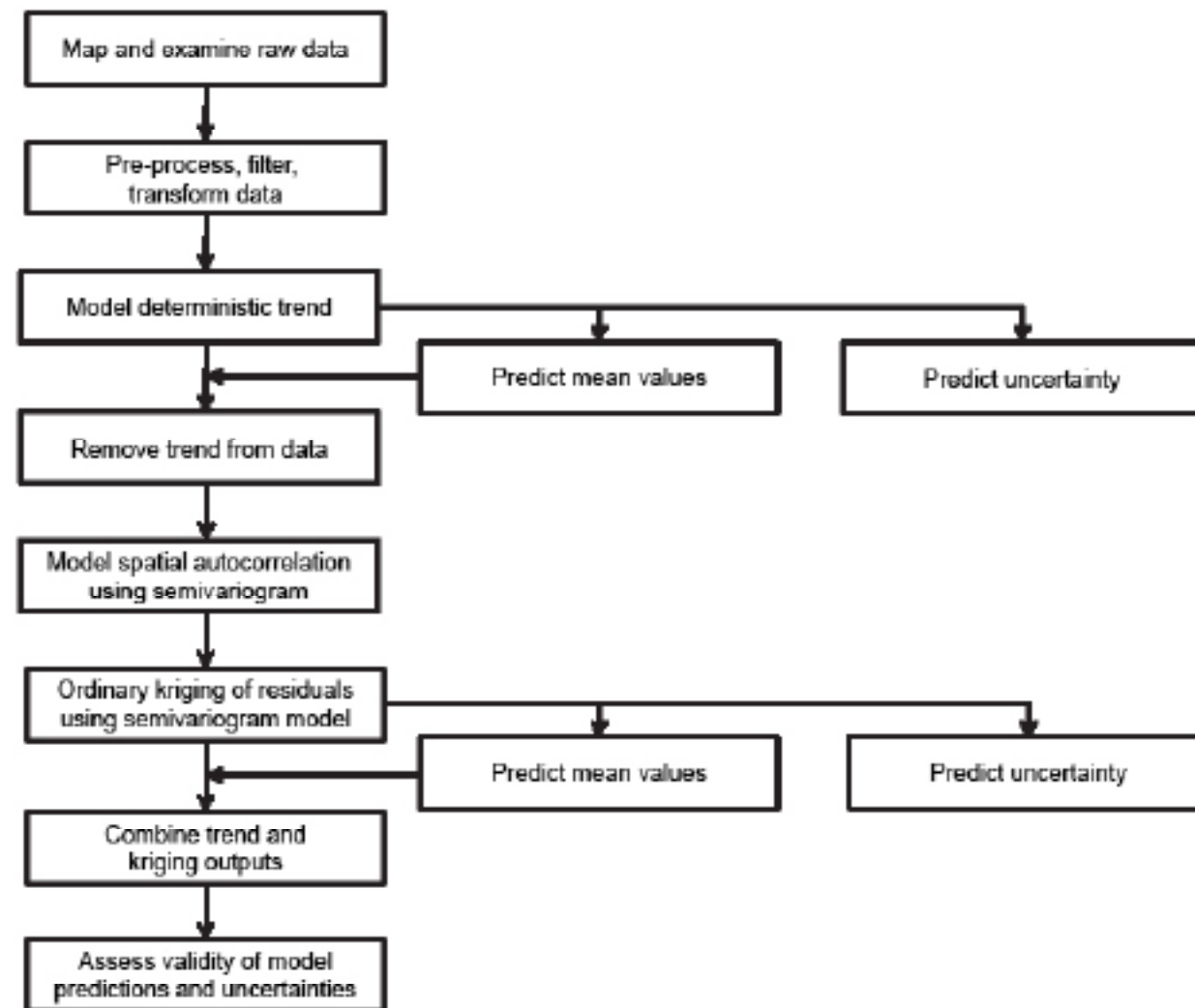


Figure 2.3. General workflow describing the geostatistical approach used to develop the predictive model for bathymetry (see sections 2.3.3 and 2.3.4 for a more detailed description of the methods).

Geostatistical models involve a number of statistical assumptions (for detailed discussions see Cressie, 1993; Chiles and Delfiner, 1999). The accuracy of model predictions and uncertainty bounds depends on varying degrees on these assumptions being met. Thus, an important part of any geostatistical analysis is model validation, which is usually done by cross-validation, a process in which some data are left out for purposes of model fitting and model predictions are tested against those data. Model predictions can also be tested against high-precision “ground-truth” datasets where such datasets are available. We use both methods to validate model predictions in this chapter (see Section 2.3.4).

2.3.2 Data Acquisition and Preparation

Raw Sounding Data

To develop a new geostatistical bathymetric model for the NY Bight, all available National Ocean Science (NOS) Hydrographic Survey Data overlapping the study area were downloaded from the National Geophysical Data Center Hydrographic Survey Database (<http://www.ngdc.noaa.gov/mgg/bathymetry/hydro.html>) on April 21, 2011. Survey measurements and metadata were extracted from raw HYD93 formatted files and exported into plain ASCII text tabular files using custom parsing scripts. Depths are represented as positive numbers with increasing depth below sea level defined by the Mean Lower Low Water (MLLW) vertical datum. Sounding data were merged with survey metadata, so that information detailing when and how each sounding was collected was retained. Sounding locations, originally in decimal degrees (NAD83 datum), were projected into a Universal Transverse Mercator projection (UTM 18N), since subsequent processing requires measurement of point-to-point distances in a Cartesian coordinate system. UTM 18N has its central meridian at 75°W and thus allows calculation of distances in our study area with negligible distortion relative to grid resolution (83.8 m).

Hydrographic soundings in the study area come from a multitude of surveys distributed between 1887 and 2004. Surveys used an assortment of positioning and sounding technologies, resulting in a patchwork of overlapping soundings collected with variable sample spacing and different precisions (Figure 2.2). In addition, survey data was processed using varying methods which created varying post-processing errors (see Calder, 2006 for a full discussion). These errors can propagate to the final model creating distortions that do not correspond to changes on the seafloor. While steps have been taken to partially correct for and reduce the impact of these data quality issues, it is important to understand that they cannot be entirely eliminated. No bathymetric model based on historical hydrographic sounding data will be completely free from such considerations.

In general, the vast majority of soundings were retained to maximize data density. However, some soundings were corrected or eliminated prior to modeling. First, based on Calder (2006), we applied a +1.48 m correction to all soundings collected by lead line to correct for the observed bias of lead line soundings compared to multibeam sonar measurements. Second, lead line and VBES surveys were identified that showed evidence of quantization due to rounding to the nearest whole fathom (resulting in an error of up to 1.8 m). Data from these surveys were eliminated when they were located within the footprint of more accurate surveys (i.e., surveys that did not exhibit quantization). Survey footprints were hand digitized at 1:50,000 in ArcGIS 10 (ESRI, 2011). Different types of rounding and conversions created surveys with varying degrees of quantization, but only those surveys with the most severe fathom-rounding quantization of 1.8 m were eliminated from analysis, and those only when more recent information was present. Other types of quantization are expected to result in errors less than 1 m. Other sources of error in raw soundings, including un-accounted for changes in vertical and tidal datums, are expected to be small (on the order of 10’s of centimeters) and are discussed in detail in Calder (2006).

Depth Stratification

The resulting hydrographic sounding database was divided into four strata based on depth thresholds (Table 2.1). Thresholds were chosen based on depth ranges that correspond to different maximum uncertainty specifications under International Hydrographic Organization (IHO) standards (S.44 Order 1 and 2, IHO 1998) and on coarse-scale changes in geomorphology (e.g., the continental shelf break). Neighboring strata overlap slightly to facilitate merging of outputs from individual strata into a continuous surface.

Table 2.1. Depths used to stratify hydrographic soundings and the corresponding number of soundings within each stratum.

DEPTH STRATUM	NUMBER OF SOUNDINGS (EXCLUDING OVERLAP)	PERCENTAGE OF SOUNDINGS	ADDITIONAL SOUNDINGS FROM OVERLAP	PERCENTAGE OF SOUNDINGS FROM OVERLAP
0-30 m	2,077,055	83.9%	0	0%
30-100 m	337,238	13.6%	176,843	34.4%
100-200 m	21,932	0.9%	9,931	31.2%
200-2,000 m	40,196	1.6%	3,517	8.0%
Total	2,476,421	100%	190,291	7.1%

Transformation

Prior to statistical modeling, depth values were transformed using the following logarithmic function to normalize error distributions:

$$Z_{\text{transform}} = \log(Z*b+a) \quad (\text{Equation 2.2})$$

where Z is depth in meters (with positive numbers representing depth below sea surface) and the transformation parameters a and b are taken from the appropriate error model for each depth stratum identified by IHO standards (a = 0.5 m, b = 0.013 when Z < 100 m [IHO S.44 Order 1] and a = 1.0 m, b = 0.023 when Z ≥ 100 m [IHO S.44 Order 2]) (IHO, 1998). This transformation was based on a standard bathymetric error model formulation (IHO, 1998; Calder, 2006), and improves homogeneity of conditional error variances within local regression and kriging neighborhoods, a desirable statistical property.

2.3.3 Development of the Bathymetric Model

The deterministic mean bathymetric trend surface was estimated using LOESS, a semi-parametric local regression technique (Cleveland and Devlin, 1988). LOESS estimates a smooth trend surface using weighted least-squares regression in local neighborhoods defined by a fixed number of points closest to each prediction location (the span, measured as a percentage of the total number of data points). Specifically, quadratic LOESS was used with a span of 1%, corresponding to an average neighborhood width of between 3 and 12 km depending on point density.

LOESS was implemented in Matlab version 7.13 (R2011b) with the Curve Fitting toolbox (The MathWorks Inc., Natick, MA). The standard Matlab toolbox function (curvefit/curvefit/+curvefit/LowessFit.m) was modified to reduce processing times and increase matrix stability. Execution speed was improved by using k-dimensional search trees (KD-Tree for MATLAB, Tagliasacchi, 2011) to identify and sort soundings in each local neighborhood. Under certain conditions local regression methods such as LOESS can exhibit instability due to limits on the precision of matrix calculations. X and Y coordinates were centered and re-scaled to minimize the possibility of matrix stability problems. The condition number of each local regression design matrix was also evaluated to diagnose areas where matrix precision might affect the accuracy of regression fits.

Local regression matrix stability was problematic when points that were very close to each other had very different values, which occasionally occurred in areas of high sounding density and resulted in gaps in the LOESS prediction surface. To eliminate gaps, soundings within a horizontal distance of ± 10 cm were identified, grouped and then dispersed with a small random nudge. Coordinates for the first occurrence of a sounding in a group were retained and subsequent coordinates were shifted by adding a uniform random number in the range ± (0.5, 1.5 m). Displacements were only accepted if they did not create conflicts (within 10 cm) with other soundings. A total of 700 soundings were modified (<0.03% of all data). Although this dispersion adds some positional error to each sounding, the displacement is negligible in relation to other sources of positioning error caused by geographic positioning systems or ship heave/pitch/roll.

A similar displacement procedure was applied to soundings that fell within 10 cm of the prediction grid coordinates. The purpose of this was to ensure that measurement and micro-scale error were filtered out of the prediction surface, because at the precise locations of original data, the kriging prediction surface exhibits

spikes due to the nugget effect. Filtering the nugget effect in this way is similar to the maximum *a posteriori* resampling technique proposed for filtering noisy bathymetric data by Goff et al. (2006).

The parametric standard error of the mean trend was estimated using a Monte Carlo approach. Specifically, the approximation method of Durban, et al. (1999) was used to estimate the variance-covariance matrix of the estimated local regression coefficients, $Var(\hat{\beta})$. The scale of the variance-covariance matrix was estimated as the sum of squares of the residuals for the whole model (i.e., the residuals of the original data from the LOESS fit at all data points), divided by (N - λ), where N is the number of observations and λ is the effective number of parameters, estimated as, $\lambda = 2*(1+[N/(N*span)])$.

Regression coefficient vectors were simulated by 1,000 draws from a multivariate normal distribution defined by mean vector $\hat{\beta}$ and covariance matrix $Var(\hat{\beta})$, and the LOESS prediction was re-calculated for each simulated regression coefficient vector. The standard error was estimated as the standard deviation of the simulated LOESS predictions at each location. The condition number of the design matrix of each local regression was also recorded as an additional diagnostic measure.

Residuals were obtained by subtracting the LOESS trend surface prediction at each data location from the observed data value. Semivariograms of residuals were then calculated and modeled in ArcGIS 10 with the Geostatistical Analyst extension (ESRI, 2011). A separate anisotropic semivariogram model was fit independently for each depth stratum (Figure 2.4, Table 2.2). The nugget effect was adjusted manually based on visual inspection and prior expectations from measurement error models (see below). The rest of the model parameters, including anisotropy ranges and direction, were fit automatically using non-linear weighted least-squares (ESRI, 2011).

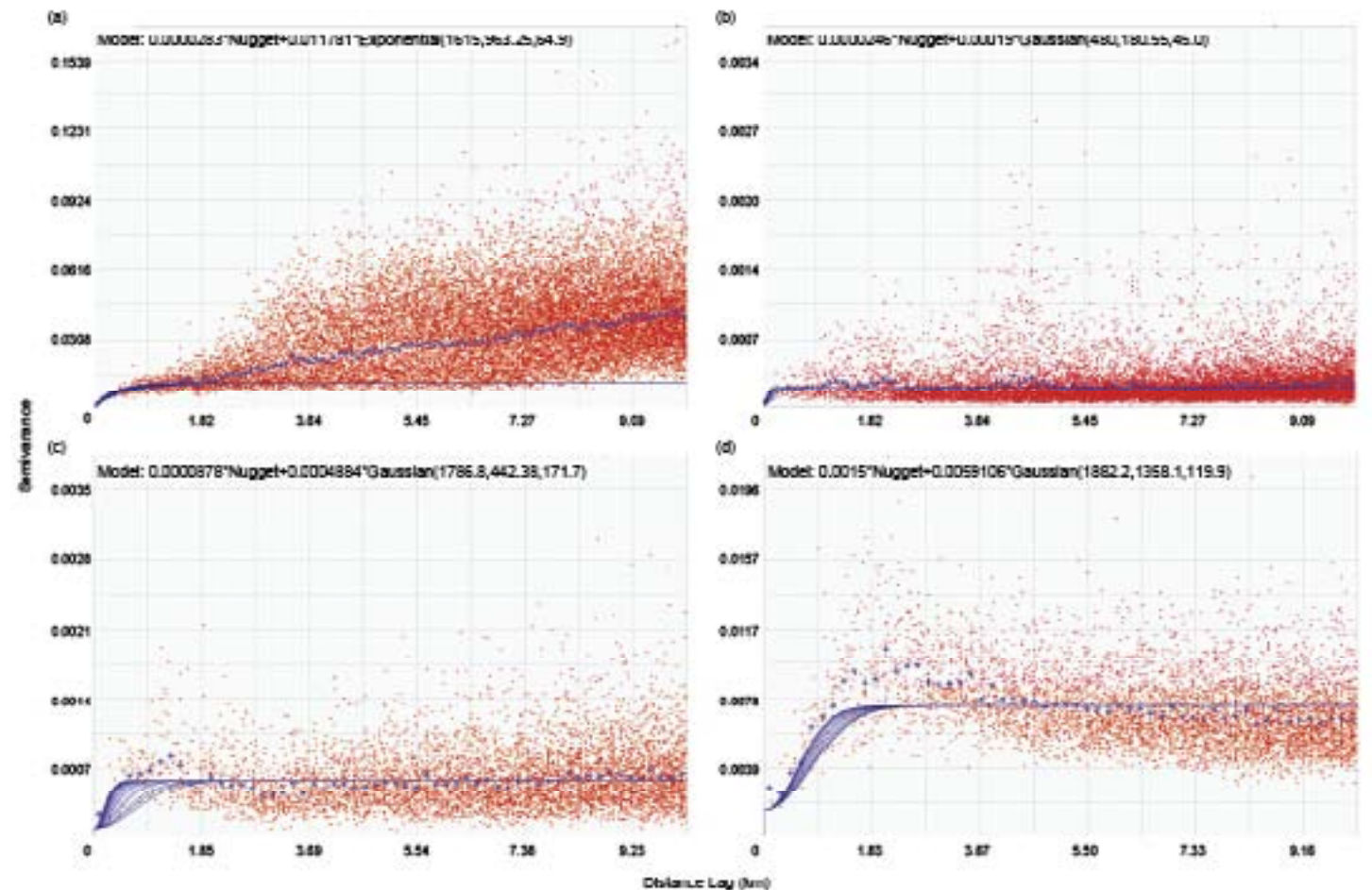


Figure 2.4. Estimated semivariograms of residuals and fitted semivariogram models for each depth stratum. (a) 0-30 m, (b) 30-100 m, (c) 100-200 m, (d) 200-2,000 m. Red dots represent sample semivariance values, blue crosses represent averaged semivariance values, solid blue lines represent directional semivariogram model fits.

Table 2.2. Semivariogram parameters for each depth stratum.

DEPTH STRATUM (m)	n	TYPE OF VARIOGRAM MODEL	NO. OF LAGS	LAG SIZE (m)	NUGGET $\times 10^{-5}$ (m)	MAJOR RANGE (m)	MINOR RANGE (m)	DIRECTION (°)*	PARTIAL SILL $\times 10^{-3}$	% OF THE SILL DUE TO THE NUGGET
0-30	2,077,055	Exp	100	100	2.83	1,615	963.25	64.86	11.8	0.2
30-100	514,081	Gau	100	100	2.46	480	180.55	45.00	0.19	11.5
100-200	31,863	Gau	175	58	8.78	1,787	442.38	171.74	0.488	15.2
200-2,000	43,713	Gau	180	56	150.0	1,882	1,358.12	119.88	5.91	20.2

Exp= exponential; Gau= Gaussian; *Clockwise from North

Nugget selection was guided by a Monte Carlo simulation of measurement error expected for each depth stratum based on maximum measurement error models defined by IHO standards (IHO S.44 Orders 1 and 2). We simulated depth observations with measurement error across the depth range of each stratum (n=100,000 points), log-transformed the simulated depths using Equation 2.2, calculated residuals from the recorded depth, and calculated the depth-averaged measurement error for each stratum in the log-transformed space. This served as a lower bound on the nugget for semivariogram fitting, which was then adjusted higher if necessary based on the best fit to empirical semivariogram plots. The rationale for this approach is that the minimum value of the nugget is equal to measurement error. Small-scale spatial features not resolved by the sample spacing (so-called “micro-scale structures”) can add to this error and raise the value of the nugget, but not lower it.

To perform ordinary kriging of residuals, semivariogram model parameters fitted in ArcGIS 10 (ESRI, 2011) were input into the KT3D module of GSLIB (Geostatistical Software Library, Deutsch and Journel, 1992). KT3D was used instead of ArcGIS 10 because of the prohibitively slow computational speed of the ArcGIS kriging implementation. KT3D was run with ordinary kriging, 8-sector search neighborhoods, a minimum search radius necessary for a gap-free kriging prediction, and a maximum search radius equal to the minimum radius times the anisotropy ratio. At least 1 and no more than 80 points (a maximum of 10 from each sector) were used to produce each kriging prediction. Table 2.3 provides more detailed information for search neighborhood parameters by stratum.

Table 2.3. Search neighborhood parameters by depth stratum.

DEPTH STRATUM (m)	MINIMUM SEARCH RADIUS (km)	MAXIMUM SEARCH RADIUS (km)	SEARCH ELLIPSOID ANGLE (°)*
0-30	3.353	2.0	64.86
30-100	5.317	2.0	45.00
100-200	12.117	3.0	171.74
200-2,000	6.929	5.0	119.88

*Clockwise from North

At each grid location for which sufficient data existed to produce a kriging prediction, the LOESS trend surface was evaluated and estimates of LOESS prediction standard error and condition number were produced. The kriging prediction, kriging variance, LOESS prediction, LOESS variance, and LOESS condition number were exported from Matlab and GSLIB formats to ESRI GRID format for post-processing using the Spatial Analyst extension in ArcGIS 10 (ESRI, 2011).

The model surface representing predicted depth for each stratum was then calculated as the sum of the LOESS and kriging prediction surfaces (see Equation 2.1). The corresponding prediction variance surface was calculated as the square root of the sum of the LOESS variance and kriging variance estimates. This calculation of the total variance assumes that the spatially structured random error component (δ and ϵ in Equation 2.1) is uncorrelated with the mean component (μ). The prediction variance was used to construct ± 1 standard error and 95% confidence interval surfaces (using the standard normal distribution critical value of 1.96).

Prediction, ± 1 standard error, and 95% confidence interval surfaces were back-transformed using the equation:

$$(\text{Exp}(Z_{\text{transform}}) - a) / b \quad (\text{Equation 2.3})$$

where $Z_{\text{transform}}$ is the depth prediction in transformed units and a and b are the error model parameters described for Equation 2.2.

Finally, the separate surfaces representing predicted depth and uncertainty for all four strata were mosaicked to generate seamless surfaces covering the whole study area. At locations with more than one prediction (i.e., where strata overlap), values for the mean (or variance) were calculated by a weighted average, where weights corresponded to the inverse of prediction variance (normalized by the sum of the weights for all the depth strata).

2.3.4 Model Validation and Accuracy Assessment

Cross-validation

A cross-validation exercise was carried out for each depth stratum to assess the accuracy of the geostatistical modeling approach. For purposes of this exercise, 50% of the data points in each stratum were selected at random for inclusion as “training data”, with the remaining points held out as “validation data.” Models were developed following the methods above applied only to the training data, and predictions were evaluated at the validation data locations. The values of the mosaicked prediction and final mosaicked prediction ± 1 standard error surfaces built from the training dataset were extracted at the validation point locations and cross-validation error statistics (Mean Average Error [MAE], Mean Average Percentage Error [MAPE], and Root Mean Square Error [RMSE]) were calculated. Since the final model was produced using the entire dataset, two times larger than the training dataset, these cross-validation statistics represent a conservative upper bound on the error statistics of the final model.

Independent Accuracy Assessment

In addition to cross-validation, geostatistical model predictions were also compared to depth predictions of the CRM (described in Section 2.1) and to a multibeam dataset, hereafter referred to as the STRATAFORM survey. The STRATAFORM survey collected soundings offshore of New York and New Jersey around 39° 12'N 72°50'W as part of the STRATAFORM project using an EM1000 MBES (Mayer et al., 1999; Nittrouer, 1999; Goff et al., 1999). The STRATAFORM survey covered 2,500 km² of seafloor in water depths ranging from 20 to 400 m and provides depth estimates for a contiguous surface at 10 m gridded resolution. Although MBES data does contain some error, for our purposes we consider it to represent the “ground truth” since accuracy and resolution of MBES surveys is much better than interpolated and compiled archival hydrographic surveys. To facilitate comparison, our 83.8 m model grid was overlaid on the 10 m STRATAFORM grid and the mean STRATAFORM values in each model grid cell were calculated. The geostatistical model and CRM, were compared to the STRATAFORM survey within the STRATAFORM survey footprint by calculating mean difference (bias), MAE, MAPE and RMSE. Comparison statistics were calculated for the entire area of overlap and for depth strata within that area (30-100 m, 100-200 m).

2.4 RESULTS AND DISCUSSION

2.4.1 Bathymetry Model Predictions

The new bathymetric model extends over the continental shelf and across the shelf slope, covering the majority of the planning area (Figure 2.5). Depth predictions ranged from 0 m at the shore to around 2,100 m on the shelf slope. Some nearshore areas, like the approach to New York Harbor, were not modeled due to processing limitations arising from extremely high data density. A few small patches in the nearshore areas off southern New Jersey and western Long Island did not have model predictions because the geostatistical model was unable to produce predictions where soundings with distinctly different measured depths occurred at virtually the same location. This occurred where older, less accurate surveys coincided with more recent, more accurate surveys.

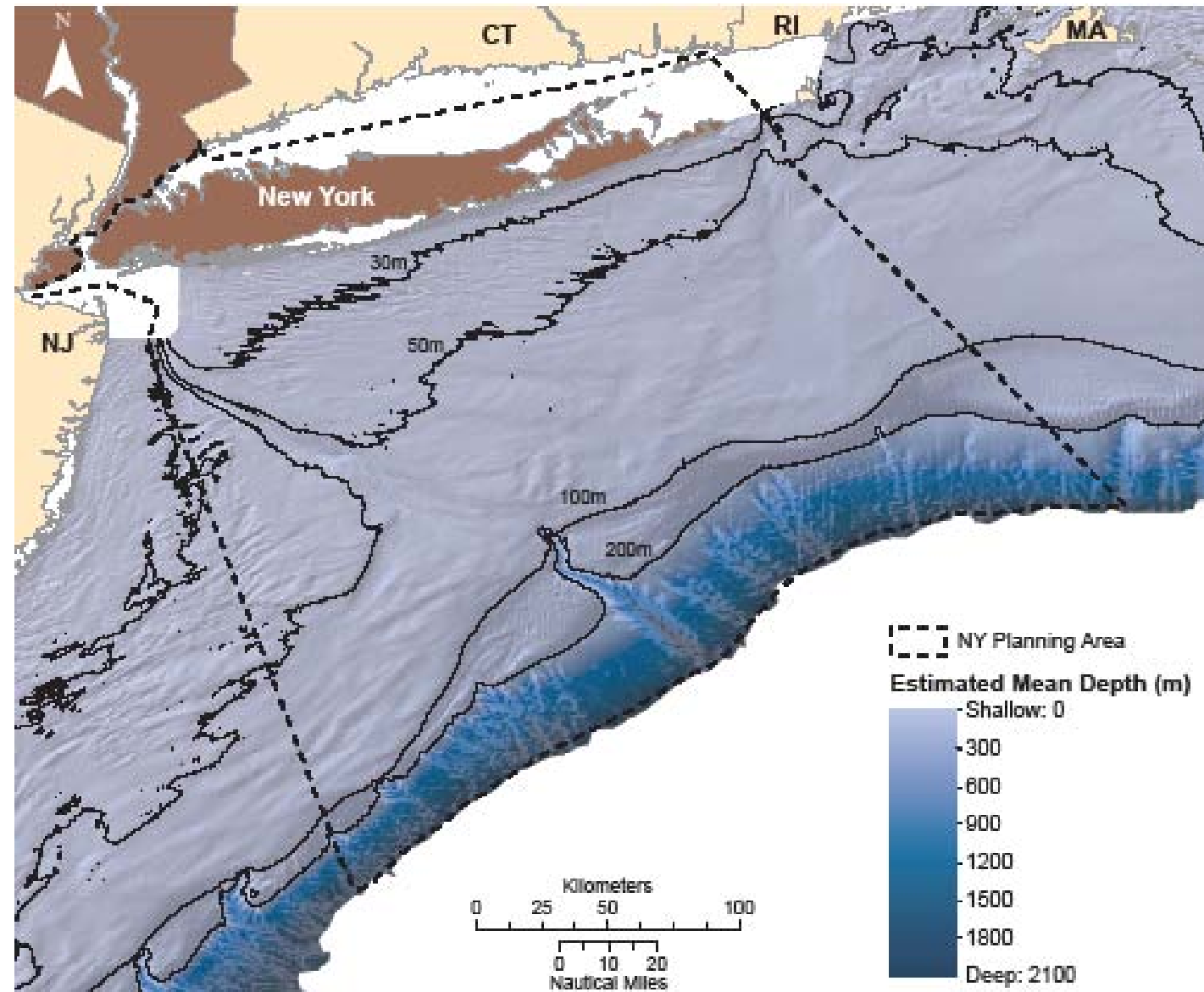


Figure 2.5. Bathymetric surface developed from the geostatistical model, draped over separate hillshade layers derived for the continental shelf (0-200 m) and the shelf slope (>200 m). Solid black lines depict depth contours derived from the bathymetric surface.

Duane et al. (1972) found that sand ridges were a dominant geomorphologic feature on most of the northeast U.S. Atlantic continental shelf. These features were evident in the bathymetry model, particularly to the west of Hudson Canyon and in the northeast of the study area. Submarine canyons, like Hudson Canyon, and shallower networks of gullies were also evident in the model along the shelf slope.

2.4.2 Bathymetry Model Uncertainty

Model standard error ranged from 0.026 m to almost 200 m over the study area (Figure 2.6). In general, model standard error was less than 5 m at depths shallower than 30 m. In this depth stratum, standard error was relatively higher (2-10 m) in areas where surveys occurred prior to 1958 (Figure 2.2). At depths from 30 m to 100 m, standard error was typically less than 2 m, but reached as much as 5 m in some areas where depths approached 100 m. Standard error typically ranged from 2-5 m for depths between 100 and 200 m but was higher (5-10 m) in some areas where depths approached 200 m at the shelf edge. Along the shelf slope, standard error increased from 10-20 m at depths closer to 200 m to greater than 50 m in areas deeper than 500 m. Although standard error generally increased with sounding depth beyond the 30 m depth contour, error was also dependent on distance between surveys. As expected, within each depth stratum, error was generally lower along survey transects where distance between soundings was shortest (lines clearly

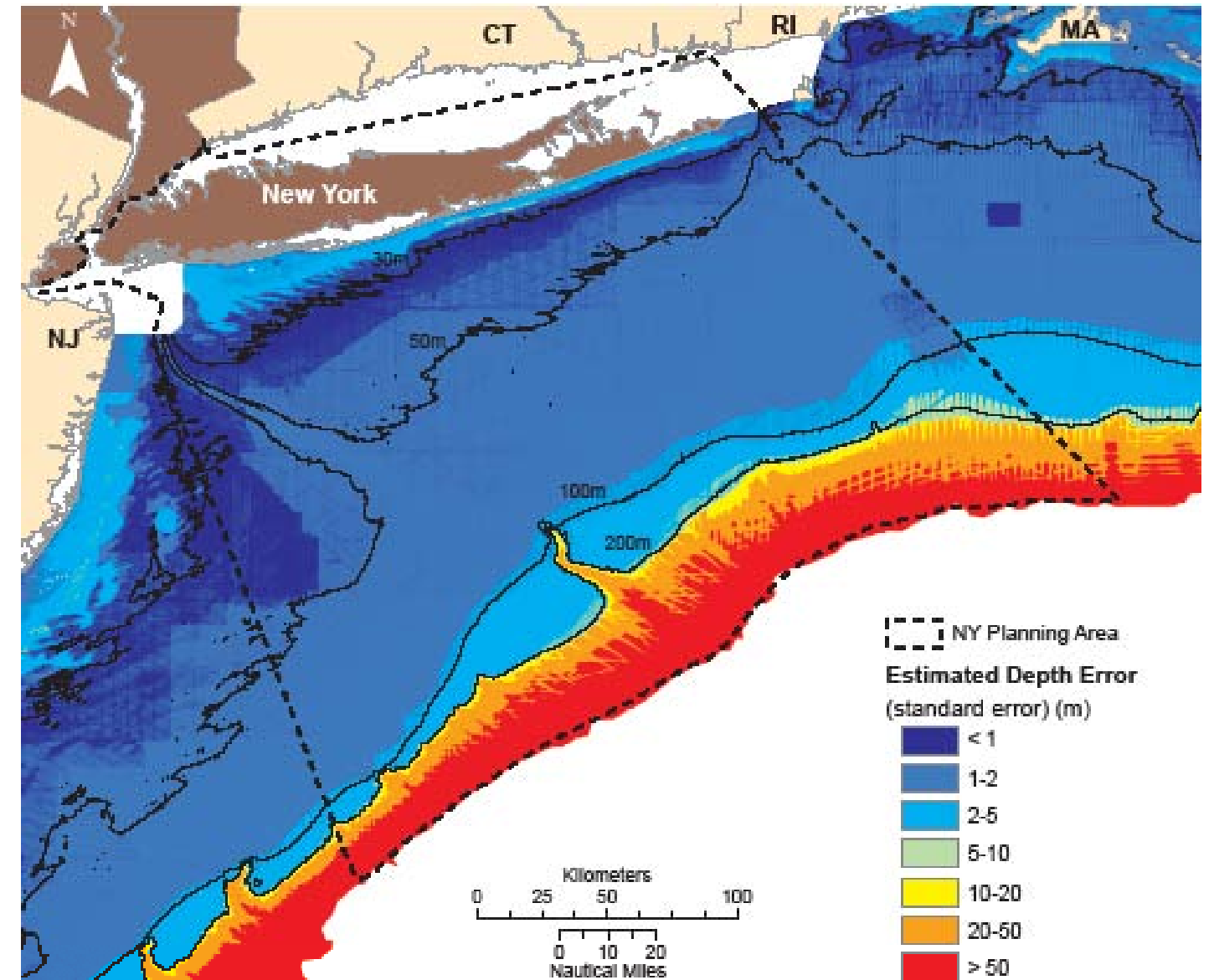


Figure 2.6. Estimated error of predictions (standard error) from the bathymetric model. Model standard error provides an indication of prediction uncertainty.

distinguishable in Figure 2.6). There were two primary reasons for higher error along the shelf slope when compared to shallow areas. First, the absolute precision of sounding instruments generally decreases with depth, and second, soundings become sparser farther offshore. There were several areas south of Hudson Canyon where sounding tracks are greater than 8 kilometers apart (Figure 2.2).

The prediction standard error surface indicates the uncertainty associated with the model prediction at each location, assuming that statistical assumptions of the model are met. Local regressions can be inaccurate as the limits of matrix precision are approached, as indicated by high condition numbers (Figure 2.7). The condition number is a diagnostic that indicates the stability of the local regression trend model at each location. Higher spatial condition number values indicate that the regression solution is less stable at that location, such that small variations in the input data (e.g., uncertainty due to measurement error) can result in large variations in the prediction. For second order polynomials, the critical spatial condition number threshold value is approximately 100, meaning that predictions should be considered with caution at locations where the spatial condition number is close to 100 and should be considered unreliable where it is greater than 100 (Golub and Van Loan, 1996). Under these conditions, the standard error surface may underestimate actual error. This occurs only in a narrow band along the southern coast of Long Island.

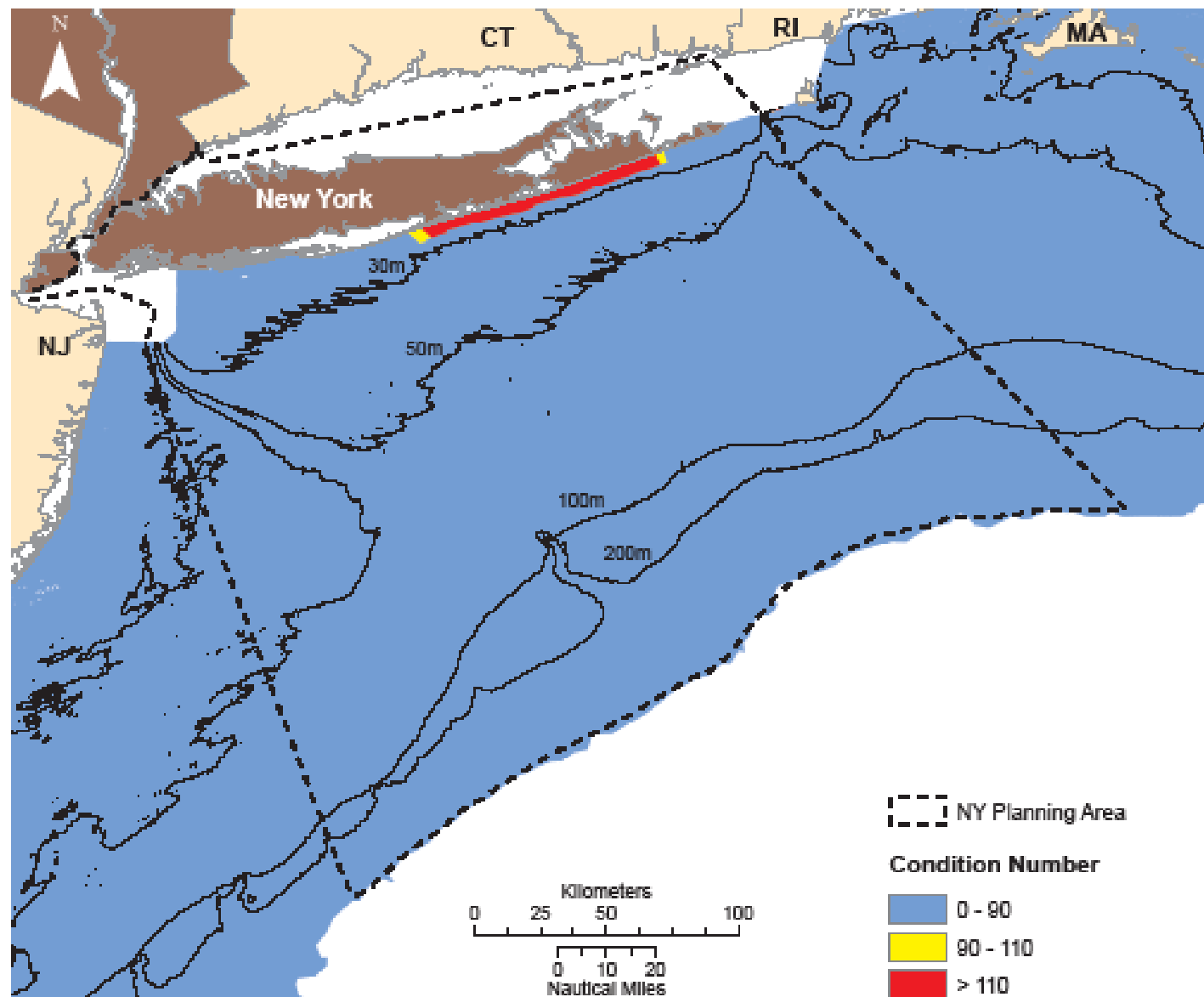


Figure 2.7. Spatial condition number from the LOESS trend model. Condition number classes reflect the threshold at which standard error predictions should be considered unreliable.

Model uncertainty was also depicted using theoretical 95% confidence intervals of the depth predictions (predicted depth $\pm 1.96 \times$ standard error) along two hypothetical transects (Transect 1 and Transect 2) that spanned from the shoreline to the shelf slope (Figure 2.8). Transect 2 differed from Transect 1 in that it cut across a submarine canyon (Hudson Canyon) at the shelf edge. Maximum and minimum depth values representing the upper and lower bounds of the 95% confidence intervals were extracted at 100 m intervals along each transect. For both transects, the width of the 95% confidence intervals generally increased with distance from shore and with depth. However, model uncertainty was greater and more variable in the 0-30 m depth stratum than it was in the 30-100 m depth stratum (Figure 2.9, Figure 2.10). At depths greater than 200 m, the 95% confidence interval widths increased dramatically with distance from shore and had an average vertical width of almost 0.25 km.

To explore how uncertainty in depth predictions may translate into horizontal uncertainty and how this uncertainty could impact management decisions (e.g., the siting of a wind farm), depth contours (30 m, 50 m, 100 m, 200 m) derived from the model prediction and from the upper and lower limits of the theoretical 95% confidence intervals ($\pm 1.96 \times$ standard error) were overlaid on the boundaries of theoretical wind farm areas within the NY study area (Figure 2.11). These theoretical wind farm areas correspond to areas outside of shipping lanes and within current depth constraints for wind farm structures. These depth contours were mapped to produce a rough estimate of the horizontal uncertainty associated with the model predictions. Within the potential

wind farm areas, transects were drawn between the 50 m depth contours derived from confidence interval limits. The transects were drawn approximately perpendicular to the 50 m depth contour derived from the model prediction at intervals of approximately 5 km.

In this region, the mean distance between the depth contours derived from the confidence interval limits was approximately 8 km with a standard deviation of almost 3 km. While this measure only represents a rough estimate of horizontal uncertainty, it suggests that depth predictions from this model and other models developed using similar data should be used with caution when high positional precision is needed.

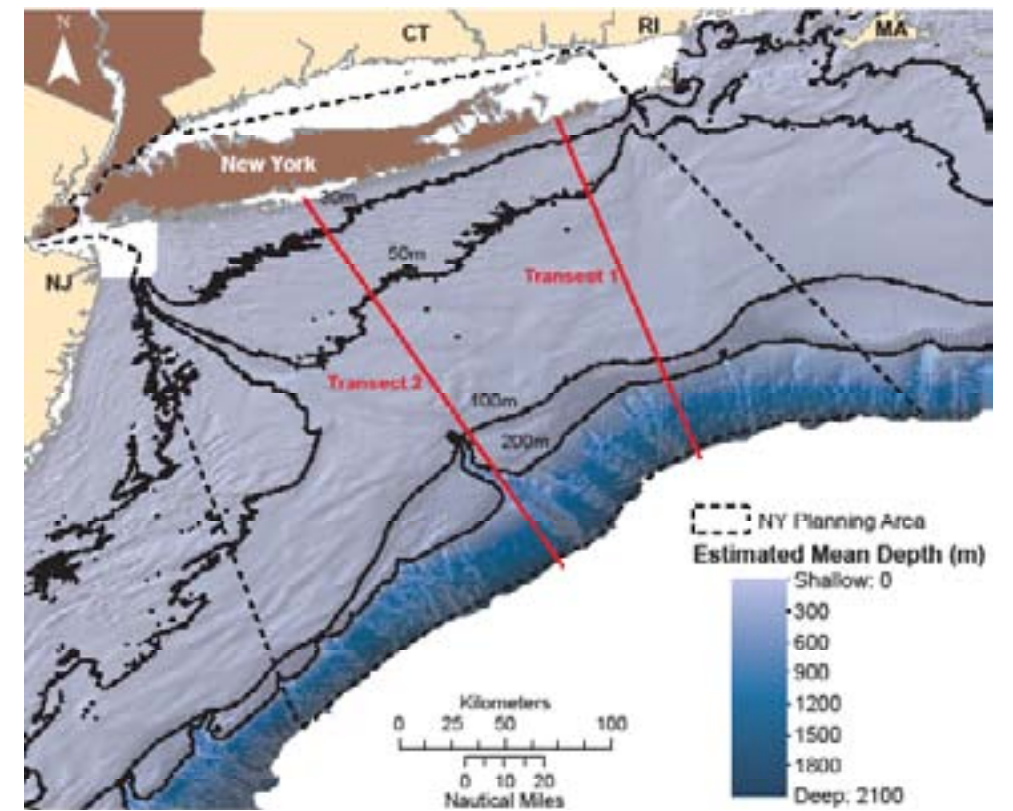


Figure 2.8. Locations of transects used to depict theoretical 95% confidence intervals of the geostatistical model predictions as a function of distance from shore and local geomorphology.

2.4.3 Cross-validation of the Training Dataset

Cross-validation results indicated that the geostatistical model performed extremely well in the 0-30 m and 30-100 m depth strata (mean absolute errors 0.60 m and 0.55 m, respectively). The model performed reasonably well in the 100-200 m depth stratum (mean absolute error of 2.1 m, or 1.40%), but model accuracy was considerably degraded in the 200-2,000 m depth stratum (mean absolute error 25.76 m, or 3.44%) (Table 2.4).

Cross-validation was also used to assess the accuracy of confidence intervals. The theoretical 68% confidence intervals (model prediction \pm standard error) are somewhat conservative for all depth strata (Table 2.5). For depths below 100 m, the theoretical 95% confidence intervals (model prediction $\pm 1.96 \times$ standard error) are slightly conservative, but the geostatistical model underestimates error at depths greater than 100 m, especially at depths greater than 200 m. For example, in the 200-2,000 m depth range model standard errors should be multiplied by a factor of 2.46, rather than the theoretical value of 1.96, to produce true 95% confidence intervals (Table 2.5).

Table 2.4. Cross-validation statistics for the geostatistical model built from the training dataset. Negative bias indicates a deep bias while positive bias indicates a shallow bias. MAE = Mean Absolute Error, MAPE = Mean Absolute Percentage Error, RMSE = Root Mean Square Error.

DEPTH STRATUM	COMPARISON STATISTIC	CROSS-VALIDATION ERROR
Overall (0-2,000 m)	Bias	-0.08 m
	MAE	1.04 m
	MAPE	6.53%
	RMSE	5.53 m
0-30 m	Bias	-0.17 m
	MAE	0.60 m
	MAPE	7.72%
30-100 m	Bias	0.02 m
	MAE	0.55 m
	MAPE	1.42%
100-200 m	Bias	0.06 m
	MAE	2.14 m
	MAPE	1.40%
200-2,000 m	Bias	2.97 m
	MAE	25.76 m
	MAPE	3.44%
	RMSE	41.23 m

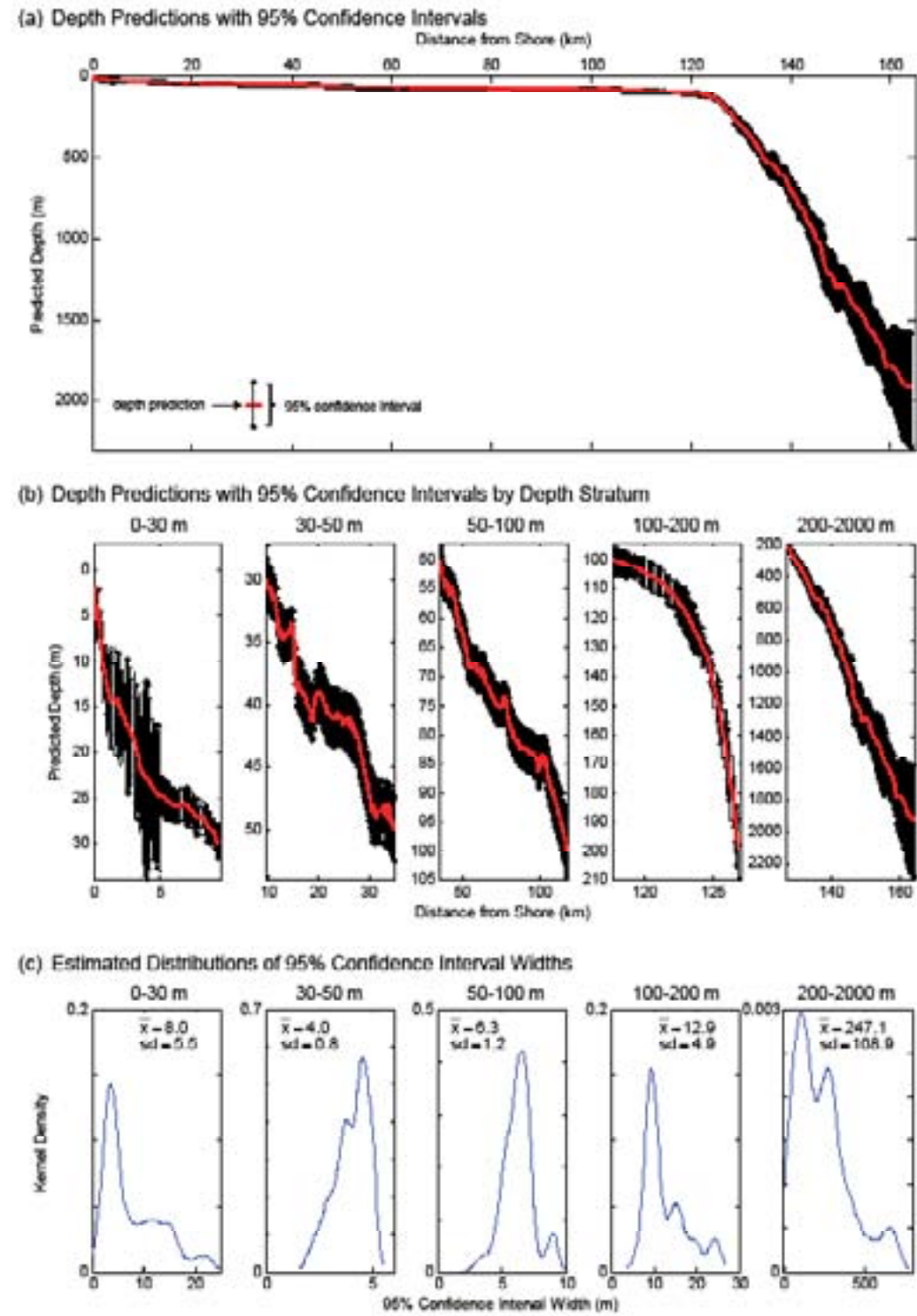


Figure 2.9. (a) Predicted depth (m) with theoretical 95% confidence intervals (± 1.96 *standard error) vs. distance from shore (km) along Transect 1. (b) Predicted depth (m) with 95% confidence intervals by depth stratum. (c) Distribution of 95% confidence interval widths with the mean (\bar{x}) and standard deviation (sd) for each depth stratum. The probability density of the confidence interval widths was estimated using a kernel density function (Särkkä 1999).

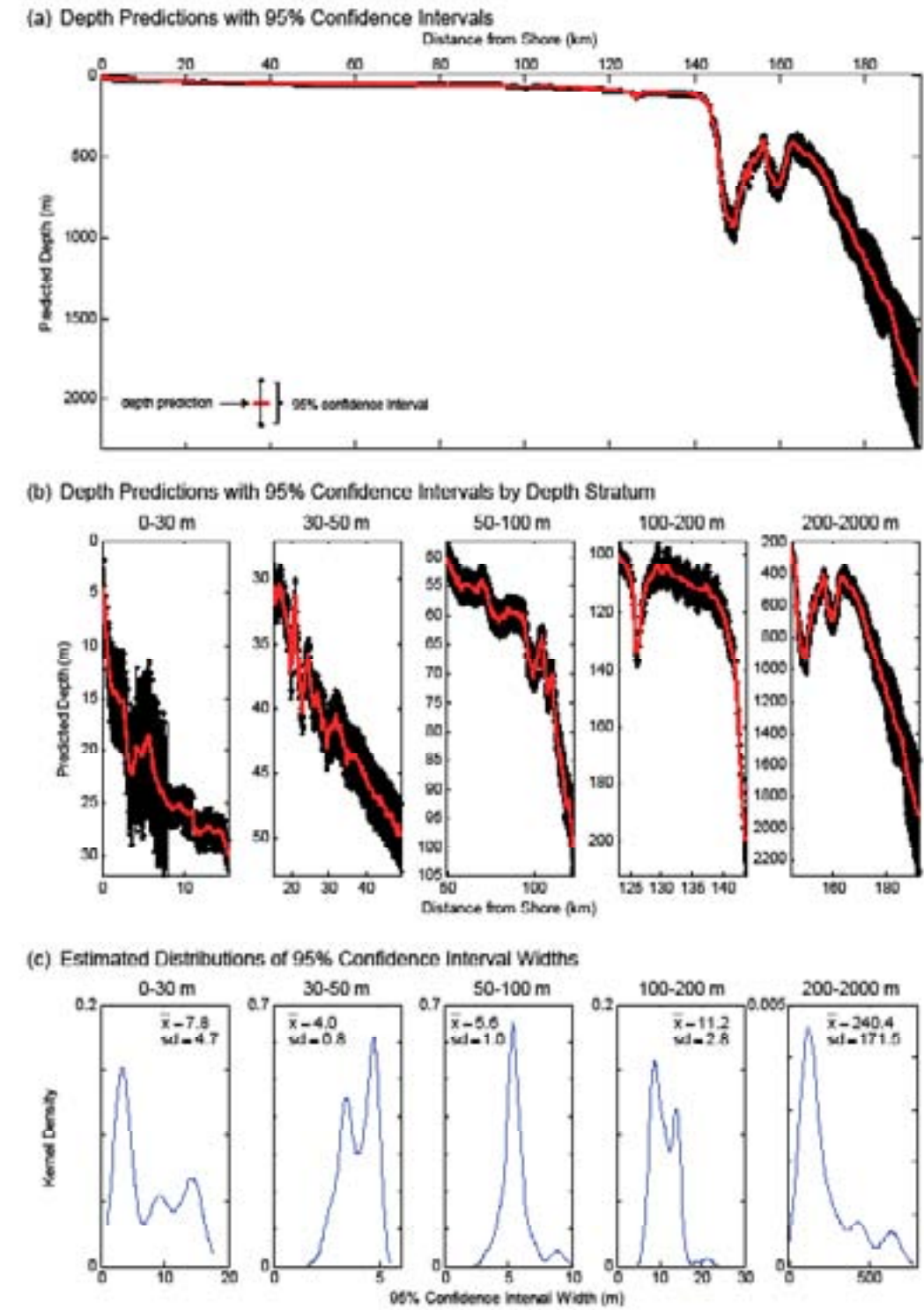


Figure 2.10. (a) Predicted depth (m) with theoretical 95% confidence intervals (± 1.96 *standard error) vs. distance from shore (km) along Transect 2. (b) Predicted depth (m) with 95% confidence intervals by depth stratum. (c) Distribution of 95% confidence interval widths with the mean (\bar{x}) and standard deviation (sd) for each depth stratum. The probability density of the confidence interval widths was estimated using a kernel density function (Särkkä 1999).

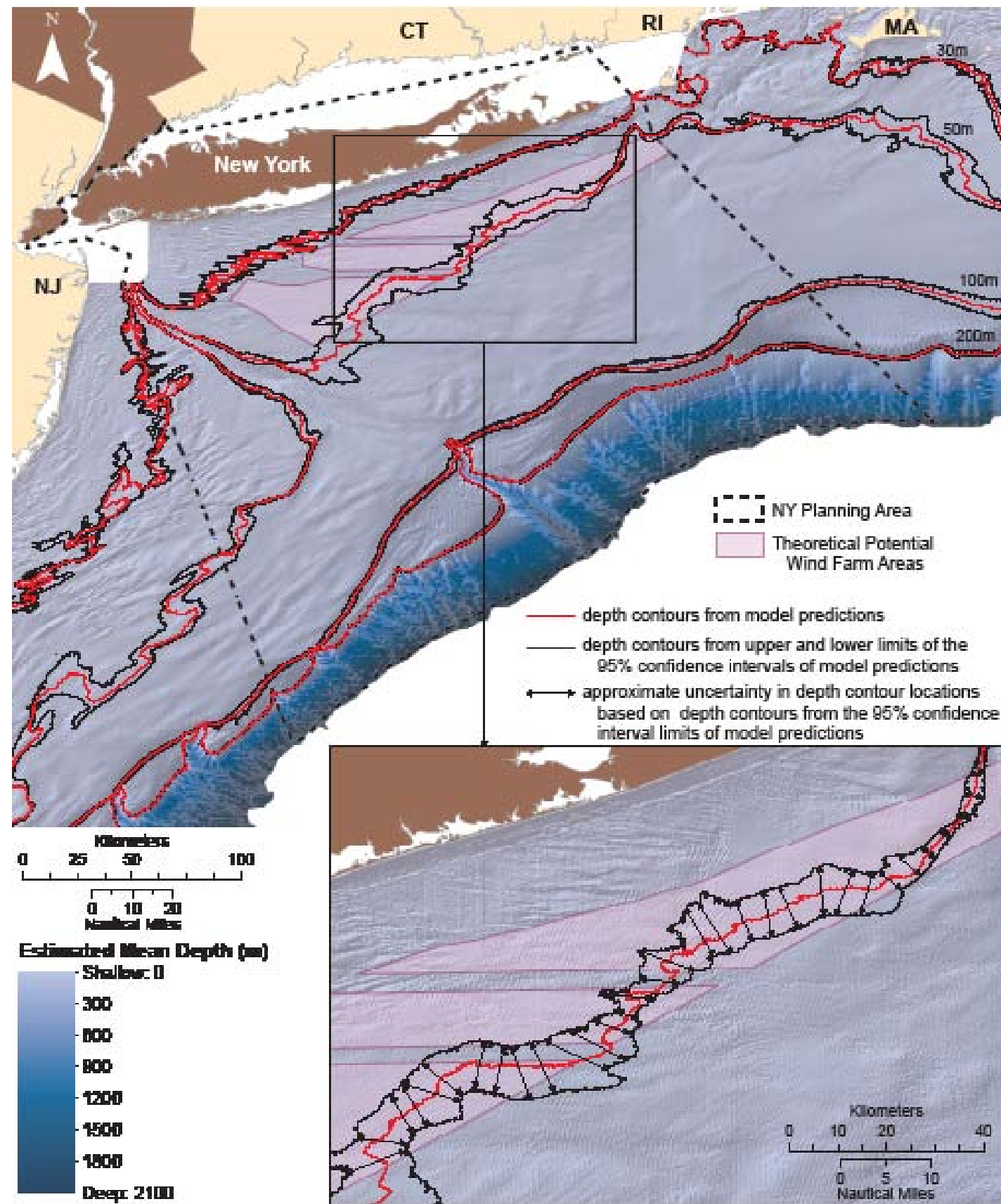


Figure 2.11. Depth contours derived from the predicted bathymetric surface and from the upper and lower limits of the theoretical 95% confidence intervals ($\pm 1.96 \times \text{standard error}$) overlaid on the predicted bathymetric surface and theoretical potential wind farm areas for New York. Within the inset map, approximate uncertainty in depth contour locations was estimated using transects approximately perpendicular to the depth contour derived from the predicted bathymetric surface.

Table 2.5. Performance of theoretical 68% and 95% confidence intervals.

DEPTH STRATUM	PERCENTAGE OF VALIDATION DATA WITHIN THEORETICAL 68% CONFIDENCE INTERVAL	STANDARD ERROR MULTIPLIER FOR 68% CONFIDENCE INTERVAL (COMPARED TO 1.0)	PERCENTAGE OF VALIDATION DATA WITHIN THEORETICAL 95% CONFIDENCE INTERVAL	STANDARD ERROR MULTIPLIER FOR 68% CONFIDENCE INTERVAL (COMPARED TO 1.96)
Overall (0-2,000 m)	87.50%	0.42	95.50%	1.84
0-30 m	87.60%	0.40	95.40%	1.86
30-100 m	87.00%	0.49	95.90%	1.77
100-200 m	88.30%	0.35	94.70%	2.04
200-2,000 m	80.80%	0.62	92.70%	2.46

2.4.4 Independent Accuracy Assessment

The STRATAFORM dataset is ideally located for an independent accuracy assessment of the geostatistical model because it extends across multiple depth strata and overlaps NOS hydrographic soundings collected using multiple sounding and positioning methods.

As a benchmark, we evaluated our model performance in comparison to the CRM in the STRATAFORM area. This may not be an entirely fair comparison, since it is possible (though not verifiable) that the CRM included some version of the STRATAFORM data; however, we proceed anyway with the caution that the CRM error statistics may be significantly better in this region than in other parts of the study area.

Overall we found that both the geostatistical model and CRM are excellent models in the 30-100 m depth range for the STRATAFORM area (mean absolute error [MAE] < 1 m, mean absolute percent error [MAPE] < 1.5%), but accuracy of both models degraded with depth in areas deeper than 100 m (Table 2.6). We found the geostatistical model did not improve upon the CRM in terms of accuracy (when comparing MAE, MAPE, and root mean-square-error [RMSE]) (Table 2.6), but it was able to provide reliable estimates of uncertainty, at least for depths less than 200 m (see Figure 2.6), and obtaining these estimates was the principal reason for undertaking a geostatistical model in the first place. For the 30-100 m and 100-200 m depth strata the percent correct within theoretical 95% confidence intervals were 97.89% and 97.06%, respectively, indicating that the confidence intervals were accurate.

Table 2.6. Results from an accuracy assessment of the geostatistical model and the coastal relief model (CRM). The new geostatistical model and the CRM are compared against the STRATAFORM data. Negative bias indicates a deep bias while positive bias indicates a shallow bias. MAE = Mean Absolute Error, MAPE = Mean Absolute Percentage Error, RMSE = Root Mean Square Error.

DEPTH STRATUM	COMPARISON STATISTIC	INDEPENDENT ACCURACY ASSESSMENT ERROR, GEOSTATISTICAL MODEL	INDEPENDENT ACCURACY ASSESSMENT ERROR, COASTAL RELIEF MODEL
Overall (30-200 m)	Bias	-0.23 m	0.21 m
	MAE	1.17 m	1.15 m
	MAPE	1.18%	1.12%
	RMSE	3.27 m	3.39 m
30-100 m	Bias	0.05 m	0.55 m
	MAE	0.90 m	0.84 m
	MAPE	1.20%	1.10%
	RMSE	1.27 m	1.15 m
100-200 m	Bias	-0.68 m	-0.35 m
	MAE	1.60 m	1.65 m
	MAPE	1.14%	1.15%
	RMSE	5.06 m	5.32 m

Results on bias were mixed. In the 30-100 m depth stratum, the geostatistical model was approximately unbiased, whereas the CRM exhibited a slight shallow bias (+0.55 m). However, in the 100-200 m depth stratum the geostatistical model exhibited more of a deep bias (-0.68 m) than the CRM (-0.35 m). These biases are small and of the magnitude expected due to known sources of error (e.g., quantization due to rounding of measurement units, changes in tidal references and vertical datums; Calder, 2006).

Taking all comparative data together, the CRM may be the best model if the average value of depth is the primary variable of interest. However, when certainty in depth estimates needs to be accounted for, then the geostatistical model should be preferred, particularly when the depths of interest are shallower than 200 m.

Examples of situations where estimates of bathymetric uncertainty may be useful include measuring the amount of habitat area falling into a given depth range, or identifying suitable construction zones for wind farms based on a depth limit (Figure 2.11). In the latter case, uncertainty can be used to define risk of additional development costs and be used to target the best areas to build within potential construction zones.

2.5 LIMITATIONS TO INTERPRETATION AND FUTURE DIRECTIONS

The geostatistical approach we have employed to create a gridded, interpolated bathymetry surface is an improvement over previous bathymetry models in that it generates a spatially explicit error map to accompany the predicted surface. The cross-validation and independent accuracy assessments show that the model performs similar to the NOAA Coastal Relief Model with the advantage of providing reliable uncertainty estimates. However, several limitations and potential improvements to our approach should be noted here to support interpretation of our models and development of future efforts. Noted limitations will also apply to the CRM and other modeling techniques. Principal limitations of our geostatistical models arise from three general factors:

- 1) data quality: integrating diverse soundings collected over time and using different methodologies results in a variety of potential distortions in the final surface,
- 2) resolution: the spatial resolution of original sample data and of the model output grid limit the minimum scale of features that can be resolved, and,
- 3) model assumptions: geostatistical models involve a number of simplifying assumptions that do not fully capture the complexity of underlying geomorphological patterns.

To help users better understand limitations and appropriate uses of this model, and to guide development of future models, we provide brief explanations and examples of these limitations below and suggest some potential improvements.

2.5.1 Data Quality

Hydrographic soundings in the study area came from a multitude of surveys spanning more than a century (1887-2004). Surveys used an assortment of positioning and sounding technologies, resulting in a patchwork of overlapping soundings collected at varying sample spacings and with different precisions. These errors can propagate to the final model creating distortions that do not correspond to changes on the seafloor.

We have not dealt explicitly with horizontal positioning error. The impact of horizontal positioning error will show up in our models as an increase in the nugget effect over the actual instrument measurement error. Some studies have integrated estimates of positioning uncertainty explicitly into spatial models (Kielland and Tubman, 1994; Jakobsson et al., 2002). Kielland and Tubman (1994) used pseudo-points about the nominal location to combine ship position uncertainties with modeling uncertainties. Jakobsson et al. (2002) used a direct simulation Monte Carlo method in which an ensemble of possible data configurations were drawn assuming a distribution of positioning errors. These approaches could be used to improve the precision of our estimates of bathymetric uncertainty by accounting for differences in positioning certainty between older and newer data.

We also did not explicitly account for differences and possible systematic biases in vertical accuracy of survey data. Archival NOS Hydrographic Survey data has been processed using varying methods over the years which have created some systematic post-processing errors (see Calder, 2006 for a full discussion). Briefly, Calder (2006) reported that archival lead line soundings (common prior to 1978) are systematically shallow-biased because of “hydrographic rounding” (a tendency to round down to the next shallowest whole fathom). Generally, the more recent VBES data appears approximately unbiased (but see below), and modern multibeam surveys offer the most precise information. Calder’s findings suggest that some older VBES soundings are also biased

because they were digitized from paper charts for which data were first rounded to the next shallowest foot or fathom (listed in the metadata as “smooth sheets digitized for NOS under contract”). It may be impossible to correct for biases in these data because the precise procedures followed were not recorded. More recent data entered directly into the database after collection by digital instruments are less likely to have systematic rounding error.

For our purposes, we applied a correction factor to lead line surveys because these were found to have a predictable, systematic error in our study area (Calder, 2006). However, we were unable to correct for probable systematic biases in other sounding methods (e.g., VBES data that went through a smooth sheet digitization). Survey metadata indicates that approximately 18% of soundings were non-lead line data that were digitized using smooth sheets, and therefore would be improved by some bias correction. We attempted to reduce the effect of these potentially biased surveys by eliminating data from those surveys where they fell within the footprint of more modern surveys known to be unbiased (directly digitized VBES and MBES). However, unfortunately, about 40% of the study area was only covered by archival lead line data and/or VBES data digitized from paper charts. These areas are less reliable and may contain systematic biases (typically shallow-biased by <2 m) that are not fully reflected in our model uncertainty estimates. In places where only older, less reliable data are available, we suggest using maps of survey age (Figure 2.2) and/or estimated survey measurement error based on the technique used for sounding (Figure 2.12) to supplement model-based uncertainty maps. These maps viewed alongside geostatistical model errors can help identify unreliable areas and areas where additional bathymetric information would improve future planning decisions.

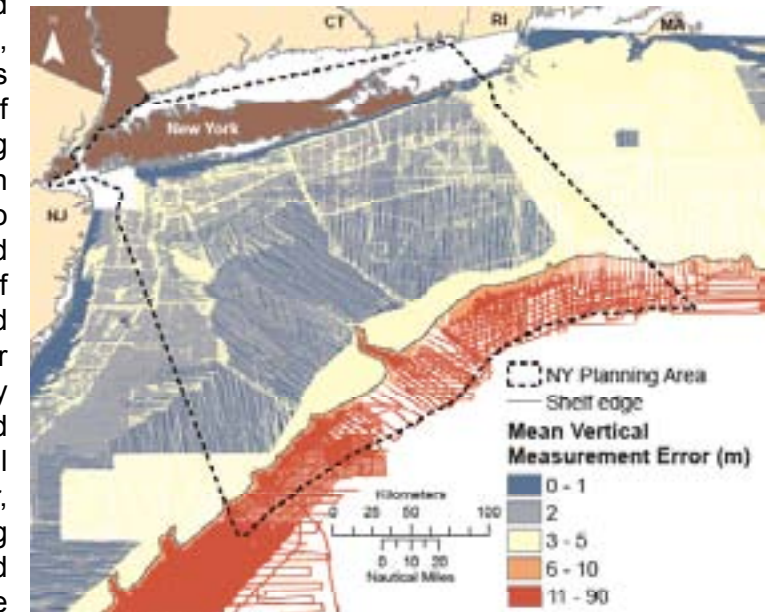


Figure 2.12. Mean estimated vertical measurement error for soundings within 1 km rectangular neighborhoods. Vertical measurement errors were estimated based on vertical sounding technology used. For some surveys this was inferred from survey age. The shelf edge corresponds to the 200 m depth contour.

We have purposefully neglected consideration of changes to the seafloor occurring over time. Temporal changes may or may not be reflected in spatially-explicit model error estimates depending on the ages of nearby surveys. We expect positional error attributed to change over time may be substantial in some areas, especially in highly dynamic areas, such as where tidal and riverine influences are great.

Finally, we note that recently developed geostatistical algorithms could be used in the future to account for heterogeneous measurement error among methods (Christensen, 2011) to improve accuracy and more appropriately weight higher quality data.

2.5.2 Resolution

The distance between soundings was not uniform across the study area (Figure 2.2). The length scale of features that can be resolved will be shorter (higher resolution) in areas with greater sounding density. Moreover, it is possible that our model-based uncertainties will underestimate true error in areas with sparse soundings, especially when very high amplitude, high frequency features are present (e.g., high frequency, short-wavelength sand waves). The chances of this and other problems arising from interactions of sample spacing and high-frequency features (e.g., aliasing) are greater when samples are both sparse and very regularly spaced. Fortunately, in our cross-validation and independent accuracy assessment we did not find evidence for significant overall underestimation of uncertainty, but localized impacts are still possible in areas with high frequency features relative to sample spacing (e.g., sand waves).

In general, fine-scale or very sharply defined features, such as erratics, deep sea reefs or man-made artifacts, will not be reliably resolved in our model. The spatial scale at which these features become visible is dependent on the relative distribution of soundings, the methods used to model spatial structure and the output resolution of maps. Although the sounding density would support resolution approaching 10 m in some limited areas (see Figure 2.2 where sounding density exceeds 100 km^{-1}), the output model grid size was $\sim 85 \text{ m}$. The minimum scale of resolved length scales is twice the output resolution, or $\sim 170 \text{ m}$. For the vast majority of the study area data density was much sparser and could only detect features at scales on the order of 10^2 m and in some areas 10^3 m . In general, new MBES and/or sidescan sonar surveys are needed if greater detectability at short spatial scales is required. In some cases, modern VBES surveys acquired with co-registered sidescan information may be used to identify some missed features. Additionally, Calder (2006) presents a unique method of integrating a variance term corresponding to “hydrographic oversight” of smaller features, but the term requires a very good understanding of the data and geomorphology.

2.5.3. Model Assumptions

A full discussion of the statistical assumptions inherent in the LOESS local regression and geostatistical approaches used here is beyond the scope of this chapter; the reader is referred to texts on the subjects (e.g., Cleveland and Devlin, 1988; Cressie, 1993; Chiles and Delfiner, 1999). However, it is important to note here that geostatistical models are not capable of reproducing the full complexity of geomorphological patterns (e.g., alluvial fans, sand waves) unless data are very dense. This is because geostatistical models describe spatial correlation as a simple function of distance between points, allowing only for very simple geometric anisotropy. Complex multi-point erosional and depositional patterns can't be resolved unless they are densely sampled. Texture-mapping approaches could possibly improve prediction of complex geomorphology (e.g., Boucher, 2009). Ultimately, however, collection of new multibeam bathymetry is preferable to any attempt to statistically reconstruct fine-level details in archival hydrographic surveys.

2.6 ACKNOWLEDGMENTS

We thank Brian Calder and Larry Mayer (The Center for Coastal and Ocean Mapping & NOAA/UNH Joint Hydrographic Center) for providing the gridded STRATAFORM multibeam data used in the accuracy assessment. Bryan Costa, Will Sautter, Tim Battista provided helpful discussions in support of this work and also assisted with data acquisition/analysis for bathymetry and vector shorelines. We are grateful to Brian Calder and John Goff for detailed technical reviews and for discussions that substantially improved this work; however, they are not responsible for any errors or omissions in the final product.

2.7 REFERENCES

Amante, C. and B.W. Eakins. 2009. ETOPO1 1 arc-minute global relief model: procedures, data sources and analysis. NOAA Technical Memorandum NESDIS NGDC-24. 19 pp.

Boucher, A. 2009. Considering complex training images with search tree partitioning. *Computers and Geosciences* 35:1151-1158.

Butman, B., W.W. Danforth, W.C. Schwab, and M.R. Buchholtz ten Brink. 1998. Multibeam bathymetric and backscatter maps of the Upper Hudson Shelf Valley and adjacent shelf, offshore of New York. U. S. Geological Survey Open-File Report 98-616.

Butman, B., T.J. Middleton, E.R. Thieler, and W.C. Schwab. 2003. Topography, shaded relief, and backscatter intensity of the Hudson Shelf Valley, offshore of New York. U. S. Geological Survey Open-File Report 03-372.

Butman, B., D.C. Twichell, P.A. Roma, B.E. Tucholke, T.J. Middleton, and J.M. Robb. 2006. Sea floor topography and backscatter intensity of the Hudson Canyon region offshore of New York and New Jersey. U.S. Geological Survey Open-File Report 2004-1441.

Calder, B.R. 2006. On the uncertainty of archive hydrographic datasets. *IEEE Journal of Oceanic Engineering* 31(2): 249-265.

Calderbank, B. 2001. Radio positioning accuracies. *Lighthouse* 59:12-15.

Chiles, J. P. and P. Delfiner. 1999. *Geostatistics: modelling spatial uncertainty*. New York: Wiley-Interscience.

Christensen, W.F. 2011. Filtered kriging for spatial data with heterogeneous measurement error variances. *Biometrics*. DOI: 10.1111/j.1541-0420.2011.01563.x.

Cleveland, W.S. and S.J. Devlin. 1988. Locally weighted regression: an approach to regression analysis by local fitting. *Journal of the American Statistical Association* 83(403):596-610.

Cressie, N.A.C. 1993. *Statistics for spatial data* (revised ed.). New York: John Wiley & Sons, Inc.

Curry, R.G. 1996. *HydroBase: a database of hydrographic stations and tools for climatological analysis*. Woods Hole Oceanographic Institution Technical Report WHOI 96-01, 44 pp.

Deutsch, C.V. and A.G. Journel. 1992. *GSLIB: Geostatistical Software Library and User's Guide*. Oxford University Press. 340 pp.

Duane, D.B., M.E. Field, E.P. Meisburger, D.J.P. Swift, and S.J. Williams. 1972. Linear shoals on the Atlantic Inner Continental Shelf, Florida to Long Island. In: Swift, D.J.P., D.B. Duane, and O.H. Pilkey (eds.). *Shelf sediment transport: process and pattern*. Stroudsburg, PA: Dowden, Hutchinson and Ross.

Durban, M., C.A. Hackett, and I.D. Currie. 1999. Approximate standard errors in semiparametric models. *Biometrics* 55(3):699-703.

Environmental Systems Research Institute, Inc. (ESRI). 2011. *ArcGIS Desktop: Release 10*. Redlands, CA: Environmental Systems Research Institute.

ESRI Online. 2011. *ArcGIS Online World Imagery service from ESRI ArcGIS Online and data partners, including imagery from agencies supplied via the Content Sharing Program*. Available from <http://www.arcgis.com/home/>, Accessed Dec 14, 2011.

Gardner, J.V., P. Dartnell, L.A. Mayer, and J.E. Hughes-Clarke. 2003. Geomorphology, acoustic backscatter, and processes in Santa Monica Bay from multibeam mapping. *Marine Environmental Research* 56:15-46.

Goff, J.A., D.J.P. Swift, C.S. Duncan, L.A. Mayer, and J. Hughes-Clarke. 1999. High resolution swath sonar investigation of sand ridge, dune and ribbon morphology in the offshore environment of the New Jersey Margin. *Marine Geology* 161:309-339.

Goff, J.A., C.J. Jenkins, and B. Calder. 2006. Maximum likelihood resampling of noisy, spatially correlated data. *Geochemistry, Geophysics, and Geosystems* 7, Q08003, DOI:10.1029/2006GC001297.

Golub, G.H. and C.F. Van Loan. 1996. *Matrix Computations*, 3rd edition. Johns Hopkins University Press.

International Hydrographic Organization. 1998. *IHO Standards for Hydrographic Surveys*, Special Publication No. 44, 4th Edition.

Jakobsson, M., B. Calder, and L. Mayer. 2002. On the effect of random errors in gridded bathymetric compilations. *Journal of Geophysical Research – Solid Earth* 107(B12).

Kielland, P. and T. Tubman. 1994. On estimating map model errors and GPS position errors: applying more science to the art of navigation. *Navigation* 41:479-499.

Kostylev, V.E., B.J. Todd, G.B.J. Fader, R.C. Courtney, G.D.M. Cameron, and R.A. Pickrill. 2001. Benthic habitat mapping on the Scotian shelf, based on multibeam bathymetry, surficial geology and sea floor photographs. *Marine Ecology Progress Series* 219:121-137.

The MathWorks Inc. 2003. *MATLAB version 7.13 (R2011b)* Natick, Massachusetts.

Mayer, L., L. Fonseca, M. Pacheco, S. Galway, J. Martinez, and T. Hou. 1999. *The STRATAFORM GIS*, U.S. Office of Naval Research (ONR), St. Andrews, Canada.

Nitrouer, C. STRATAFORM: overview of its design and synthesis of its results. *Marine Geology* 154(1-4):3-12.

Särkkä, S. 1999. *Kernel1 function (for MATLAB)*. Downloaded November 2011.

Schwab, W.C., W. Corso, M.A. Alison, J.F. Denny, L. Lotto, W.W. Danforth, D.S. Foster, T.F. O'Brien, D.A. Nichols, B.J. Irwin, and K.F. Parolski. 1997a. Mapping the sea floor geology offshore of the New York-New Jersey metropolitan area using sidescan sonar: preliminary report. U.S. Geological Survey Open-File Report 97-61.

Schwab, W.C., M.A. Allison, W. Corso, L.L. Lotto, B. Butman, M. Buchholtz ten Brink, J. Denny, W.W. Danforth, and D.S. Foster. 1997b. Initial results of high-resolution sea-floor mapping offshore of the New York - New Jersey metropolitan area using sidescan sonar. *Northeastern Geology and Environmental Sciences* 19(4):243-262.

Tagliasacchi, A. 2011. *KD-Tree (Library for MATLAB)*. Downloaded August 2011 from <http://www.mathworks.com/matlabcentral/fileexchange/21512-kd-tree-for-matlab>.

Tobler, W. 1970. A computer movie simulating urban growth in the Detroit region. *Economic Geography* 46:234-240.

This page intentionally left blank.

Surficial Sediments

Matthew Poti^{1,2,3}, Brian Kinlan^{1,2}, and Charles Menza²

3.1. SUMMARY

Mapping seafloor features, including sediment characteristics and distribution, provides crucial information for a number of coastal and marine spatial planning applications. Seafloor maps can be used to help identify critical habitat areas for benthic organisms (e.g., clams, corals, demersal fish), select appropriate offshore construction sites, and plan sand/gravel mining operations.

Predictive models of mean grain size, sediment composition, and hard bottom occurrence were developed for the New York study area (Figure 1.2). These new models build upon the data compilations and analytical frameworks laid out by Goff et al. (2008), Poppe et al. (2005) and Greene et al. (2010), respectively. For mean grain size and sediment composition, the models



Image 3.1. Example of sand waves. Photo credit: NOAA/CCMA/Biogeography Branch.

provide continuous, gridded spatially-explicit prediction surfaces and corresponding uncertainty estimates. The hard bottom occurrence model also provides a continuous gridded prediction surface representing the likelihood of hard bottom occurrence. All information was mapped on the same 30 arc-second horizontal resolution grid used to characterize ocean habitat and seabird variables in Chapters 4 and 5 of this report.

3.2. BACKGROUND

The New York study area, like other broad continental shelf regions in the northeastern United States, is characterized by spatially variable seafloor features that have formed as a result of dynamic marine geological processes, particularly the dramatic (>100 m) rise in sea level following the last glaciation (Williams et al., 2006; Goff et al., 2008). The present distribution of surficial sediments in the region reflects deposition, erosion, and other sedimentological processes during this period of sea level rise (Williams et al., 2006).

The continental shelf within the study area has relatively simple topography and slopes gently from the shore to the shelf edge 100-150 km from shore (Allen et al., 1983). The seafloor on the continental shelf is composed mostly of sand which grades to silt and clay in deeper areas (Poppe et al., 1994). The relatively homogeneous seafloor is interrupted by sporadic relic sand and gravel ridges, exposed sandstone and bedrock, dumping sites, dredge disposal sites, and artificial reefs (e.g., shipwrecks, lost cargo, submerged pipelines). The most pronounced topographic features in the study area are the Hudson Shelf Valley, which crosses the entire shelf at the southern end of the study area (Butman et al., 2003), and many shelf edge incisions made by submarine canyons. The Hudson Canyon connects to the Hudson Shelf Valley and is the largest submarine canyon on the U.S. Atlantic continental margin (Butman et al., 2006).

Mapping seafloor sediment characteristics is challenging, in part, because of the high variability of sediment characteristics at relatively short spatial scales. Characterization of physical features of the seafloor is often limited by the availability of comprehensive sampling across a wide range of spatial scales (Goff et al., 2008). Traditional bottom grab, core, trawl and camera surveys are limited in their spatial coverage. One solution to this

¹ Consolidated Safety Services, Inc.

² Biogeography Branch, Center for Coastal Monitoring and Assessment, National Centers for Coastal Ocean Science, National Ocean Service, National Oceanic and Atmospheric Administration

³ Corresponding author: Matthew.Poti@noaa.gov

problem developed in recent decades is the use of acoustic backscatter information to characterize physical properties of seafloor sediments (e.g., Lathrop et al., 2006; De Falco et al., 2010; Harris and Stokesbury, 2010; Brown et al., 2011).

Multibeam and sidescan sonar surveys completed in the New York study area (see Figure 2.1) recorded acoustic backscatter or reflectance data. If appropriately processed, this information can provide fine-scale sediment composition maps in areas of coverage. Acoustic backscatter data is not, however, uniformly available across the NY study area. Moreover, Goff et al. (2008) stressed geographic variability in the relationship between acoustic backscatter and sediment characteristics owing to differences in environmental factors like bathymetric slope and water column properties. They suggested that extensive direct sampling of surficial sediments is needed to assess the correlation between backscatter intensity and sediment character from region to region, which limits its utility to densely ground-truthed areas.

An alternative method is to statistically model the spatial distribution of sediment using large databases assembled from many surveys. Goff et al. (2008) proposed and illustrated this method using the recently compiled U.S. Geological Survey (USGS) Atlantic Coast usSEABED database (Reid et al., 2005). The usSEABED database provides an extensive and heterogeneous collection of seabed survey data derived from a number of sources. The database includes both “extracted” information derived from analytical measurements and “parsed” information that is inferred from word-based descriptions (Reid et al., 2005). Goff et al. (2008) found that usSEABED parsed and extracted mean grain size data were suitable for use in sediment mapping even though data were collected using a range of methodologies across several decades, provided they were appropriately quality-controlled and bias-corrected. The predictive models described in this chapter are built on quality-controlled and bias-corrected usSEABED data.

Two notable additional mapping efforts have produced sediment grain size distribution maps for the U.S. Atlantic coast. First, the USGS Continental Margin Mapping (CONMAP) Program developed a coarse-scale sediment grain size distribution map for the U.S. East Coast continental margin through the analysis and compilation of thousands of sediment samples, many of which are part of usSEABED. The CONMAP sediment data layer is a vector dataset with polygons classified according to the dominant surficial sediment type (Poppe et al., 2005). The metadata provided with the CONMAP sediment data layer indicates that this dataset does not capture localized features of sediment distribution and should be used mainly to describe regional trends in sediment grain size distribution (Poppe et al., 2005). It is therefore useful mainly as a qualitative mapping aid. Second, as part of the Northwest Atlantic Marine Ecoregional Assessment, The Nature Conservancy (TNC) produced a map of soft sediment characteristics using an interpolation of mean grain size point data from the usSEABED sediment database (Greene et al., 2010). A point dataset of hard bottom locations derived from the usSEABED dataset and National Marine Fisheries Service (NMFS) bottom trawl survey data was overlaid on the soft sediment map to identify hard bottom areas (Greene et al., 2010). The TNC maps were aimed at broad scale regional planning and did not provide a spatial assessment of map accuracy.

The present study aims to build on previous mapping efforts by developing maps more appropriate for fine scale planning decisions in the NY study area, with spatially explicit accuracy maps.

3.3. METHODS

3.3.1. Study Region and Grid

Predictions for mean grain size, sediment composition and the likelihood of hard bottom occurrence were made on a 30 arc-second spatial resolution geographic grid spanning the New York study area. The same grid was applied to predict oceanographic variables (Chapter 4) and seabird distributions (Chapter 6). The 30 arc-second grid has a north-south linear dimension of 0.927 km and an average east-west linear dimension of 0.814 km in the study area. For simplicity, decimal degrees were used to keep track of grid cell centroids and measure distances using a simple elliptical geodetic approximation; the effects of this simplifying assumption were negligible given the size of our study region and grid configuration (potential errors in linear distances < 50% of grid cell horizontal resolution).

3.3.2. Mean Grain Size

Data Preparation

We obtained the quality-controlled, bias-corrected, merged parsed and extracted database of mean sediment grain size (ϕ) described in Goff et al. (2008) from the lead author of that study (Dr. John Goff, University of Texas at Austin). Mean grain size is reported in ϕ units, where $\phi = -\log_2(\text{mean grain diameter in mm})$ (Krumbein and Sloss 1963). In this scale, gravel corresponds to -6 to -1 ϕ , sand corresponds to -1 to 4 ϕ , and mud corresponds to 4 to 12 ϕ .

Goff’s dataset was derived from the publicly available usSEABED Atlantic Coast Offshore Surficial Sediment Data Release, version 1.0 (Reid et al., 2005). The original usSEABED extracted and parsed datasets were filtered to remove records that did not relate to surficial sediments. At locations with multiple records pertaining to surficial sediments, mean grain size was averaged. Since the laboratory-based analyses used to generate the extracted data may exclude hard components like shell and gravel and may therefore introduce a bias toward finer particles (Williams et al., 2006; Harris and Stokesbury, 2010), the parsed data were bias-corrected as described in Goff et al. (2008) prior to merging the extracted and parsed data. Goff’s data covered only the mid-Atlantic portion of the U.S. Atlantic coast. We extracted a subset of the data including the NY study area for further analysis.

Development of the Mean Grain Size Model

A geostatistical modeling approach was used to predict a continuous, gridded surface for surficial sediment mean grain size from scattered sediment survey point data and to generate corresponding spatially-explicit uncertainty estimates. The same general modeling approach used for the bathymetry prediction and described in Section 2.3.1 was used for this analysis and is not reiterated here (see Cressie 1993 and Figure 2.3 for work flow). All geostatistical modeling steps were performed in ArcGIS 10 using the Spatial Analyst and Geostatistical Analyst toolboxes (ESRI 2011a).

The deterministic mean trend was estimated using local polynomial interpolation (LPI), a semi-parametric local regression technique that creates a prediction surface by fitting polynomial functions of a specified degree to data in overlapping search neighborhoods defined by a constant search radius, or bandwidth (ESRI 2011a). LPI uses weighted least-squares regression, with weights equal to 0 outside the search neighborhood, and a Gaussian function of distance inside the search neighborhood. LPI was chosen over other techniques because it provides approximate parametric confidence intervals, and because bandwidth can be adjusted to ensure that only broad-scale trends are captured, leaving more localized information in residuals. LPI outputs are a prediction surface, an approximate parametric prediction standard error surface, indicating the uncertainty associated with the prediction at each location, and a spatial condition number surface, indicating the stability of the local regression model at each location. Higher spatial condition number values indicate that the solution is less stable, such that small variations in the input data (e.g., uncertainty due to measurement error) can result in large variations in the prediction. For second order polynomials, the critical spatial condition number threshold value is 100 (Golub and Van Loan, 1996), meaning that predictions should be considered with caution at locations where the spatial condition number is close to 100 and should be considered unreliable where it is greater than 100. We used second degree (quadratic) polynomials, an eight sector circular search neighborhood with 1 decimal degree bandwidth (~111 km), and Gaussian kernel weights. At least 10 and no more than 250 data from each sector were used to produce each trend prediction. The eight-sector neighborhood search was used to mitigate the effects of uneven sample distribution on the trend surface estimation.

Residuals were obtained by subtracting the trend surface prediction at each data location from the observed data value. Residuals were checked for normality by examining histogram and normal QQ plots. A sample semivariogram of the residuals was then calculated in ArcGIS 10 using the Geostatistical Analyst extension (ESRI, 2011a). Lag size was selected based on examining the distribution of nearest-neighbor distances, choosing the smallest lag size that would allow sufficient samples to estimate semivariance values near the origin. Anisotropy (i.e., changes in spatial autocorrelation due to direction) was checked using directional semivariograms. To model spatial autocorrelation in residuals, a constrained weighted least squares algorithm was used to fit an exponential anisotropic model to the sample semivariogram (model parameters in Table 3.1).

Fitted semivariogram model parameters were used to perform ordinary kriging (OK) of the residuals in ArcGIS 10 using eight-sector search neighborhoods and anisotropic search neighborhood radii equal to the radii of the anisotropic semivariogram model. At least 5 and no more than 25 data points from each sector were used to produce kriging predictions on a 30 arc-second grid. Kriging predictions were generated at the centroid of each grid cell. We confirmed that centroids did not intersect with data point locations, so that the nugget effect (measurement error and small-scale variance) was “filtered out” of the kriging prediction. This resulted in a desirable noise reduction in the prediction surface, equivalent to the maximum a posteriori resampling algorithm used by Goff et al. (2006, 2008).

Table 3.1. Semivariogram parameters for the mean grain size model.

DATA	n	TYPE OF VARIOGRAM MODEL	NO. OF LAGS	LAG SIZE (km) ^b	NUGGET	MAJOR RANGE (km) ^b	MINOR RANGE (km) ^b	DIRECTION (°) ^c	PARTIAL SILL	% OF THE SILL DUE TO THE NUGGET
Mean Grain Size ^a	14,612	Exp	50	1.11	1.26	24.44	12.22	288.05	0.98	56.25

a - in ϕ units, where $\phi = -\log_2(\text{mean grain diameter in mm})$; b - converted from decimal degrees to kilometers using 111.1 km/decimal degree;

c - clockwise from North; Exp = Exponential

The model surface representing the predicted mean grain size was calculated as the sum of the trend (LPI) and residual (kriging) prediction surfaces. The corresponding prediction standard error surface was calculated as the square root of the sum of the trend and kriging prediction variances (errors in the trend and residual surfaces are assumed to be independent). The final prediction and prediction standard error surfaces were exported as ESRI grids with the extent and spatial resolution described in Section 3.3.1. An error mask was applied to the output grids to exclude areas where the kriging standard error was greater than 97.5% of the residual sample standard deviation. This error mask was applied to all surficial sediment outputs for consistency.

In addition to the prediction and prediction standard error maps, a vector dataset with polygons classified by mean grain size classes was generated by assigning each grid cell a mean grain size class using the classification scheme of Wentworth (1922). Finally, the probability of mean grain size exceeding the thresholds 25.6 cm ($\phi < -8$, boulders and larger), 6.4 cm ($\phi < -6$, cobbles and larger), 2 mm ($\phi < -1$, pebbles and larger), and 0.062 mm ($\phi < 4$, very fine sand and larger) were mapped, by integrating under the normal distribution defined for each grid cell by the OK prediction mean and variance.

3.3.3. Sediment Composition

Data Preparation

Seabed survey data from the usSEABED Atlantic Coast Offshore Surficial Sediment Data Release, version 1.0 (Reid et al., 2005) parsed and extracted databases were used to develop models of the fractional composition of mud, sand, and gravel in surficial sediments in the study area. Data were downloaded from the USGS publications website (<http://pubs.usgs.gov/ds/2005/118/htmldocs/usseabed.htm>). The dataset provided by Dr. Goff for the mean grain size analysis was not used for sediment composition modeling because it did not include percentages of mud, sand, and gravel. The survey point data was filtered to remove duplicate points and points not relating to surficial sediments. Survey records were removed if the “sample phase” attribute for the database record indicated that the sample was clearly not from surficial sediments (e.g., from the bottom of the sample core). When multiple records referred to the same sample core, the record that described the top of the sample core (as indicated by the “sample top” attribute) was retained and the other records were removed. When multiple records pertaining to surficial sediments existed at a location, values for percent mud, percent sand, and percent gravel were averaged. When the sum of all fractions exceeded 100%, each of the mud, sand, and gravel percentages was divided by the sum to re-normalize sums to 100% (sums were seldom greater than 110% so any error introduced by this re-normalization procedure would be small). Separate datasets for each sediment type were extracted, excluding records with “no data” for the given sediment type (but including 0% values). Percentages were converted to fractional values between 0 and 1 for subsequent processing.

Development of the Sediment Composition Models

The same geostatistical approach used to model mean grain size (see Section 3.3.2) was applied separately to each of the individual sediment type datasets. The deterministic mean trend was fit using the same LPI parameters as described for the mean grain size model in Section 3.3.2. Specific exponential anisotropic models for each sediment type were fitted to the sample semivariogram as described in Section 3.3.2 (model parameters are shown in Table 3.2). Fitted semivariogram model parameters were used to perform ordinary kriging (OK) following the same procedures outlined in Section 3.3.2.

Table 3.2. Semivariogram parameters for the sediment composition models.

DATA	n	TYPE OF VARIOGRAM MODEL	NO. OF LAGS	LAG SIZE (km) ^a	NUGGET	MAJOR RANGE (km) ^a	MINOR RANGE (km) ^a	DIRECTION (°) ^b	PARTIAL SILL	% OF THE SILL DUE TO THE NUGGET
Mud Fraction	30,126	Exp	50	1.11	0.064	24.44	12.22	82.44	0.15	29.91
Sand Fraction	30,127	Exp	50	1.11	0.082	24.44	12.22	77.87	0.16	33.88
Gravel Fraction	30,115	Exp	50	1.11	0.04	24.44	12.22	141.5	0.045	47.06

a - converted from decimal degrees to kilometers using 111.1 km/decimal degree; b - clockwise from North; Exp = Exponential

Maps representing the predicted fraction for each sediment type were calculated as the sum of the trend (LPI) and residual (kriging) prediction surfaces. The corresponding prediction standard error surfaces were calculated as the square root of the sum of the trend and kriging prediction standard error surfaces (errors in the trend and residual surfaces are assumed to be independent). The final prediction and prediction standard error surfaces were exported as ESRI grids with the extent and spatial resolution described in Section 3.3.1. An error mask was applied to the output grids as described in Section 3.3.2.

Following Goovaerts (1997) and Deutsch and Journel (1998) each sediment type prediction surface was corrected for order violations by setting values less than zero to zero and values greater than one to one and by dividing each prediction value by the sum of the three prediction surfaces where their sum exceeded one. Where the sum was less than one we did not divide by the sum of the prediction surfaces, as some sediment could have been neither mud, sand, nor gravel (e.g., clay).

In addition to the prediction and prediction standard error maps for each sediment type, a vector dataset with polygons classified by sediment texture classes was generated by assigning each grid cell a sediment texture class using the Folk classification scheme (Folk 1954, 1974) based on the predicted ratios of sediment types.

3.3.4. Hard Bottom Occurrence

Data Preparation

An integrated point dataset of known hard bottom locations was built from three sources of seabed survey data and used to develop a prediction surface for the likelihood of hard bottom occurrence. First, we identified locations in the usSEABED Atlantic Coast Offshore Surficial Sediment Data Release, version 1.0 (Reid et al., 2005) parsed and extracted databases where the Shepard code for the point was “solid” or the rock membership value was greater than zero (for description of the rock membership value see Reid et al., 2005). Second, we searched the “National Oceanic and Atmospheric Administration (NOAA)/National Ocean Service (NOS) and U.S. Coast and Geodetic Survey (USCGS) Bottom Type Descriptions from Hydrographic Surveys” database archived at the NOAA National Geophysical Data Center (NOAA NGDC 2011) for point locations where hydrographic survey annotations had described the bottom type as hard or rocky. Third, The Nature Conservancy (TNC) provided a hard bottom point dataset compiled from information in the usSEABED database (Reid et al., 2005) and the National Marine Fisheries Service (NMFS) bottom trawl dataset as part of the Northwest Atlantic Marine Ecoregional Assessment (Greene et al., 2010; J. Greene, pers. comm.;

M. Fogarty, pers. comm.). We merged points from these three data sources and removed surveys with identical geographic coordinates. Sample distribution bias can have strong effects on presence-only models (Phillips et al., 2009; Elith et al., 2011). To create a dataset with more uniformly distributed sample effort, we removed hard bottom points in densely surveyed nearshore areas.

Development of the Hard Bottom Occurrence Model

In contrast to other predictive models developed in this report, a geostatistical model could not be applied to the hard bottom point data, because the available hard bottom datasets were restricted to presences, rather than absences, of hard bottom. The lack of absence data arises because hard bottom is very patchily distributed even at very small scales (centimeters to meters). A point sample such as a sediment core that brings up soft sediment does not preclude the presence of hard bottom in the immediate vicinity. Any geostatistical model developed using the unreliable absence data would be heavily biased and uninformative. Reliable absence data for hard bottom generally requires diver, remotely operated vehicle (ROV), photo, video, or acoustic backscatter data that continuously covers large swaths of area; generally impractical in deeper waters.

For this reason, a maximum entropy (MaxEnt) model was used to predict the likelihood of hard bottom occurrence by combining the presence-only hard bottom point dataset with potential predictor variables (Phillips et al., 2006; Phillips and Dudik, 2008). This approach can be thought of as creating a “suitability map” for the presence of hard bottom patches, analogous to habitat suitability maps developed for organisms (Elith et al., 2011). A full description of the MaxEnt algorithm is beyond the scope of this document (see Elith et al., 2011). Briefly, MaxEnt produces an estimate of the relative likelihood of a feature’s occurrence at each location in a specified grid, assuming that presences take on the most spatially random (uniform) distribution possible under the constraint that for each environmental predictor variable the expected value from the estimated distribution matches its observed mean (Elith et al., 2006; Phillips et al., 2006; Peterson et al., 2007). MaxEnt models are trained on a subset of the data and validated by testing predictions on remaining data. MaxEnt has been shown to perform well compared to other presence-only approaches (Elith et al., 2006; Phillips and Dudik, 2008), and is readily implemented using free, open-source software (Phillips et al., 2006, downloadable at <http://www.cs.princeton.edu/~schapire/maxent/>).

Environmental predictor variables used to train the model of hard bottom occurrence included mean grain size, depth, slope, slope of slope, bathymetric variance, distance from shore, signed distance from shelf, sea surface chlorophyll concentration, and turbidity. All of these predictors are described in Chapters 4 and 6, with the exception of bathymetric variance (calculated as the standard deviation of the depth in ~900 m rectangular neighborhoods). The same transformations described in Appendix 6.B were applied to mean grain size, depth, slope, slope of slope, distance from shore, signed distance from shelf, chlorophyll, and turbidity. Although transformation is not strictly necessary for MaxEnt, we found that transforming predictors improved cross-validation model performance. Eighty percent of the hard bottom presence points were used to build (train) the model and 20% of the points were randomly withheld to test the model. MaxEnt is more robust than regression techniques to the inclusion of large sets of potential predictor variables (Elith et al., 2011), so no model selection was carried out to reduce the size of this predictor set.

MaxEnt provides three post-hoc assessments of the relative importance of predictor variables. First, the MaxEnt program provides a summary of how much each predictor contributes to the gain of the model, accumulated for each predictor over the course of the training algorithm. Second, the MaxEnt program randomly permutes the values for each predictor (one at a time) and determines the resulting decrease in the area under the training model receiver operating characteristic curve (AUC). This provides a measure of how strongly the model depends on each predictor. Third, the MaxEnt program estimates predictor importance using a jackknife approach, in which it re-runs the model for each predictor, first building the model with all variables except the predictor of interest, and then building the model with only the predictor of interest. If a predictor is highly correlated with the other predictors, withholding it will have little impact on model performance. Therefore, an important and non-redundant predictor will have high explanatory power by itself and its omission from the model will result in a significant reduction in predictive power.

The final map of the “hard bottom occurrence likelihood index” consisted of a logistic transformation of MaxEnt’s raw output to produce a smooth index between 0 and 1 (this is the default output of the MaxEnt program). It is related to the probability of occurrence, but is not strictly a probability (Elith et al., 2011). It should be considered an index of the relative likelihood of hard bottom occurrence, rather than a strict measure of the probability of encountering hard bottom. All of the issues and caveats related to interpretation of ecological models based on presence-only data are applicable (Elith et al., 2011).

3.3.5. Model Validation

The performance of mean grain size and sediment composition models was evaluated by two methods: leave-one-out cross-validation and qualitative comparison to an independent sidescan sonar backscatter dataset. Leave-one-out cross validation of kriging predictions was performed in ESRI Geostatistical Analyst (ESRI 2011a) as described in Goovaerts (1997). Cross-validation statistics were calculated as described in ESRI (2011b). Qualitative comparisons to acoustic backscatter data followed Goff et al. (2008). Model prediction maps were presented alongside existing 100-120 kHz backscatter data collected by USGS in the New York Bight region (Schwab et al., 2000; Schwab et al., 2002) and visually interpreted. In general, acoustic backscatter intensity is lower where there are fine sediments and higher where there are coarse sediments (Ferrini and Flood, 2006; DeFalco et al., 2010).

In addition to qualitative comparison with acoustic backscatter data, the hard bottom occurrence model performance was evaluated using cross-validation on the 20% of data withheld from training. Cross-validation performance was evaluated using the Area-Under-Curve (AUC) statistic of the receiver operating characteristic (ROC)-like MaxEnt output (Fielding and Bell, 1997). Traditional ROC curves plot the true positive rate (sensitivity) versus the false positive rate (1 – specificity) for the range of potential threshold values, with the AUC statistic providing a measure of how well the model maximizes the true positive rate for low values of the false positive rate. The AUC statistic ranges from 0.5 (no better than random) to 1.0 (a perfect prediction). An AUC statistic greater than 0.75 is generally indicative of a potentially useful model, and ROC curves for high performing models will approach the upper left corner of the plot (Fielding and Bell, 1997; Peterson et al., 2007). The ROC-like analysis used by MaxEnt differs in that it substitutes the fractional predicted area for the specificity since there is no absence data from which to measure specificity (the true negative rate). As a result the maximum achievable AUC is less than one (Phillips et al., 2006).

3.4. RESULTS AND DISCUSSION

3.4.1. Mean Grain Size

Model Predictions

The model of mean grain size extended just past the continental shelf edge and provided predictions of mean grain size for the majority of the study area. The model did not extend into Long Island Sound (LIS) because Goff et al. (2008) did not include LIS in their quality-controlled dataset. An additional reason for excluding LIS was that the geostatistical model developed for the open ocean system (most of the study area) would not have applied to the geomorphologically distinct, enclosed Long Island Sound system. The model did not extend far past the continental shelf edge due to lack of sufficient sampling effort. The model predicted that much of the seafloor is covered by sediment with a mean grain size characteristic of coarse to medium sand (0-2 ϕ), with areas having mean grain size characteristic of finer sand and silt (4-6 ϕ) within the upper reaches of the Hudson Shelf Valley, offshore of the shelf break, and in the area of the Block Island Delta and Block Island Valley. The model predicted that mean grain sizes characteristic of coarse to medium sand covered ~60% of the study area, mean grain sizes characteristic of fine to very fine sand covered ~32% of the study area and mean grain sizes characteristics of silt covered ~8% of the study area (Figure 3.1, Figure 3.2, Table 3.3).

Model Uncertainty

Model standard error ranged from ~1.2 ϕ units for grid cells with a very high density of seafloor surveys to ~1.6 ϕ units for grid cells farthest from survey locations, such as the area farthest offshore (Figure 3.3). Model uncertainty of this magnitude corresponds to theoretical 95% confidence intervals (± 1.96 *standard error) ranging from the mean grain size prediction ± 2.4 ϕ units in densely surveyed areas to the prediction ± 3.2 ϕ units where surveys were more sparse. For example, a mean grain size prediction of 1 ϕ in a densely

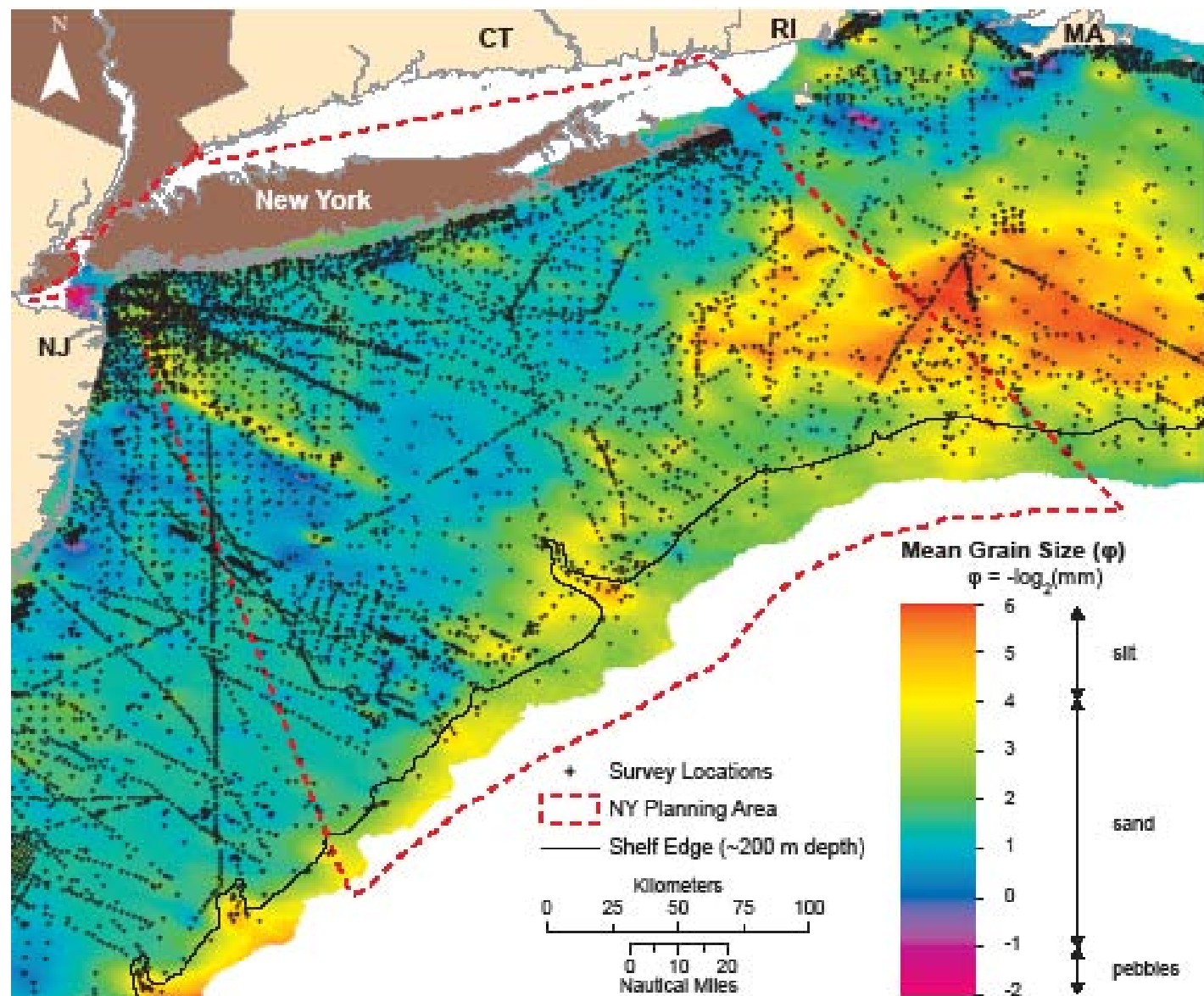


Figure 3.1. Predicted mean grain size of surficial sediments from kriging interpolation of mean grain size data in the Mid-Atlantic Bight. Mean grain size is in ϕ units, where $\phi = -\log_2(\text{mean grain diameter in mm})$. Data courtesy of J. Goff (University of Texas at Austin), derived from USGS usSEABED database (Reid et al., 2005).

surveyed area could have a theoretical 95% confidence interval of $(-1.4 \phi, 3.4 \phi)$. In this case, the mean grain size prediction corresponds to coarse sand, but the confidence interval limits range from very fine pebbles to very fine sand. Given that sediment surveys in areas offshore of the continental shelf break were quite sparse and prediction accuracy in these areas is worse than in nearshore areas, model predictions offshore of the shelf break should be used with caution.

The predicted probabilities of exceeding mean grain size thresholds of 25.6 cm ($\phi < -8$, boulders and larger), 6.4 cm ($\phi < -6$, cobbles and larger), 2 mm ($\phi < -1$, pebbles and larger), and 0.062 mm ($\phi < 4$, very fine sand and larger) generally followed spatial patterns in mean grain size predictions. This is expected since these probability calculations assume a normal distribution of sediment grain sizes around the mean. The probabilities of having a mean grain size less than -8ϕ (boulders and larger) or less than -6ϕ (cobbles and larger) were essentially zero across the entire study area (Figure 3.4a, b). This does not mean that boulders and cobbles do not occur, only that they are almost never the mean grain size over any appreciable area (they are always mixed with other, finer sediment types), and/or they are very erratic in their occurrence (occurring only as isolated departures from the mean). The probability of having a mean grain size less than -1ϕ (pebbles and larger) was very low across most of the study area, but there were areas of higher probability corresponding

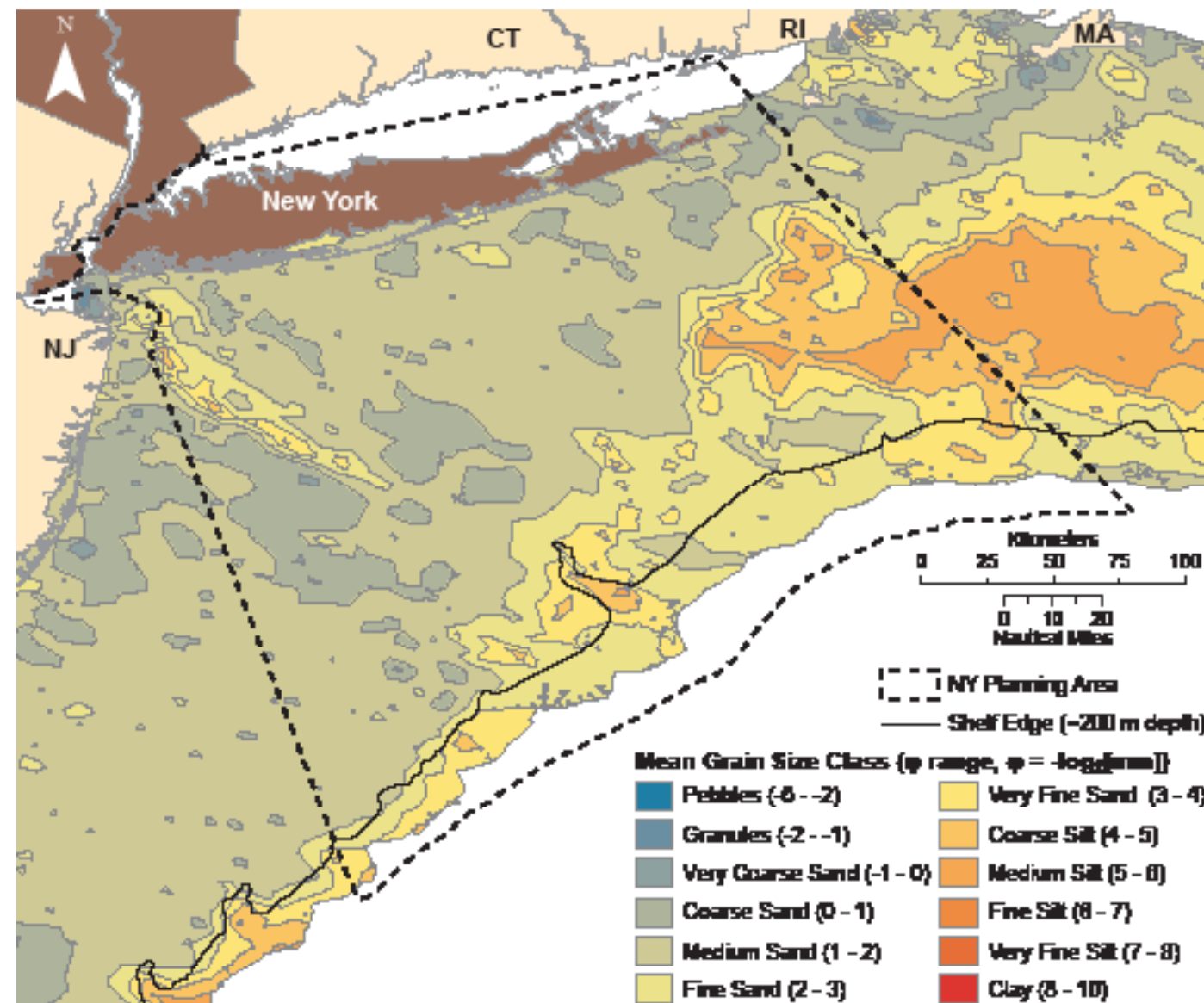


Figure 3.2. Distribution of predicted surficial sediment mean grain size classes, derived from kriging interpolation of mean grain size data in the Mid-Atlantic Bight. Mean grain size classes are defined based on Wentworth (1922). Data courtesy of J. Goff (University of Texas at Austin), derived from USGS usSEABED database (Reid et al., 2005).

Table 3.3. Total area and percent area of predicted mean grain size classes in the study area.

MEAN GRAIN SIZE CLASS ^a	MEAN GRAIN SIZE (ϕ) ^b	MEAN GRAIN SIZE (METRIC)	PREDICTED TOTAL AREA (km ²)	PREDICTED PERCENT AREA
Pebbles	-6 - -2	4 mm - 6.4 cm	1	0
Granules	-2 - -1	2 mm - 4 mm	12	0
Very Coarse Sand	-1 - 0	1 mm - 2 mm	38	0.1
Coarse Sand	0 - 1	0.5 mm - 1 mm	4,978	12.2
Medium Sand	1 - 2	0.25 mm - 0.5 mm	19,613	47.9
Fine Sand	2 - 3	0.125 mm - 0.25 mm	8,607	21.0
Very Fine Sand	3 - 4	0.062 mm - 0.125 mm	4,402	10.8
Coarse Silt	4 - 5	0.031 mm - 0.062 mm	2,525	6.2
Medium Silt	5 - 6	0.016 mm - 0.031 mm	734	1.8
Fine Silt	6 - 7	0.008 mm - 0.016 mm	0	0
Very Fine Silt	7 - 8	0.004 mm - 0.008 mm	0	0
Clay	8 - 10	0.001 mm - 0.004 mm	0	0

a - from Wentworth (1922)

b - $\phi = -\log_2(\text{mean grain diameter in mm})$

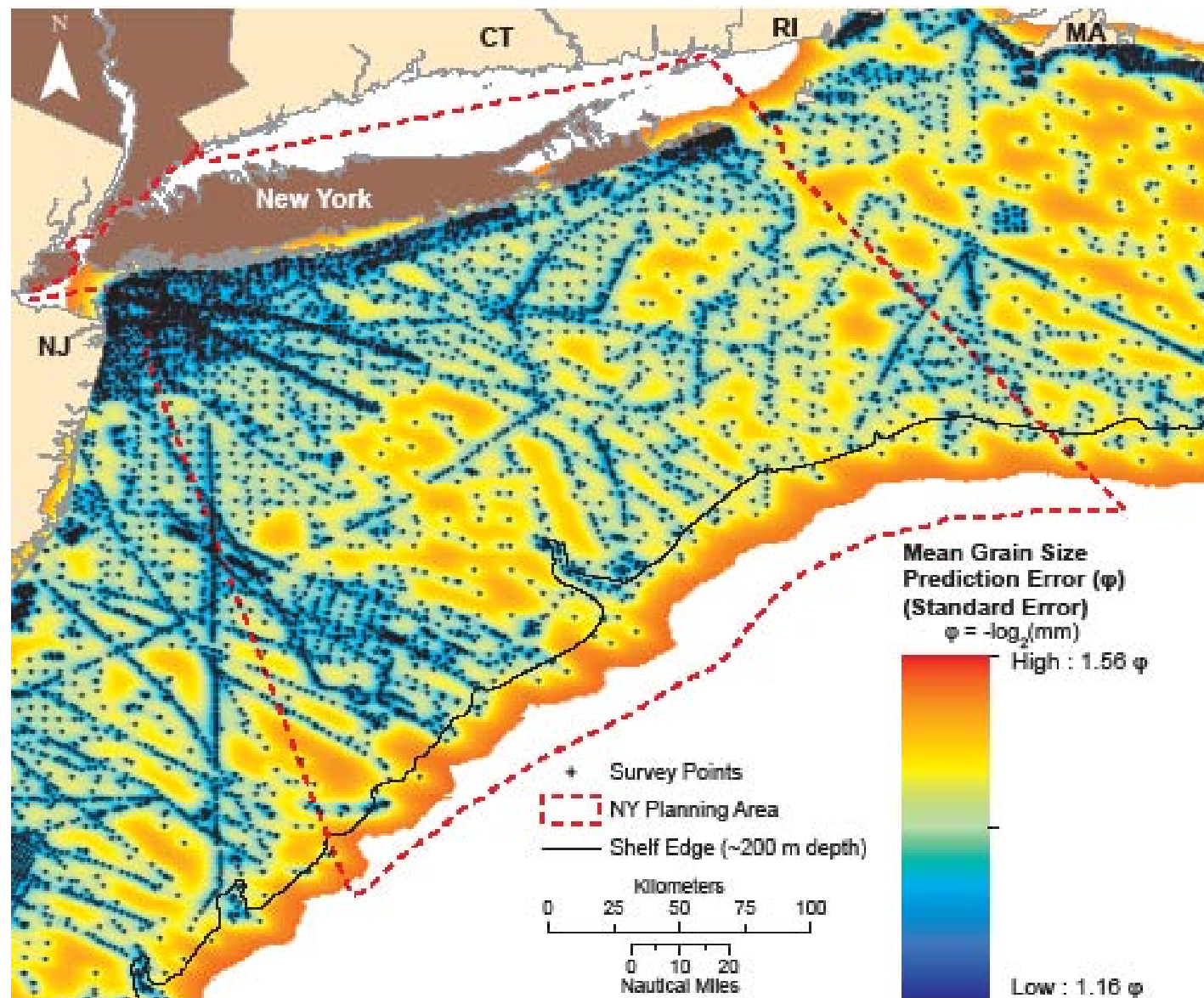


Figure 3.3. Surficial sediment mean grain size prediction standard error (in ϕ units, $\phi = -\log_2[\text{mean grain diameter in mm}]$) from kriging interpolation of the mean grain size data in the Mid-Atlantic Bight. Data courtesy of J. Goff (University of Texas at Austin), derived from USGS usSEABED database (Reid et al., 2005).

well with the areas mapped as pebbles by the mean grain size prediction model (Figure 3.1, Figure 3.4c). The probability of having a mean grain size less than 4ϕ (very fine sand and larger) was high across the study area, with areas of near zero probability corresponding to areas that were mapped as silt (Figure 3.1, Figure 3.4d).

Probabilities for each mean grain size threshold were also mapped with values standardized by the maximum probability values (Figure 3.5). These maps emphasize areas where the mean grain size has the highest relative likelihood of exceeding the indicated thresholds. Panels (a) and (b) of Figure 3.5 should be interpreted with some caution since the highest probabilities are near zero for thresholds of less than -8ϕ (boulders and larger) or less than -6ϕ (cobbles and larger).

Model Validation

Leave-one-out cross-validation of the mean grain size prediction model yielded a root-mean-square error (RMSE) of 1.4ϕ , which was reasonable given the magnitude of grain size measurement error (estimated to be on the order of 1ϕ unit; J. Goff, University of Texas at Austin, personal communication, February 11,

2011) and allowing for unresolved small-scale variance and model specification error. Cross-validation also indicated that the prediction errors were unbiased (mean standardized prediction error was near zero) and the assessment of prediction uncertainty was valid since the root-mean-square standardized error was close to one (Table 3.4).

Although the mean grain size prediction model was mapped at a considerably lower spatial resolution (30 arc-second grid cells have an average linear dimension of ~ 800 - 900 meters in the study area) than the USGS acoustic backscatter data (4 m grid cells) from Schwab et al. (2002), comparison of the mean grain size prediction map to the USGS backscatter data provided a qualitative assessment of the accuracy of the predictions for overlapping areas. In general, areas of high backscatter intensity (lighter shades) were associated with areas predicted to have coarser sediments, such as the areas labeled A and C in Figure 3.6. Also, the Hudson Shelf Valley (area labeled B in Figure 3.6) had low backscatter intensity and was predicted to have finer sediments. These comparisons were consistent with the conclusions of Ferrini and Flood (2006) and De Falco et al. (2010), who found that acoustic backscatter intensity is generally lower where there are fine sediments and higher where there are coarse sediments. However, the matchup is clearly not perfect, and without detailed calibration of backscatter to ground-truth samples it is difficult to say whether deviations between the two maps are due to inaccurate model predictions or variation in the backscatter surface not associated with sediment variation.

3.4.2. Sediment Composition

Model Predictions

Models of sediment composition provided predictions for most of the study area, from the southern shore of Long Island, where survey density was greatest, to just past the continental shelf edge (Figure 3.7).

The mud fraction model predicted that seafloor surficial sediments were composed

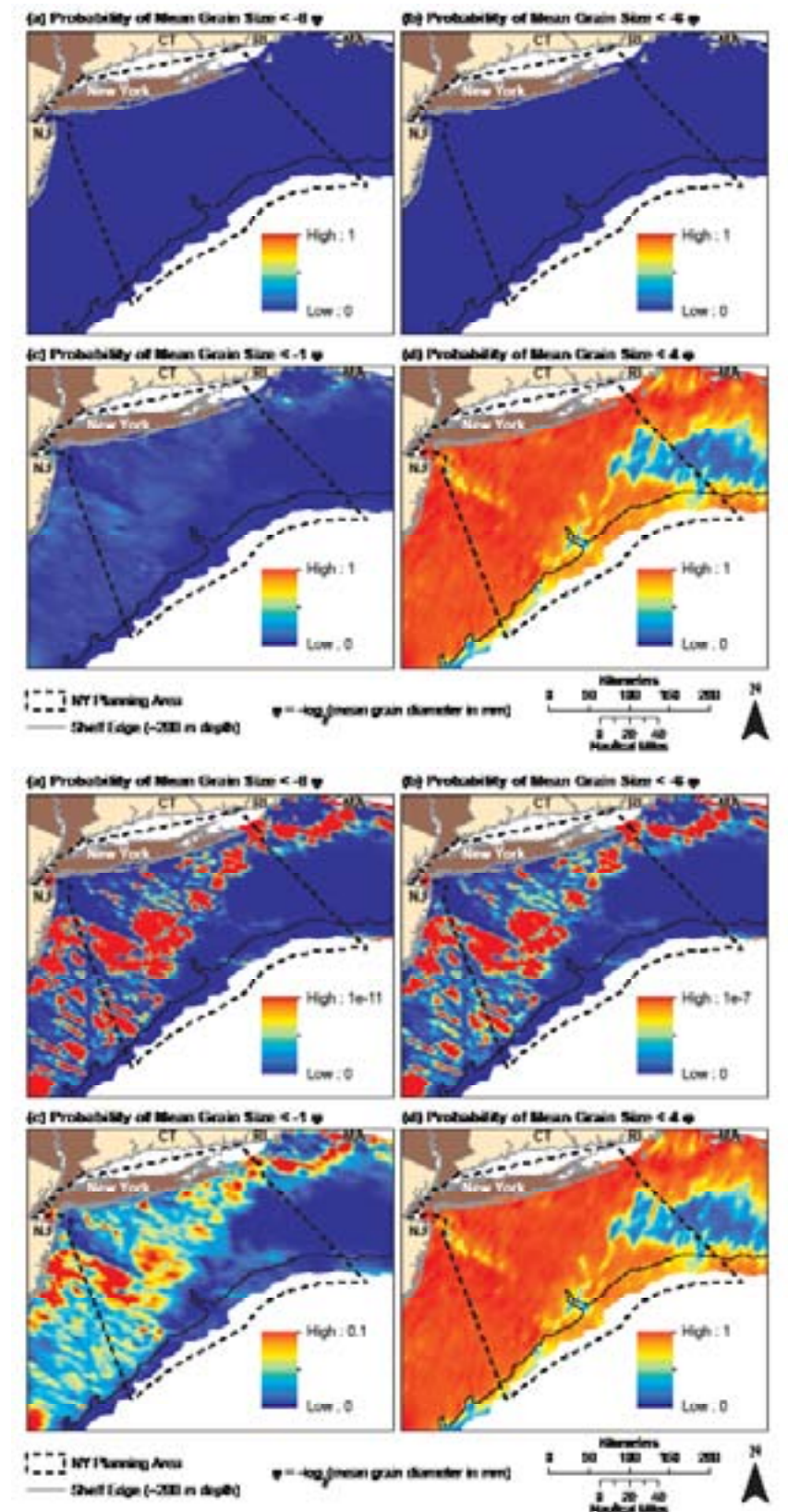


Figure 3.4 (top). Maps of the probability that surficial sediment mean grain size (in ϕ units, $\phi = -\log_2[\text{mean grain diameter in mm}]$) is less than threshold values of (a) -8ϕ (boulders and larger), (b) -6ϕ (cobbles and larger), (c) -1ϕ (pebbles and larger), and (d) 4ϕ (sand and larger). Figure 3.5 (bottom). Same as Figure 3.4, with probability values standardized by maximum probability of each corresponding threshold map. Values were adjusted to emphasize areas with the highest probabilities of exceeding each of the mean grain size thresholds. Data courtesy of J. Goff (University of Texas at Austin), derived from USGS usSEABED database (Reid et al., 2005).

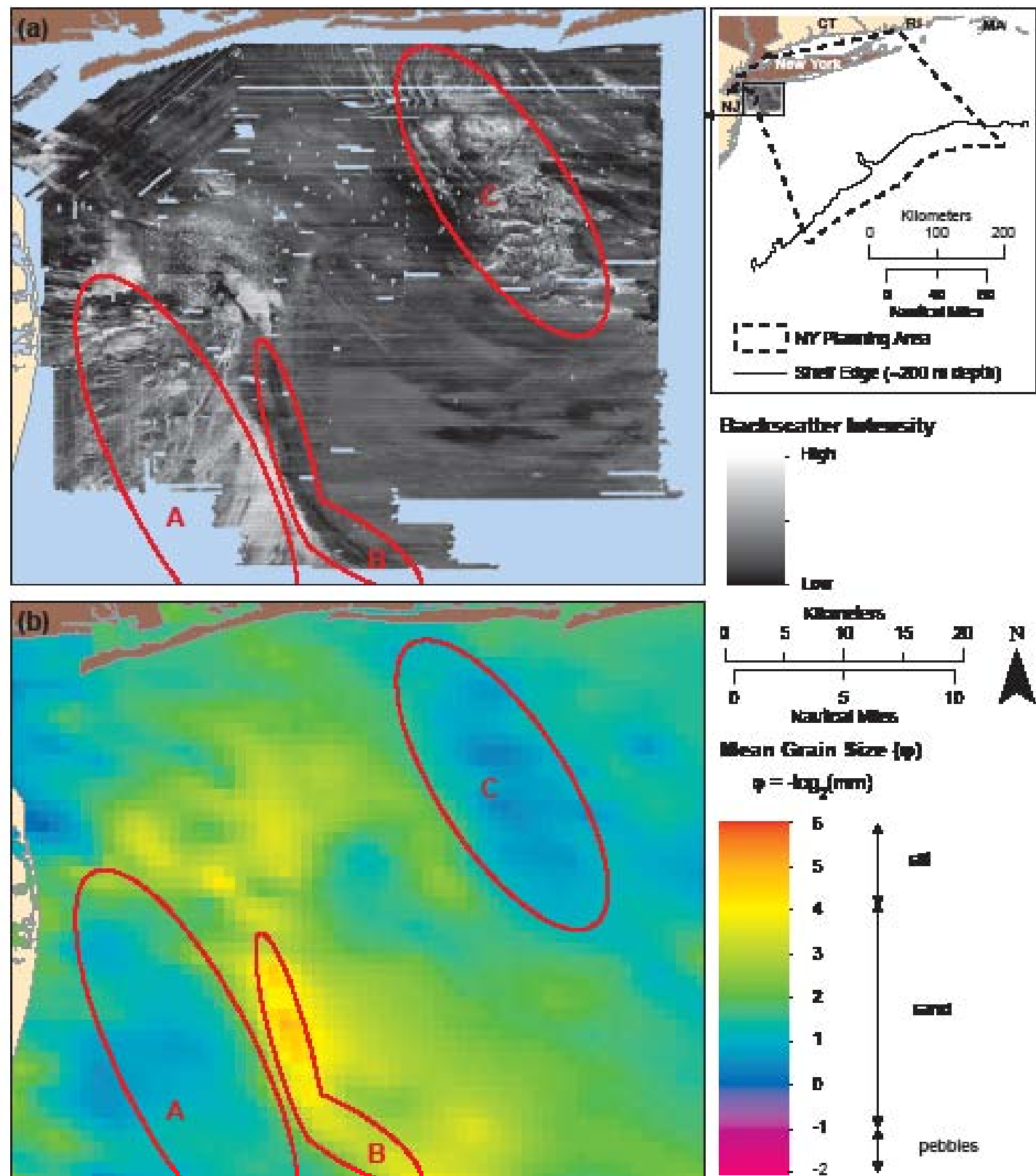


Figure 3.6. Comparison of overlapping portions of the (a) USGS acoustic backscatter data (from Schwab et al., 2002) and (b) surficial sediment mean grain size prediction (in ϕ units, $\phi = -\log_2[\text{mean grain diameter in mm}]$). In general, higher backscatter intensity indicates coarser sediments (e.g., coarse sand, pebbles) while lower backscatter intensity indicates finer sediments (e.g., sand and silt). Mean grain size data courtesy of J. Goff (University of Texas at Austin), derived from USGS usSEABED database (Reid et al., 2005).

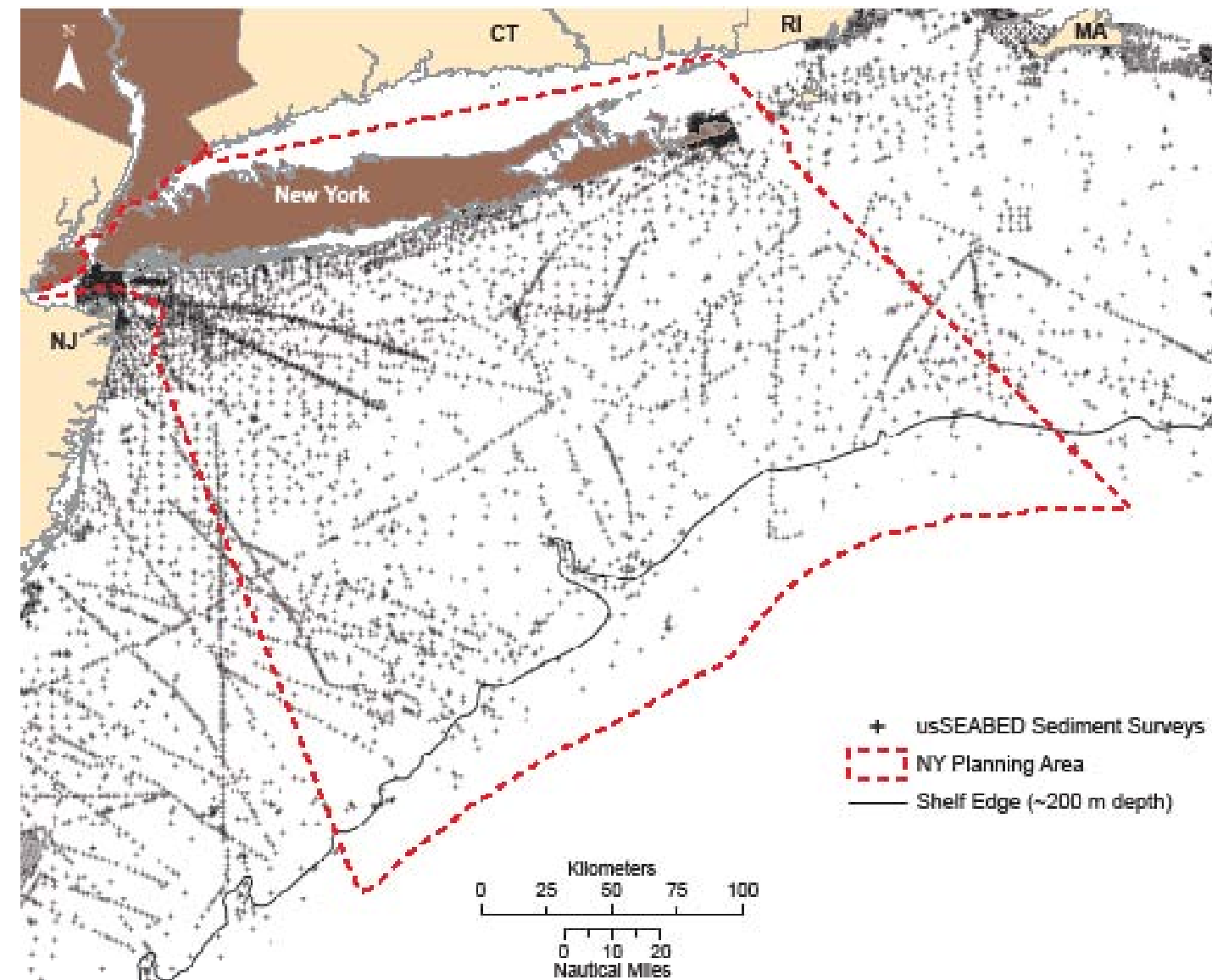


Figure 3.7. Locations of usSEABED sediment survey data in the study area. Data courtesy of USGS usSEABED database (Reid et al., 2005).

mostly of mud in several areas, including in the Hudson Shelf Valley, in and around the Hudson Canyon, along the continental shelf slope, and over a large swath south of Martha's Vineyard and Rhode Island between the 50 m and 100 m contours (Figure 3.8a). The sand fraction model predicted that surficial sediments were composed mostly of sand throughout most of the study area (Figure 3.8b), with the exception being those areas predicted to have mud-dominated sediments by the mud fraction model. The gravel fraction model predicted that surficial sediments were composed mostly of gravel in only a few small areas (Figure 3.8c). These areas corresponded to those mapped as pebbles or granules by the model of mean grain size (Figure 3.1). Under Folk's classification scheme (Folk 1954, 1974), just over half of the study area was mapped as gravelly sand or slightly gravelly sand (Figure 3.8d, Table 3.5). Another ~30% of the study area was mapped as having a mix of mud and sand with slight amounts of gravel. An almost negligible area was mapped as having predominantly gravel.

Table 3.4. Cross-validation statistics for the mean grain size model.

DIAGNOSTIC STATISTIC	VALUE
Bias	-0.0007
Root-Mean-Square Error (RMSE)	1.4090
Mean Standardized Prediction Error	-0.0004
Root-Mean-Square Standardized Error	1.0920

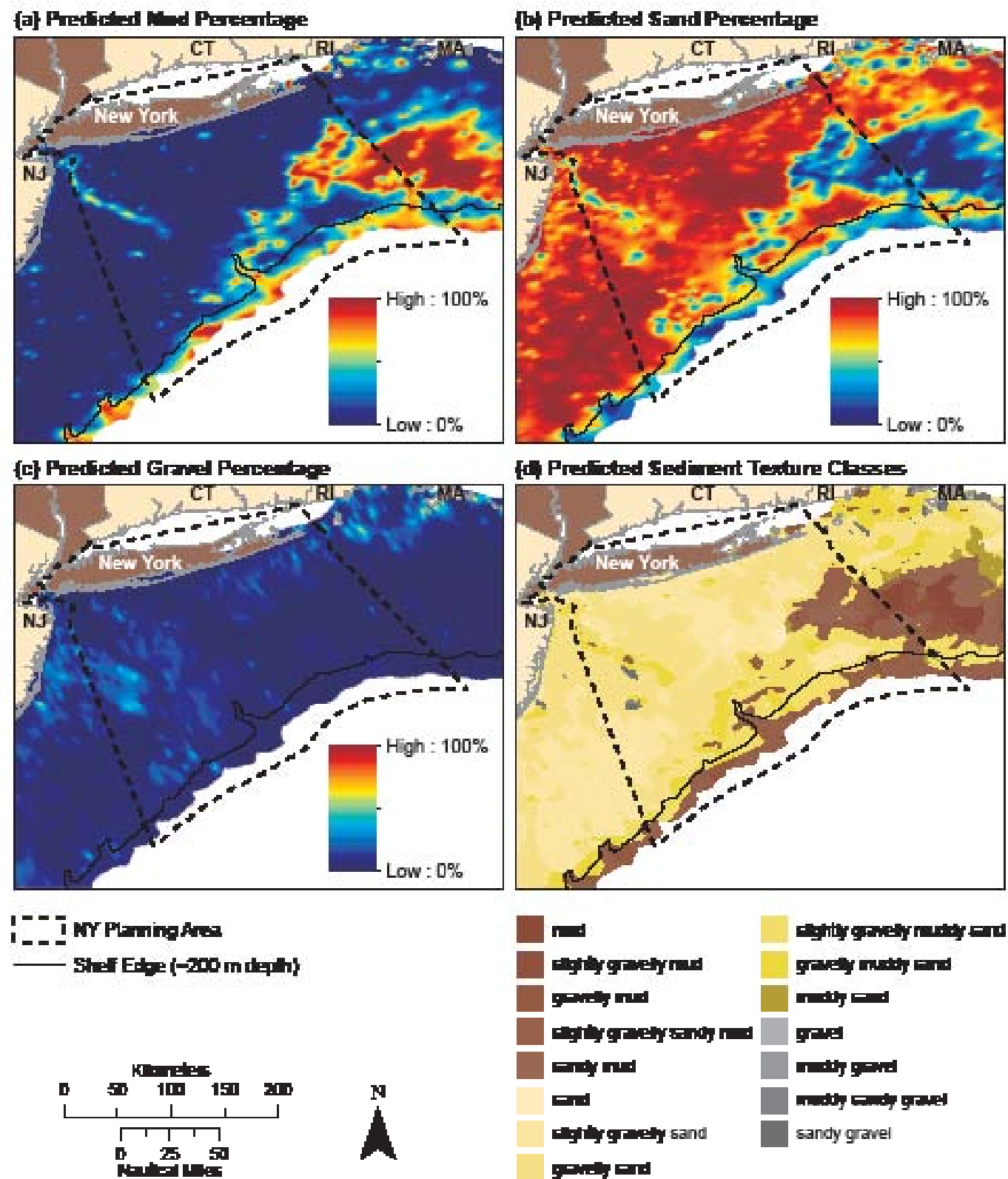


Figure 3.8. Surficial sediment composition maps from kriging interpolations of usSEABED sediment composition data in the Mid-Atlantic Bight. (a) Predicted mud percentage, (b) predicted sand percentage, (c) predicted gravel percentage, (d) distribution of predicted sediment texture classes. Sediment texture classes were assigned based on the ratios of the predicted mud, sand, and gravel fractions according to Folk (1954, 1974). Data courtesy of USGS usSEABED database (Reid et al., 2005).

Model Uncertainties

For all three sediment types, model uncertainties were lowest in densely surveyed areas and highest in unsurveyed areas, particularly farthest offshore of the continental shelf break. Model prediction standard error was lowest for the gravel fraction model (Figure 3.9), which was the least encountered sediment type in sediment samples. As with the mean grain size model, given that sediment surveys in areas offshore of the continental shelf break were sparse and prediction accuracy in these areas is worse than in nearshore areas, model predictions offshore of the shelf break should be used with caution.

Model Validation

Cross-validation of the sediment composition models yielded RMSE values ranging from 23% for gravel to 32% for sand (Table 3.6). The somewhat high RMSE values were not surprising given the heterogeneous nature of the data (laboratory analyzed vs. interpretation of written descriptors) and the potential bias toward finer particles for some of the sediment surveys (discussed in Goff et al., 2008). Cross-validation indicated that prediction errors were unbiased (mean standardized prediction errors were near zero) and the assessments of prediction uncertainty were valid since the root-mean-square standardized errors were close to one (Table 3.6). Given the relatively high RMSE values, all three sediment composition models should be used with caution and with the knowledge that available data can only provide moderately reliable predictions at investigated spatial scales. Although there are discernible broad-scale spatial patterns, the composition of sediment in any given point sample is highly variable and difficult to predict.

Table 3.5. Total area and percent area of predicted sediment texture classes in the study area.

SEDIMENT TEXTURE CLASS ^a	DESCRIPTION ^a	PREDICTED TOTAL AREA (km ²)	PREDICTED PERCENT AREA
mud	"gravel < 0.01%, sand : mud < 1:9"	61	0.1
slightly gravelly mud	"0.01-5% gravel, sand : mud < 1:9"	408	1.0
gravelly mud	"5-30% gravel, sand : mud < 1:1"	788	1.9
slightly gravelly sandy mud	"0.01-5% gravel, sand : mud from 1:9 to 1:1"	5158	12.6
sandy mud	"gravel < 0.01%, sand : mud from 1:9 to 1:1"	918	2.2
sand	"gravel < 0.01%, sand : mud > 9:1"	774	1.9
slightly gravelly sand	"0.01-5% gravel, sand : mud > 9:1"	9,352	22.9
gravelly sand	"5-30% gravel, sand : mud > 9:1"	12,353	30.2
slightly gravelly muddy sand	"0.01-5% gravel, sand : mud from 1:1 to 9:1"	6,812	16.7
gravelly muddy sand	"5-30% gravel, sand : mud from 1:1 to 9:1"	3,488	8.5
muddy sand	"gravel < 0.01%, sand : mud from 1:1 to 9:1"	472	1.2
gravel	> 80% gravel	0	0
muddy gravel	"30-80% gravel, sand : mud < 1:1"	11	0
muddy sandy gravel	"30-80% gravel, sand : mud from 1:1 to 9:1"	87	0.2
sandy gravel	"30-80% gravel, sand : mud > 9:1"	211	0.5

a - from Folk 1954, 1974.

Table 3.6. Cross-validation statistics for the sediment composition models.

Diagnostic Statistic	SEDIMENT COMPOSITION MODEL		
	Mud Fraction	Sand Fraction	Gravel Fraction
Bias	-0.000004	-0.000420	0.000140
Root-Mean-Square Error (RMSE)	0.266200	0.320800	0.227200
Mean Standardized Prediction Error	-0.000076	-0.000620	0.000340
Root-Mean-Square Standardized Error	0.862400	0.943400	1.005900

The gravel fraction prediction model was compared to USGS acoustic backscatter data from Schwab et al. (2002) to provide a qualitative accuracy assessment of predictions for overlapping areas. Although the gravel fraction model was mapped at a considerably coarser spatial resolution (~800-900 m grid cells) than the backscatter data (4 m grid

cells), a general spatial correspondence was observed over broad spatial scales. Areas of high backscatter intensity (lighter shades) were generally associated with areas predicted to be gravelly (A and C in Figure 3.10) and the narrow region of low backscatter intensity in the Hudson Shelf Valley (B in Figure 3.10) roughly corresponded to areas predicted to be sand or mud. As noted previously, the matchup is clearly not perfect, and without detailed calibration of backscatter to ground-truth samples it is difficult to say whether deviations between the two maps are due to inaccurate model predictions or variation in the backscatter surface not associated with sediment variation.

3.4.3. Hard Bottom Occurrence

Model Prediction

The MaxEnt model output indicated a relatively high likelihood of hard bottom occurrence in nearshore areas and in the vicinity of canyon features just offshore of the continental shelf break (e.g., Hudson Canyon) (Figure 3.11). The model also corresponded well to the mean grain size model in that it predicted a low likelihood of hard bottom occurrence in areas mapped as fine particles. It is important to note that the model does not provide any indication of the size of predicted hard bottom features, and does not necessarily relate to the proportion of substrate that is hard bottom at a given location. Rather, the model provides a relative index of the likelihood that at least one hard bottom point would occur if an area was sampled a sufficient number of times. An area predicted as having a high likelihood of hard bottom occurrence may in fact be dominated by non-hard bottom substrate. For example, the nearshore areas in the study area were predicted to have a high likelihood of hard bottom occurrence by the MaxEnt model, but the mean grain size and sand fraction models suggest they are predominantly sandy. Taken together, the models suggest that the nearshore areas have a surface composed primarily of sandy sediments but with widely distributed (although not abundant) hard bottom components such as large boulders, bedrock, or highly consolidated sediments. This example stresses the importance of supplementing information derived from one aspect of sediment character (e.g., mean grain size) with additional information to provide a more complete characterization of surficial sediment distribution.

The MaxEnt model output indicated that the predictor variables distance from shore, slope of slope, depth, and signed distance from shelf were most important in determining the distribution of hard bottom presences, relative to the other predictors included in the set, when measured in terms of their contribution to regularized model gain (Table 3.7). According to the jack-knifing outputs, signed distance from shelf, distance from shore, and depth had the greatest individual predictive power (Figure 3.12). The model built without signed distance to shelf showed a significant decrease in gain, which suggested that this predictor was important and not redundant (i.e., not highly correlated with other predictors). Interestingly, surface

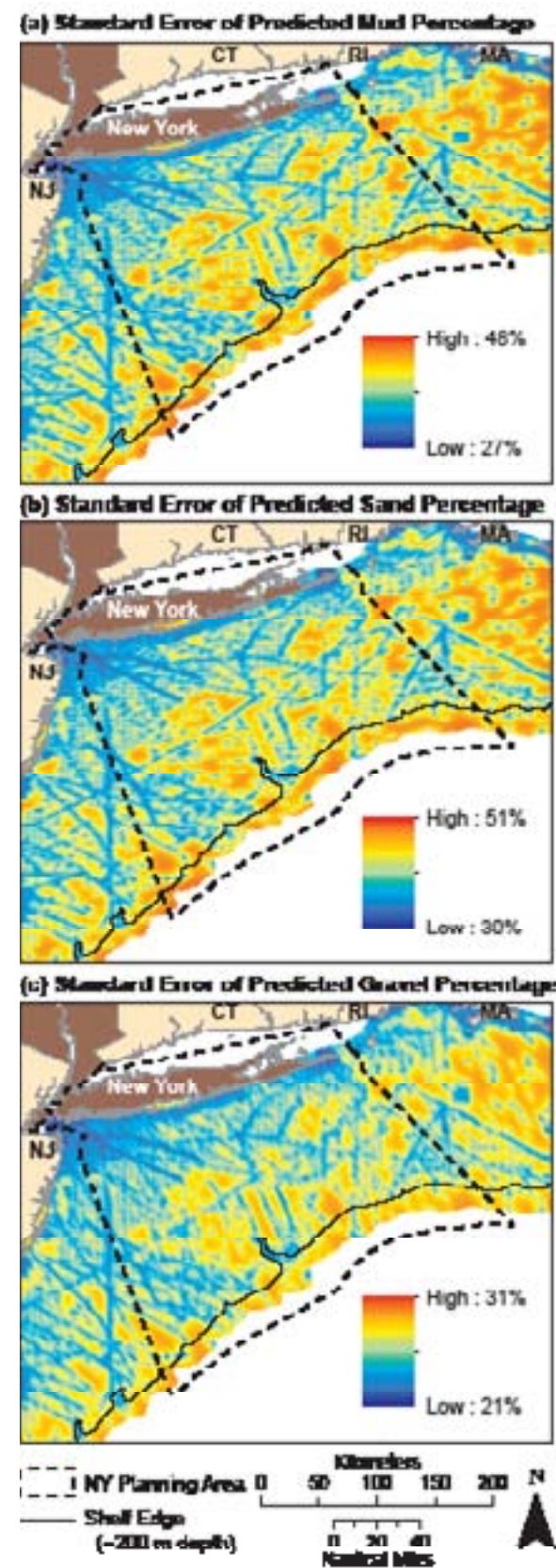


Figure 3.9. Standard error maps for (a) predicted mud percentage, (b) predicted sand percentage, and (c) predicted gravel percentage of surficial sediments from kriging interpolations of usSEABED sediment composition data in the Mid-Atlantic Bight. Data courtesy of USGS usSEABED database (Reid et al., 2005).

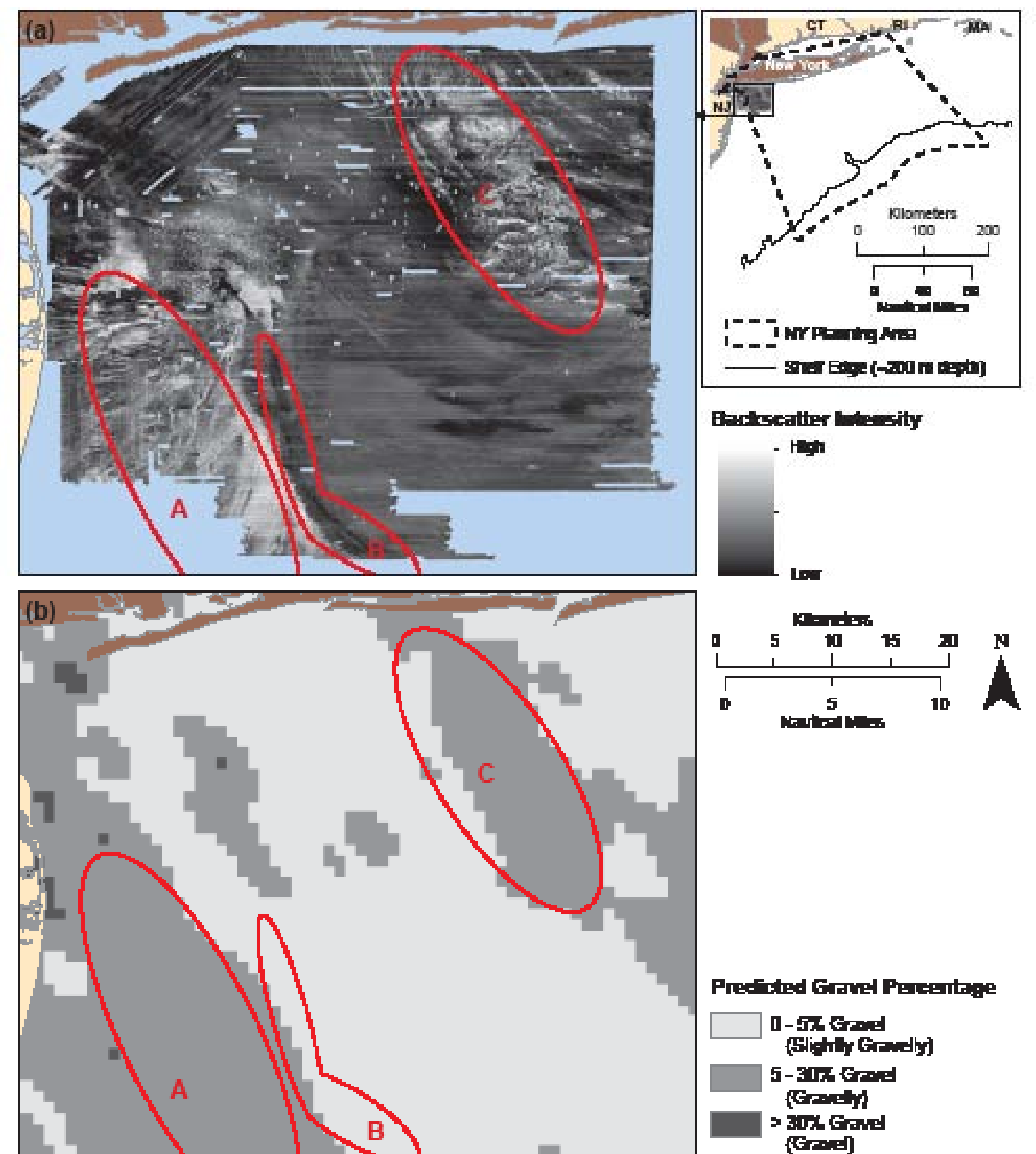


Figure 3.10. Comparison of overlapping portions of the (a) USGS acoustic backscatter data (from Schwab et al., 2002) and (b) the predicted gravel percentage in surficial sediments. In general, higher backscatter intensity indicates coarser sediments (e.g., gravel) while lower backscatter intensity indicates finer sediments (e.g., sand and mud). Sediment survey data courtesy of USGS usSEABED database (Reid et al., 2005).

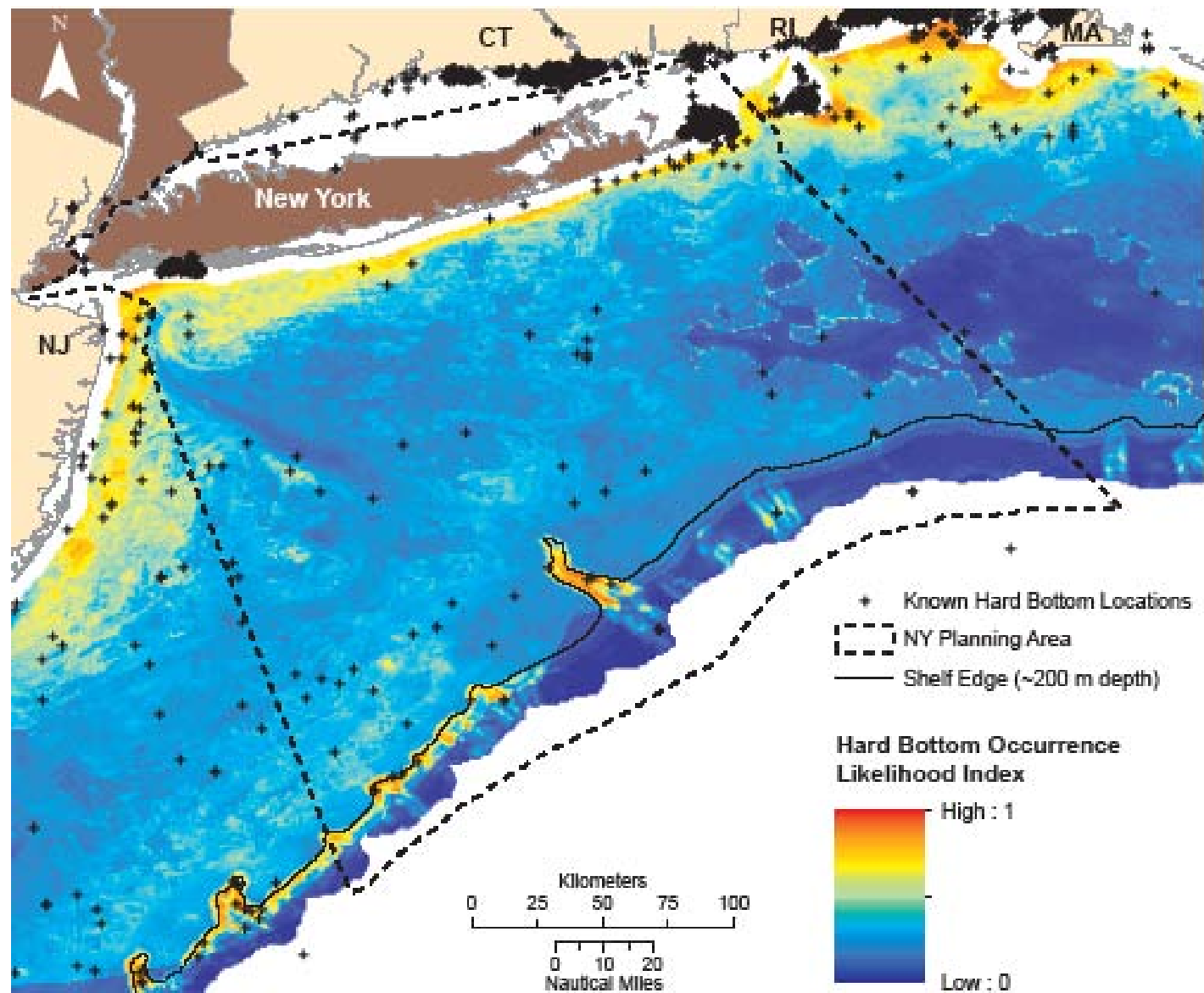


Figure 3.11. MaxEnt model of hard bottom occurrence. Map depicts the predicted relative likelihood of hard bottom occurrence from the maximum entropy model. Data courtesy of USGS usSEABED database (Reid et al., 2005), NOS Hydrographic (NOAA NGDC 2011), and The Nature Conservancy (Greene et al., 2010; J. Greene, The Nature Conservancy, personal communication, March, 2011; M. Fogarty, NMFS, personal communication, March, 2011).

chlorophyll concentration had low predictive power by itself, but its omission resulted in the greatest decrease in the predictive power of the model. This suggested that important information may be contained in the interaction of surface chlorophyll concentration with one or more of the other predictors.

Model Validation

The MaxEnt ROC-like analysis indicated good model performance, with a training AUC of 0.832 and test AUC of 0.730 (Figure 3.13). This indicates that ~73% of the time a randomly selected true hard bottom location will have a higher predicted probability of hard bottom presence than would any randomly selected location in the study area.

Table 3.7: Relative contributions of predictor variables to the MaxEnt model for hard bottom occurrence (based on cumulative regularized gain estimates).

PREDICTOR VARIABLE	PERCENT CONTRIBUTION
distance from shore	26.4
slope of slope	17.6
depth	16.0
signed distance from shelf	15.0
mean grain size	8.9
slope	6.8
surface chlorophyll concentration	4.1
turbidity	3.3
bathymetric variance	1.9

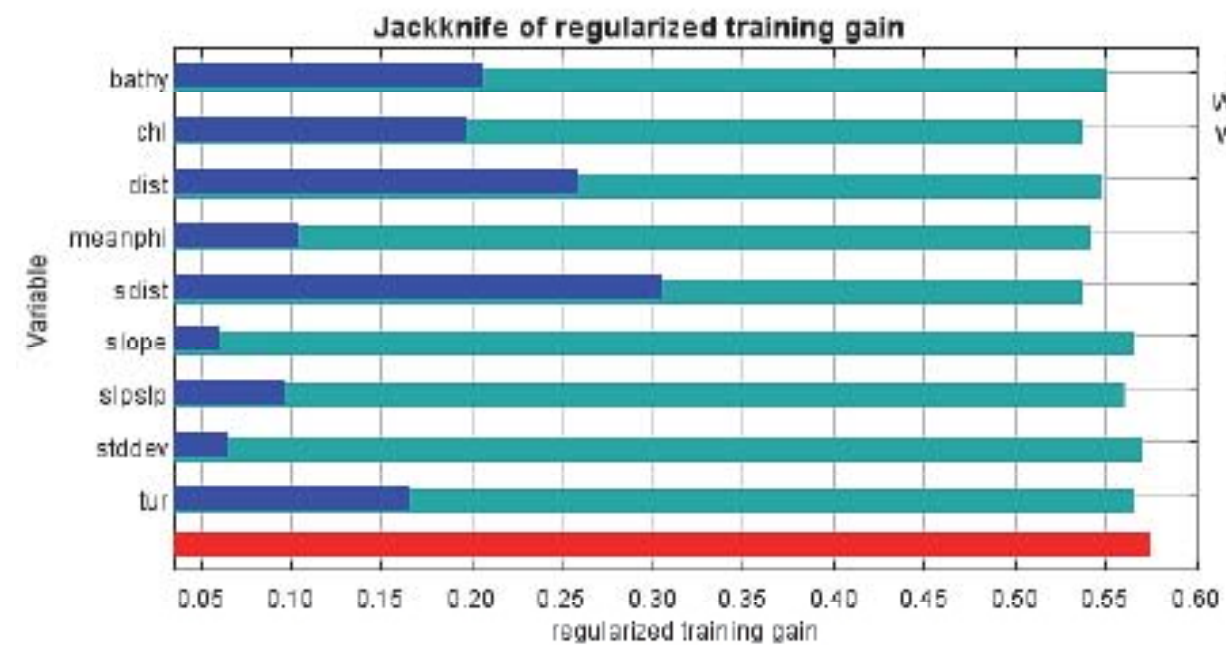


Figure 3.12. Jackknife test of predictor variable importance for the MaxEnt model of hard bottom occurrence. Blue bars indicate regularized training gain for models built with each predictor individually. Green bars indicate regularized training gain for models built with all other predictors and can be compared to the red bar, which indicates the regularized training gain for a model built using all the predictors, to determine how much the regularized training gain decreases with the omission of each predictor. Predictor variables: bathy = depth, chl = sea surface chlorophyll concentration, dist = distance from shore, meanphi = sediment mean grain size, sdist = signed distance from shelf, slope = slope, slpslp = slope of slope, stdev = bathymetric variance, tur = turbidity.

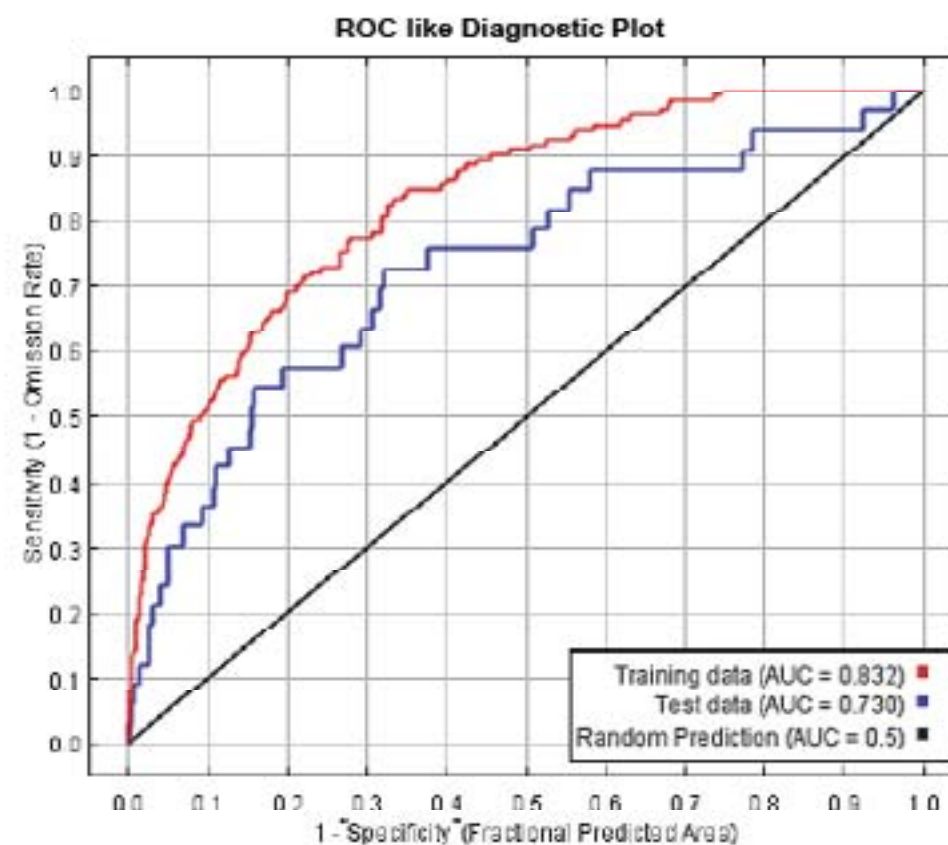


Figure 3.13. Receiver operating characteristic-like (ROC-like) curve for the MaxEnt model of hard bottom occurrence.

Although the model was mapped at a considerably lower spatial resolution (30 arc-second grid cells have an average linear dimension of ~800-900 m in the study area) compared to the USGS acoustic backscatter data (4 m grid cells) from Schwab et al. (2002), comparison of the predicted hard bottom occurrence likelihood index map to the USGS backscatter data revealed some qualitative spatial association between areas of high backscatter intensity (lighter shades) and areas predicted to have a high probability of hard bottom presence by the model (Figure 3.14).

3.5. Limitations to Interpretation

Mean Grain Size and Sediment Composition Models

As with the bathymetry model (Chapter 2), the density of usSEABED survey locations affected mean grain size and sediment composition model uncertainty estimates. In the study area, survey density was highest nearshore and was considerably lower in offshore areas. Although the mean grain size model and sediment composition models seemed to capture meso-scale (10's to 100's of km) spatial patterns across the study area (e.g., predictions of silt in major depositional areas), the models likely missed finer scale patterns in sediment distribution, especially in areas where the spatial density of sampling was low. The length scale of features that can be resolved will generally be no shorter than twice the local average distance between samples. Regardless of sample density, because the spatial resolution of the output model grid is approximately 800 m, the minimum length scale of features that can be resolved is approximately 1.6 km. While sediment survey density in nearshore areas may support the development of a model at a finer spatial resolution, areas with fewer survey data (such as offshore of the continental shelf break) limit the resolving power of the model. As a result, none of the models presented in this chapter can be used to directly predict the locations of smaller features such as hard bottom patches or cold water coral reefs.

There are also limitations to the reliability of the mean grain size and sediment composition models that are related to issues with sediment sample processing. As described previously and discussed in detail by Goff et al. (2008), the laboratory-based analyses used to generate the usSEABED extracted data often exclude hard components like shell and gravel and may therefore introduce a bias toward finer particles. Goff et al. (2008) found that a simple correction (subtracting 0.5ϕ from extracted data) removed the average bias between extracted and parsed mean grain size datasets. We used that bias correction, but note that it may not apply equally across the whole study area or all time periods and surveys. The model could still have under-predicted coarse sediments in some areas dominated by extracted data. Moreover, even parsed data may exhibit a bias against very large grains (especially cobbles and boulders) if they were excluded by mechanical sampling devices or removed in pre-processing. For the sediment composition models, we used both extracted and parsed datasets without applying any bias correction to account for the exclusion of hard components in the extracted data. As a result, the models were likely biased toward finer particles and may under-predict the fraction of gravel particles.

Other issues arise from the long time span over which samples were collected. Samples in the usSEABED database were collected over multiple decades, and thus variability in grain size and sediment composition data likely includes a temporal component in addition to spatial variability. It is possible that a sample collected in 1970 no longer reflects the true state of the seafloor, but it was used in the model as such. Also, positional uncertainty for survey locations was considerably greater for data collected decades ago.

Mean grain size is a suitable measure of sediment character at survey sites where sediment composition has a unimodal distribution, since mean grain size will represent the typical size of sediment particles in the sample. However, if the distribution of sediments in a sample is bimodal or multi-modal, then mean grain size will not indicate the typical size of sediment particles at the survey site (and in fact very few particles in the sample may be this size). For example, the mean grain size for a sample of gravelly-mud sediments could correspond to sand, even though sand may not be part of the sample. The mud, sand, and gravel fraction models can be used in conjunction with the mean grain size models to mitigate this limitation.

Given that previous maps of sediment composition consisted of point data depicting the dominant sediment type at each location (e.g., Williams et al., 2006), the maps developed here represent a considerable advance over previously available information. However, given the limitations associated with the use of the usSEABED

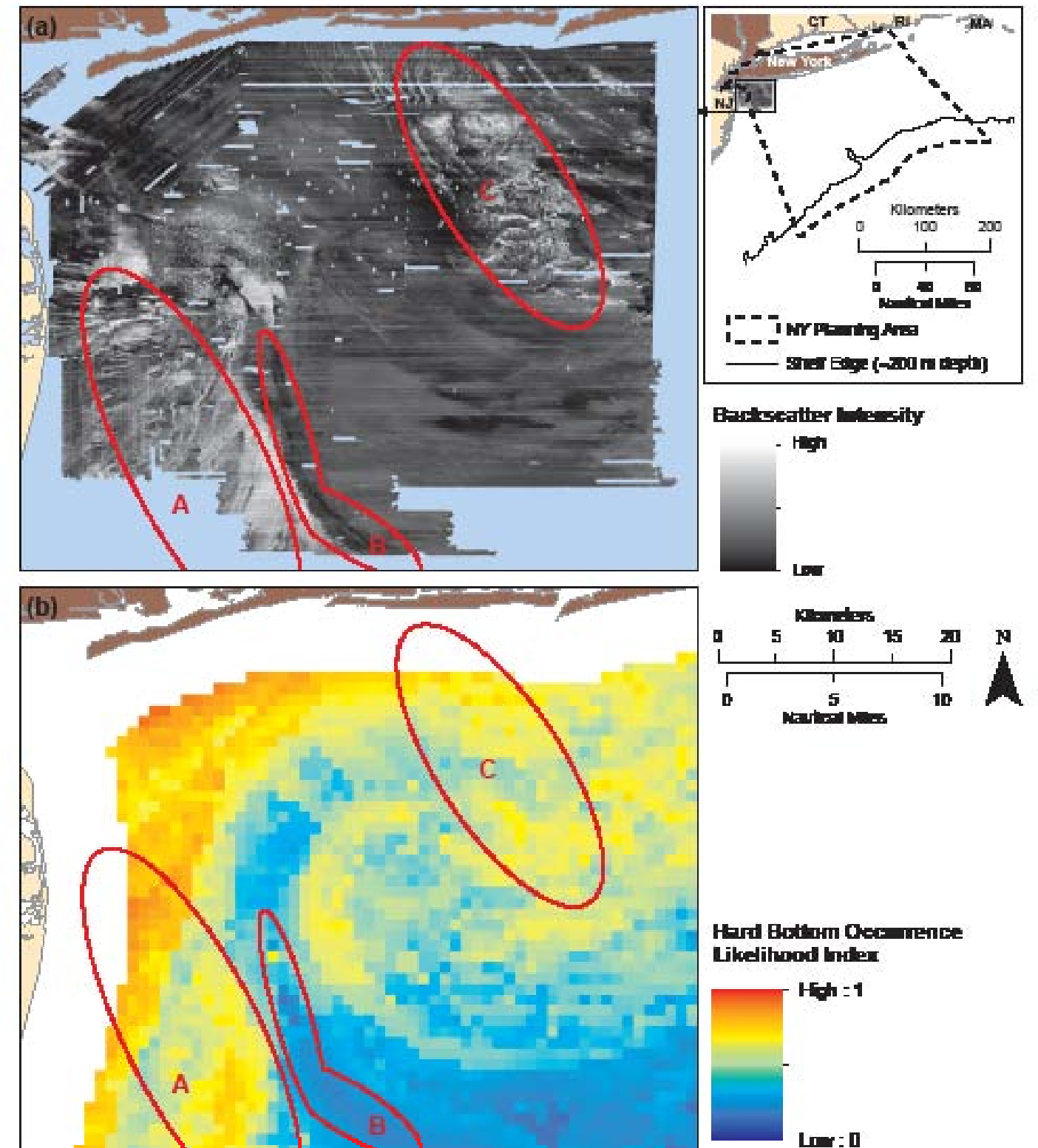


Figure 3.14. Comparison of overlapping portions of the (a) USGS acoustic backscatter data (from Schwab et al., 2002) and (b) the predicted hard bottom occurrence likelihood index. Higher backscatter intensity indicates coarser sediments (e.g., gravel) while lower backscatter intensity indicates finer sediments (e.g., sand and mud). Hard bottom data courtesy of USGS usSEABED database, NOS Hydrographic database (NOAA NGDC 2011), and The Nature Conservancy (Greene et al., 2010; J. Greene, pers. comm.; M. Fogarty, pers. comm.).

sediment data, the maps of predicted mean grain size and sediment composition fractions should be used primarily to describe general patterns in sediment distribution. Maps of model uncertainty can be used to identify areas where additional survey data are needed and for risk analyses related to decision-making under uncertainty.

Hard Bottom Occurrence Model

The MaxEnt model of the likelihood of hard bottom occurrence performed well in the cross-validation ROC-like analysis. However, there are a number of limitations to the interpretation of this presence-only model, and it should be considered an experimental product.

First, the environmental predictor variables used to characterize hard bottom locations were at a considerably coarser spatial resolution than most hard bottom features on the seafloor (e.g., individual boulders, patches of exposed bedrock). As a result, the value associated with a given hard bottom point for a predictor may misrepresent the actual value at that precise location. Finer-scale environmental predictor data would enable the model to characterize hard bottom locations more accurately in terms of the environmental predictors, and as a result model predictions would be more reliable.

Second, MaxEnt solutions using presence-only data require that sampling effort is distributed homogeneously over the study area or that biases are known and integrated into the model. We know that sampling effort was heterogeneously distributed and that there were significantly more samples collected close to shore, but we don't know exactly how effort is distributed. Because we were concerned about sample bias we excluded a large number of hard bottom locations in nearshore areas. Sample bias can result in model predictions that are overfit to more densely surveyed areas (Phillips et al., 2009; Elith et al., 2011). Because of limitations related to sample bias and the inability of MaxEnt models to identify prevalence, Elith et al. (2011) suggest that presence-absence modeling methods should be used if presence-absence survey data is available. However, reliable hard bottom absence data was not available in the study area.

Third, unlike the mean grain size and sediment composition models, the MaxEnt output did not provide a spatial map of prediction uncertainties. Therefore, it was not possible to assess changes in prediction certainty associated with the location of input data or its variability. Lastly, the model did not provide any indication of the size of predicted hard bottom features. Rather, the model provided only an indication of the likelihood of at least one hard bottom point sample occurring at a given location. This, of course, depends on sample effort – but as previously noted the heterogeneity in effort is not explicitly included in the model.

Additional fundamental limitations to models developed from presence-only data are discussed in detail by Elith et al. (2011); anyone interested in quantitative application of the hard bottom model results should thoroughly read and understand the limitations discussed in that article.

Previous maps of hard bottom locations in the study area consisted of point data depicting survey locations where hard bottom features were observed, with no indication of the relative likelihood of occurrence across the study area (Greene et al., 2010). Therefore, in spite of the limitations associated with presence-only modeling, the model of hard bottom occurrence developed here provides additional information at unsampled locations that has previously been unavailable, and may be useful to spatial planning until detailed hard bottom distribution data can be collected.

3.6. ACKNOWLEDGMENTS

We thank Jenn Greene and Mark Anderson (The Nature Conservancy) and Michael Fogarty (NMFS) for providing hard bottom point data used by Greene et al. (2010) in the Northwest Atlantic Ecoregional Assessment and John Goff (University of Texas at Austin) for providing surficial sediment grain size data. Bryan Costa, Will Sautter, and Timothy Battista of the NOAA Biogeography Branch provided helpful discussions in support of this work and also assisted with data acquisition/analysis for bathymetry and vector shorelines. John Goff and Brian Calder provided detailed reviews that improved an earlier version of this chapter. However, any errors or omissions are the sole responsibility of the authors.

3.7. REFERENCES

Allen, J.S., R.C. Beardsley, J.O. Blanton, W.C. Boicourt, B. Butman, L.K. Coachman, A. Huyer, T.H. Kinder, T.C. Royer, J.D. Schumacher, R.L. Smith, and W. Strurges. 1983. Physical oceanography of continental shelves. *Rev. Geophys. Space Phys.* 21:1149-1181.

Brown, C.J., B.J. Todd, V.E. Kostylev, and R.A. Pickrill. 2011. Image-based classification of multibeam sonar backscatter data for objective surficial sediment mapping of Georges Bank, Canada. *Continental Shelf Research* 31:S110-S119.

Butman, B., T.J. Middleton, E.R. Theiler, and W.C. Schwab. 2003. Topography, shaded relief and backscatter intensity of the Hudson Shelf Valley, offshore of New York: U.S. Geological Survey Open-File Report 03-372. <http://pubs.usgs.gov/of/2003/of03-372/>.

Butman, B., D.C. Twichell, P.A. Rona, B.E. Tucholke, T.J. Middleton, and J.M. Robb. 2006. Sea floor topography and backscatter intensity of the Hudson Canyon region offshore of New York and New Jersey: U.S. Geological Survey Open-File Report 2004-1441, version 2.0. <http://pubs.usgs.gov/of/2004/1441/>.

Cressie, N.A.C. 1993. *Statistics for spatial data* (revised ed.). New York: John Wiley & Sons, Inc.

De Falco, G., R. Tonielli, G. Di Martino, S. Innangi, S. Simeone, and I.M. Parnum. 2010. Relationships between multibeam backscatter, sediment grain size, and *Posidonia oceanica* seagrass distribution. *Continental Shelf Research* 30:1941-1950.

Deutsch, C.V. and A.G. Journel. 1998. *GSLIB: Geostatistical software library and user's guide* (second ed.). New York: Oxford University Press.

Elith, J., C.H. Graham, R.P. Anderson, M. Dudík, S. Ferrier, A. Guisan, R.J. Hijmans, F. Huettmann, J.R. Leathwick, A. Lehmann, J. Li, L.G. Lohmann, B.A. Loiselle, G. Manion, C. Moritz, M. Nakamura, Y. Nakazawa, J. M. Overton, A.T. Peterson, S.J. Phillips, K.S. Richardson, R. Scachetti-Pereira, R.E. Schapire, J. Sobero'n, S. Williams, M.S. Wisz, and N.E. Zimmermann. 2006. Novel methods improve prediction of species' distributions from occurrence data. *Ecography* 29:129-151.

Elith, J., S.J. Phillips, T. Hastie, M. Dudik, Y.E. Chee and C.J. Yates. 2011. A statistical explanation of MaxEnt for ecologists. *Diversity and Distributions* 17:43-57.

Environmental Systems Research Institute, Inc. (ESRI). 2011a. *ArcGIS Desktop: Release 10*. Redlands, CA: Environmental Systems Research Institute.

Environmental Systems Research Institute, Inc. (ESRI). 2011b. *ArcGIS Desktop 10 Resource Center. Cross Validation (Geostatistical Analyst)*. URL: <http://help.arcgis.com/en/arcgisdesktop/10.0/help/index.html#//003000000000z000000.htm>.

Ferrini, V.L. and R.D. Flood. 2006. The effects of fine-scale surface roughness and grain size on 300 kHz multibeam backscatter intensity in sandy marine sedimentary environments. *Marine Geology* 228:153-172.

Fielding, A.H. and J.F. Bell. 1997. A review of methods for the assessment of prediction errors in conservation presence/absence models. *Environmental Conservation* 24:38-49.

Fogarty, Michael. 2011. NOAA National Marine Fisheries Service (NMFS). Northeast Fisheries Science Center. Personal communication.

Folk, R.L. 1954. The distinction between grain size and mineral composition in sedimentary rock nomenclature. *Journal of Geology* 62:344-359.

Folk, R.L. 1974. *The petrology of sedimentary rocks*. Austin, TX: Hemphill Publishing Co. 182 pp.

Goff, J.A. 2011. University of Texas at Austin. Personal communication.

Goff, J.A., C.J. Jenkins, and B. Calder. 2006. Maximum likelihood resampling of noisy, spatially correlated data. *Geochemistry, Geophysics, and Geosystems* 7, Q08003, doi:10.1029/2006GC001297.

Goff, J.A., C.J. Jenkins, and S.J. Williams. 2008. Seabed mapping and characterization of sediment variability using the usSEABED data base. *Continental Shelf Research* 28:614-633.

Golub, G.H. and C.F. Van Loan. 1996. *Matrix Computations*, 3rd edition. Johns Hopkins University Press.

Goovaerts, P. 1997. *Geostatistics for natural resources evaluation*. New York: Oxford University Press.

Greene, J.K. 2011. The Nature Conservancy. Eastern U.S. Division. Personal Communication.

Greene, J.K., M.G. Anderson, J. Odell, and N. Steinberg, eds. 2010. *The Northwest Atlantic Marine Ecoregional Assessment: Species, Habitats and Ecosystems. Phase One*. The Nature Conservancy, Eastern U.S. Division, Boston, MA. URL: <http://www.nature.org/ourinitiatives/regions/northamerica/areas/easternusmarine/explore/index.htm>.

Harris, B.P. and K.D.E. Stokesbury. 2010. The spatial structure of local surficial sediment characteristics on Georges Bank, USA. *Continental Shelf Research* 30:1840-1853.

Krumbein, W.C. and L.L. Slass. 1963. *Stratigraphy and sedimentation*. San Francisco: W.H. Freeman. 660 pp.

Lathrop, R.G., M. Cole, N. Senyk, and B. Butman. 2006. Seafloor habitat mapping of the New York Bight incorporating sidescan sonar data. *Estuarine, Coastal and Shelf Science* 68:221-230.

National Oceanic and Atmospheric Administration (NOAA) National Geophysical Data Center (NGDC). 2011. NOAA National Ocean Service (NOS) and U.S. Coast and Geodetic Survey (USCGS) Bottom Type Descriptions from Hydrographic Surveys. NGDC Data Set G10163. Online database. <http://www.ngdc.noaa.gov/geosamples/survey.jsp>. Accessed June 29, 2011.

Peterson, A.T., M. Papes, and M. Eaton. 2007. Transferability and model evaluation in ecological niche modeling: a comparison of GARP and Maxent. *Ecography* 30:550-560.

Phillips, S.J., R.P. Anderson, and R.E. Schapire. 2006. Maximum entropy modeling of species geographic distributions. *Ecological Modelling* 190:231-259.

Phillips, S.J. and M. Dudik. 2008. Modeling of species distributions with Maxent: new extensions and a comprehensive evaluation. *Ecography* 31:161-175.

Phillips, S.J., M. Dudik, J. Elith, C.H. Graham, A. Lehmann, J. Leathwick, and S. Ferrier. 2009. Sample selection bias and presence-only distribution models: implications for background and pseudo-absence data. *Ecological Applications* 19:181-197.

Poppe, L.J., J.S. Schlee, and H.J. Knebel. 1994. Map showing distribution of surficial sediment on the Mid-Atlantic continental margin, Cape Cod to Albemarle Sound. USGS. USGS United States Geological Survey (US Department of the Interior). Misc. Invest. Sen, Map I-1987-D.

Poppe, L.J., S.J. Williams, and V.F. Paskevich. 2005. U.S. Geological Survey East-Coast Sediment Analysis: Procedures, Database, and GIS Data: Open-File Report 2005-1001, U.S. Geological Survey, Coastal and Marine Geology Program, Woods Hole Science Center, Woods Hole, MA.

Reid, J.M., J.A. Reid, C.J. Jenkins, M.E. Hastings, S.J. Williams, and L.J. Poppe. 2005. usSEABED: Atlantic coast offshore surficial sediment data release: U.S. Geological Survey Data Series 118, version 1.0. <http://pubs.usgs.gov/ds/2005/118/>.

Schwab, W.C., J.F. Denny, B. Butman, W.W. Danforth, D.S. Foster, B.A. Swift, L.L. Lotto, M.A. Allison, and E.R. Thieler. 2000. Seafloor characterization offshore of the New York-New Jersey metropolitan area using sidescan-sonar: U.S. Geological Survey Open-File Report 00-295. <http://pubs.usgs.gov/of/2000/of00-295>.

Schwab, W.C., J.F. Denny, D.S. Foster, L.L. Lotto, M.A. Allison, E. Uchupi, W.W. Danforth, B.A. Swift, E.R. Thieler, and B. Butman. 2002. High resolution quaternary seismic stratigraphy of the New York Bight continental shelf: U.S. Geological Survey Open-File Report 02-152. <http://pubs.usgs.gov/of/2002/of02-152/>.

Wentworth, C.K. 1922. A scale of grade and class terms for elastic sediments. *The Journal of Geology* 30:377-392.

Williams, S.J., M.A. Arsenault, L.J. Poppe, J.A. Reid, J.M. Reid, and C.J. Jenkins. 2006. Surficial sediment character of the New York-New Jersey offshore continental shelf region: a GIS compilation. U.S. Geological Survey Open- File Report 2006-1046. Online at <http://pubs.usgs.gov/of/2006/1046>.

Oceanographic Setting

Brian Kinlan^{1,2}, Matthew Poti^{1,2} and Charles Menza^{1,3}

4.1. SUMMARY

In this chapter data on several dynamic oceanographic variables, including water column stratification, sea surface temperature (SST), surface chlorophyll, surface turbidity, and near-surface zooplankton biomass are compiled for the New York study area (Figure 1.2). Data are gridded to a common 30 arc-second resolution and long-term average (climatological) ocean conditions are mapped by season (spring [Mar-May], summer [Jun-Aug], fall [Sep-Nov], winter [Dec-Feb]). These datasets are intended to quantify spatial variation in long-term average patterns of physical and biological oceanographic variables.



Image 4.1. The ocean is a dynamic environment. Photo credit: Edward Moran

4.2. BACKGROUND

The hydrography of the study area is characterized by a strong seasonal cycle, considerable freshwater runoff, and interactions among three distinct large-scale water masses. These water masses produce strong spatial and temporal heterogeneity in both biological and physical parameters, and define biogeographic regions that are often clearly delimited by temperature and/or salinity fronts, although the exact position of these fronts shifts seasonally and inter-annually. Over the shelf, water is relatively cold and fresh, and comes from the Labrador Current via a continuous equatorward coastal current system (Chapman and Beardsley, 1989). The northward-flowing warm equatorial waters of the Gulf Stream pass farther offshore. Between these two and over the slope lies a water mass, commonly called Slope Water, which is a mixture of shelf water and the Gulf Stream.

The frontal boundary between shelf and slope masses is highly dynamic and changes due to wind forcing, gravitational flow, and large scale alterations in atmospheric circulation patterns such as those associated with the North Atlantic Oscillation (NAO) (Pershing et al., 2001). Changes in the relative position of these water masses not only affect physical parameters, such as water temperature, but also species distributions. For instance an infamous 1882 tilefish kill offshore of New Jersey has been attributed to colder-than-usual water temperatures and a low NAO index (Marsh et al., 1999).

Productivity on the shelf is generally nitrogen-limited and therefore is greatest wherever inorganic nitrogen-containing nutrients are supplied, typically by processes such as runoff from rivers and estuaries, turbulent mixing in warm core rings, wind-driven upwelling intrusions of slope water, and intense tidal mixing at shoals. Frontal boundaries and stratification between water masses inhibit mixing, but strong winds, upwelling, and eddies can provide sufficient energy to promote mixing and introduce nutrients. Upwelling occurs south of Long Island during periods of southwesterly winds and during the passage of storms (Walsh et al., 1978). Warm core rings resulting from Gulf Stream meanders occur, but are less frequent than at George's Bank (Ingham et al., 1982).

The shelf's water column stratifies in the spring and summer from warming and freshwater inputs. Stratification isolates warm, well-mixed surface water from cold deeper water and deprives the upper (euphotic) zone of nutrients. During stratification, primary productivity is highest nearshore where periodic coastal upwelling and

¹ Center for Coastal Monitoring and Assessment, National Centers for Coastal Ocean Science, National Ocean Service, National Oceanic and Atmospheric Administration

² Consolidated Safety Services, Inc.

³ Corresponding author: Charles.Menza@noaa.gov

runoff can provide nutrients. Offshore productivity is limited to the pycnocline where phytoplankton can get nutrients via diffusive fluxes. In late summer, stratification breaks down due to storms and surface cooling. By winter the entire water column over the shelf is well-mixed and a sharp frontal zone separates cold, fresh nearshore water from warmer, more-saline slope water.

4.3. METHODS

In this section, data sources are identified and methods used to interpolate data onto a consistent sampling grid are described. All datasets are co-registered on the same 30 arc-second sampling grid used in Chapters 3 and 6 and clipped to the same study area spatial extent (Figure 1.2). Since sea surface temperature (SST), stratification, chlorophyll, turbidity, and zooplankton biomass are time-varying environmental variables dominated by seasonal variability, long-term average (climatological) ocean conditions were mapped by season (spring [Mar-May], summer [Jun-Aug], fall [Sep-Nov], winter [Dec-Feb]).

Data processing was carried out using ArcGIS 9.3.1 with the Spatial Analyst extension (Environmental Systems Research Group [ESRI], Redlands, CA), Geostatistical Analyst extension (ESRI), XTools Pro 6.2.1 for ArcGIS 9.x (Data East LLC, Novosibirsk, Russia), and Hawth's Tools for ArcGIS 9.x (Beyer, 2004).

Water Column Stratification

Seasonal climatologies of water column stratification were obtained from The Nature Conservancy (TNC) and are described in TNC's Northwest Atlantic Marine Ecoregional Assessment (NAMERA) Phase I Report (Greene et al., 2010; Shumway et al., 2010). Stratification estimates were originally provided to TNC by Dr. Grant Law and subsequently provided to us with permission from the original author (G. Law, pers. comm.). Briefly, three-dimensional ocean temperature and salinity data were interpolated from a database of conductivity-temperature-depth (CTD) casts, using the OAX5 optimal-analysis algorithm (Hendry and He, 1996). CTD casts came from a compilation of Hydrobase (described in Curry, 1996), NOAA National Marine Fisheries Service databases (described in Mountain, 2003), Fisheries and Ocean Canada databases (described in Gregory, 2004), and South-Atlantic Bight oceanographic data (described in Blanton et al., 2003) (for details see Shumway, 2010 and Law, 2011). Stratification was calculated by subtracting the optimally interpolated seawater density (measured in $\text{kg}\cdot\text{m}^{-3}$) at 50 meters from the surface seawater density, then averaged to create a 1980 – 2007 climatology (Shumway, 2010). Note that by this definition, stratification is usually negative, corresponding to less dense warmer and/or fresher water occurring on top of more dense colder and/or more saline water. More negative values indicate greater stratification.

The stratification climatology was provided on a 5 arc-minute grid and bi-linearly resampled to the 30 arc-second model grid. We did not explicitly characterize the accuracy of this dataset, but previous accuracy assessments of hydrographic data interpolation in this region suggest relative error on the order of 50% (Taylor and Mountain, 2003). Given this level of uncertainty, and that the original resolution of this dataset is coarser than any of the predictors used in this analysis (spacing between sample points typically 1-10 km or further), this layer should be used with caution for planning scales finer than ~10 km and for any application requiring precise knowledge of stratification at any particular time and place. Better resolution and accuracy might be obtained from more recent data-assimilating numerical ocean models. An improved high-resolution gridded stratification climatology should be a priority for this region.

Stratification in the study area was greatest in the spring and summer (Figure 4.1). In these months, stratification was higher over a broad area of the shelf, decreasing towards the shelf edge and eastwards to Nantucket shoals. In fall, stratification is greatest in the middle of the shelf, with more mixing along shore and to the east and west of the study area. In winter stratification is low compared to other seasons. Relative to the seasonal mean, it is higher nearshore, especially near the Hudson River and east of Long Island Sound.

Sea Surface Temperature (SST)

Seasonal climatologies of sea surface temperature (SST) were obtained by averaging monthly composites from the National Aeronautics and Space Administration (NASA) Pathfinder 1.1 km Advanced Very High Resolution Radiometer (AVHRR) SST archive for the Northwest Atlantic region, 1985-2001 (Wolfeich, 2011), maintained at the University of Rhode Island (URI) and available publicly via OpenDAP (Cornillion et al.,

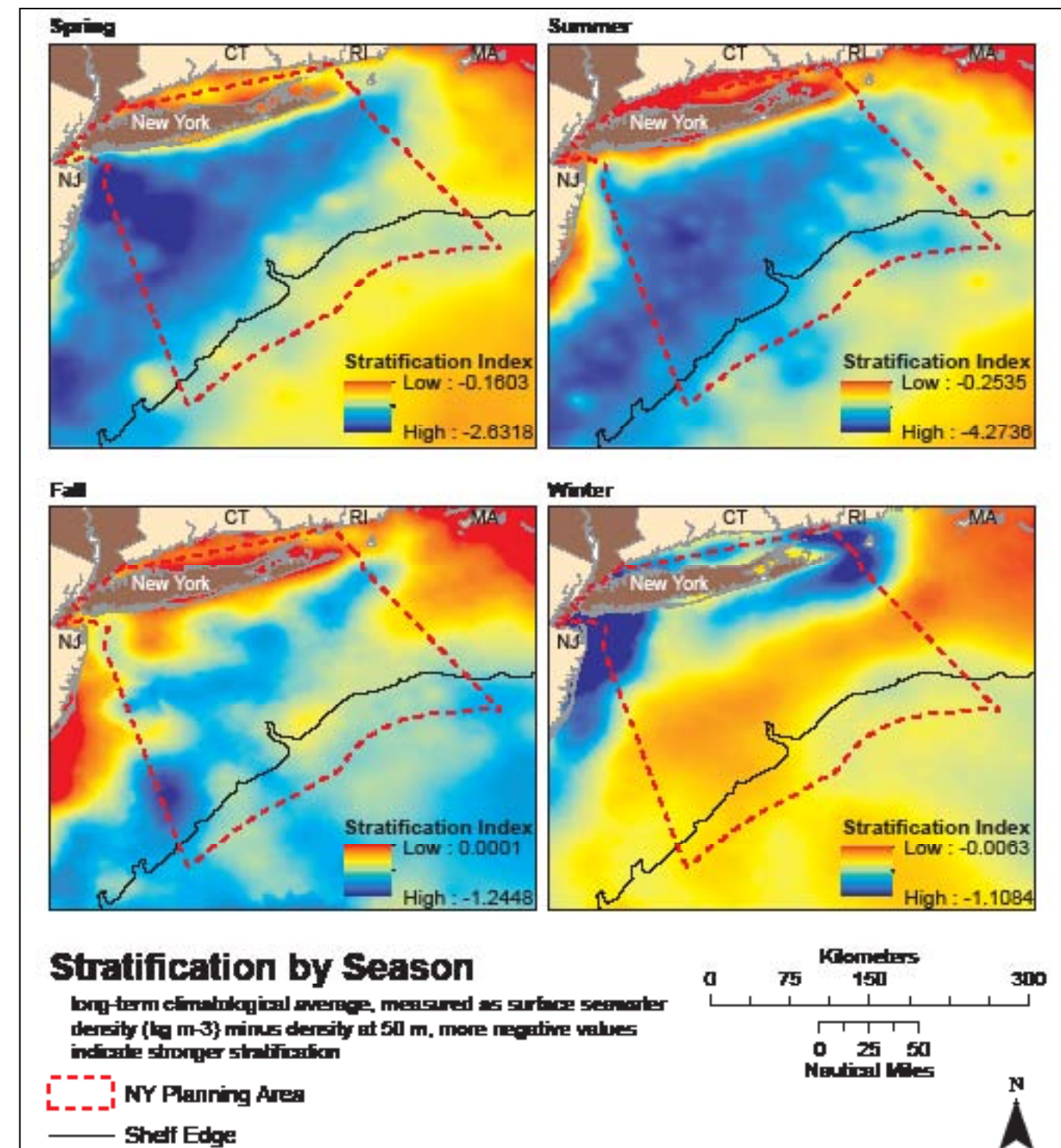


Figure 4.1: Seasonal stratification climatology maps for spring (upper left), summer (upper right), fall (lower left) and winter (lower right). Data courtesy of G. Law (Oregon Health Sciences University), J. Greene (The Nature Conservancy), NOAA Fisheries, Fisheries and Ocean Canada, Woods Hole Oceanographic Institution (Hydrobase), and B. Blanton (University of North Carolina-Chapel Hill).

2003) at the following URL: http://satdat1.gso.uri.edu/.opendap/Pathfinder/Northwest_Atlantic/1km/declouded/contents.html. Radiometry data from AVHRR instruments mounted on NOAA satellites was processed using the Pathfinder Algorithm (Casey et al., 2010). Details of the algorithm and processing are provided at the following URL: http://satdat1.gso.uri.edu/.opendap/Pathfinder/Pathfinder1km/pathfinder_1km.html

Data were bi-linearly resampled to the 30 arc-second model grid. Given the quality flags that were applied, accuracy of the satellite SST estimates is expected to be approximately $\pm 1^\circ$ Celsius (about 5% for the range of temperatures in our region) although this can degrade close to land (Casey and Cornillion, 1999). The long time period of averaging resulted in gap-free coverage over the study area except in pixels immediately

adjacent to land. SST was generally warmer offshore of the continental shelf break relative to nearshore areas and varied seasonally, with considerable warming of nearshore areas from spring to summer (Figure 4.2). Climatological SST differed little between summer and fall.

Surface Chlorophyll and Turbidity

As a proxy for surface primary productivity, seasonal climatologies of chlorophyll a concentration for the period 1998-2006 were extracted from high-resolution (~1.1 km) SeaWiFS satellite data processed using standard NASA ocean biology processing group (OBPG) reprocessing 5.1 algorithms (Franz and Thomas, 2005). Similarly, as a proxy for sea surface turbidity, seasonal climatologies of normalized Lw-670nm for the period 1998-2006 were extracted from the same imagery. All SeaWiFS processing was done by the Coastal Oceanographic Assessment Status and Trends (COAST) Branch (NOAA/NOS/NCCOS/CCMA/COAST), following previously documented methods (Franz

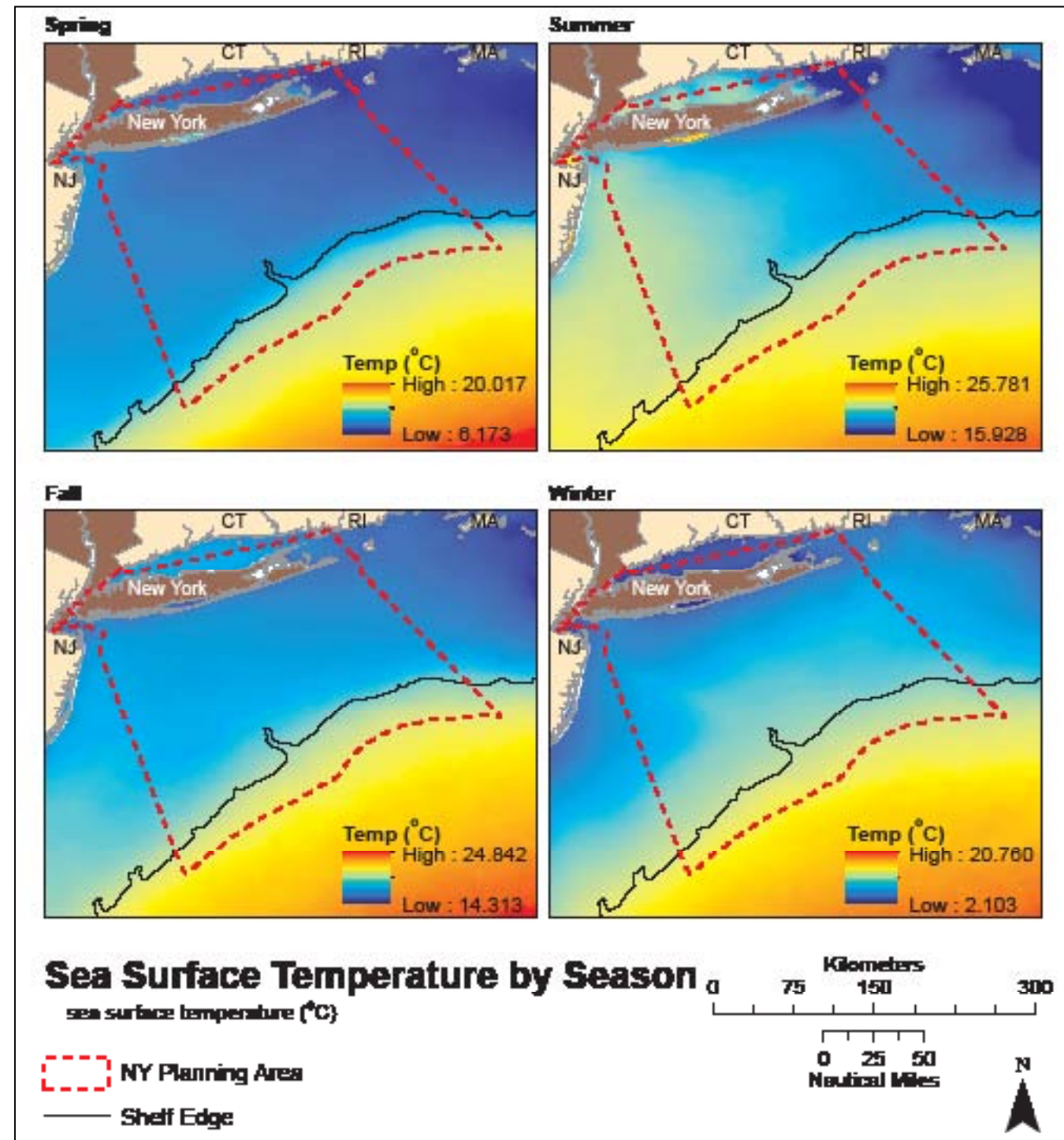


Figure 4.2: Seasonal sea surface temperature climatology maps for spring (upper left), summer (upper right), fall (lower left) and winter (lower right). Data courtesy of C. Wolfriech (University of Rhode Island).

and Thomas, 2005; Pirhalla et al., 2009), except a despeckling filter was also applied (Gonzalez and Woods, 1992). Accuracy statistics of ocean color imagery have been reviewed extensively (Franz et al., 2007); under ideal conditions SeaWiFS error tolerances are <5% for water-leaving radiances and <35% for chlorophyll a; however, errors can be substantially higher in coastal waters (Franz et al., 2007). The long time period of averaging resulted in gap-free coverage over the study area except in pixels adjacent to land.

Chlorophyll a concentrations changed by seasons, but showed similar broad-scale spatial patterns (Figure 4.3). Concentrations were highest in the summer and lowest in the winter. In all months, concentrations were highest neashore and in Long Island Sound and low over most of the shelf and offshore of the continental shelf break. Turbidity showed a similar spatial pattern, but was highest in the spring (Figure 4.4).

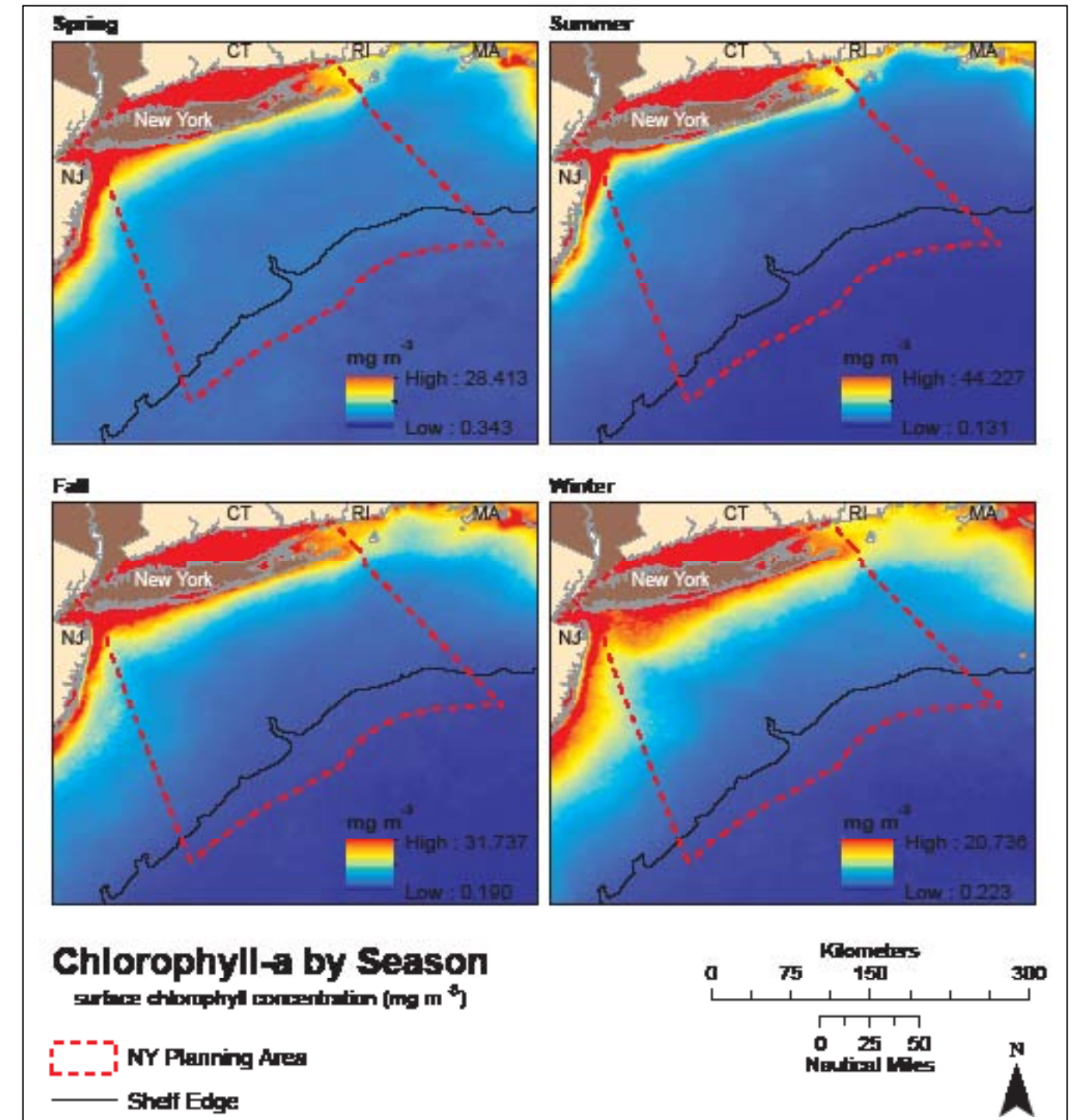


Figure 4.3: Seasonal chlorophyll a climatology maps for spring (upper left), summer (upper right), fall (lower left) and winter (lower right). Data from the Sea-viewing Wide Field-of-view Sensor (SeaWiFS) satellite, processed by D. Pirhalla and V. Ransibrahmanakul (NOAA/NOS/NCCOS/CCMA/COAST). Raw SeaWiFS imagery provided by NASA under research/educational agreement with GeoEye, Inc.

Near-surface Zooplankton Biomass

Point estimates of zooplankton biomass (mean displacement volume per volume of water strained) were obtained from the NOAA National Marine Fisheries Service's (NMFS) Copepod database. The all-taxa zooplankton global compilation was used, available at: http://www.st.nmfs.noaa.gov/plankton/atlas/data_src/copepod-2010__4000000-compilation.txt.

In the study region, we found 3,122 records of zooplankton biomass from 1966-2001. These were grouped by season and processed using ordinary kriging (with locally quadratic detrending) to produce a gridded seasonal climatology at the required resolution. We pooled observations over time to estimate the long-term climatological spatial mean. Ordinary kriging was used because the data exhibited approximately stationary

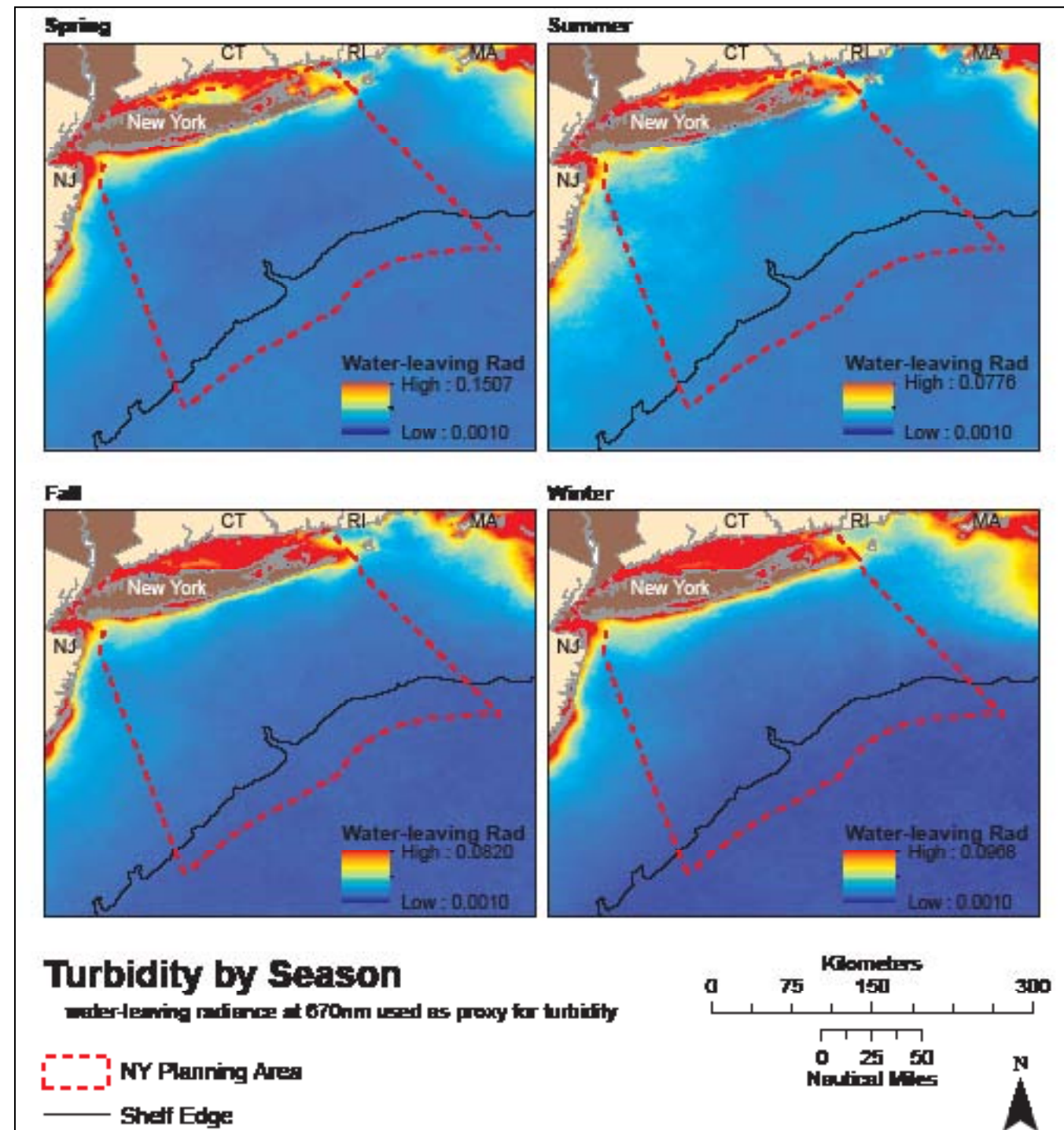


Figure 4.4: Seasonal turbidity climatology maps for spring (upper left), summer (upper right), fall (lower left) and winter (lower right). Water-leaving radiance values are normalized to reflect the fraction of incident light reflected, and thus are dimensionless numbers between 0 and 1. Data courtesy of D. Pirhalla and V. Ransibrahmanakul (NOAA/NOS/NCCOS/CCMA/COAST), imagery was provided by NASA under a research/educational agreement with GeoEye, Inc.

(though geometrically anisotropic) spatial autocorrelation over the study region after trend removal. Ordinary kriging was found to perform better than inverse-distance weighting (IDW) based on leave-one-out cross-validation. Predictions were not made where the variogram model explained <2.5% of the total variance (i.e., areas far from data points). Relative cross-validation RMSE was 27% averaged across all seasons (spring 35%, summer 20%, fall 24%, winter 27%). Geostatistical analyses were carried out using Geostatistical Analyst for ArcGIS 9.3 (ESRI).

Zooplankton biomass was greatest in the fall, with patches of relatively high biomass south of Long Island and outside of the study area offshore of New Jersey (Figure 4.5). In the spring, summer and winter zooplankton biomass was heterogeneously distributed and showed different spatial patterns.

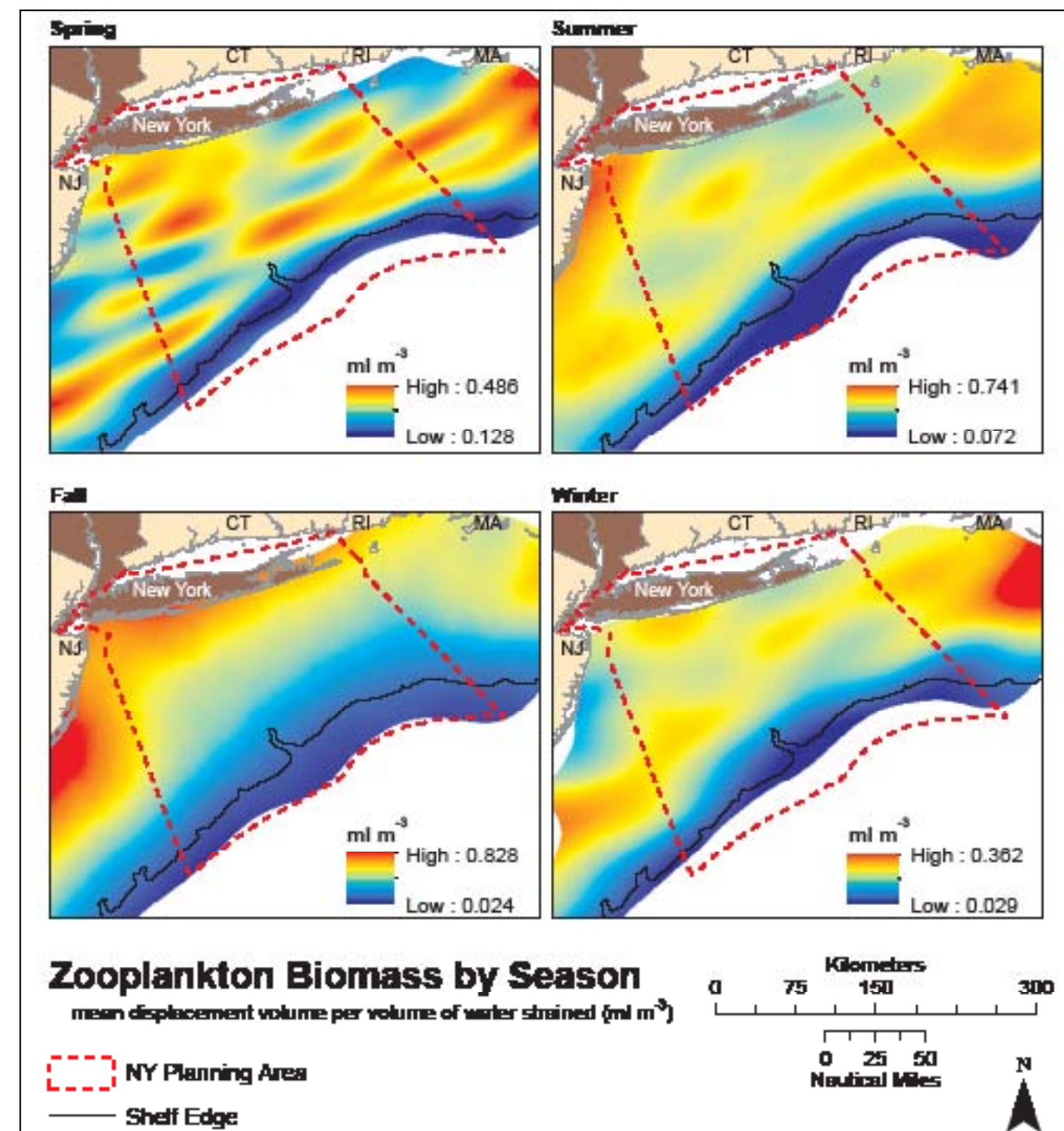


Figure 4.5: Seasonal zooplankton climatology maps for spring (upper left), summer (upper right), fall (lower left) and winter (lower right). Data courtesy of the NOAA National Marine Fisheries Service Copepod database.

4.4. ACKNOWLEDGMENTS

We thank Jenn Greene and Mark Anderson (The Nature Conservancy) and Dr. Grant Law (Oregon Health Sciences University) for providing stratification climatology data, Doug Pirhalla and Varis Ransibrahmanakul (NOAA/NOS/NCCOS/CCMA/COAST Branch) for providing SeaWiFS climatologies, and Carl Wolfeich (URI) for providing 1.1 km Pathfinder SST data. SeaWiFS data are used here for research and educational purposes only in accordance with an agreement between NASA and GeoEye, Inc. (Herndon, VA), which operates the SeaWiFS instrument. The Pathfinder algorithm and data processing steps for AVHRR SST data were originally developed at University of Miami, Rosenstiel School of Marine and Atmospheric Science. Zooplankton data was courtesy of the public NOAA NMFS Copepod database. Brian Calder (University of New Hampshire Center for Coastal and Ocean Mapping) and John Goff (University of Texas at Austin) provided technical reviews that improved this chapter, though any errors or omissions are the sole responsibility of the authors.

4.5 REFERENCES

- Beyer, H.L. 2004. Hawth's Analysis Tools for ArcGIS. Available at <http://www.spataleecology.com/htools>.
- Blanton, B.O., A. Aretxabaleta, F. Werner, and H. Seim. 2003. Monthly climatology of the continental shelf waters of the South Atlantic Bight. *J. Geophys. Res.* 108 (C8): 3264, doi: 10.1029/2002JC001609.
- Casey, K. and P. Cornillon. 1999. A comparison of satellite and in situ-based sea surface temperature climatologies. *J. Climate* 12: 1848–1863.
- Casey, K.S., T.B. Brandon, P. Cornillon, and R. Evans. 2010. "The Past, Present and Future of the AVHRR Pathfinder SST Program", in *Oceanography from Space: Revisited*, eds. V. Barale, J.F.R. Gower, and L. Alberotanza, Springer. DOI: 10.1007/978-90-481-8681-5_16
- Chapman, D.C. and R.C. Beardsley. 1989. On the origin of shelf water in the Middle Atlantic Bight. *Journal of Physical Oceanography* 19(3):384–391.
- Cornillon, P., J. Gallagher and T. Sgouros. 2003. OPeNDAP: Accessing Data in a Distributed, Heterogeneous Environment, *Data Science Journal* 2:164-174.
- Curry, R.G. 1996. Hydrobase - A database of hydrographic stations and tools for climatological analysis, Woods Hole Oceanog. Inst. Tech. Rep., WHOI-96-01, 44 pp.
- Franz, B.A. and D. Thomas. 2005. Overview of MODIS/Aqua Ocean Color Processing & Distribution. NASA Ocean Biology Processing Group. Online publication. Retrieved from: http://oceancolor.gsfc.nasa.gov/DOCS/MODISA_processing.htm
- Franz, B.A., S.W. Bailey, P.J. Werdell, and C.R. McClain. 2007. Sensor-independent approach to the vicarious calibration of satellite ocean color radiometry. *Appl. Optics* 46:5068–5082.
- Gonzalez, R. and R. Woods. 1992. *Digital Image Processing*. Addison-Wesley Publishing Company. 191 pp.
- Greene, J.K., M.G. Anderson, J. Odell, and N. Steinberg, (eds). 2010. *The Northwest Atlantic Marine Ecoregional Assessment: Species, Habitats and Ecosystems. Phase One*. The Nature Conservancy, Eastern U.S. Division, Boston, MA. URL: <http://www.nature.org/ourinitiatives/regions/northamerica/areas/easternusmarine/explore/index.htm>.
- Gregory, D.N. 2004. *Climate: A Database of Temperature and Salinity Observations for the Northwest Atlantic DFO Can. Sci. Advis. Sec. Res. Doc. 2004/075*
- Hendry, R. and I. He. 1996. Technical Report on Objective Analysis (OA) Project. Unpublished document available at URL: http://www2.mar.dfo-mpo.gc.ca/science/ocean/coastal_hydrodynamics/Oax/download/techrep.ps
- Ingham, M.C., R.S. Armstrong, J.L. Chamberlin, S.K. Cook, D.G. Mountain, R.J. Schlitz, J.P. Thomas, J.J. Bisagni, J.F. Paul and C.E. Warsh. 1982. Summary of the Physical Oceanographic Processes and Features Pertinent to Pollution Distribution in the Coastal and Offshore Waters of the Northeastern United States, Virginia to Maine. NEMP Oceanography Summary Report. NEMP-IV-82-C-004. Washington, DC: U.S. Department of Commerce.
- Law, G. 2011. Center for Coastal Margin Observation and Prediction, Oregon Health and Science University. Personal Communication via emails with B. Kinlan, C. Menza, and M. Poti, March 2011 – August 2011.
- Marsh, R.B., B. Petrie, C.R. Weidman, R.R. Dickson, J.W. Loder, C.G. Hannah, K. Frank and K. Drinkwater. 1999. The 1882 tilefish kill – a cold event in shelf waters off the north-eastern United States? *Fish. Oceanography* 8:39-49.
- Mountain, D.G. 2003. Variability in the properties of Shelf Water in the Middle Atlantic Bight, 1977–1999. *J. Geophys. Res.* 108, NO. C1, 3014, doi:10.1029/2001JC001044.
- Pershing, A.J., C.H. Greene, C. Hannah, D. Sameoto, E. Head, D.G. Mountain, J.W. Jossie, M.C. Benfield, P.C. Reid, and T.G. Durban. 2001. Oceanographic responses to climate in the Northwest Atlantic. *Oceanography* 14:76-82.

Pirhalla, D.E., V. Ransibrahmanakul, and R. Clark. 2009. An Oceanographic Characterization of the Olympic Coast National Marine Sanctuary and Pacific Northwest: Interpretive Summary of Ocean Climate and Regional Processes Through Satellite Remote Sensing. NOAA Technical Memorandum NOS NCCOS 90. Silver Spring, MD. 55 pp.

Shumway, C., K. Ruddock, and M. Clark. 2010. Physical Oceanography. Chapter 4 In: Greene, J.K., M.G. Anderson, J. Odell, and N. Steinberg (eds.). The Northwest Atlantic Marine Ecoregional Assessment: Species, Habitats and Ecosystems. Phase One. The Nature Conservancy, Eastern U.S. Division, Boston, MA.

Taylor, M.H. and D. Mountain. 2003. The role of local wintertime atmospheric heat flux in determining springtime temperature variability in the northern Middle Atlantic Bight during 1965–1973. *Continental Shelf Research* 23:377–386.

Walsh, J.J., T.E. Whitley, F.W. Barvenik, C.D. Wirick, and S.O. Howe. 1978. Wind events and food chain dynamics within New York Bight. *Limnol. Oceanogr.* 23:659-683.

Wolfteich, C. 2011. Web document: URI/NASA AVHRR Pathfinder 1km SST Archive. Retrieved April 2011 from http://satdat1.gso.uri.edu/opendap/Pathfinder/Pathfinder1km/pathfinder_1km.html

Deep Sea Corals

Dave Packer¹ and Dan Dorfman^{2,3,4}

5.1. SUMMARY

Deep sea corals are benthic invertebrates known to inhabit cold and deep waters throughout the globe, including the Atlantic waters offshore of the State of New York. Many are slow growing, long-lived, and exhibit complex, branching forms of growth that, while providing valuable habitat for other species, also makes them particularly susceptible to damage from fishing gear and other anthropogenic impacts. Within the New York State offshore study area there are 5,619 records of known deep sea coral locations within the deep sea coral geodatabase of NOAA's Deep-sea Coral Research and Technology Program (DSCRTP). Of these, 4,625 are of sea pens and the remaining 994 are stony corals, true soft corals, or gorgonians. The two most abundant species of sea pens are typically found in the soft sediments on the continental shelf. Most of the stony corals in this region are solitary organisms and are often found on soft substrates as well. Many of the true soft corals and gorgonians were typically found on gravel and rocky outcrops around the continental slope. Several species are found around Hudson Canyon (Figure 5.1); there are very few records from the literature of deep sea corals within the Canyon itself.



Figure 5.1 White sea pens (*Stylatula elegans*) on muddy sand from 119 m on the outer continental shelf near Hudson Canyon (left). Solitary hard coral (*Dasmomillia lymani*) on shelly sand from 108 m on the rim of Hudson Canyon (right). Photo credit: P.C. Valentine, USGS.

We have a very incomplete picture of deep sea coral distribution and abundance in the northeastern U.S. region and offshore of New York, and the overall quantity and quality of deep sea coral habitat is unknown. There is also a dearth of information on their natural history, as well as difficulties with their taxonomy. Deep sea corals in this region face a range of anthropogenic threats from fishing, gas and oil drilling, and ocean acidification due to global warming.

Obviously, in order to better preserve and protect deep corals and deep coral habitat off the northeastern U.S. and offshore of New York, there needs to be: 1) an increased mapping and survey effort; 2) more basic research on deep coral taxonomy, life history, habitat requirements, species associations, etc.; and finally, 3) quantification on the susceptibility of deep corals to anthropogenic impacts. There are currently efforts underway, under the auspices of the New England Fishery Management Council (NEFMC), in coordination the Mid-Atlantic Fishery Management Council (MAFMC), to protect deep sea corals within the New York State offshore study area. Several approaches to management and conservation are being evaluated and the DSCRTP and NOAA's National Marine Fisheries Service (NMFS) Northeast Fisheries Science Center (NEFSC) will be conducting a three year regional investigation into deep sea coral distribution, biology, and ecology from fiscal year (FY) 2013 through FY2015.

5.2. INTRODUCTION

Deep sea corals are benthic invertebrates known to inhabit cold and deep waters throughout the globe, including the Atlantic waters offshore of the State of New York. While considerable attention has been given to tropical and subtropical corals and coral reefs, deep sea corals have only recently been researched and managed for

¹ Coastal Ecology Branch, Ecosystems Processes Division, Northeast Fisheries Science Center, National Marine Fisheries Service, National Oceanic and Atmospheric Administration

² Biogeography Branch, Center for Coastal Monitoring and Assessment, National Centers for Coastal Ocean Science, National Ocean Service, National Oceanic and Atmospheric Administration

³ Consolidated Safety Services, Inc.

⁴ Corresponding author: dan.dorfman@noaa.gov

their habitat value. Unlike shallow water corals, deep sea corals can be found in cold water habitats throughout the globe in a wide range of depths. Deep sea corals can be found from near the surface to about 3,000 m depth, although NOAA generally defines them as occurring >50 m on continental shelves, slopes, canyons, and seamounts. Deep sea corals are suspension feeders, but unlike most tropical and subtropical corals, do not require sunlight and do not have symbiotic algae (zooxanthellae) to meet their energy needs. Deep sea corals can occur as small, solitary individuals or as structure-forming corals that provide vertical structure above the seafloor that can be utilized by other species; the latter includes both branching corals that form a structural framework (e.g., reefs) as well as individual branching coral colonies. Because deep sea corals are slow-growing, long-lived, and often have complex, branching forms of growth, they are highly susceptible to anthropogenic impacts (such as from fishing gear). These life history traits also compromises their recovery from disturbances over short time periods.

Deep sea corals in the northeastern U.S. belong to three major taxonomic groups (Figure 5.2). There are the Hexacorals (or Zoantharia), which include the hard or stony corals (Scleractinia); the Ceriantipatharians which includes the black and thorny corals (Antipatharia), and finally there are the Octocorals (or Alcyonaria), with flexible, partly organic skeletons that include the true soft corals (Alcyonacea), gorgonians (Gorgonacea or sea fans and sea whips), and sea pens (Pennatulacea). Scleractinians identified in the northeastern U.S. number 16 species, Antipatharians number possibly four or perhaps more species, Alcyonaceans number nine species, Gorgonaceans number 21 species, and Pennatulaceans number 21 species. Among all three groups, there appear to be a suite of species (see below) that occurs at depths of less than 500 m (shelf and upper slope), and a separate suite that occurs at depths greater than 500 m (lower slope and rise). One species of hard coral and one alcyonacean occur in water less than 50 m deep.

Phylum	Class	Subclass	Order	Family (# species)	
Cnidaria	Anthozoa (true corals and sea pens)	Ceriantipatharia	Antipatharia (black corals)	Antipathidae (17)	
				Leiposiphidae (13)	
				Schizopathidae (27)	
		Hexacorallia {-Zoantharia} {true corals}	Scleractinia {stony corals}	Caryophyllidae (8)	
				Dendrophyllidae (2)	
		Octocorallia {-Alcyonaria} {octocorals}	Alcyonacea {soft corals}	Flabellidae (4)	
				Fungiacyathidae (1)	
				Rhizangiidae (1)	
				Gorgonacea (sea fans and sea whips)	Alcyoniidae (3)
					Clavariidae (2)
Nephthidae (4)					
Pennatulacea {sea pens and sea pensies}	Gorgonacea (sea fans and sea whips)	Acanthogorgiidae (1)			
		Anthothelidae (1)			
		Chrysogorgiidae (4)			
		Isidae (4)			
		Paragorgiidae (1)			
		Paramuriceidae (4)			
		Pennatulidae (6)			
		Pennatulacea {sea pens and sea pensies}	Pennatulacea {sea pens and sea pensies}	Anthraptidae (3)	
				Furculetidae (1)	
				Halipteridae (1)	
Kaphobelemeridae (3)					
Pennatulidae (1)					
Protaptidae (3)					
Rensidae (1)					
Schaeptelidae (2)					
Umbellulidae (2)					
Virgulariidae (2)					

Figure 5.2. Deep sea coral taxonomy for those species found in the northeastern U.S. from Maine to Cape Hatteras including four seamounts (Bear, Physalia, Mytilus, and Retriever) off of Georges Bank that lie within the Exclusive Economic Zone (EEZ).

5.2.1. Studies of Deep Sea Corals in the Northeast Region

Off the northeastern U.S., deep sea corals have been noted since the surveys of Verrill in the 19th century (Verrill, 1862; 1878a, b; 1879; 1884) and as fisheries bycatch since that period. Theroux and Wigley (1998) described the distribution of deep sea corals in the northwest Atlantic, based on samples taken from 1956-1965. They often do not distinguish between taxonomic groups; e.g., stony corals such as *Astrangia* sp. and *Flabellum* sp. are lumped together with the various types of anemones in the subclass Zoantharia. Theroux and Wigley (1998) also discussed the soft corals, gorgonians, as well as the sea pens. They were present along the outer margin of the continental shelf and on the slope and rise, and were sparse and patchy in all areas, particularly in the northern section. Theroux and Wigley (1998) found that they were not collected in samples taken at < 50 m in depth, and were most abundant between 200-500 m. Identified species include gorgonians, such as *Acanella* sp., *Paragorgia*

arborea, and *Primnoa reseda* (now *resedaeformis*, see Cairns and Bayer [2005]) and the soft coral *Alcyonium* sp. Gorgonians and soft corals were collected from gravel and rocky outcrops (Theroux and Wigley, 1998).

Watling and Auster (2005) noted two distinct distributional patterns for the gorgonians and soft corals in the northwest Atlantic. Most are deepwater species that occur at depths > 500 m; these include species of gorgonians in the genera *Acanthogorgia*, *Acanella*, *Anthothela*, *Lepidisis*, *Radicipes*, and *Swiftia*, and soft corals in the genera *Anthomastus* and *Clavularia*. Other species occur throughout shelf waters to the upper continental slope and include the gorgonians *P. arborea*, *P. resedaeformis*, and species in the genus *Paramuricea*. Both *P. arborea* and *P. resedaeformis* are considered widespread off the northeastern U.S.; *P. resedaeformis* has been reported south to off Virginia Beach, Virginia. The majority of records for *Acanthogorgia armata*, *P. arborea*, and *P. resedaeformis* come from Lydonia, Oceanographer, and Baltimore submarine canyons.

Dr. Barbara Hecker and her colleagues surveyed the deep sea corals and epibenthic fauna of the continental margin and several canyons off the northeastern U.S. in the 1980s via submersible and towed camera sled (Hecker et al., 1980, 1983). Corals were denser and more diverse in the canyons, and some species, such as those restricted to hard substrates, were found only in canyons while the soft substrate types were found both in canyons and on the continental slope (Hecker and Blechschmidt, 1980). For a complete discussion of Hecker's and others' surveys and research on deep sea corals as well as a thorough review of deep sea coral presence and distribution in the northeastern U.S., see Packer et al. (2007).

In the Mid-Atlantic Bight, many of the topographic features characteristic of other deep sea coral habitats are absent. The relatively small amount of hard substrate in this area occurs in conjunction with submarine canyons or are artificial reefs or shipwrecks. The main physiographic feature off of New York State is the Hudson Shelf Valley and Canyon, extending from the inner-continental shelf, at about the 40 m isobath, onto the continental slope. Sediments over the Mid-Atlantic shelf are fairly uniformly distributed, and are primarily composed of sand, with isolated patches of coarse-grained gravel and fine-grained silt and mud deposits (Stevenson et al., 2004). Deep sea corals that grow on soft bottom habitats (e.g., sea pens, some stony corals) are more common here than in other U.S. regions, especially on the shelf. Deep sea corals have been seen on the shelf around Hudson Canyon and in the head of the Canyon (discussed below).

Although the mid-Atlantic shelf is mostly soft bottom and devoid of major structure forming deep sea corals, in the relatively shallow nearshore region off Delaware and Maryland there are patch areas of hard bottom containing significant stands of the sea whip *Leptogorgia virgulata* (Gorgoniidae), which may be a northern range extension for this species. These hard bottom areas include natural rocky bottom as well as wrecks and artificial reefs, at depths as little as 8 m for the wreck/artificial reef areas, and can be less than 16 km from shore. These "shallow-dwelling" deep sea corals may not fit into the standard definition of deep sea corals, but these habitats are all known to support high densities of species that prefer structure, such as black sea bass (*Centropristis striata*) and tautog (*Tautoga onitis*), as well as flounder, so they may be important habitats in need of protection. Surveys have not yet been conducted to see if similar nearshore coral patch habitat occurs adjacent to other mid-Atlantic states like New York, but it seems unlikely that it would be restricted to Maryland and Delaware.

Despite the aforementioned faunal surveys, our knowledge of the temporal and spatial distribution and abundance of deep sea corals off the northeastern U.S., as well as some aspects of their basic biology and habitat requirements, is severely limited, so their overall population status is difficult to determine. That, along with questions about their taxonomy, makes it difficult, if not impossible, to determine whether there have been changes in deep coral occurrence or abundance over time. (There is, however, more information on deep coral distribution and habitat requirements in Canadian waters; e.g., the Northeast Channel [Mortensen and Buhl-Mortensen, 2004]). NEFSC groundfish and shellfish surveys from the Gulf of Maine to Cape Hatteras have collected corals as part of their bycatch for several decades, but there are many data gaps (e.g., corals were not properly identified or quantified) which precludes using the data to assess any long-term population trends.

The environmental parameters of Mid-Atlantic Bight deep sea corals are also unknown, but Leverette and Metaxas (2005) developed predictive models to determine areas of suitable habitat for *P. arborea* and *P. resedaeformis* along the Canadian Atlantic continental shelf and shelf break. Several environmental factors including slope, temperature, chlorophyll *a*, current speed and substrate were included in the analysis. Their results showed that the habitat requirements differed between the two gorgonians. *P. arborea* occurred predominantly in steeply sloped environments and on rocky substrates, while the habitat for *P. resedaeformis* was more broadly distributed and located in areas with high current speed, rocky substrates and a temperature range between 5-10°C.

There have been some more recent, targeted surveys off of New England using trawls and remotely operated vehicles (ROVs). In 2003, 2004, and 2005, surveys were conducted of several seamounts in the New England and Corner Rise Seamount chains (the latter is approximately 400 km to the east of the New England Seamount chain, and nearly midway between the east coast of the U.S. and the Mid-Atlantic Ridge) funded by NOAA's Office of Ocean Exploration and National Undersea Research Program. The cruises were multidisciplinary in nature, but the goals included studying the distribution and abundance of deep corals relative to the prevailing direction of currents; collecting specimens for studies of reproductive biology, genetics, and ecology; and studying species associations.

5.2.2. The Role of Deep Sea Corals as Habitat

Deep sea corals provide habitat for other marine life, increase habitat complexity, and contribute to marine biodiversity (Lumsden et al., 2007). The role of deep sea corals as possible habitats for fishes has been studied in other regions. The corals in the *Primnoa*, *Lophelia*, and *Oculina* genera have been the most studied. Several studies have documented that certain fish commonly occur in the vicinity of corals more often than in areas without corals. In the northwest Atlantic, this has been noted for redfish in the Northeast Channel near Georges Bank (Mortensen et al., 2005). Redfish may take advantage of structure on the bottom as a refuge from predation, as a focal point for prey, and for other uses. However, in a survey of habitats in the Jordan Basin in the Gulf of Maine containing coral assemblages (primarily from the genera *Paragorgia*, *Paramuricea*, and *Primnoa*), Auster (2005) found that densities of redfish were not significantly different between dense coral habitats and dense epifauna habitats. However, the density of redfish in these two habitats was higher than in the outcrop-boulder habitat containing sparse epifauna. While this shows that a habitat without deep corals can support similar densities of fish to a habitat containing corals, Auster (2005) states that it is the actual distribution of each habitat type throughout a region that will ultimately determine the role such habitats play in the demography of particular species and communities. Deep sea coral habitats are fairly rare in the Gulf of Maine, but boulder-cobble habitats containing dense epifauna are not. Auster (2005) suggests that deep sea corals do have some effect on the distribution and abundance of fishes, but by themselves may not support high density, unique or high diversity fish communities. The corals do provide important structural attributes of habitat, but may not be functionally different than structures provided by other dense epifaunal assemblages.

There are few data available about invertebrate species associations with deep corals off the northeastern U.S. More is known about the species associations of deep corals and invertebrates from other regions. However, recent research suggests that deep corals are important components of benthic communities, providing structure and refuge for various other invertebrate species (e.g., Lumsden et al., 2007; Mosher and Watling, 2009).

5.3. OBJECTIVES

This chapter will focus on describing the distribution of those deep sea corals found off New York State, from nearshore to the continental slope, based on historical surveys and databases. When examining the information available on the distribution of corals in the area offshore from New York State it is important to note that the historical surveys are far from comprehensive and the taxonomy and identification of many of these deep sea corals are open to question, so the presence, distribution, and abundance of these deep sea corals should be interpreted with caution. The national DSCTRP and NEFSC will be conducting a three year intensive investigation on the distribution, ecology and status of deep sea corals off the northeastern U.S. beginning in FY2013.

5.4. METHODS

The primary source of data used for this analysis was the Cold-water Coral Geographic Database developed by the USGS with support from the DSCRTP. The USGS Cold-Water Coral Geographic Database (CoWCoG) consolidates the known locations of deep sea corals in the eastern US and provides a tool for researchers and managers interested in studying, protecting, and/or utilizing cold-water coral habitats in the Gulf of Mexico and western North Atlantic Ocean. The database makes information about the locations and taxonomy of deep sea corals available to the public in an easy-to-access form while preserving the scientific integrity of the data. The database includes over 1,700 entries, mostly from published scientific literature, museum collections, and other databases (Scanlon et. al., 2010).

This database was supplemented with additional records provided by the Watling et al. database (2003), the Theroux and Wigley database (1998), the Smithsonian Institution's National Museum of Natural History and NMFS NEFSC's National Systematics Lab, the archives of the former National Undersea Research Center, surveys by Dr. Barbara Hecker and her colleagues (e.g., Hecker et al., 1980, 1983), Peter Auster of the University of Connecticut, and the NEFSC. Many of these records were obtained through a data mining project sponsored by the DSCRTP. For the complete list of northeast deep sea coral references, see Packer et al. (2007). It should be noted that the distribution maps presented in this chapter show presence only; i.e., they only describe where deep corals that could be identified were observed or collected. Since all areas have not been surveyed and since some specimens were not identified, the true distributions of many of these species remain unknown. However, these combined databases represent the best available georeferenced data on the presence of deep corals in the northeast region.

5.5. RESULTS

There are a total of 5,619 records of known deep sea corals for the study area (Table 5.1). Of these, 4,625 are for sea pens (Pennatulacea; Figure 5.3). The most common and fairly widespread species found in the deeper parts of the continental shelf are *Pennatula aculeata* (common sea pen) (Langton et. al., 1990) and *Stylatula elegans* (white sea pen). *P. aculeata* has been reported down to depths of 3,300 m. *S. elegans* is abundant on the mid-Atlantic coast outer shelf (Figure 5.3) and has been found as deep as 800 m. Unlike most other deep sea corals, sea pens live in muddy or other soft sediments, anchored in place by a swollen, buried peduncle. Some species are capable of retracting part or the entire colony into the sediment when disturbed. Observation suggests that sea pens are resistant to physical disturbance, although growth and population dynamics have not been investigated, but because of their ubiquity they are generally not of concern for biodiversity or ecosystem management.

Table 5.1: Number of deep sea coral records in the study area as a total and by taxonomic order.

TAXONOMIC ORDER	COUNT
All Deep Sea Corals	5,619
Pennatulacea	4,625
Scleractinia	338
Alcyonacea	365
Gorgonacea	291

The remaining 994 records are observations of hard and soft corals, mostly from the shelf and slope. There are 338 records of stony corals (Scleractinia; Figure 5.4). These observations occur between 14 and 2,654 meters depth. Most of the stony corals in this region are solitary organisms and are often found on soft substrates. Species observed included *Dasmosmilia lymani* (Figure 5.1), *Flabellum alabastrum*, and *Astrangia* sp. (most likely *Astrangia poculata*, which can occur in very shallow water, at depths of only a few meters).

There are 365 records of true soft corals (Alcyonacea; Figure 5.5). These observations were made between 30 meters and 3,506 meters, with notable concentrations occurring at the shelf edge between 100 and 200 meters and again between 2,000 and 3,000 meters depth. Species observed included, *Capnella florida*, *Anthomastus grandiflorus*, *Anthomastus agassizii*, and *Gersemia fruticosa*. *Gersemia rubiformis* is very numerous in nearshore records throughout the northeast.

There are 291 records of Gorgonians occurring between 310 and 3,206 meters, predominantly deeper than 600 meters (Figure 5.6). Species observed included *Acanella arbuscula*, *Acanthogorgia armata*, *Anthothela grandiflora*, *Lepidisis caryophyllia*, *P. arborea*, *Paramuricea grandis*, *P. resedaeformis*, *Swiftia casta*, and *Radicipes gracilis*.

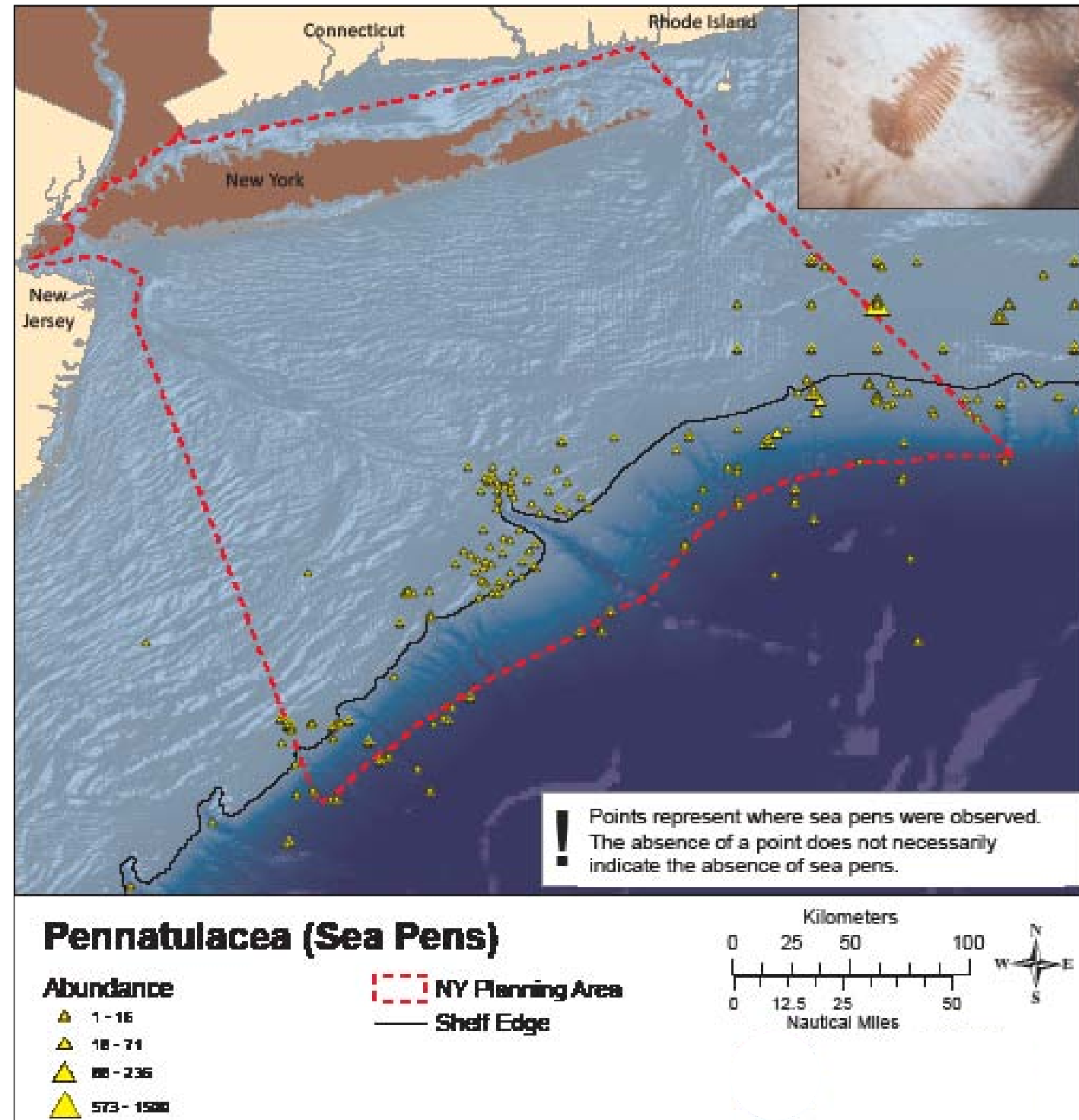


Figure 5.3. Observed Pennatulacea locations.

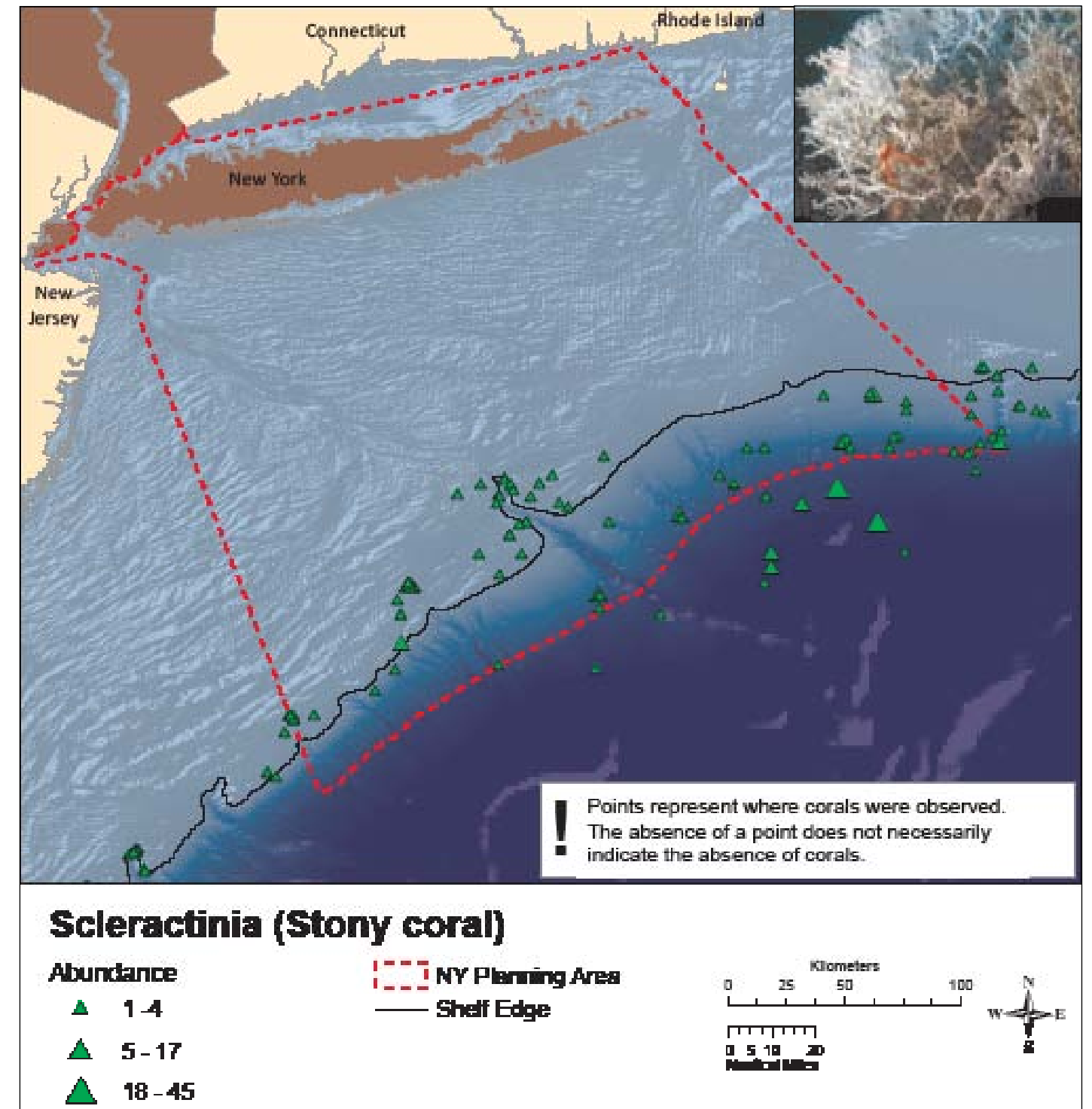


Figure 5.4. Observed Scleractinea locations.

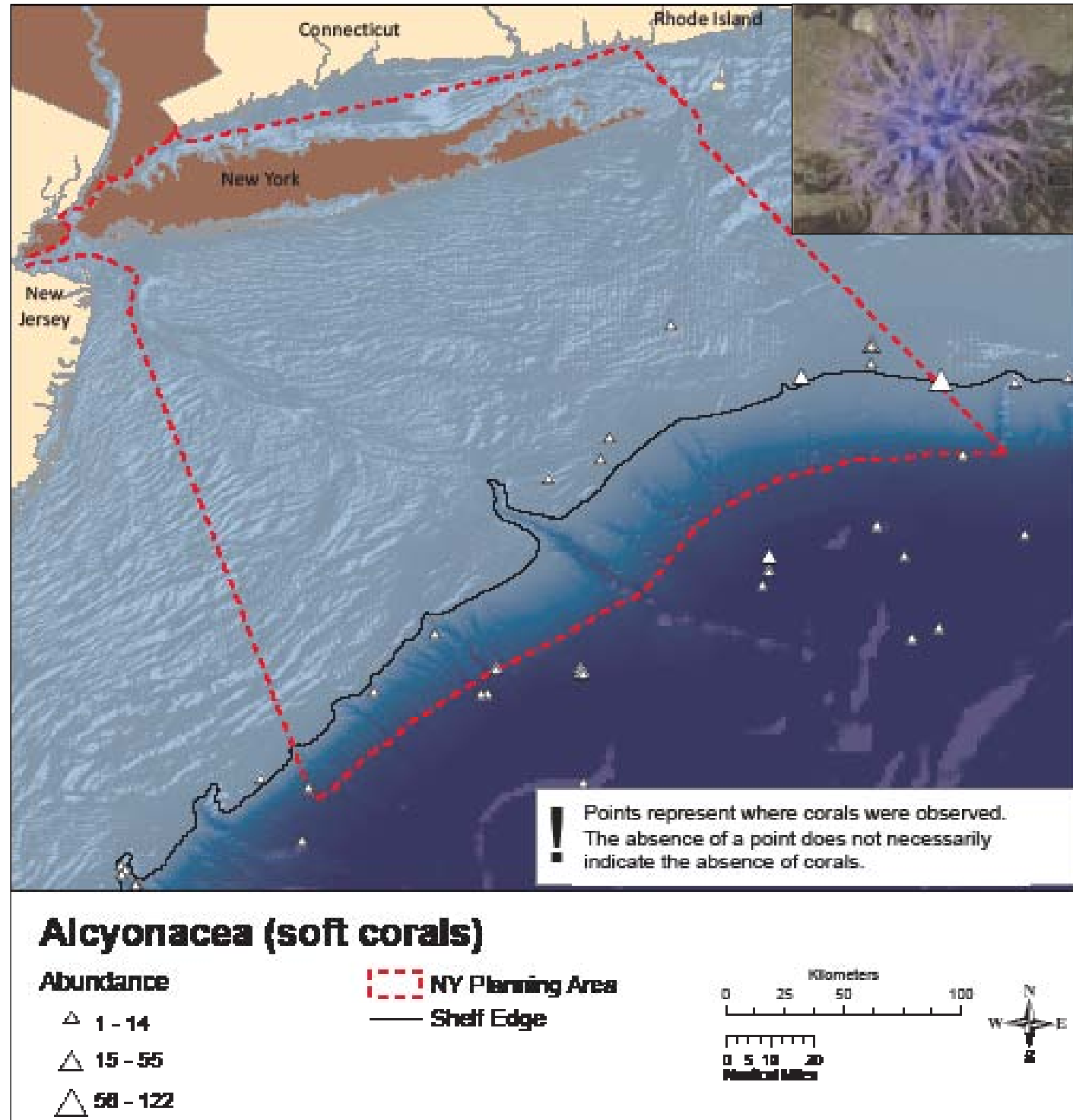


Figure 5.5. Observed Alcyonacea locations.

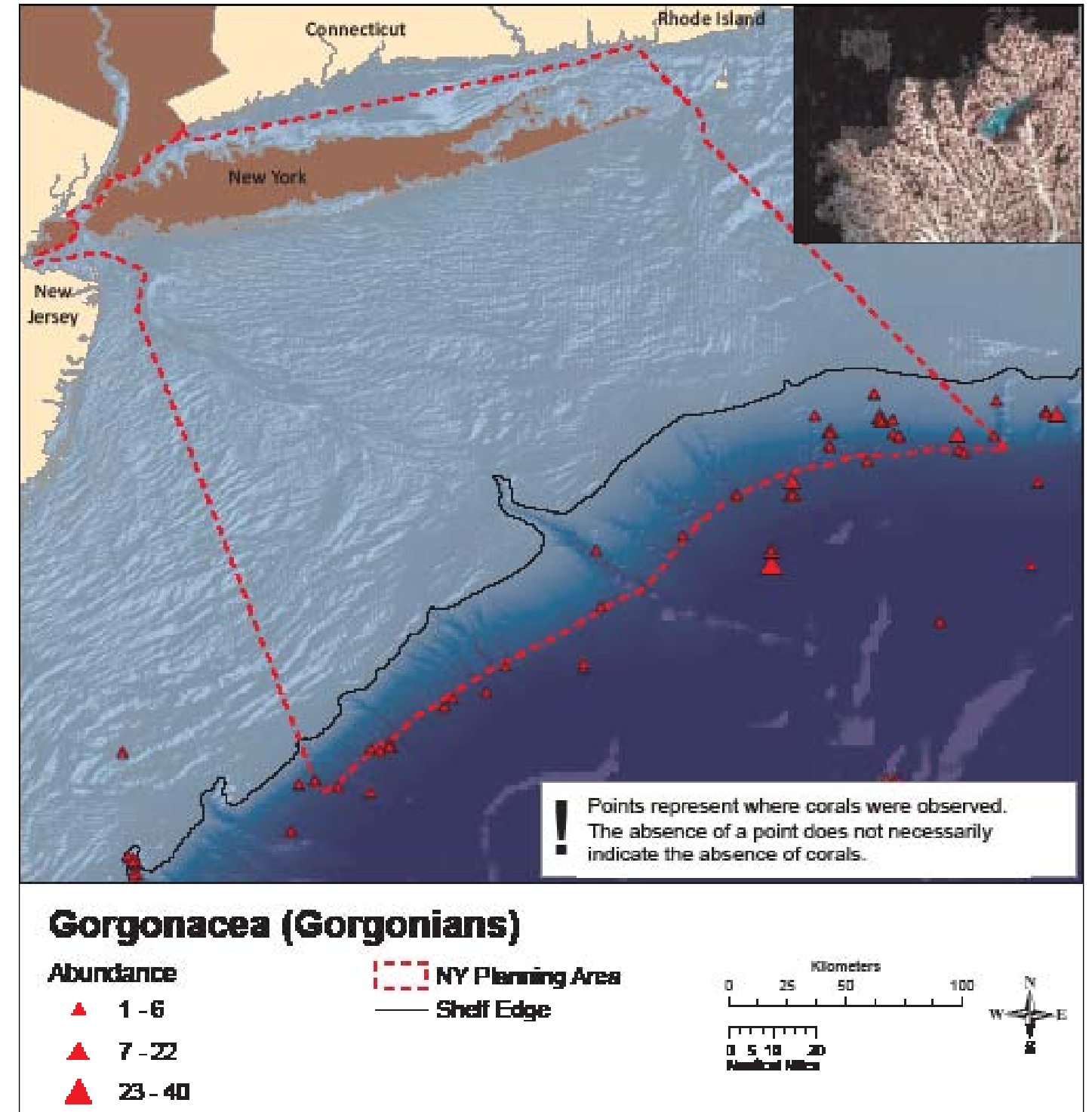


Figure 5.6. Observed Gorgonacea locations.

Hudson Canyon

Deep sea corals have been seen on the shelf around Hudson Canyon and in the head of the Canyon. For example, a survey by Guida¹ of benthic habitats on the shelf around Hudson Canyon in 2001, 2002, and 2004 found the solitary stony coral *D. lymani* at a number of sites at depths ranging from 100 to 200 m (Figure 5.7). They were particularly abundant, occurring in patches in a narrow band along the canyon's rim near its head at depths of 105-120 m; local densities within those patches exceeded 200 polyps m², but densities elsewhere were much lower. Other records of deep sea corals around Hudson Canyon can be found in Packer et al. (2007). However, the only evidence of deep corals occurring deep within the canyon itself comes from Hecker and Blechschmidt (1980), who found abundant populations of the soft coral *Eunephthya fructosa* (same as *G. fructosa*?), but only in the deeper portion of the canyon. This may be due to the predominance of soft substrate within the Canyon itself, although recent mapping surveys (Guida¹) have found evidence of hard bottom areas that may serve as deep sea coral habitat.

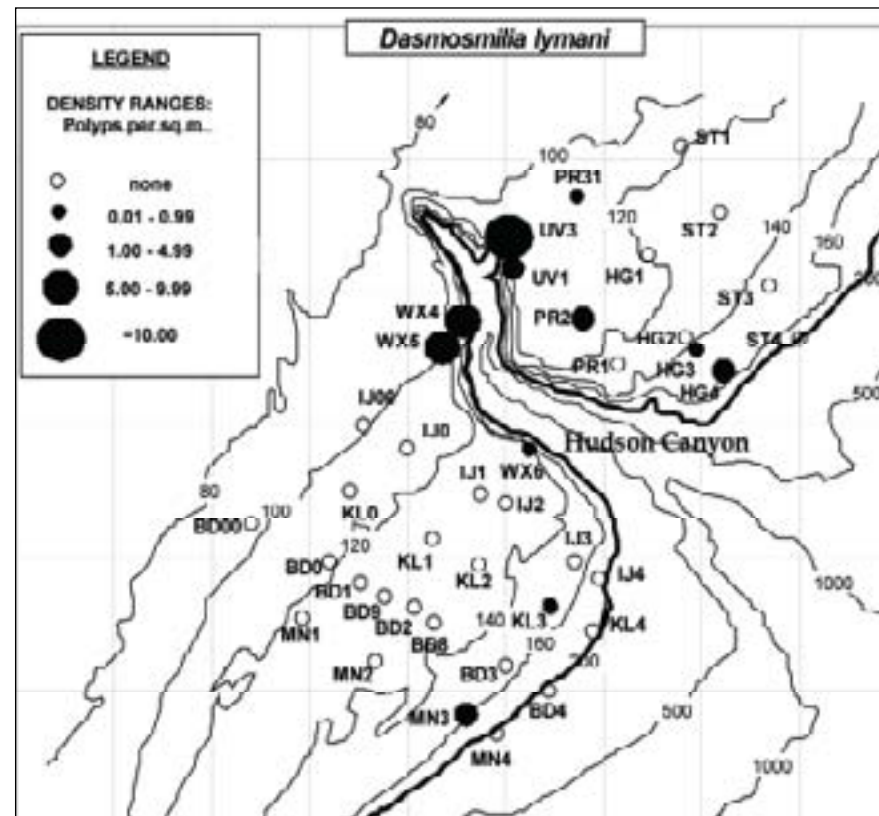


Figure 5.7. Distribution and approximate densities (polyps per square meter) of the solitary stony coral *Dasmomilia lymani* in samples from the Mid-Atlantic shelf around Hudson Canyon (Guida¹). Data obtained from still photos and trawl samples taken during October and November 2001, 2002, and August 2004.

In addition to deep sea corals, there are records of sponges around Hudson Canyon, a result of a single research effort by Guida¹. Structure forming sponges are expected to play a similar role to deep sea corals by providing potential habitat for other species. Sponges were observed at 22 locations, with densities ranging from 0.1 to > 100/sq dm (Figure 5.8). An effort is currently underway to obtain and document records of sponge occurrences off the northeastern U.S. (e.g., from the Smithsonian Institution's database).

An additional map is included showing both deep sea corals and sponges in a single image. (Figure 5.9)

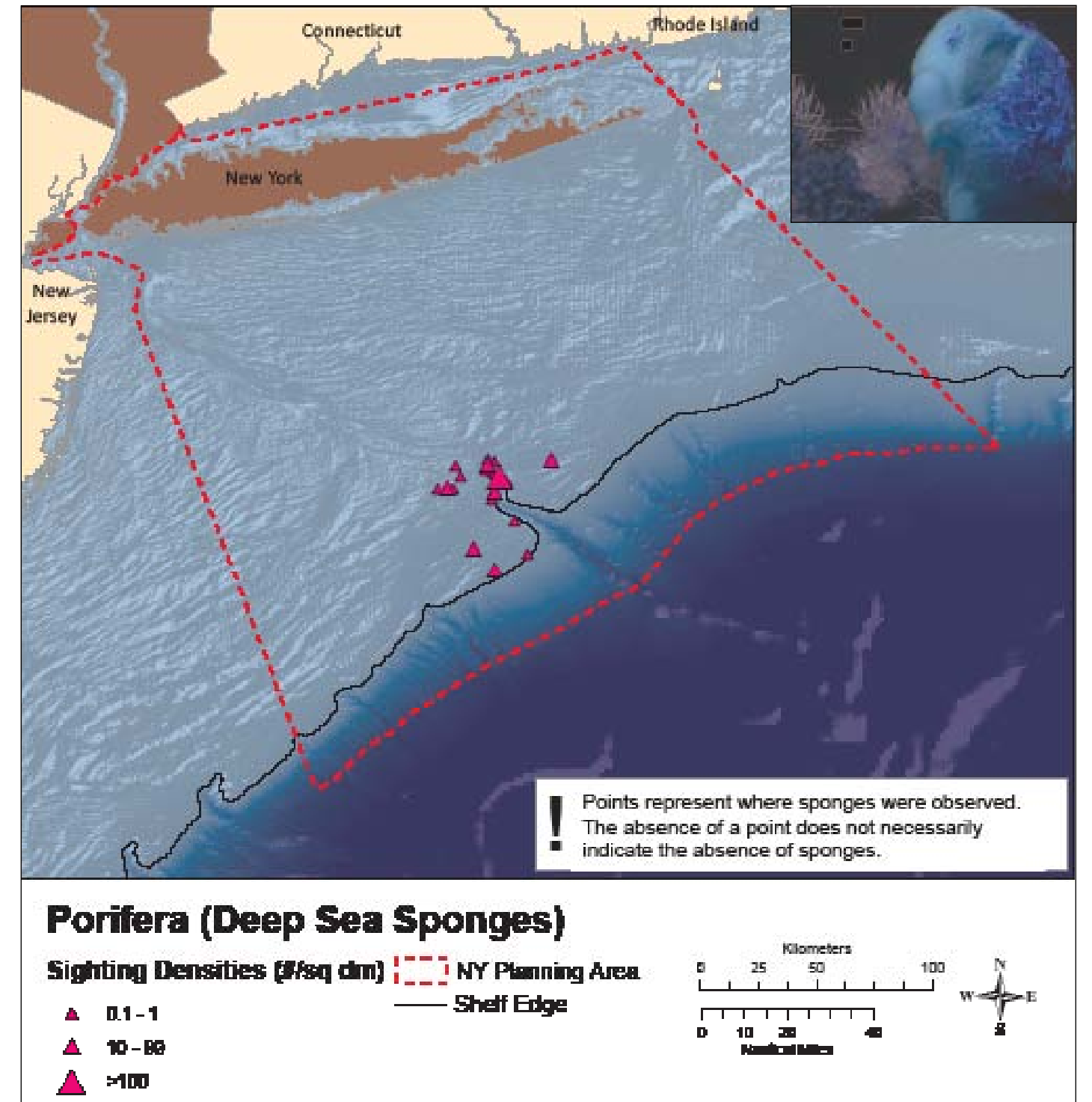


Figure 5.8. Observed deep sea sponge locations.

¹ Guida, V. 2004. Unpubl. data. NOAA, NMFS, NEFSC, James J. Howard Marine Sciences Laboratory, 74 Magruder Road, Sandy Hook Highlands, NJ 07732.

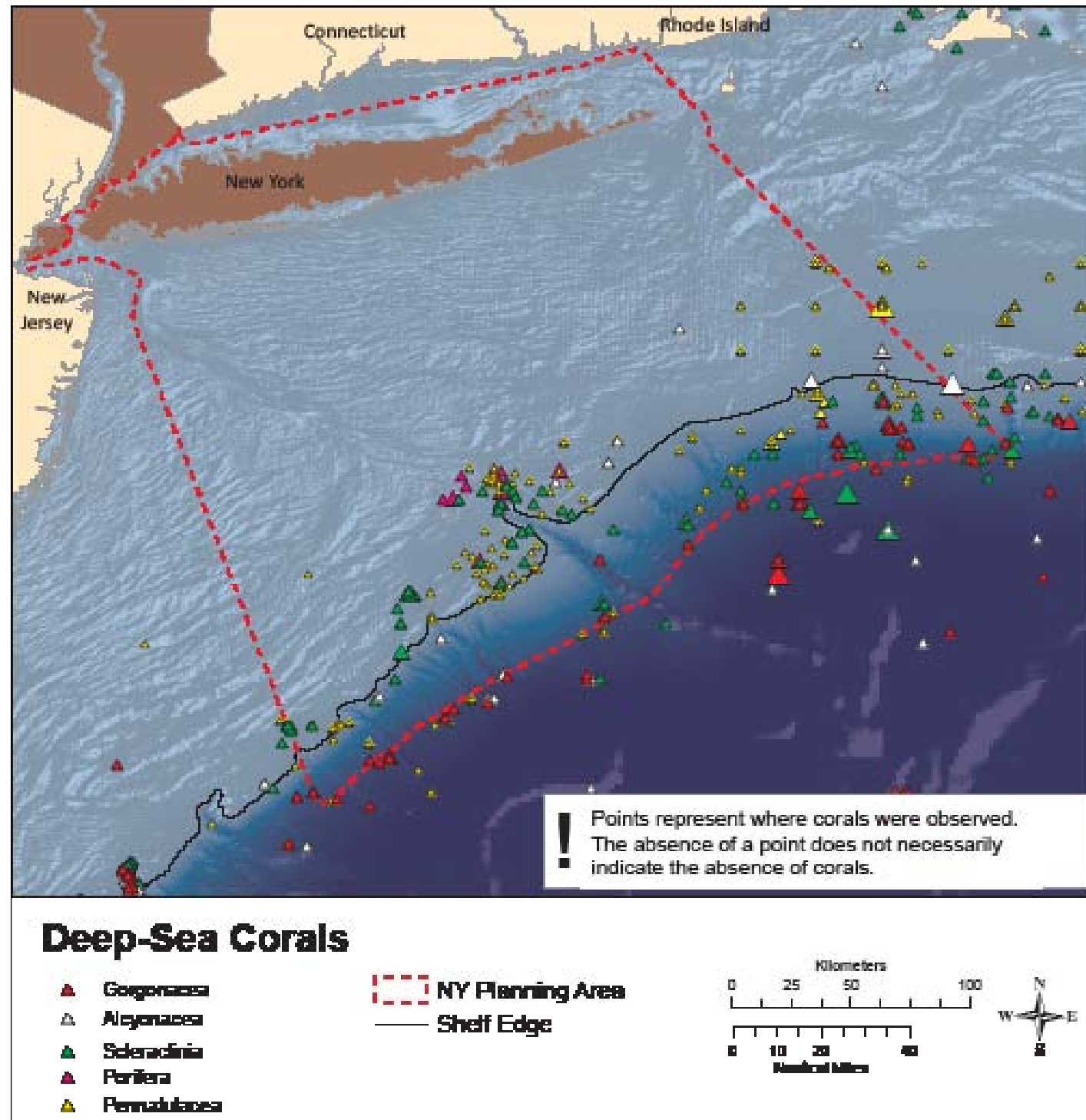


Figure 5.9. Observed deep sea coral and sponge locations.

Northeast Region
 Our knowledge of the distribution of deep sea corals for the Northeast Region (Maine - North Carolina) is incomplete, so conclusions drawn from existing data should be considered preliminary. The known distribution of corals in the region is shown in Figure 5.10. Distribution of corals in the region is similar to the distribution found within the study area, with concentrations occurring on the shelf edge and shelf break.

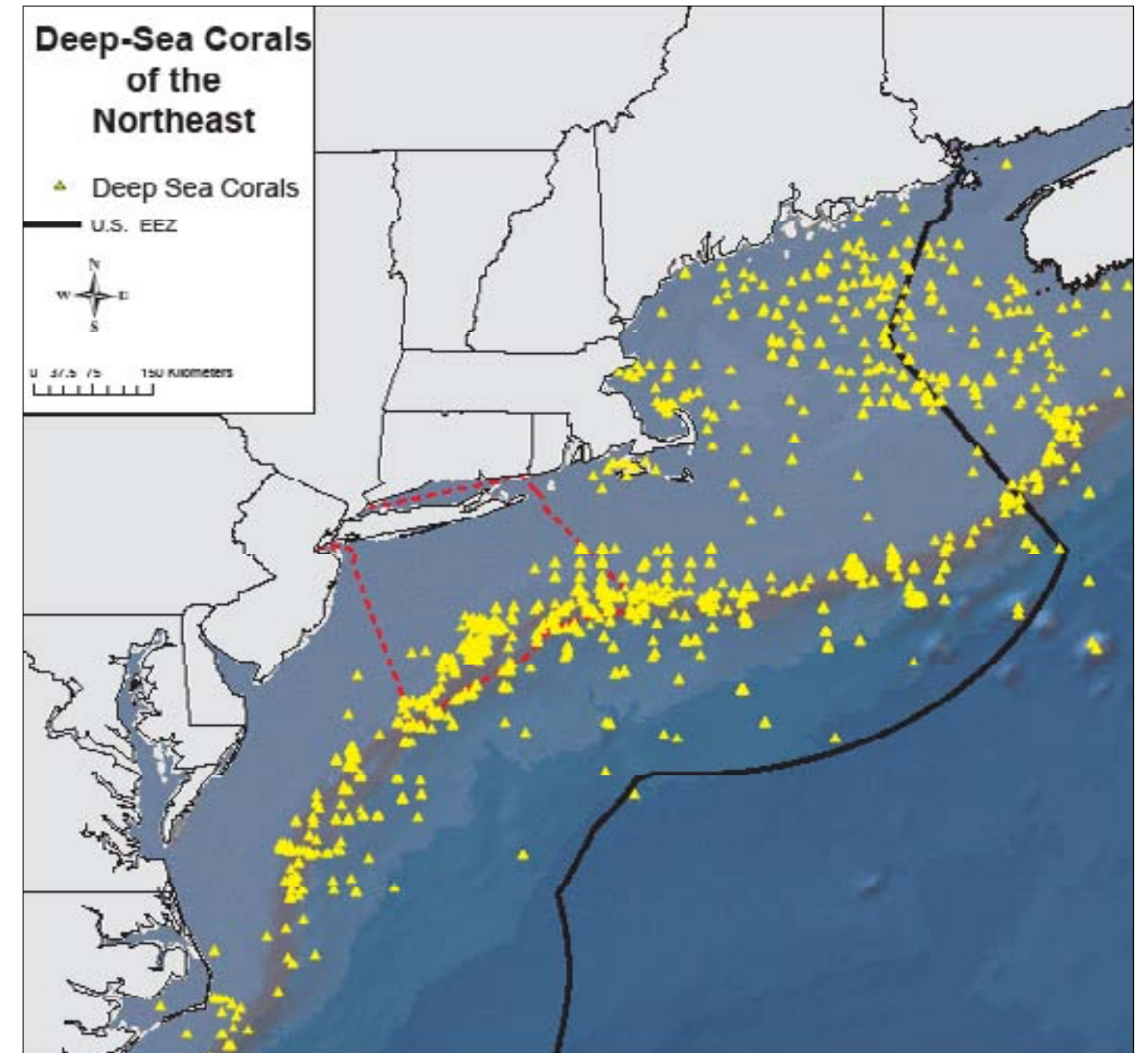


Figure 5.10. Known deep sea coral locations for the Northeast Region.

5.6. DISCUSSION

Deep sea corals provide habitat for other marine life, increase habitat complexity, and contribute to marine biodiversity, and their destruction could impact other marine species. Anecdotal data from surveys as well as reports from fishermen, who have brought corals up as bycatch since the 19th century, suggest that deep sea corals have become less common or their distributions have been reduced due to the impacts of bottom fishing (e.g., off New England); fishing has had significant effects on deep sea coral populations in other regions. Deep corals are especially susceptible to damage by fishing gear because of their often fragile, complex, branching form of growth above the bottom. Also, they grow and reproduce at very slow rates, with some estimates on the scale of hundreds of years. Recruitment rates may also be low, which makes their recovery from disturbances difficult over short time periods. Of the various fishing methods, bottom trawling has been found to be particularly destructive (e.g., Rogers, 1999; Hall-Spencer et al., 2001; Koslow et al., 2001; Krieger, 2001; Fosså et al., 2002; Freiwald, 2002).

The effects of current and historic fishing efforts on deep sea coral and coral habitats in the northeastern U.S. have not been quantified. The types of fishing gear used in the region include fixed gear, such as longlines, gillnets, and pots and traps, as well as trawls and dredges. Fixed gear can be lost at sea, where it can continue to damage corals. In Canada, longlines have been observed entangled in deep sea corals such as *Paragorgia* and *Primnoa* and may cause breakage (Breeze et al., 1997; Mortensen et al., 2005). Bottom trawling was found to have a larger impact on deep sea corals compared to longlining (e.g., damage to *Primnoa* off Alaska [Krieger, 2001]). The northeastern U.S. fisheries that have the highest likelihood of occurring near concentrations of known deep sea coral habitats (e.g., in canyon and slope areas) are the monkfish or goosefish and tilefish fisheries, and the red crab and offshore lobster pot fisheries.

Other potential threats to deep sea corals in this region include possible oil and gas drilling in the deeper parts of the shelf, and ocean acidification due to global warming. Deep sea coral communities may be uniquely vulnerable to changes in ocean chemistry associated with ocean acidification due to increased atmospheric CO₂ from the combustion of fossil fuels (Guinotte et al., 2006). The ocean acts as the largest net sink for CO₂, absorbing this gas from the atmosphere and then storing carbon in the deep ocean. Oceanic uptake of CO₂ drives the carbonate system to lower pH and lower saturation states of the carbonate minerals calcite and aragonite, the materials used to form supporting skeletal structures in many major groups of marine organisms, including corals (Kleypas et al., 2006). This change in ocean chemistry will reduce the ability of corals; i.e., stony corals, to lay down calcium carbonate skeletons (calcification). There is evidence that the rate of CO₂ increase in the deep ocean has been occurring at a pace double that of shallow waters and therefore the effect of ocean acidification on deep sea corals could be significant (e.g., Bates et al., 2002; Guinotte et al., 2006). The ability for organisms to calcify decreases in the deep ocean naturally with latitude, temperature, and pressure, causing an increased concern for deep sea corals in the near future. There are also areas in the ocean where a natural boundary, known as the 'saturation horizon', exists below which organisms may have difficulty forming calcium carbonate. This is due to the physical factors already mentioned that decrease calcification in the deep ocean, but as CO₂ levels increase the saturation horizon will become shallower. This would severely limit the distribution of deep sea corals in certain parts of the ocean (The Royal Society, 2005).

In 2005, NEFMC and MAFMC, with the NEFMC as the lead, approved the designation of Oceanographer and Lydonia Canyons (located off New England on the continental slope south of the Georges Bank fishing grounds; approximately 116 square nautical miles) as Habitat Closed Areas (HCA) and added these areas to the NEFMC's network of HCAs (or marine protected areas). These new HCAs are closed indefinitely to fishing with bottom trawls and bottom gillnets in order to minimize the impacts of the monkfish fishery on Essential Fish Habitat (EFH) in these deep sea canyons and on the structure-forming organisms therein, including deep sea corals. Veatch and Norfolk Canyons are also protected under the Tilefish Management Plan and are closed to bottom-tending gear. Recently, a working group of the NEFMC has developed a series of proposals for the designation of specific deep sea coral protection zones off the northeastern U.S. using the discretionary authorities under the Magnuson-Stevens Act Section 303(b). They have also developed a range of possible management options for those zones and suggestions for future research.

Areas where deep sea corals are present should be considered vulnerable marine ecosystems and efforts are underway to extend protection to these valuable natural resources. The NOAA Strategic Plan for Deep Sea Coral and Sponge Ecosystems encourages avoidance of adverse impacts of non-fishing activities on deep sea coral and sponge ecosystems. Impacts to deep sea corals and sponge ecosystems should be evaluated when considering off-shore development of energy facilities and infrastructure.

Packer et al. (2007) outline some of the research priorities for the deep sea corals in this region. To better preserve and protect them, first there needs to be increased mapping and survey efforts, and more basic research is needed on their taxonomy, life history, habitat requirements, water chemistry, species associations, etc. Predictive modeling for individual species of deep sea corals has assisted research and monitoring efforts in other regions (e.g., Davies and Guinotte, 2011) and is recommended for this region in order to support planning and management decisions. There needs to be a better understanding of how anthropogenic impacts (e.g., fishing, ocean acidification, oil and gas drilling) affect the deep sea corals of this region. As mentioned previously, the DSCRTP and NEFSC are planning to conduct deep sea coral fieldwork off the northeastern U.S., including the MAFMC and NEFMC regions, in 2013-15.

5.7. REFERENCES

- Auster, P. 2005. Are deep-water corals important habitats for fishes? In: Freiwald, A. and A. Roberts (eds.). Cold-water corals and ecosystems. Berlin, Heidelberg: Springer-Verlag. p. 643-656.
- Bates, N.R., A.C. Pequignet, R.J. Johnson, and N. Gruber. 2002. A short-term sink for atmospheric CO₂ in subtropical mode water of the North Atlantic Ocean. *Nature* 420: 489-493.
- Breeze, H., D.S. Davis, M. Butler, and V. Kostylev. 1997. Distribution and status of deep sea corals off Nova Scotia. Marine Issues Committee Special Publication Number 1, Ecology Action Center, Halifax, NS. 58 p.
- Cairns, S.D. and F.M. Bayer. 2005. A review of the genus *Primnoa* (Octocorallia: Gorgonacea: Primnoidae), with the description of two new species. *Bull. Mar. Sci.* 77: 225-256.
- Davies, A.J. and J.M. Guinotte. 2011. Global Habitat Suitability for Framework-Forming Cold-Water Corals. *PLoS ONE* 6(4): e18483. Doi:10.1371/journal.pone.0018483.
- Fosså, J.H., P.B. Mortensen, and D.M. Furevik. 2002. The deep-water coral *Lophelia pertusa* in Norwegian waters: Distribution and fishery impacts. *Hydrobiologia* 471: 1-12.
- Freiwald, A. 2002. Reef-forming cold-water corals. In: Wefer, G., Billet, D., Hebbeln, D., Jorgensen, B.B., Schluter, M., Van Weering, T. (eds.). Ocean margin systems. Berlin, Germany: Springer-Verlag. p. 365-385.
- Guinotte, J.M., J. Orr, S. Cairns, A. Freiwald, L. Morgan, and R. George. 2006. Will human-induced changes in seawater chemistry alter the distribution of deep sea scleractinian corals? *Frontiers Ecol. Environ.* 4: 141-146.
- Hall-Spencer, J., V. Allain, and J.H. Fosså. 2001. Trawling damage to Northeast Atlantic ancient coral reefs. *Proc. Royal Soc. London Ser. B-Biol. Sci.* 269: 507-511.
- Hecker, B. and G. Blechschmidt. 1980. Final historical coral report for the canyon assessment study in the Mid- and North Atlantic areas of the U.S. outer continental shelf: epifauna of the northeastern U.S. continental margin. Appendix A. In: Canyon assessment study. U.S. Dep. Int., Bur. Land Manage., Washington, DC, No. BLM-AA551-CT8-49.
- Hecker, B., G. Blechschmidt, and P. Gibson. 1980. Final report for the canyon assessment study in the Mid- and North Atlantic areas of the U.S. outer continental shelf: epifaunal zonation and community structure in three Mid- and North Atlantic canyons. In: Canyon assessment study. U.S. Dep. Int., Bur. Land Manage., Washington, DC, No. BLM-AA551-CT8-49. p. 1-139.
- Hecker, B., D.T. Logan, F.E. Gandarillas, and P.R. Gibson. 1983. Megafaunal assemblages in Lydonia Canyon, Baltimore Canyon, and selected slope areas. In: Canyon and slope processes study: Vol. III, biological processes. Final report for U.S. Dep. Int. Mineral Manage. Ser. No. 14-12-001-29178. p. 1-140.
- Kleypas, J.A., R.A. Feely, V.J. Fabry, C. Langdon, C.L. Sabine, and L.L. Robbins. 2006. Impacts of ocean acidification on coral reefs and other marine calcifiers: a guide for future research. Workshop Rep., 18-20 April 2005, St. Petersburg, FL, sponsored by NSF, NOAA, U.S.G.S. 88 p.
- Koslow, J.A., K. Gowlett-Holmes, J.K. Lowry, T. O'Hara, G.C.B. Poore, and A. Williams. 2001. Seamount benthic macrofauna off southern Tasmania: community structure and impacts of trawling. *Mar. Ecol. Prog. Ser.* 213: 111-125.
- Krieger, K.J. 2001. Coral (*Primnoa*) impacted by fishing gear in the Gulf of Alaska. In: Willison, J.H.M., J. Hall, S.E. Gass, E.L.R. Kenchington, M. Butler, and P. Doherty (eds.). Proceedings of the First International Symposium on Deep sea Corals. Ecology Action Center, Halifax, NS. p. 106-116.
- Langton, R.W., E.W. Langton, R.B. Theroux, and J.R. Uzmann. 1990. Distribution, behavior and abundance of sea pens, *Pennatula aculeata*, in the Gulf of Maine. *Mar. Biol.* 107: 463-469.
- Leverette, T.L. and A. Metaxas. 2005. Predicting habitat for two species of deep-water coral on the Canadian Atlantic continental shelf and slope. In: Freiwald, A. and A. Roberts. (eds.) Cold-water corals and ecosystems. Berlin, Heidelberg: Springer-Verlag. p. 467-479.

Lumsden, S.E., T.F. Hourigan, A.W. Bruckner, and G. Dorr. (eds.). 2007. The state of deep coral ecosystems of the United States. NOAA Tech. Memo. CRCP-3.

Mortensen, P.B. and L. Buhl-Mortensen. 2004. Distribution of deep-water gorgonian corals in relation to benthic habitat features in the Northeast Channel (Atlantic Canada). *Mar. Biol.* 144: 1223-1238.

Mortensen, P.B., L. Buhl-Mortensen, D.C. Gordon, Jr., G.B.J. Fader, D.L. McKeown, and D.G. Fenton. 2005. Effects of fisheries on deep-water gorgonian corals in the Northeast Channel, Nova Scotia (Canada). In: Barnes, P.W. and J.P. Thomas (eds.). Benthic habitats and the effects of fishing. *Am. Fish. Soc. Symp.* 41: 369-382.

Mosher, C.V. and L. Watling. 2009. Partners for life: a brittle star and its octocoral host. *Mar. Ecol. Prog. Ser.* 397: 81-88.

Packer, D.B., D. Boelke, V. Guida, L.-A. McGee. 2007. State of deep coral ecosystems in the northeastern US region: Maine to Cape Hatteras. In: Lumsden, S.E., T.F. Hourigan, A.W. Bruckner, and G. Dorr (eds.). The state of deep coral ecosystems of the United States. NOAA Tech. Memo. CRCP-3. p. 195-232.

Rogers, A.D. 1999. The biology of *Lophelia pertusa* (Linnaeus 1758) and other deep-water reef-forming corals and impacts from human activities. *Internat. Rev. Hydrobiol.* 84: 315-406.

The Royal Society. 2005. Ocean acidification due to increasing atmospheric carbon dioxide. The Royal Society Policy Doc. 12/05, June 2005. Cardiff, UK: The Clyvedon Press Ltd. p.1-57.

Scanlon, K.M., R.G. Waller, A.R. Sirotek, J.M. Knisel, J.J. O'Malley, and S. Alesandrini. 2010. USGS cold-water coral geographic database - Gulf of Mexico and Western North Atlantic Ocean, Version 1.0. US Geological Survey. Open File Report 2008-1351.

Stevenson, D.K., L. Chiarella, D. Stephan, R. Reid, K. Wilhelm, J. McCarthy, and M. Pentony. 2004. Characterization of the fishing practices and the marine benthic ecosystems of the northeast U.S. shelf, and an evaluation of the potential effects of fishing on Essential Fish Habitat. NOAA Tech. Memo. NMFS-NE-181.

Theroux, R.B. and R.L. Wigley. 1998. Quantitative composition and distribution of the macrobenthic invertebrate fauna of the continental shelf ecosystems of the northeastern United States. NOAA Tech. Rep. NMFS-140. 240 p.

Verrill, A.E. 1862. Notice of a *Primnoa* from Georges Bank. *Proc. Essex Inst., Salem, MA* 3: 127-129.

Verrill, A.E. 1878a. Notice of recent additions to the marine fauna of the eastern coast of North America. *Am. J. Sci. Arts Ser. 3*, 16: 207-215.

Verrill, A.E. 1878b. Notice of recent additions to the marine fauna of the eastern coast of North America, No. 2. *Am. J. Sci. Arts Ser. 3* (16): 371-379.

Verrill, A.E. 1879. Notice of recent additions to the marine fauna of the eastern coast of North America, No. 5. *Am. J. Sci. Arts Ser. 3* (17): 472-474.

Verrill, A.E. 1884. Notice of the remarkable marine fauna occupying the outer banks of the southern coast of New England. *Am. J. Sci. Arts Ser. 3* (28): 213-20.

Watling, L. and P. Auster. 2005. Distribution of deep-water Alcyonacea off the northeast coast of the United States. In: Freiwald, A., A. Roberts (eds.). Cold-water corals and ecosystems. Berlin, Heidelberg: Springer-Verlag. p. 259-264.

Watling, L., P. Auster, I. Babb, C. Skinder, and B. Hecker. 2003. A geographic database of deepwater alcyonaceans of the northeastern U.S. continental shelf and slope. Version 1.0 CD-ROM. Nat. Undersea Res. Cent., Univ. Conn., Groton.

This page intentionally left blank.

Predictive Modeling of Seabird Distribution Patterns in the New York Bight†

Brian P. Kinlan^{1,2}, Charles Menza¹, and Falk Huettmann³

6.1. SUMMARY

In this chapter we develop and present maps of the seasonal and annual distributions of selected seabird species and species groups in the New York study area (the NY Bight, Figure 1.2). The maps are based on seabird-environment statistical models fit to visual shipboard seabird observational data collected as part of a standardized survey program from 1980-1988. Models are developed for single species and for species groups, and then combined to produce “hotspot” maps depicting multi-species abundance and diversity patterns. In addition to a large geodatabase of standardized offshore seabird surveys, the predictive models developed here make use of spatially explicit environmental data products from long-term archival satellite, oceanographic, hydrographic, and biological databases that were developed and discussed in Chapter 4. Seabird distribution maps produced include seasonal and annual relative indices of occurrence and abundance, with associated maps depicting metrics of certainty. All information is mapped on the same 30 arc-second (less than one kilometer) horizontal resolution grid used to characterize surficial sediments and ocean habitat variables in Chapters 3 and 4.



Image 6.1. Cory's Shearwater and Wilson's Storm-Petrels.
Photo by: David Pereksta, BOEM

High-resolution, contiguous predictive maps of seabird distributions and maps depicting accuracy of model predictions were two critical information gaps identified in discussions with New York State's Department of State, Ocean and Great Lakes Program. These products are expected to be useful contributions to offshore spatial planning, particularly for activities that may affect seabirds or their habitats.

6.2. DEFINITION OF SEABIRDS

In this chapter we operationally define seabirds as all avian species regularly sighted over marine waters. Given this definition, most species included in this chapter belong to the following taxonomic orders: Charadriiformes (gulls, terns, auks, phalaropes), Pelecaniformes (gannets, pelicans, and cormorants), and Procellariiformes (shearwaters, fulmars, petrels). These species generally derive the majority of their nutrition from marine productivity. Some species in the orders Anseriformes (ducks, geese, swans) and Gaviiformes (loons) are also included in our operational definition, but most seafaring species in this order rely only partially on the marine environment. Many of the species presented in this chapter, especially those preferring more nearshore habitats, also fall under various definitions for shorebirds or waterbirds. We also note that although some Falconiformes (falcons, osprey) can be pelagic, and some passerine birds can be observed offshore from time to time, we did not include them in this study due to lack of data.

¹ National Oceanic and Atmospheric Administration, National Ocean Service, National Centers for Coastal Ocean Science, Center for Coastal Monitoring and Assessment, Biogeography Branch, 1305 East West Hwy, SSMC-4, N/SCI-1, Silver Spring, MD 20910-3281.

² Consolidated Safety Services, Inc., 10301 Democracy Lane, Suite 300, Fairfax, Virginia 22030

³ EWHALE lab, Biology and Wildlife Department, Institute of Arctic Biology, University of Alaska-Fairbanks, Fairbanks, Alaska 99775-7000.

† Author contributions: BPK led design of research, obtained and processed data, carried out all analyses, interpreted results, and wrote the document. CM assisted with research design, data processing, results interpretation, and writing. FH contributed to the discussion and interpretation of results.

6.3. SEABIRD ECOLOGY IN THE NEW YORK BIGHT

Seabirds are a conspicuous and ecologically important component of coastal and marine ecosystems. They are typically long-lived (15-70 years), move over broad ranges and feed at a variety of trophic levels. As such, they are responsive to changes in the marine and coastal environment and can be useful indicators of cumulative biological, physical and chemical changes in marine ecosystems. However, because seabirds are highly mobile, long-lived, and occupy a dynamic environment, observations and predictive models of their spatial and temporal distributions present a formidable challenge (see Section 6.6.).

The New York study area is located along the Atlantic Flyway, one of four major American migration routes for migrating waterfowl, shorebirds, predatory birds, songbirds and seabirds. Along the Flyway, coastal and marine habitats provide shelter and food for birds at stopover sites between wintering areas (generally to the south) and breeding areas (generally to the north, but some species, such as the Great Shearwater, Sooty Shearwater, and Wilson's Storm-Petrel, are southern hemisphere breeders). The Flyway is generally considered to follow the Atlantic shoreline, but some species like the Manx Shearwater and Arctic Tern migrate out at sea, far from land (Guilford et al., 2009; Egevang et al., 2010).

Most species are temporary residents gathering food in pelagic and coastal habitats as they overwinter during the non-breeding season, stopover during migration, or breed during the summer months. The community of seabirds in the study area is constantly changing and a dominant species in one season may not be observed in other seasons. For instance, Wilson's Storm-Petrel is one of the most abundant species in the summer months, but is practically absent from surveys in the winter.

Most species found in the study area breed elsewhere, but at least 10 seabird species breed along New York's mainland shores, on Long Island and on a few smaller offshore islands (New York State Ornithological Association, Breeding Bird survey). The main breeding season lasts from May to early September (Forbush, 1929; Bull, 1974; Harrison, 1978), during which time seabirds use the study area to acquire food critical to brood success. Breeders usually arrive earlier and stay later than the breeding seasons to prepare for breeding and migration to overwintering sites. In the maps shown later in this report, the breeding period is best reflected by "summer" data.

Seabirds occupy an assortment of ecological niches and thus exhibit a range of spatial distributions. Some species spend the majority of time along coastal shorelines, while others live offshore coming to land only to breed. As in terrestrial ecosystems, some marine areas are more important than others; however few regions of the ocean are entirely free of seabirds at all times. "Hotspots," or "persistent aggregations" of seabirds, defined here as areas where higher-than-average abundance (or diversity) of seabirds is frequently observed, are often located where food availability is high and/or where the required effort to obtain food is comparatively low. Elevated food availability can be natural (e.g., areas of high ocean productivity) or anthropogenic (e.g., areas of fishery discards and human refuse disposal). Hotspots of abundance and/or species diversity may also form near breeding areas and along migratory pathways. Due to the strong seasonal signal in the NY marine and coastal environment, the location of seabird hotspots is likely to vary not only among species but among seasons even for the same species.

Understanding environmental, biological/ecological and anthropogenic processes that affect seabird behaviors is critical to understanding seabird distributions. Many studies have shown a strong correlation between seabird distribution and biophysical variables, including sea surface temperature, mixed-layer depth (stratification), the location of prey and subsurface predators, weather, and distance to nesting sites (e.g., Schneider 1990, 1997; Ballance et al., 2001; Daunt et al., 2003; Yen et al., 2004; Friedland et al., 2012). In this chapter we take advantage of some of these environmental relationships to generalize from sighting data to make predictions about seabird occurrence and abundance at unsurveyed locations.

In addition to biophysical variables, seabird communities are tightly linked to many human activities, including fishing, hunting, coastal development, shipping, and resource extraction. The present-day seabird community structure must be viewed in the context of both past and present conditions and impacts, both human and natural. For instance, humans have drastically altered the population levels of Common Terns and Herring

Gulls. Credible reports identify Common Tern nesting sites with hundreds of thousands of birds in the Northwest Atlantic in the late 19th century (Brewster, 1879). Now, the population consists of approximately 40,000 pairs, almost half of which are found in New York (Nisbet, 2002). Common Terns were hunted for use in the hatmaking industry in the late 19th century, but modern threats include habitat destruction and disturbance, chemical pollution, rat predation on eggs, and competition with expanding populations of large gulls often fed by byproducts of human activities (BirdLife International, 2012). In 1900 the U.S. Herring Gull population numbered 8,000 breeding pairs and was entirely located in Maine. This followed a long period during which the species was intensively hunted for eggs and feathers (Pierotti and Good, 1994). Now there are greater than 100,000 pairs and it is one of the most common species found in the New York study area (Andrews, 1990). The increase is attributed to protection from hunting, increased waste from fisheries, and decreased competition for small fish and invertebrates, as human impacts reduced abundances of large top predators (Pierotti and Good, 1994).



Image 6.2. Wilson's and Leach's Storm-Petrels.
Photo by: David Pereksta, BOEM

Interactions between fisheries and seabirds have been well documented worldwide, with both increases and decreases to regional seabird populations linked to fishing activity (Tasker et al., 2000; Furness, 2003; Tasker and Furness, 2003; Votier et al., 2004; Lotze and Milewski, 2004). Distributions are also affected; for example, discards from large-scale trawling operations can attract extremely large, but transient, aggregations of seabirds. Bartumeus et al. (2010) found that fishery discards distort seabird movement patterns at regional scales, and modify the natural way in which seabirds explore the seascape to look for resources.

6.4. THREATS TO SEABIRDS

Currently, the greatest threats to seabirds in the region are generally considered to be habitat destruction/alteration, nesting disturbance, the direct (e.g., mortality in bycatch) and indirect (e.g., overfishing, lights) impacts of fisheries (Tasker et al., 2000; Votier et al., 2004), other seabirds (Drury, 1965), oil spills, and climate change (Riou et al., 2011). Since seabirds are mobile and interact with multiple environmental and anthropogenic stressors over vast geographic distances and long lifetimes, it is important to consider cumulative impacts and their synergies in evaluating threats to seabirds.

Many species migrate long distances between breeding and wintering sites. Along the way they can cross multiple ecosystems and geopolitical boundaries. For example, the Arctic Tern migrates an average of 71,000 km a year, crosses two oceans and flies adjacent to four continents (Egevang et al., 2010). Seabird movements also mean that seabirds are affected by environmental changes at local, regional and global scales. Examples of seabird threats that may occur outside of the study area, but impact populations in the study area, include watershed and coastal development, predators on nest sites, overfishing, bycatch, oil spills, and climate change.

There is evidence that climate change may pose increasing threats to seabird populations in the future. Anthropogenic changes in primary and secondary productivity in the Northwest Atlantic have already propagated up the food chain, affecting seabird breeding success (Riou et al., 2011). Anthropogenic effects on food webs may interact with natural interdecadal variability in ocean climate and productivity and regional-to-global scale changes in the ocean-atmosphere system driven by human activities to cause serious cumulative impacts (Sandvik and Erikstad, 2008). Links between natural and human climate changes and seabird population dynamics are an active area of research (Sandvik and Erikstad, 2008; Riou et al., 2011).

Potential impacts of offshore alternative energy production facilities (e.g., wind turbines, ocean thermal energy conversion, and marine hydrokinetic devices) on marine avifauna are also an active area of investigation. A full review of the literature on offshore energy platform effects on seabirds is beyond the scope of this report. For useful entry points into the relevant literature, see Drewitt and Langston, 2006; Hueppop et al., 2006; Hatch and Brault, 2007; Allison et al., 2008; and Watts, 2010. The effects of offshore wind farms on birds are likely to be highly variable, and will depend on a wide range of factors including: the type of construction, the habitats affected and the number and species of birds present (Drewitt and Langston, 2006). The principal potential impacts are thought to be: collision mortality, displacement of foraging areas and migration routes, and habitat change and loss from platform installation, operation and maintenance. Vulnerability to and likelihood of these impacts varies in a species, place and time-dependent manner (Allison et al., 2008). Spatial information on seabird abundance, diversity and habitat is therefore essential to reduce potential risks from offshore wind development.

6.5. MANAGEMENT AND CONSERVATION STATUS

Several domestic laws, Executive Orders and international treaties provide protection for seabirds. Multiple species found in the study area are listed by state, federal and international conservation listing agencies as species of conservation concern because of declining or already small population. Table 6.1 lists species identified by the U.S. Fish and Wildlife Service as species of conservation concern in the mid-Atlantic that “without additional conservation actions, are likely to become candidates for listing under the Endangered Species Act” (USFWS, 2008).

Species listing under the Endangered Species Act (ESA) of 1973 can have significant impacts to offshore spatial management decisions. For instance, ESA prohibits federal agencies from authorizing, funding or carrying out actions that “destroy or adversely modify” designated critical habitat of species on the federal endangered species list. This authority applies to all federal waters and although this regulatory aspect does not apply directly to State waters, large-scale development projects typically require a federal permit. Critical habitat protection is only one provision of the ESA. Others include take prohibitions and a requirement that Federal agencies consult on potential adverse effects to listed (threatened or endangered) species pursuant to Section 7. In addition, non-federal entities are required to get a Section 10(a)(1)(B) permit if their proposed action will result in take of a listed species. A full discussion of the implications of the ESA for marine and coastal activities that may impact listed bird species is beyond the scope of this document; the reader is referred to Baur and Irvin (2009) as an entry point and recent review of ESA law and policy.

Table 6.1. Birds of conservation concern identified by the U.S. Fish and Wildlife Service for the New England/Mid-Atlantic Coast (Bird Conservation Region 30 [BCR30]) and birds listed under the Endangered Species Act (ESA). Species shaded in grey are commonly observed greater than 10 km from shore.

Roseate Tern (*)	Buff-breasted Sandpiper (nb)
Red-throated Loon (nb)	Short-billed Dowitcher (nb)
Least Tern (c)	Pied-billed Grebe
Gull-billed Tern	Horned Grebe (nb)
Great Shearwater (nb)	Black Skimmer
Audubon's Shearwater (nb)	Short-eared Owl (nb)
American Bittern	Whip-poor-will
Least Bittern	Red-headed Woodpecker
Snowy Egret	Loggerhead Shrike
Bald Eagle (b)	Brown-headed Nuthatch
Peregrine Falcon (b)	Sedge Wren
Black Rail	Wood Thrush
Wilson's Plover	Blue-winged Warbler
American Oystercatcher	Golden-winged Warbler
Solitary Sandpiper (nb)	Prairie Warbler
Lesser Yellowlegs (nb)	Cerulean Warbler
Upland Sandpiper	Worm-eating Warbler
Whimbrel (nb)	Kentucky Warbler
Hudsonian Godwit (nb)	Henslow's Sparrow
Marbled Godwit (nb)	Nelson's Sharp-tailed Sparrow
Red Knot (<i>rufa</i> ssp.) (a) (nb)	Saltmarsh Sharp-tailed Sparrow
Semipalmated Sandpiper (Eastern) (nb)	Seaside Sparrow (c)
Purple Sandpiper (nb)	Rusty Blackbird (nb)

(*) ESA listed, (a) ESA candidate, (b) ESA delisted, (c) non-listed subspecies or population of Threatened or Endangered species, (nb) non-breeding in this BCR

In addition to the ESA, which affects listed species, the Migratory Bird Treaty Act (MBTA) of 1918, as amended, protects all species of seabirds in the U.S. The MBTA makes it unlawful in most cases to take, kill, possess, transport or import migratory birds, their eggs or their nests. The USFWS and Department of Justice are allowed enforcement discretion. To date enforcement has focused on persons or operations that have taken birds with blatant disregard for the law. In general, offshore enforcement of both MBTA and ESA poses a significant and unresolved challenge. The provisions of the MBTA apply equally to federal and non-federal entities, except where exempted (e.g., selected military activities). Table 6.1 summarizes the USFWS species of concern for the Bird Conservation Region (BCR) including the New York Bight.



Image 6.3. Double-crested Cormorant. Photo by: David Pereksta, BOEM

Additional federal efforts for seabird conservation include: Executive Order 13186 - Responsibilities of Federal Agencies To Protect Migratory Birds, which was implemented in 2001, the Fish and Wildlife Conservation Act of 1980, and guidelines of the Magnuson-Stevens Fishery Conservation and Management Act of 1976, as reauthorized. In the latter, Fisheries Management Councils must select measures that, to the extent practicable, minimize seabird bycatch and bycatch mortality. In doing so, Councils are advised to consider effects on both seabirds and other protected species (e.g., marine mammals, sea turtles).

New York State's Environmental Conservation Law (ECL) supplements federal laws to help conserve seabirds in State waters. For instance, New York makes its own list of endangered, threatened and species of special concern to supplement the federal list and has similar prohibitions (§ 11-0535). New York also has its own conservation measures like the Bird Conservation Area (BCA) program. The BCA program integrates bird conservation interests into agency planning, management and research projects and to date has set aside 52 areas in the State to safeguard and enhance populations in important habitats. To date, bird conservation areas have been created for terrestrial and estuarine systems, but not for pelagic systems.

The New York Department of State (NY DOS) is currently leading an effort to formalize the process of identifying significant offshore habitats for wildlife, which could lead to identification of important habitats for seabirds. The procedures used to identify, evaluate and recommend areas for protection are being taken from NY State's procedures previously used in coastal waters (Ozard, 1984). The data and maps presented in this report are intended as a resource to support identification of significant habitats to coastal and pelagic seabirds.

6.6. CHALLENGES OF UNDERSTANDING SEABIRD DISTRIBUTION AND ABUNDANCE

Seabirds are highly mobile organisms that range widely and respond to shifting and dynamic features in their physical and biological environment at time scales from minutes to years. Developing contiguous distribution maps at the relatively fine spatial scales (0.5-5 km horizontal resolution or better) needed for offshore planning off NY is a formidable challenge, not least because any discernible long-term average spatial patterns must be inferred from incomplete observations on a process with a tremendous amount of inherent variation.

Traditionally, offshore seabird distribution data has been represented by atlases using spatially aggregated observations at coarse spatial resolutions of 10-15 kilometers or greater (Jespersen, 1924; Moore, 1951; Powers, 1983). Often, non-quantitative data (sightings collected anecdotally outside of standardized surveys) are incorporated into these general descriptions of a species' range. Such coarse descriptions are helpful for some regional monitoring, assessment and planning purposes, but are inappropriate for detailed spatial planning decisions. Increasingly, state and local managers are being asked to make resource management

decisions at much finer resolutions. For instance, the U.S. Department of the Interior (DOI) Bureau of Ocean Energy Management (BOEM) divides the Outer Continental Shelf (OCS) into leasing blocks for energy leasing purposes that are approximately 5x5 kilometers (length x width), and it is anticipated that areas as small as 1/16th of a lease block could be leased. Maps in most seabird atlases are too coarse to differentiate seabird communities in 5x5 km lease blocks, let alone the smaller areas that are being considered. One of the objectives of this chapter is to develop maps at the spatial scales that managers are using to make decisions in the waters offshore of NY.

Improving the spatial resolution of predictive maps of seabird distribution requires dealing with two issues that arise at fine spatial scales: data gaps, and the inevitable increase in uncertainty associated with making predictions at finer spatial scales. To address the problem of discontinuous data (data gaps), we adopt a predictive spatial statistical modeling approach. This approach takes advantage of the increased availability of biophysical data at fine spatial resolutions and over broad spatial extents (see Chapters 2, 3, 4), along with statistical modeling techniques that analyze and generalize the spatial information contained in observations (see Appendix 6.A). We combine regression (generalized linear modeling [Fox, 2008]) and geostatistical (kriging [Cressie, 1993; Chiles and Delfiner, 1999]) approaches in a statistical modeling framework to predict the long-term average probability of occurrence and relative abundance of a variety of seabird species and groups. In this approach, both seabird-environment linkages and spatial autocorrelation are used to make predictions about unobserved locations from the scattered available data. We note that our approach does not attempt to predict the location of individual birds at a particular time. Rather, we model the long-term average pattern (called the 'spatial climatology') of seabird occurrence and abundance. The spatial climatological approach is a useful way to map persistent patterns in the distribution of dynamic organisms (e.g., Santora and Reiss, 2011), and is less data-intensive than individual-based approaches.

A second challenge of fine-resolution mapping of a dynamic, incompletely sampled spatial process like seabird abundance is characterizing and conveying uncertainty. Uncertainty in predictive maps of a dynamic living resource (e.g., seabird populations) comes from several sources, including sampling, measurement error, and the intrinsic dynamics of the resource itself (e.g., migration, mortality, reproduction) in conjunction with natural and anthropogenic changes in the environment. When environmental variables are used as predictors, they are often also measured with uncertainty, and/or may only serve as indirect proxies of the underlying driving mechanisms (e.g., water column stratification may correlate with prey availability). It is important to understand and communicate uncertainties to ensure there is an awareness of the limitations inherent in the use of static maps to represent dynamic resources. Our choice of the regression-geostatistical modeling framework allows us to produce maps quantifying how uncertainty varies over space. We also employ a battery of diagnostic statistics (e.g., error magnitude, prediction skill, receiver operating characteristic [ROC] curve analysis, and cross-validation statistics) to assess model accuracy, validity, and performance. Cross-validation diagnostic statistics are particularly important because they provide an integrated assessment of model performance given uncertainties and possible violations of model assumptions.

6.7. SUMMARY OF PREVIOUS STUDIES RELEVANT TO THE STUDY REGION

Much is known about birds in inland, estuarine and coastal habitats of New York, but less information is available for offshore habitats. Collecting data in offshore habitats is expensive and few datasets provide a comprehensive depiction of the seabird community over many years, seasons and places. The data used for this report come from the Manomet Bird Observatory (MBO) Seabird and Cetacean Assessment Program (CSAP) database, which contains species-specific



Image 6.4. Common Tern.
Photo by: David Pereksta, BOEM

sightings from multiple years (1980-1988). Spatially, temporally, and taxonomically, the MBO CSAP database is the most comprehensive single available information source on seabird distribution for the study area.

Two more recent regional offshore seabird survey efforts are underway that will likely eventually surpass the MBO CSAP in spatial and temporal intensity of effort: seabird observations conducted on NOAA Fisheries Service (NMFS/NEFSC) Ecosystem Monitoring and Herring Acoustic Survey cruises regularly from 2006 to present (contact: Dr. Richard Veit, Professor, City University of New York, College of Staten Island, richard.veit@csi.cuny.edu), and AMAPPS surveys conducted starting in 2010 (Contact: Mr. Michael Simpkins, Branch Chief, NOAA/NEFSC/READ/Protected Species Branch, michael.simpkins@noaa.gov). It is recommended that New York State closely monitor the progress of these efforts and use these data to assess possible changes in seabird distribution and abundance since the period in the 1980's when the MBO CSAP was collected.



Image 6.5. Red Phalarope. Photo by: David Pereksta, BOEM

As part of an ongoing study funded by the U.S. DOI Bureau of Ocean Energy Management (BOEM), the USGS Patuxent Wildlife Research Center (PWRC) has been assembling a compendium of offshore avian survey data in the U.S. Atlantic (O'Connell et al., 2009; Spiegel and Johnston, 2011; see also <http://www.boemre.gov/eppd/PDF/EPPDStudies/CompendiumAvianInformation.pdf>). The Atlantic Seabird Compendium (ASC) currently includes >250,000 seabird occurrence records from >80 datasets, including all of the datasets identified above. USGS plans to make most of this database publicly available in the near future through the US Fish & Wildlife Service (USFWS), although there may be some limitations on distribution due to the proprietary nature of some datasets. Metadata and summary data are already available (Spiegel and Johnston, 2011; USGS, 2012).

Other resources for seabird data include online databases such as the Ocean Biogeographic Information System Spatial Ecological Analysis of Megavertebrate Populations (OBIS-SEAMAP; <http://seamap.env.duke.edu/>) and the Global Biodiversity Information Facility (GBIF; resource: <http://www.gbif.org/>). In the preparation of this report we have extensively searched all of these resources. Again, at the time of publication, despite its age, the MBO CSAP represents the most comprehensive, long-term single database available to characterize the marine avifauna of the NY region.

Payne et al. (1984) used an early version of the MBO CSAP database to analyze the distribution and abundance of seabirds in 13 subregions from Nova Scotia to Cape Hatteras. Their report provided seasonal density estimates of seabirds at coarse spatial scales (e.g., Southern New England Inner shelf, Mid-Atlantic Outer Shelf), which may be useful for regional ocean planning. Hoopes et al. (1993) presented summary analyses based on the full 1980-1988 MBO CSAP dataset. More recently Huettmann and Diamond (2000, 2001), and Pittman and Huettmann (2006) used the MBO CSAP dataset and additional sighting information collected in Canadian waters (the Programme Intégré de Recherches sur les Oiseaux Pélagiques [PIROP] database) to assess seabird distribution patterns at medium resolution (5 arc-minutes or ~9 km). The reader is referred to Huettmann (2000) and Pittman and Huettmann (2006) for a detailed characterization of the distribution of survey effort and other background information on the PIROP and MBO CSAP databases. Huettmann and Diamond (2000, 2001) tracked migration patterns of nine species in the northwest Atlantic Ocean, including some parts of the New York study area.

Pittman and Huettmann (2006) derived spatially-explicit and quantitative information on the distribution and diversity of seabirds within the Gulf of Maine, as part of an ecological assessment for the Stellwagen Bank

National Marine Sanctuary. They used a boosted regression tree (BRT) approach to develop statistical models and produce medium resolution (~9x9 km grid) predictive maps of seabird relative prevalence. In the present chapter, we use a generalized linear model (GLM)-based regression approach instead of the BRT approach, use a wider set of environmental covariates, use relative abundance information as well as relative prevalence, and employ a different statistical framework (regression-kriging) that allows us to produce finer spatial resolution predictions by accounting for spatial autocorrelation.



Image 6.6. South Polar Skua.
Photo by: David Pereksta, BOEM

It should be noted that a smaller project by the New York State Energy Research and Development Authority (NYSERDA) used the MBO dataset to assess potential avian impacts of a proposed Long Island – New York City offshore wind project (NYSERDA, 2010). Their report provides a list of species and a review of their biology and potential impacts, but does not map or assess distribution.

We also note that a variety of datasets other than the MBO CSAP exist for coastal areas near the study area, including: surveys of Long Island's beach-nesting shorebird habitats (NY and TNC, 1991), New York's Christmas Bird Count, the North American Breeding Bird Survey, The Audubon Society's eBird counts, and compilations of surveys by the US Fish and Wildlife Service. The Nature Conservancy used New York State and US Fish and Wildlife surveys to identify critical habitats for Roseate Terns, Least Terns, Piping Plovers and Harlequin Ducks along Long Island's shores. These studies may be useful for nearshore spatial planning, although it is important to realize they do not provide information on the presence or absence of birds outside of nearshore areas.

Rhode Island and New Jersey, two states adjacent to New York, have conducted systematic studies of their offshore waters to establish ecological baselines for use in coastal and marine spatial planning (Paton et al., 2010; GMI, 2010). These studies are recent, reliable and extend over offshore habitats adjacent to their corresponding States, some of which partially overlap but do not cover the New York study area.

Finally, we are aware of three additional datasets that overlap very small portions of the study area. The Massachusetts Audubon Society conducted surveys from 2002 to 2006 to assess the potential effect of wind farm development on avifauna in Nantucket sound. Surveys were conducted from fixed-wing aircraft at 500 feet above the water surface and by boat. These data are proprietary but are contained in the USGS ASC database mentioned above (O'Connell et al., 2009). The Minerals Management Service (now the Bureau of Ocean Energy Management) funded a winter survey of coastal mid-Atlantic seabirds that extended from southern Virginia to the northern border of New Jersey. This survey covered from the coast offshore to at least 12 nautical miles, and was conducted in 2001-2002 and 2002-2003. These data are public and included in the USGS ASC database (O'Connell et al., 2009). As part of studies related to the Cape Wind project, Energy Management, Inc. commissioned boat and aerial surveys of Nantucket Sound from 2002 to 2004. These data are proprietary and have not been publicly released, but metadata are available in the USGS ASC database (O'Connell et al., 2009).

6.8. METHODS

This section provides an overview of how the MBO CSAP seabird database (Figure 6.1) was used, in conjunction with environmental covariates, to fit spatial statistical models and produce predictive maps of seabird distribution and relative abundance in the NY region representative of the period from 1980-1988. Figures 6.2 and 6.3 provide an outline and example of the key processing steps. Tables 6.2, 6.4 and 6.5 and Figures 6.1 and 6.4 summarize the input data. The statistical methods used are covered in greater detail in Appendix 6.A and Online Supplement 6.2. The sources and processing of the environmental covariate data are covered in greater detail in Chapter 4, Appendix 6.B and Online Supplement 6.1.

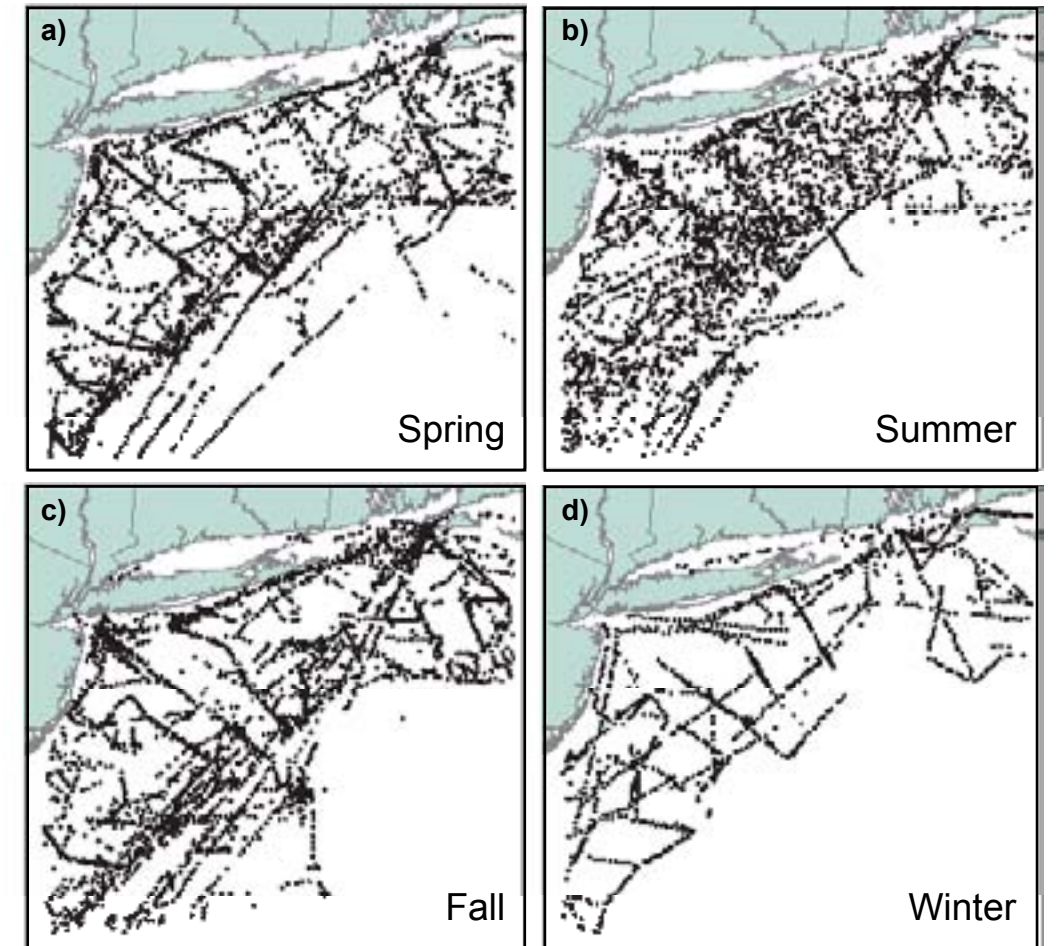


Figure 6.1. Locations (centroids) of all unique MBO CSAP seabird survey transects sampled between April 1980 and October 1988 in a)Spring, b)Summer, c)Fall, and d)Winter.

6.8.1. Study region and grid

The same study region and 30 arc-second geographic grid described in Chapter 4 of this report was used for all seabird environmental variables and model predictions. The 30 arc-second grid has a north-south linear dimension of 0.927 km and an average east-west linear dimension of 0.714 km in the study region (average = 0.814 km). This resolution is approximately 400 times finer than previous 10 arc-minute maps and 100 times finer than 5 arc-minute maps. For simplicity, we have chosen to use decimal degrees to keep track of grid cell centroids, and measure distances using a simple elliptical geodetic approximation; the effects of this simplifying assumption are negligible given the size of our study region and grid configuration (potential errors in linear distances <50% of grid cell horizontal resolution).

6.8.2. Seabird survey data

Seabird sightings data for the study region were extracted from the Manomet Bird Observatory's (MBO) Cetacean and Seabird Assessment Program (CSAP) database. The former MBO is currently named the Manomet Center for Conservation Sciences (MCCS). This is one of the largest pelagic seabird data sets in the world, providing exceptional spatial and temporal resolution for the Northwest Atlantic for the period from 1980-1988. As discussed above (Section 6.7.), this is the best currently available single source for seabird abundance and distribution data in the study region; other, smaller and/or more narrowly focused datasets exist, and future efforts to synthesize those data could result in improved coverage and accuracy in specific areas and/or for certain species. The MBO database was provided directly by staff at the MCCS to the NOAA Biogeography Branch in 2006 (Pittman and Huettmann, 2006). We extracted only quantitative survey data (i.e., data from fixed time, standardized surveys as described below) from the CSAP database. The following filtering criteria were used: OBTYP=1 (quantitative surveys only), ANTYPE=1 (seabirds) or 0 (confirmed absence of any seabird species), and transect centroid falling on or within the study area shown in Chapter 1, Figure 1.2. Field names refer to fields in the digital database outputs supplied to us by MCCS.

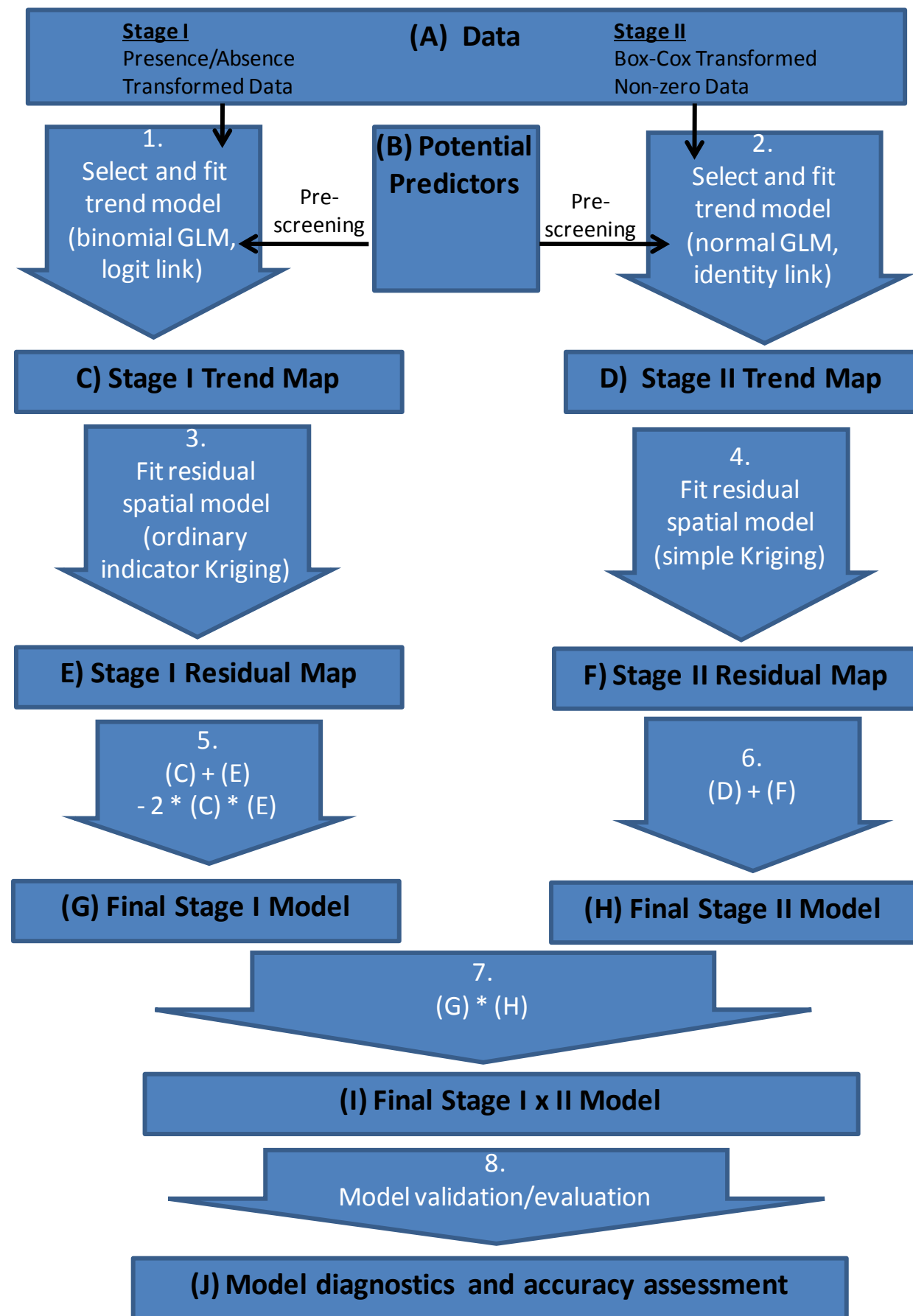


Figure 6.2. Flowchart of seasonal predictive mapping process for seabirds. Letters represent geospatial inputs/ outputs. Numbers represent process steps. For details, see Figure 6.3, Section 6.8.6. and Appendix 6.A.

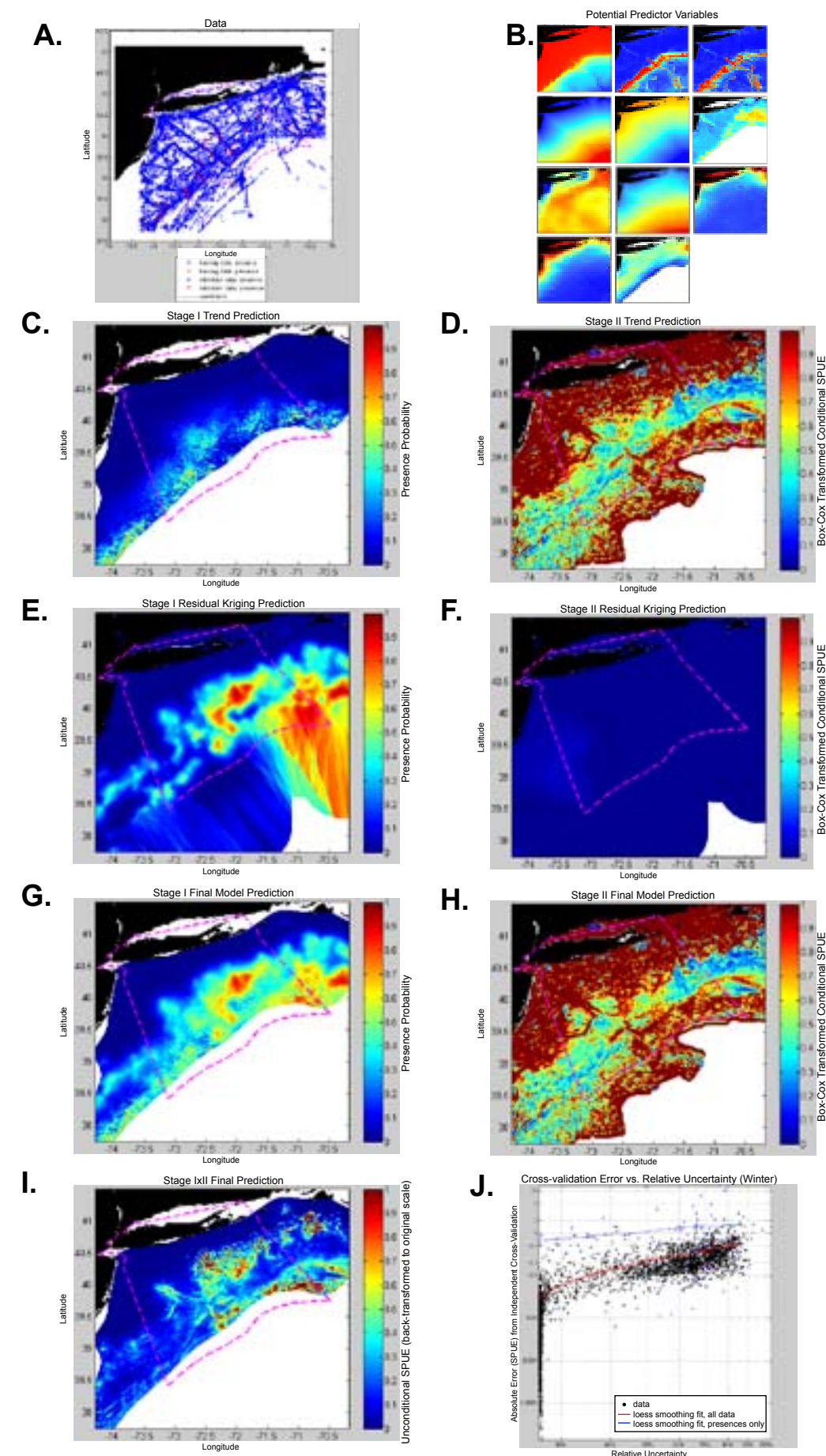


Figure 6.3. Example geospatial information from each step of the seasonal predictive modeling process (example images are from the Dovekie winter model). Panel letters correspond to the letters in the model flowchart (Figure 6.2).

Notes:

i) Maps in this figure are intended only as examples of the modeling process and should not be used in place of the final Dovekie maps presented in Figure 6.12 and in Appendix 6.C.

ii) For a full depiction of the predictor variables shown in panel B, see Figure 6.4 and Appendix 6.B.

iii) Panels D, E, F, and H show prediction maps before error-masking to eliminate unreliable predictions far from data points.

iv) Panels D, F, and H show model predictions in Box-Cox transformed units that are not linearly related to the original SPUE units.

v) Stage II panels (D, F, and H) refer to conditional SPUE (SPUE when the species is present).

vi) Final Stage I x II model results (Panel I) are presented in back-transformed units (the original SPUE units of No. indiv./km²/15-min), and represent the expected value of unconditional SPUE (the expected average over many repeated measurements at the same location if zeros are included in the average), which is the final output of the model.

vii) See Appendix 6.A for details of statistical methods.

viii) Pink dashed lines depict outline of NY planning area.

Table 6.2. Species recorded by MBO CSAP quantitative surveys (1980-1988) in the study region, and groupings used for analysis*.

COMMON NAME	FAMILY	SCIENTIFIC NAME
Species Individually Mapped		
Black-legged Kittiwake	Laridae	<i>Rissa tridactyla</i>
Common Tern	Sternidae	<i>Sterna hirundo</i>
Common Loon	Gaviidae	<i>Gavia immer</i>
Cory's Shearwater	Procellariidae	<i>Calonectris diomedea</i>
Dovekie	Alcidae	<i>Alle alle</i>
Great Black-backed Gull	Laridae	<i>Larus marinus</i>
Great Shearwater	Procellariidae	<i>Puffinus gravis</i>
Herring Gull	Laridae	<i>Larus argentatus smithsonianus</i>
Laughing Gull	Laridae	<i>Larus atricilla</i>
Northern Fulmar	Procellariidae	<i>Fulmarus glacialis</i>
Northern Gannet	Sulidae	<i>Morus bassanus</i>
Pomarine Jaeger	Stercorariidae	<i>Stercorarius pomarinus</i>
Sooty Shearwater	Procellariidae	<i>Puffinus griseus</i>
Wilson's Storm-Petrel	Hydrobatidae	<i>Oceanites oceanicus</i>
Alcids, Less Common		
Alcidae		
Atlantic Puffin	Alcidae	<i>Fratercula arctica</i>
Common Murre	Alcidae	<i>Uria aalge</i>
Thick-billed Murre	Alcidae	<i>Uria lomvia</i>
Razorbill	Alcidae	<i>Alca torda</i>
Unidentified sightings in the family Alcidae	Alcidae	n/a
Coastal Waterfowl (Eiders, Mergansers, Scoters, Ducks, Loons)		
Anatidae, Gaviidae		
White-winged Scoter	Anatidae	<i>Melanitta fusca</i>
Black Scoter	Anatidae	<i>Melanitta nigra</i>
Surf Scoter	Anatidae	<i>Melanitta perspicillata</i>
Long-tailed Duck	Anatidae	<i>Clangula hyemalis</i>
Red-throated Loon	Gaviidae	<i>Gavia stellata</i>
Red-breasted Merganser	Anatidae	<i>Mergus serrator</i>
Common Eider	Anatidae	<i>Somateria mollissima</i>
Unidentified species in families Anatidae and Gaviidae	Anatidae, Gaviidae	n/a
Jaegers		
Stercorariidae		
Parasitic Jaeger	Stercorariidae	<i>Stercorarius parasiticus</i>
Long-tailed Jaeger	Stercorariidae	<i>Stercorarius longicaudus</i>
Unidentified sightings of Jaegers	Stercorariidae	n/a
Phalaropes		
Scolopacidae		
Red Phalarope	Scolopacidae	<i>Phalaropus fulicaria</i>
Red-necked Phalarope	Scolopacidae	<i>Phalaropus lobatus</i>
Unidentified sightings of Phalaropes	Scolopacidae	n/a
Shearwaters, Less Common		
Procellariidae		
Manx Shearwater	Procellariidae	<i>Puffinus puffinus</i>
Audubon's Shearwater	Procellariidae	<i>Puffinus lherminieri</i>
Unidentified sightings in the family Procellariidae	Procellariidae	n/a

Table 6.2 cont. Species recorded by MBO CSAP quantitative surveys (1980-1988) in the study region, and groupings used for analysis*.

COMMON NAME	FAMILY	SCIENTIFIC NAME
Small Gulls, Less Common		
Laridae		
Ring-billed Gull	Laridae	<i>Larus delawarensis</i>
Bonaparte's Gull	Laridae	<i>Larus philadelphia</i>
Storm-Petrels, Less Common		
Hydrobatidae		
Leach's Storm-Petrel	Hydrobatidae	<i>Oceanodroma leucorhoa</i>
Band-rumped Storm-Petrel	Hydrobatidae	<i>Oceanodroma castro</i>
White-faced Storm-Petrel	Hydrobatidae	<i>Pelagodroma marina</i>
Unidentified species in the family Hydrobatidae	Hydrobatidae	n/a
Terns, Less Common		
Sternidae		
Royal Tern	Sternidae	<i>Sterna maxima</i>
Arctic Tern	Sternidae	<i>Sterna paradisaea</i>
Roseate Tern	Sternidae	<i>Sterna dougallii</i>
Least Tern	Sternidae	<i>Sterna antillarum</i>
Sooty Tern	Sternidae	<i>Onychoprion fuscatus</i>
Bridled Tern	Sternidae	<i>Sterna anaethetus</i>
Forster's Tern	Sternidae	<i>Sterna forsteri</i>
Unidentified sightings in the family Sternidae	Sternidae	n/a
Unidentified Gulls		
Laridae		
Unidentified sightings in the family Laridae	Laridae	n/a
**Cormorants		
Phalacrocoracidae		
Double-crested Cormorant	Phalacrocoracidae	<i>Phalacrocorax auritus</i>
Great Cormorant	Phalacrocoracidae	<i>Phalacrocorax carbo</i>
Unidentified sightings of Cormorants	Phalacrocoracidae	n/a
**Rare Visitors		
Anatidae, Laridae, Stercorariidae		
Canada Goose	Anatidae	<i>Branta canadensis</i>
American Black Duck	Anatidae	<i>Anas rubripes</i>
Brant	Anatidae	<i>Branta bernicla</i>
Bufflehead	Anatidae	<i>Bucephala albeola</i>
Mallard	Anatidae	<i>Anas platyrhynchos</i>
Glaucous Gull	Laridae	<i>Larus hyperboreus</i>
Lesser Black-backed Gull	Laridae	<i>Larus fuscus</i>
Iceland Gull	Laridae	<i>Larus glaucoides glaucoides</i>
Little Gull	Laridae	<i>Larus minutus</i>
South Polar Skua	Stercorariidae	<i>Stercorarius maccormicki</i>
Unidentified sightings of Ducks and Geese	Anatidae	n/a
**Skuas, Less Common		
Stercorariidae		
Great Skua	Stercorariidae	<i>Stercorarius skua</i>
Unidentified sightings of Skuas	Stercorariidae	n/a

* Species with one or more sightings in standardized quantitative surveys by the Manomet Bird Observatory Cetacean and Seabird Assessment Program (MBO CSAP) during the period April 1980 to October 1988.

** No predictive modeling was carried out for these groups due to limited sample size.

Survey methods have been previously described (Powers et al., 1980; Powers, 1983; Payne et al., 1984; Huettmann, 2000). Briefly, a small number of expert observers were trained in standardized survey methods and placed on research vessels undertaking a wide variety of surveys, including NOAA Fisheries Service groundfish, scallop, and plankton surveys, US Coast Guard surveys, and US EPA surveys. Observers conducted surveys in

Table 6.3. Definition of seasons.

SEASON	ABBREVIATION*	START DATE	END DATE
Spring	SP	March 1	May 31
Summer	SU	June 1	August 31
Fall	FA	September 1	November 30
Winter	WI	December 1	February 28**

*Abbreviations used in some labels and figures.
**February 29 in leap years.

Table 6.4. Summary of numbers of identifiable species, unidentified types, and contributions to species richness of each mapped species and group.

SPECIES OR GROUP NAME	# OF POSITIVELY IDENTIFIED SPECIES IN GROUP	# OF UNIDENTIFIED CATEGORIES IN GROUP	MINIMUM CONTRIBUTION TO SPECIES RICHNESS	MAXIMUM CONTRIBUTION TO SPECIES RICHNESS
Individually mapped species				
Black-legged Kittiwake	1	0	1	1
Common Loon	1	0	1	1
Common Tern	1	0	1	1
Cory's Shearwater	1	0	1	1
Dovekie	1	0	1	1
Great Black-backed Gull	1	0	1	1
Great Shearwater	1	0	1	1
Herring Gull	1	0	1	1
Laughing Gull	1	0	1	1
Northern Fulmar	1	0	1	1
Northern Gannet	1	0	1	1
Pomarine Jaeger	1	0	1	1
Sooty Shearwater	1	0	1	1
Wilson's Storm-Petrel	1	0	1	1
Subtotals	14	0	14	14
Modeled species groups				
Alcids, less common	4	4	1	4
Coastal Waterfowl	7	3	1	7
Jaegers	2	1	1	2
Phalaropes	2	1	1	2
Shearwaters, less common	2	2	1	2
Small Gulls, less common	2	0	1	2
Storm-Petrels, less common	3	1	1	3
Terns, less common	7	2	1	7
Unidentified gulls	0	2	0	0
Subtotals	29	16	8	29
Non-modeled species groups				
Cormorants	2	1	1	2
Rare Visitors	10	2	1	10
Skuas, less common	1	1	1	1
Subtotals	13	4	3	13
GRAND TOTALS				
Modeled	43	16	22	43
Not modeled	13	4	3	13
All	56	20	25	56

Table 6.5. Numbers of unique shipboard survey locations in which each species or species group was seen, overall and by season.

SPECIES OR GROUP NAME	TOTAL N	N SPRING	N SUMMER	N FALL	N WINTER
Individually mapped species					
Black-legged Kittiwake	1,391	260	2	469	660
Common Loon	217	112	4	60	41
Common Tern	171	57	80	33	1
Cory's Shearwater	458	3	301	153	1
Dovekie	161	37	0	27	97
Great Black-backed Gull	2,172	788	176	587	621
Great Shearwater	951	33	502	407	9
Herring Gull	4,252	1,671	282	1,565	734
Laughing Gull	404	47	115	236	6
Northern Fulmar	392	228	43	45	76
Northern Gannet	2,302	1,142	9	537	614
Pomarine Jaeger	130	14	7	108	1
Sooty Shearwater	205	88	114	3	0
Wilson's Storm-Petrel	1,680	300	1172	207	1
Species groups					
Alcids, less common	147	80	0	5	62
Coastal Waterfowl	300	120	0	67	113
Jaegers	79	13	8	58	0
Phalaropes	294	247	7	36	4
Shearwaters, less common	196	16	93	87	0
Small Gulls, less common	210	53	3	110	44
Storm-Petrels, less common	225	46	126	53	0
Terns, less common	127	57	49	21	0
Unidentified gulls	291	55	19	163	54
Cormorants	66	13	9	21	23
Rare Visitors	42	18	1	11	12
Skuas, less common	36	12	2	11	11
Special category					
No birds sighted	2,299	511	847	812	129
Number of unique locations	9,148	2,549	2,674	2,777	1,148

15-minute periods, where each period was considered an individual transect. In a small number of instances (313 data points, less than 1.5% of the data records) the actual survey time was slightly less than 15-minutes (7 to 14-minutes); this deviation from the standard protocol was considered minor and no explicit correction was made (it is partially accounted for simply by the corresponding decrease in transect area -- for a given ship speed, a shorter time transect will be shorter in length and area). Seabirds were identified to the lowest possible taxonomic level, usually species, and counted within a fixed strip width of 300 m at one side of the ship, traveling on a straight course, at a constant speed (generally 8-12 knots). The starting point, constant bearing, and constant speed during each fixed 15-minute survey period were recorded using the ship's instruments, and used to define the area of the rectangular strip covered by the survey. For purposes of this analysis, unless otherwise noted, the centroid of each rectangular strip was used to define its spatial location.

In the NY study region, transect length averaged 4.3 km (SD=0.8 km), ranging from 0.4 to 6.5 km, and transect area averaged 4.4 km² (SD=2.9 km²), ranging from 0.1 to 20 km². Average nearest-neighbor distance between transect centroids ranged from 2.8 km to 3.6 km depending on season, and the minimum nearest-neighbor distances ranging from 0.03 km to 0.26 km, depending on season (Figure 6.1). Given this spatial distribution of observations, the minimum length scale of features that can be resolved in all seasons is approximately 0.5

Table 6.6. Summary of seasons chosen for predictive modeling.

SPECIES OR GROUP	SEASON				NUMBER OF SEASONS MODELED
	SPRING	SUMMER	FALL	WINTER	
Individually mapped species					
Black-legged Kittiwake	Modeled	Not modeled	Modeled	Modeled	3
Common Loon	Modeled	Not modeled	Modeled	Modeled	3
Common Tern	Modeled	Modeled	Modeled	Not modeled	3
Cory's Shearwater	Not modeled	Modeled	Modeled	Not modeled	2
Dovekie	Combined*	Absent†	Combined*	Modeled	1
Great Black-backed Gull	Modeled	Modeled	Modeled	Modeled	4
Great Shearwater	Not modeled	Modeled	Modeled	Not modeled	2
Herring Gull	Modeled	Modeled	Modeled	Modeled	4
Laughing Gull	Modeled	Modeled	Modeled	Not modeled	3
Northern Fulmar	Modeled	Modeled	Modeled	Modeled	4
Northern Gannet	Modeled	Not modeled	Modeled	Modeled	3
Pomarine Jaeger	Not modeled	Not modeled	Modeled	Not modeled	1
Sooty Shearwater	Modeled	Modeled	Not modeled	Absent†	2
Wilson's Storm-Petrel	Modeled	Modeled	Modeled	Not modeled	3
			Subtotal		38
Species groups					
Alcids, less common	Modeled	Absent†	Not modeled	Modeled	2
Coastal Waterfowl	Modeled	Absent†	Modeled	Modeled	3
Jaegers	Not modeled	Not modeled	Modeled	Absent†	1
Phalaropes	Modeled	Not modeled	Not modeled	Not modeled	1
Shearwaters, less common	Not modeled	Modeled	Modeled	Absent†	2
Small Gulls, less common	Modeled	Not modeled	Modeled	Modeled	3
Storm-Petrels, less common	Modeled	Modeled	Modeled	Absent†	3
Terns, less common	Modeled	Modeled	Not modeled	Absent†	2
Unidentified gulls	Modeled	Not modeled	Modeled	Modeled	3
Cormorants	Not modeled	Not modeled	Not modeled	Not modeled	0
Rare Visitors	Not modeled	Not modeled	Not modeled	Not modeled	0
Skuas, less common	Not modeled	Not modeled	Not modeled	Not modeled	0
			Subtotal		20
Special category					
No birds sighted**	Modeled	Modeled	Modeled	Modeled	4
			Subtotal		4
Total number of seasonal predictive models					62

* Sightings from these seasons were combined with sightings from Winter for modeling.

† Species or group not detected in the Manomet dataset in this season.

**Surveys that specifically noted the absence of any seabirds were modeled separately.

km (this is determined by the greater of: the minimum transect length, or twice the minimum nearest-neighbor distance). Thus the grid resolution chosen for the present study (~0.8 km) approaches the finest possible resolution given the limits of the data. This is one reason that cross-validation, described below, is essential to characterize the accuracy of final mapped predictions. Cross-validation accuracy assessments take into account horizontal positional error as well as other sources of uncertainty.

The CSAP database contained 16,899 species sighting and abundance records (plus 2,299 records of surveys in which no seabirds were sighted, i.e., confirmed absences) from quantitative transect surveys at 9,099 unique locations in our study area, spanning the time period from April 20, 1980 to October 3, 1988 (a total of 9,148 unique survey locations in all seasons; Figure 6.1, Tables 6.2, 6.4, 6.5). The age of this dataset is an admitted

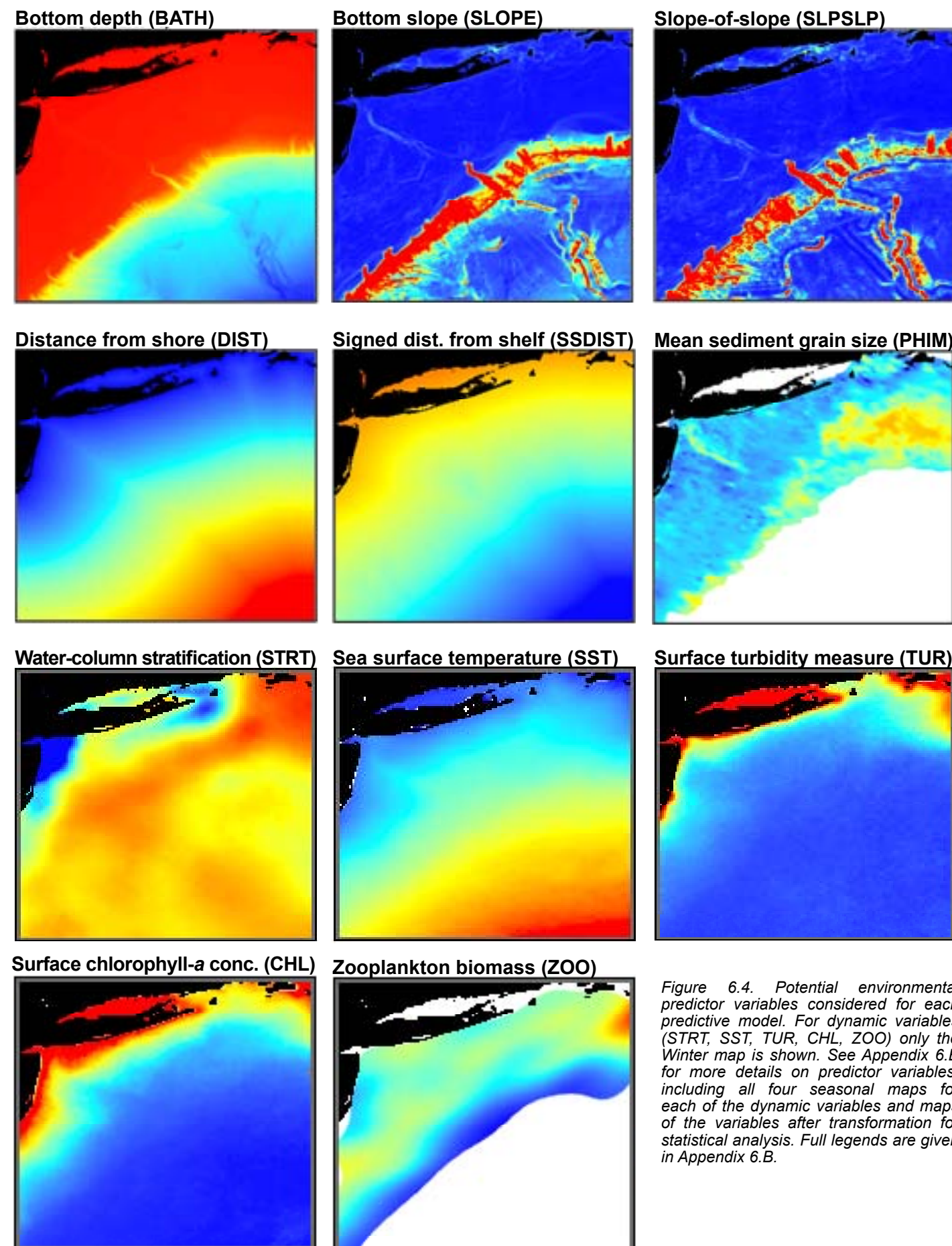


Figure 6.4. Potential environmental predictor variables considered for each predictive model. For dynamic variables (STRT, SST, TUR, CHL, ZOO) only the Winter map is shown. See Appendix 6.B for more details on predictor variables, including all four seasonal maps for each of the dynamic variables and maps of the variables after transformation for statistical analysis. Full legends are given in Appendix 6.B.

limitation of this analysis, and implications of using data that are 24-32 years old at the time of the present report's publication (2012) are discussed in Appendix 6.A (Section 6.A.14.) and in the Discussion (Section 6.10.). Fifty-six identifiable species of seabirds and waterfowl were recorded (Table 6.2, Table 6.4). These species were organized into groups for modeling purposes where necessary due to small sample sizes (see below and Table 6.2, Table 6.4, Table 6.5, Table 6.6). All "unidentified" bird sighting categories were identified at least to family level, which allowed assignment of those sighting records to appropriate groups. Most of the "unidentified" categories are likely to represent species positively identified elsewhere in the database that could not be positively identified in a particular sighting record, rather than species not otherwise represented in the database (although it is possible that a few of the "unidentified" records truly represent species not recorded elsewhere). Fifty-six is thus a conservative estimate of the number of seabird and opportunistically seafaring species present in the 1980-1988 period in the NY Bight study region. Since the MBO CSAP surveys were ship-based and most survey effort was focused >10 km offshore (Pittmann and Huettmann, 2006), the total number of species that may be observed over nearshore waters could be substantially higher.

Temporal patterns of seabird occurrence were summarized with monthly histograms (Appendix 6.C), and used to further divide bird occurrence into seasons for modeling as described in Section 6.8.3. Although the Manomet dataset provides good coverage for offshore environments, survey effort is reduced within 10 km of shore (Pittmann and Huettmann, 2006), and excludes most of Long Island Sound. To alleviate the effects of this bias on temporal occurrence histograms for nearshore species (species spending substantial amounts of time <10 km from shore), we obtained non-quantitative data from an online dataset (eBird, <http://ebird.org/content/ebird>). The eBird dataset consists of opportunistic publicly available bird observations made by recreational and professional bird watchers and was developed by the Cornell Lab of Ornithology and National Audubon Society. Seabird sighting frequencies were extracted from the open access eBird database in November, 2011 for the New England/Mid Atlantic Bird Conservation Region, and used to produce monthly histograms of sighting frequency that are presented alongside the CSAP histograms for comparison (see Appendix 6.C).

6.8.3. Processing of quantitative seabird data for analysis

Observations were separated by season; season definitions are given in Table 6.3. For each season, unique survey locations were identified (2,549 locations in spring, 2,674 locations in summer, 2,777 locations in fall, 1,148 locations in winter), defining the sampling configuration for each season (Figure 6.1). For each species or group sighting record in each season, the "COUNT" field of the CSAP database (number of birds of that species observed during the timed survey) was divided by the corresponding survey tract area to yield an index of relative abundance that was standardized by both time (15-minutes) and area (km² of transect footprint), which we will hereafter refer to as sightings per unit effort (SPUE). Units of SPUE are individual birds detected per square kilometer per 15-minute survey. When species were grouped (see below), the "COUNT" field was summed over all species in the group occurring in a given survey. Because observers were searching for all seabird species during surveys conducted at each unique location, the absence of a species record at one of these points generated an SPUE of 0 for that species at that location in that season. Note that these calculations assume perfect detectability; the implications of this assumption are discussed in Appendix 6.A (Section 6.A.14.). It was very uncommon for surveys to be centered at precisely the same location in the same season more than once over the 9 survey years (this occurred 6 times in spring, 2 in summer, 12 in fall, and 2 in winter). Where this did occur, we used the weighted average SPUE for each species at that location, with weights proportional to survey tract areas (surveys with greater tract area received greater weight).

This process resulted in four sets (one for each season) of georeferenced point measurements of SPUE, representing all seabird sightings that occurred in each season over the 9-year survey period. These datasets were coded in two ways for further analysis:

- (1) as binary variables indicating the **occurrence** (presence [1] or absence [0]) of a given species or group (Figure 6.2A: Stage I), and,
- (2) as non-zero continuous variables representing the relative index of **abundance** (SPUE) of each observed species at each location where it was present (Figure 6.2B: Stage II).

Note the distinction between measures of **occurrence**, which refer to the frequency with which a species was sighted among independent 15-minute surveys, and **abundance**, which refers to the number of individuals

of a given species or species group sighted within a 15-minute survey, scaled to the transect area surveyed (SPUE). Note, also, that because detectability was not accounted for and individuals were not tracked over time, the indices of occurrence used here are not equivalent to the true frequencies of occurrence and indices of abundance are not equivalent to population abundance; they are only relative proxy measures.

6.8.4. Grouping and selection of species for modeling

All individually identified species with 40 or more sightings in at least one season (Spring, Summer, Fall, Winter; defined in Section 6.8.3.) were selected for predictive modeling (Table 6.5, Table 6.6). Remaining species were grouped according to shared ecological and life history patterns and/or shared spatial and temporal patterns of occurrence (Table 6.2, Appendix 6.C; Pittmann and Huettmann, 2006), and groups were modeled where 40 or more sightings occurred in at least one season. Remaining groups had no more than 23 sightings in any one season and were considered too rare to model. For each species or group, a season was only modeled if at least 40 records existed for that season, with the following exceptions: Common Terns were modeled in Fall despite only 33 sighting records, and Dovekie sighting records from Fall (n=27) and Spring (n=37) were combined with Winter (n=97) observations (Table 6.6). For groups and/or individual species that were not modeled, as well as for seasons in which a given species or group was too rare to model, point maps of all occurrences are presented.

We note that other modeling methods might be capable of generating reliable predictions when fewer than 40 records are present, but feel the uncertainties involved in extrapolating predictions from so few data make raw point maps of occurrence more suitable for these limited data cases, unless other information is available to predict distribution of these species based on biological characteristics and environmental preferences. The abundance of these birds is most conservatively treated as unknown (not zero) at locations in between sample points; the range of observed abundances over the entire study area can be used as a guide to the range of possible values at unsampled locations.

6.8.5. Potential environmental predictors

Based on available high-resolution data coverage within our study region and previous studies of environmental correlates of seabird distribution and abundance, we identified 11 potential environmental predictor variables (Figure 6.4, Chapter 4, Appendix 6.B, Online Supplement 6.1). Short codes used to refer to each predictor are given in parentheses: bottom depth (BATH), bottom slope (SLOPE), bottom slope-of-the-slope (SLPSLP), mean grain size of bottom surficial sediments (PHIM), linear distance from shore (DIST), signed linear distance from the shelf edge (SSDIST), sea surface temperature (SST), water column stratification (STRT), sea surface chlorophyll concentration (CHL), sea surface turbidity (TUR), and near surface zooplankton biomass (ZOO). It is important to note that this was only the candidate predictor set; a model selection process described below (Section 6.8.7.) narrowed down the set of predictor variables that contributed to any particular species/group model in any particular season. We also wish to emphasize this is not a comprehensive list of all potential environmental influences on seabird abundance in the area, but instead is limited by such factors as the availability of high-resolution datasets collected over sufficiently long time frames to allow calculation of climatologies.

The 11 identified predictors (Figure 6.4) were derived from 6 types of data: bathymetry and coastline, surficial sediments, water-column sampling, satellite ocean surface temperature, satellite ocean surface color, and ship-based plankton tows (Chapter 4). These datasets are described individually in Chapter 4, Appendix 6.B, and Online Supplement 6.1. For time-varying predictors (SST, STRT, CHL, TUR, ZOO), long-term average (climatological) ocean conditions were mapped by season (defined as in Table 6.3). Due to constraints of data availability, the climatological period of the environmental variables does not always match that of the seabird survey data. The implicit assumption is that the long-term climatological patterns of ocean conditions are reflective of the 1980-1988 period. Implications of this assumption are discussed in Appendix 6.A (Section 6.A.14.).

All grid processing was carried out using ArcGIS 9.3.1 with the Spatial Analyst extension (Environmental Systems Research Group [ESRI], Redlands, CA), Geostatistical Analyst extension (ESRI), XTools Pro 6.2.1 for ArcGIS 9.x (Data East LLC, Novosibirsk, Russia), and Hawth's Tools for ArcGIS 9.x (Beyer, 2004). All

predictor grids were co-registered on the 30 arc-second sampling grid (Chapter 4) and clipped to the spatial extent of the study area (Chapter 1, Figure 1.2). Grids were exported from ArcGIS in the .FLT binary floating point raster format for subsequent processing. All environmental predictors used in this study and associated metadata are available by contacting the corresponding author.

Some predictors were gridded or re-sampled using interpolation algorithms (e.g., kriging, bilinear interpolation). Uncertainty in predictors resulting from interpolation was ignored for purposes of model formulation; that is, predictor values at each location were treated as perfectly known. This is likely to cause parametric estimates of uncertainty to underestimate prediction uncertainty when predictions are made at locations not included in model fitting. We address this uncertainty with the model evaluation, cross-validation, and uncertainty calibration procedures described in Appendix 6.A (Section 6.A.12.). Chapter 4, Appendix 6.B, and Online Supplement 6.1 also provide estimates of the relative uncertainty of each predictor layer as it is discussed.

6.8.6. Seasonal predictive modeling

A flowchart of the seasonal predictive modeling process is shown in Figure 6.2. In this figure, capital letters indicate the geospatial data and statistics that form the inputs and outputs of the modeling process. Numbers represent steps of the modeling process that transform geospatial information from step to step. Appendix 6.A, Statistical Methods, gives a detailed explanation of each process step and relevant equations and references.

For each season with sufficient data within each species/group selected for predictive modeling, we model the transect estimates of SPUE as point samples (located at the centroid of each transect) of two spatial random processes, Stage I and Stage II (Figure 6.2A). Stage I uses binary (presence/absence) data from the MBO CSAP surveys (Figure 6.2A, left). Stage II uses relative abundance (SPUE) observations for each species or group from the same surveys, but does not consider locations where SPUE=0 (i.e., Stage II only considers observations where the species is present) (Figure 6.2A, right). This two-stage modeling approach has been successfully applied to model marine species distributions (Stefánsson, 1996; Ver Hoef and Jansen, 2007; Winter et al., 2011) and performs well in tests of alternative species distribution models (Potts and Elith, 2006).

Within each stage of the model, we use a regression-kriging (RK) model framework to account for both seabird-environment relationships and spatial structure (Hengl et al., 2007). Both Stage I and Stage II models include two components: a trend model that uses a generalized linear model (GLM) (Figure 6.2: boxes C, D and steps 1, 2) and incorporates environmental predictors (Figure 6.2B), and a geostatistical model that accounts for spatial autocorrelation in the residuals from the GLM (Figure 6.2: boxes E, F and steps 3, 4). Statistically, this involves an assumption that the spatial processes are separable into trend and residual components. That is, at each location the observed value can be modeled as a sum of a deterministic linear combination of known predictor values (trend), and a realization of a spatial random field (residual). For more detailed discussion and mathematical treatment of RK models, see Hengl et al. (2007). Implications of the assumption of separability are discussed in Appendix 6.A (Section 6.A.14.).

The trend (Figure 6.2C, D) and residual (Figure 6.2E, F) components of the Stage I and Stage II models are combined probabilistically (Stage I: Figure 6.2 step 5) or additively (Stage II: Figure 6.2 step 6) to yield the final, combined Stage I (Figure 6.2G) and Stage II (Figure 6.2H) models. Stage I and Stage II are then multiplied (Figure 6.2 step 7) to produce the final prediction of relative abundance (Figure 6.2I), the expected long-term average SPUE in repeated 15-minute standardized surveys randomly scattered in time within the modeled season during the 1980-1988 survey period. The multiplication of Stage I and Stage II arises from the fact that Stage I is the probability of presence, and Stage II is the abundance when present (Appendix 6.A).

The final Stage I x II model prediction is then used to calculate a variety of model validation and evaluation statistics (Figure 6.2 box J and step 8), which are reported in the diagnostic tables shown later in this document, and in Appendix 6.C and Online Supplement 6.2. Due to the number and variety of diagnostic statistics calculated, they are not described in detail here. However, the most important diagnostic statistics are derived from a procedure called cross-validation (Cressie, 1993; Goovaerts, 1997; Deutsch and Journel, 1998; Hengl et al., 2007; Ross, 2007; Fox, 2008). In this procedure, 50% of the data for each species/group in each season

are selected at random to be used to fit the model (the “training set”). The remaining 50% of data form the “validation set” (also called the “holdout set”). The model fit using only the training set is subsequently used to predict observations in the validation set, allowing an independent assessment of the accuracy and predictive performance of the model when confronted with new data. Cross-validation is a powerful tool that allows assessment not only of prediction accuracy, but of the degree to which modeled uncertainty values capture the true uncertainty encountered in out-of-training-set prediction.

Although models were fit using only 50% of data (the training set), the final maps presented in this document and in Appendices 6.C and 6.D were produced by applying the final model to the *entire* dataset (training and validation sets combined). Thus the cross-validation diagnostic statistics provide a conservative estimate of model performance, as the final maps are based on a dataset which is twice the size of the training and validation subsets. Online Supplement 6.2 provides detailed diagnostic reports on each step of the model fitting process, and shows the maps produced using the restricted 50% training subset.

Figure 6.3 provides an example of each of the lettered inputs and outputs in the Figure 6.2 flowchart, using the example of the Dovekie (*Alle alle*) winter seasonal model. Figure 6.4 shows the potential environmental predictor set, with only the winter panel shown for dynamic variables (SST, STRT, CHL, TUR, ZOO). Note that the predictor variables shown in Figure 6.4 are untransformed, whereas transformed versions of some variables were used for statistical modeling. Transformed versions, and all four seasonal panels for dynamic variables, can be found in Appendix 6.B.

Unless otherwise noted, all predictive modeling analyses were carried out in Matlab R2011a (version 7.12.0.635; The Mathworks, Natick, MA), with the Statistics, Mapping, and Image Processing toolboxes (Mathworks), mGstat (Hansen, 2009, <http://mgstat.sourceforge.net/>), ROC (Cardillo, 2008), partest (Cardillo, 2008), lowess (Burkey, 2009), ploterr (Zörgiebel, 2008), boxcoxlm (Dror, 2006), and additional custom code available by contacting the authors. Geostatistical algorithms (kriging, generalized least squares estimation of trend model coefficients, variogram estimation, and variogram model fitting) were implemented by calling the program gstat (standalone version 2.5.1; Pebesma and Wesseling, 1998; <http://www.gstat.org/>) from within Matlab, with the help of the mGstat toolbox. GLM model selection was carried out by calling the R package glmulti (Calcagno and Mazancourt, 2010; Calcagno, 2011; [<http://cran.r-project.org/web/packages/glmulti/index.html>]) from within Matlab. All Matlab code is available from the corresponding author on request.

6.8.7. Generation of annual maps

The seasonal modeling process described in Figure 6.2, Section 6.8.6., and Appendix 6.A was repeated for each species and species group, in each season for which sufficient data existed to estimate the model (Table 6.6). Seasonal predictions were then summed to produce annual climatological maps of SPUE for each species and species group (Appendix 6.A., Section 6.A.13.). Seasonal Stage I predictions (presence probability maps) were also combined probabilistically to produce “integrated annual presence probability” maps, which reflect the probability of each grid cell being occupied in at least one season of the year, assuming independence of seasonal predictions (Appendix 6.A., Section 6.A.13.).

Relative uncertainty of the annual SPUE and annual integrated presence probability maps was calculated as the weighted average of the seasonal Stage I and Stage IxII relative uncertainty estimates, respectively, with weights proportional to the overall frequency of species occurrence in that season. In this way, the annual relative uncertainty maps were weighted to reflect periods when the species was most prevalent. Mathematical details of the relative uncertainty calculations are given in Appendix 6.A (Section 6.A.11.).

“High”, “Medium”, and “Low” *certainty* classes (corresponding to low, medium, and high *uncertainty*, respectively) were assigned based on the relative uncertainty value (Section 6.A.11.). The High certainty class was defined by relative uncertainty values ≤ 0.50 , the Medium certainty class was defined by relative uncertainty values > 0.5 but ≤ 0.65 , and the Low certainty class was defined by relative uncertainty values > 0.65 . These certainty classes were based on inspection of the cross-validation error vs. relative uncertainty calibration plots presented as part of each species/group profile in Appendix 6.C.

6.8.8. Hotspot analysis

To examine “hotspots” (or “coldspots”) of particularly high (or low) seabird abundance, species richness, and diversity (a combined measure of species richness and evenness), we combined results from the individually mapped species and species groups. We combined maps in two ways:

1. Using only species that were individually mapped (see Table 6.2).
2. Using both species that were individually mapped and species groups (Table 6.2).

Results of (1) and (2) were qualitatively similar and so we show only the second set of results, that is, maps derived from a combination of individually mapped species and species groups. Both seasonal and annual species/group maps were combined to produce seasonal and annual hotspot maps. For additional information on the rationale behind hotspot analyses, see Box 6.3.

6.8.8.1. Abundance

Abundance hotspots are defined as concentrations of large numbers of individual seabirds, regardless of species. To calculate annual abundance hotspot maps, predicted SPUE annual climatology maps were summed, with the sum taken at each grid cell location over all species and groups for which predictions were available. Seasonal maps were calculated in a similar way, and are presented in Appendix 6.D.

6.8.8.2. Species richness

To calculate species richness hotspot maps, we chose an arbitrary threshold to define a species as functionally present; if its predicted abundance in the final annual SPUE climatology map was $\geq T$, where T = the 10th percentile of the observed relative abundance (SPUE) of the species when present, divided by 10. After applying this threshold to each species map (i.e., values $<$ threshold were set to 0 and values \geq threshold were set to 1), the resulting binary presence/absence maps were summed to produce the annual species richness hotspot map. Seasonal maps were produced in a similar way using the seasonal SPUE climatologies (Stage I/II maps).

Since groups contain more than one species, they could potentially contribute more than 1 unit to species richness. An upper bound on group contribution to richness was calculated by repeating the summation after multiplying each binary group presence/absence map by the number of true species in the group (not including any unidentified types). The ‘unidentified gull’ group was excluded from all species richness analyses because it had no identifiable species.

Final richness maps show the midpoint between the lower bound on species richness, assuming each group contributed just one species, and the upper bound, assuming all species in a group were present. These maps likely over-represent actual species richness observable at any given time and location, since not all species in a group are equally common, and since even common and abundant species are highly mobile and will not be observed in every survey even at the locations of their highest predicted abundance. They are only intended as a relative index of potential long-term species richness at each location (the number of species likely to be encountered over long periods of time, such as the ~9-year MBO CSAP study period).

6.8.8.3. Diversity

Species richness alone can over-represent the effective diversity of an area if many species are present only at very low abundances relative to their abundance elsewhere. We found this to be the case for our maps of species richness, and so we also report the common Shannon diversity index (H') (Krebs, 1989). Because this index requires the total number of species to remain the same to allow comparison from one location to another, species that were not present at a given location were assigned a very low abundance (SPUE = 0.0001), chosen to be at least 10 times lower than any observed SPUE in the dataset. For this analysis, each group was counted as a single species, regardless of the number of species in the group. Unidentified gulls were included and counted as a single species.

Like species richness, the diversity index hotspot maps will likely overestimate the diversity observed at any instant in time. Instead, they are intended to represent the long-term potential diversity of an area, based on model predictions.

6.8.8.4. Hotspot uncertainty

As a general guide to the level of certainty about each of the hotspot maps (abundance, richness, and diversity), we calculated a weighted average of the relative uncertainty maps associated with each annual and seasonal predicted SPUE climatology map. Weights used were proportional to the frequency of the species in the corresponding season or year (similar to the weighting scheme used for seasonal maps described in Appendix 6.A [Section 6.A.13.]). This resulted in the final hotspot relative uncertainty maps (see Appendix 6.D).

“High”, “Medium”, and “Low” certainty classes (corresponding to low, medium, and high uncertainty, respectively) were assigned based on the relative uncertainty value in the same manner as for the other annual maps (see Section 6.8.7.). Hotspot certainty classes are presented as overlays on Figures 6.35-6.37.

6.9. RESULTS

Seasonal predictive modeling was carried out for 58 season/species combinations and for the ‘no birds sighted’ category in 4 seasons (Table 6.6). In all, 44 species were modeled in the 58 seasonal models. 14 species were modeled individually, and 30 species were modeled as part of the 9 modeled species groups. These groups also included sightings from 15 categories not identified to species level, but still identifiable to group level (all sightings were identified at least to family level). 17 species/types were too rare in the study area to model: 3 Cormorant species, the South Polar Skua, 10 rare visitor/migrant species, and 4 unidentified types that fell into one of these three groups (Table 6.2).

Overall, diagnostic statistics indicated that most models were successful in describing some aspects of species distribution, although model performance varied over space and from species to species. Environmental predictors contributed significantly to the predictive ability of most models. Figure 6.5 summarizes the relative importance of different environmental predictor variables across the seasonal predictive models. The relative importance of different model components (trend model, spatial model, ‘white noise’ error term) varied from Stage I to Stage II and among species/groups, although similarities in model structure were often observed across different seasons for a given species/group (Figure 6.6). ‘White noise’ refers to random variability that is not spatially structured and is not predictable based on available environmental variables; therefore, models with higher white noise components have less predictive power. It can be thought of as indicating a higher degree of expected variability around the mean if the same spot were visited repeatedly, even under identical environmental conditions. Model performance also varied, and any application of these models should consider the performance metrics most relevant to the application in question. Figure 6.7 summarizes several selected seasonal model diagnostic statistics. Table 6.7 summarizes some cross-validation performance diagnostics from seasonal predictive models. More detailed information about model performance is given in the species summaries that follow (Box 6.1) and in Appendix 6.C and Online Supplement 6.2.

Box 6.1 describes the Annual Predictive Model Summaries that were produced for each species and group. Maps of predicted long-term average annual relative abundance (SPUE) for each of the 14 individually modeled species are shown in Figures 6.8 to 6.21, and maps for the 9 modeled species groups are shown in Figures 6.22 to 6.30. Three additional species groups (Cormorants, Skuas, and Rare visitors) had insufficient data to model; only point-estimates of SPUE at transect centroids are shown for these non-modeled species (Figures 6.31-6.33). These are followed by a predictive model of an index of the frequency and extent of 15-minute surveys in which no seabirds were detected (Figure 6.34A) and the probability for each grid location of at least one ‘no birds sighted’ survey occurring during one of the four seasonal periods (Figure 6.34B). The index of ‘no birds sighted’ is measured in units of km² transect area in which no birds were detected per 15-minute survey. Box 6.2 discusses the interpretation and potential utility of the ‘no birds sighted’ model. Following the species, group, and ‘no birds sighted’ models, hotspot analyses of abundance, richness, and diversity are presented (Figures 6.35 to 6.37) and discussed (Box 6.3). Finally, a point map is presented of sightings for species of particular concern (Figure 6.38).

As described in Box 6.1, all maps are accompanied by a data summary table. Where predictive modeling was done, predictor summary tables and diagnostic summary tables are also included. Box 6.1 describes the color coding used in these tables to provide an overall assessment of the relative performance of a model.

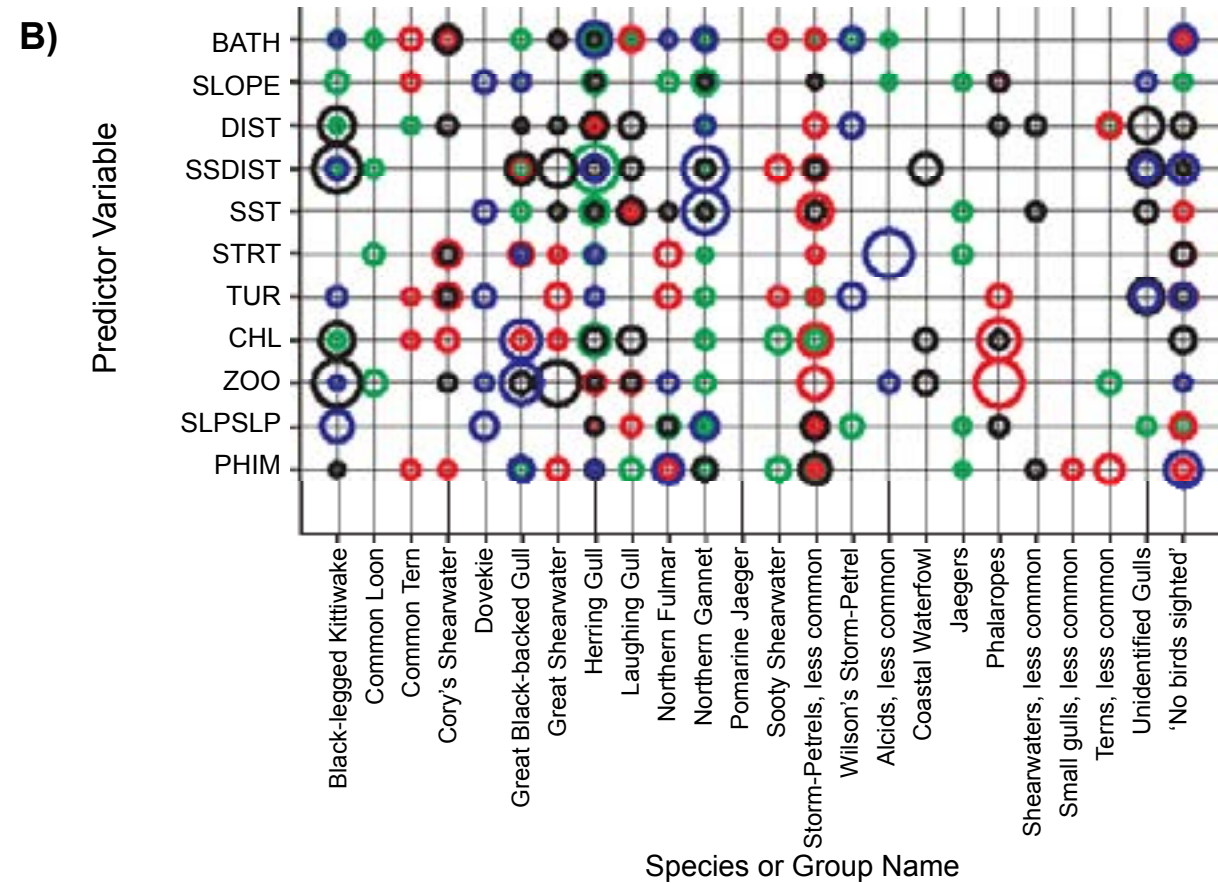
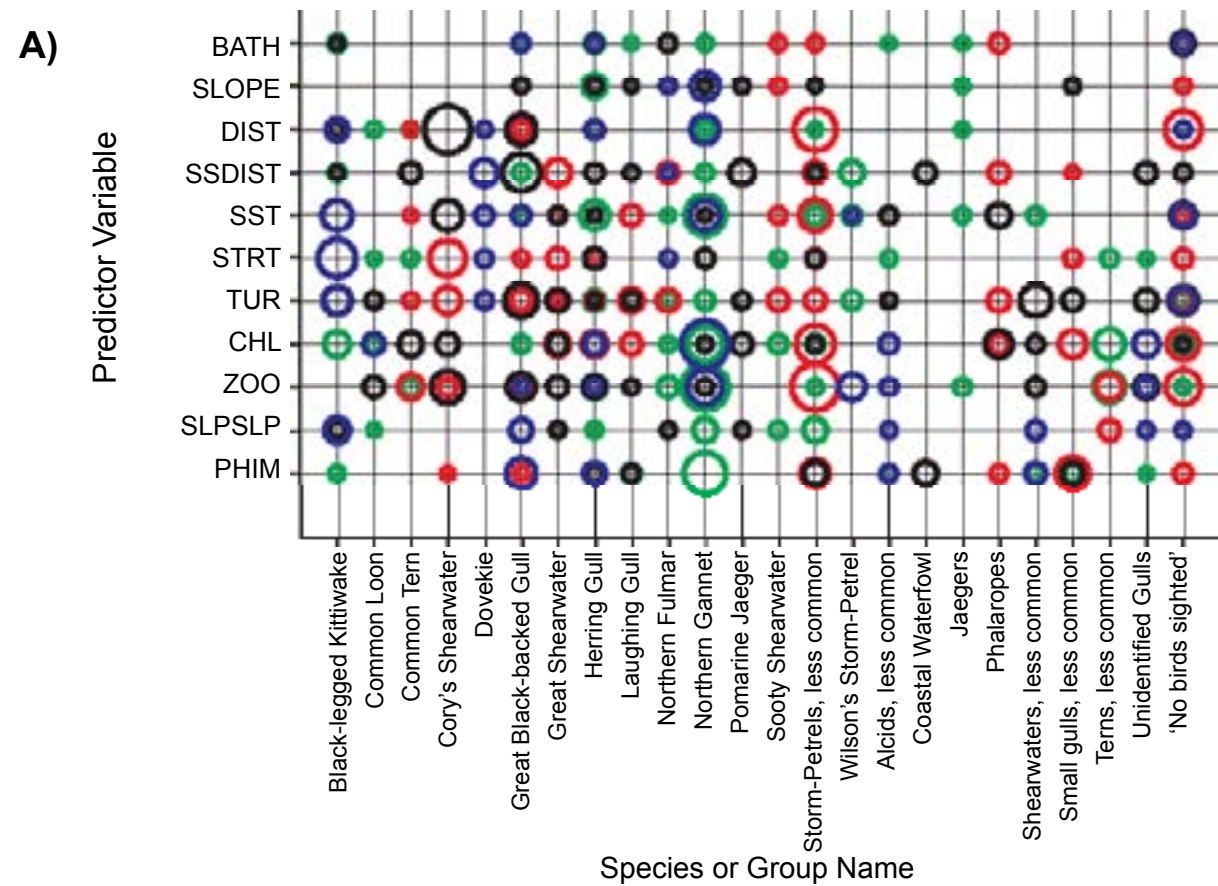


Figure 6.5. Summary of environmental predictor variable importance in the seasonal predictive models. For each species or group modeled (horizontal axis) and each potential predictor variable (vertical axis), bubbles are plotted for each season in which the predictor was included in the GLM trend model (green=spring, red=summer, black=fall, blue=winter). The diameter of the bubble plotted for each season is proportional to the magnitude of the standardized simple slope (sum of main effect slope and all interaction effect slopes in which a given predictor variable occurs), a measure of predictor variable influence in the fitted trend model. A) Stage I Trend Model predictor importance. B) Stage II Trend Model predictor importance. For details on simple slopes calculations see Appendix 6.A and Online Supplement 6.2. Online Supplement 6.2 also includes bar plots that indicate the sign of each predictor's influence, information that is not included here (only absolute magnitudes are indicated by bubble size in this plot).

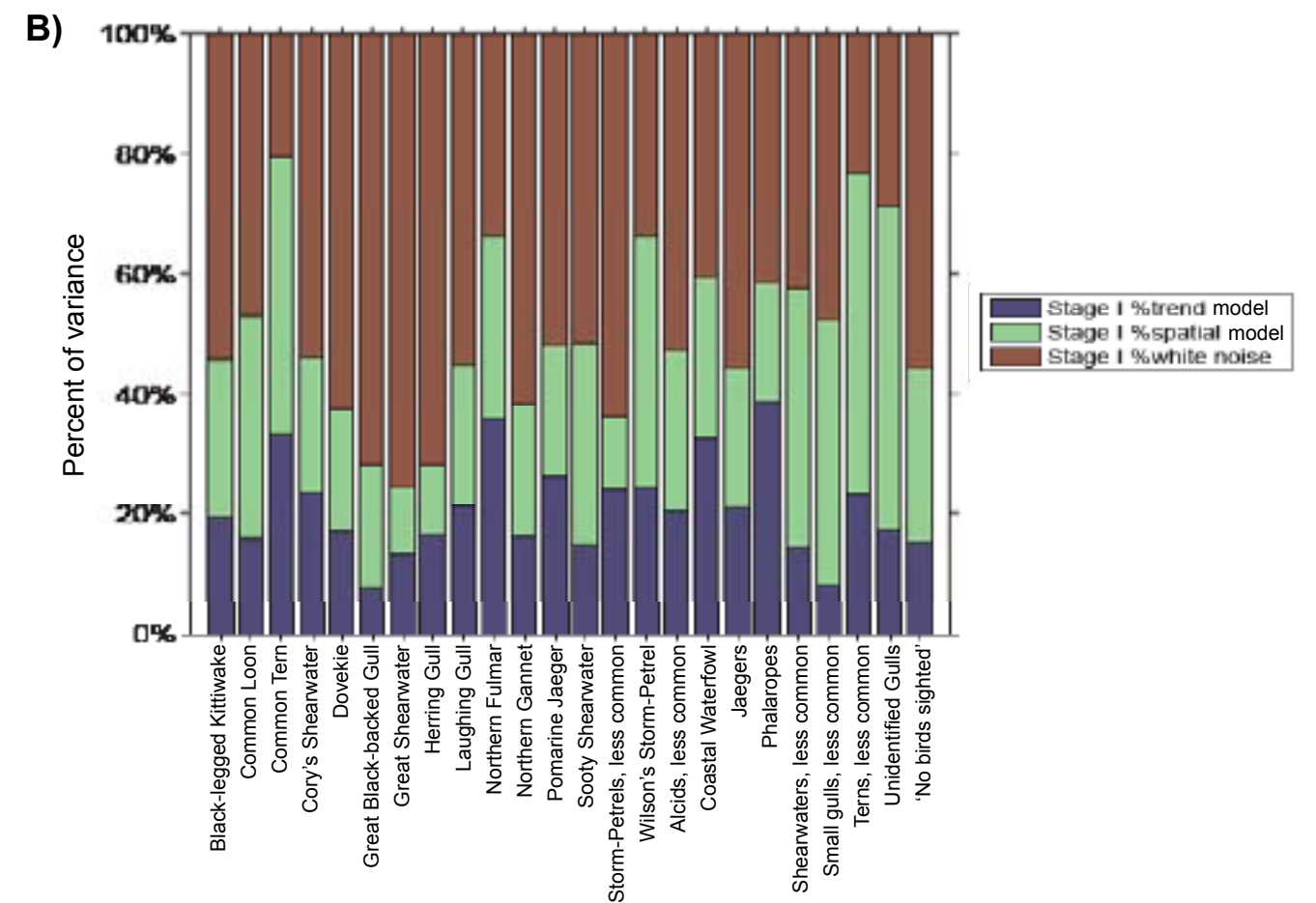
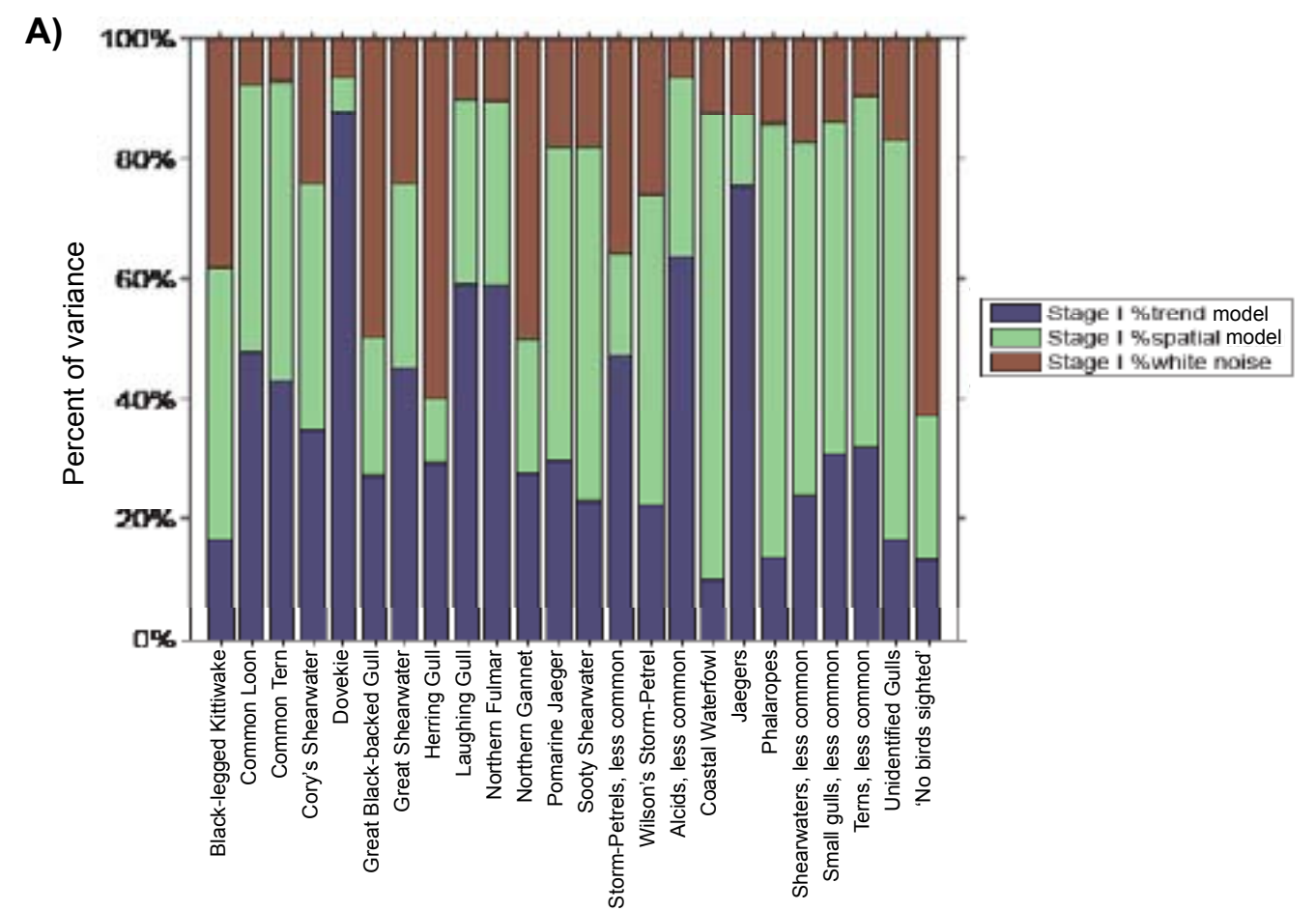


Figure 6.6. Summary of variance partitioning in model fits among the trend component, spatial component (residual variogram 'sill') and white noise component (residual variogram 'nugget'), for A) Stage I (Occurrence Model), and, B) Stage II (Abundance-when-present Model). For details of variance component calculations, see Appendices 6.A and 6.C and Online Supplement 6.2.

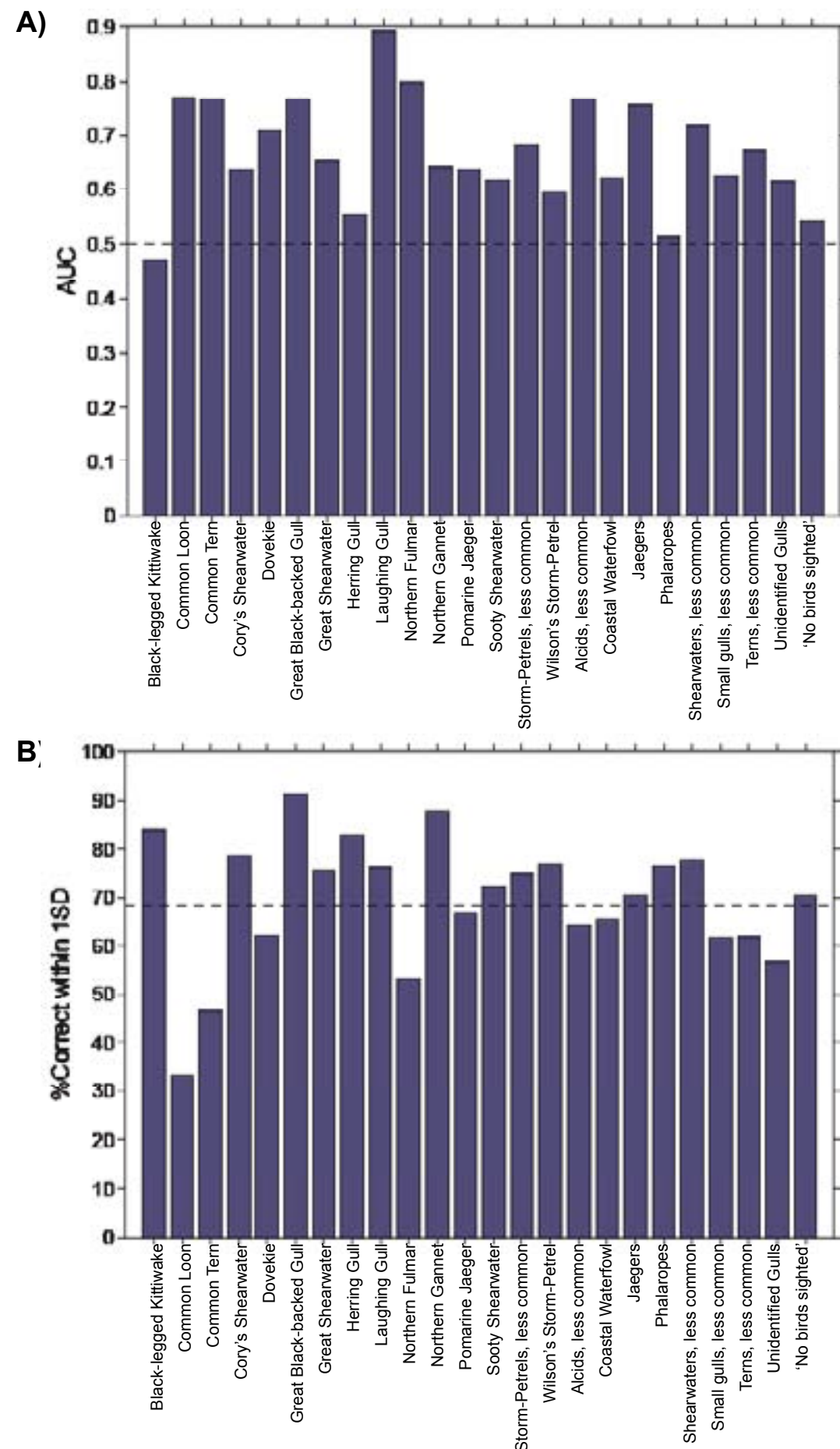


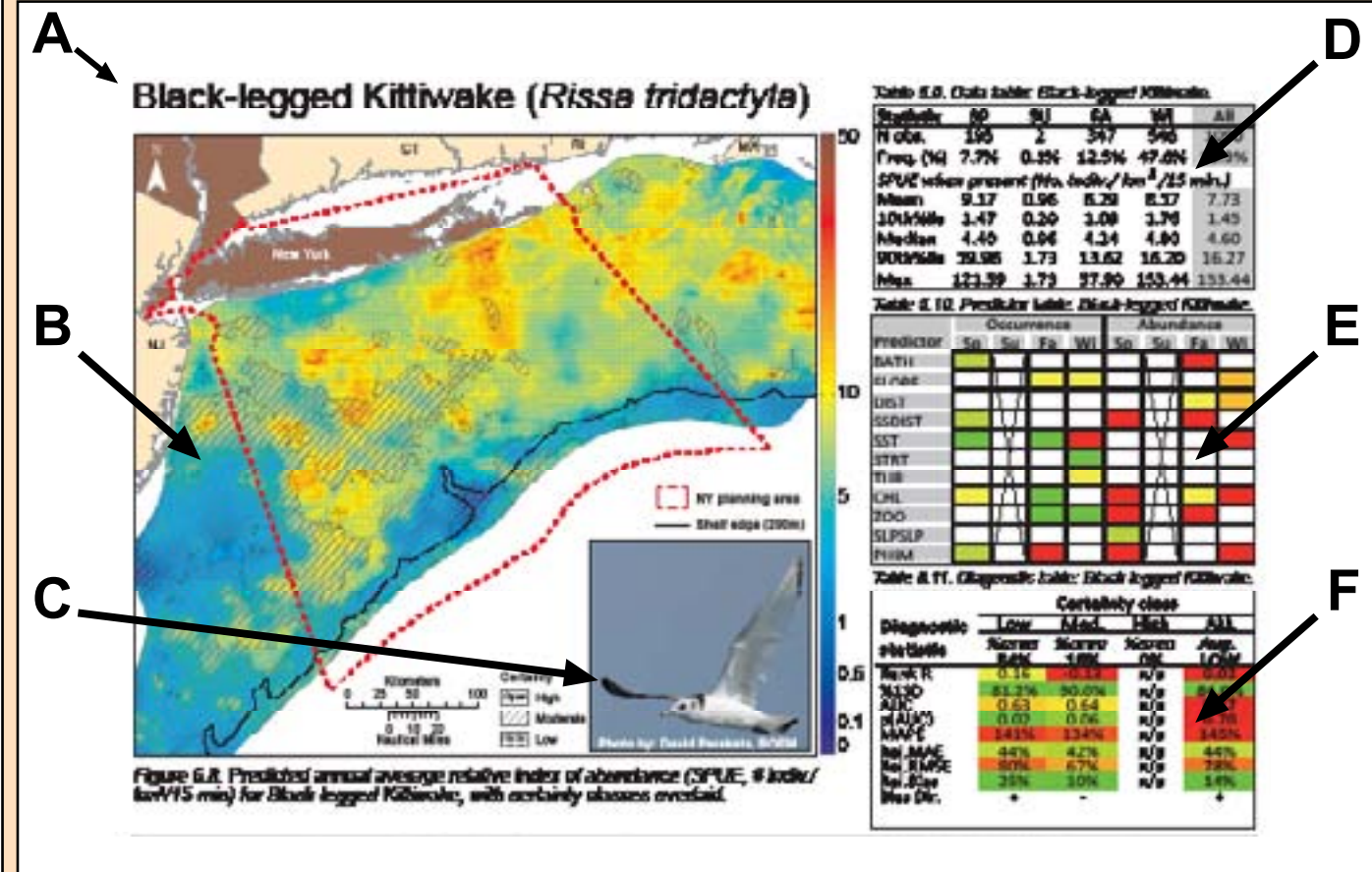
Figure 6.7. Summary of annual cross-validation model diagnostic statistics. A) Stage I – Cross-validation AUC; reference line is plotted at the threshold value of 0.5 below which the model has no predictive value. B) Stage II - cross-validation % correctly predicted within parametric 1 S.D. confidence intervals; reference line is plotted at the theoretical target value of 68.3%.

Table 6.7 Summary of cross-validation diagnostic statistics for annual models*.

SPECIES OR GROUP NAME	DIAGNOSTIC STATISTICS**							
	Rank R	%1SD	AUC	p(AUC)	MAPE	Rel. MAE	Rel. RMSE	Rel. Bias
Species								
Black-legged Kittiwake	0.02	84.0%	0.47	0.7011	145%	44%	78%	14%
Common Loon	-0.04	33.3%	0.77	0.0000	258%	40%	67%	41%
Common Tern	0.26	46.7%	0.77	0.0000	579%	24%	34%	18%
Cory's Shearwater	0.20	78.6%	0.64	0.0000	112%	22%	69%	5%
Dovekie	0.20	62.3%	0.71	0.0000	216%	5%	15%	5%
Great Black-backed Gull	0.32	91.4%	0.77	0.0000	134%	33%	46%	7%
Great Shearwater	0.07	75.6%	0.65	0.0000	221%	27%	65%	-1%
Herring Gull	0.13	82.8%	0.56	0.3192	176%	43%	70%	-11%
Laughing Gull	0.33	76.1%	0.89	0.0000	161%	15%	28%	0%
Northern Fulmar	0.21	53.3%	0.80	0.0000	396%	60%	101%	46%
Northern Gannet	0.17	87.9%	0.64	0.0095	259%	32%	48%	0%
Pomarine Jaeger	0.30	66.7%	0.64	0.0012	590%	11%	15%	9%
Sooty Shearwater	0.28	72.4%	0.62	0.0025	135%	19%	27%	21%
Storm-Petrels, less common	0.24	61.5%	0.63	0.0072	306%	18%	25%	22%
Wilson's Storm-Petrel	0.29	75.2%	0.68	0.0000	396%	45%	95%	-17%
Mean	0.20	69.9%	0.68	n/a	272%	29%	52%	11%
Groups								
Alcids, less common	0.22	76.7%	0.59	0.0509	158%	23%	33%	26%
Coastal Waterfowl	0.20	64.3%	0.77	0.0000	395%	22%	66%	14%
Jaegers	-0.16	65.4%	0.62	0.0213	471%	13%	25%	10%
Phalaropes	0.16	70.6%	0.76	0.0000	908%	23%	77%	-9%
Shearwaters, less common	-0.05	76.5%	0.51	0.3915	156%	21%	32%	26%
Small gulls, less common	0.16	77.8%	0.72	0.0011	131%	27%	32%	34%
Terns, less common	0.52	61.9%	0.67	0.0047	874%	26%	39%	28%
Unidentified Gulls	0.14	56.8%	0.62	0.0173	291%	21%	27%	26%
Mean	0.15	68.7%	0.66	n/a	423%	22%	41%	19%
Special category								
'No birds sighted'	0.13	70.6%	0.54	0.2539	63%	297%	466%	433%

*Cross-validation was performed by aggregating data and predictions in 10x10 cell (~9x9 km) bins. This was necessary because cross-validation data locations did not match up exactly from season to season. See Appendices 6.A and 6.C for details.
**Diagnostic statistics are explained in Box 6.1, Table B.

Box 6.1. Predictive modeling summary guide.



PREDICTIVE MODELING SUMMARY GUIDE

On the following pages the annual predictive models for each species and species group are summarized in a standardized layout like the example above. The elements of this model summary are as follows:

A. Common name (Scientific name) of the species; or Group name (number of species)

B. Annual climatological predicted relative abundance (Sightings Per Unit Effort [SPUE], No. indiv./km²/15-minute survey). Predicted SPUE is indicated by the color gradient, which is logarithmically scaled as indicated by the color bar at right. Certainty classes are overlaid on model predictions, as indicated in the legend of the first figure in the series (Figure 6.8). The NY planning area and the shelf edge are denoted by a magenta dotted line and a solid black line, respectively (see legend in Figure 6.8).

C. A photo of an individual of the species, or of one representative species in the group.

D. Data summary table. The input data used to fit and test the model are summarized by season and over all seasons. "N obs." indicates the number of independent surveys in which a species or group was sighted; "Freq. (%)" is the relative frequency of sighting; the rest of the table reports statistics of non-zero data only (relative abundance when the species was present).

E. Predictor summary table. This table summarizes the variables included in each of the seasonal trend GLM models for Occurrence (Stage I) and Abundance (Stage II). P-values for Bonferroni-corrected post-hoc significance tests of each effect (minimum p-value considering main effect and any interactions in which the variable occurs) are indicated by color shading (Box Table A).

Variables that were not included are indicated by white squares. Seasons that were not modeled are indicated by an "X" through the corresponding columns of the table.

Box 6.1: Table A. Color shading for P-values.

Color	P-value
Red	p>0.1
Orange	p<0.1
Yellow	p<0.05
Light green	p<0.01
Green	p<0.001

F. Diagnostic summary table. The first row of this table reports the percentage of the NY study area that falls into each certainty class ("Low", "Med", "High" columns), and the certainty class that would be assigned based on the average relative uncertainty value calculated over the whole NY study area ("ALL" column). The rest of the table reports cross-validation error statistics for each certainty class (based on the 50% of the data that were withheld from model fitting). Cells are color coded based on whether the results of each diagnostic can be considered "excellent" (green), "fair" to "good" (yellow), or "poor" (red). See Box 6.1: Table B for a list of the diagnostic statistics, notes on how they were calculated, and values used to define the "excellent", "fair to good", and "poor" categorization. Note that the color-coding of diagnostic statistics should be considered a general guideline to model performance; the usefulness of model predictions in any specific case often depends on the details of the application. One diagnostic statistic may be important for one application, but irrelevant for another.

Box 6.1: Table B. Description of diagnostic statistics and color-coding of diagnostic tables. Cutoff values for "Poor", "Fair", "Good", and "Excellent" are subjective and qualitative categories and are intended as an interpretative aid, not a formal statistical test.

Diagnostic statistic	Description	Calculated with	Poor	Fair to Good	Excellent
Rank R	Spearman rank correlation coefficient of observed vs. predicted	Non-zero cross-validation data	x<0.05	0.05≤x<0.3	x≥0.3
%1SD	Percent of observations within +/- 1 standard deviation (or standard error) confidence intervals of predicted value; theoretical expectation is 68%	Non-zero cross-validation data	x<20%	20%≤x<50%	x≥50%
AUC	Area Under Curve statistic; area under the receiver operating characteristic (ROC) curve	All binary cross-validation data (presence/absence); maximum predicted probability in bin used as ROC classifier	x<0.55	0.55≤x<0.75	x≥0.75
p(AUC)	p-Value for significance test of the AUC statistic	Non-zero cross-validation data	x>0.20	0.20≥x>0.01	x≤0.01
MAPE	Mean Absolute Percentage Error = mean(obs-pred /obs)*100%	Non-zero cross-validation data	x>150%	150%≥x>50%	x≤50%
Rel.MAE	Relative Mean Absolute Error (expressed as a % of the 90th percentile - 10th percentile range of the data)	All cross-validation data	x>100%	100%≥x>25%	x≤25%
Rel.RMSE	Relative Root Mean Square Error (expressed as a % of the 90th percentile - 10th percentile range of the data)	All cross-validation data	x>100%	100%≥x>25%	x≤25%
Rel.Bias	Relative Absolute Bias (expressed as a % of the 90th percentile - 10th percentile range of the data)	All cross-validation data	x>100%	100%≥x>25%	x≤25%
Bias Dir.	Sign (+ or -) of the Bias statistic. + indicates predicted value tends to be greater than observed value.	All cross-validation data	n/a	n/a	n/a

The maps shown in the main section of this report (Figures 6.8 to 6.37) are annual climatological maps. Full model profiles including seasonal maps for each species and group (and the “no birds sighted” category) are given in Appendix 6.C. These profiles include overlays of original data points on model predictions, the seasonal predictions that went into each annual map, more detailed quantitative maps of relative uncertainty, details on the structure of each model, histograms showing the temporal occurrence of each species/group, and results of the cross-validation accuracy assessment for each model. Similar seasonal profiles for hotspot analyses are given in Appendix 6.D. Readers interested in application of the models presented in this report are urged to consult Appendices 6.C and 6.D to evaluate seasonal variation in model predictions, and the performance of each model in independent cross-validation.

Below, very brief notes are given on predictive model results for each species and group, in relation to species life history and occurrence in the study area. These notes are intended only as an initial introduction and qualitative description of model results; the maps and diagnostics presented in figures, tables, appendices, and online supplements convey more detailed results for each species.

6.9.1. Species notes

Black-legged Kittiwake (*Rissa tridactyla*)

The Black-legged Kittiwake (Figure 6.8, Tables 6.9-11) is one of the most abundant and frequently sighted species in the study area. The majority of sightings were made between late fall and early spring. The species breeds along coasts in the Arctic and sub-Arctic in summer, and winters out at sea along the Pacific and Atlantic coasts, including the study area. Predicted abundance was highest in the north and central parts of the study area, especially south of the eastern tip of Long Island, in the Hudson Shelf Valley vicinity, and south of Nantucket Shoals. This pattern was fairly consistent across seasons. Model predictive ability was marginal with a high proportion of white noise (unpredictable random variation) and poor ROC performance. However, some of the other diagnostic statistics indicate acceptable performance, especially in the “medium” certainty class.

Common Loon (*Gavia immer*)

The Common Loon (Figure 6.9, Tables 6.12-14) is a coastal species during the non-breeding season (i.e., outside of summer), and this is reflected in model predictions. Hotspots of predicted abundance occur all along the shore, especially in the vicinity of New York Bay, the NJ shore, Long Island, Block Island, and Martha’s Vineyard. Loons are fairly commonly sighted nearshore in spring, fall, and winter, and range furthest offshore in spring; otherwise patterns were consistent across seasons. Model predictive ability was generally good, with low white noise, excellent overall ROC performance, and excellent performance in the ‘high’ certainty class that dominated the study area. The small white (blank) spot southeast of Block Island is a place where predictions were masked out because they were both extremely high (beyond the range of the data) and extremely uncertain (beyond the threshold over which we considered predictions too uncertain to map, and unsupported by any nearby data points). The high values around the edges of this blank spot are also fairly uncertain. Expert judgement is that this apparent hotspot is not likely to be real (D. Veit and P. Paton, pers. comms.). Also, because this is a highly coastal species, and the coverage of the Manomet dataset is poor nearshore, the abundance estimates for this species may be biased low. For example, the RI SAMP study (Paton et al., 2010) found that Common Loons were relatively common in RI waters in the winter.

Common Tern (*Sterna hirundo*)

Although the Common Tern (Figure 6.10, Tables 6.15-17) is the most widespread tern species in North America it is relatively infrequent in the study area dataset (<3% prevalence). This is likely partially due to the poor coverage of the MBO CSAP data in very nearshore areas: the species prefers coastal habitats along the ocean, rivers and lakes, which abut, but are not part of the study area. The largest Common Tern colony in the region (15,000+ individuals) is on Great Gull Island at the east end of Long Island Sound. There is an influx of Common Terns into more offshore waters in April and May, with peak abundance in the summer breeding months and trailing off into December. The model predictions reflect this seasonal pattern and the expected nearshore distribution. The species is listed as Threatened by New York. Predicted abundance is highest nearshore, especially south of Long Island. The area of high predicted abundance near Jamaica Bay is well-supported by data offshore, but not by any nearshore data points, and so should be interpreted with

caution in light of the data distribution shown in Appendix 6.C. The spatial pattern is consistent across seasons. Model predictive ability was good, with low white noise, excellent overall ROC performance, and excellent performance in the ‘high’ certainty class that dominated the study area. Model predictions were more uncertain and variable in fall, when the species was less abundant.

Cory’s Shearwater (*Calonectris diomedea*)

Cory’s Shearwater (Figure 6.11, Tables 6.18-20) is a large seabird found across the Northern Atlantic and seldom seen near land except during breeding. Since it breeds on islands in the eastern North Atlantic and Mediterranean, it is not regularly seen close to shore in North America. It is commonly found where water masses mix. Most sightings in the study area are made during the summer and fall. Abundance predictions peak offshore and the abundance trend follows a general southwest to northeast pattern along the shelf edge, with a more expansive distribution to the north and east. The apparent hotspots south of Block Island and near Nantucket Shoals are not well-supported by data (they are based primarily on extrapolation of environmental relationships) and therefore should be considered hypothetical until tested with additional survey data. Model predictive ability indicated by error statistics and ROC analysis is fair to good where certainty is high. However, the white noise component of the model is moderately high indicating a high degree of unpredictable random variability in abundance at any given location. This is consistent with findings of the more recent Rhode Island SAMP study, which found significant interannual variation in the abundance of this species in offshore areas (Paton et al., 2010). It should also be noted that this species is attracted to fishing vessels and may be influenced by fishing patterns.

Dovekie (*Alle alle*)

Dovekies (Figure 6.12, Tables 6.21-23) are almost strictly pelagic, coming ashore only to breed on cliffs in areas far north of the NY Bight. Sightings are uncommon in the study area except offshore in winter, but when Dovekies are seen, they exhibit clear spatial and temporal patterns. Dovekies are most common in the winter months and there is an obvious preference for warmer waters above the shelf slope and in the middle of the study area, northwest of Hudson Canyon. This is consistent with Dovekie’s tendency to concentrate in this region near temperature fronts and aggregations of copepods and similarly sized zooplankton (D. Veit, pers. comm.). Model predictive ability in ROC analysis was fair to good; abundance when sighted was highly variable (high Stage II white noise). This species may recently have increased in abundance (e.g., Paton et al., 2010) and the patterns depicted here should be compared to more recent data.

Great Black-Backed Gull (*Larus marinus*)

The Great Black-Backed Gull (Figure 6.13, Tables 6.24-26) is a coastal species found in the North Atlantic and Palearctic, breeding on coasts in North America and Europe. The study area is towards the southern limit of this species’ distribution (breeds south to North Carolina; ranges to Florida in winter), which may explain why sightings are more common in the northern part of the study area. Most sightings are made between July and November during breeding months and there are confirmed observations of breeding on Long Island. Relatively certain predictions of high abundance were made throughout the northeast portion of the study domain, including the vicinity of Block Island southeast to the shelf edge, and Martha’s Vineyard south to the shelf edge. High abundances were also predicted near the coast and along the shelf edge. The onshore-offshore distribution varied somewhat with season (Appendix 6.C). Though highly variable (white noise component was high), presence predictions were generally excellent and error statistics were acceptable even for the ‘low’ certainty class.

Great Shearwater (*Puffinus gravis*)

The Great Shearwater (Figure 6.14, Tables 6.27-29) is one of only a few species found in the NY Bight that migrate from breeding grounds in the Southern Hemisphere to wintering grounds in the Northern Hemisphere. Migration follows a quasi-circular route moving up the western edge of the Atlantic in spring-summer and returning along the eastern Atlantic. Sightings in the study area occur primarily in summer and fall. Low abundance was predicted over most of the study area, suggesting that the birds remain primarily offshore during migration and generally follow the shelf edge. A broad, moderate concentration of abundance occurs in the center of the NY planning area, just south of Long Island extending south and southeast to the shelf edge and east past Nantucket Shoals. This pattern of abundance is similar to that of other shearwaters (e.g., Cory’s

Shearwater). Presence predictions were fair to good; abundance when seen was highly variable (high white noise). Error statistics were fair to good in higher certainty classes.

Herring Gull (*Larus argentatus smithsonianus*)

The Herring Gull (Figure 6.15, Tables 6.30-32) is a very widespread and abundant seabird in the study area. It is a year-round resident and breeds along the coasts. Especially high abundance occurs at the mouth of the Hudson River, along the south shore of Long Island, south of Nantucket at the eastern edge of the domain, and scattered other locations throughout the domain. This species is attracted to ships, and the high abundances off New York Harbor and south of Martha's Vineyard may be due to birds aggregating at fishing trawlers (and thus not reliable long-term hotspots). A clear and dramatic change in spatial distribution occurs over the course of a year (see Appendix 6.C). Sightings are distributed across the shelf during winter, spring and fall, but are rare greater than 50 km from shore during the summer breeding months. Very high white noise components indicate a highly variable, transient pattern of distribution, and error statistics are correspondingly poor; however, the model predicted the range of variability well (%1SD statistics) and ROC statistics were excellent in the 'medium' certainty class.

Laughing Gull (*Leucophaeus atricilla*)

The Laughing Gull (Figure 6.16, Tables 6.33-35) breeds along the eastern Atlantic with the greatest abundances seen south of the study area, though it is fairly common in NY. The study area is relatively close to the northern limit of the Laughing Gull breeding distribution (which extends as far north as Nova Scotia and New Brunswick). Predictions of highest abundance and occurrence are made within 50 km of shore and near the Hudson River and New Jersey coasts, and are consistent across spring, summer, and fall seasons. Sightings in the winter and early-spring are more rare; this species winters in the mid-Atlantic and to the south. Model predictions of presence are excellent, though abundance when seen is fairly variable. Predictions in the 'high' certainty class are excellent; 'medium' certainty predictions are less good.

Northern Fulmar (*Fulmarus glacialis*)

The Northern Fulmar (Figure 6.17, Tables 6.36-38) is a gull-like relative of albatrosses and shearwaters. Most sightings are made between January and June (winter-spring). The majority of sightings are offshore, between 75 km from shore and the shelf edge, although sightings occur somewhat closer to shore in the northeast of the study area, offshore of Martha's Vineyard and Nantucket. Patterns are consistent across seasons. Performance in ROC analysis was good, and diagnostics are excellent for the high certainty class which covers about half the study area.

Northern Gannet (*Morus bassanus*)

The Northern Gannet (Figure 6.18, Tables 6.39-41) is one of the most abundant and widespread species of seabird in the study area. It is frequently sighted between October and April and exhibits distinct spatial patterns among seasons, with more offshore sightings in spring. In the winter most individuals are seen in the mid-to-inner shelf towards the southern part of the domain, in the spring throughout the domain and especially along the shelf edge, and in the fall in the inner to mid-shelf with peaks near Nantucket Shoals and Long Island. This species is known to aggregate to areas of fishing activity, and so its spatial distribution may have changed since the 1980's with shifting patterns of fishing effort. In particular, large aggregations of Northern Gannets were observed in association with foreign factory trawler boats in the 1980's, and similar aggregations have not been observed since those boats stopped frequenting the region (D. Veit, pers. comm.). Thus, the hotspots near the shelf break require confirmation from more recent data before being considered persistent aggregations. Both the two-pulse fall and spring migrant pattern and the tendency to aggregate to fishing boats have been confirmed by recent studies in the area (Paton et al., 2010). Model predictive performance is poor to fair, depending on certainty class; the Stage II white noise component (unpredictability in abundance when present) is very high.

Pomarine Jaeger (*Stercorarius pomarinus*)

The Pomarine Jaeger (Figure 6.19, Tables 6.42-44) is a skua occasionally seen offshore of New York in the fall (<4% frequency). Very few sightings are made in other seasons. Areas of highest abundance are predicted along the shelf edge, and south of Nantucket shoals. It is possible that these aggregations are due to the presence of fishing trawlers and are not reliable long-term hotspots (D. Veit, pers. comm.). This species is

seldom if ever observed close to shore. Model predictive performance was excellent for the high certainty class, but model uncertainty tended to underestimate uncertainty seen in cross-validation, due to the highly skewed abundance distribution.

Sooty Shearwater (*Puffinus griseus*)

The Sooty Shearwater (Figure 6.20, Tables 6.45-47) breeds on islands off southern South America and New Zealand and spends summers in the North Pacific and Atlantic. Most sightings in the study area are between April and July (spring-summer). Predictions show a clear preference for the shelf edge during the spring, similar to other shearwaters in the study area. Predictions of high abundance are also made in discrete areas in the spring and summer south of central Long Island and south of Nantucket Island, respectively. Model performance was generally fair, but excellent in the ~20% of the study area with 'high' certainty.

Wilson's Storm-Petrel (*Oceanites oceanicus*)

Wilson's Storm-Petrel (Figure 6.21, Tables 6.48-50) is one of the most common species seen in summer in the study area, and is also present in spring and fall. It breeds in Antarctic and sub-Antarctic seas, but ranges to the Northern Pacific, Atlantic and Indian Oceans during summer months. The majority of sightings in the study area are between May and September (spring, summer, and fall). Areas of high abundance are predicted fairly uniformly over the shelf, increasing offshore. Abundances extend into the nearshore in the northern part of the study area in summer. Though white noise is high, indicating a high degree of unpredictability in abundance, ROC analysis showed good predictive ability. Model diagnostics in the 'high' certainty class indicated excellent performance.

6.9.2. Group notes

Less Common Alcids

The Less Common Alcids group (Figure 6.22, Tables 6.51-53) includes the Atlantic Puffin, Common Murre, Razorbill, Thick-billed Murre, and unidentified species in the Family Alcidae. These species are generally rare in the study area, though frequency of sightings reaches 5% in winter. They occur in winter and spring, and very rarely in fall. Predictions are uncertain and cross-validation results are poor. Generally there appears to be an area of elevated abundance along the shelf especially in the northeast of the domain, south of Nantucket shoals. ROC analysis shows very little predictive success, though more certain predictions do have better cross-validation error statistics, indicating that when the group is present the abundance predictions are fairly good. The Rhode Island SAMP study found that the Razorbill and Common Murre have become much more common than earlier surveys in this region in recent years, so analysis of newer survey data will be important to an improved assessment of this group (Paton et al., 2010).

Coastal Waterfowl

Coastal Waterfowl (Figure 6.23, Tables 6.54-56), as defined here, are a diverse group including scoters, ducks, mergansers, eiders and other waterfowl in the family Anatidae, plus Red-throated Loons (family Gaviidae). We note that loons are not generally considered to be waterfowl (usually this term refers to species in the family Anatidae) but are included here because the Red-throated Loon sightings in the Manomet dataset were spatio-temporally similar to the true waterfowl sightings in the region, and Red-throated Loons were not seen enough to model separately (likely due in part to their low detectability; these birds tend to dive when moving ships are approaching [P. Paton, pers. comm.]). These species occur near coastlines and islands throughout the study area, both inside and outside of Long Island Sound, northeast around Block Island, Nantucket, and Martha's Vineyard, and southwest along the NJ shore. Highest abundances are seen in spring. Distributions are generally consistent across seasons. Statistically, model performance is generally excellent, especially with regard to occurrence. Error statistics are good in the high certainty class, except the model-predicted confidence intervals under-predict error (the %1SD statistic is well below its theoretical target of 68.3%). However, there are significant caveats. Stage II white noise is high, indicating that although occurrence is highly predictable, the observed abundance when seen exhibits a high degree of unpredictable random variability. Moreover, because the Manomet dataset had very few nearshore surveys in winter when seaducks are most abundant, and also because Red-throated Loons and seaducks tend to avoid ships, the winter estimate of abundance for this group is likely to be a severe underestimate. Finally, because this group encompasses a large number of species, species-specific inferences cannot be made. If particular species of waterfowl are

of concern, additional data will be necessary to facilitate species-specific modeling. We note that much better data sources exist for wintering seabirds (e.g., Zipkin et al., 2010).

Jaegers

Jaegers (Figure 6.24, Tables 6.57-59) are rare in the study area, only exceeding a frequency of 0.5% in fall (when they reach a frequency of 2%). They are occasional in spring and summer and absent in winter. The only season for which sufficient data were available to model was fall. The model performs fairly well for high certainty areas, given limited data, but the high abundances predicted at the edges of the domain (along the shelf edge) have low certainty. ROC analysis indicates high sensitivity but with a high false positive rate. Other cross-validation statistics suggest caution is necessary in applying this model.

Phalaropes

Phalaropes (Figure 6.25, Tables 6.60-62) were only present at high enough frequency to model in spring. They are pelagic in distribution, concentrating at the shelf edge, especially in the central and eastern part of the domain. Model performance is good to excellent especially in the high certainty class that covers half the domain. Model-predicted uncertainty bounds tend to underestimate observed variability in abundance when seen.

Less Common Shearwaters

The Less Common Shearwaters (Figure 6.26, Tables 6.63-65) group includes the Manx Shearwater, Audubon's Shearwater and unidentified species in the Family Procellariidae. Most sightings occur in the spring, summer and fall, with a peak in summer. Highest abundance is predicted in summer along the eastern end of Long Island and Block Island and near Nantucket Shoals, though uncertainty is high for some of these areas. Otherwise, scattered sightings are made offshore out to the shelf edge throughout the study area in spring, summer, and fall. Audubon's Shearwaters are more common offshore, where they are mixed with Manx Shearwater sightings. Manx Shearwaters dominate nearshore sightings off the eastern tip of Long Island. Abundance and frequency are generally greater in the center and northeast than the southwest of the region. However, model performance in cross-validation is poor and results of this model should be used with caution.

Less Common Small Gulls

The Less Common Small Gulls (Figure 6.27, Tables 6.66-68) group includes the Ring-billed Gull and Bonaparte's Gull. The group is fairly rare in the study area (<4%); most prevalent in the fall and winter. Both of these species are migrants passing through the area in these seasons; summer breeding grounds are in boreal North America. High abundances are predicted along the Hudson shelf valley and to its south, and near the east end of Long Island. Insufficient sightings were made in very nearshore coastal areas to characterize distribution accurately, as indicated by the high uncertainty in these areas. Spatial distribution was consistent across seasons. Model performance in cross-validation was fair.

Less Common Storm-Petrels

The Less Common Storm-Petrels group (Figure 6.28, Tables 6.69-71) includes the Leach's Storm-Petrel, Band-rumped Storm-Petrel, White-faced Storm-Petrel (rarely), and unidentified species in the Family Hydrobatidae. Species in this group are very rare except in summer, when frequency of sighting approaches 5%. Areas of highest predicted abundance are scattered offshore along the shelf edge, slightly higher toward the south. Distribution is fairly consistent across seasons, with a subtle southward shift in summer. Occasional sightings occur at the east end of Long Island, primarily in summer, and in the Hudson Shelf Valley vicinity. Leach's Storm-Petrel was the most common species sighted and the only one positively identified in the nearshore. Overall, model performance is fair to poor for SPUE, but presence prediction diagnostics are good for the 'high' certainty class. A very high Stage II white noise component means abundance when seen is very hard to predict.

Less Common Terns

The Less Common Terns group (Figure 6.29, Tables 6.72-74) includes the Roseate, Least, Royal, Arctic, Sooty, Bridled, Caspian, and Forster's Terns and unidentified species in the Family Sternidae. The first two species are listed as endangered and threatened, respectively, by New York. The Roseate Tern is also federally listed

as Endangered by the USFWS. Most sightings are in the summer breeding months and are within 50 km of shore. Cross-validation shows presence/absence predictions are acceptable, but abundance predictions are poor except for the most certain areas (generally places far offshore where the species' are virtually certain to be absent). Given the sample sizes used to fit these models and the marginal performance statistics, caution should be used in applying SPUE predictions; presence/absence predictions can be used, but should also be treated with some caution. Caution should also be exercised because this group lumps many species, some of which are known to have different spatial distributions, and because the group contains more "Unidentified Tern" sightings than positively identified species sightings. These model results should be used as a starting point for forming hypotheses about distribution patterns which should be tested with further sampling and combined with additional species-specific survey data and expert opinion before being used for decision-making purposes. We note that Caspian Terns are now commonly seen in Rhode Island waters (Paton et al., 2010), but no Caspian Terns were positively identified in the Manomet dataset.

Unidentified Gulls

The Unidentified Gulls group (Figure 6.30, Tables 6.75-77) could consist of a variable set of species depending on the location within the study area and the time of year. This group had enough sightings to model in fall, winter, and spring, but not summer, suggesting that its members breed elsewhere and are passing through the area in spring/fall or overwintering. Another possibility is that many of the unidentified gulls could be juveniles; juvenile gulls can be very difficult to identify. The low numbers in summer are consistent with this hypothesis as young gulls would not yet be fledged at that point. The peak predicted abundance is in fall near Martha's Vineyard. Abundance is also predicted nearshore throughout the study area (with smaller peaks near the mouth of Long Island Sound, near Nantucket Shoals, and near New York Bay). This pattern is fairly consistent across seasons. Cross-validation performance is acceptable to good in the medium and high uncertainty classes, though there is high white noise in Stage I and the model-predicted confidence intervals are too small (low %1SD). Overall, model results for this group should be treated with caution as the identity of the component species is unknown, possibly variable over time and space, and possibly overlapping with some of the other, positively identified, gull species and groups that were modeled separately.

6.9.3. Non-modeled species groups

Cormorants

Cormorants (Figure 6.31, Table 6.78) are infrequent in the Manomet database, due in part to poor sampling in very nearshore areas. Point sightings of cormorants are most common in winter and are clustered near the east end of Long Island, Block Island, Martha's Vineyard, New York Bay, and southwest of Great Peconic Bay. More data is necessary to assess the spatial distribution of cormorants in offshore waters of NY if they are of particular interest. In the winter, when most common, unidentified birds were probably mainly Great Cormorants (P. Paton, pers. comm.).

Rare Visitors

The Rare Visitors group (Figure 6.32, Table 6.79) consists of species that are non-breeding, transient, and rare in the study area. Sightings are very infrequent (<1% total) and scattered around the study area with little obvious spatial pattern. If any of these species (listed in Table 6.2) are of particular interest, detailed additional studies will have to be performed.

Less Common Skuas

The Less Common Skuas group (Figure 6.33, Table 6.80) includes the Great Skua and unidentified sightings of skuas (species in the family Stercorariidae that are not Jaegers). The unidentified skuas are very likely to have been either poorly seen Great Skuas or South Polar Skuas, as these are the only two skua species recorded in the western North Atlantic. Sightings of this group are very infrequent in the study area (<1%). Most sightings are in the fall months, similar to the Pomarine Jaeger. Sightings generally occur offshore along the outer continental shelf, and are slightly more concentrated toward the south-central part of the domain near the shelf. If the Great Skua or other skuas thought to be represented by this group are of particular concern, more detailed studies or additional data collection and modeling should be conducted.

6.9.4. 'No birds sighted'

Figure 6.34A shows the annual predicted index of abundance of surveys that result in no sightings of seabirds (measured by multiplying the predicted probability of occurrence by the predicted transect area in which no birds were detected, in km²). Figure 6.34B shows the probability of at least one survey in any season resulting in "no birds sighted" (i.e., the annual integrated presence probability, calculated as if the 'no birds sighted' category were a species). Tables 6.81, 6.82, and 6.83 summarize the input data, predictors, and diagnostic statistics, respectively, for the 'no birds sighted' model.

The eastern end of Long Island and areas near Block Island and Martha's Vineyard have a lower probability than average of experiencing times without seabirds (i.e., most surveys in these areas see seabirds). The inner shelf in the Long Island Platform vicinity, about 10-30 km offshore, has an above average probability of experiencing times without seabirds. The patterns vary somewhat from season to season, and predictive performance of the model is fair to poor (high white noise, marginal error statistics). The reader should be particularly cautious of high predicted "no birds sighted" values within 10 km of shore as Manomet survey coverage drops off rapidly in the nearshore. Nonetheless, there are discernible spatial patterns that may be useful as an alternative to abundance hotspot maps to identify areas of potentially reduced conflict between ocean uses and seabirds.

6.9.5. Hotspots

Predicted hotspots of abundance for all modeled species combined (Figure 6.35) occur along the coast, especially along the Hudson Shelf Valley and in scattered areas throughout the shelf, particularly near Nantucket Shoals. The onshore-offshore gradient in abundance is consistent with many previous studies of seabirds in this region, and recent intensive survey work in New Jersey and Rhode Island.

Species richness hotspots (Figure 6.36) are scattered throughout the center and northeast of the study area, extending south-southeast from Long Island to the shelf edge, and between Long Island and Nantucket Shoals. Low diversity predicted beyond the shelf edge is unreliable, as indicated by the uncertainty overlay. Very nearshore predictions are also unreliable throughout the domain. This is consistent with increased species richness along the Atlantic Flyway. The patchy, uneven pattern of the species richness predictions is a result of the discrete nature of this variable (there can only be whole numbers of species) combined with the necessity of choosing a somewhat arbitrary threshold to define a species as present or absent at a given location.

The predicted Shannon diversity index (Figure 6.37) shows a smoother pattern that is distinct from the richness and abundance patterns. It reveals hotspots and coldspots of diversity scattered throughout the shelf, with highest diversity in the northeast of the study area near Nantucket and at the mouth of Long Island Sound.

It is important to remember that concentrations of abundance and diversity can form and disperse rapidly, because seabirds are highly mobile, and interact with dynamic ecological resources and processes. Thus, the patterns displayed here reflect the considerable variability in concentrations of seabird abundance over the 9-year observation period (1980-1988). For example, hotspots may form in entirely different locations in different years resulting in multiple hotspots in the final map, not all of which form in any given year or season. It is also important to note that uncertainty accumulates when predictive statistical models are combined, a fact that is reflected in the uncertainty maps. Reliable hotspot predictions can only be produced in places where data is sufficiently dense for all species.

6.9.6. Point Maps of Seabirds of Concern

Figure 6.38 shows the locations of sightings for four species of particular concern: the Roseate Tern, Common Tern, Least Tern, and Common Loon. The Piping Plover, listed as endangered by New York, was not in the Manomet dataset and therefore was not mapped. Most species of concern are sighted within 50 km of shore. Noticeable concentrations of sightings occur south of Jamaica and Great South bays. It is important to note that Figure 6.38 presents point sightings, not results of a predictive model. No information can be assumed regarding the presence or absence of the species in between sample points. With the exception of the Common Loon, these species were too rare to produce individual species predictive models. The remaining species were included in the predictive model for "Less Common Terns."

Black-legged Kittiwake (*Rissa tridactyla*)

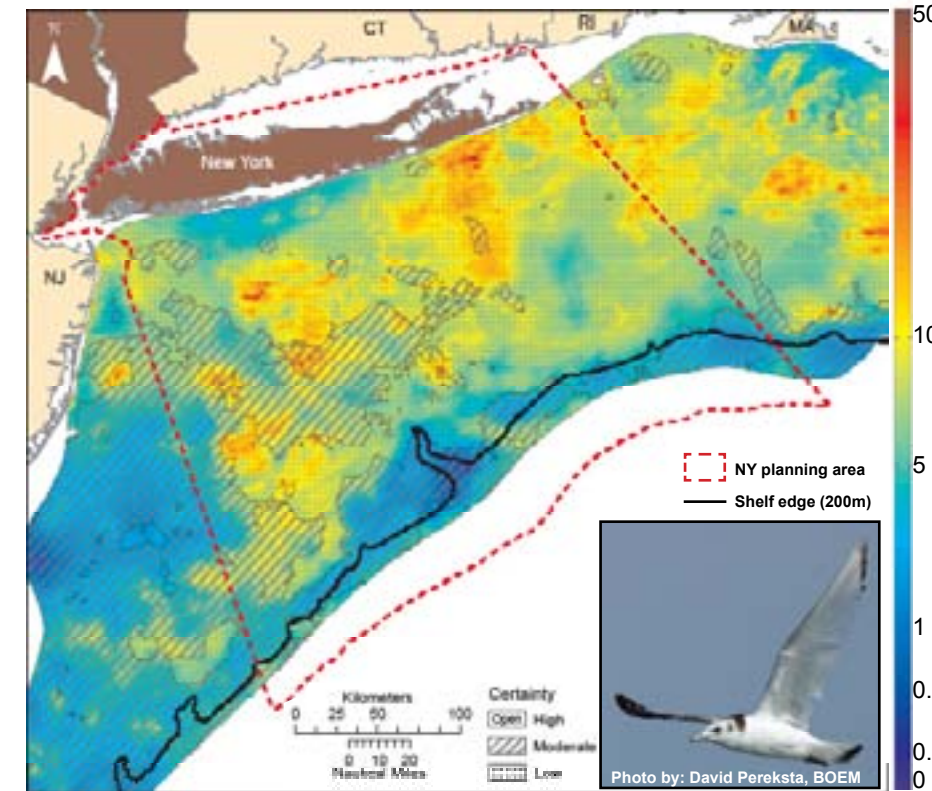


Figure 6.8. Predicted annual average relative index of abundance (SPUE, # indiv./km²/15-min) for Black-legged Kittiwake, with certainty classes overlaid.

Table 6.9. Data table: Black-legged Kittiwake.

Statistic	SP	SI	FA	WI	All
N obs.	195	2	397	546	1090
Freq. (%)	7.7%	0.1%	12.5%	47.6%	11.9%
SPUE when present (No. indiv./km ² /15 min.)					
Mean	9.17	0.96	6.29	8.17	7.73
1DthNdr	1.47	0.20	1.09	1.76	1.45
Median	4.40	0.96	4.24	4.80	4.60
5DthNdr	19.96	1.73	13.62	16.20	16.27
Max	121.59	1.73	57.90	153.44	153.44

Table 6.10. Predictor table: Black-legged Kittiwake.

Predictor	Occurrence				Abundance			
	Su	Su	Fa	Wi	Su	Su	Fa	Wi
BATH								
SLOPE								
ENST								
SSDIST								
SST								
STRT								
TUR								
CHI								
ZOO								
PIP/P								
PHM								

Table 6.11. Diagnostic table: Black-legged Kittiwake.

Diagnostic statistic	Certainty class			
	Low Score	Med Score	High Score	All Avg.
Rank R	0.16	0.13	n/a	0.02
%SD	81.2%	90.0%	n/a	84.0%
AIC	0.63	0.64	n/a	0.47
p(AIC)	0.02	0.06	n/a	0.70
MAPE	141%	154%	n/a	145%
Rel.MAE	44%	42%	n/a	44%
Rel.RMSE	80%	67%	n/a	78%
Rel.Bias	25%	10%	n/a	14%
Min. Err.	+	-	n/a	+

Common Loon (*Gavia immer*)

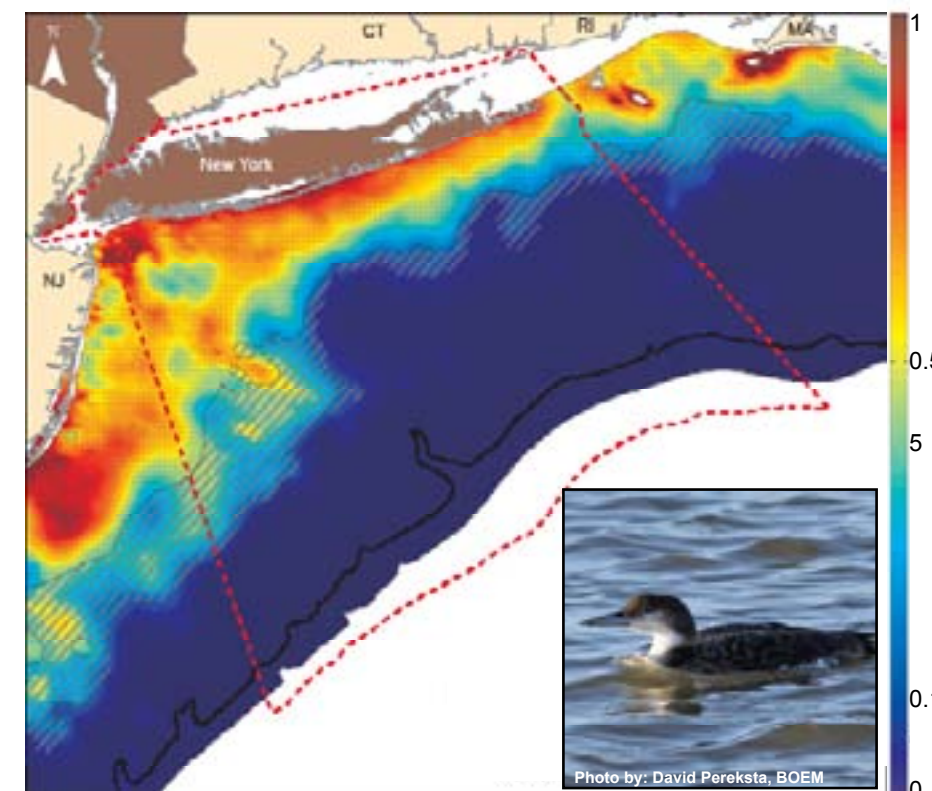


Figure 6.9. Predicted annual average relative index of abundance (SPUE, # indiv./km²/15-min) for Common Loon, with certainty classes overlaid (see legend in Figure 6.8).

Table 6.12. Data table: Common Loon.

Statistic	SP	SI	FA	WI	All
N obs.	132	9	60	40	216
Freq. (%)	4.9%	0.1%	2.2%	3.5%	2.4%
SPUE when present (No. indiv./km ² /15 min.)					
Mean	0.59	0.51	0.28	0.46	0.48
1DthNdr	0.16	0.27	0.10	0.12	0.13
Median	0.36	0.49	0.18	0.24	0.27
5DthNdr	0.92	0.80	0.54	1.17	0.80
Max	9.49	0.80	1.97	2.53	9.49

Table 6.13. Predictor table: Common Loon.

Predictor	Occurrence				Abundance			
	Su	Su	Fa	Wi	Su	Su	Fa	Wi
BATH								
SLOPE								
ENST								
SSDIST								
SST								
STRT								
TUR								
CHI								
ZOO								
PIP/P								
PHM								

Table 6.14. Diagnostic table: Common Loon.

Diagnostic statistic	Certainty class			
	Low Score	Med Score	High Score	All Avg.
Rank R	0.08	0.33	n/a	0.04
%SD	16.0%	66.7%	n/a	33.3%
AIC	0.58	0.57	n/a	0.77
p(AIC)	0.13	0.27	n/a	0.00
MAPE	208%	90%	n/a	256%
Rel.MAE	40%	17%	n/a	40%
Rel.RMSE	82%	24%	n/a	67%
Rel.Bias	87%	27%	n/a	41%
Min. Err.	+	+	n/a	+

Common Tern (*Sterna hirundo*)

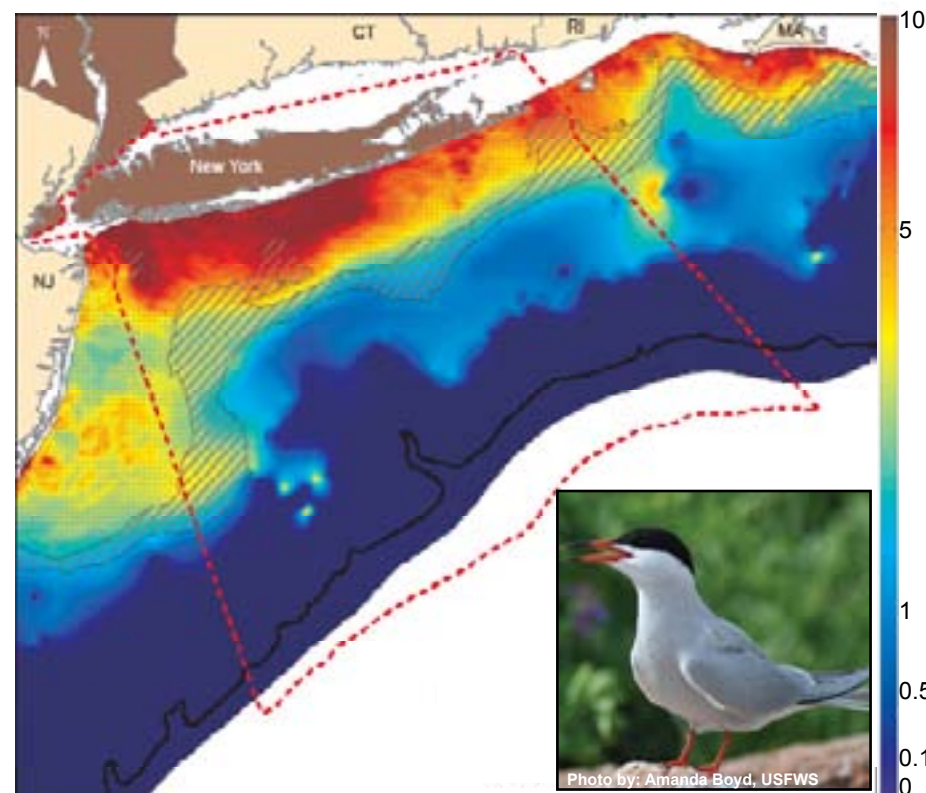


Figure 6.10. Predicted annual average relative index of abundance (SPUE, # indiv./km²/15-min) for Common Tern, with certainty classes overlaid (see legend in Figure 6.8).

Table 6.15. Data table: Common Tern.

Statistic	SP	SU	FA	WI	All
N obs.	56	76	32	1	165
Freq. (%)	2.2%	2.8%	1.2%	0.1%	1.8%
SPUE when present (No. indiv./km ² /15 min.)					
Mean	6.61	5.08	3.88	0.27	5.34
10th%ile	0.48	0.28	0.33	0.27	0.33
Median	2.63	2.52	1.32	0.27	2.52
50th%ile	11.70	12.30	9.16	0.27	12.42
Max	48.43	27.20	20.16	0.27	48.43

Table 6.16. Predictor table: Common Tern.

Predictor	Occurrence				Abundance			
	Su	Su	Fa	Wi	Su	Su	Fa	Wi
BATH								
SLOPE								
DIST								
SSDIST								
SST								
STRT								
TUR								
EHI								
ZOO								
SI P S I P								
BHIM								

Table 6.17. Diagnostic table: Common Tern.

Diagnostic	Certainty class			
	Low	Med	High	All
Statistic	Score	Score	Score	Avg.
Rank 12	24%	11%	65%	HIGH
%AIC	0.58	n/a	0.57	0.26
%AIC	42.3%	n/a	71.4%	46.7%
AIC	0.46	n/a	0.69	0.77
p(AIC)	0.05	n/a	0.05	0.00
MAPE	285%	n/a	183%	578%
Rel. MAPE	37%	n/a	6%	24%
Rel. RMSE	48%	n/a	10%	34%
Rel. Bias	54%	n/a	3%	18%
Obs. Dir.	+		+	+

Table 6.18. Data table: Cory's Shearwater.

Statistic	SP	SU	FA	WI	All
N obs.	3	297	153	1	454
Freq. (%)	0.1%	11.1%	5.5%	0.1%	5.0%
SPUE when present (No. indiv./km ² /15 min.)					
Mean	0.33	1.80	0.73	0.22	1.45
10th%ile	0.24	0.24	0.15	0.22	0.20
Median	0.30	0.65	0.45	0.22	0.60
50th%ile	0.45	2.40	1.44	0.22	2.16
Max	0.45	104.99	17.60	0.22	104.99

Table 6.19. Predictor table: Cory's Shearwater.

Predictor	Occurrence				Abundance			
	Su	Su	Fa	Wi	Su	Su	Fa	Wi
BATH								
SLOPE								
DIST								
SSDIST								
SST								
STRT								
TUR								
EHI								
ZOO								
SI P S I P								
BHIM								

Table 6.20. Diagnostic table: Cory's Shearwater.

Diagnostic	Certainty class			
	Low	Med	High	All
Statistic	Score	Score	Score	Avg.
Rank 12	34%	16%	50%	MED
%AIC	-0.03	-0.21	0.57	0.20
%AIC	63.5%	80.0%	97.6%	78.6%
AIC	0.57	0.55	0.67	0.64
p(AIC)	0.05	0.31	0.00	0.00
MAPE	129%	115%	71%	112%
Rel. MAPE	55%	18%	11%	22%
Rel. RMSE	101%	48%	31%	69%
Rel. Bias	8%	10%	1%	5%
Obs. Dir.	+	+	+	+

Cory's Shearwater (*Calonectris diomedea*)

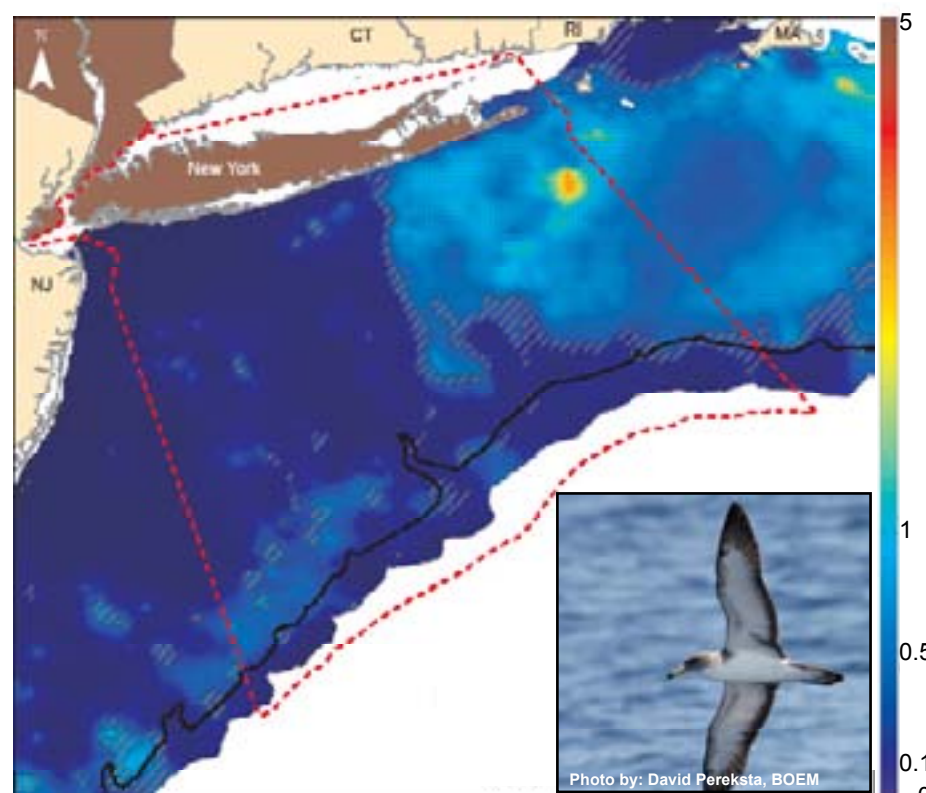


Figure 6.11. Predicted annual average relative index of abundance (SPUE, # indiv./km²/15-min) for Cory's Shearwater, with certainty classes overlaid (see legend in Figure 6.8).

Dovekie (*Alle alle*)

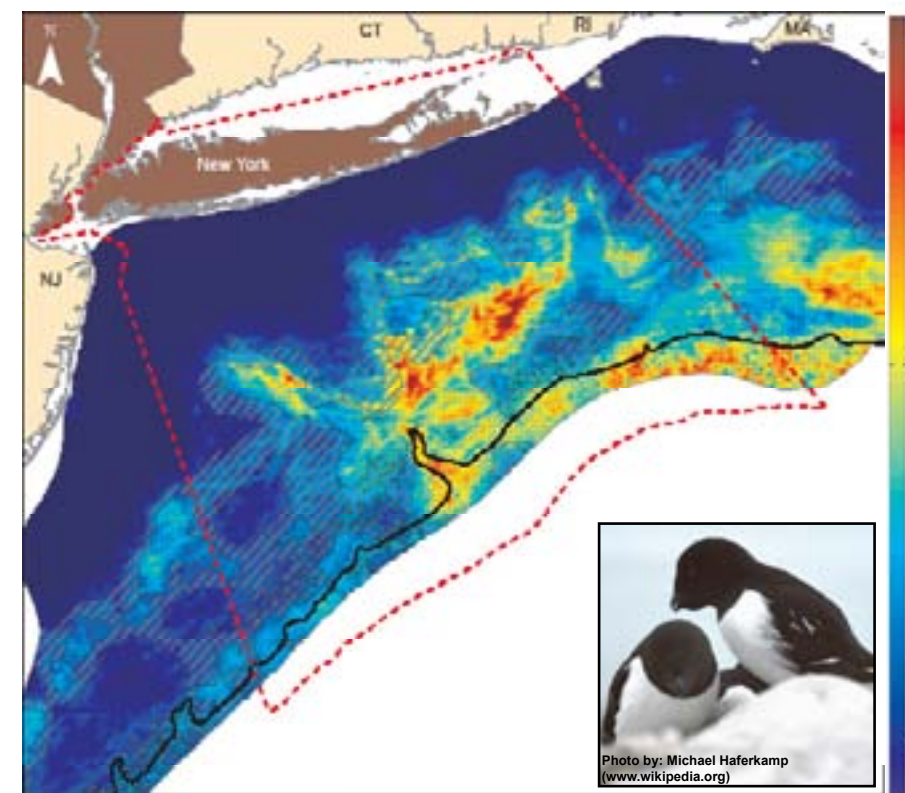


Figure 6.12. Predicted annual average relative index of abundance (SPUE, # indiv./km²/15-min) for Dovekie, with certainty classes overlaid (see legend in Figure 6.8).

Table 6.21. Data table: Dovekie.

Statistic	SP	SU	FA	WI	All
N obs.	37	0	27	97	161
Freq. (%)	1.5%	0.0%	1.0%	8.1%	1.8%
SPUE when present (No. indiv./km ² /15 min.)					
Mean	1.80		1.12	1.48	1.49
10th%ile	0.18		0.18	0.16	0.16
Median	0.90		0.60	0.56	0.65
50th%ile	5.17		1.01	1.10	1.13
Max	13.44		5.10	20.52	20.52

Table 6.22. Predictor table: Dovekie.

Predictor	Occurrence				Abundance			
	Su	Su	Fa	Wi	Su	Su	Fa	Wi
BATH								
SLOPE								
DIST								
SSDIST								
SST								
STRT								
TUR								
EHI								
ZOO								
SI P S I P								
BHIM								

Table 6.23. Diagnostic table: Dovekie.

Diagnostic	Certainty class			
	Low	Med	High	All
Statistic	Score	Score	Score	Avg.
Rank 12	1%	2%	4%	MED
%AIC	-0.12	0.20	0.24	0.20
%AIC	58.6%	66.7%	63.6%	62.3%
AIC	0.51	0.68	0.71	0.71
p(AIC)	0.40	0.00	0.01	0.00
MAPE	231%	163%	237%	216%
Rel. MAPE	9%	3%	3%	5%
Rel. RMSE	30%	6%	8%	15%
Rel. Bias	9%	7%	2%	5%
Obs. Dir.	+	+	+	+

Great Black-backed Gull (*Larus marinus*)

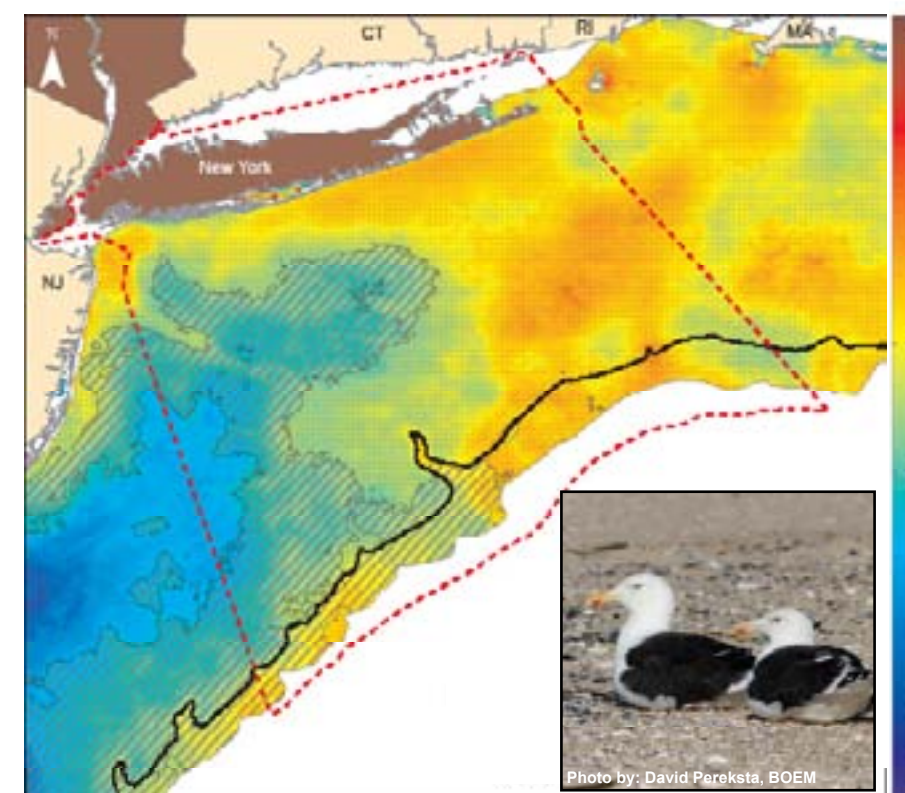


Figure 6.13. Predicted annual average relative index of abundance (SPUE, # indiv./km²/15-min) for Great Black-backed Gull, with certainty classes overlaid (see legend in Figure 6.8).

Table 6.24. Data table: Great Black-backed Gull.

Statistic	SP	SU	FA	WI	All
N obs.	624	1,49	506	468	1,747
Freq. (%)	24.5%	5.6%	18.2%	40.8%	19.1%
SPUE when present (No. indiv./km ² /15 min.)					
Mean	0.29	6.83	7.78	0.47	8.62
10th%ile	1.01	1.46	0.44	2.29	0.96
Median	5.10	5.40	4.80	5.87	5.22
50th%ile	16.23	12.80	17.10	19.50	17.10
Max	284.38	85.79	92.69	320.85	320.85

Table 6.25. Predictor table: Great Black-backed Gull.

Predictor	Occurrence				Abundance			
	Su	Su	Fa	Wi	Su	Su	Fa	Wi
BATH								
SLOPE								
DIST								
SSDIST								
SST								
STRT								
TUR								
EHI								
ZOO								
SI P S I P								
BHIM								

Table 6.26. Diagnostic table: Great Black-backed Gull.

Diagnostic	Certainty class			
	Low	Med	High	All
Statistic	Score	Score	Score	Avg.
Rank 12	0.2%	0.3%	0.3%	LOW
%AIC	87.7%	96.4%	100.0%	91.4%
AIC	0.40	0.55	1.00	0.77
p(AIC)	0.62	0.30	0.00	0.00
MAPE	148%	83%	294%	154%
Rel. MAPE	42%	25%	17%	35%
Rel. RMSE	55%	36%	21%	46%
Rel. Bias	6%	11%	8%	7%
Obs. Dir.	+	+	-	+

Great Shearwater (*Puffinus gravis*)

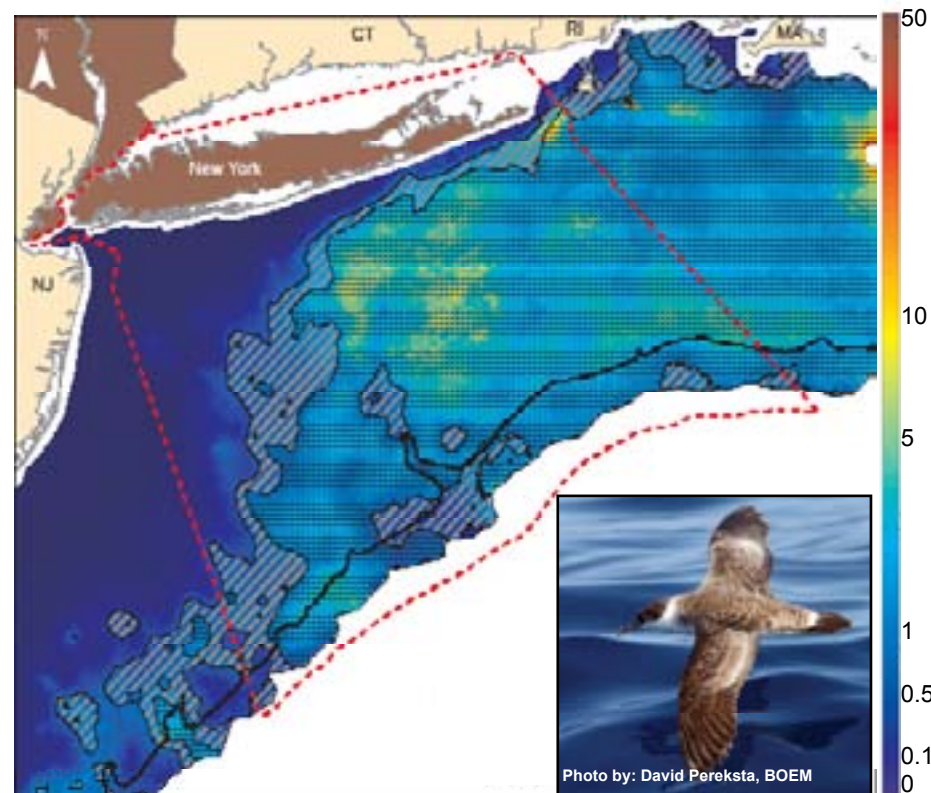


Figure 6.14. Predicted annual average relative index of abundance (SPUE, # indiv./km²/15-min) for Great Shearwater, with certainty classes overlaid (see legend in Figure 6.8).

Table 6.27. Data table: Great Shearwater.

Statistic	SP	SLI	FA	WI	All
N obs.	33	197	404	9	943
Freq. (%)	1.3%	18.6%	14.5%	0.8%	10.3%
SPUE when present (No. indiv./km ² /15 min.)					
Mean	0.58	2.80	1.75	0.29	2.27
10th%ile	0.14	0.27	0.22	0.18	0.24
Median	0.48	0.80	0.65	0.24	0.72
90th%ile	2.10	4.66	3.60	0.50	3.97
Max	7.80	223.54	79.19	0.80	223.54

Table 6.28. Predictor table: Great Shearwater.

Predictor	Occurrence				Abundance			
	Sp	Su	Fa	Wi	Sp	Su	Fa	Wi
BATH								
SLOPE								
DIST								
SSDIST								
SST								
STRT								
TUR								
CHI								
ZOO								
SLPSP								
PHIM								

Table 6.29. Diagnostic table: Great Shearwater.

Diagnostic statistic	Certainty class			
	Low Score	Med Score	High Score	All Avg. LOW
Rank R	0.04	0.03	0.21	0.07
%ASD	71.2%	92.6%	81.3%	75.6%
AUC	0.64	0.55	0.76	0.65
p(AUC)	0.00	0.22	0.00	0.00
MAPE	267%	89%	104%	221%
Rel.MAC	39%	16%	9%	27%
Rel.RMSE	85%	27%	27%	65%
Rel.Dias	1%	3%	2%	1%
New Dir.	-	+	-	-

Laughing Gull (*Leucophaeus atricilla*)

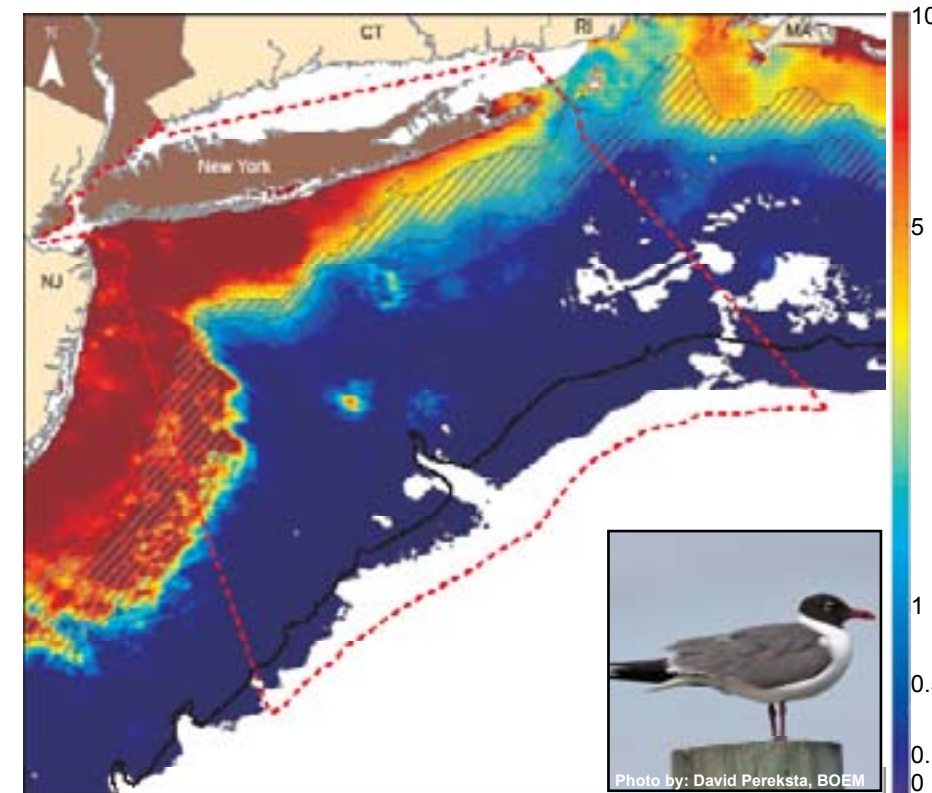


Figure 6.16. Predicted annual average relative index of abundance (SPUE, # indiv./km²/15-min) for Laughing Gull, with certainty classes overlaid (see legend in Figure 6.8).

Table 6.33. Data table: Laughing Gull.

Statistic	SP	SLI	FA	WI	All
N obs.	46	108	208	6	368
Freq. (%)	1.8%	4.0%	7.5%	0.5%	4.0%
SPUE when present (No. indiv./km ² /15 min.)					
Mean	3.86	16.14	6.08	0.74	8.67
10th%ile	0.74	1.27	0.36	0.15	0.36
Median	2.76	10.08	3.52	0.70	4.52
90th%ile	8.35	36.96	13.74	1.54	19.73
Max	29.16	131.99	67.67	1.60	131.39

Table 6.34. Predictor table: Laughing Gull.

Predictor	Occurrence				Abundance			
	Sp	Su	Fa	Wi	Sp	Su	Fa	Wi
BATH								
SLOPE								
DIST								
SSDIST								
SST								
STRT								
TUR								
CHI								
ZOO								
SLPSP								
PHIM								

Table 6.35. Diagnostic table: Laughing Gull.

Diagnostic statistic	Certainty class			
	Low Score	Med Score	High Score	All Avg. HIGH
Rank R	0.27	0.82	0.43	0.33
%ASD	64.5%	100.0%	100.0%	76.1%
AUC	0.58	0.79	0.72	0.69
p(AUC)	0.19	0.00	0.03	0.00
MAPE	920%	63%	158%	161%
Rel.MAC	61%	7%	2%	15%
Rel.RMSE	115%	9%	5%	28%
Rel.Dias	7%	5%	1%	0%
New Dir.	-	+	+	+

Herring Gull (*Larus argentatus smithsonianus*)

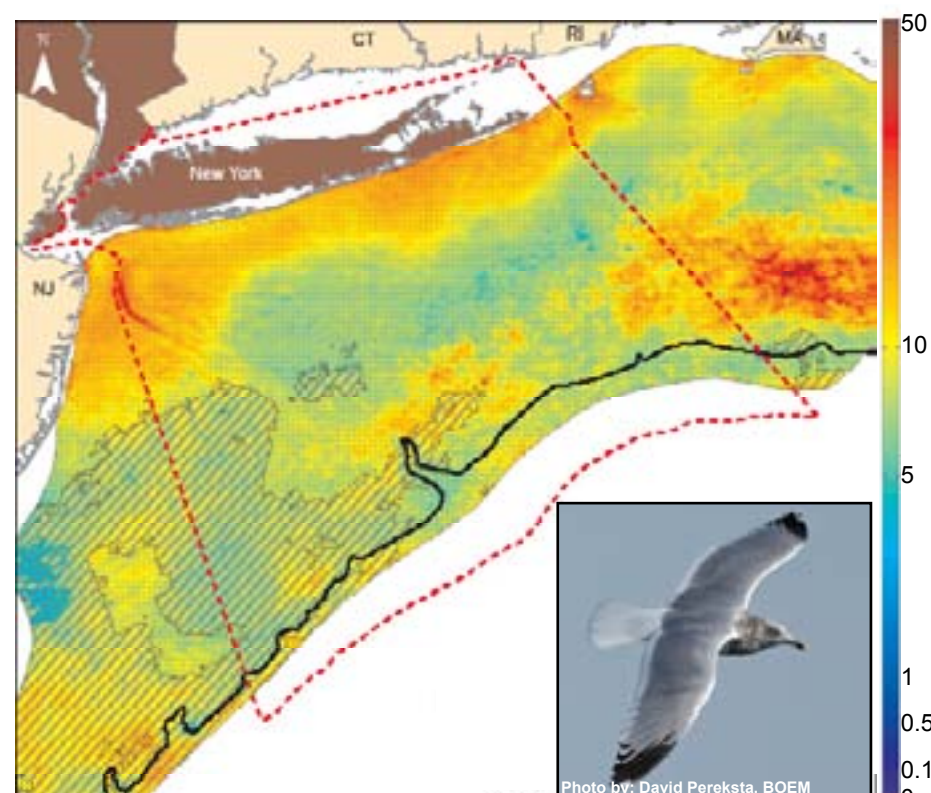


Figure 6.15. Predicted annual average relative index of abundance (SPUE, # indiv./km²/15-min) for Herring Gull, with certainty classes overlaid (see legend in Figure 6.8).

Table 6.30. Data table: Herring Gull.

Statistic	SP	SLI	FA	WI	All
N obs.	1219	245	1128	580	3172
Freq. (%)	47.8%	9.2%	40.6%	50.5%	34.7%
SPUE when present (No. indiv./km ² /15 min.)					
Mean	15.14	10.02	10.12	8.34	11.71
10th%ile	0.94	0.80	0.72	1.68	0.90
Median	7.20	5.20	6.35	5.76	6.30
90th%ile	27.85	19.35	21.60	15.93	22.29
Max	411.52	393.57	165.91	200.38	411.52

Table 6.31. Predictor table: Herring Gull.

Predictor	Occurrence				Abundance			
	Sp	Su	Fa	Wi	Sp	Su	Fa	Wi
BATH								
SLOPE								
DIST								
SSDIST								
SST								
STRT								
TUR								
CHI								
ZOO								
SLPSP								
PHIM								

Table 6.32. Diagnostic table: Herring Gull.

Diagnostic statistic	Certainty class			
	Low Score	Med Score	High Score	All Avg. MED
Rank R	0.12	0.09	n/a	0.13
%ASD	81.7%	100.0%	n/a	82.8%
AUC	0.58	n/a	n/a	0.56
p(AUC)	0.24	n/a	n/a	0.32
MAPE	185%	61%	n/a	170%
Rel.MAC	45%	17%	n/a	43%
Rel.RMSE	74%	24%	n/a	70%
Rel.Dias	11%	8%	n/a	11%
New Dir.	-	-	-	-

Northern Fulmar (*Fulmarus glacialis*)

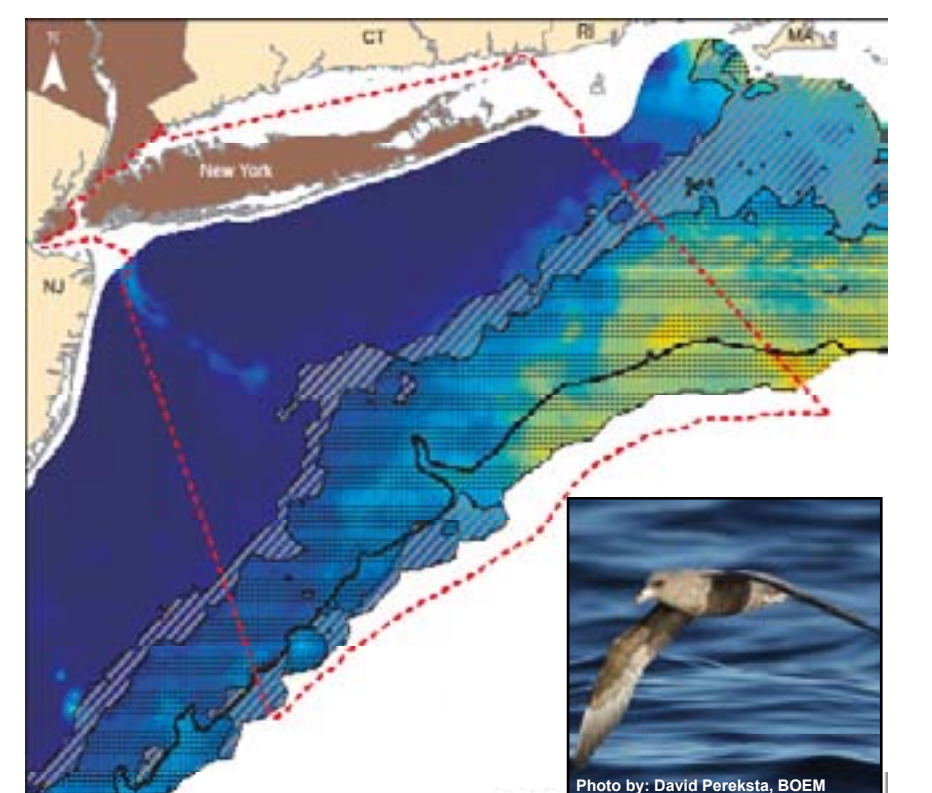


Figure 6.17. Predicted annual average relative index of abundance (SPUE, # indiv./km²/15-min) for Northern Fulmar, with certainty classes overlaid (see legend in Figure 6.8).

Table 6.36. Data table: Northern Fulmar.

Statistic	SP	SLI	FA	WI	All
N obs.	228	43	45	76	392
Freq. (%)	8.9%	1.6%	1.6%	6.6%	4.3%
SPUE when present (No. indiv./km ² /15 min.)					
Mean	0.63	1.10	0.31	0.58	0.63
10th%ile	0.13	0.23	0.13	0.13	0.13
Median	0.36	0.72	0.26	0.27	0.36
90th%ile	1.21	2.56	0.60	1.02	1.18
Max	13.40	7.20	0.80	5.60	13.40

Table 6.37. Predictor table: Northern Fulmar.

Predictor	Occurrence				Abundance			
	Sp	Su	Fa	Wi	Sp	Su	Fa	Wi
BATH								
SLOPE								
DIST								
SSDIST								
SST								
STRT								
TUR								
CHI								
ZOO								
SLPSP								
PHIM								

Table 6.38. Diagnostic table: Northern Fulmar.

Diagnostic statistic	Certainty class			
	Low Score	Med Score	High Score	All Avg. MED
Rank R	0.01	0.30	n/a	0.21
%ASD	38.9%	70.0%	n/a	53.3%
AUC	0.63	0.54	n/a	0.80
p(AUC)	0.10	0.38	n/a	0.00
MAPE	476%	459%	n/a	396%
Rel.MAC	78%	80%	n/a	60%
Rel.RMSE	138%	126%	n/a	101%
Rel.Dias	62%	84%	n/a	46%
New Dir.	+	+	-	+

Northern Gannet (*Morus bassanus*)

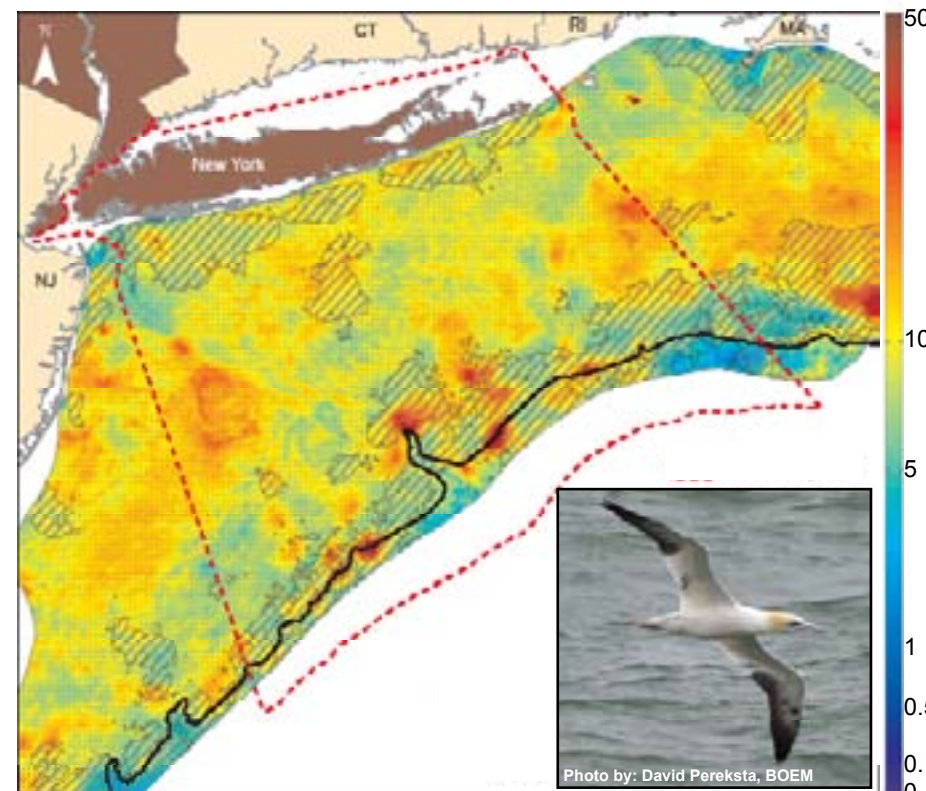


Figure 6.18. Predicted annual average relative index of abundance (SPUE, # indiv./km²/15-min) for Northern Gannet, with certainty classes overlaid (see legend in Figure 6.8).

Table 6.39. Data table: Northern Gannet.

Statistic	SP	SU	FA	WI	All
N obs.	815	9	385	493	1802
Freq. (%)	15.9%	0.3%	13.9%	42.9%	19.7%
SPUE when present (No. indiv./km ² /15 min.)					
Mean	18.79	2.98	8.85	10.63	14.36
10th%ile	1.80	0.82	1.72	2.73	1.96
Median	8.10	2.56	5.40	7.54	7.20
90th%ile	40.80	6.48	18.65	20.23	28.80
Max	604.30	7.20	104.39	78.39	604.30

Table 6.40. Predictor table: Northern Gannet.

Predictor	Occurrence				Abundance			
	Su	Su	Fa	Wi	Su	Su	Fa	Wi
BATH								
SLOPE								
DIST								
SSDIST								
SST								
STRT								
TUR								
CHI								
ZOO								
SLPSP								
PHIM								

Table 6.41. Diagnostic table: Northern Gannet.

Diagnostic statistic	Certainty class			
	Low	Med	High	All
Rank R	62%	37%	3%	LOW
Mean	0.07	0.30	n/a	0.17
%SD	89.9%	83.3%	n/a	87.9%
AIC	0.59	0.55	n/a	0.64
p(AIC)	0.20	0.31	n/a	0.01
MAPE	112%	548%	n/a	250%
Rel.MAE	28%	30%	n/a	32%
Rel.RMSE	39%	61%	n/a	48%
Rel.Dias	2%	4%	n/a	0%
Dias Dir.	-	+		

Sooty Shearwater (*Puffinus griseus*)

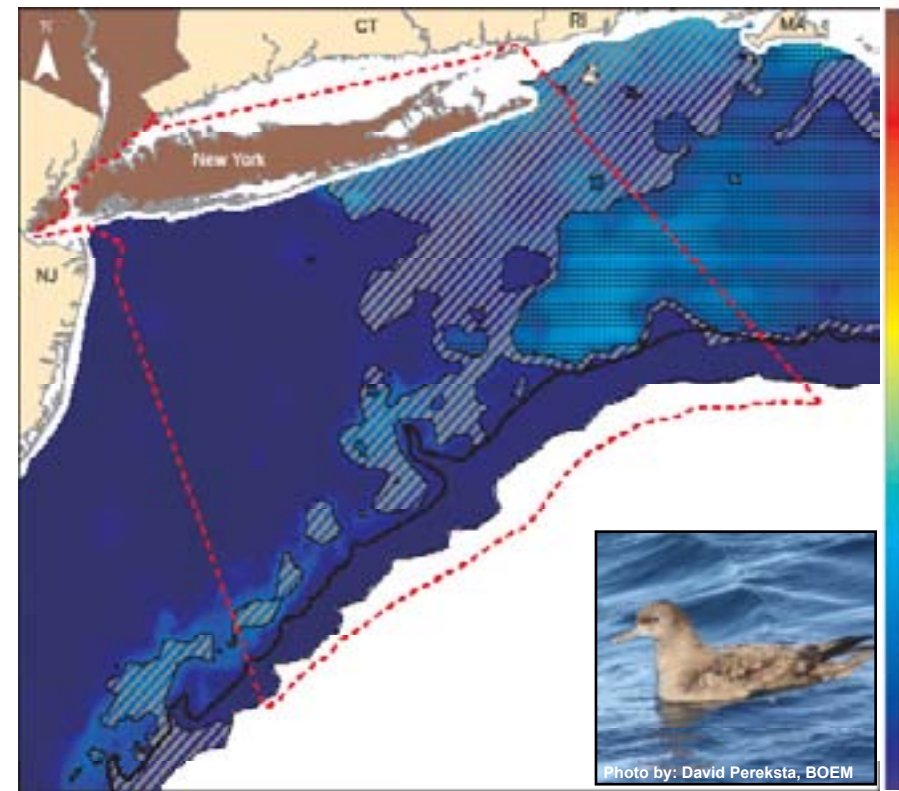


Figure 6.20. Predicted annual average relative index of abundance (SPUE, # indiv./km²/15-min) for Sooty Shearwater, with certainty classes overlaid (see legend in Figure 6.8).

Table 6.45. Data table: Sooty Shearwater.

Statistic	SP	SU	FA	WI	All
N obs.	88	114	3	0	205
Freq. (%)	3.5%	4.3%	0.1%	0.0%	2.2%
SPUE when present (No. indiv./km ² /15 min.)					
Mean	0.50	0.70	0.73	-	0.61
10th%ile	0.15	0.16	0.14	-	0.16
Median	0.36	0.38	0.27	-	0.36
90th%ile	1.20	1.62	1.96	-	1.35
Max	2.16	9.90	1.96	-	9.90

Table 6.46. Predictor table: Sooty Shearwater.

Predictor	Occurrence				Abundance			
	Su	Su	Fa	Wi	Su	Su	Fa	Wi
BATH								
SLOPE								
DIST								
SSDIST								
SST								
STRT								
TUR								
CHI								
ZOO								
SLPSP								
PHIM								

Table 6.47. Diagnostic table: Sooty Shearwater.

Diagnostic statistic	Certainty class			
	Low	Med	High	All
Rank R	11%	30%	52%	HIGH
Mean	0.46	0.38	0.24	0.28
%SD	59.1%	62.5%	65.0%	72.4%
AIC	0.51	0.48	0.65	0.62
p(AIC)	0.63	0.62	0.03	0.00
MAPE	110%	116%	96%	135%
Rel.MAE	24%	12%	10%	19%
Rel.RMSE	38%	18%	20%	27%
Rel.Dias	31%	33%	9%	21%
Dias Dir.	+	+	+	+

Pomarine Jaeger (*Stercorarius pomarinus*)

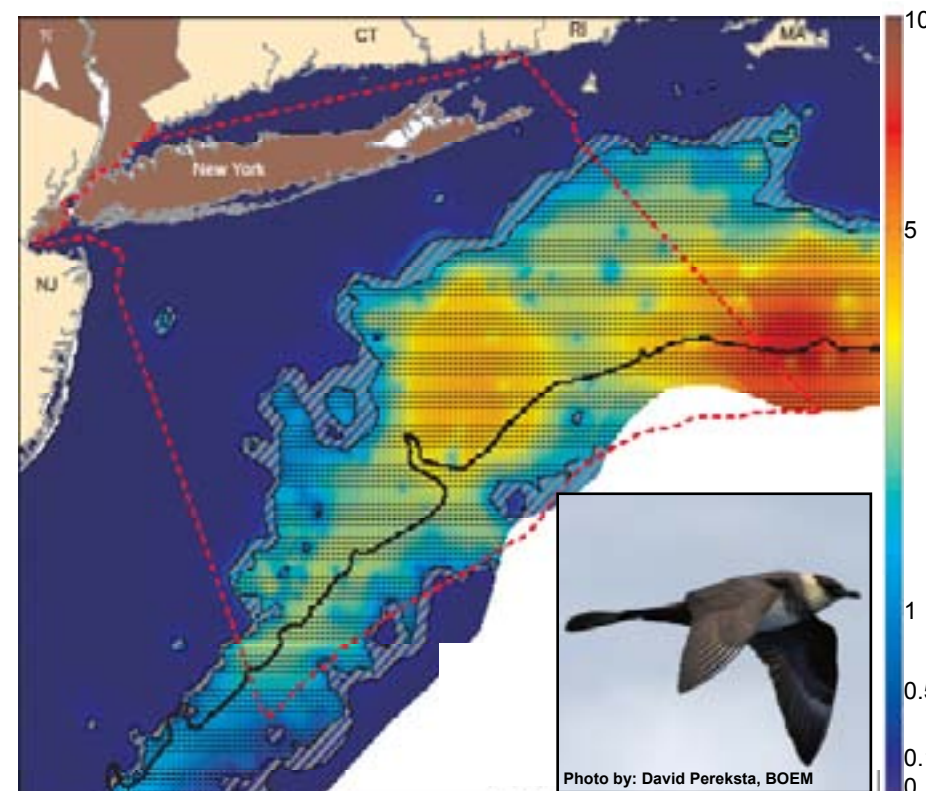


Figure 6.19. Predicted annual average relative index of abundance (SPUE, # indiv./km²/15-min) for Pomarine Jaeger, with certainty classes overlaid (see legend in Figure 6.8).

Table 6.42. Data table: Pomarine Jaeger.

Statistic	SP	SU	FA	WI	All
N obs.	24	6	101	3	122
Freq. (%)	0.5%	0.2%	3.6%	0.1%	1.3%
SPUE when present (No. indiv./km ² /15 min.)					
Mean	1.36	1.67	6.23	0.27	5.50
10th%ile	0.20	0.72	0.20	0.27	0.21
Median	0.36	1.21	3.36	0.27	2.80
90th%ile	4.58	11.89	14.92	0.27	13.35
Max	4.58	12.60	43.20	0.27	43.20

Table 6.43. Predictor table: Pomarine Jaeger.

Predictor	Occurrence				Abundance			
	Su	Su	Fa	Wi	Su	Su	Fa	Wi
BATH								
SLOPE								
DIST								
SSDIST								
SST								
STRT								
TUR								
CHI								
ZOO								
SLPSP								
PHIM								

Table 6.44. Diagnostic table: Pomarine Jaeger.

Diagnostic statistic	Certainty class			
	Low	Med	High	All
Rank R	95%	18%	5%	NSD
Mean	0.12	0.09	0.05	0.30
%SD	50.0%	100.0%	80.0%	66.7%
AIC	0.51	0.77	0.73	0.64
p(AIC)	0.41	0.01	0.00	0.00
MAPE	400%	107%	85%	590%
Rel.MAE	11%	3%	1%	11%
Rel.RMSE	18%	5%	3%	15%
Rel.Dias	20%	5%	1%	9%
Dias Dir.	+	+	+	+

Wilson's Storm-Petrel (*Oceanites oceanicus*)

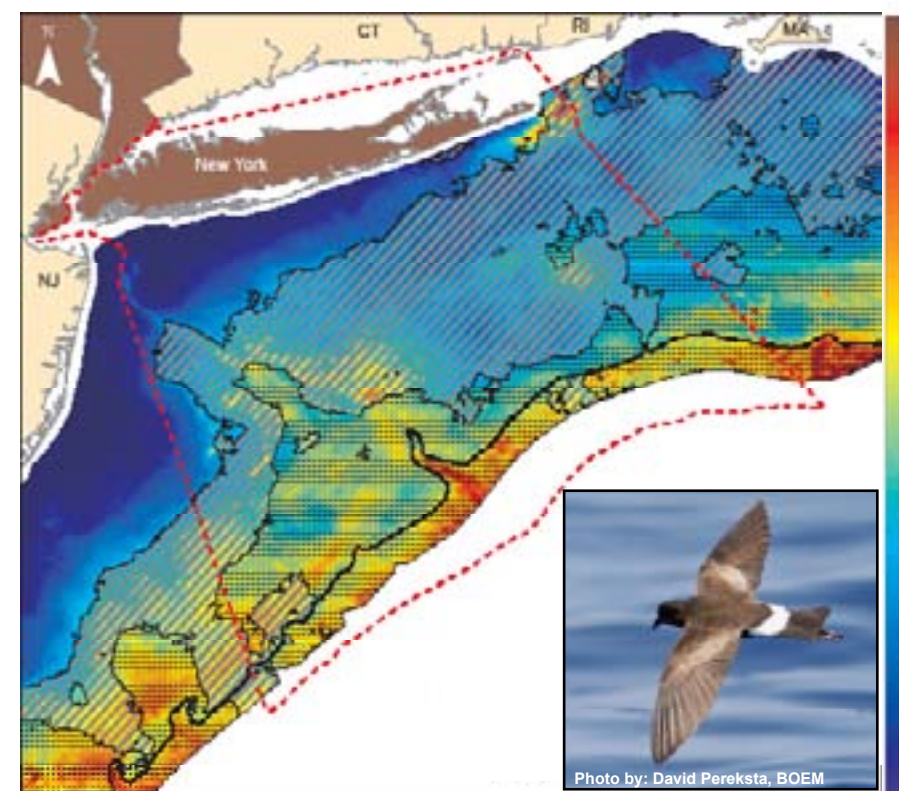


Figure 6.21. Predicted annual average relative index of abundance (SPUE, # indiv./km²/15-min) for Wilson's Storm-Petrel, with certainty classes overlaid (see legend in Figure 6.8).

Table 6.48. Data table: Wilson's Storm-Petrel.

Statistic	SP	SU	FA	WI	All
N obs.	289	1149	206	1	1650
Freq. (%)	11.7%	42.8%	7.4%	0.1%	18.0%
SPUE when present (No. indiv./km ² /15 min.)					
Mean	2.27	3.63	2.85	0.11	3.28
10th%ile	0.19	0.36	0.28	0.13	0.33
Median	0.72	1.20	0.72	0.13	0.98
90th%ile	5.76	7.20	3.99	0.13	6.40
Max	49.60	125.99	135.99	0.13	135.99

Table 6.49. Predictor table: Wilson's Storm-Petrel.

Predictor	Occurrence				Abundance			
	Su	Su	Fa	Wi	Su	Su	Fa	Wi
BATH								
SLOPE								
DIST								
SSDIST								
SST								
STRT								
TUR								
CHI								
ZOO								
SLPSP								
PHIM								

Table 6.50. Diagnostic table: Wilson's Storm-Petrel.

Diagnostic statistic	Certainty class			
	Low	Med	High	All
Rank R	90%	96%	3%	NSD
Mean	0.18	0.24	0.10	0.20
%SD	70.4%	78.9%	80.0%	75.2%
AIC	0.56	0.54	0.74	0.68
p(AIC)	0.23	0.26	0.01	0.00
MAPE	501%	230%	207%	386%
Rel.MAE	81%	27%	4%	45%
Rel.RMSE	140%	55%	10%	95%
Rel.Dias	42%	4%	1%	17%
Dias Dir.	-	-	+	-

Alcids, less common (4 species)

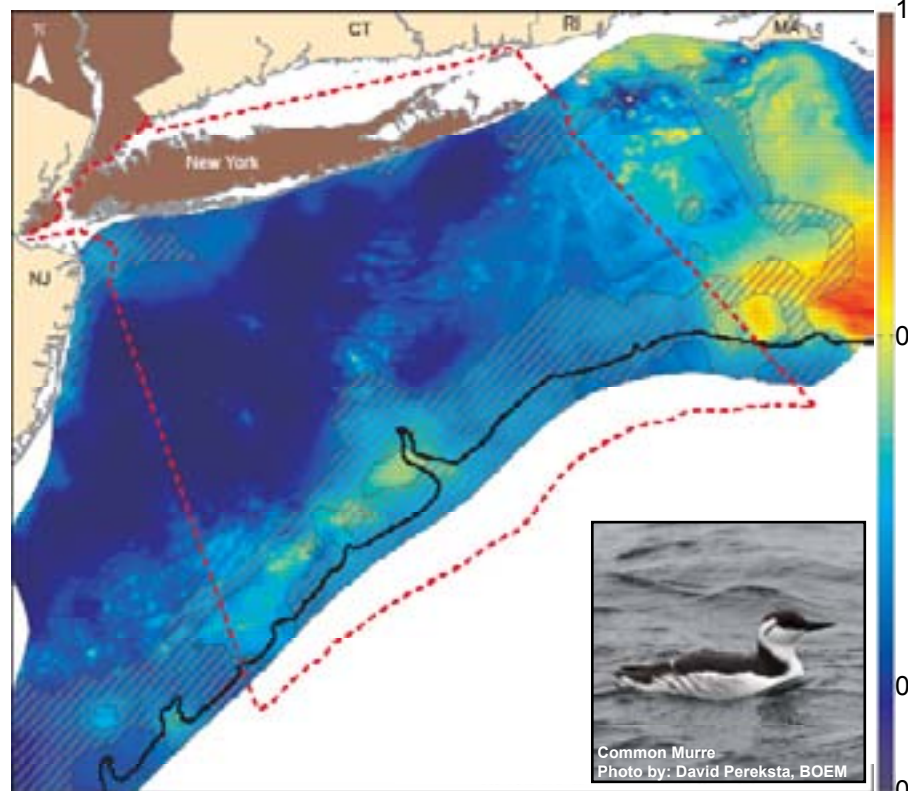


Figure 6.22. Predicted annual average relative index of abundance (SPUE, # indiv./km²/15-min) for Less Common Alcids with certainty classes overlaid (see legend in Figure 6.8).

Table 6.51. Data table: Alcids, less common.

Statistic	SP	SU	FA	WI	All
N obs.	76	0	5	58	139
Freq. (%)	3.0%	0.0%	0.2%	5.1%	1.5%
SPUE when present (No. indiv./km ² /15 min.)					
Mean	0.32	-	0.27	0.25	0.30
10th%ile	0.13	-	0.08	0.11	0.11
Median	0.24	-	0.12	0.20	0.22
90th%ile	0.72	-	0.72	0.70	0.72
Max	1.44	-	0.72	1.03	1.44

Table 6.52. Predictor table: Alcids, less common.

Predictor	Occurrence				Abundance			
	Su	Su	Fa	Wi	Su	Su	Fa	Wi
BATH								
SLOPE								
EINT								
SSDIST								
SST								
STRT								
TUR								
EHI								
ZOO								
%PSP								
PHM								

Table 6.53. Diagnostic table: Alcids, less common.

Diagnostic	Certainty class			
	Low	Med	High	All
Statistic	Score	Score	Score	Avg.
	7%	75%	60%	18%
Rank R	-0.71	0.08	0.46	0.22
%SSD	71.4%	55.6%	92.9%	76.7%
AIC	0.63	0.56	0.53	0.59
p(AIC)	0.14	0.28	0.36	0.03
MAPE	94%	104%	104%	198%
Rel.MAE	26%	15%	12%	21%
Rel.RMSE	34%	29%	18%	33%
Rel.Dias	71%	28%	11%	26%
Dias Dir.	+	+	+	+

Jaegers (2 species)

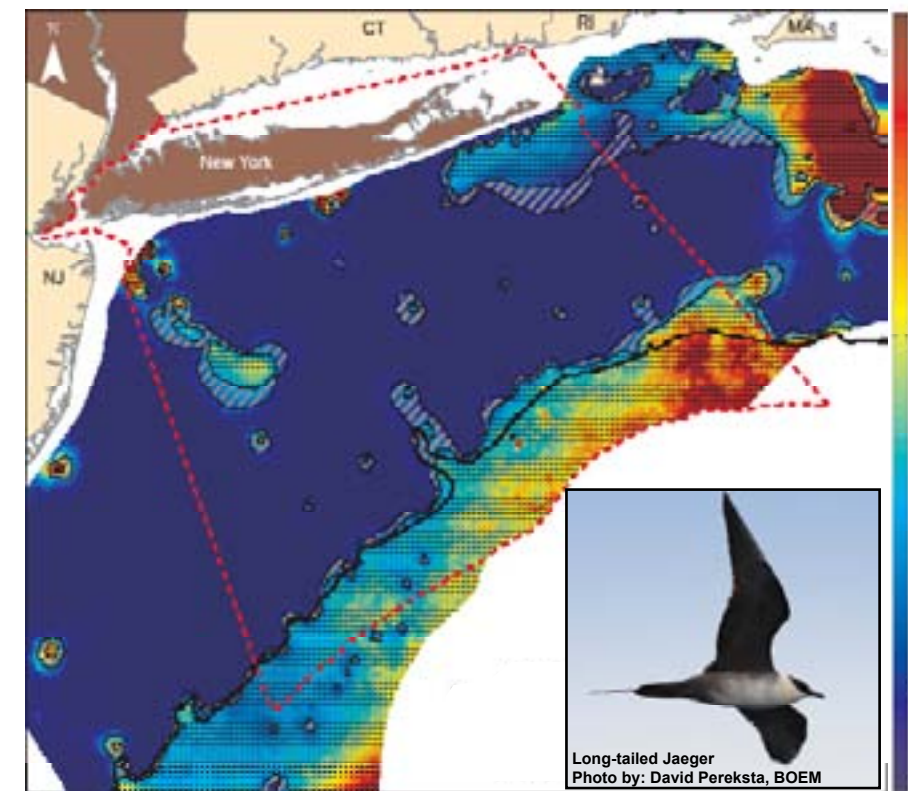


Figure 6.24. Predicted annual average relative index of abundance (SPUE, # indiv./km²/15-min) for Jaegers, with certainty classes overlaid (see legend in Figure 6.8).

Table 6.57. Data table: Jaegers.

Statistic	SP	SU	FA	WI	All
N obs.	13	8	56	0	77
Freq. (%)	0.5%	0.3%	2.0%	0.0%	0.8%
SPUE when present (No. indiv./km ² /15 min.)					
Mean	2.23	2.52	1.68	-	1.90
10th%ile	0.17	0.24	0.13	-	0.15
Median	1.81	1.81	0.78	-	0.36
90th%ile	6.87	9.24	5.51	-	6.16
Max	9.16	10.80	11.52	-	11.52

Table 6.58. Predictor table: Jaegers.

Predictor	Occurrence				Abundance			
	Su	Su	Fa	Wi	Su	Su	Fa	Wi
BATH								
SLOPE								
EINT								
SSDIST								
SST								
STRT								
TUR								
EHI								
ZOO								
%PSP								
PHM								

Table 6.59. Diagnostic table: Jaegers.

Diagnostic	Certainty class			
	Low	Med	High	All
Statistic	Score	Score	Score	Avg.
	17%	17%	67%	18%
Rank R	-0.23	-0.03	-0.49	-0.16
%SSD	60.0%	66.7%	70.0%	65.4%
AIC	0.58	0.70	0.45	0.62
p(AIC)	0.28	0.06	0.72	0.02
MAPE	1420%	692%	148%	473%
Rel.MAE	30%	10%	2%	13%
Rel.RMSE	43%	15%	4%	25%
Rel.Dias	31%	9%	1%	10%
Dias Dir.	+	+	+	+

Coastal Waterfowl (7 species)

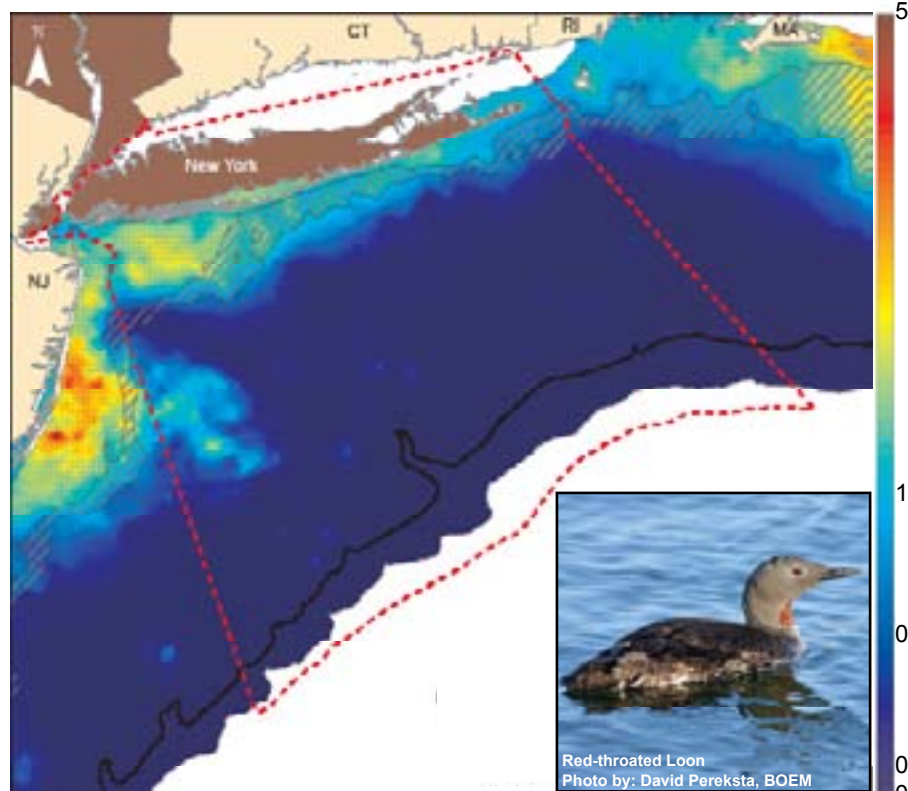


Figure 6.23. Predicted annual average relative index of abundance (SPUE, # indiv./km²/15-min) for Coastal Waterfowl, with certainty classes overlaid (see legend in Figure 6.8).

Table 6.54. Data table: Coastal Waterfowl.

Statistic	SP	SU	FA	WI	All
N obs.	99	0	58	79	236
Freq. (%)	3.9%	0.0%	2.1%	6.9%	2.6%
SPUE when present (No. indiv./km ² /15 min.)					
Mean	131.67	-	1.89	9.38	58.84
10th%ile	0.21	-	0.13	0.17	0.16
Median	0.72	-	0.40	0.77	0.57
90th%ile	9.41	-	4.81	18.38	8.76
Max	11999	-	25.20	158.54	11999

Table 6.55. Predictor table: Coastal Waterfowl.

Predictor	Occurrence				Abundance			
	Su	Su	Fa	Wi	Su	Su	Fa	Wi
BATH								
SLOPE								
EINT								
SSDIST								
SST								
STRT								
TUR								
EHI								
ZOO								
%PSP								
PHM								

Table 6.56. Diagnostic table: Coastal Waterfowl.

Diagnostic	Certainty class			
	Low	Med	High	All
Statistic	Score	Score	Score	Avg.
	8%	6%	66%	18%
Rank R	0.14	n/a	-0.17	0.20
%SSD	45.5%	n/a	88.9%	66.7%
AIC	0.49	n/a	0.70	0.77
p(AIC)	0.56	n/a	0.02	0.00
MAPE	310%	n/a	566%	395%
Rel.MAE	25%	n/a	24%	22%
Rel.RMSE	79%	n/a	67%	66%
Rel.Dias	15%	n/a	14%	14%
Dias Dir.	+	-	+	+

Phalaropes (2 species)

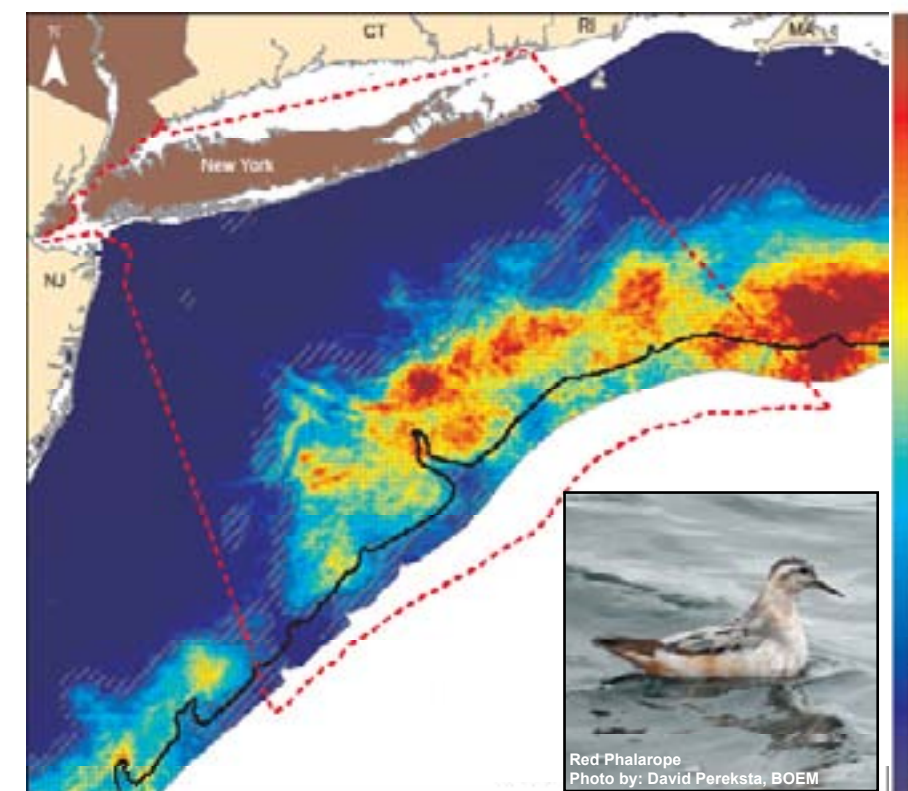


Figure 6.25. Predicted annual average relative index of abundance (SPUE, # indiv./km²/15-min) for Phalaropes, with certainty classes overlaid (see legend in Figure 6.8).

Table 6.60. Data table: Phalaropes.

Statistic	SP	SU	FA	WI	All
N obs.	230	7	33	4	274
Freq. (%)	9.0%	0.3%	1.2%	0.3%	3.0%
SPUE when present (No. indiv./km ² /15 min.)					
Mean	60.72	0.40	2.58	1.81	51.31
10th%ile	0.47	0.33	0.39	0.60	0.41
Median	3.57	0.40	1.05	1.17	2.93
90th%ile	69.69	0.80	6.77	1.98	48.60
Max	4880	0.80	14.40	1.98	4880

Table 6.61. Predictor table: Phalaropes.

Predictor	Occurrence				Abundance			
	Su	Su	Fa	Wi	Su	Su	Fa	Wi
BATH								
SLOPE								
EINT								
SSDIST								
SST								
STRT								
TUR								
EHI								
ZOO								
%PSP								
PHM								

Table 6.62. Diagnostic table: Phalaropes.

Diagnostic	Certainty class			
	Low	Med	High	All
Statistic	Score	Score	Score	Avg.
	54%	16%	40%	18%
Rank R	0.13	0.08	-0.57	0.16
%SSD	68.1%	76.2%	77.8%	70.6%
AIC	0.40	0.54	0.80	0.76
p(AIC)	0.64	0.31	0.00	0.00
MAPE	1822%	638%	172%	908%
Rel.MAE	46%	16%	0%	23%
Rel.RMSE	159%	41%	2%	77%
Rel.Dias	19%	7%	0%	9%
Dias Dir.	-	-	+	-

Shearwaters, less common (2 species)

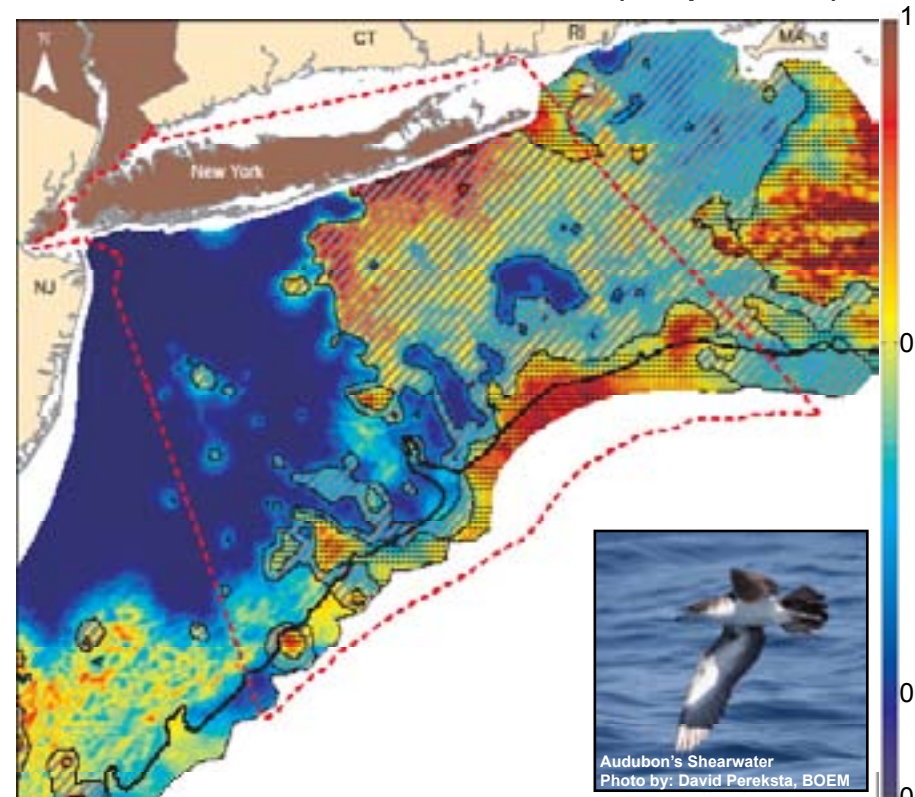


Figure 6.26. Predicted annual average relative index of abundance (SPUE, # indiv./km²/15-min) for Less common Shearwaters with certainty classes overlaid (see legend in Figure 6.8).

Table 6.63. Data table: Shearwaters, less common

Statistic	SP	SU	FA	WI	All
N obs.	15	91	87	0	193
Freq. (%)	0.6%	3.4%	3.1%	0.0%	2.1%
SPUE when present (No. indiv./km ² /15 min.)					
Mean	0.40	0.76	0.97	-	0.83
10th%ile	0.16	0.17	0.20	-	0.20
Median	0.33	0.44	0.54	-	0.47
90th%ile	0.72	1.50	1.60	-	1.44
Max	1.10	8.68	12.77	-	12.27

Table 6.64. Predictor table: Shearwaters, less common

Predictor	Occurrence				Abundance			
	Su	Su	Fa	Wi	Su	Su	Fa	Wi
BATH								
SLOPE								
DIST								
SSDIST								
SST								
STRT								
TUR								
CHI								
ZOO								
SI P S I P								
BHM								

Table 6.65. Diagnostic table: Shearwaters, less common.

Diagnostic statistic	Certainty class			
	Low	Med	High	All
Rank R	1.00	0.99	0.99	0.99
%SD	20.0%	90.0%	84.7%	78.5%
AUC	0.75	0.60	0.54	0.51
p(AUC)	0.03	0.15	0.27	0.30
MAPE	104%	150%	128%	156%
Rel.MAE	34%	20%	13%	21%
Rel.RMSE	53%	29%	18%	32%
Rel.Dias	55%	37%	14%	26%
N/A	+	+	+	+

Storm-Petrels, less common (3 species)

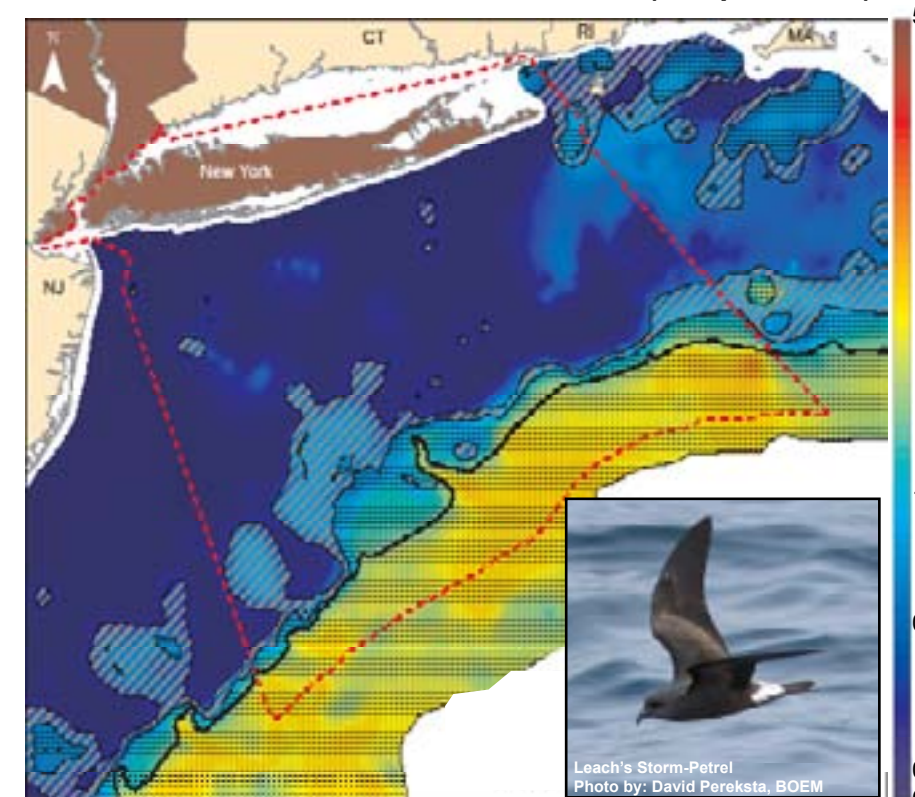


Figure 6.28. Predicted annual average relative index of abundance (SPUE, # indiv./km²/15-min) for Less Common Storm-Petrels with certainty classes overlaid (see legend in Figure 6.8).

Table 6.69. Data table: Storm-Petrels, less common.

Statistic	SP	SU	FA	WI	All
N obs.	45	122	52	0	219
Freq. (%)	1.9%	4.6%	1.9%	0.0%	2.4%
SPUE when present (No. indiv./km ² /15 min.)					
Mean	0.95	1.49	0.97	-	1.26
10th%ile	0.18	0.31	0.16	-	0.24
Median	0.48	0.80	0.65	-	0.72
90th%ile	2.52	3.37	1.93	-	2.62
Max	4.80	17.28	9.82	-	17.28

Table 6.70. Predictor table: Storm-Petrels, less common.

Predictor	Occurrence				Abundance			
	Su	Su	Fa	Wi	Su	Su	Fa	Wi
BATH								
SLOPE								
DIST								
SSDIST								
SST								
STRT								
TUR								
CHI								
ZOO								
SI P S I P								
BHM								

Table 6.71. Diagnostic table: Storm-Petrels, less common.

Diagnostic statistic	Certainty class			
	Low	Med	High	All
Rank R	0.20	0.24	0.04	0.24
%SD	23.5%	90.0%	91.7%	61.5%
AUC	0.68	0.58	0.58	0.63
p(AUC)	0.01	0.22	0.20	0.01
MAPE	272%	95%	140%	306%
Rel.MAE	22%	6%	0%	18%
Rel.RMSE	26%	8%	9%	25%
Rel.Dias	51%	21%	4%	22%
N/A	+	+	+	+

Small Gulls, less common (2 species)

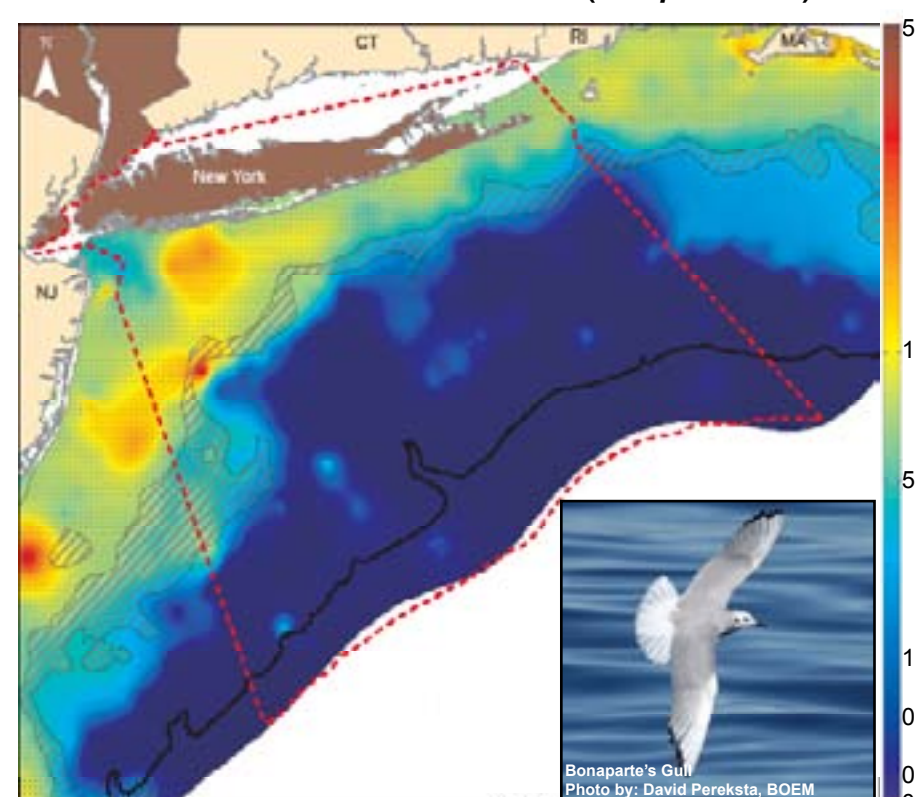


Figure 6.27. Predicted annual average relative index of abundance (SPUE, # indiv./km²/15-min) for Less Common Small gulls with certainty classes overlaid (see legend in Figure 6.8).

Table 6.66. Data table: Small Gulls, less common.

Statistic	SP	SU	FA	WI	All
N obs.	49	3	80	38	180
Freq. (%)	1.9%	0.1%	3.2%	3.3%	2.0%
SPUE when present (No. indiv./km ² /15 min.)					
Mean	12.45	7.80	1.63	8.44	7.11
10th%ile	0.67	0.36	0.58	1.38	0.69
Median	3.20	1.44	2.69	2.80	2.83
90th%ile	21.55	21.60	7.65	9.92	10.70
Max	241.58	21.60	20.88	95.39	241.58

Table 6.67. Predictor table: Small Gulls, less common.

Predictor	Occurrence				Abundance			
	Su	Su	Fa	Wi	Su	Su	Fa	Wi
BATH								
SLOPE								
DIST								
SSDIST								
SST								
STRT								
TUR								
CHI								
ZOO								
SI P S I P								
BHM								

Table 6.68. Diagnostic table: Small Gulls, less common.

Diagnostic statistic	Certainty class			
	Low	Med	High	All
Rank R	0.30	n/a	1.00	0.15
%SD	75.0%	n/a	83.3%	77.8%
AUC	0.48	n/a	0.89	0.72
p(AUC)	0.29	n/a	0.00	0.00
MAPE	121%	n/a	101%	131%
Rel.MAE	19%	n/a	10%	27%
Rel.RMSE	30%	n/a	14%	32%
Rel.Dias	62%	n/a	11%	34%
N/A	+	n/a	+	+

Terns, less common (7 species)

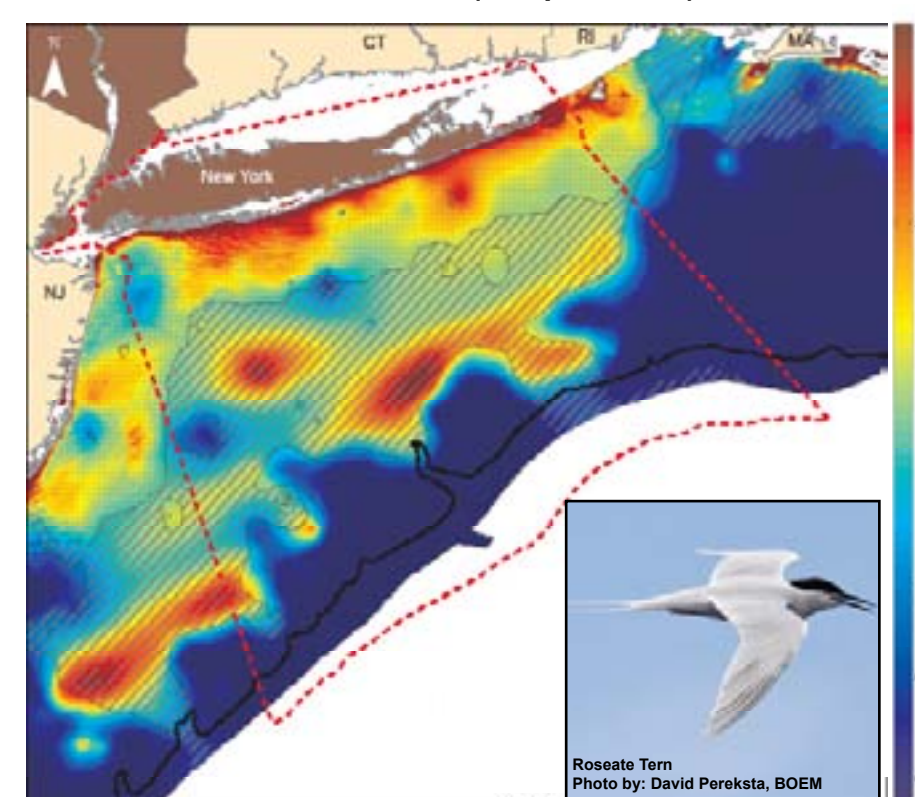


Figure 6.29. Predicted annual average relative index of abundance (SPUE, # indiv./km²/15-min) for Less Common Terns with certainty classes overlaid (see legend in Figure 6.8).

Table 6.72. Data table: Terns, less common.

Statistic	SP	SU	FA	WI	All
N obs.	53	46	23	0	120
Freq. (%)	2.1%	1.7%	0.8%	0.0%	1.3%
SPUE when present (No. indiv./km ² /15 min.)					
Mean	5.91	2.42	2.17	-	3.92
10th%ile	0.20	0.33	0.20	-	0.24
Median	1.83	1.07	0.98	-	1.31
90th%ile	9.89	5.03	5.78	-	7.89
Max	59.73	21.77	17.60	-	59.73

Table 6.73. Predictor table: Terns, less common.

Predictor	Occurrence				Abundance			
	Su	Su	Fa	Wi	Su	Su	Fa	Wi
BATH								
SLOPE								
DIST								
SSDIST								
SST								
STRT								
TUR								
CHI								
ZOO								
SI P S I P								
BHM								

Table 6.74. Diagnostic table: Terns, less common.

Diagnostic statistic	Certainty class			
	Low	Med	High	All
Rank R	0.54	n/a	0.30	0.52
%SD	50.0%	n/a	60.0%	61.9%
AUC	0.59	n/a	0.51	0.67
p(AUC)	0.17	n/a	0.46	0.00
MAPE	956%	n/a	680%	874%
Rel.MAE	25%	n/a	10%	26%
Rel.RMSE	41%	n/a	18%	39%
Rel.Dias	51%	n/a	8%	28%
N/A	+	n/a	+	+

Unidentified Gulls (0 species*)

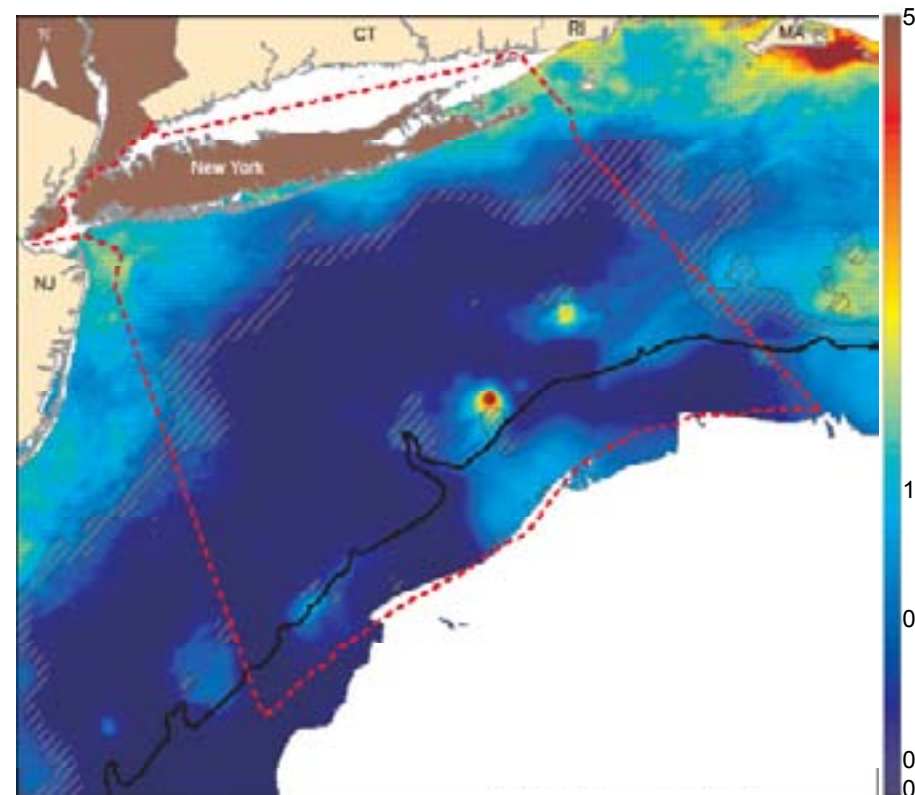


Table 6.75. Data table: Unidentified Gulls.

Statistic	SP	SU	FA	WI	All
N obs.	55	19	357	53	284
Freq. (%)	2.2%	0.7%	5.7%	4.6%	3.1%
SPUE when present (No. indiv./km ² /15 min.)					
Mean	2.13	1.38	0.77	1.33	1.18
10th%ile	0.16	0.12	0.16	0.13	0.14
Median	0.48	0.33	0.48	0.45	0.48
90th%ile	2.00	3.06	1.59	2.11	1.80
Max	71.11	11.70	10.28	15.30	71.11

Table 6.76. Predictor table: Unidentified Gulls.

Predictor	Occurrence				Abundance			
	Su	Su	Fa	Wi	Su	Su	Fa	Wi
BATH								
SLOPE								
DIS1								
SSDIST								
SST								
STRT								
TUR								
CHI								
ZOO								
SLPSP								
BHM								

Table 6.77. Diagnostic table: Unidentified Gulls.

Diagnostic statistic	Certainty class				Avg. All
	Low	Med	High	All	
Rank R	21%	12%	67%	100%	100%
Mean	0.07	-0.35	-0.16	0.14	0.14
MAE	10.8%	60.0%	100.0%	56.8%	56.8%
MAE	0.52	0.67	0.55	0.62	0.62
p(AUC)	0.42	0.60	0.80	0.62	0.62
MAPE	104%	235%	115%	203%	203%
Rel.MAE	20%	11%	6%	21%	21%
Rel.RMSE	29%	17%	9%	27%	27%
Rel.Disc	40%	21%	0%	26%	26%
Disc Eff.	+	+	+	+	+

Figure 6.30. Predicted annual average relative index of abundance (SPUE, # indiv./km²/15-min) for Unidentified Gulls, with certainty classes overlaid (see legend in Figure 6.8).

*This group contains two categories of unidentified gulls in the family Laridae, but no positively identifiable species.

Cormorants (2 species)

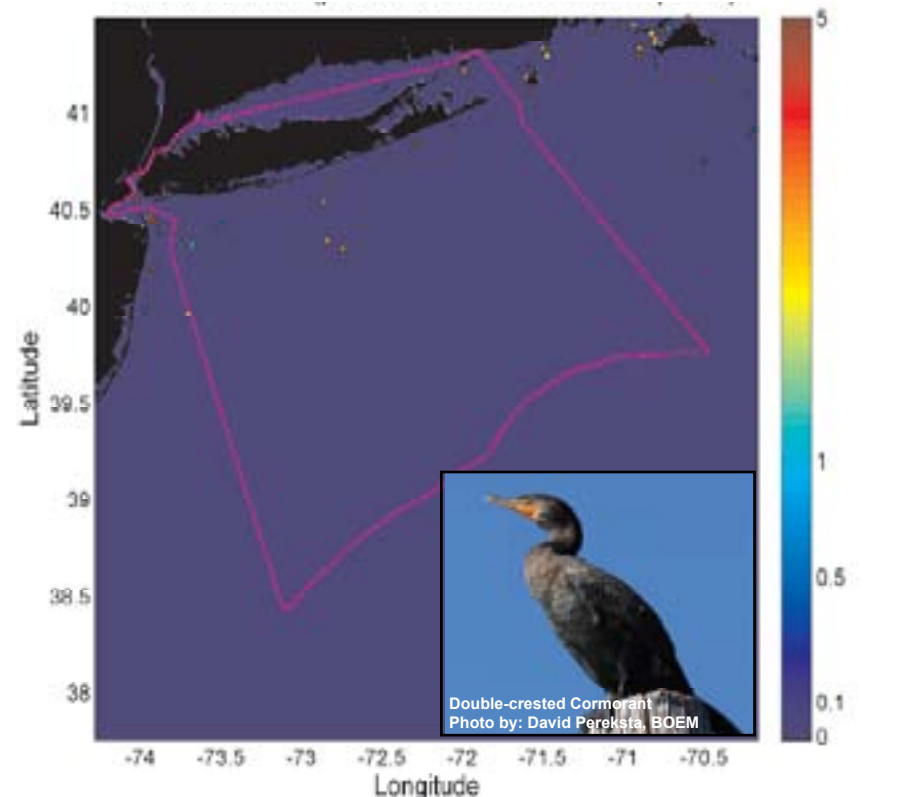


Table 6.78. Data table: Cormorants.

Statistic	SP	SU	FA	WI	All
N obs.	12	9	20	19	60
Freq. (%)	0.5%	0.3%	0.7%	1.7%	0.7%
SPUE when present (No. indiv./km ² /15 min.)					
Mean	6.23	7.63	9.99	3.53	6.85
10th%ile	0.15	1.77	0.22	0.25	0.21
Median	0.38	2.88	3.75	2.74	2.72
90th%ile	22.68	21.30	35.97	8.99	20.23
Max	61.92	24.53	48.68	14.48	61.92

Figure 6.31. Point observations of the relative abundance index (SPUE, # indiv./km²/15-min) for Cormorants. Dark blue shading indicates unsampled areas; no predictive modeling was done for this species group due to insufficient data.

Rare Visitors (10 species)

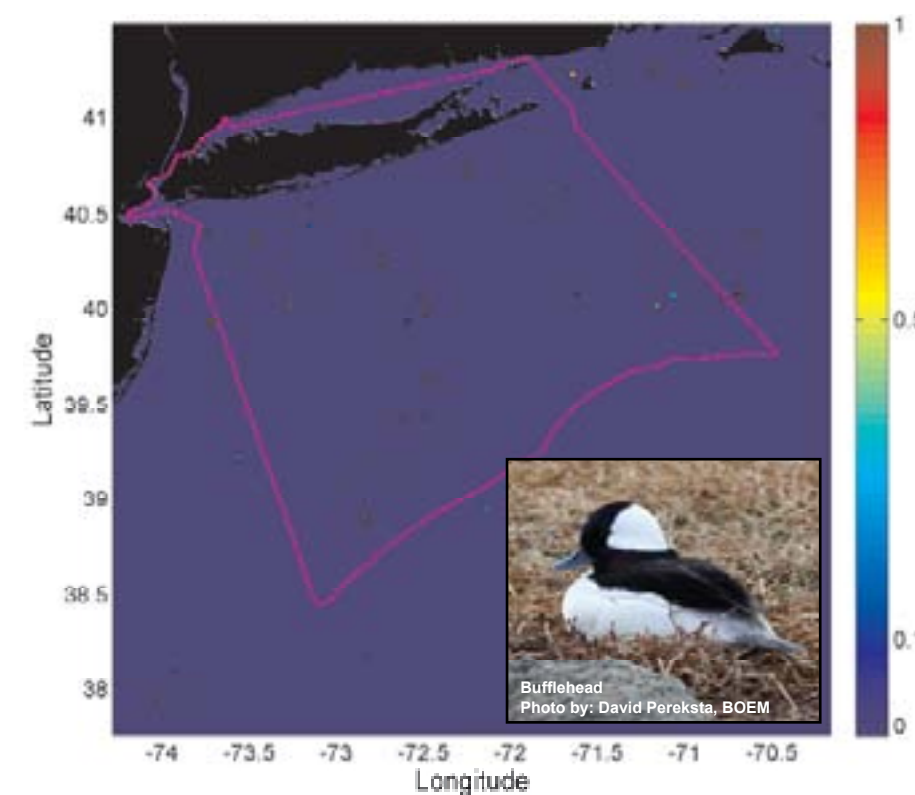


Table 6.79. Data table: Rare Visitors.

Statistic	SP	SU	FA	WI	All
N obs.	18	1	10	11	40
Freq. (%)	0.7%	0.0%	0.4%	1.0%	0.4%
SPUE when present (No. indiv./km ² /15 min.)					
Mean	2.35	0.09	1.81	1.40	1.89
10th%ile	0.14	0.09	0.10	0.19	0.12
Median	2.14	0.09	0.53	1.03	1.17
90th%ile	5.22	0.09	6.16	4.10	4.89
Max	7.49	0.09	8.00	5.45	8.00

Figure 6.32. Point observations of the relative abundance index (SPUE, # indiv./km²/15-min) for Rare Visitors. Dark blue shading indicates unsampled areas; no predictive modeling was done for this species group due to insufficient data.

Skuas, less common (1 species)

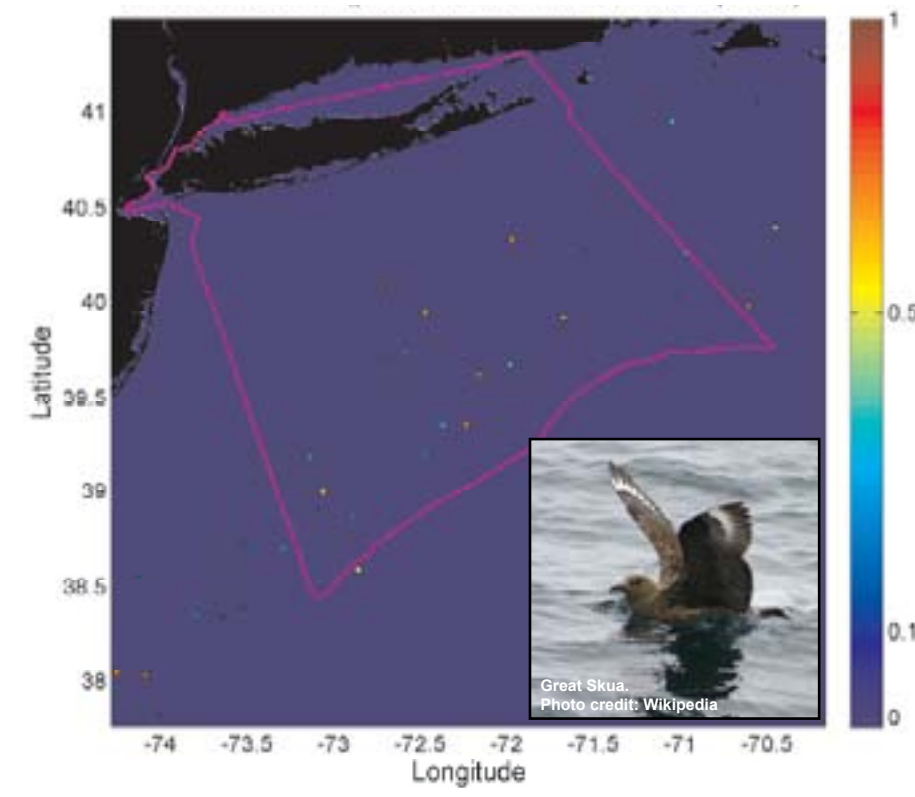


Table 6.80. Data table: Skuas, less common.

Statistic	SP	SU	FA	WI	All
N obs.	12	2	11	11	36
Freq. (%)	0.5%	0.1%	0.4%	1.0%	0.4%
SPUE when present (No. indiv./km ² /15 min.)					
Mean	0.40	0.65	0.25	0.40	0.37
10th%ile	0.15	0.33	0.12	0.11	0.13
Median	0.30	0.65	0.24	0.27	0.27
90th%ile	0.72	0.98	0.45	0.72	0.72
Max	0.72	0.98	0.48	0.72	0.98

Figure 6.33. Point observations of the relative abundance index (SPUE, # indiv./km²/15-min) for Less Common Skuas. Dark blue shading indicates unsampled areas; no predictive modeling was done for this species group due to insufficient data.

'No birds sighted'

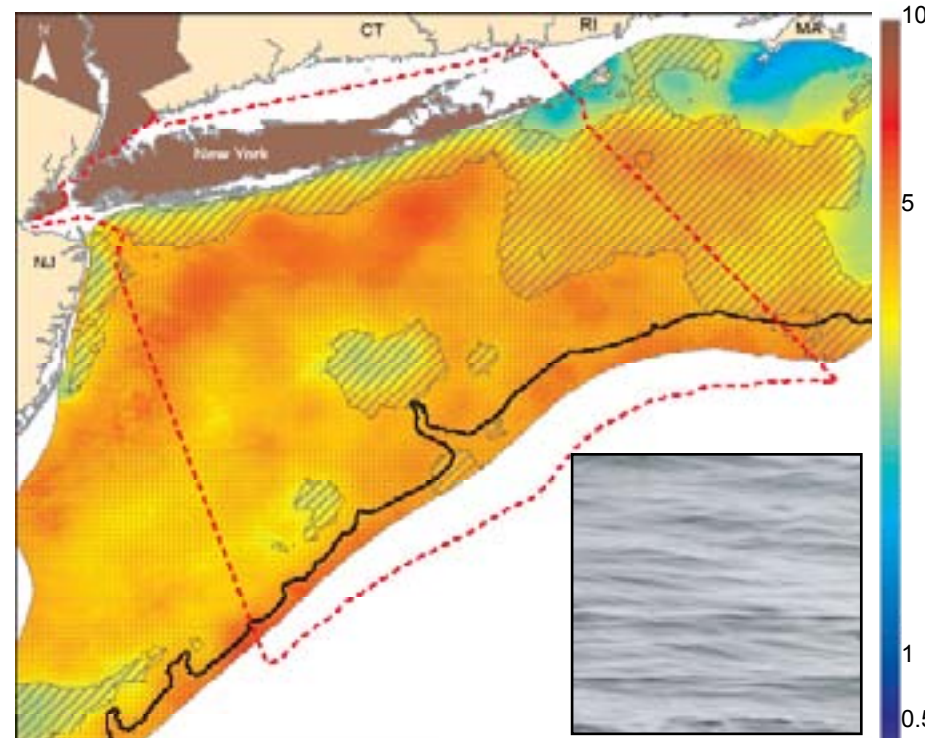


Figure 6.34A. Predicted annual average relative index of survey effort resulting in 'No birds sighted' observations, with error class overlay. Units are km² of transect area in which no birds were sighted in a 15-minute survey. Legend as in Figure 6.8.

Table 6.81. Data table: 'No birds sighted'.

Statistic	SP	SU	FA	WI	All
N obs.	509	838	799	329	2275
Freq. (%)	20.0%	31.7%	28.8%	11.2%	24.9%
'No birds sighted' index (km² / 15 min. survey)					
Mean	0.75	0.82	0.90	0.78	0.83
10th%ile	0.65	0.65	0.65	0.68	0.65
Median	0.72	0.72	0.72	0.72	0.72
90th%ile	0.80	0.96	1.03	0.90	0.90
Max	1.80	3.60	7.20	1.20	7.20

Table 6.82. Predictor table: 'No birds sighted'.

Predictor	Occurrence				Abundance			
	Sp	Su	Fa	Wi	Sp	Su	Fa	Wi
BATH	+							
SLOPE								
DIS1								
SSDIST								
SST								
STRT								
TUR								
CHI								
ZOO								
SLIPSP								
PHIM								

Table 6.83. Diagnostic table: 'No birds sighted'.

Diagnostic statistic	Certainty class				Avg. LOW
	Low	Med	High	All	
Rank R	-0.17	-0.36	-0.34	0.13	
Mean	69.1%	70.0%	80.0%	70.6%	
MAE	0.48	0.58	0.55	0.54	
MAUC	0.57	0.23	0.39	0.25	
MAPE	66%	49%	50%	63%	
Rel.MAE	323%	277%	201%	297%	
Rel.MAUC	541%	357%	256%	460%	
Rel.MAPE	453%	454%	296%	433%	
Disc. Eff.	+	+	+	+	

Box 6.2. Notes on the 'No birds sighted' analyses

In the course of the MBO CSAP standardized visual surveys, observers recorded instances when no seabirds of any kind were sighted in a standardized 15-minute observation period. We analyzed these 'No birds sighted' observations using the same predictive statistical model as for other species and groups, with one exception: instead of SPUE, the 'relative abundance' of 'No birds sighted' was measured as the area (in km²) of the transect in which no birds were sighted.

The maps at left (Figure 6.34 A and B) may be useful as an alternative or supplement to hotspot maps (Figures 6.35-6.37) to identify areas of potentially high or low conflict between seabird and human uses of ocean habitat.

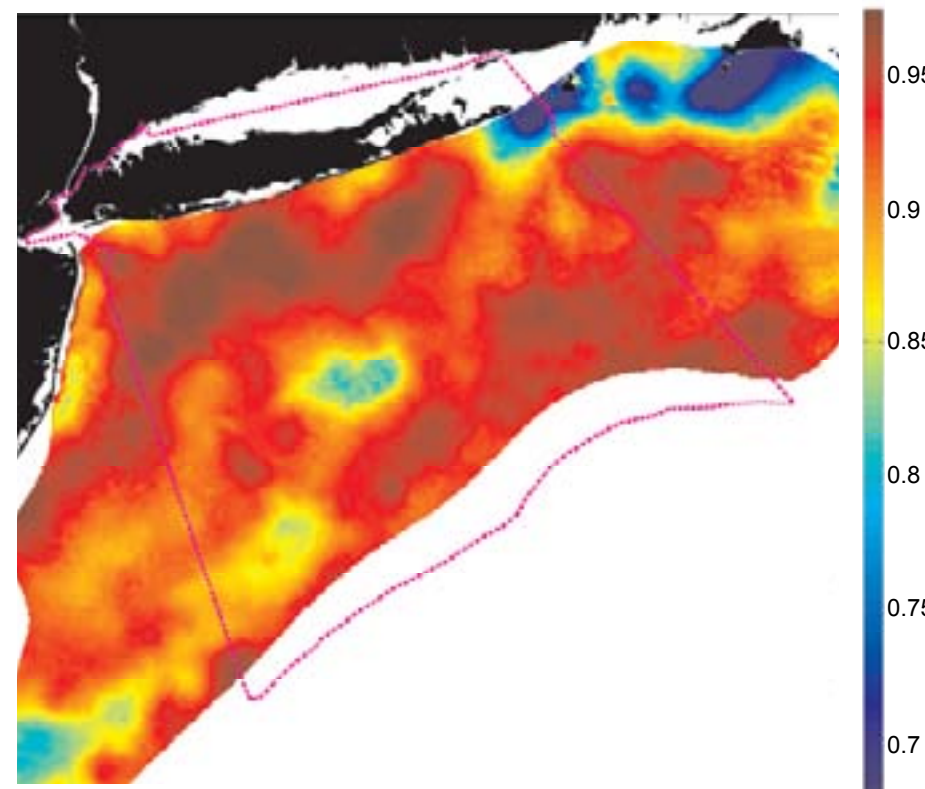


Figure 6.34B. Predicted annual integrated probability of a 'No birds sighted' observation. Units are probability of 'no birds sighted' in a 15-min. survey in at least one of the four seasons. Annual integrated presence probability was calculated as described in Appendix 6.A. For associated certainty map, see Appendix 6.C.

Box 6.3. Notes on Hotspot Analyses

Abundance and diversity are two important metrics of ecosystem structure. Concentrations of abundance can indicate areas that are important to multiple species for feeding, reproduction, migration, refuge from unfavorable conditions (storms, predators), and other important aspects of seabird life cycles. These may be apparent in annual distributions, or occur only seasonally due to varying environmental conditions and timing of life cycles.

Abundance hotspots alone do not give a complete picture of important areas for seabirds, because they can be driven by the presence of only one or a few very abundant species. Areas of high diversity, as measured by the Shannon diversity index (H'), represent places where diverse bird communities form aggregations of many species in which even rarer species are relatively well-represented. These may represent convergences of environmental conditions suitable for many species, or may arise from species interactions. Regardless of the reason for high diversity, diversity hotspots are often considered of high conservation value because of the relatively high number of species that can be protected in a relatively small area.

Beyond their ecological importance, hotspots of abundance and diversity are important for marine spatial planning because they represent areas where large numbers of individual birds and/or large numbers of bird species may be affected by human activities. Diversity hotspots may also be of value for non-consumptive human activities such as bird-watching.

On this page and the pages that follow, annual predicted abundance hotspots (Figure 6.35), species richness hotspots (Figure 6.36), and Shannon diversity index hotspots (Figure 6.37) are shown.

Abundance Hotspots

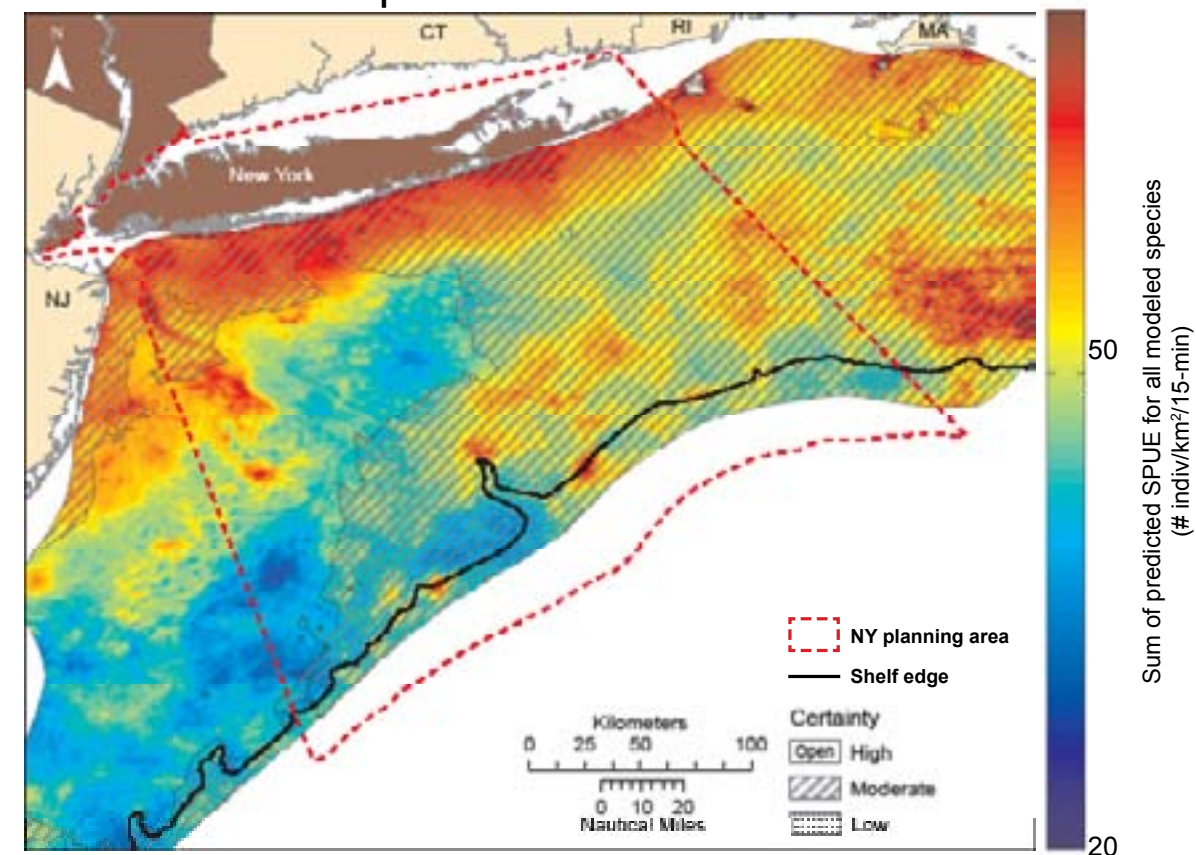


Figure 6.35. Predicted seabird abundance hotspot map.

Richness Hotspots

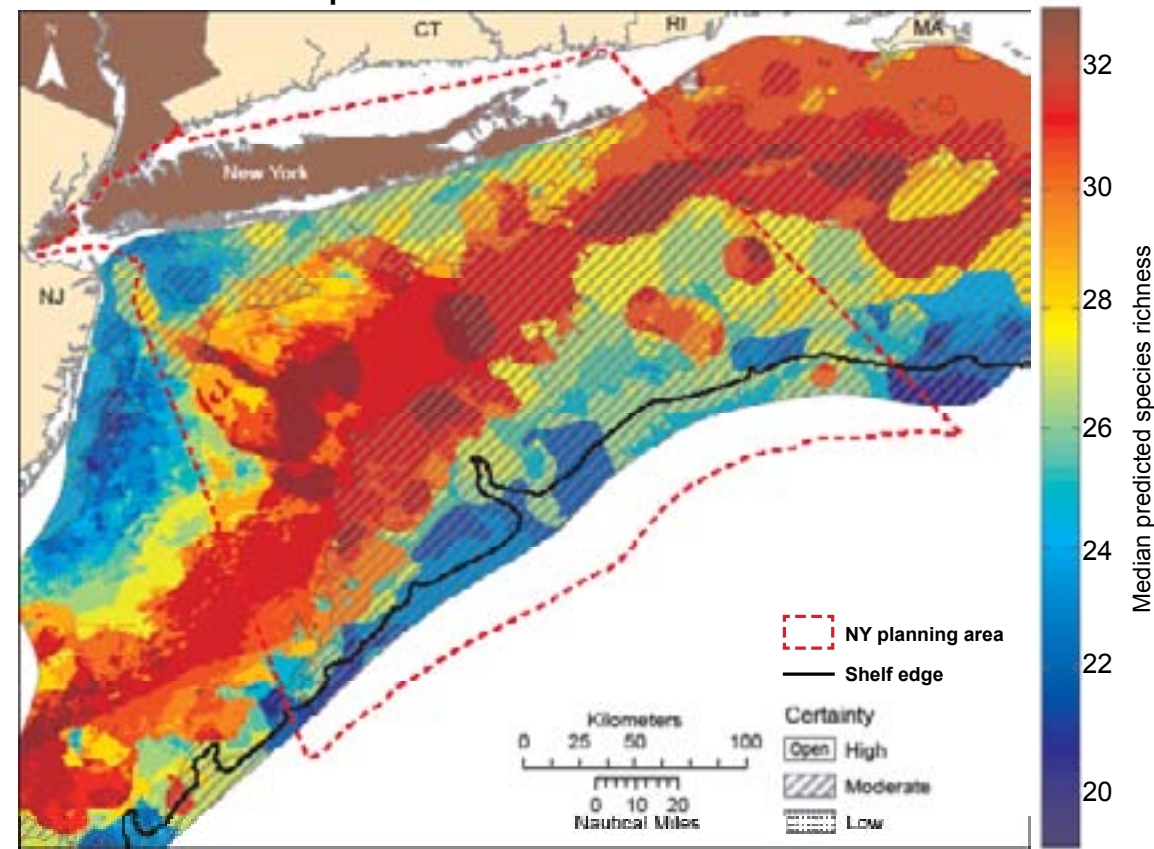


Figure 6.36. Predicted species richness hotspot map.

Diversity Hotspots

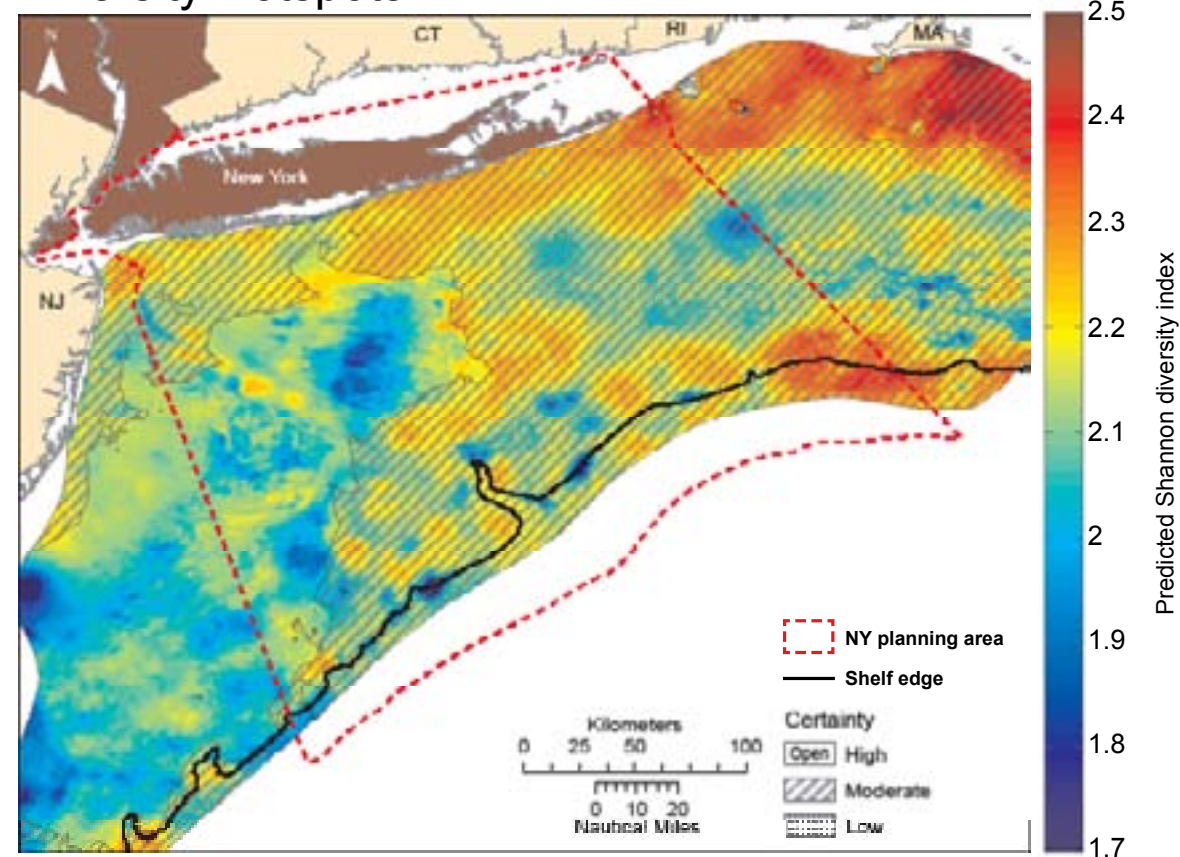
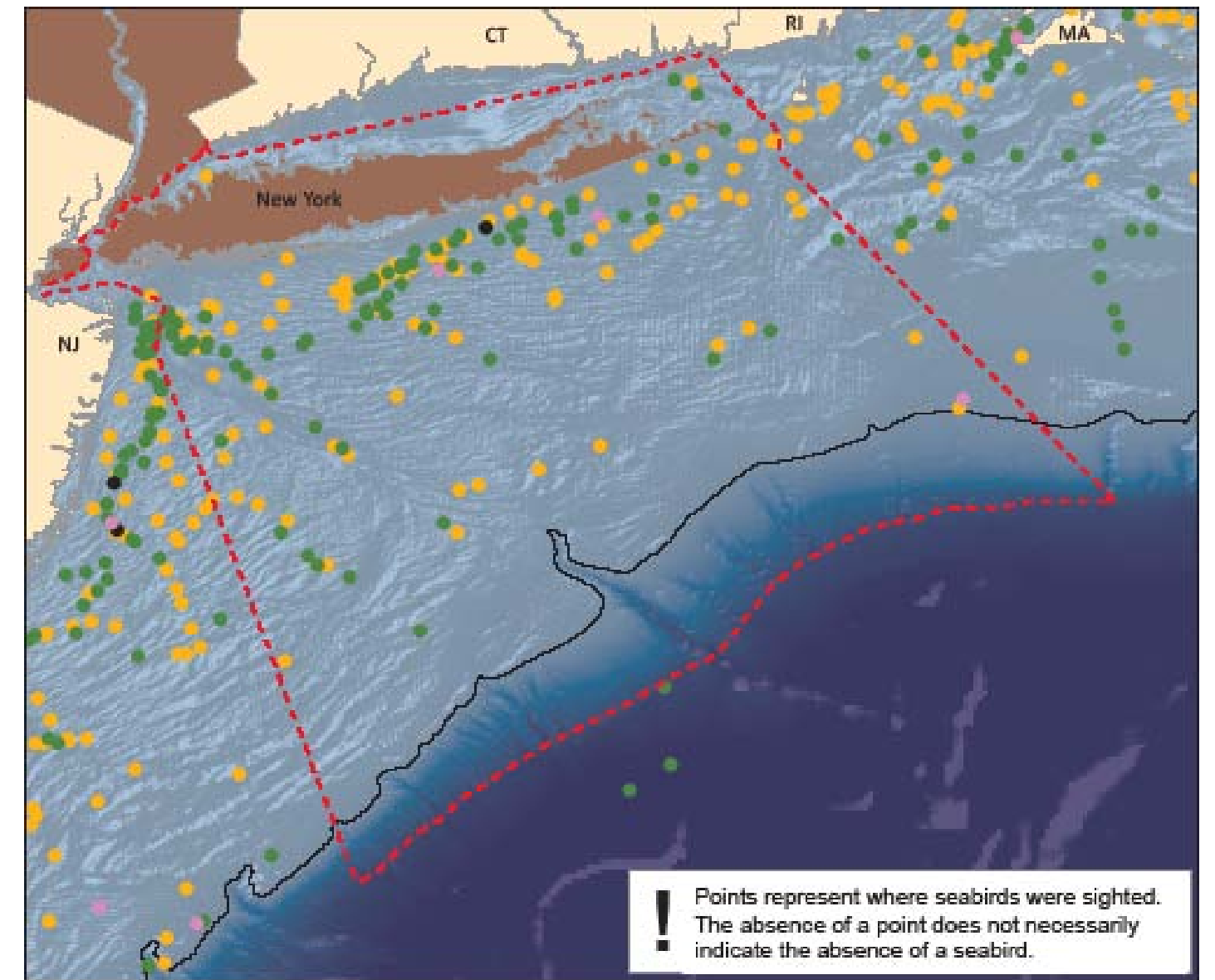


Figure 6.37. Predicted Shannon species diversity index hotspot map.

Sightings Data for Species of Concern



Seabirds of Concern Distribution

Sighting Locations by Species

- Least Tern
- Roseate Tern
- Common Loon
- Common Tern

NY Planning Area

— Shelf Edge

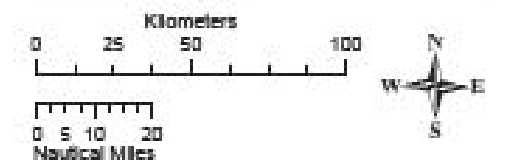


Figure 6.38. Point map of raw sightings data for species of concern. This map shows the location of sightings in the Manomet dataset for four species of seabirds listed as endangered, threatened or of special concern by New York's Department of Environmental Conservation: the Roseate Tern (*Sterna dougallii dougallii*), Common Tern (*Sterna hirundo*), Least Tern (*Sternula antillarum*), and Common Loon (*Gavia immer*). The Piping Plover (*Charadrius melodus*), listed as endangered by New York, was not in the Manomet dataset and therefore was not mapped.

6.10. DISCUSSION

The spatial models, data, and associated statistics presented in this chapter provide information on the long-term annual and seasonal spatial distribution of the marine avifauna offshore of NY. Results focus on identifying areas of likely and possible persistent aggregations of seabird species, species groups, and communities (multi-species hotspot/coldspot analyses) in the NY Bight. These maps are expected to be of high utility for marine spatial planning decisions involving seabirds in the NY Bight.

This report provides information on the long-term annual and seasonal spatial distribution of seabirds in the NY region, which is one important consideration for design of spatial management strategies. Such long-term average maps, known as “spatial climatologies,” are useful for characterizing long-term average patterns of abundance and occurrence of organisms in space (e.g., Santora and Reiss, 2011). However, it is important to emphasize that climatological mapping is only one step towards developing an effective and defensible management and conservation strategy for seabird populations. Consideration of species’ differential sensitivity to different offshore activities, and differences in population-level vulnerability to mortality or other demographic changes will also be critical to a comprehensive evaluation of risks posed by offshore management actions (Drewitt and Langston, 2006; Hueppop et al., 2006; Hatch and Brault, 2007; Allison et al., 2008; Watts, 2010). The climatological seabird occurrence and abundance models presented here should be viewed as measures of the potential exposure of different species to the effects of spatial management actions, rather than a direct measure of risk (Crichton, 1999). Although beyond the scope of this report, future work should address the incorporation of “exposure models” using the information generated here into comprehensive risk analyses for specific types of proposed management and/or development activities.

We wish to urge several cautions regarding inference of hotspots and coldspots of abundance from the maps in this report. First, the reader is urged to consult both the certainty class overlays presented on Figures 6.8-6.37 and the diagnostic statistics presented in associated tables. Second, if a particular hot or coldspot is of interest, the reader should consider consulting Appendix 6.C to determine whether that feature occurs in all seasons or only in particular seasons, whether it is directly supported by data points or is merely inferred from environmental conditions, and whether the model cross-validation plots indicate good performance outside the training data set. Third, if an important decision is to be made on the basis of a particular feature seen in model predictions, we would recommend several independent efforts to confirm model findings:

- Examination of original Manomet data to determine whether the hot or coldspot persisted over many years consistently or was only sporadic
- Collection of new survey data to confirm findings
- Consultation with local experts

In particular, hotspots or coldspots based only on extrapolation from environmental conditions, with no nearby data points, should be considered hypotheses to be tested rather than certainties. The data point overlay maps in Appendix 6.C are very useful for distinguishing such features from those that are directly supported by data points.

Similar cautions apply about judging the persistence of a hotspot or coldspot seen in the model predictions presented here. In defining “persistence”, the spatial climatological modeling approach we take does not account for how observations are spread over time. Several high observations in a small area can lead to a predicted hotspot, but they may all have occurred in the same year. One way to evaluate whether a hotspot is persistent over time within a year is to compare seasonal maps. However, to assess inter-annual persistence it is necessary to go back to the original data and examine the years in which observations associated with each potential hot or coldspot were made.

Similar cautions should be observed with multi-species abundance, richness, and diversity hotspot maps. Appendix 6.D gives a detailed account of the performance of these models in a leave-50%-out cross-validation test, and should be used as a guide to interpreting multi-species hotspot model results. In particular, it is important to note that while the hotspot maps do a good job at predicting the relative values of abundance,

richness, and diversity, the predicted values tend to be systematically higher than what is actually observed in any single 15-minute survey. This issue is discussed in Appendix 6.D and correction factors are presented, based on cross-validation, which could be applied if the absolute values of summed abundance, richness, or diversity are important.

Consideration of temporal changes and population, community, and ecosystem dynamics will also be critical to any long-term management strategy. Many dynamic aspects of seabird ecology are not directly captured by the maps presented here. Seabirds interact with a highly dynamic environment where the location of food resources, competition and threats are constantly moving. Consequently, seabird habitats are variable in distribution, time, and extent with changing human activities and environmental biophysical parameters of the marine ecosystem. The age of the data used to develop the models presented here means that the patterns can only strictly be viewed as representative of the 1980’s. Generalization to the present day requires an assumption that the human and natural environment has not changed. This assumption is likely to be more valid for some species than others, and in some areas than others (see Section 6.9.1., Species Notes). Similarly, our results assume that the climatological patterns of ocean conditions (including sea surface temperature, stratification, chlorophyll, turbidity, and zooplankton) have not undergone substantial shifts over the period from 1980-present. In reality, ocean climate is known to vary in ways that influence seabird distribution (e.g., Zipkin et al., 2010), further underscoring the need for collection and analysis of more up-to-date comprehensive regional seabird surveys.

The importance of different environmental predictors varied from species to species and often among seasons for a given species (Figure 6.5). Different predictors were sometimes important for Stage I (presence/absence) models when compared to Stage II (abundance-when-present) models. Overall, dynamic ocean climate variables like surface chlorophyll, surface turbidity, zooplankton, sea surface temperature, and stratification were often important, but for certain species static predictors like distance from shore and bathymetry were of equal or greater importance. Species that are more strongly correlated with dynamic oceanographic variables are more likely to be affected by long-term trends in ocean climate; thus, Figure 6.5 could be used to identify species more likely to be affected by ocean climate shifts.

Ideally, the information in this report would serve as an initial guide to be followed up by more current, detailed studies or syntheses of more recent data for selected areas of interest. Information presented here could be supplemented with a meta-analysis including other seabird survey datasets, non-quantitative observations, unpublished reports, and reports from the primary scientific literature. Section 6.7. identifies several existing datasets that would be useful in a meta-analysis. Additional data as well as additional modeling could supplement and improve our understanding of any particular species and area. New modeling technologies are constantly emerging; machine learning techniques such as TreeNet, RandomForest and others are likely to outperform GLM-based approaches for modeling trend surfaces and should be explored in the future (Oppel et al., 2012).

Several additional caveats should be considered when exploring the results presented in this report. The following is a non-exhaustive list (other, more technical caveats are discussed in Section 6.A.14.):

- Data used in seabird assessments are biased towards species which are larger, commonly seen, conspicuous, abundant and/or attracted to ships. Birds that are small, rare, nocturnal or avoid ships were likely undercounted (see Tasker, 1984 for species/group detection information).
- Predictions quantify the expected long-term average relative abundance of a species or species group, when averaged over time. A prediction of high abundance does not mean many individuals will be sighted there all the time; the hotspot may only occur periodically, and many individual observations may still be zero even if the long-term average abundance is high.
- Predictions made in Long Island Sound, nearshore (<5 km from land) and off the shelf slope (waters deeper than 2,000 m) can be highly uncertain, because little survey effort occurred in these areas.
- Sightings per unit effort are a relative index of abundance and should not be confused with an absolute population estimate.

Implications of the first point about detectability and attraction are particularly important to consider. Estimates of detectability require frequent, replicated repeat surveys over the same area, and therefore are not possible with the Manomet dataset. However, future targeted survey efforts may be able to estimate differences in detectability for different species with methods similar to the Manomet methods. In that case, the model estimates presented here could be updated to reflect differences in detectability. Biases due to attraction are more difficult to correct. Certain species are more likely to be affected by detectability and attraction issues than others. For example, as noted in Section 6.9.1., Northern Gannets are attracted to fishing trawlers, and the presence of large factory trawlers near the shelf break in the 1980's may have influenced some of the apparent hotspots for this species. Conversely, most terns are smaller and harder to detect or identify to species-level, and their abundance is probably underestimated. Diving birds like cormorants and dovekeys also have lower detectability because they are sometimes underwater. These issues underscore the importance of treating the measures of relative abundance presented here as proxies for the real underlying patterns, and considering them in the light of other datasets, the life history of each species, and independent local expert opinion.

Notwithstanding these caveats and the inevitable uncertainties associated with modeling a complex, dynamic community from scattered data, the maps presented here represent the first high-resolution depiction of spatial patterns in the marine avifauna of New York, and as such, represent an important step towards design of effective spatial conservation, management, and sustainable use strategies for New York's offshore waters.

6.11. ACKNOWLEDGMENTS

We gratefully acknowledge Allan O'Connell, Andrew Gilbert, Beth Gardner, Simon Pittman, Tim Battista, Chris Caldwell, Mark Monaco, Grant Law, Jennifer Greene, Mark Anderson, Chris Bruce, Brian Smith, Jeff Herter, Greg Capobianco, John Manderson, John Goff, Robert Gamble, Dick Veit, Peter Paton, David Pereksta, James Woehr, and David Bigger for valuable discussions over the course of this project. Andrew Gilbert, David Pereksta, Simon Pittman, Dick Veit, and Peter Paton provided detailed technical and content reviews that greatly improved this chapter. However, all interpretations and any errors or omissions are our own. The preparation of this document would not have been possible without Sarah D. Hile, Alicia Clarke, and Jamie Higgins (NOAA Biogeography Publications Team), Tracy Gill, Matt Poti, and Sarah Kullbom. We are also grateful to Patricia E. Leonard (Cornell Lab of Ornithology), Jeff Herter (NY DOS), Greg Capobianco (NY DOS) and the Manomet Center for Conservation Sciences (Manomet, Massachusetts) for their contributions to this study. Seabird photos for this document were graciously provided by David Pereksta from his personal collection, and also by the Cornell Lab of Ornithology (CLO), U.S. Fish and Wildlife Service (USFWS), U.S. Geological Survey (USGS), Armin Rose, Dick Daniels, Bruce Worden and Wikipedia.

Chapter 6: Online Supplements

Online Supplements can be found by going to <http://oceanservice.noaa.gov/programs/nccos/welcome.html> and searching on the keywords: *New York Spatial Plan*

Online Supplement 6.1: Predictor variable transformation details

This document provides additional detail on the statistical preparation of potential predictor variables for analysis.

Online Supplement 6.2: Species and group seasonal models, full diagnostic reports

This Online Supplement is presented in the form of an HTML document providing links to full diagnostic reports from each of the seasonal species/group predictive models.

6.12. REFERENCES

- Allison, T., E. Jedrey, and S. Perkins. 2008. Avian issues for-offshore wind development. *Marine Technology Society Journal*. 42 (2): 28-38. doi: 0025-3324.
- Amante, C. and B.W. Eakins. 2009. ETOPO1 1 Arc-Minute Global Relief Model: Procedures, Data Sources and Analysis. NOAA Technical Memorandum NESDIS NGDC-24, 19 pp, March 2009. URL: <http://www.ngdc.noaa.gov/mgg/global/global.html>
- Andrews, R. 1990. Coastal waterbird colonies: Maine to Virginia, 1984-85. U.S. Fish and Wildlife Service Newton Corner, MA.
- Ballance LT, D.G. Ainley, and G.L. Hunt, Jr. 2001. Seabird Foraging Ecology. In: J.H. Steele, S.A. Thorpe and K.K. Turekian (eds.) *Encyclopedia of Ocean Sciences*, vol. 5. Academic Press, London. pp. 2636-2644.
- Bartumeus, F., L. Giuggioli, M. Louzao, V. Bretagnolle, D. Oro, and S.A. Levin. 2010. Fishery discards impact on seabird movement patterns at regional scales. *Curr. Biol.* 20:215–222.
- Baur, D.C. and W.R. Irvin. 2009. *Endangered Species Act: Law, Policy, and Perspectives*. 2nd edition. American Bar Association. 457 pp.
- Beauchamp, G. 2011. Fit of aggregation models to the distribution of group sizes in Northwest Atlantic seabirds. *Mar Ecol Prog Ser* 425:261-268.
- Beyer, H. L. 2004. Hawth's Analysis Tools for ArcGIS. Available at <http://www.spatialecology.com/htools>
- BirdLife International. 2012. Species factsheet: *Sterna hirundo*. Downloaded from <http://www.birdlife.org> on 05/02/2012.
- Bjorck, A. 1996 *Numerical Methods for Least Squares Problems*. SIAM. 408 pp.
- Blanton, B.O., A. Aretxabaleta, F. Werner, and H. Seim. 2003. Monthly climatology of the continental shelf waters of the South Atlantic Bight. *J. Geophys. Res.*, 108 (C8), 3264, doi:10.1029/2002JC001609.
- Box, G.E.P. and D.R. Cox. 1964. An analysis of transformations (with discussion). *J. R. Statist. Soc.* B26:211-52.
- Brewster, W. 1879. The terns of the New England coast. *Bulletin of the Nuttall Ornithological Club*, 4:13-22.
- Bull, J. 1974. *Birds of New York state*. Doubleday/Natural History Press, Garden City, New York. Reprint, 1985 (with Supplement, Federation of New York Bird Clubs, 1976), Cornell Univ. Press, Ithaca, New York.
- Burkey, J. 2009. Matlab function 'lowess.m': LOWESS, Locally Weighted Scatterplot Smoothing for linear and non-linear data (enhanced). 16 Dec 2008 (Updated 27 Oct 2009). Downloaded 13 Aug 2011 from URL: <http://www.mathworks.com/matlabcentral/fileexchange/22470-lowess-locally-weighted-scatterplot-smoothing-for-linear-and-non-linear-data-enhanced>
- Calder, B.R. 2006. On the Uncertainty of Archive Hydrographic Datasets, *IEEE Journal of Oceanic Engineering*, v. 31.
- Calcagno, V. and C. Mazancourt. 2010. glmulti: An R Package for Easy Automated Model Selection with (Generalized) Linear Models. *Journal of Statistical Software* 34(12):1-29.
- Calcagno, V. 2011. R Package <glmulti> version 1.0.1. Manual: <http://cran.r-project.org/web/packages/glmulti/glmulti.pdf>, Software: <http://cran.r-project.org/web/packages/glmulti/index.html>
- Cardillo, G. 2006. Matlab toolbox <partest>. Clinical test performance: the performance of a clinical test based on the Bayes theorem. URL: <http://www.mathworks.com/matlabcentral/fileexchange/12705>
- Cardillo, G. 2008. Matlab toolbox <ROC>. ROC curve: compute a Receiver Operating Characteristics curve. URL: <http://www.mathworks.com/matlabcentral/fileexchange/19950>
- Casey, K. and P. Cornillon. 1999. A comparison of satellite and in situ-based sea surface temperature climatologies. *J. Climate*, 12, 1848–1863.
- Casey, K.S., T.B. Brandon, P. Cornillon, and R. Evans. 2010. "The Past, Present and Future of the AVHRR Pathfinder SST Program", in *Oceanography from Space: Revisited*, eds. V. Barale, J.F.R. Gower, and L. Alberotanza, Springer. DOI: 10.1007/978-90-481-8681-5_16
- Chiles, J.P. and P. Delfiner. 1999. *Geostatistics, Modelling Spatial Uncertainty*, Wiley-Interscience.
- Cornillon, P., J. Gallagher, and T. Sgouros. 2003. OPeNDAP: Accessing Data in a Distributed, Heterogeneous Environment, *Data Science Journal* 2:164-174.

Cragg, J.G. 1971. Some statistical models for limited dependent variables with application to the demand for durable goods. *Econometrica* 39: 829–844.

Cressie, N.A. 1993. *Statistics for spatial data*. John Wiley & Sons, Ontario, Canada.

Crichton, D. 1999. The risk triangle. In Ingleton, J. (ed.), *Natural Disaster Management*, Tudor Rose, London, pp. 102-103.

Curry, R.G. 1996. Hydrobase - A database of hydrographic stations and tools for climatological analysis, Woods Hole Oceanog. Inst. Tech. Rep., WHOI-96-01, Woods Hole Oceanog. Inst., Woods Hole, MA. 44 pp.

Daunt, F., G. Peters, B. Scott, D. Gremillet, and S. Wanless. 2003. Rapid-response recorders reveal interplay between marine physics and seabird behaviour. *Marine Ecology Progress Series* 255:283-288.

Deutsch, C.V. and A.G. Journel. 1998. *GSLIB: Geostatistical Software Library: and User's Guide*, second ed. Oxford University Press, New York, NY, 369 pp.

Draper, N.R. and D.R. Cox. 1969. On distributions and their transformations to normality. *Journal of the Royal Statistical Society, Series B*, 31, 472-476.

Drewitt, A.L. and R.H.W. Langston. 2006. Assessing the Impacts of Wind Farms on Birds. *Ibis* 148:29-42.

Dror, H. 2006. Matlab function: 'boxcoxl'. URL: <http://www.mathworks.com/matlabcentral/fileexchange/10419-box-cox-power-transformation-for-linear-models>.

Drury, W.H. 1965. Gulls vs. terns: Clash of coastal nesters. *Massachusetts Audubon* 1965:207-211.

Egevang, C., I.J. Stenhouse, R.A. Phillips, A. Petersen, J.W. Fox, and J.R.D. Silk. 2010. Tracking of Arctic Terns *Sterna paradisaea* reveals longest animal migration. www.pnas.org/cgi/doi/10.1073/pnas.0909493107

Forbush, E.H. 1929. *Birds of Massachusetts and other New England states*. Vol. 3. Mass. Dept. of Agriculture, Boston. 466 pp.

Fox, J. 2008. *Applied Regression Analysis, Linear Models, and Related Methods*. Sage Publishing. 2nd edition. Chapter 15.

Friedland, K., J.P. Manning, J.S. Link, J.R. Gilbert, A.T. Gilbert, and A.F. O'Connell, Jr. 2012. Variation in wind and piscivorous predator fields affecting the survival of Atlantic salmon, *Salmo salar*, in the Gulf of Maine. *Fisheries Ecology and Management* 19:22-35.

Furness, R. W. 2003. Impacts of fisheries on seabird communities. *Sci. Mar.* 67(suppl. 2), 33–45.

Gonzalez, R. and R. Woods. 1992. *Digital Image Processing*, Addison-Wesley Publishing Company, p 191.

GMI (Geo-Marine, Inc.). 2010. New Jersey Department of Environmental Protection Baseline Studies Final Report Volume II: Avian Studies. Final Report.

Goff, J.A., C.J. Jenkins, and S.J. Williams. 2008. Seabed mapping and characterization of sediment variability using the usSEABED data base. *Continental Shelf Research* 28 (2008) 614–633.

Goovaerts, P. 1997. *Geostatistics for natural resources evaluation*. Oxford, New York, Oxford University Press.

Guilford T., J. Meade, J. Willis, R.A. Phillips, D. Boyle, S. Roberts, M. Collett, R. Freeman, and C.M. Perrins. 2009. Migration and stopover in a small pelagic seabird, the Manx shearwater *Puffinus puffinus*: insights from machine learning. *Proceedings of the Royal Society B*, 276 (1660), 1215-1223.

Greene, J.K., M.G. Anderson, J. Odell, and N. Steinberg, eds. 2010. *The Northwest Atlantic Marine Ecoregional Assessment: Species, Habitats and Ecosystems. Phase One*. The Nature Conservancy, Eastern U.S. Division, Boston, MA. URL: <http://www.nature.org/ourinitiatives/regions/northamerica/areas/easternusmarine/explore/index.htm>

Hansen, T.M. 2009. mGStat Manual. <http://mgstat.sourceforge.net/mGstat.pdf> Software available from: <http://mgstat.sourceforge.net/>

Harrison, C. 1978. *A field guide to the nests, eggs and nestlings of North American birds*. Collins, Cleveland, Ohio.

Hatch, J.J. and S. Brault. 2007. Collision Mortalities at Horseshoe Shoal of Bird Species of Special Concern. Report no.5.3.2-1 Cape Wind Associates.

Hendry, R. and I. He. 1996. Technical Report on Objective Analysis (OA) Project. Unpublished document available at URL: http://www2.mar.dfo-mpo.gc.ca/science/ocean/coastal_hydrodynamics/Oax/download/techrep.ps

- Hengl, T., G.M.B. Heuvelink, and A. Stein. 2004. A generic framework for spatial prediction of soil variables based on regression-kriging. *Geoderma* 122(1-2):75-93.
- Hengl, T., G.M.B. Heuvelink, and D.G. Rossiter. 2007. About regression-kriging: from equations to case studies. *Computers and Geosciences*, 33(10):1301-1315.
- Hoopes, E.M., P.M. Cavanagh, C.R. Griffin, and J.T. Finn. 1994. Synthesis of information on marine and coastal birds of the Atlantic coast: abundance, distribution, and potential risks from oil and gas activities, 3 vols. Prepared by Massachusetts Cooperative Fish and Wildlife Research Unit, University of Massachusetts, Amherst, MA. Prepared for U.S. Department of the Interior, Minerals Management Service, Herndon, VA.
- Hueppop, O.D., J., K-M. Exo, E. Fredrich, and R. Hill. 2006. Bird Migration Studies and Potential Collusion Risk with Offshore Wind Turbines. *British Ornithologist's Union. Ibis*, 148:90-109.
- Huettmann, F. 2000. Environmental Determination of Seabird Distribution. Unpublished PhD Thesis. Atlantic Cooperative Wildlife Ecology Research Network (ACWERN). Faculty of Forestry and Environmental Management. University of New Brunswick (UNB), Fredericton, New Brunswick, Canada.
- Huettmann, F. and A.W. Diamond. 2000. Seabird migration in the Canadian North Atlantic: moulting locations and movement patterns of immatures. *Canadian Journal of Zoology* 33:1-25.
- Huettmann, F. and A.W. Diamond. 2001. Seabird colony locations and environmental determination of seabird distribution: A spatially explicit seabird breeding model in the Northwest Atlantic. *Ecological Modeling* 141:261-298.
- Isaaks, E.H. and R.M. Srivastava. 1989. An introduction to applied geostatistics. Oxford Univ. Press, New York.
- Jespersion, D. 1924. On the frequency of birds over the high Atlantic Ocean. *Nature* 114:281-283.
- Krebs, C. 1989. *Ecological Methodology*. HarperCollins, New York.
- Laidler, K.J. 1997. *Chemical Kinetics*, Third Edition, Benjamin-Cummings.
- Law, G. 2011. Center for Coastal Margin Observation and Prediction, Oregon Health and Science University. Pers. comm. by email with B. Kinlan and C. Menza, March 2011.
- Lotze, H. and I. Milewski. 2004. Two centuries of multiple human impacts and successive changes in a North Atlantic food web. *Ecological Applications* 14(5):1428-1447.
- Moore, H.B. 1951. The seasonal distribution of oceanic birds in the western North Atlantic. *Bulletin of Marine Science for the Gulf and Caribbean* 1:1-14.
- Nisbet, I.C.T. 2002. Common Tern (*Sterna hirundo*). In A. Poole and F. Gill, eds. *The birds of North America*, No 618. The Academy of Natural Sciences, Philadelphia, and the American Ornithologists' Union, Washington D.C.
- NY and TNC (New York Department of State Division of Coastal Resources and Waterfront Revitalization and The Nature Conservancy). 1991. Long Island's beach-nesting shorebird habitat: Protection and Management of a vulnerable resource. Draft Report.
- NYSERDA. 2010. <http://www.nysesda.org/publications/li-nyc-collaborative-task3b--avianriskassessment-final-100110-wappendix.pdf>
- NASA OBPG (Ocean Biology Processing Group). 2005. SeaWiFS Reprocessing 5.1 URL:<http://oceancolor.gsfc.nasa.gov/REPROCESSING/SeaWiFS/R5.1/>
- NOAA National Geophysical Data Center (NGDC). 2010. U.S. Coastal Relief Model. Retrieved 23 June 2010 from URL: <http://www.ngdc.noaa.gov/mgg/coastal/crm.html>
- O'Connell, Jr., A.F., B. Gardner, A.T. Gilbert, and K. Laurent. 2009. Compendium of Avian Occurrence Information for the Continental Shelf Waters along the Atlantic Coast of the United States (Database Section: Seabirds). A final report for the U.S. Department of the Interior, Minerals Management Service, Atlantic OCS Region, Herndon, VA. 50 pp. Contract No. M08PG20033.
- Oppel, S., A. Meirinho, I. Ramirez, B. Gardner, A. O'Connell, and M. Louzao. 2012. Comparison of five modelling techniques to predict the spatial distribution and abundance of seabirds. *Biological Conservation*.
- Ozard, J.W. 1984. Technical Memorandum: Procedures used to identify, evaluate and recommend areas for designation as "Significant Coastal Fish And Wildlife Habitats". Grant Number: NA-82-AA-D-CZ068.

- Pardo-Igúzquiza, E. 1999. VARFIT: a fortran-77 program for fitting variogram models by weighted least squares. *Computers & Geosciences*, Volume 25, Issue 3, April 1999, pp 251-261.
- Paton, P., K. Winiarski, C. Trocki and S. McWilliams. 2010. Spatial distribution, abundance, and flight ecology of birds in nearshore and offshore waters of Rhode Island. Interim Technical Report for the Rhode Island Ocean Special Area Management Plan 2010. Department of Natural Resources Science, University of Rhode Island.
- Payne, P.M., L.A. Seltzer and A.R. Knowlton. 1984. Distribution and density of cetaceans, marine turtles and seabirds in the shelf waters of the Northeastern United States, June 1980-December 1983, based on shipboard observations. Final report to the National Marine Fisheries Service Northeast Fish. Sci. Cent. in fulfillment of contract NA-81-FA-C-023. Manomet Bird Observatory, Manomet, MA, 246 pp.
- Pebesma, E.J. and C.G. Wesseling. 1998. Gstat, a program for geostatistical modelling, prediction and simulation. *Computers and Geosciences*, 24(1):17-31.
- Pierotti, R.J. and T.P. Good. 1994. Herring Gull (*Larus argentatus*), *The Birds of North America Online* (A. Poole, ed.). Ithaca: Cornell Lab of Ornithology; Retrieved from the Birds of North America Online: <http://bna.birds.cornell.edu/bna/species/124> doi:10.2173/bna.124
- Pirhalla, D.E., V. Ransibrahmanakul, and R. Clark. 2009. An Oceanographic Characterization of the Olympic Coast National Marine Sanctuary and Pacific Northwest: Interpretive Summary of Ocean Climate and Regional Processes Through Satellite Remote Sensing. NOAA Technical Memorandum NOS NCCOS 90. Silver Spring, MD. 55 pp.
- Pittman, S. and F. Huettmann. 2006. Chapter 4 - Seabird Distribution and Diversity. In: *An Ecological Characterization of the Stellwagen Bank National Marine Sanctuary Region: Oceanographic, Biogeographic, and Contaminants Assessment*. Battista, T., R. Clark, and S. Pittman (eds.). Prepared by NCCOS's Biogeography Team in cooperation with the National Marine Sanctuary Program. Silver Spring, MD. NOAA Technical Memorandum NCCOS 45.
- Potts, J.M. and J. Elith. 2006. Comparing species abundance models. *Ecological Modeling* 199:153-163.
- Powers, K.D. 1983. Pelagic distributions of marine birds off the northeastern United States. NOAA Technical Memorandum NMFS-F/NEC-27. U.S. Department of Commerce, Washington D.C. 202 pp.
- Powers, K.D., G.L. Pittman, and S.J. Fitch. 1980. Distribution of marine birds on the mid- and north-Atlantic U.S. outer continental shelf. Technical Progress Report. U.S. Department of Energy, Washington D.C. 165 pp.
- Reid, J.M., J.A. Reid, C.J. Jenkins, M.E. Hastings, S.J. Williams and L.J. Poppe. 2005. usSEABED: Atlantic coast offshore surficial sediment data release: U.S. Geological Survey Data Series 118, version 1.0. URL: <http://pubs.usgs.gov/ds/2005/118/>
- Riou, S., C.M. Gray, M. Brooke, P. Quillfeldt, J.F. Masello, C. Perrins, and K.C. Hamer. 2011. Recent impacts of anthropogenic climate change on a higher marine predator in western Britain. *Marine Ecology Progress Series* 422:105-112.
- Roberts, C.M., G. Branch, R.H. Bustamante, J.C. Castilla, J. Dugan, B.S. Halpern, K.D. Lafferty, H. Leslie, J. Lubchenco, D. McArdle, M. Ruckelshaus and R.R. Warner. 2003. Application of ecological criteria in selecting marine reserves and developing reserve networks. *Ecological Applications* 13 (Supplement): 215-228.
- Ross, S.M. 2007. Introduction to probability models. 9th edition. Academic Press, 782 pp. Chapter 3.
- Sandvik, H. and K.E. Erikstad. 2008. Seabird life histories and climatic fluctuations: a phylogenetic-comparative time series analysis of North Atlantic seabirds. *Ecography* 31:73-83.
- Santora, J.A. and C.S. Reiss. 2011. Geospatial variability of krill and top predators within an Antarctic submarine canyon system. *Marine Biology* 158:2527-2540. DOI 10.1007/s00227-011-1753-0
- Schneider, D.C. 1990. Seabirds and fronts: A brief overview. *Polar Research* 8:17-22.
- Schneider, D.C. 1997. Habitat selection by marine birds in relation to water depth. *Ibis* 139:175-178.
- Shumway, C., K. Ruddock, and M. Clark. 2010. Physical Oceanography. Chapter 4 In: *Greene, J.K., M.G. Anderson, J. Odell, and N. Steinberg, eds. 2010. The Northwest Atlantic Marine Ecoregional Assessment: Species, Habitats and Ecosystems. Phase One. The Nature Conservancy, Eastern U.S. Division, Boston, MA.*
- Sokal, R.R. and F.J. Rohlf. 1995. *Biometry. The Principles and Practice of Statistics in Biological Research*. Third Edition. New York: W.H. Freeman and Company.
- Soluri, E.A. and V.A. Woodson. 1990. World Vector Shoreline. *International Hydrographic Review*, LXVII(1).

- Spiegel, C. and S. Johnston. 2011. Compendium of Avian Occurrence Information for the Continental Shelf Waters along the Atlantic Coast of the United States (Database Section: Shorebirds). A final report for the U.S. Department of the Interior, Bureau of Energy Management, Regulation, and Enforcement, Atlantic OCS Region, Herndon, VA. 27 pp. Contract No. M08PG20033//Interagency Agreement between USGS and USFWS, Region 5, Division of Migratory Birds, Hadley, MA.
- Stefánsson, G. 1996. Analysis of groundfish survey abundance data: combining the GLM and delta approaches. *ICES Journal of Marine Science*, 53:577–588.
- Tasker, M.L., P.H. Jones, T. Dixon, and B.F. Blake. 1984. Counting seabirds at sea from ships: a review of methods employed and a suggestion for a standardized approach. *The Auk* 101:567-577.
- Tasker, M.L., C.J. Camphuysen, J. Cooper, S. Garthe, W.A. Montevecchi, and S.J.M. Blaber. 2000. The impacts of fishing on marine birds. *ICES Journal of Marine Science* 57:531-547.
- Tasker, M.L. and R.W. Furness. 2003. Seabirds as monitors of the marine environment. ICES Cooperative Research Report No. 258. International Council for the Exploration of the Sea, Copenhagen, Denmark. 73 pp.
- U.S. Fish and Wildlife Service. 2008. Birds of Conservation Concern 2008. United States Department of Interior, Fish and Wildlife Service, Division of Migratory Bird Management, Arlington, Virginia. 85 pp. [Online version available at <<http://www.fws.gov/migratorybirds/>>]
- Ver Hoef, J.M. and J.K. Jansen. 2007. Space-time zero-inflated count models of Harbor seals. *Environmetrics* 18:697–712.
- Votier, S.C., R.W. Furness, S. Bearhop, J.E. Crane, R.W.G. Caldow, P. Catry, K. Ensor, K.C. Hamer, A.V. Hudson, E. Kalmbach, N.I. Klomp, S. Pfeiffer, R.A. Phillips, I. Prieto, and D.R. Thompson. 2004. Changes in fisheries discard rates and seabird communities. *Nature* 427:727-730.
- Watts, B.D. 2010. Wind and Waterbirds: Establishing sustainable mortality limits within the Atlantic Flyway. Center for Conservation Biology Technical Report Series, CCBTR-10-05. College of William and Mary/Virginia Commonwealth University Williamsburg, VA. 43 pp.
- Winter, A., Y. Jiao and J.A. Browder. 2011. Modeling Low Rates of Seabird Bycatch in the U.S. Atlantic Longline Fishery. *Waterbirds*, 34(3):289-303. DOI: 10.1675/063.034.0304
- Wolfeich, C. Web document: URI/NASA AVHRR Pathfinder 1km SST Archive. Retrieved April 2011 from http://satdat1.gso.uri.edu/opendap/Pathfinder/Pathfinder1km/pathfinder_1km.html
- Yen, P.P.W., W.J. Sydeman, and D.K. Hyrenbach. 2004. Marine bird and cetacean associations with bathymetric habitats and shallow-water topographies: implications for trophic transfer and conservation. *Journal of Marine Systems* 50:79-99.
- Yorio, P. 2009. Marine protected areas, spatial scales, and governance: implications for the conservation of breeding seabirds. *Conservation Letters* 2(4):171-178.
- Zipkin, E.F., B. Gardner, A.T. Gilbert, A.F. O'Connell, Jr., J.A. Royle, and E.D. Silverman. 2010. Distribution patterns of wintering sea ducks in relation to the North Atlantic Oscillation and local environmental characteristics. *Oecologia* 163:893-902.
- Zörgiebel, F. 2008. Matlab function: <ploterr.m>. Downloaded May 2011. URL: <http://www.mathworks.com/matlabcentral/fileexchange/22216-ploterr>

Appendix 6.A. Statistical Methods

6.A.1. Model overview

We adopt a two-stage approach that separates a model of the presence probability of a species from a model of its relative abundance when it is present. This approach has been successfully used to model highly zero-inflated marine distribution data (e.g., Stefánsson, 1996; Ver Hoef and Jansen, 2007; Winter et al., 2011). This technique is also referred to in the statistical literature as a hurdle model (Cragg, 1971; Potts and Elith, 2006; Ver Hoef and Jansen 2007). In our case we refer to the two parts of the model as Stage I and Stage II. Stage I models the probability, $p_i(x,y)$, that species or group i is observed in a survey at location (x,y) in a given season (models were repeated for each season, but seasonal subscripts are omitted for simplicity):

$$p_i(x,y) \equiv \text{Prob}(i \text{ observed at } \langle x,y \rangle \text{ in a single 15-minute survey}) \quad \text{Eq. 1 (Stage I)}$$

Here, $p_i(x,y)$ is treated as a spatial random variable whose value is a probability; the details of how it is modeled are discussed below and in Sections 6.A.4., 6.A.5., and 6.A.6. We do not distinguish between observation and presence; the probability $p_i(x,y)$ is assumed to be equal to the probability that the species was actually present during a single 15-minute survey conducted over the 9-year study period. In other words, probability of detection when the species is present is assumed to be 1; consequences of this assumption are discussed in Section 6.A.14.

Stage II models $E\{Z_i(x,y) \mid P_i(x,y)=1\}$, the long-term mean of the observed relative abundance (SPUE), $Z_i(x,y)$, of species or group i at location (x,y) when the species or group is present:

$$E\{Z_i(x,y) \mid P_i(x,y)=1\} \quad \text{Eq. 2 (Stage II)}$$

Here $Z_i(x,y)$ is a continuous random variable representing relative abundance (number of individuals sighted per 15-minute survey per km² of survey area), and $P_i(x,y)$ is a Bernoulli random variable whose probability of success in a single trial is given by $p_i(x,y)$. Note that $E\{A|B\}$ represents the conditional expectation operator, which returns the expected value (arithmetic average over many trials) of the random variable A, given the value of the random variable B. This expected value can be thought of as the average SPUE that would have been recorded if the same location had been visited many times, instead of only once, during the 9-year survey period, and only non-zero values were included in the average. In this model, the observed value of SPUE at each location is our single observation of the random variable $Z_i(x,y)$, conditional on the outcome of $P_i(x,y)$ at that location (0 if species i is absent, 1 if present). Over a 9-year period, assuming 6 hours of potential survey per day, approximately 20,000 temporally non-overlapping surveys *could have been* conducted at each location in each season. If hypothetical repeat surveys were conducted and averaged (excluding zero observations), then the value of that average would approach that of equation 2 as the number of repeat surveys increased, if the relevant assumptions outlined in Section 6.A.14. are also met.

The MBO seabird data, processed as described in Section 6.8.3., are conceptually modeled as a set of outcomes of the purely spatial (non-temporal) random variables $P_i(x,y)$ (Stage I) and $Z_i(x,y)$ conditional on $P_i(x,y)=1$ (Stage II). This relies on the basic assumption that the parameters that define these random variables (described in more detail below) do not vary over time within a season or among survey years. Implications of this assumption are discussed in Section 6.A.14. The use of spatial random variables without an explicit temporal component is termed a spatial climatological approach and has been used elsewhere to map “hotspots” and “coldspots” in long-term average patterns of species distribution (e.g., Santora and Reiss, 2011). The word climatology in this context means long-term average.

Both Stage I and Stage II of the model are themselves comprised of two sub-models: a trend model and a residual model, described in more detail below. The trend models are implemented as generalized linear models (GLMs), and predict large-scale variation in a species’ distribution from environmental variables. The residual models are implemented as geostatistical models (kriging) to account for spatial autocorrelation in the residuals from the trend (Cressie, 1993; Pebesma, 1998).

The GLM trend component was necessary because exploratory data analysis showed that both probability of presence (Stage I) and abundance when a species is present (Stage II) showed large-scale trends that were related to environmental variables. Notably, presence/absence often showed different large-scale spatial patterns than abundance when the species was present, motivating the two-stage approach. Other types of trend models are possible, and could be explored in future work (e.g., generalized additive models, classification and regression trees).

The geostatistical component was necessary because the data are clustered and unevenly distributed in space, and preliminary analysis after removal of large-scale trends with GLM revealed autocorrelation in the spatial pattern of residuals. When this is the case, spatial dependence must be explicitly modeled to obtain unbiased estimates of GLM coefficients, as well as to properly model uncertainty at unsampled locations (Cressie, 1993; Chiles and Delfiner, 1999). A major advantage of the hybrid GLM-geostatistical approach is that predictions are accompanied by spatially explicit estimates of uncertainty, because spatial dependence in error fields is explicitly modeled (Pebesma, 1998).

The final seasonal model prediction of SPUE is the product of Stage I and Stage II maps, which gives the unconditional expected value of $Z_i(x,y)$:

$$E\{Z_i(x,y)\} = P_i(x,y) * E\{Z_i(x,y) | P_i(x,y)=I\} \quad \text{Eq. 3 (Stage I x II)}$$

This result follows directly from application of basic laws of probability and conditional expectation for random variables (Cragg, 1971; Ross, 2007). The final predicted value represents the average number of birds that would be seen if a site was surveyed repeatedly (using the same standardized 15-minute surveys), *including times when the species was not seen as values of 0*.

The seasonal modeling process can be summarized as follows. For each species and group, for each season that can be modeled, the following steps are performed:

1. Transform potential predictor variables for linearity. See Section 6.A.2. below.
2. Divide data into training and validation (“holdout”) subsets for cross-validation purposes. See Section 6.A.3. below.
3. Stage I trend model: Use a GLM (binomial distribution, logit link) to generate a predictive map of the mean probability of species occurrence. See Section 6.A.4. below.
4. Stage I residual model: Use ordinary indicator kriging (OIK) to predict the “residual” probability map, where “residual” is defined as the probability that the regression model leads to an incorrect classification of the presence state ($P_i(x,y)$) of a given location. See Section 6.A.5. below.
5. Final Stage I model: Adjust the trend-predicted probability map using the kriged residual probability map from step 4. The trend from step 3 and residual from step 4 are combined using probability laws. See Section 6.A.6. below.
6. Stage II trend model: Use a GLM (normal distribution, identity link) to generate a predictive map of the mean abundance of a species when it is present. Data were transformed for normality for this part of the analysis using a Box-Cox type transformation (Box and Cox 1964), described further below, and back-transformed for final maps. See Section 6.A.7. below.
7. Stage II residual model: Use Simple Kriging (SK) to predict residual map of the regression model of abundance. See Section 6.A.8. below.
8. Final Stage II model: Add the trend map from step 6 and the residual map from step 7. See Section 6.A.9. below.
9. Final Stage I x II model prediction: Multiply the predicted probability of occurrence at each location by the predicted abundance if present to produce the final prediction of the expected value (long-term average) of abundance at each location. See Section 6.A.10. below.

10. Relative uncertainty calculation: scaled relative uncertainty values were calculated for the trend, residual, and final models for Stage I and Stage II, and for the final Stage IxII prediction. See Section 6.8.11. below.
11. Model evaluation, cross-validation, and relative uncertainty calibration. See Section 6.A.12. below.

The sections below describe each of these steps in detail.

6.A.2. Transformation of potential predictor variables for linearity

Transforming independent variables in a multiple linear regression context for normality, centrality, and homogeneity of variance is often desirable for stabilizing estimates of regression parameters, and can also help to linearize relationships between predictors and response (Sokal and Rohlf, 1995). The family of power-law transformations studied by Box and Cox (1964) is particularly useful for improving both normality and linearity. A Box-Cox transformation is defined as follows, where X denotes the original variable and X^* the transformed variable:

$$X^* = \begin{cases} X^\lambda, & \text{if } \lambda \neq 0 \\ \ln(X), & \text{if } \lambda = 0 \end{cases} \quad \text{Eq. 4}$$

A maximum-likelihood procedure (Box and Cox, 1964; Dror, 2006) was used to estimate the Box-Cox transformation parameter λ for each potential predictor variable, and guide the final choice of stabilizing transformation for each predictor. *A priori* knowledge about the types of transformations likely to be justified for different types of variables was also considered (Sokal and Rohlf, 1995). Predictor transformations expressions are shown in Table 6.A.1.

Note that the transformation of some of these variables changes the sign of the linear relationship between variable and response; care must therefore be taken in interpreting the signs of regression coefficients for transformed predictors. Details of transformation choices and pre- and post-transformation distributions are given in Appendix 6.B. and Online Supplement 6.1.

Table 6.A.1. Predictor variable transformations.

PREDICTOR VARIABLE	TRANSFORMATION EXPRESSION	NOTES
BATH	$X^*=(1-x)^{-0.4}$	For all $X \leq 0$
SLOPE	$X^*=X^{-0.4}$	
DIST	$X^*=X^{0.6}$	
SSDIST	$X^*=X$	Not transformed
SST	$X^*=11605/(X+273.15)$	Arrhenius transform (Laidler, 1997)
STRT	$X^*=X$	Not transformed
TUR	$X^*=1/X$	
CHL	$X^*=1/(X+1)$	
ZOO	$X^*=X$	Not transformed
SLPSLP	$X^*=X^{-0.3}$	
PHIM	$X^*=1/(X+3)$	

Transformed predictor variables were centered and standardized prior to each GLM fit, using the set of values of each predictor variable at the data locations under consideration (centering and standardization was performed each time just prior to running the GLM, because different patterns of missing predictor data could cause different data points to be used, requiring re-centering and re-standardization).

6.A.3. Selection of training and validation subsets for cross-validation

50% of the observation locations were selected at random to be used in subsequent model-fitting (henceforth referred to as the training set), with the remaining 50% withheld for cross-validation (henceforth referred to as the validation or holdout set). All model selection and model fitting (Sections 6.A.4. to 6.A.10.) was carried out using only the training set. Cross-validation statistics were calculated by comparing model predictions at the holdout locations to the true data values at the holdout locations. Final predictive maps, however, used all available data by applying the models selected and fit based on training data to the entire original dataset. Cross-validation error estimates are thus conservative in the sense that they were derived from a model fit to a dataset one half the size of the final dataset.

6.A.4. Stage I trend model

The trend component of the Stage I model, $\mu_i^I(x,y)$, was estimated as follows.

Observed data $Z_i(x,y)$ were first transformed to a binary indicator variable $P_i(x,y)$, whose value was 1 if $Z_i(x,y) > 0$ and 0 otherwise. The initial set of 11 potential predictor variables was then pre-screened to remove any predictors whose pattern of missing values would too greatly influence the data points that could be used to estimate the GLM. Pre-screening criteria are given in Table 6.A.2.

Table 6.A.2. Criteria for inclusion of a predictor variable in the set of potential predictors evaluated for a given seasonal Stage I or Stage II GLM model ("pre-screening criteria"). The set of points for which both data and predictor values were available had to meet all of these criteria for a predictor variable to be considered.

CRITERION	CONDITION
Fraction of all data eliminated	$\leq 30\%$
Fraction of presences eliminated	$\leq 20\%$
Fraction of absences eliminated	$\leq 50\%$
Number of presences remaining	≥ 15

Predictor variables not excluded in the pre-screening process were centered, standardized, and the R package 'glmulti' (Calcagno and Mazancourt, 2010; Calcagno, 2011) was used to search for the model with lowest AICc from the set of possible generalized linear models, allowing two-way interaction effects to be included, but requiring that both corresponding main effects be in the model if an interaction term were to be included (marginality requirement). GLM model used a binomial distribution with a logit link function (Fox, 2008).

The search method used depended on the size of the possible model space, which was restricted by the elimination of some potential predictors in the pre-screening stage (above) and by an upper bound on the number of terms determined by the number of observations. The number of terms in a model (not including the intercept) was restricted to be no greater than the number of observations divided by 10 (Sokal and Rohlf, 1995; Fox, 2008). If the number of predictors and/or maximum number of terms was sufficiently small, then the model space was searched exhaustively for the model with the lowest corrected Akaike's Information Criterion (AICc; Sokal and Rohlf, 1995). If the number of predictors and/or maximum number of terms was intermediate, then a genetic algorithm with the default parameters and stopping criteria of $\Delta AIC = 0.5$, $\text{conseq} = 5$ was used (Calcagno and Mazancourt, 2010; Calcagno, 2011). If the number of predictors and/or maximum number of terms was too large for the genetic algorithm to enumerate the model space, then an exhaustive search was performed of all possible models with 5 or fewer main effects (allowing for two-way interactions within each subset).

The selected model structure was then fit to the data using Matlab Statistics Toolbox function 'glmfit', which implements standard Generalized Linear Model fitting by iteratively re-weighted least-squares (Bjorck, 1996; Fox, 2008). As before, a binomial distribution and logit link function were used. Use of binomial distributions and logit link functions involves assumptions that are discussed in Section 6.A.14. Parametric ± 1 standard error confidence bounds on GLM estimates were calculated using Matlab function 'glmval' (following equations in Fox, 2008).

A standard array of GLM diagnostics was produced, including effect tests, deviance goodness-of-fit tests, several 'pseudo-R²' measures designed for logistic regression, residual leverage and influence plots, and a variety of other diagnostic measures (for details see diagnostic tables in main text and Online Supplement 6.2). An ROC curve analysis was also performed to assess accuracy of the Stage I trend prediction (see Online Supplement 6.2).

6.A.5. Stage I residual model

The residual component of the Stage I model, $\varepsilon_i^I(x,y)$, was estimated as follows.

First, ROC curve analysis was used to determine the optimal cutoff value of the trend probability, $\mu_i^I(x,y)$, to use for classifying the presence/absence data (Cardillo, 2008). ROC curve analysis identifies the cutoff probability for classification that optimizes the tradeoff between sensitivity and specificity, given a training dataset. This cutoff was then applied to transform the trend prediction map $\mu_i^I(x,y)$ into a binary classification

map (0=predicted absence, 1=predicted presence). Use of this ROC curve method to classify the trend can result in global bias of the classification toward the less-common class (usually presences), and the implications of this are discussed in Section 6.A.14.

A binary indicator variable (the "misclassification indicator") was then created that took the value 1 if the binary classification map based on the trend was correct at a data location, and 0 if not. Indicator variograms were estimated and modeled from this misclassification indicator, and Ordinary Indicator Kriging (OIK) was used to produce a map of predicted misclassification probabilities. Kriging predictions >1 or <0 were set to 1 or 0, respectively, to satisfy order relations for probabilities (Deutsch and Journel, 1998; Pebesma, 1998), and the resulting map was the residual component of Stage I, $\varepsilon_i^I(x,y)$. Because misclassification of 0's as 1's and 1's as 0's were considered equivalent, the OIK geostatistical model makes the assumption that the spatial patterns of misclassification of 1's and 0's are equivalent (symmetry). Implications of this symmetry assumption are discussed in Section 6.A.14.

Variogram models were fit automatically by a non-linear weighted least-squares minimization algorithm (Pebesma, 1998; Pardo-Igúzquiza, 1999), using weights proportional to N/h^2 (the number of pairs of observations used to estimate each observation divided by the square of the lag distance), as described by Pebesma (1998). Following standard geostatistical practice, the functional form of the variogram and an initial-guess parameter set was specified prior to the least-squares minimization by inspection of the empirical variogram (Issaks and Srivistava, 1989; Cressie, 1993; Deutsch and Journel, 1998; Chiles and Delfiner, 1999).

OIK produces parametric estimates of uncertainty (kriging standard error) for each location in the residual prediction map (Pebesma, 1998; Deutsch and Journel, 1998). An ROC curve analysis was also performed to assess accuracy of the Stage I residual prediction (see Online Supplement 6.2).

6.A.6. Final Stage I model

Because the trend and residual components of the Stage I model are probabilities, they can be combined using the laws of conditional probability to arrive at the full Stage I model as follows (Ross, 2007):

$$p_i(x,y) = \text{Prob}([\text{trend model predicts } i \text{ is present AND trend model is not wrong}] \text{ OR } [\text{trend model predicts } i \text{ is not present AND trend model is wrong}]) \quad \text{Eq. 5}$$

which can be translated to,

$$p_i(x,y) = \mu_i^I(x,y) \cdot (1 - \varepsilon_i^I(x,y)) + (1 - \mu_i^I(x,y)) \cdot \varepsilon_i^I(x,y) \quad \text{Eq. 6}$$

which simplifies to the final Stage I model:

$$p_i(x,y) = \mu_i^I(x,y) + \varepsilon_i^I(x,y) - 2 \cdot \mu_i^I(x,y) \cdot \varepsilon_i^I(x,y) \quad \text{Eq. 7}$$

Parametric ± 1 SE confidence intervals for the final Stage I model, $p_i(x,y)$, were derived by applying Equation 7 to the parametric confidence intervals for $\mu_i^I(x,y)$ and $\varepsilon_i^I(x,y)$ calculated using the GLM model and the geostatistical (OIK) model, respectively.

6.A.7. Stage II trend model

The trend component of the Stage II model, $\mu_i^{II}(x,y)$, was estimated as follows.

Data at non-zero locations were first transformed for normality using a Box-Cox power transform (see Section 6.A.2.) whose parameter λ was chosen by a maximum likelihood procedure (Figure 6.A.1) (Box and Cox, 1964; Dror, 2006). Power-law family models have recently been found to outperform other often-used statistical models (e.g., Poisson) for describing distributions of seabird group sizes in our study region (Beauchamp, 2011), lending further motivation to the use of the Box-Cox family of transformations for this purpose.

The initial set of 11 potential predictor variables was then pre-screened to remove any predictors whose pattern of missing values would too greatly influence the data points that could be used to estimate the GLM. Pre-screening criteria are given in Table 6.A.2.

The predictor variables were centered, standardized, and the R package 'glmulti' (Calcagno and Mazancourt, 2010; Calcagno, 2011) was used to search for the model with lowest AICc in the same way described for Stage I (Section 6.A.4.), except that in this case the GLM model used a normal distribution with an identity link function (Fox, 2008).

The selected model structure was then fit to the data using Matlab Statistics Toolbox function 'glmfit', which implements standard Generalized Linear Model fitting by iteratively re-weighted least-squares (Bjorck, 1996; Fox, 2008). A normal distribution and identity link function were used. Use of the normal distribution here involves assumptions that are discussed in Section 6.A.14. Parametric ± 1 standard error uncertainty bounds on GLM estimates were calculated using Matlab function 'glmval' (following equations in Fox, 2008).

Because spatial autocorrelation biases the estimation of GLM parameters, we followed an iterative procedure to fit the final GLM in gstat (Pebesma, 1998; Chiles and Delfiner, 1999).

1. Calculate residuals and estimate residual variogram (see Section 6.8.).
2. Re-calculate fit with gstat, using residual variogram
3. Re-calculate residuals and repeat fitting with gstat (steps 2 and 3) until residual variogram has converged (determined by inspection).

A standard array of GLM diagnostics was produced, including effect tests, goodness-of-fit F tests, R^2 and several 'pseudo- R^2 ' measures to allow comparison with the Stage I logistic regression, residual leverage and influence plots, and a variety of other diagnostic measures (for details, see diagnostic tables in main text and Online Supplement 6.2).

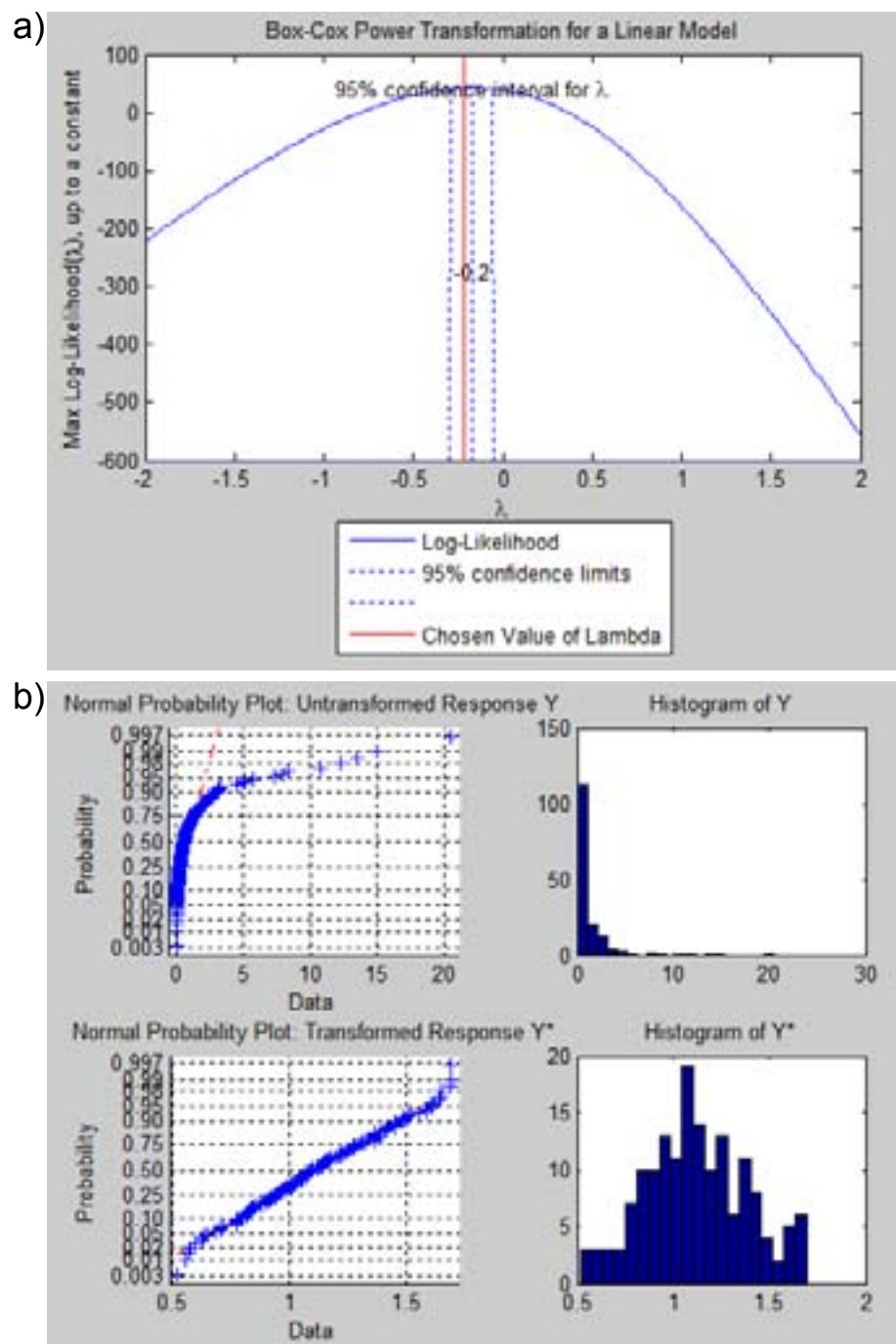


Figure 6.A.1 Box-Cox transformation of non-zero relative abundance (SPUE) data. Example for Dovekie in Winter. (a) selection by maximum likelihood procedure. (b) normal probability plots and histograms before and after transformation.

6.A.8. Stage II residual model

The residual component of the Stage II model, $\varepsilon_i''(x,y)$, was estimated as follows.

First, residuals from the trend model fit were calculated by subtracting the observed values from predicted values. Residuals were calculated in Box-Cox transformed space to satisfy normality assumptions of geostatistical methods. Residual variograms were then estimated and modeled using gstat, and Simple Kriging (SK) was used to produce a map of predicted residuals. The resulting map was the residual component of Stage II, $\varepsilon_i''(x,y)$.

Variogram models were fit automatically by a non-linear weighted least-squares minimization algorithm (Pebesma, 1998; Pardo-Igúzquiza, 1999), using weights proportional to N/h^2 (the number of pairs of observations used to estimate each observation divided by the square of the lag distance), as described by Pebesma (1998). Following standard geostatistical practice, the functional form of the variogram and an initial-guess parameter set was specified prior to the least-squares minimization by inspection of the empirical variogram (Issaks and Srivistava, 1989; Cressie, 1993; Deutsch and Journel, 1998; Chiles and Delfiner, 1999).

SK was also used to produce parametric estimates of uncertainty (kriging standard error) for each location in the residual prediction map (Pebesma, 1998; Deutsch and Journel, 1998).

6.A.9. Final Stage II model

In Box-Cox transformed space, the final Stage II model is simply the sum of trend and residual components:

$$E\{Z_i^{Transformed}(x,y) | P_i(x,y)=1\} = \mu_i''(x,y) + \varepsilon_i''(x,y) \quad \text{Eq. 8}$$

The result can be back-transformed to yield a prediction in the original units of SPUE:

$$E\{Z_i(x,y) | P_i(x,y)=1\} = \begin{cases} (E\{Z_i^{Transformed}(x,y) | P_i(x,y)=1\})^{1/\lambda}, & \text{if } \lambda \neq 0 \\ \exp(E\{Z_i^{Transformed}(x,y) | P_i(x,y)=1\}), & \text{if } \lambda = 0 \end{cases} \quad \text{Eq. 9}$$

Back-transforms were constrained to lie between 0 and 110% of the observed data maximum.

Parametric ± 1 SE confidence intervals for the final back-transformed Stage II model, $E\{Z_i(x,y) | P_i(x,y)=1\}$, were derived by applying Equations 8 and 9 to the parametric confidence intervals for $\mu_i''(x,y)$ and $\varepsilon_i''(x,y)$ calculated using the GLM model and the geostatistical (SK) model, respectively.

6.A.10. Final Stage I x II model

Stage I and Stage II models were combined as described in Section 6.A.1. (Equation 3) to produce each seasonal predictive map of the unconditional expected value of SPUE, which we will refer to as the "Stage I x II" prediction map or $E\{Z_i(x,y)\}$. Specifically, $E\{Z_i(x,y)\}$ is equal to the product of Equation 9 (the final back-transformed Stage II prediction) and Equation 7 (the final Stage I model prediction). Note that the Stage I x II predictions are in back-transformed units (SPUE).

Parametric uncertainty bounds (± 1 SE) for the final Stage I x II maps were obtained by plugging the confidence intervals for $\mu_i^I(x,y)$, $\varepsilon_i^I(x,y)$, $\mu_i''(x,y)$, and $\varepsilon_i''(x,y)$ described above into equations 7 and 9 and multiplying equation 7 by equation 9 for each set of uncertainty bounds.

6.A.11. Relative uncertainty calculations

In order to simplify comparison of uncertainties among different model components, uncertainties were converted to relative values that fall between 0 and 1, with 0 representing low uncertainty (high certainty) and 1 representing high uncertainty (low certainty). To further aid in interpretation, relative certainty classes were defined as follows: high certainty class (relative uncertainty ≤ 0.5), medium certainty class ($0.5 < \text{relative uncertainty} \leq 0.65$), and low certainty class (relative uncertainty > 0.65). The implications of a particular relative

uncertainty value or certainty class for model performance can be determined by examining the diagnostic tables in the main text, which give cross-validation performance error statistics for each certainty class, and the cross-validation relative uncertainty calibration plots in Appendix 6.C. (described in Section 6.A.12. below).

6.A.11.1. Stage I

The relative uncertainty of Stage I model predictions is expressed as the scaled negative log (odds ratio), *SNLOR*. The negative log odds ratio, *NLOR*, is the negative natural logarithm of the ratio of the odds of correct binary classification (absence= 0, presence= 1) using the Stage I model to the odds of correct binary classification under a null model:

$$NLOR = -\ln\left(\frac{Odds_{model}}{Odds_{null}}\right) \quad \text{Eq. 10}$$

To calculate the odds of correct classification under the Stage I model, $Odds_{model}$, we first consider uncertainty of the Stage I model prediction relative to the cutoff probability c used for binary classification (in this case, the optimal cutoff probability determined by ROC curve analysis). The uncertainty around the Stage I model prediction p can be modeled by a normal curve on the logit scale, with mean equal to the Stage I prediction and standard deviation equal to the larger of the upper and lower 1SE confidence intervals:

$$z_p \sim N(\text{logit}[p], \max(\text{logit}[p^{+1SE}] - \text{logit}[p], \text{logit}[p] - \text{logit}[p^{-1SE}])). \quad \text{Eq. 11}$$

Then the probability of the true predicted value lying above the cutoff probability c is given by

$$p_{above} = \text{Prob}(z_p > \text{logit}(c)), \quad \text{Eq. 12}$$

and the probability of the true predicted value falling below the cutoff probability is

$$p_{below} = \text{Prob}(z_p < \text{logit}(c)). \quad \text{Eq. 13}$$

The classifier itself is subject to error, which we estimate by its performance in cross-validation: the true positive (\hat{p}_{TP}), true negative (\hat{p}_{TN}), false positive (\hat{p}_{FP}), and false negative (\hat{p}_{FN}), rates of the classifier from the cross-validation confusion matrix at cutoff value c . The odds of correct classification using the Stage I model can then be calculated as:

$$SNLOR = \frac{\ln\left(\frac{Odds_{model}^{max}}{Odds_{null}}\right) - \ln\left(\frac{Odds_{model}}{Odds_{null}}\right)}{\ln\left(\frac{Odds_{model}^{max}}{Odds_{null}}\right) - \ln\left(\frac{Odds_{model}^{min}}{Odds_{null}}\right)} \quad \text{Eq. 14}$$

To calculate the odds of correct classification under a null model, $Odds_{null}$, we consider a null model in which the true and predicted presence/absence (1/0) states are given by Bernoulli random variables with probabilities p_1 (equal to the global prevalence of the species) and c (equal to the optimal cutoff probability from ROC curve analysis), respectively. Then the null odds of correct classification are:

$$Odds_{null} = \frac{p_{obs} \cdot \hat{p}_{TP} + p_{abs} \cdot \hat{p}_{TN}}{p_{obs} \cdot \hat{p}_{FP} + p_{abs} \cdot \hat{p}_{FN}} \quad \text{Eq. 15}$$

For a given set of cross-validation error rates (\hat{p}_{TP} , \hat{p}_{TN} , \hat{p}_{FP} , and \hat{p}_{FN}), the minimum and maximum possible values of the *NLOR* are:

$$Odds_{null} = \frac{(1-p_1) \cdot c + p_1 \cdot (1-c)}{(1-p_1) \cdot (1-c) + p_1 \cdot c} \quad \text{Eq. 16}$$

The scaled *NLOR*, *SNLOR*, is calculated so that *SNLOR*=0 at the minimum possible value of the *NLOR* and *SNLOR*=1 at the maximum possible value of the *NLOR*:

$$Odds_{model}^{min} = \min\left(\frac{\hat{p}_{TP}}{\hat{p}_{FP}}, \frac{\hat{p}_{TN}}{\hat{p}_{FN}}\right), \quad Odds_{model}^{max} = \max\left(\frac{\hat{p}_{TP}}{\hat{p}_{FP}}, \frac{\hat{p}_{TN}}{\hat{p}_{FN}}\right) \quad \text{Eq. 17}$$

Values of *SNLOR* closer to 0 indicate model predictions that have relatively high odds of being correct compared to a null model (high certainty), whereas values closer to 1 indicate model predictions that have relatively low odds of being correct compared to a null model (low certainty). Relative uncertainties were calculated in this way for the Stage I trend, Stage I residual, and the final Stage I model, using the cross-validation ROC curve cutoff c and cross-validation error rates (\hat{p}_{TP} , \hat{p}_{TN} , \hat{p}_{FP} , and \hat{p}_{FN}) determined from the ROC analysis of trend, residual, and final Stage I predictions, respectively. Below, the final Stage I relative uncertainty is denoted $\sigma^{I,rel}(x,y)$, and is equal to the value of *SNLOR* for the final Stage I model for species/group i at location (x,y) .

6.A.11.2. Stage II

Relative uncertainty of Stage II trend, residual, and final model predictions were calculated as the ratio of prediction variances to the appropriate error variance (trend prediction variance: total sample variance minus residual variogram sill; residual variance: residual variogram sill; final prediction variance: total sample variance). Below, the final Stage II relative uncertainty is denoted $\sigma^{II,rel}(x,y)$.

6.A.11.3. Stage IxII

The relative uncertainty of final Stage IxII model predictions was calculated by combining the relative uncertainties of final Stage I and Stage II models as follows:

$$\sigma_i^{IxII,rel}(x,y) = p_i(x,y) \cdot [\sigma_i^{II,rel}(x,y)] + (1-p_i(x,y)) \cdot \sigma_i^{I,rel}(x,y) \quad \text{Eq. 18}$$

The rationale behind equation 18 is that the Stage II relative uncertainty applies if the species is present (which is true with probability $p_i(x,y)$), whereas the Stage I relative uncertainty applies if the species is absent (which is true with probability $[1-p_i(x,y)]$).

6.A.12. Model evaluation and uncertainty calibration

In addition to the standard GLM effect tests and diagnostics, model predictive performance was evaluated in and out of the training set using a variety of error statistics, error plots and ROC curve analysis. As a final summary of model performance in cross-validation and aid to the reader in interpreting relative uncertainty values for the final Stage IxII model, an uncertainty calibration plot was produced. For each location in the holdout set, the model developed from training data was used to predict the value at that location, and the magnitude of the difference between actual and predicted values (absolute error) was plotted versus the Stage I x II relative uncertainty value (Appendix 6.C.). Robust linear loess smoothing lines (Burkey, 2009) are plotted to show how actual out-of-set average prediction errors relate to parametric relative uncertainty estimates. Separate lines are plotted for overall error, and error when the species or group was present (since most species are relatively rare in any given survey, presences are harder to predict than absences). Similar relative uncertainty calibration plots are produced for Stage I predictions (presence/absence).

Uncertainty calibration plots, ROC analyses, error statistics, and other model evaluation diagnostics are included in the diagnostic tables in the main report, in Appendix 6.C., and in Online Supplement 6.2.

6.A.13. Combination of seasonal climatological maps to produce annual climatological maps

For each species and species group i , seasonal maps of climatological SPUE (Stage IxII predictions) were combined to produce annual maps as follows:

$$E\{Z_i(x,y)\}^{annual} = \sum_{\text{all seasons } j} E\{Z_i(x,y)\}_j \quad \text{Eq. 19}$$

Using the laws of probability and the expectation operator (Ross, 2007), this procedure can be shown to yield an unbiased estimate of the SPUE prediction for the entire year, given that (1) each seasonal model prediction is the unconditional expected value of SPUE, $Z_i(x,y)$, and, (2) the seasons are defined as non-overlapping and together cover the entire climatological year. These two conditions are true by definition.

Annual integrated presence probability maps were produced by combining the seasonal climatological presence probability predictions (Stage I predictions), assuming statistical independence of the seasonal probabilities. Given 4 seasons, there are 15 possible ways in which a species or group can be present in at least one season. Represented as four digit binary codes, these are: 1000, 0100, 0010, 0001, 1100, 1010, 1001, 0110, 0011, 0101, 1110, 1011, 1101, 0111, 1111. The probabilities of each of these outcomes was summed to produce the annual integrated presence probability, $p_i(x,y)^{\text{annual}}$, which is equivalent to the annual climatological site occupancy probability for species/group i each location (x,y) .

To estimate the relative uncertainty associated with each annual map, the weighted average of the corresponding seasonal relative uncertainty maps was calculated, using the frequencies of occurrence of the species in each season as weights. For the annual SPUE map the relative uncertainty is given by:

$$\sigma_i^{\text{all,rel}}(x,y)^{\text{annual}} = \sum_{\text{all seasons } j} \left[\frac{\sigma_i^{\text{all,rel}}(x,y) \cdot f_{i,j}}{\sum_j f_{i,j}} \right] \quad \text{Eq. 20}$$

For the annual integrated presence probability map relative uncertainty, the relative uncertainty is given by:

$$\sigma_i^{\text{rel}}(x,y)^{\text{annual}} = \sum_{\text{all seasons } j} \left[\frac{\sigma_i^{\text{rel}}(x,y) \cdot f_{i,j}}{\sum_j f_{i,j}} \right] \quad \text{Eq. 21}$$

It can be shown that these relative uncertainties are monotonically related to the variance of the annual prediction error, but this relationship will not necessarily be linear for two reasons (Ross, 2007):

1. The relative uncertainty of Stage I predictions is based on a log-odds ratio, and,
2. Seasonal estimates of $Z_i(x,y)$ may not be uncorrelated, and therefore summation of variances, unlike summation of expected values, is not necessarily a linear operator.

Thus we rely on uncertainty calibration plots (plots of cross-validation error vs. relative uncertainty, Section 6.A.12.) to interpret the precise meaning of the relative uncertainty value for each species/group annual model.

6.A.14. Summary and implications of model assumptions

The seasonal predictive modeling approach described above makes a number of assumptions. To the extent these assumptions are violated, accuracy of predictions and uncertainty estimates may suffer. In this section we briefly review the major assumptions and their implications. The degree to which violations of model assumptions affect the performance of any given seasonal model can be assessed by considering the cross-validation performance statistics described in 6.A.12 and reported in the main text diagnostic tables, Appendix 6.C, and Online Supplement 6.2.

Important general assumptions:

- *Stationarity of pattern over time within seasons and among years*
Statistically, stationarity in this context means that the region-wide mean, variance, and spatial structure of abundance and occurrence patterns do not change over the time period we studied. Ecologically, stationarity implies that the ecosystem has not undergone any fundamental shifts in patterns and processes (e.g., climate trends, ocean climate regime shifts, introduced species, changes in patterns

of human activities like fishing). If this assumption is violated, temporal variation will show up as non-spatially structured error (“white noise”) in the model result. Model parameters and predictions may also be biased (cross-validation errors will not be centered at 0). The predicted spatial pattern may be an amalgam of different patterns that occurred at different time periods (e.g., “smearing” of hotspots that moved from year to year). If there are major changes in the underlying processes, the model will also be less generalizable to other time periods.

- *Stationarity of environmental predictor climatologies*
The use of long-term climatologies of time-varying environmental predictors (such as SST and stratification), assumes that the long-term seasonal mean spatial patterns of these variables have not changed over time. Major changes in the underlying environmental patterns and processes will make the model less generalizable to other time periods.
- *Unbiased year-to-year sampling (no temporal effect included)*
If the sampling pattern is non-random within seasons and/or across years, GLM parameter estimates and parametric uncertainties could be biased and inaccurate. This problem will be exacerbated if the assumptions of temporal stationarity of predictors and response are also violated. The Manomet survey was conducted on ships of opportunity, so samples were not random in space or time; therefore some biases due to unbalanced effort are expected.
- *Perfect detectability; freedom from other kinds of sample bias*
To the extent that a given species or species group is not perfectly detectable by the sampling protocol, relative occurrence and abundance indices will be biased compared to true abundance and occurrence values. Predictions from this model should be considered relative, rather than absolute, estimates of occurrence and abundance. In addition to detectability, similar biases can result from attraction of certain species to the survey platform (boats). Finally, systematic study biases may exist in the types of species that were recorded. For example, we found very few records of passerines in the Manomet dataset, even though there is evidence of offshore sightings of these species from other sources. These and other birds that are rare but not absent in the offshore may require other survey and modeling approaches if they are of conservation concern.
- *Constant relationship between sampling effort, relative indices of occurrence and abundance, and true values of occurrence and abundance*
Not only are species unlikely to be perfectly detectable, the relationship between our relative indices of occurrence and abundance and the true values of occurrence and abundance could vary in time and space, depending on differences in observers, weather conditions, animal behavior, etc. Such variation introduces an un-accounted for source of measurement error into data.

Important Stage I assumptions

- *Binomial distribution and logit link function*
To the extent that these distributional assumptions are violated, trend predictions may be biased and parametric confidence intervals inaccurate.
- *Use of receiver operating characteristic (ROC) curve optimal cutoff analysis to classify residuals from the trend model*
Use of the ROC classifier may introduce bias into the final presence probability estimates at the expense of balancing overall sensitivity and specificity.
- *Symmetry assumption for misclassification probability field*
Misclassification of absences as presences may not show the same spatial pattern as misclassification of presences as absences; if that is the case, then model predictions may be biased and the model may perform better for one type of misclassification than for others, even though parametric uncertainty estimates are the same.

Important Stage II assumptions

- *Normality and linearity of Box-Cox transformed predictors and responses in the Stage II trend model*
We assume that the Box-Cox transform in Stage II is sufficient to achieve normality of residual variances

and linearity of underlying response-predictor relationships. Since the underlying seabird relative abundance data are based on counts (divided by transect area to create a quasi-continuous density estimate), this requires that we assume the continuous Box-Cox transformed Gaussian distribution used to represent non-zero relative abundance is an adequate approximation to the underlying discrete probability distribution. The appropriateness of these assumptions is difficult to test directly and the reader should rely on cross-validation performance statistics to judge the extent to which these assumptions were approximately correct.

- *Trans-Gaussian assumption in the Stage II residual (geostatistical) model*
Simple Kriging also assumes approximate normality; therefore the adequacy of the Box-Cox transformation to achieve normality of the residual distribution is also important to the accuracy of the kriging prediction (especially the validity of the kriging variance).
- *Back-transform issues (extrapolation of the CDF tail)*
When back-transforming Stage II predictions, we have arbitrarily cut off the upper end of the distribution at 110% of the data maximum, which may not always be appropriate. This is only expected to influence the highest predicted values.

Important Stage IxII assumptions

- *Separability of abundance and presence/absence patterns*
We have assumed that abundance is conditionally independent of presence/absence (that is, abundance can be modeled independently of presence probability). If this assumption is violated, then the Stage IxII estimates will be biased. The direction of this bias will depend on the sign of the dependence, and on the Box-Cox transformation parameter. The degree of bias in predictions can be assessed (and corrected for) by examining cross-validation bias statistics in the diagnostic tables.

Important assumptions of annual maps

- *Seasonal estimates of expected SPUE, $Z_i(x,y)$, are uncorrelated with each other.*
If seasonal estimates of SPUE are positively correlated with each other, then the summation of unconditional expected values will still be correct but the relationship between actual prediction error and the predicted relative uncertainty value will be affected. The cross-validation uncertainty calibration plots should be used as a guide to the true relationship between relative uncertainty and prediction error for each annual model.
- *Seasonal estimates of presence probability $p_i(x,y)$ are independent of each other.*
If presence probabilities are not independent from season to season, then the integrated annual presence probability maps will over or underestimate annual site occupancy probability, depending on the sign of the dependence.

Appendix 6.B. Environmental Predictor Variables

6.B.1. Overview

The set of 11 potential predictor variables considered in this study are listed in the body of this chapter (Section 6.8.5.) and the statistical transformations applied prior to inclusion in regression models are discussed in Appendix 6.A. (Section 6.A.2.). This appendix provides additional detail about the potential predictor variables, including maps of each predictor before and after the transformations discussed in Appendix 6.A were applied (Figures 6.B.1 through 6.B.11). Additional detail about the choice of transformations is provided in Online Supplement 6.1.

6.B.2 Bathymetry and coastline (BATH, SLOPE, SLPSLP, DIST, SSDIST)

Depth data was extracted from the 3 arc-second (approximately 84 m in our study area) horizontal resolution NOAA U.S. Coastal Relief Model (CRM) (NOAA National Geophysical Data Center [NGDC] 2010), and merged with the 1 arc-minute (approximately 1.6 km in our study area) ETOPO1 database (Amante and Eakins 2009) in offshore areas not covered by the CRM (the ETOPO1 database was projected to match the CRM and bilinearly resampled to the 83.9 m CRM cell size prior to merging). See Chapter 2 for more information about different bathymetry datasets in this region. Depths below the MLLW vertical datum were negative. Depths greater than +2 in the CRM dataset (i.e., elevations of 2 meters above MLLW or higher) were set to +2. The merged dataset was then reprojected to geographic coordinates (WGS84 datum) and smoothed (rectangular block-average using the centroids of the 83.9m grid cells) to the 30 arc-second model grid. Any cells whose block-averaged depth value at the final 30 arc-second resolution was >0 were set to 0, so that all depth values were <=0.

To reduce the amplitude of potential artifacts from merging and resampling of bathymetry datasets, to reduce the influence of outlier points known to exist in both CRM (NOAA NGDC 2010) and ETOPO1 (Amante and Eakins 2009) datasets, and to allow for the likely imprecision of any possible influence of bottom topography on above-surface bird distribution, the 30 arc-second merged bathymetry grid was reprojected to the UTM18N coordinate system, resampled bilinearly to the original 83.9m CRM grid resolution, filtered with a 21x21 cell (1.8 x 1.8 km) Gaussian blur kernel ($1\sigma = 220$ m; filter calculated to 4σ and weights re-normalized to sum to 1) (Gonzalez and Woods 1992) and then rectangular block-averaged back to the 30 arc-second grid, using centroids of the 83.9m projected grid to identify block members. The result was the BATH predictor grid.

Slope was calculated on the filtered bathymetry while still at 83.9 m resolution, as the maximum percentage change

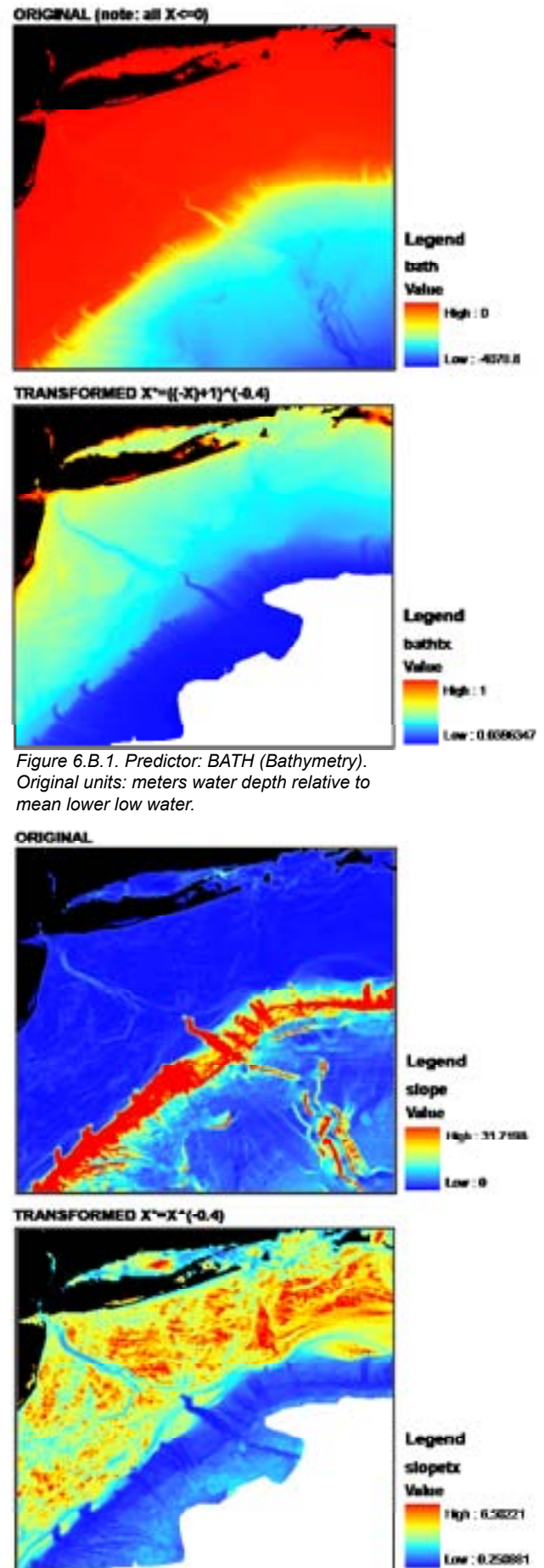


Figure 6.B.1. Predictor: BATH (Bathymetry). Original units: meters water depth relative to mean lower low water.

Figure 6.B.2. Predictor: SLOPE (Bathymetric slope). Original units: %

in depth from each 30 arc-second grid cell to its 4 neighbors. The calculated slope was then filtered again with a 21x21 cell Gaussian blur kernel and a 21x21 cell box kernel. The result was rectangular block-averaged back to 30 arc-second grid, resulting in the SLOPE predictor grid.

Slope-of-slope was calculated as the slope of the doubly filtered slope grid while still at 83.9 m resolution. This calculation was subsequently filtered with a 21x21 cell Gaussian blur kernel and a 21x21 cell box kernel, and block-averaged to the 30 arc-second grid, resulting in the SLPSLP predictor grid.

As a result of the filtering and block-averaging operations, the bathymetry, slope, and slope-of-slope predictor values in each 30 arc-second grid cell represent a weighted average of "local" bottom topographic characteristics. In the case of BATH, information in each focal grid cell can come from up to 1.6 km away from the grid centroid (using 3σ as the effective cutoff distance of the Gaussian filter). In the case of SLOPE, due to additional filtering steps, information in each focal grid cell can come from up to 3.1 km away from the centroid. In the case of SLPSLP, this distance is 4.7 km. Thus these three predictors, in addition to quantifying different features of benthic topography, also contain information deriving from several different topographic scales.

Error statistics of bathymetry derived from the same underlying data as the CRM are described in Chapter 2 of this report, and bathymetric uncertainty for this region has also been studied by Calder (2006). Slope and slope-of-slope have additional error because they are multiple-point statistics. Over most of the study area, relative errors will typically be <5% for depth, <10% for slope, and <20% for slope-of-slope.

Distance from shore (DIST) was calculated by measuring the shortest straight-line distance (in km in UTM18N projected coordinates) from the centroid of each grid cell to the 1:250,000 World Vector Shoreline (Soluri and Woodson 1990), which was found to agree within ± 0.5 km with the contour of the 0 m isobath in the original CRM bathymetry dataset in our study region, and thus considered of sufficient accuracy given the chosen grid resolution. For grid cells whose centroids fell on land, distance to shore was set to 0. Distance from shelf edge (SSDIST) was calculated by measuring the shortest straight-line distance (in km in UTM18N projected coordinates) from the centroid of each grid cell to the shelf edge, defined as the 200 m isobath. Distances from grid cells offshore of the 200 m

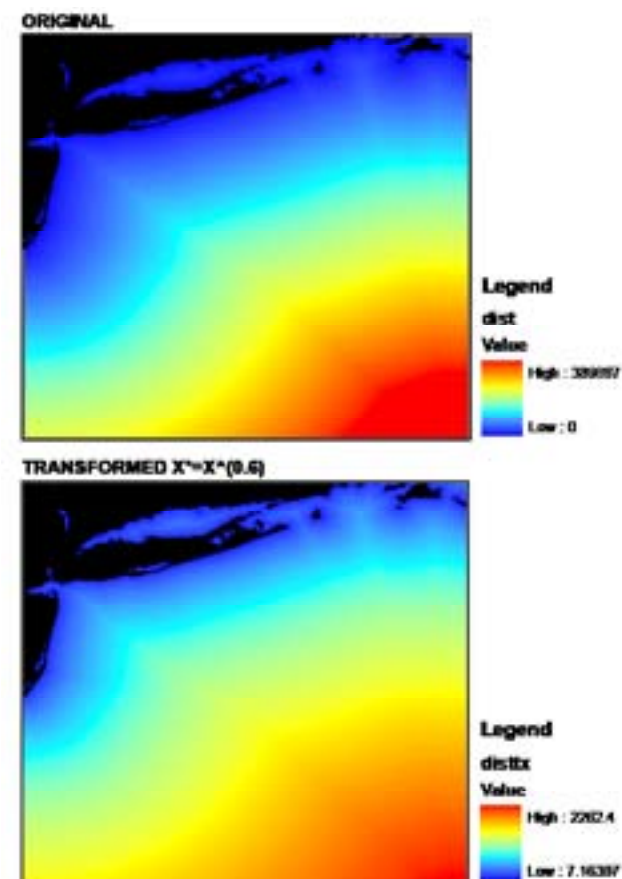


Figure 6.B.3. Predictor: DIST (Distance from shore). Original units: meters.

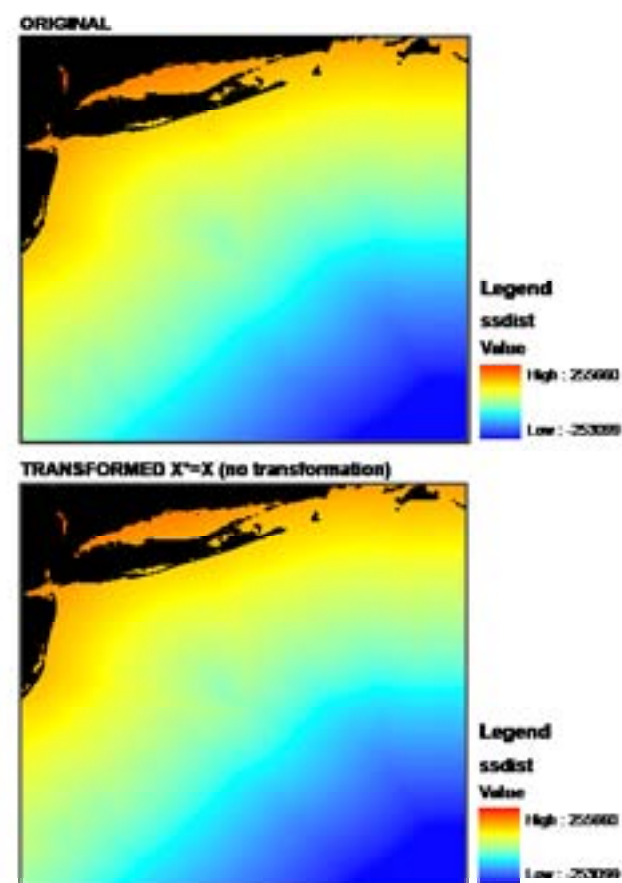


Figure 6.B.4. Predictor: SSDIST (Signed distance from shelf-break). Original units: meters.

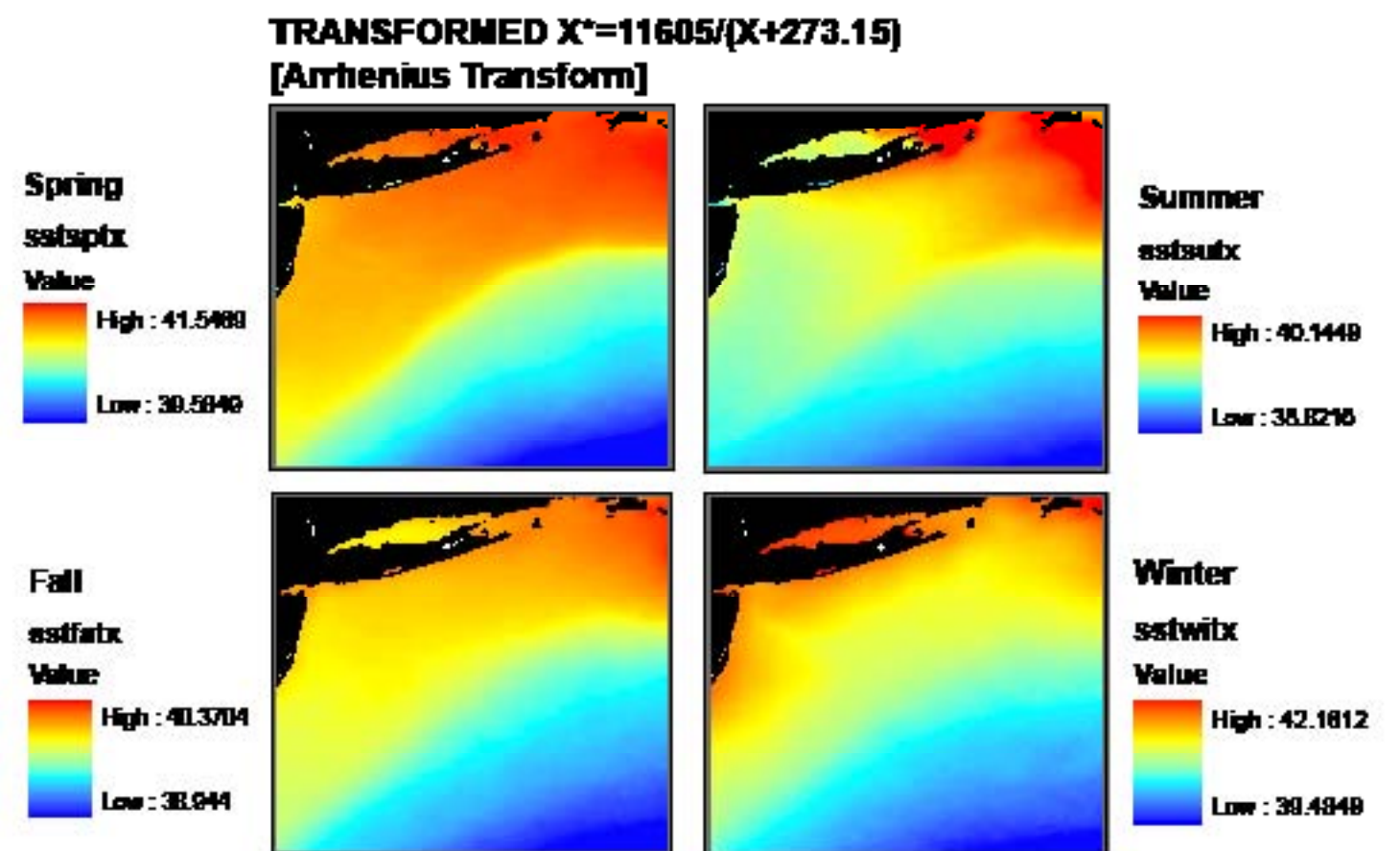
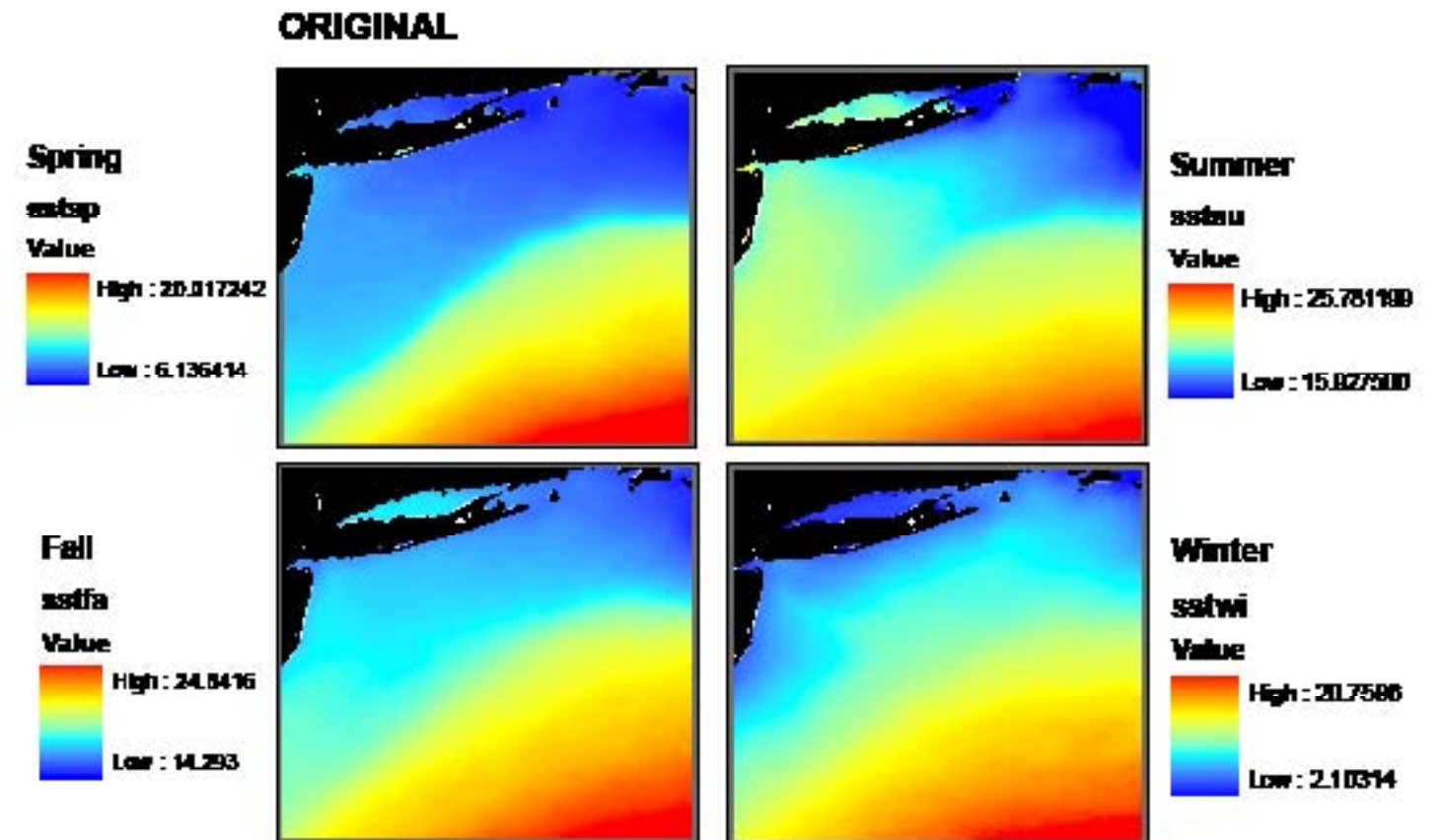


Figure 6.B.5. Predictor: SST (Sea Surface Temperature). Original units: °C

isobaths were assigned a negative sign, whereas distances from inshore cells were assigned positive signs. For purposes of this measurement a line feature representing the -200 m isobath contour was created by contouring the merged, smoothed bathymetry product using ESRI Spatial Analyst's contour tool. Although these distances were measured in the projected UTM18N system, their values were recorded on the same 30 arc-second model grid as other variables, and represent distances from the geographic centroids of those grid cells. Based on the scales and uncertainties of the source data, errors in these distances are of the order 0.5-2 km, or about 1 to 2%.

Finally, a land mask was created by finding cells of the 30 arc-second model grid within which $\geq 51\%$ of the contained CRM values (based on centroids) had positive depth values (i.e., land). Model predictions were not produced for these predominantly land-covered grid cells.

6.B.3 Benthic surficial sediments (PHIM)

The USGS usSEABED bottom sample database for the Atlantic coast of the US (Reid et al., 2005) was used as described in Chapter 3 of this report to create gridded maps of mean ϕ (where $\phi = \text{Log}_2[\text{surficial sediment grain size in mm}]$). Dr. John Goff kindly provided a quality-controlled version of the merged usSEABED parsed and extracted datasets, which included unpublished updates to the usSEABED database, selected only surficial sediment records, eliminated duplicates and spurious records, and applied the bias correction of Goff et al. (2008) to the parsed values. Goff's quality-controlled dataset of mean ϕ estimates was interpolated using ordinary kriging (with locally quadratic trend) to produce estimates of mean ϕ on the 30 arc-second model grid (PHIM). See Chapter 3 for characterization of uncertainty in of mean grain size predictions.

6.B.4 Pelagic environmental variables (STRT, SST, TUR, CHL, ZOO)

Seasonal climatologies of the following pelagic environmental variables were taken from Chapter 4 of this report (Section 4.3). These variables included water column stratification (STRT) from optimally-interpolated vertical profiles of temperature and salinity, sea surface temperature (SST) from satellite data, surface chlorophyll-a concentration (CHL) and a turbidity proxy (TUR) from satellite ocean color data, and zooplankton biomass from near-surface plankton tows (ZOO).

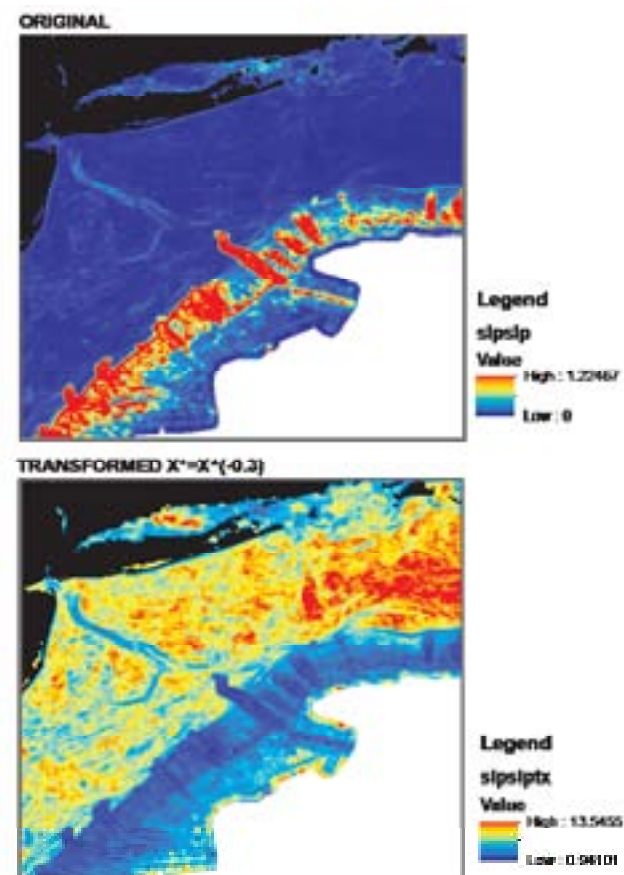


Figure 6.B.6. Predictor: SLPSLP (Slope of the bathymetric slope). Original units: % of %.

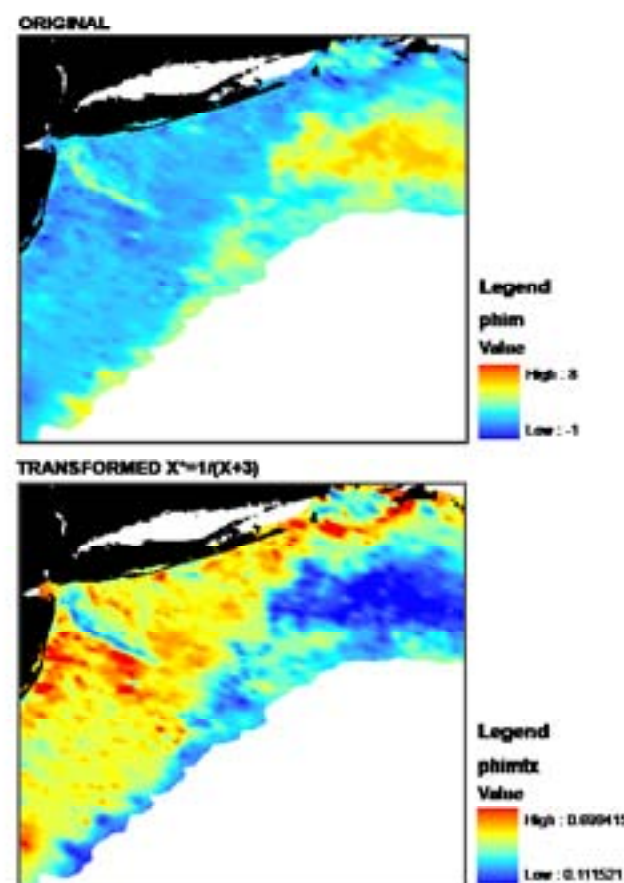


Figure 6.B.7. Predictor: PHIM (Mean phi of surficial sediments). Original units: mean \log_2 (grain size in mm) of surficial sediments.

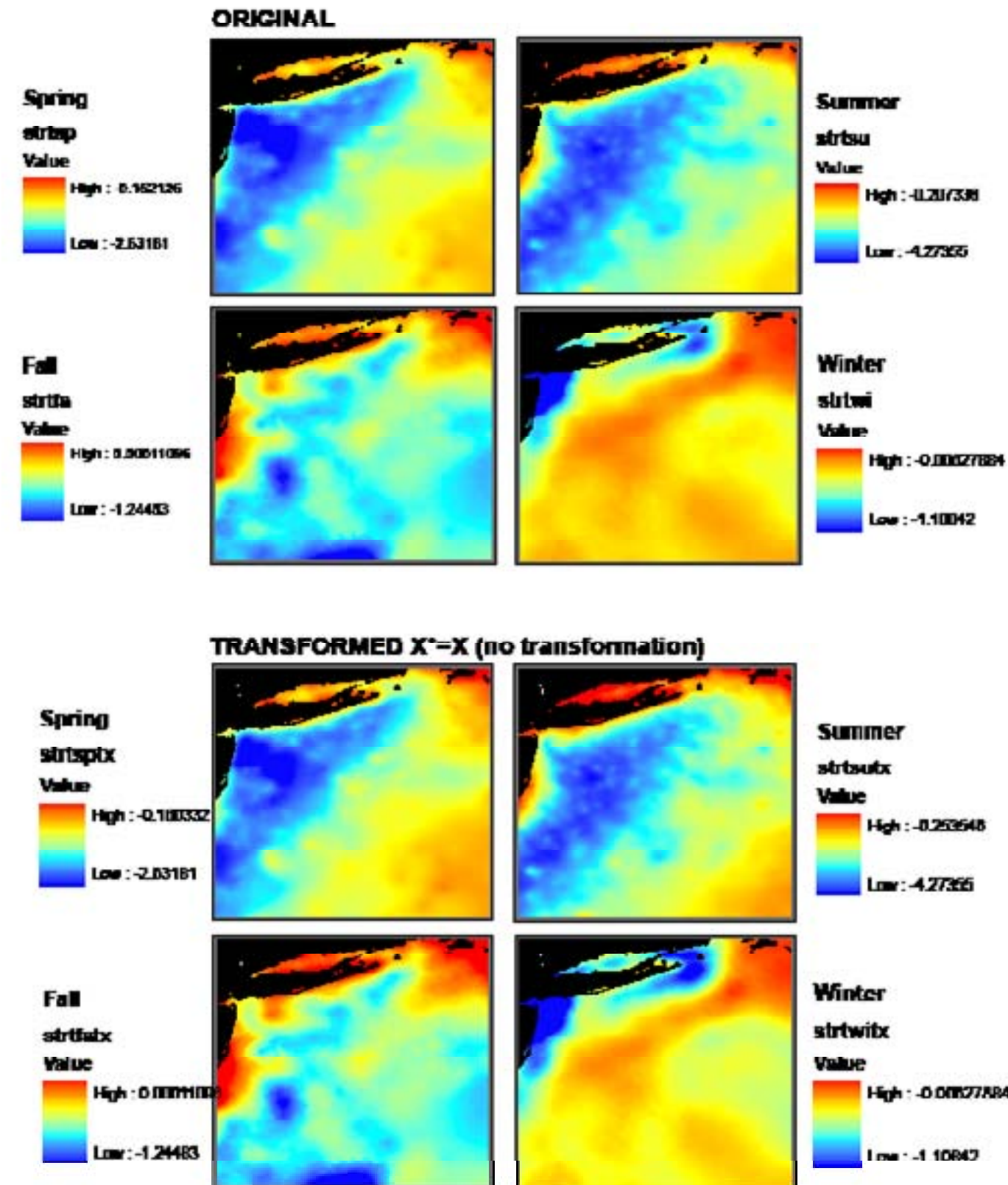


Figure 6.B.8. Predictor: STRT (Water-column Stratification). Original units: long-term climatological average stratification, measured as surface seawater density (kg m^{-3}) minus density at 50 m. More negative values indicate stronger stratification.

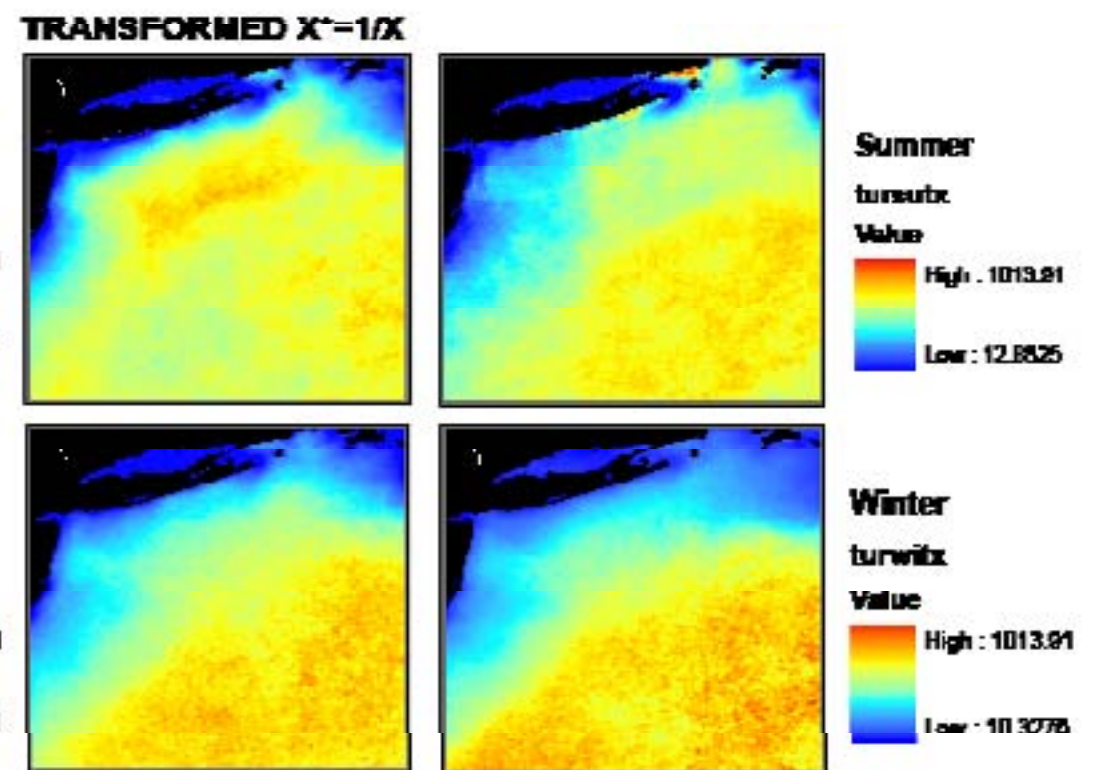
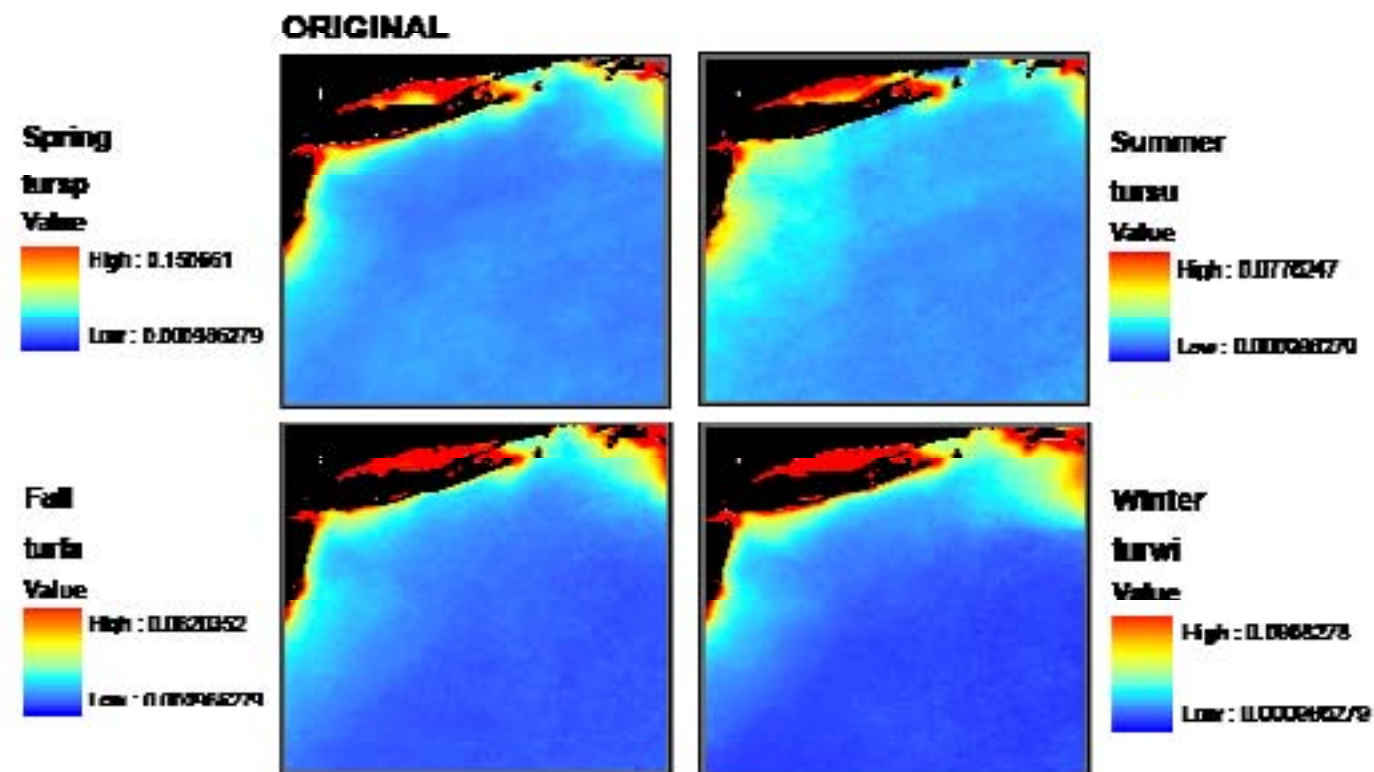


Figure 6.B.9. Predictor: TUR (Turbidity proxy). Original units: Normalized water-leaving radiance at 670 nm.

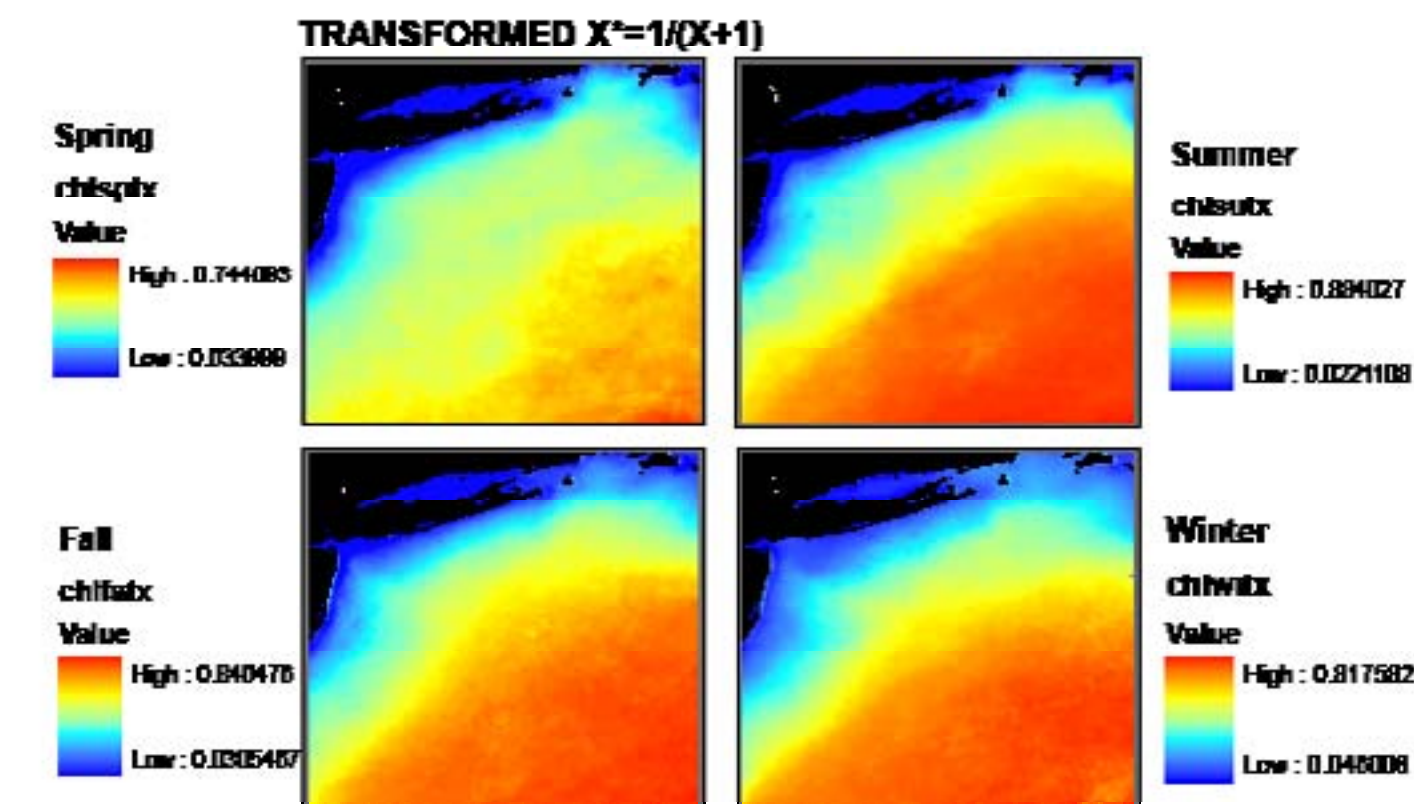
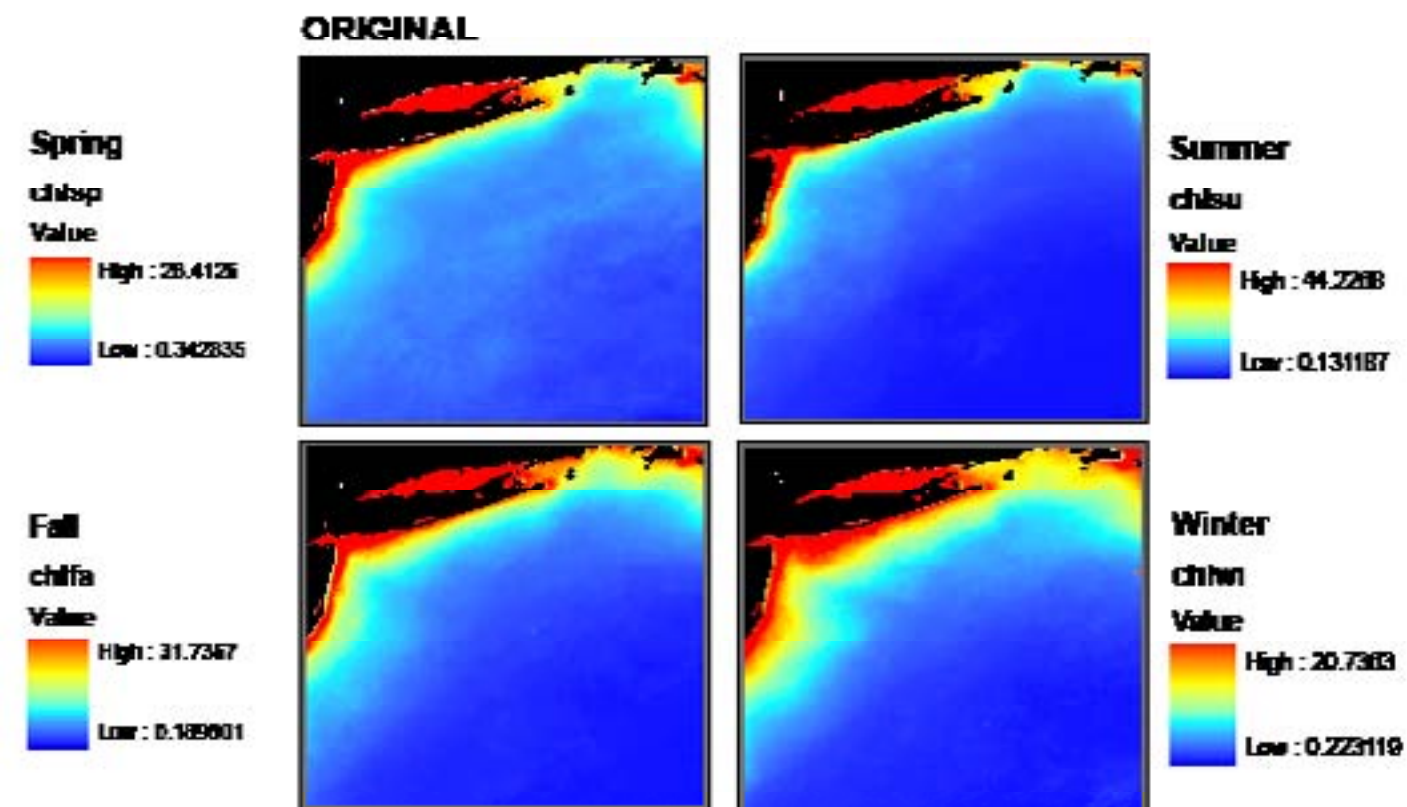


Figure 6.B.10. Predictor: CHL (Surface chlorophyll-a concentration). Original units: $mg\ m^{-3}$

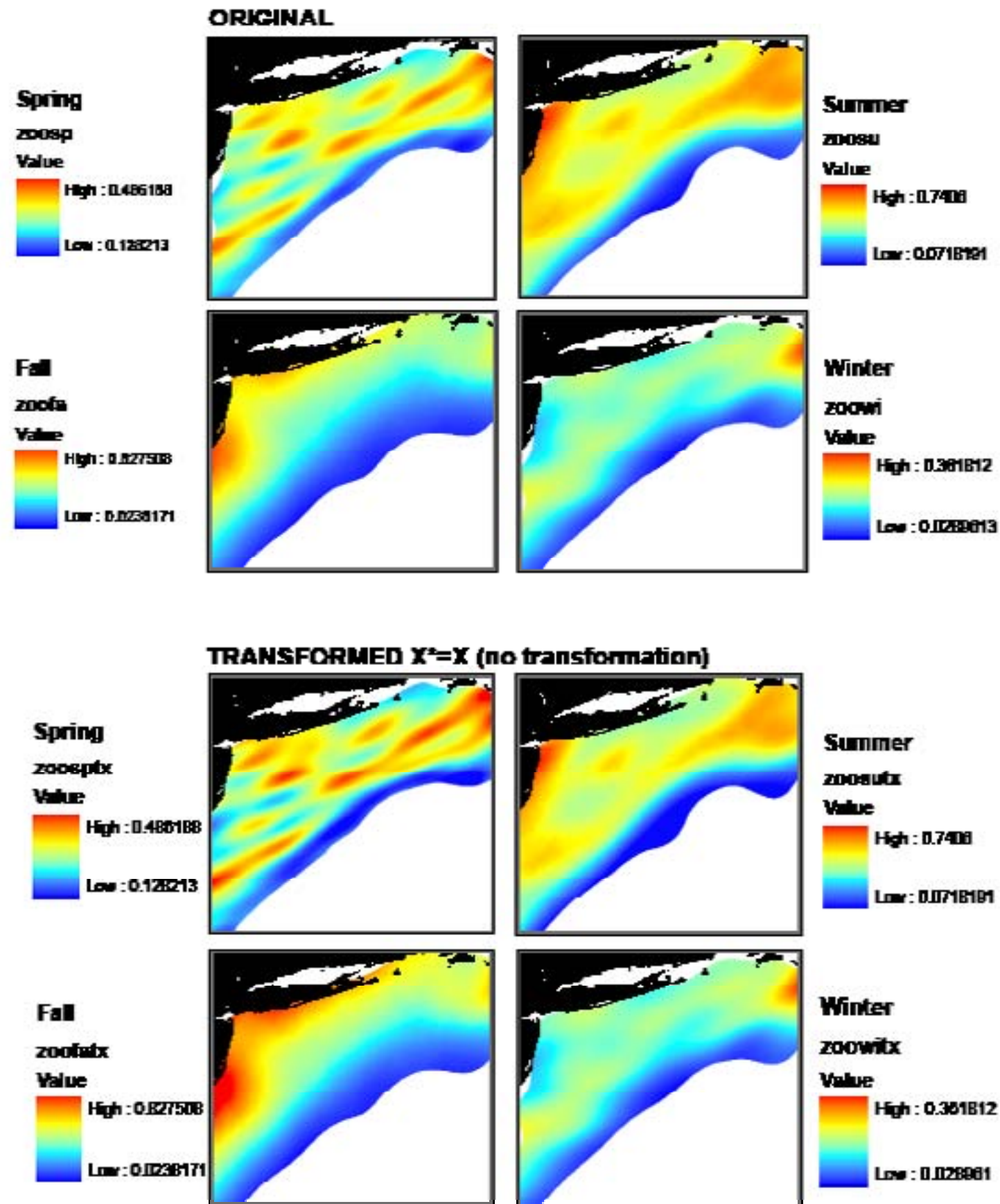


Figure 6.B.11. Predictor: ZOO (Zooplankton biomass). Original units: mean displacement volume per volume of water strained (ml m⁻³).

Appendix 6.C. Species and Group Seasonal Profiles

Black-legged Kittiwake	172
Common Loon	174
Common Tern	176
Cory's Shearwater	178
Dovekie	180
Great Black-backed Gull	182
Great Shearwater	184
Herring Gull	186
Laughing Gull	188
Northern Fulmar	190
Northern Gannet	192
Pomarine Jaeger	194
Sooty Shearwater	196
Wilson's Storm-Petrel	198
'No birds sighted'	200
Alcids, less common	202
Coastal Waterfowl	204
Jaegers	206
Phalaropes	208
Shearwaters, less common	210
Small Gulls, less common	212
Storm-Petrels, less common	214
Terns, less common	216
Unidentified Gulls	218
Non-modeled Groups	220
Cormorants (2 species)	220
Skuas, less common	220
Rare Visitors (10 species)	220

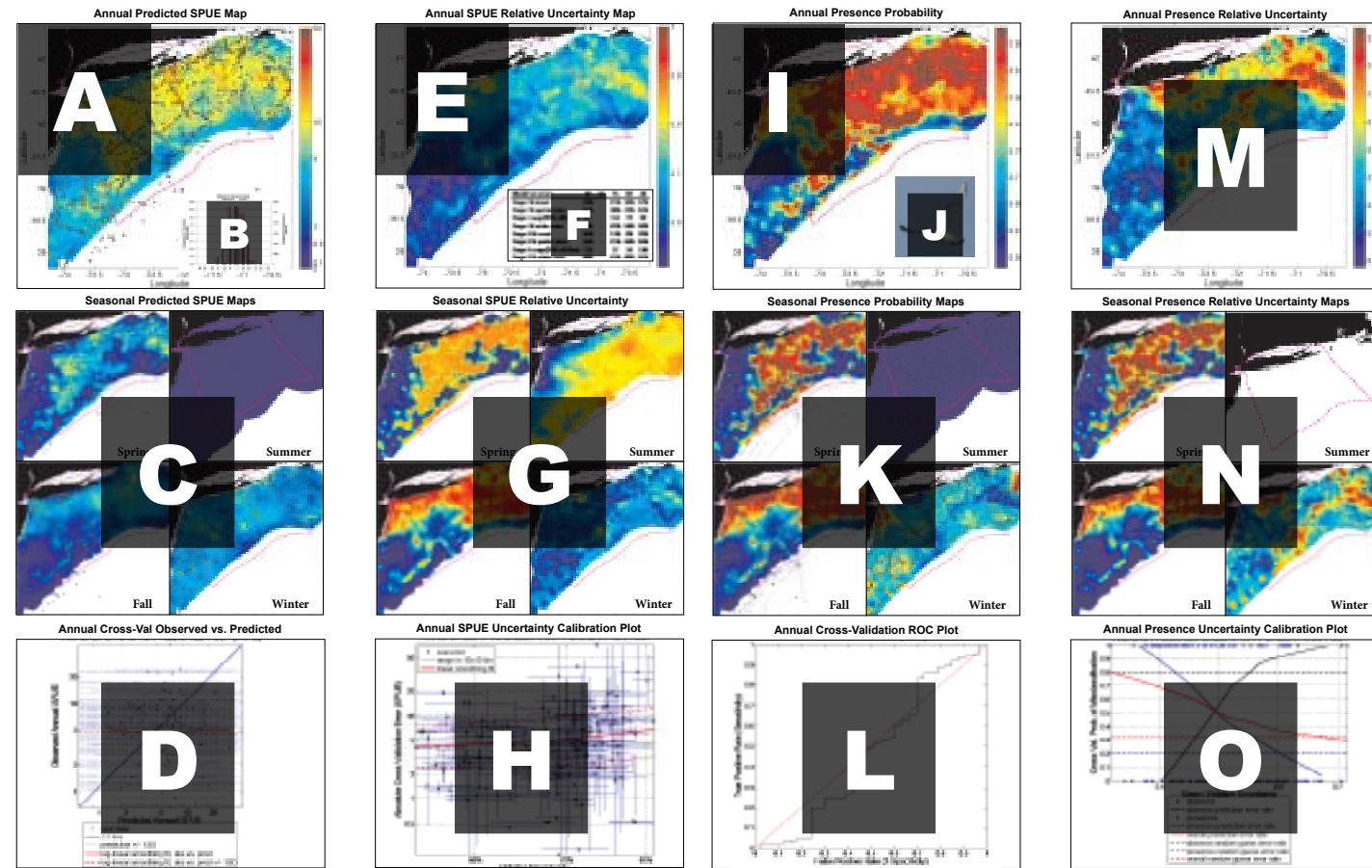


Figure 6.C.1. Guide to the elements presented in each species/group seasonal model profile. A shrunk-down image of an example two-page model profile spread is shown, with capital letters marking the different graphic elements as they are described in Section 6.C.1.

6.C.1. Profile interpretation guide

This appendix presents two-page profiles for each modeled species and group giving more detailed results of predictive models of abundance and presence/absence. In each profile, the annual and seasonal predictive maps are shown with original data points overlaid for comparison, annual and seasonal maps of relative model uncertainty are given, separate maps are shown for abundance (sightings per unit effort, SPUE) and for occurrence (probability of presence), and model fit and model uncertainty plots based on cross-validation are provided to help assess model accuracy.

Rather than number and caption each figure and table in these profiles repetitively, we have developed this profile interpretation guide that explains each element of the 24 two-page profiles that follow. Figure 6.C.1 (above) is a schematic illustration of the layout of each profile. The large white letters in transparent black boxes indicate each element of the layout. Each element, lettered A through O, is explained below:

- A.** Annual climatological (long-term average) predictive map of relative abundance. SPUE is used as a proxy for abundance. Cool colors represent low and warm colors represent high SPUE. Land is represented by black, areas with insufficient data to make a prediction are white, and the offshore planning area identified by New York DOS is shown by a dotted magenta line. All non-zero SPUE data (training and validation datasets) are overlaid as colored dots on the same colorscale as the gridded SPUE predictions.
- B.** Monthly pattern of occurrence - Temporal histogram showing frequency of occurrence by month. Data is presented from two complementary sources to more fully capture pelagic and nearshore species. The Manomet dataset (red bars) was collected offshore by ship-based surveys and the eBird dataset (blue bars) consists mostly of onshore and nearshore surveys. Differences between histograms from the two datasets may represent an onshore-offshore distributional gradient.

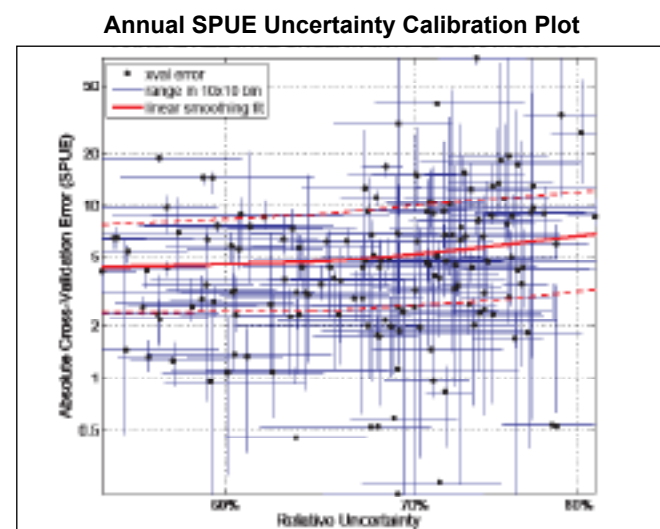
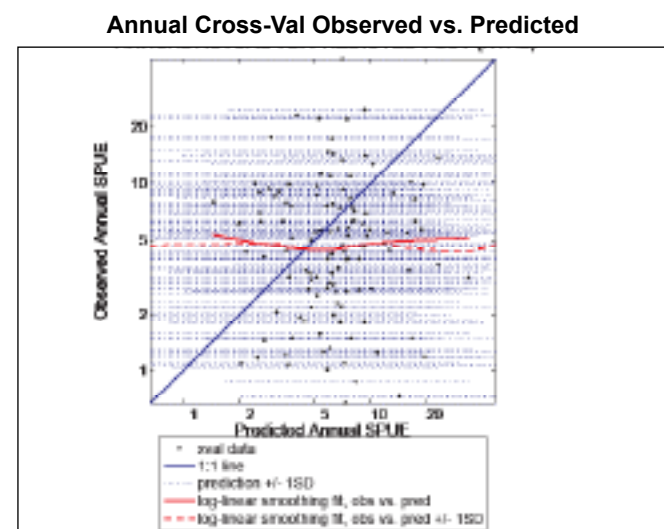
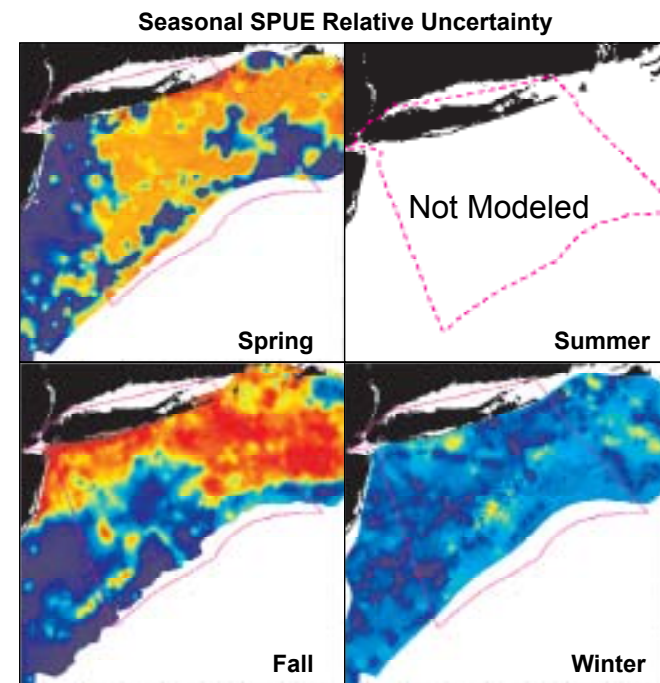
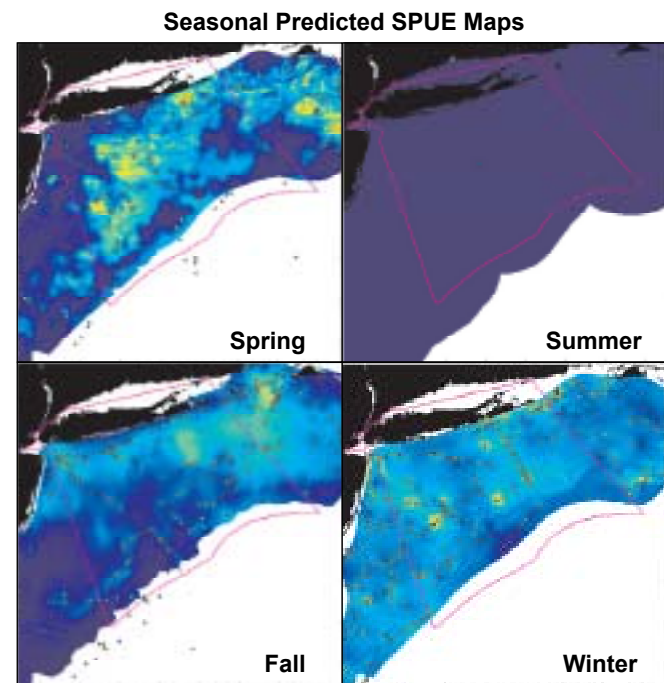
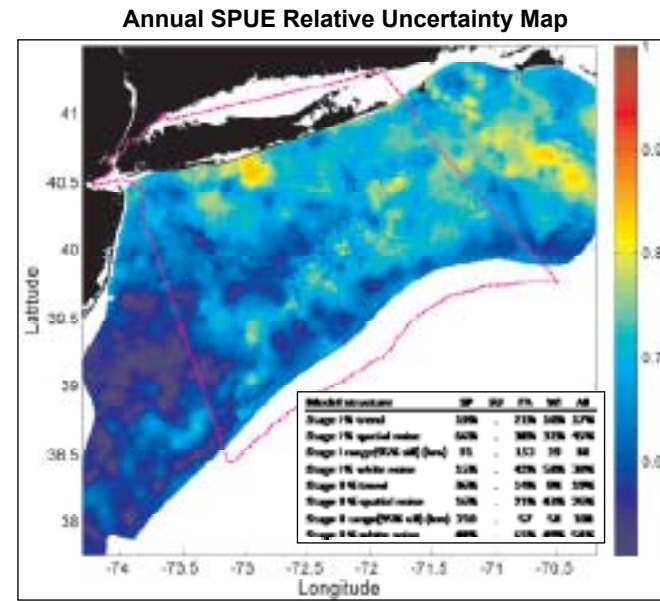
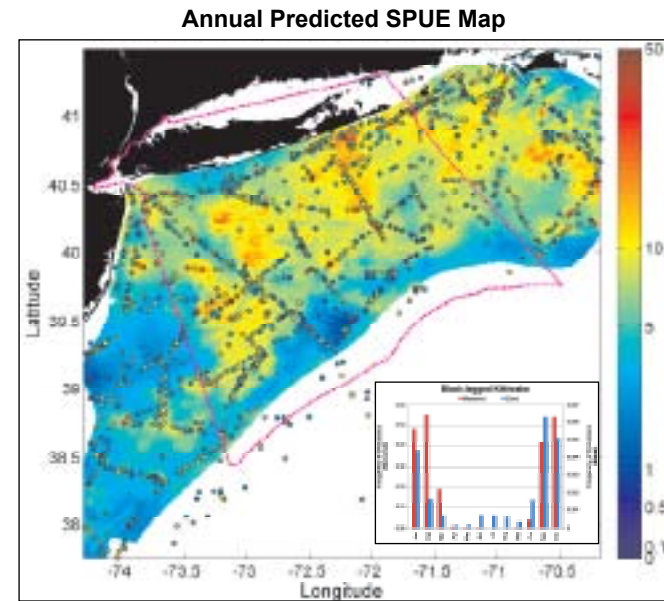
- C.** Seasonal climatological (long-term average) predictive maps of relative abundance (SPUE, No. indiv. / km² / 15-min). All non-zero SPUE data (training and validation datasets) for each season are overlaid as colored dots on the same colorscale as the gridded SPUE predictions.
- D.** Cross-validation Observed vs. Predicted plot (mean observed vs. mean predicted SPUE in 10x10 cell bins [~9x9 km]). Binning was necessary because cross-validation data points did not exactly coincide across seasons.
- E.** Distribution of mean relative uncertainty – Map showing relative uncertainty in the Stage IxII predictive model. Uncertainty is a function of distance from survey locations, spatial autocorrelation and accuracy of the trend regressions. Relative uncertainty values closer to 0 represent predictions that are expected, on average, to have lower error; values closer to 1 represent predictions that are expected, on average, to have greater error.
- F.** Model structure table, showing percentages of variance attributable to each component of the model and the length scales of spatial autocorrelation, for each season and averaged over all seasons.
- G.** Seasonal relative uncertainty maps. See Appendix 6.A., Section 6.A.11.
- H.** Cross-validation relative uncertainty calibration plot for annual SPUE (using mean predicted abundance and the mean value of the annual Stage IxII relative uncertainty for each 10x10 cell [~9x9 km] bin). See Appendix 6.A., Section 6.A.12. for details.
- I.** Annual integrated predicted probability of presence. Probability of species being present in at least one of the modeled seasons. See Appendix 6.A., Section 6.A.13. for details. Seasons modeled for each species are shown in Table 6.6.
- J.** Representative photo of species or one species in a species group.
- K.** Seasonal predicted probability of presence (Stage I final model prediction). Absence data are indicated by small black dots, and presence data are indicated by larger open black circles.
- L.** Annual cross-validation ROC plot for presence/absence prediction, using maximum probability in 10x10 cell bins [~9x9 km] as the predictor of whether at least one presence was observed in that bin. Red line indicates 1:1, black line is ROC curve. Small blue dot indicates the optimal operating point on the ROC curve, used to determine the threshold that optimizes the tradeoff between sensitivity and specificity.
- M.** Relative uncertainty of annual presence probability prediction.
- N.** Seasonal maps of relative uncertainty of presence probability prediction.
- O.** Cross-validation relative uncertainty calibration plot for annual integrated presence probability (using maximum predicted probability and the mean value of the Stage I relative uncertainty for each 10x10 cell [~9x9 km] bin). Note that presence, absence, and overall error rates reflect the tradeoff between sensitivity and specificity; some error rates may go up even as relative uncertainty goes down. The relative uncertainty is based on the overall odds of the model prediction being correct compared to a null model; see Appendix 6.A. for details.

6.C.2. A note on error masking

Throughout all sections of this chapter, white space on maps is used to indicate places where predictions either were not made (due to insufficient seabird survey data or insufficient information on environmental predictors), or were considered too unreliable to display. For some species and groups, we developed two versions of the “error masks” used to hide unreliable predictions: a more conservative mask that is used in the main body of this report, and a less conservative mask that is used here in Appendix 6.C. The affected species/groups are: Great Shearwater, Sooty Shearwater, Wilson’s Storm-Petrel, Pomarine Jaeger, Northern Fulmar, Less Common Storm-Petrels, Less Common Shearwaters, and Jaegers. We use the less conservative masks here in Appendix 6.C. in order to show the maximum extent of model predictions, and allow the user to judge for themselves whether predictions are well-supported by data (original data points are overlaid on maps and uncertainty maps are presented alongside each prediction map). The user is cautioned to closely examine the distribution of data and the uncertainty maps, as well as diagnostic plots such as the cross-validation uncertainty calibration, to determine the degree of confidence appropriate for any particular prediction. Users should be especially careful when drawing inferences about “hotspots” or “coldspots” that are not supported by any nearby data points; these result solely from extrapolation from environmental conditions, and should be considered only potential hot or cold spots until those areas are actually surveyed. For example, predictions made in Long Island Sound for species with no presence data points in the Sound are unreliable. Such predictions have been masked out in the maps presented in the main body of this report, but may not always be masked out by the less conservative masks in this Appendix or Online Supplement 6.2.

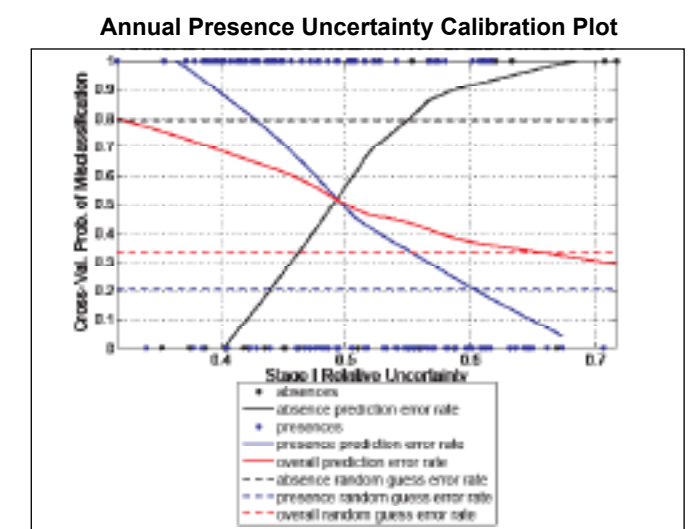
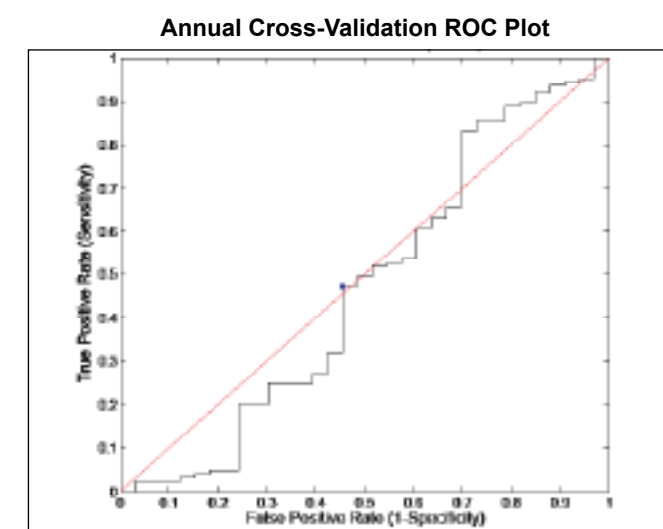
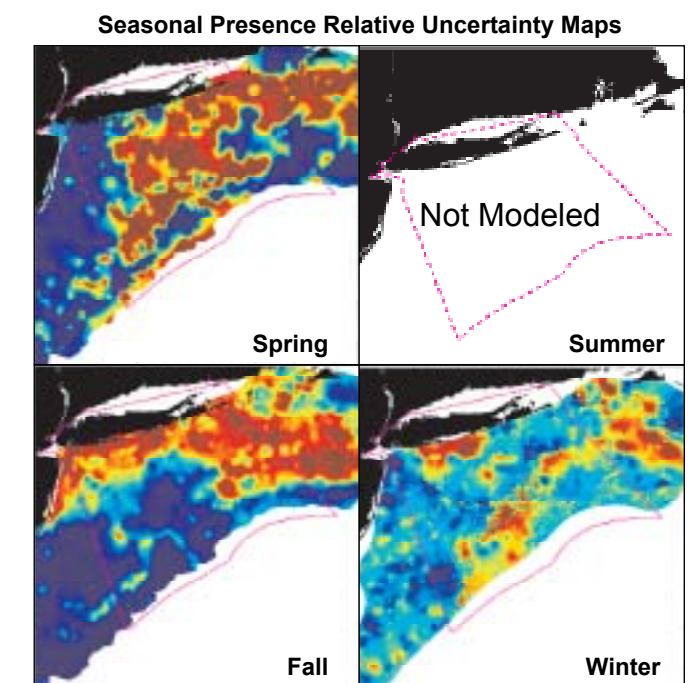
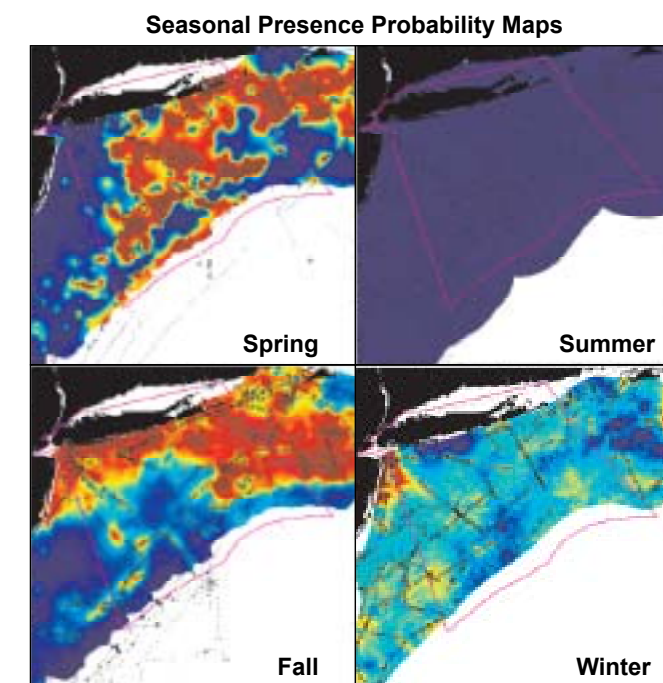
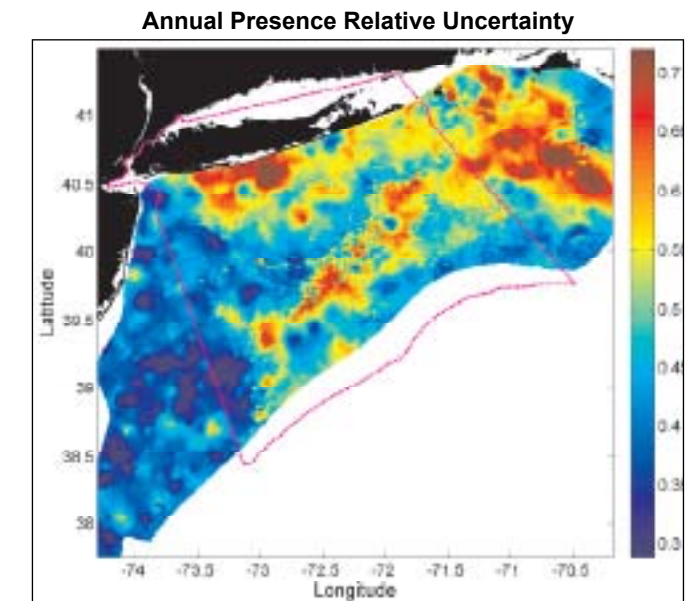
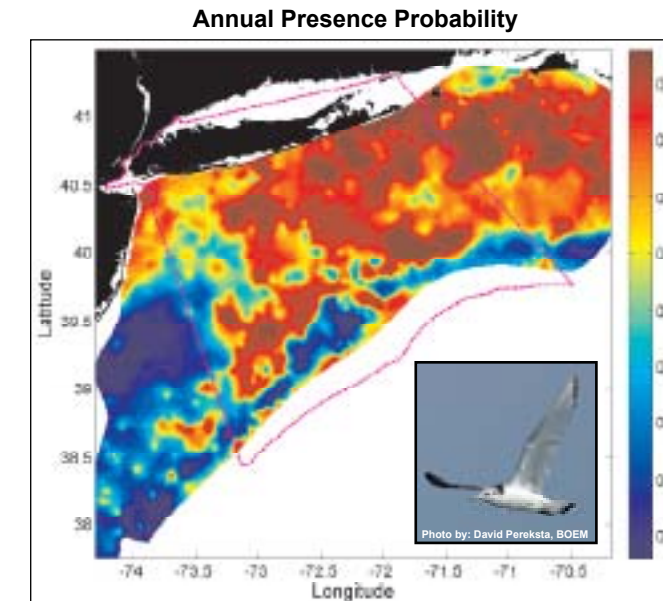
Black-legged Kittiwake

Stage I x II: Relative Abundance Predictive Model



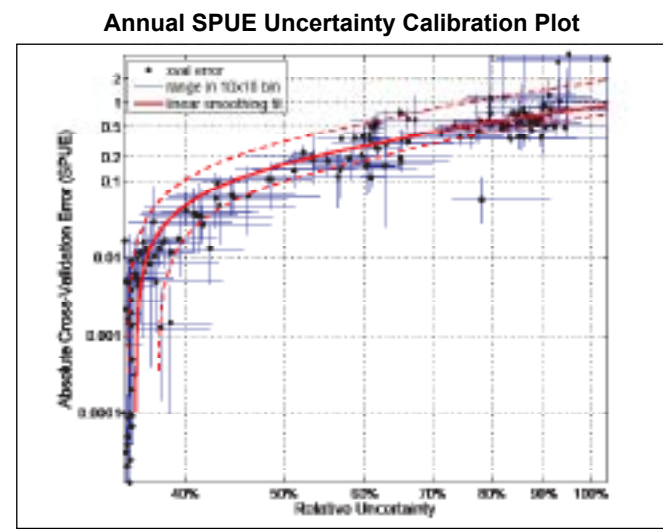
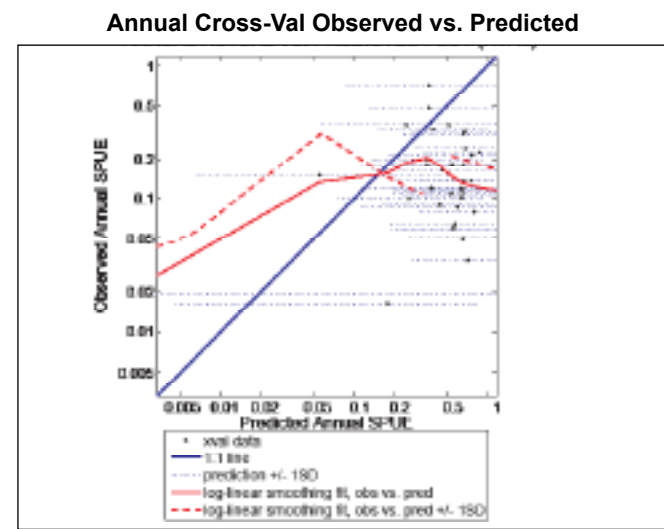
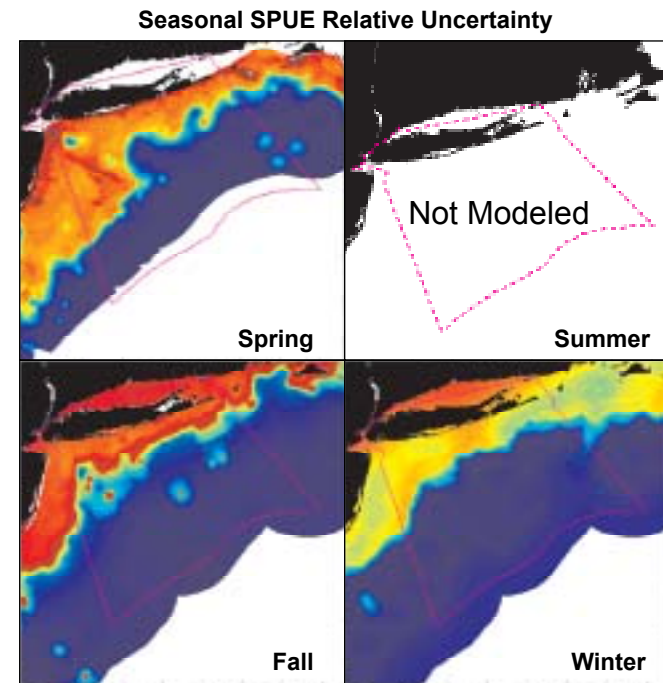
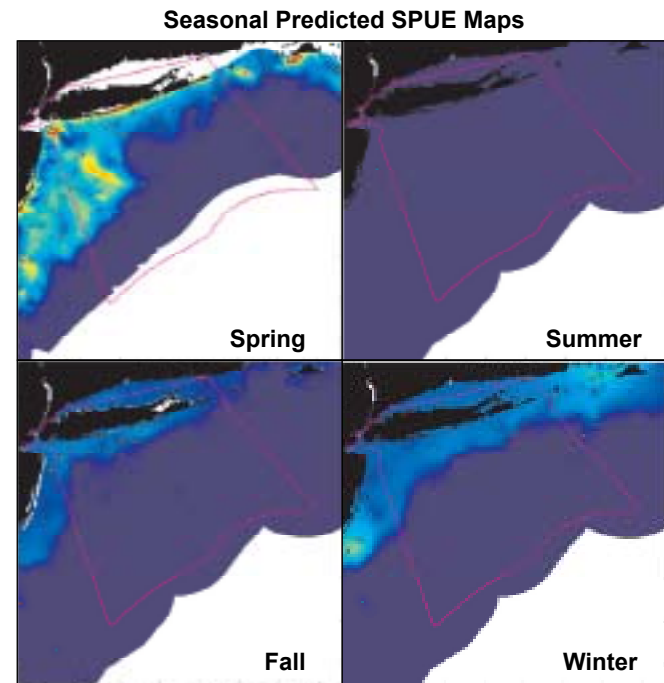
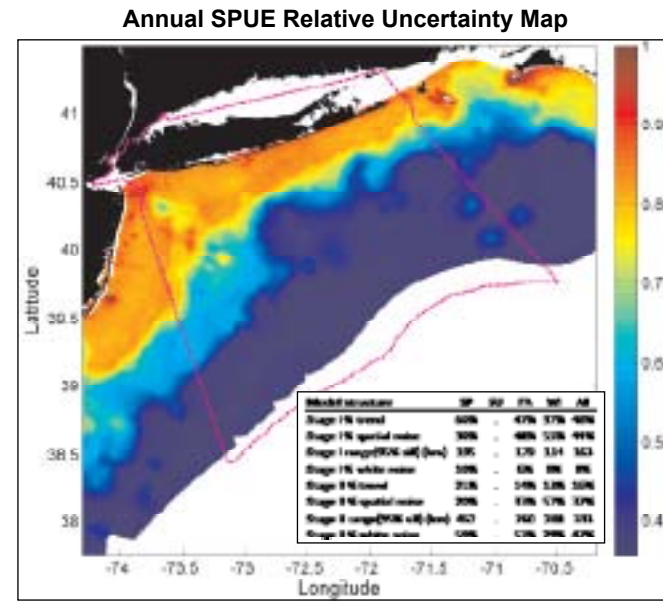
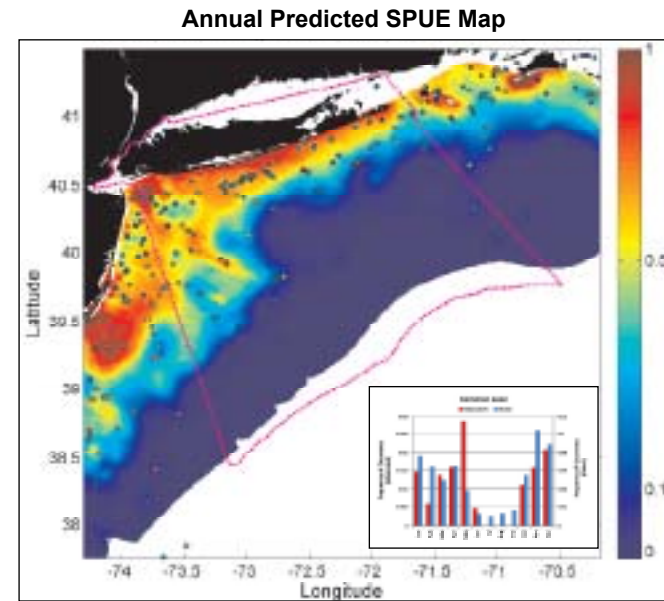
Black-legged Kittiwake

Stage I: Presence Probability Predictive Model



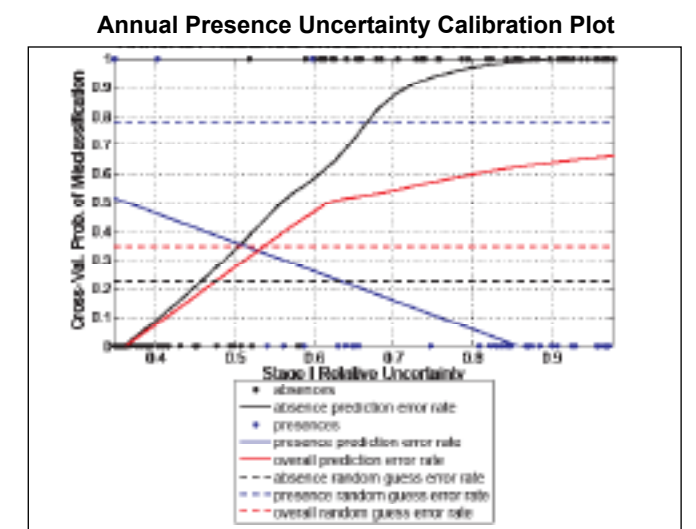
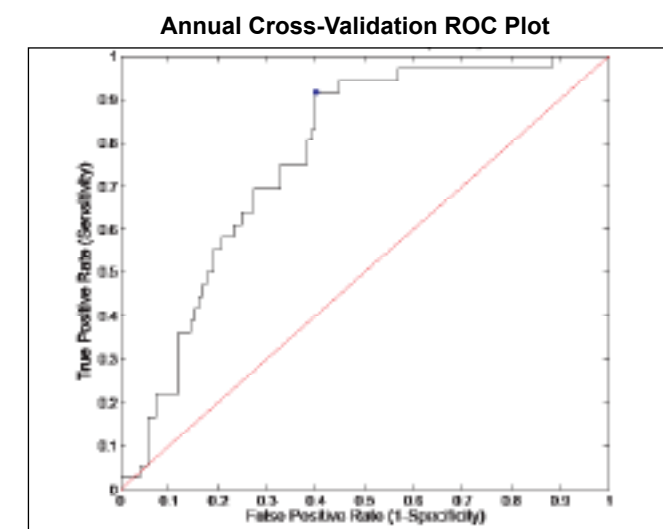
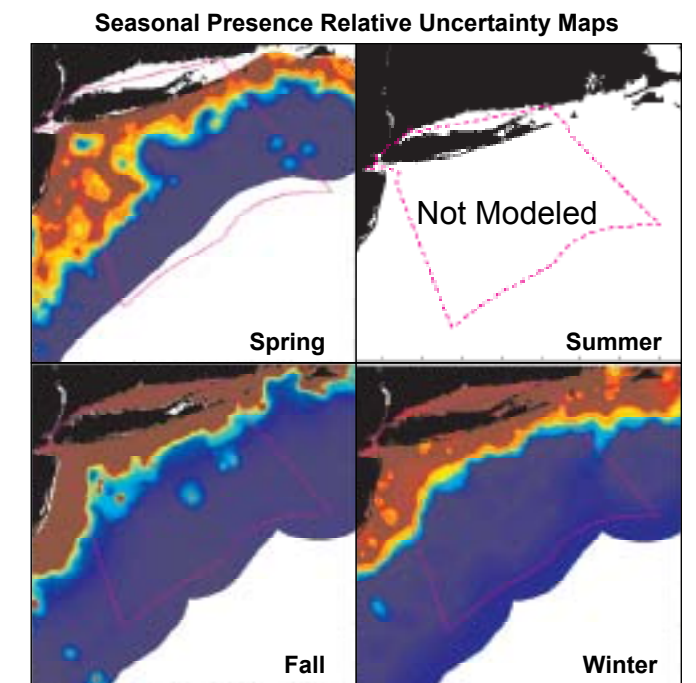
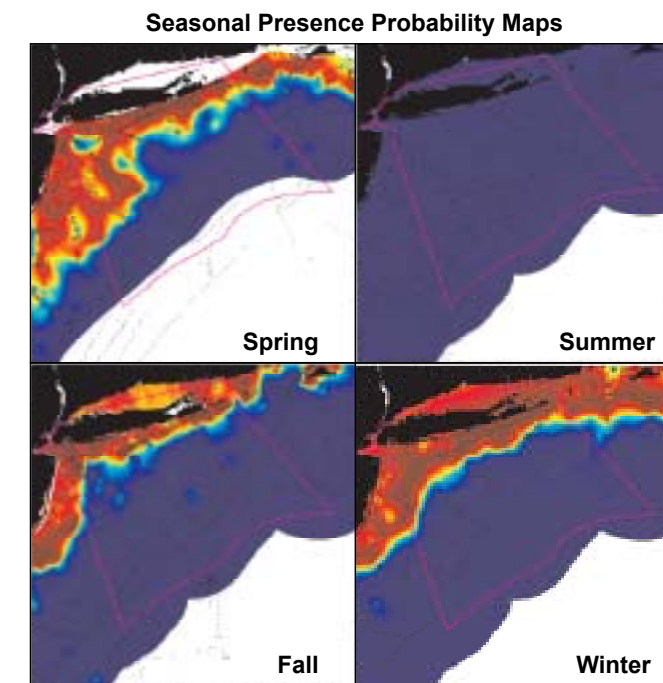
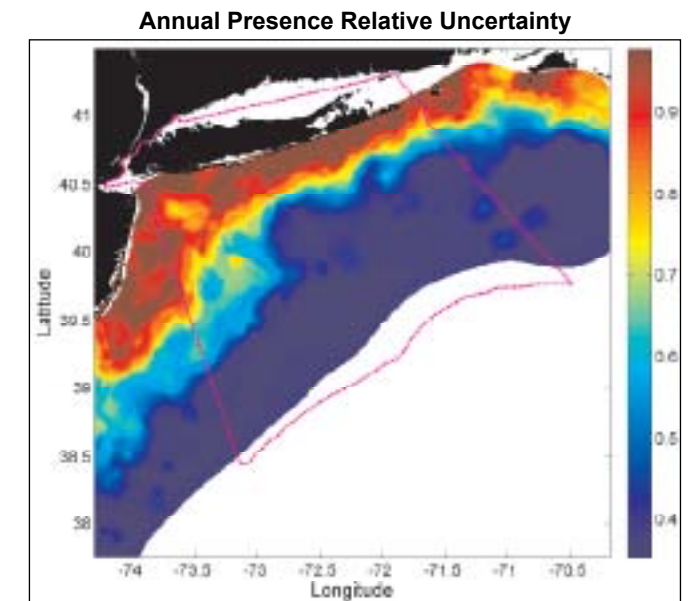
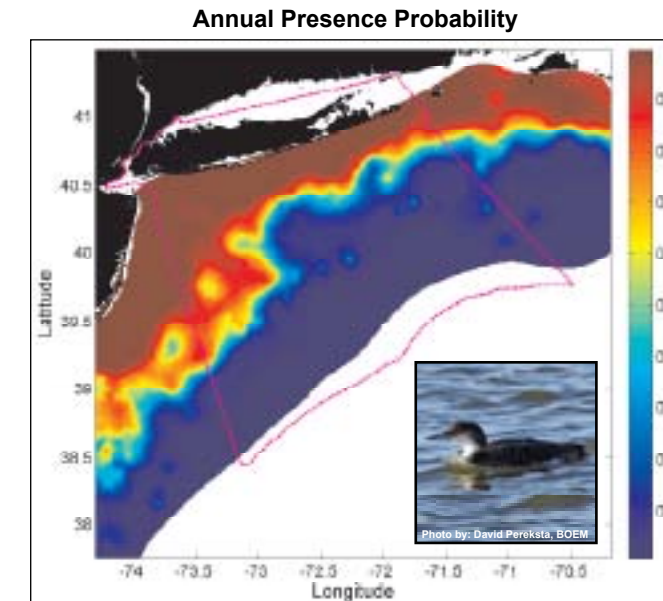
Common Loon

Stage I x II: Relative Abundance Predictive Model



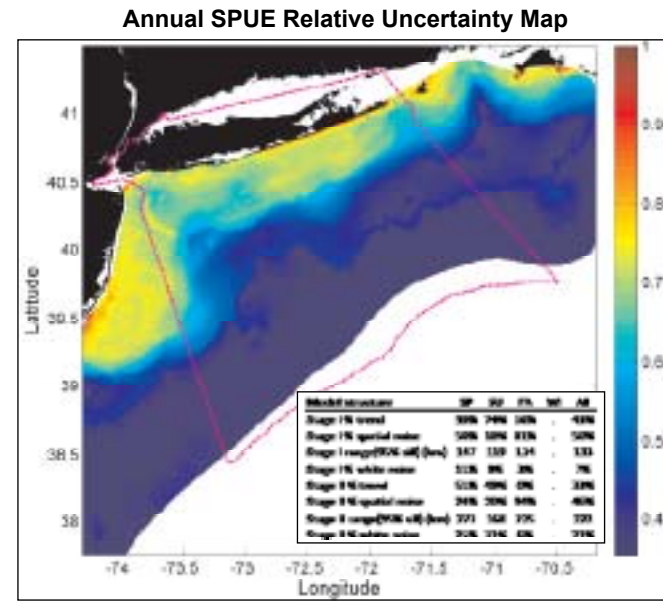
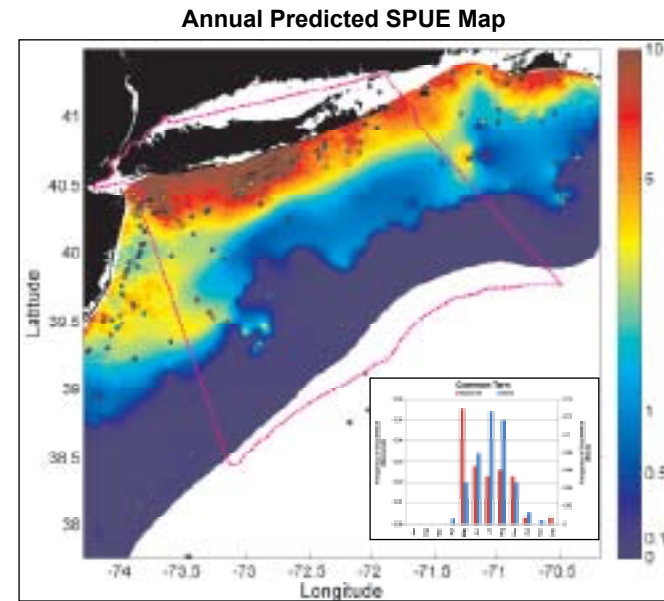
Common Loon

Stage I: Presence Probability Predictive Model



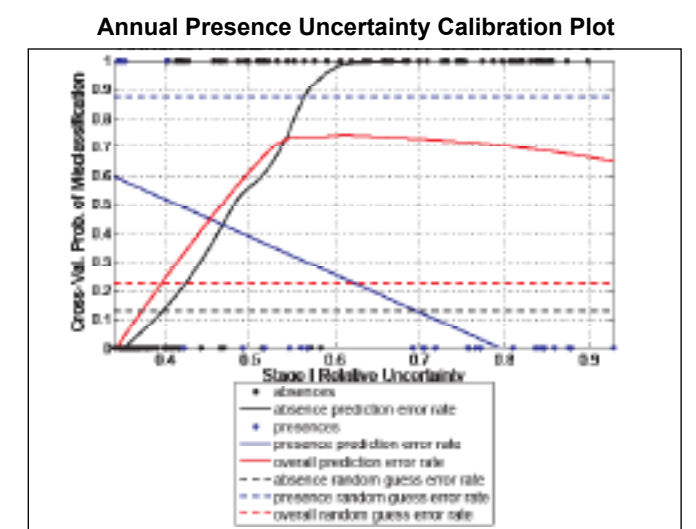
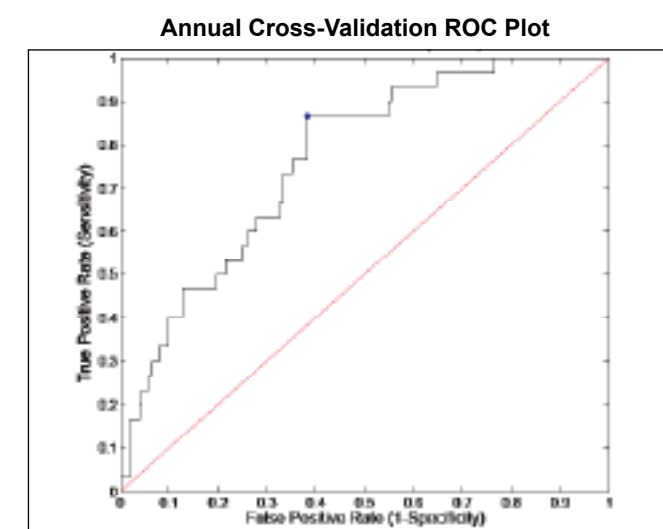
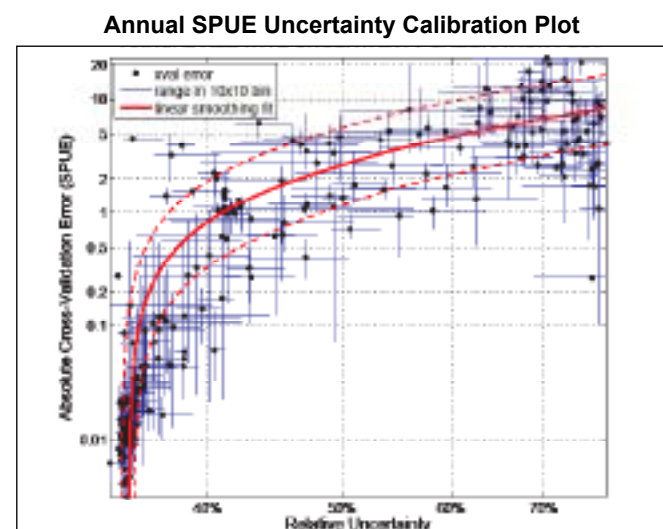
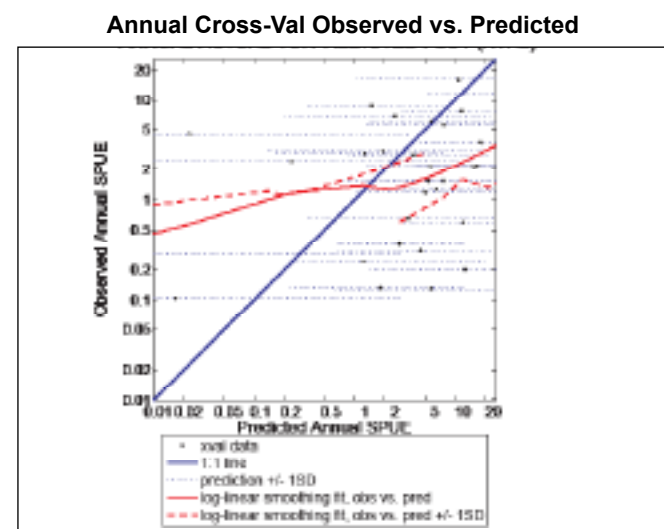
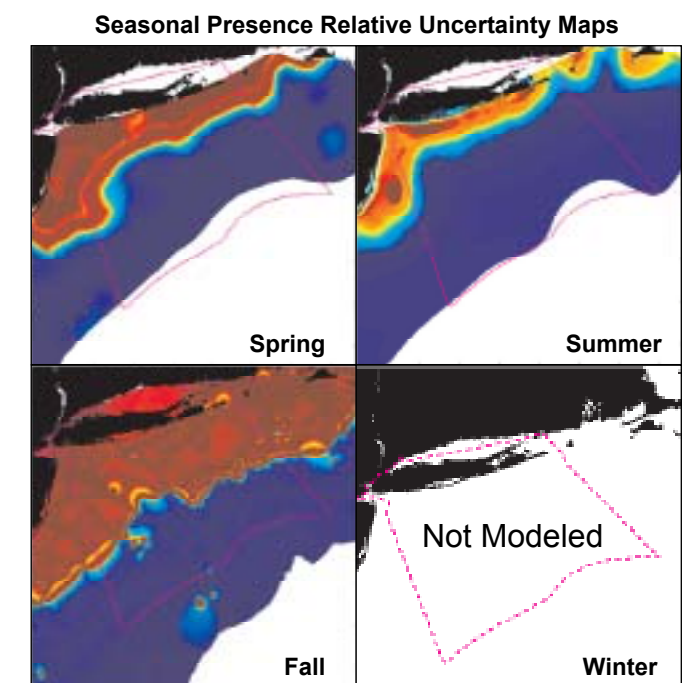
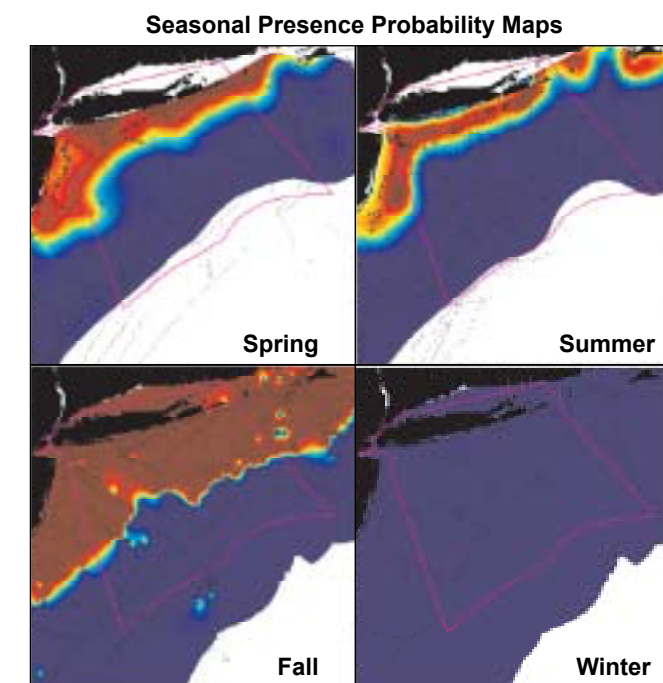
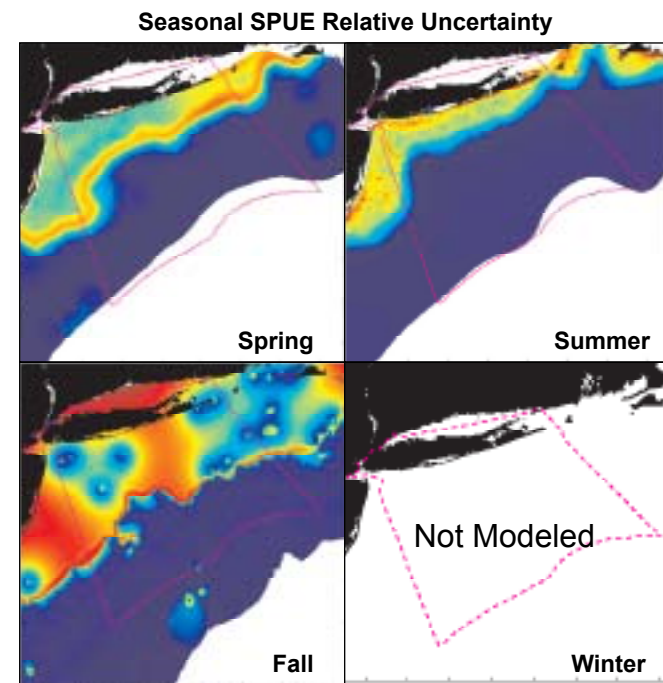
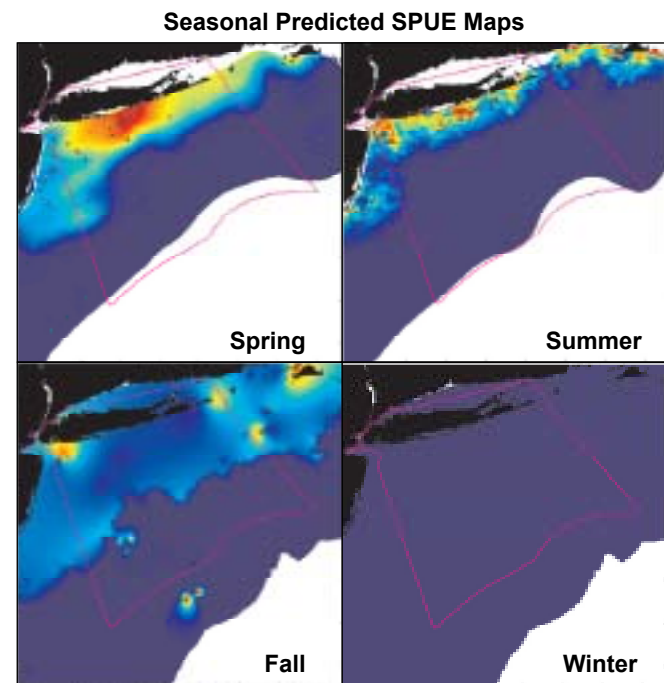
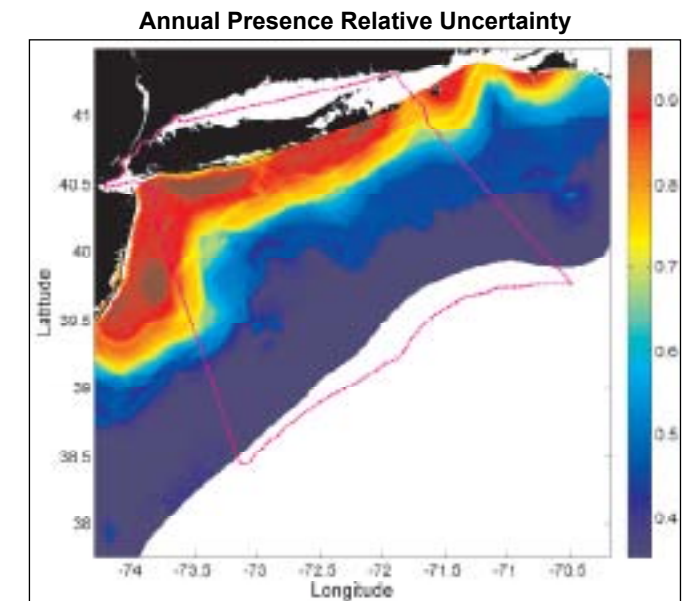
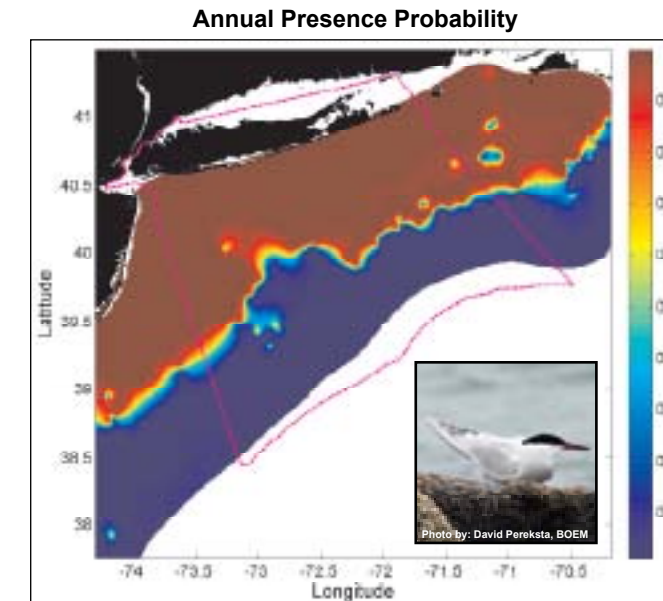
Common Tern

Stage I x II: Relative Abundance Predictive Model



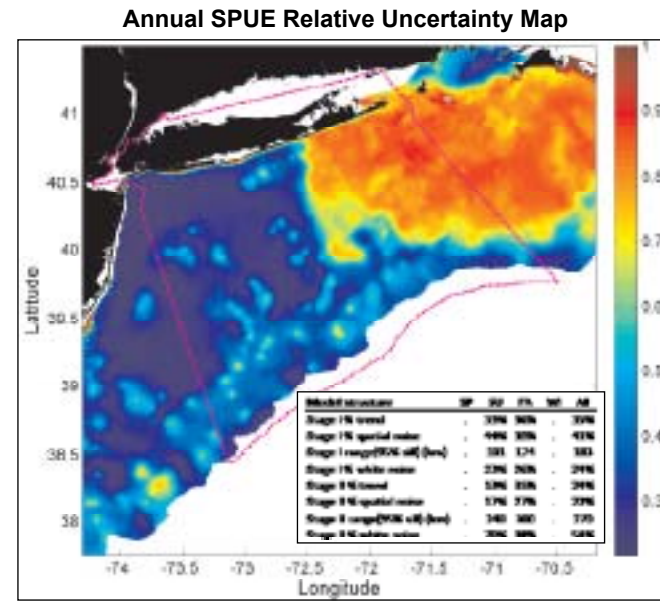
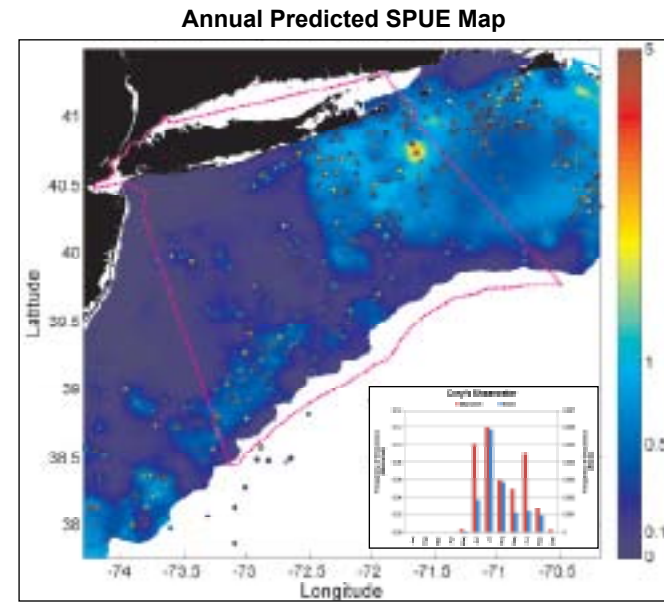
Common Tern

Stage I: Presence Probability Predictive Model



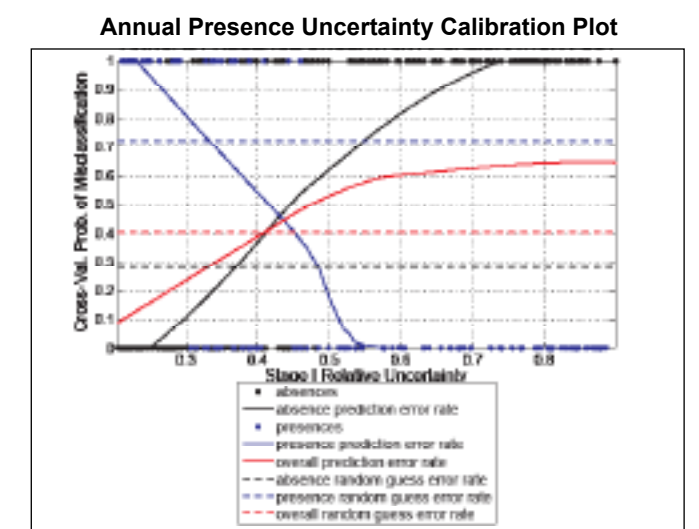
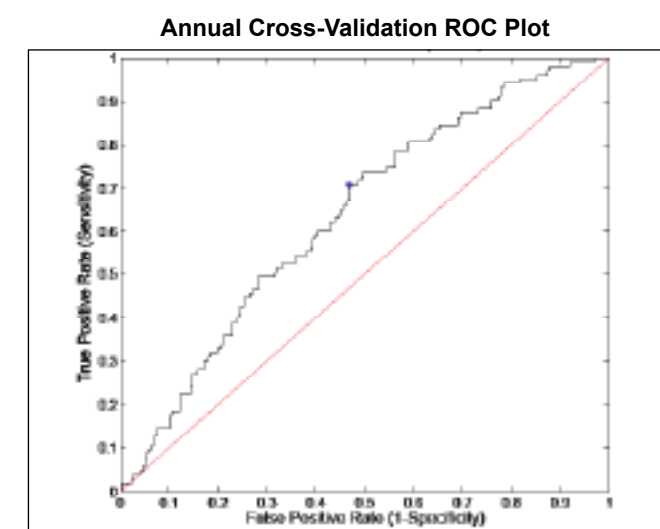
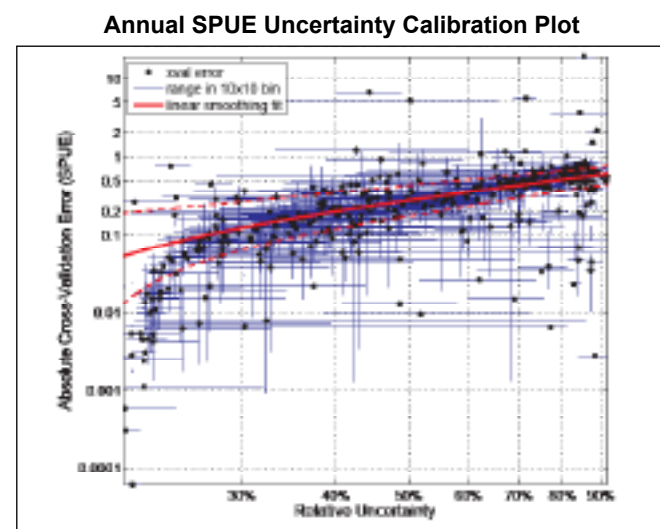
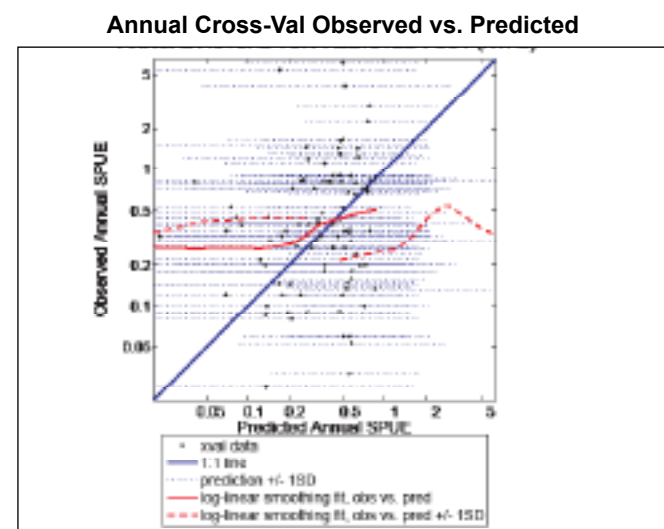
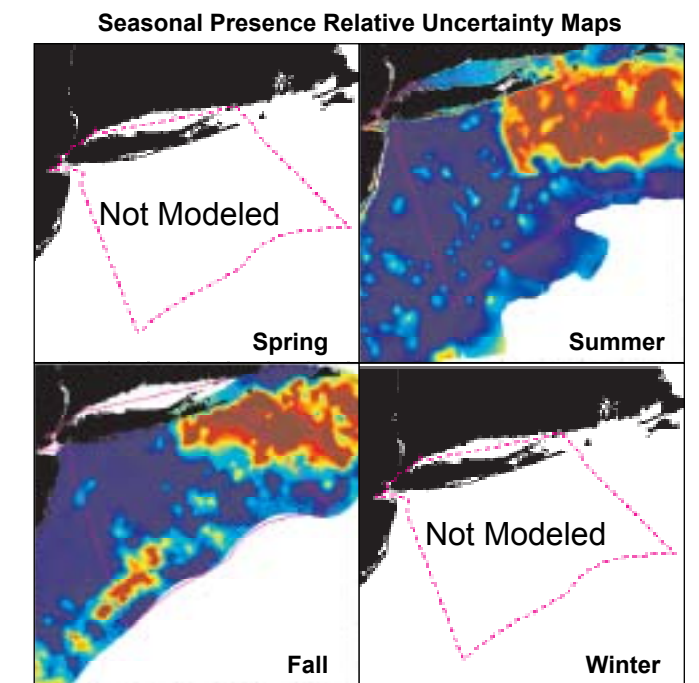
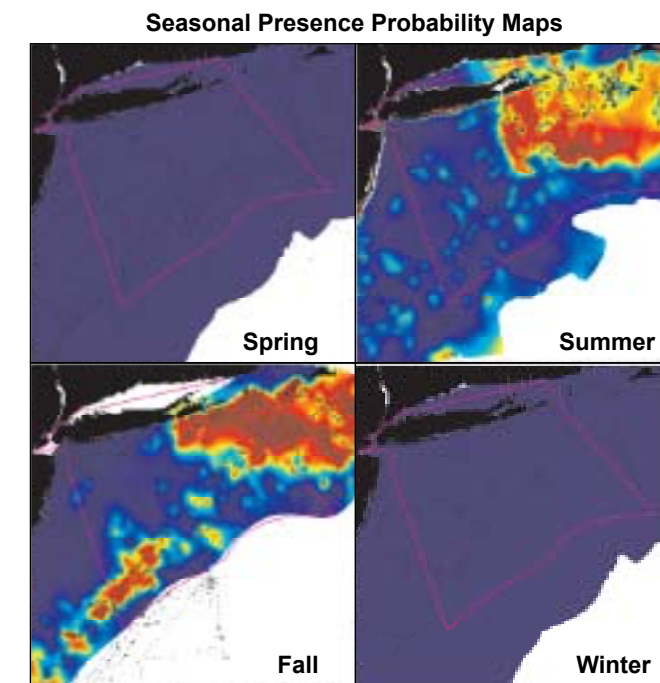
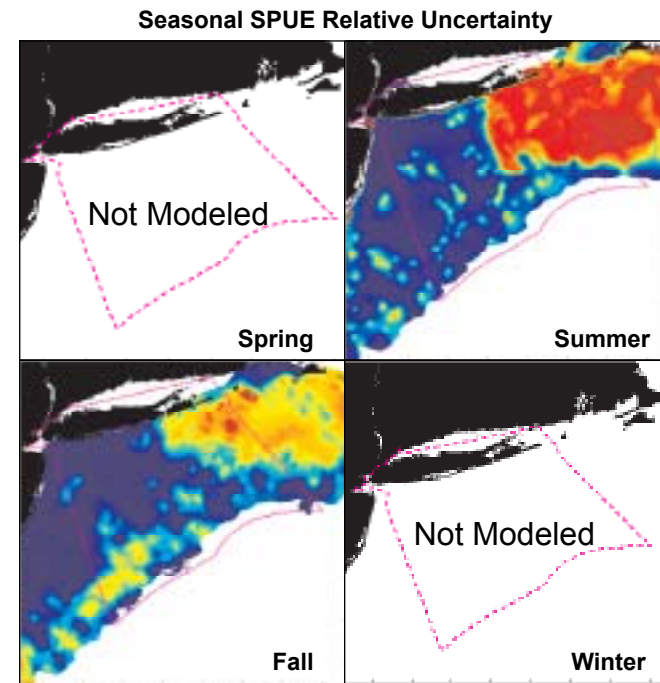
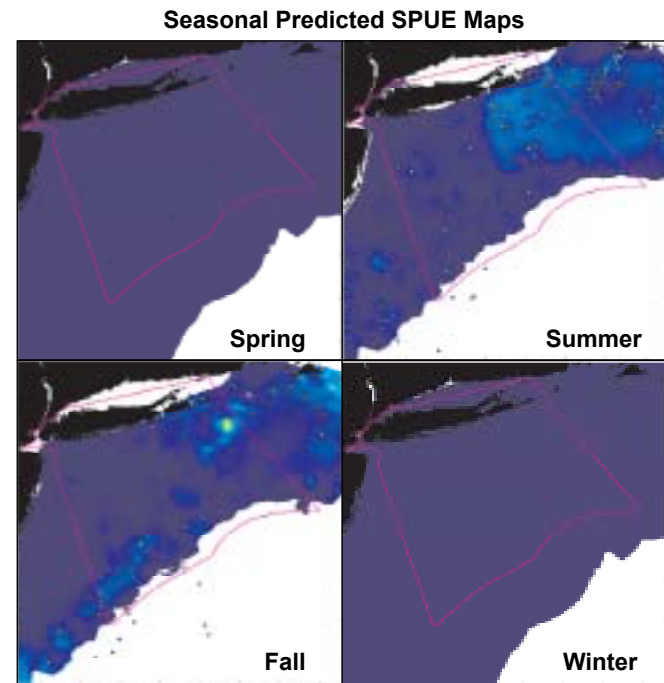
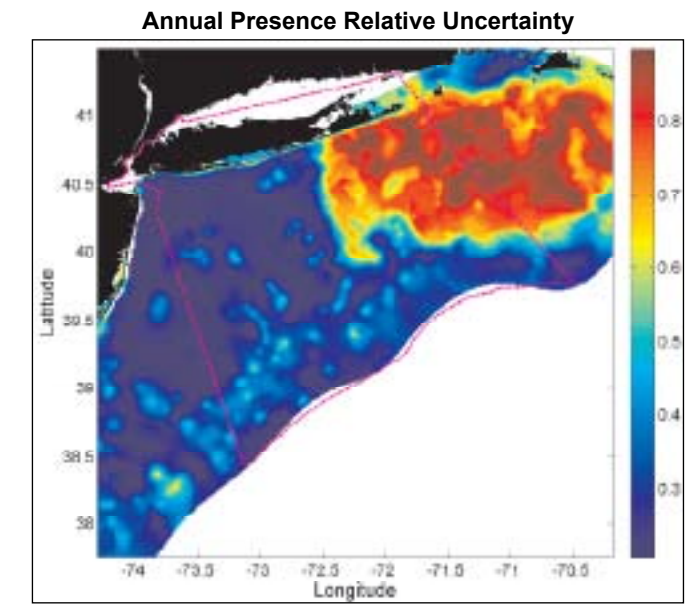
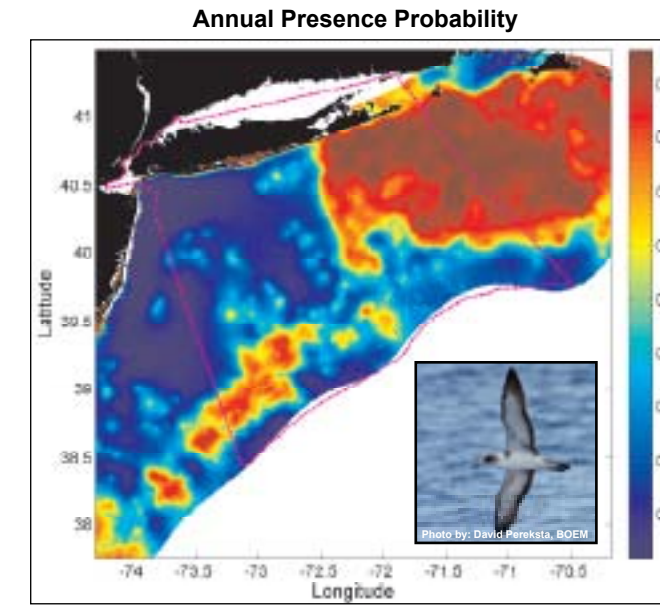
Cory's Shearwater

Stage I x II: Relative Abundance Predictive Model



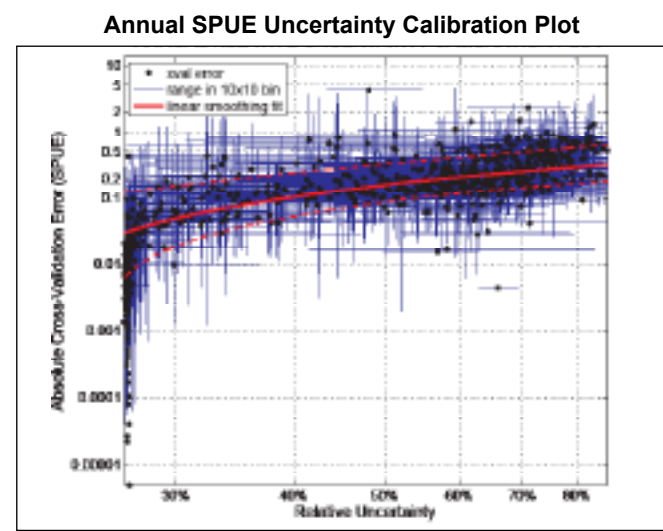
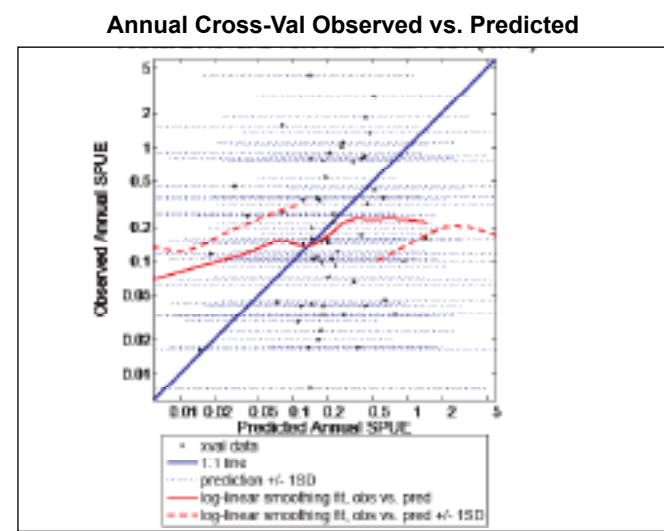
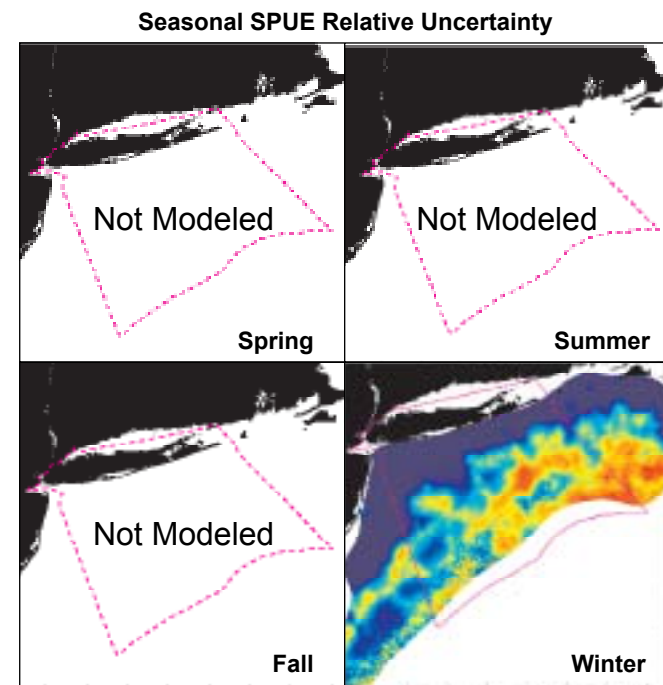
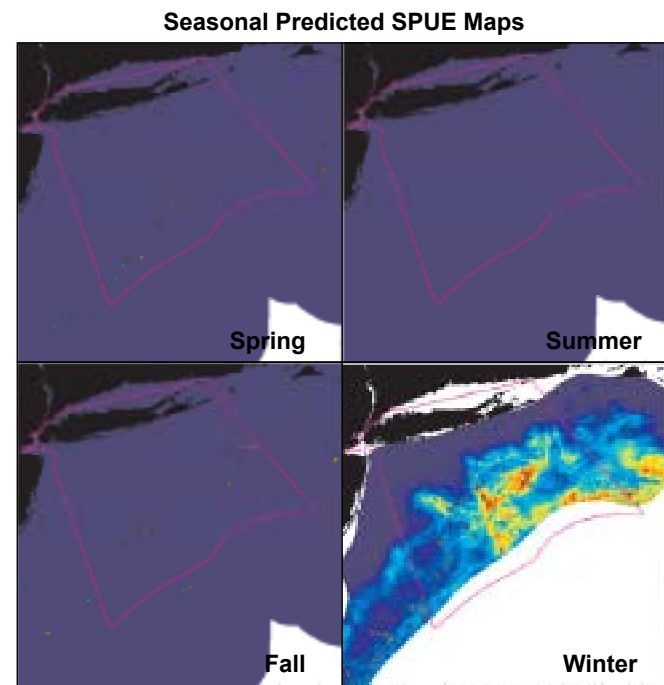
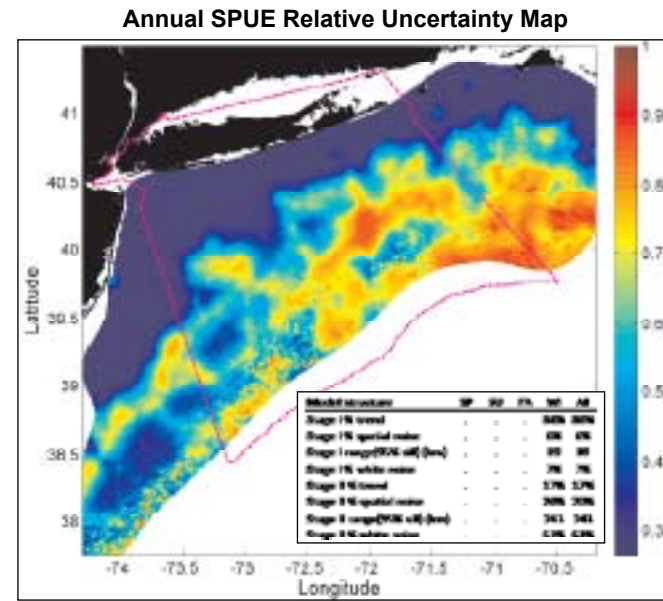
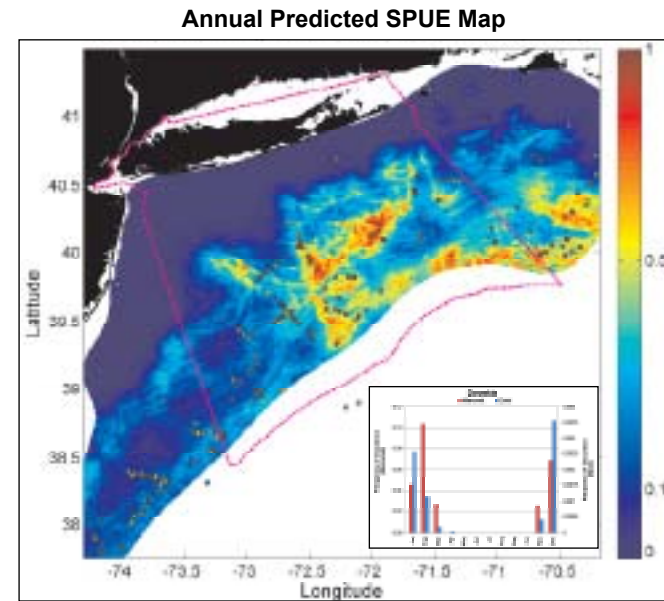
Cory's Shearwater

Stage I: Presence Probability Predictive Model



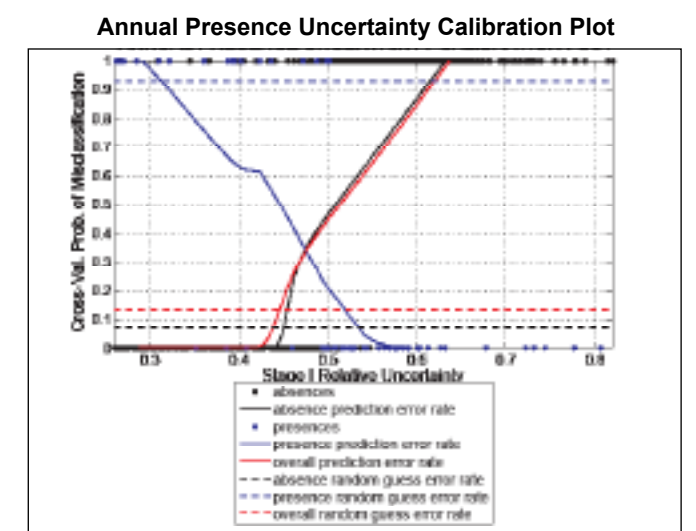
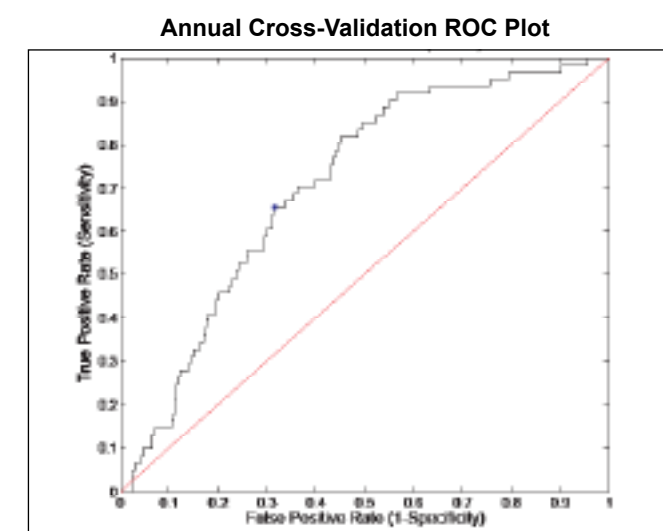
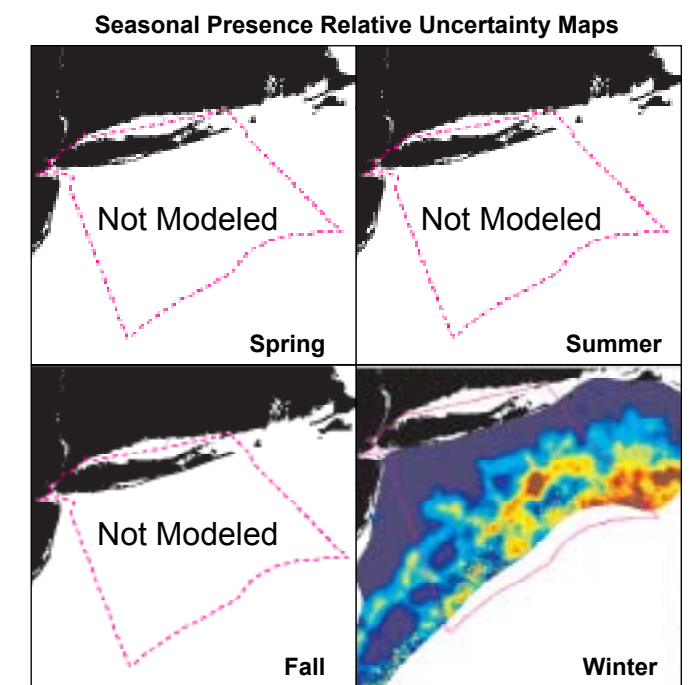
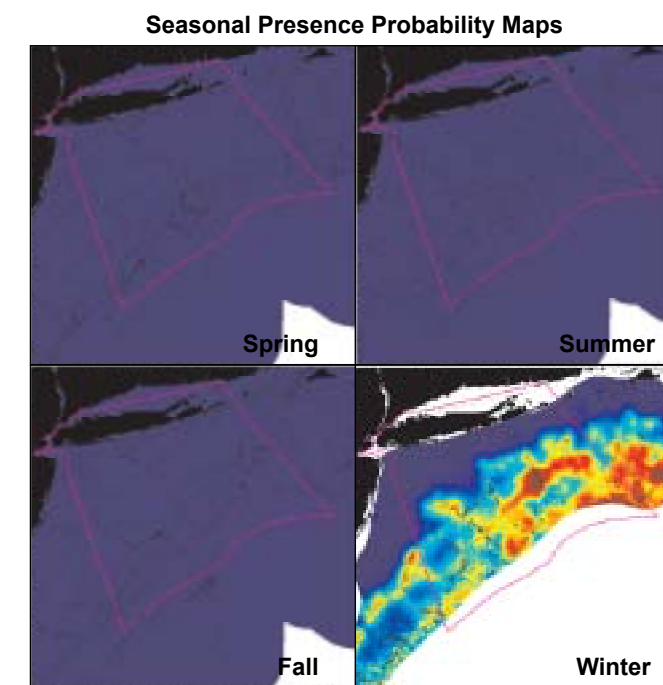
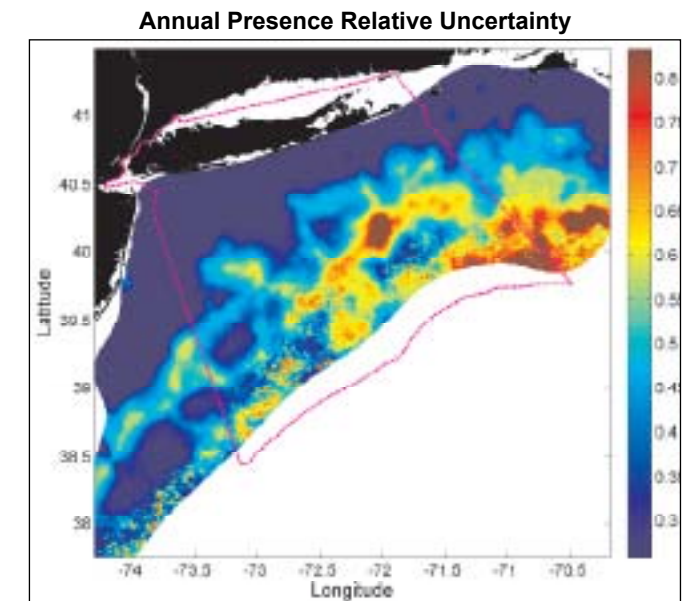
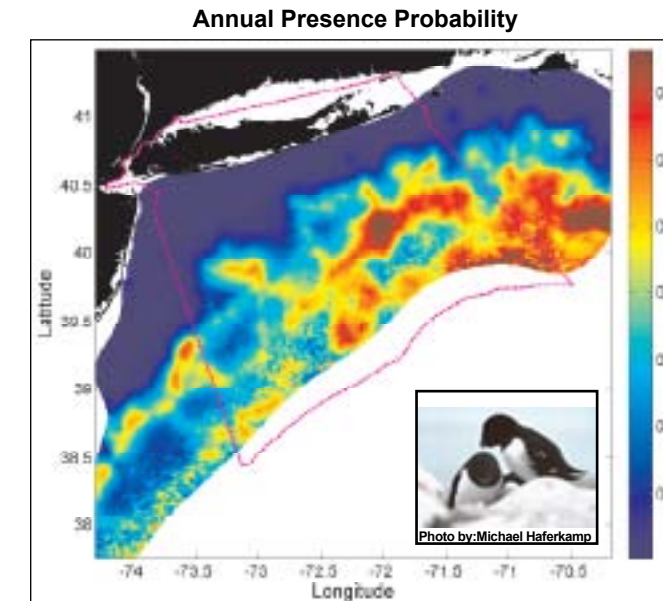
Dovekie

Stage I x II: Relative Abundance Predictive Model



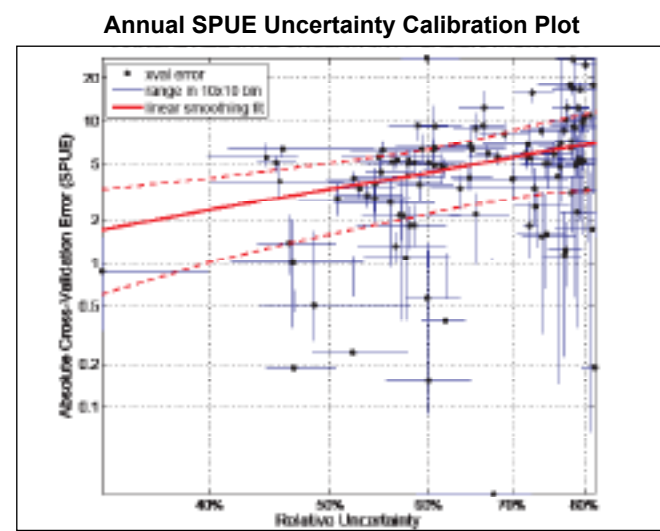
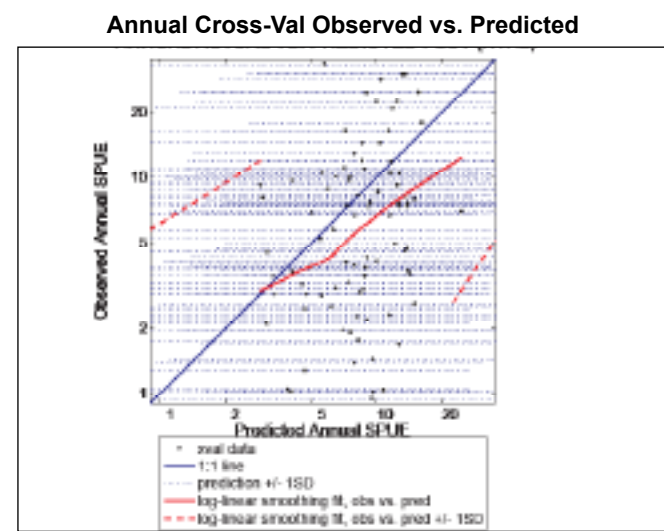
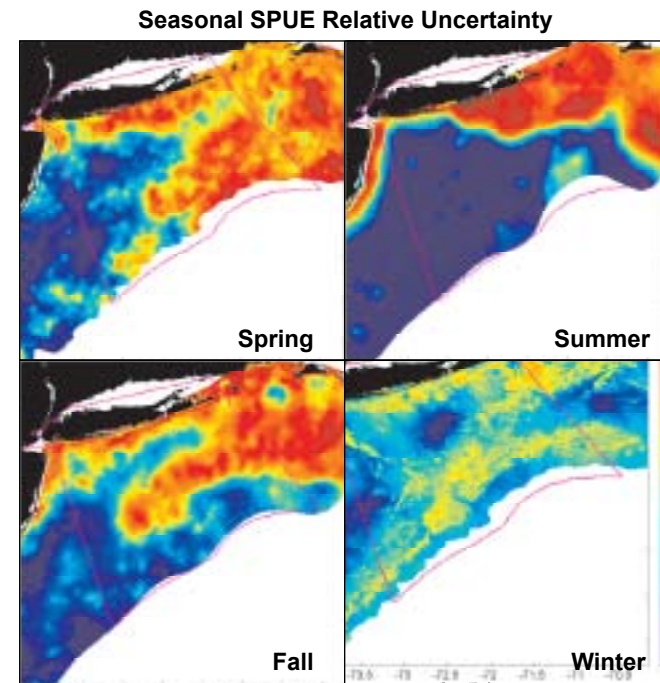
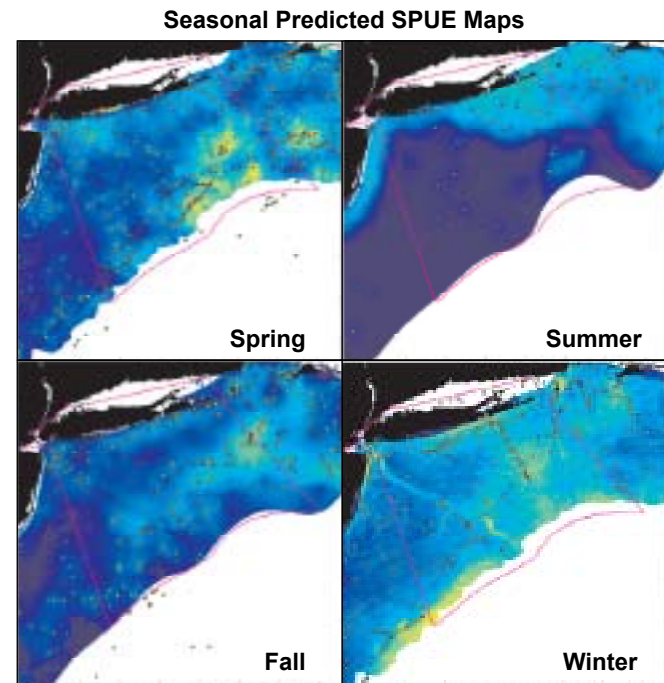
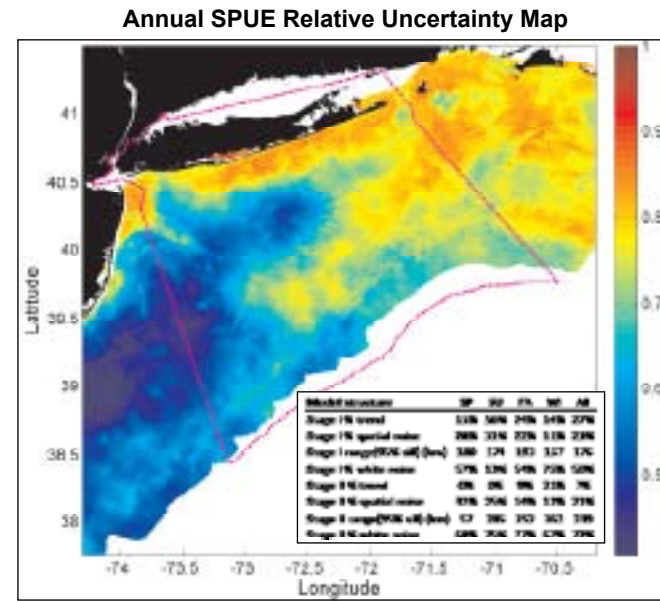
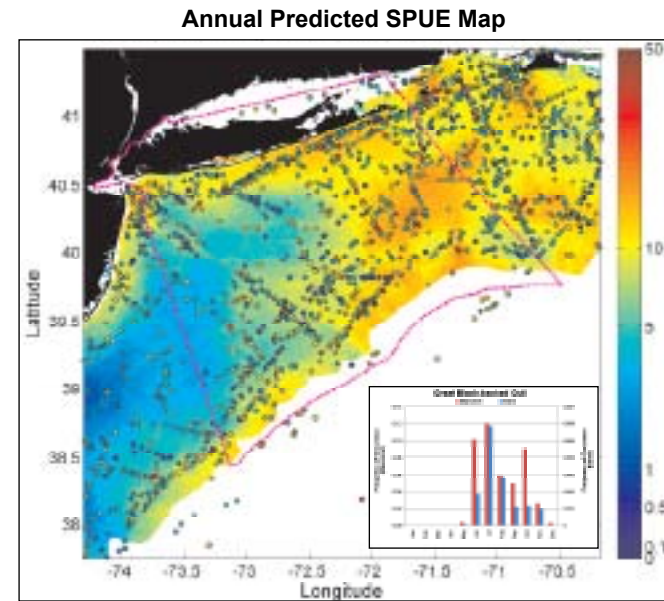
Dovekie

Stage I: Presence Probability Predictive Model



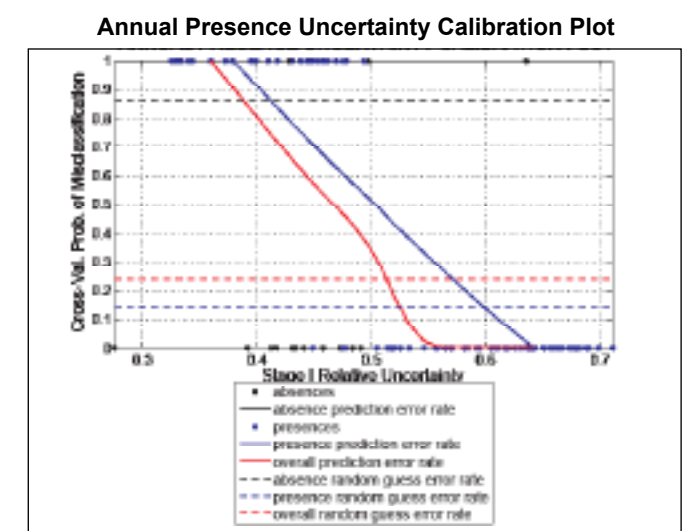
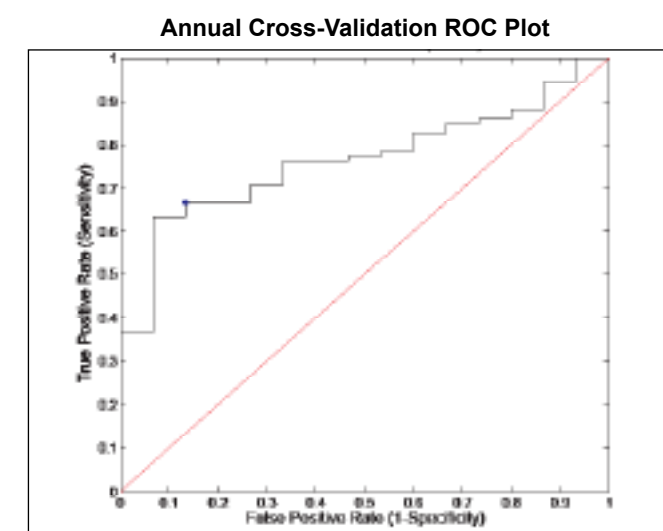
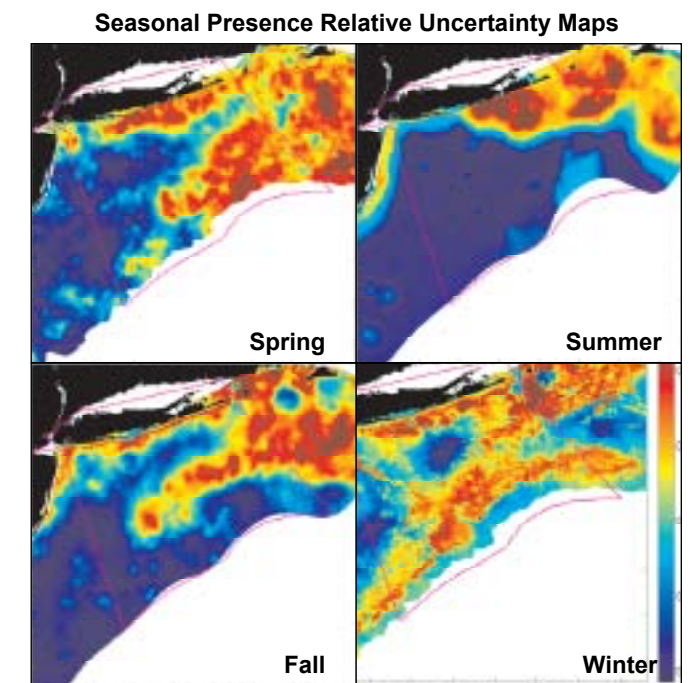
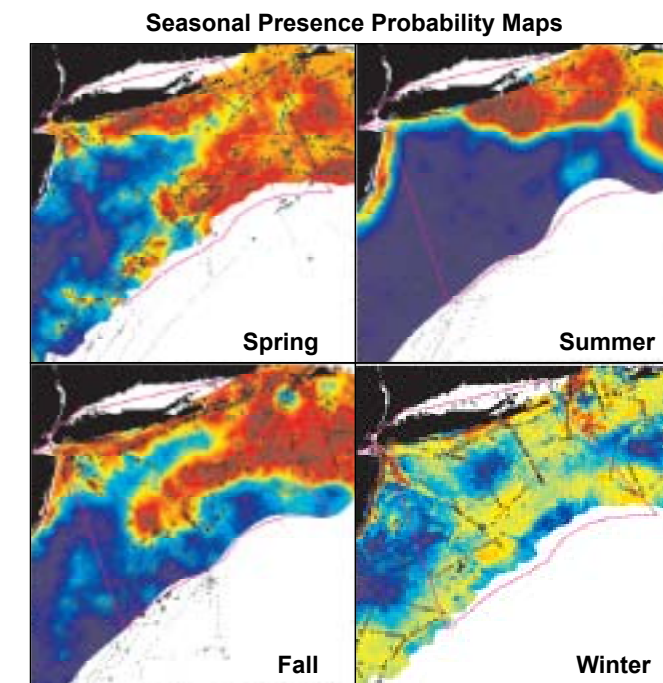
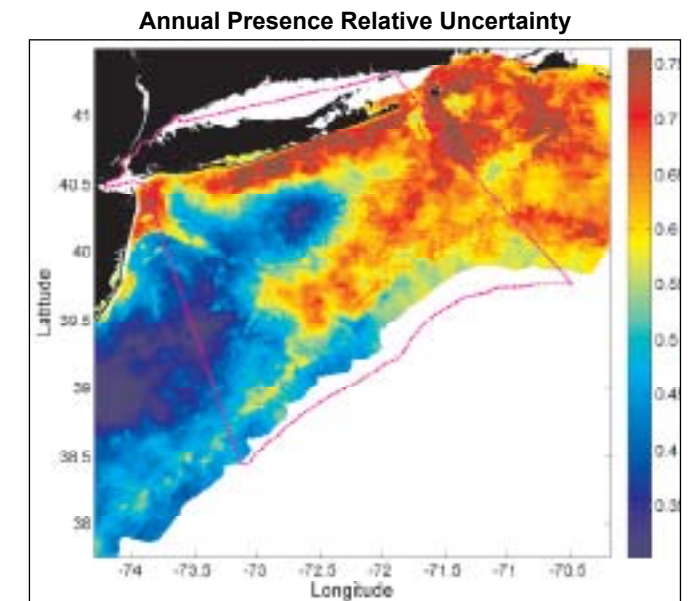
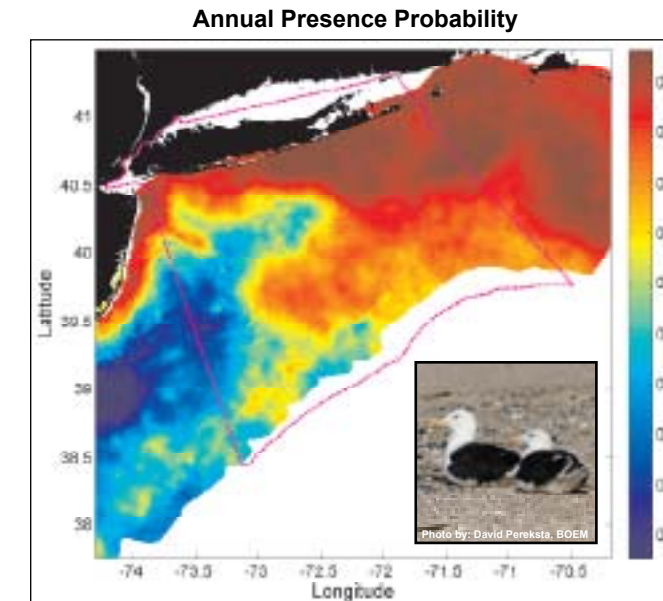
Great Black-backed Gull

Stage I x II: Relative Abundance Predictive Model



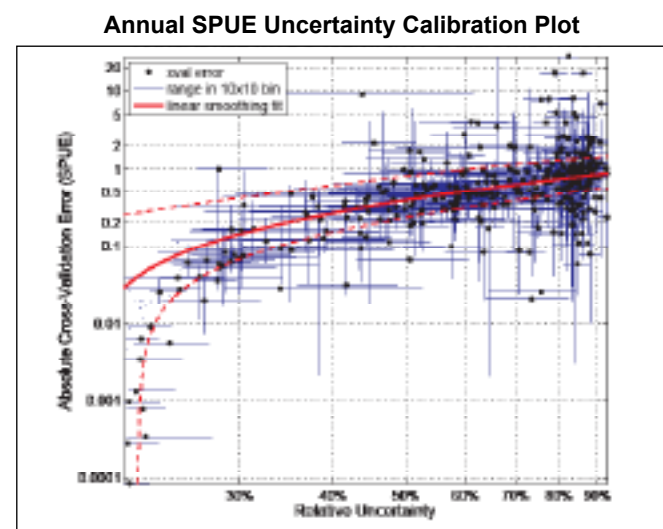
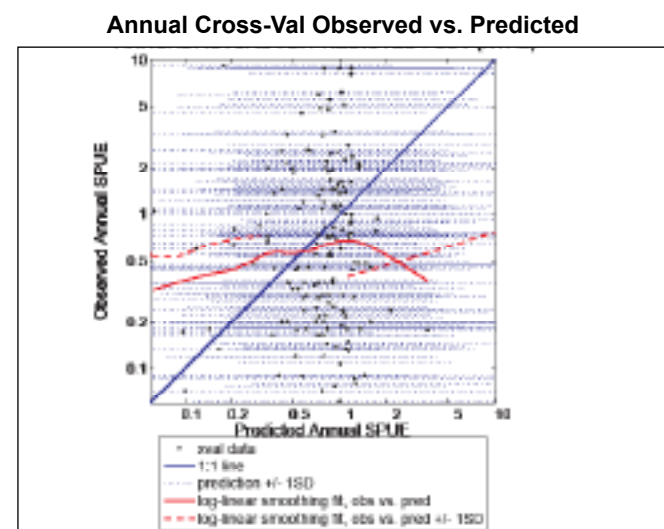
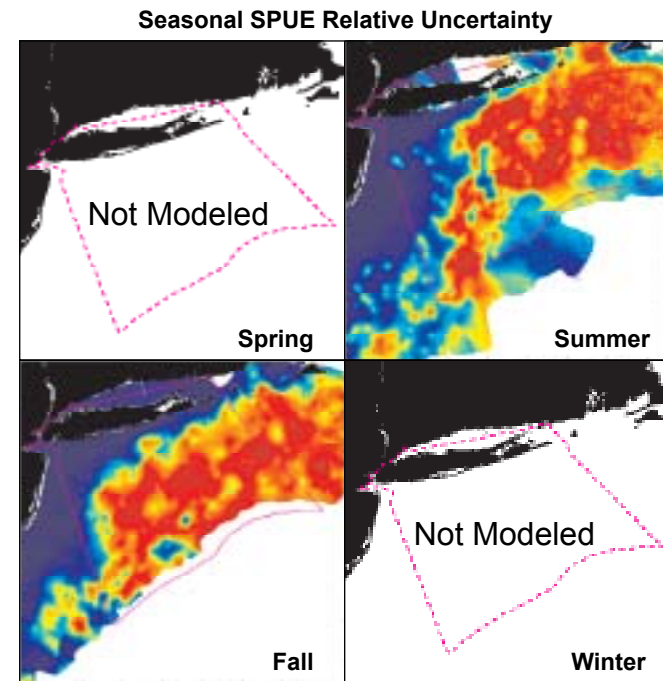
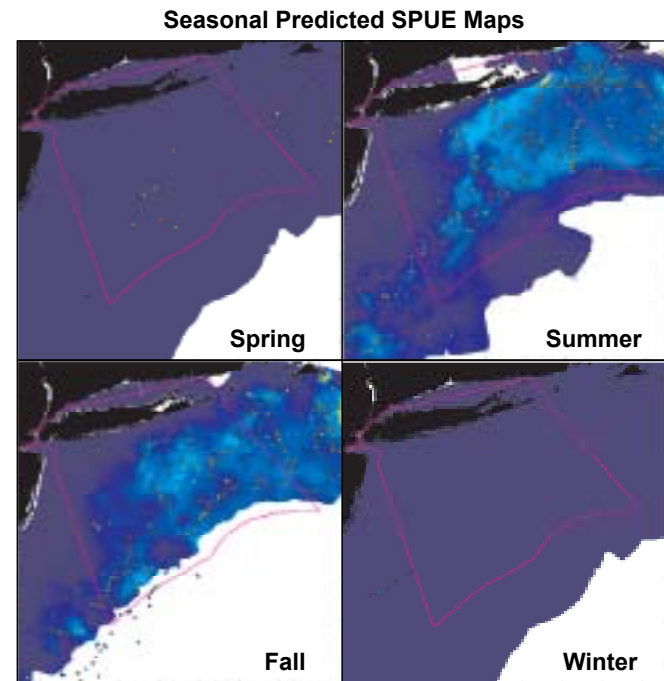
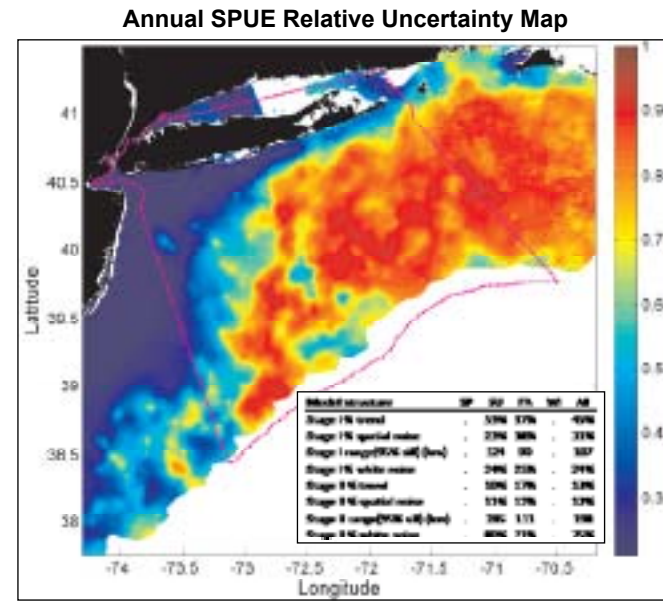
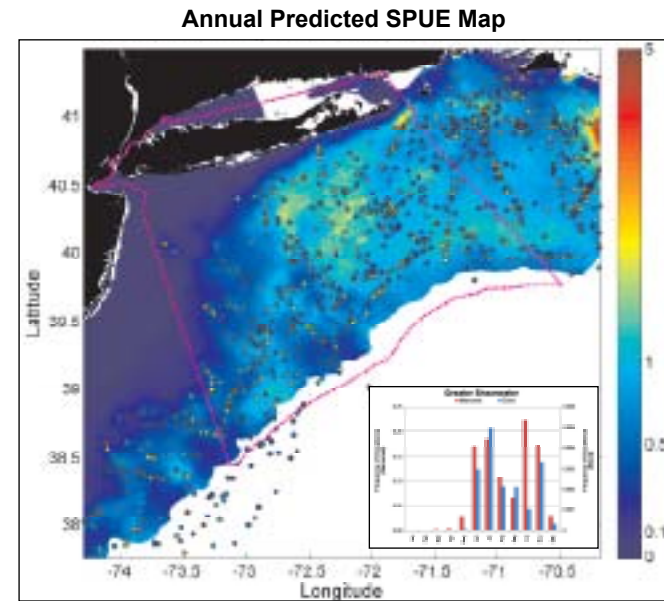
Great Black-backed Gull

Stage I: Presence Probability Predictive Model



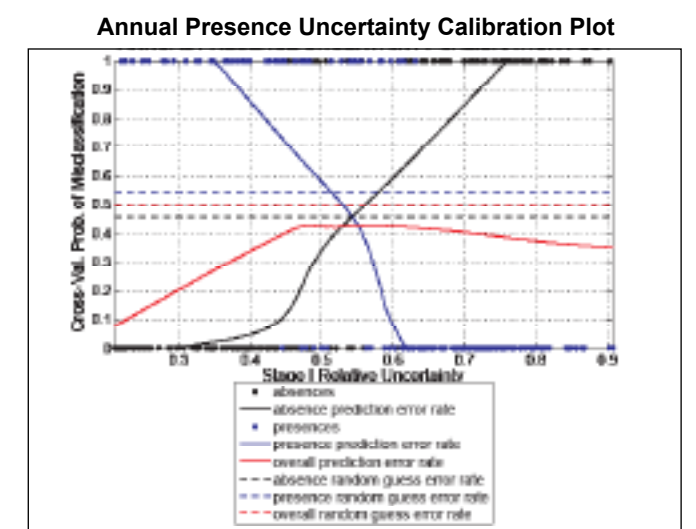
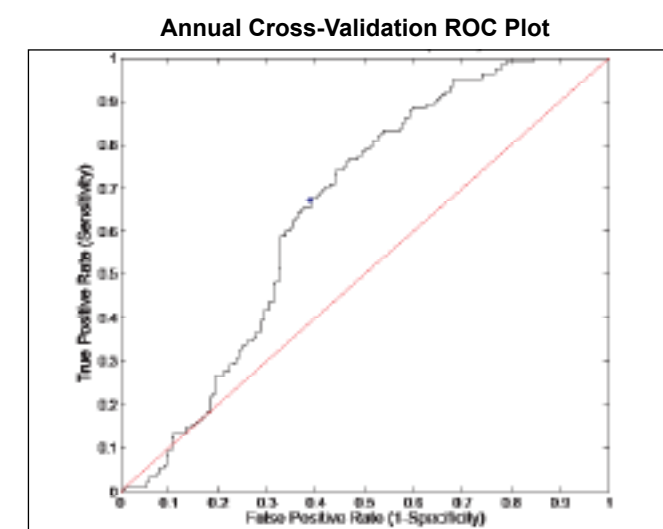
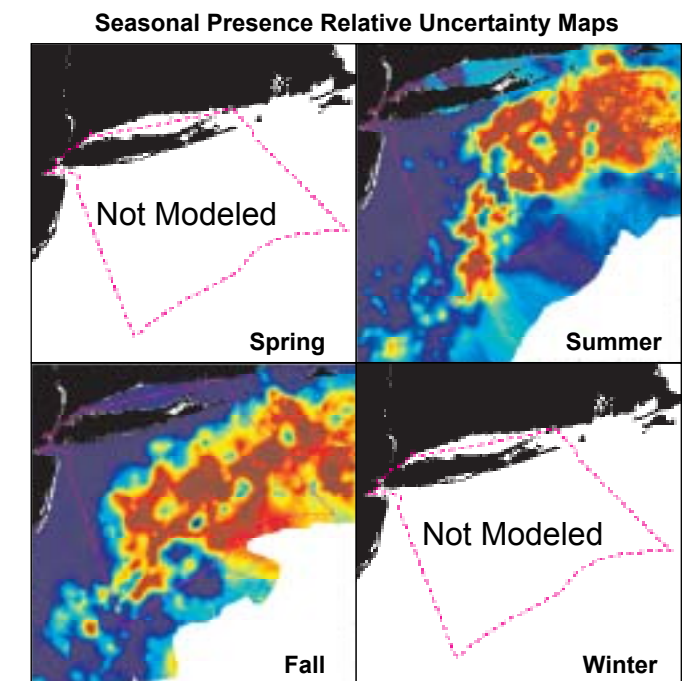
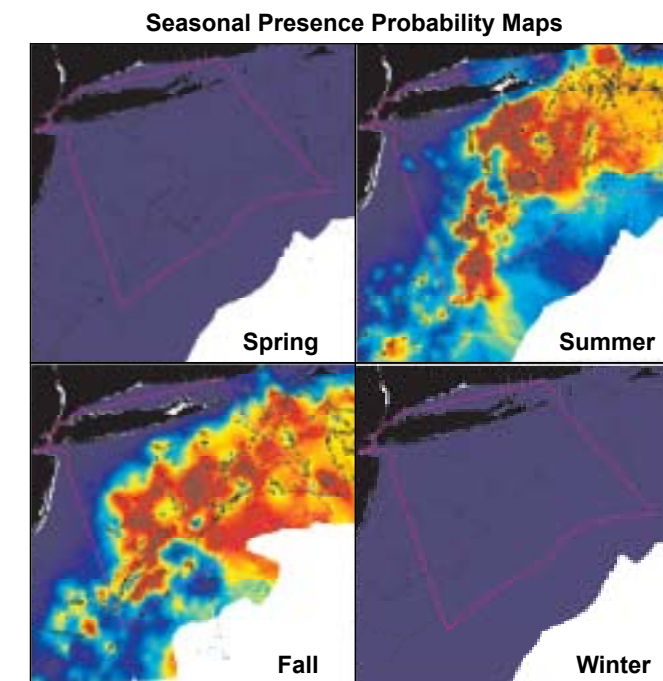
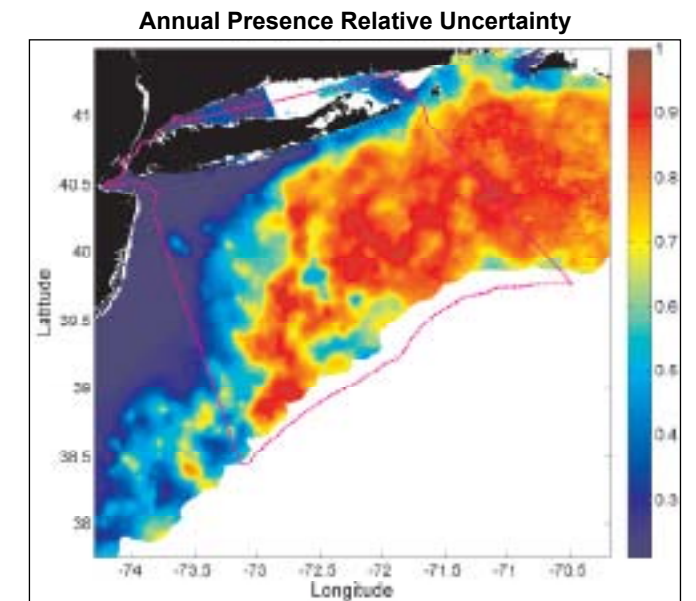
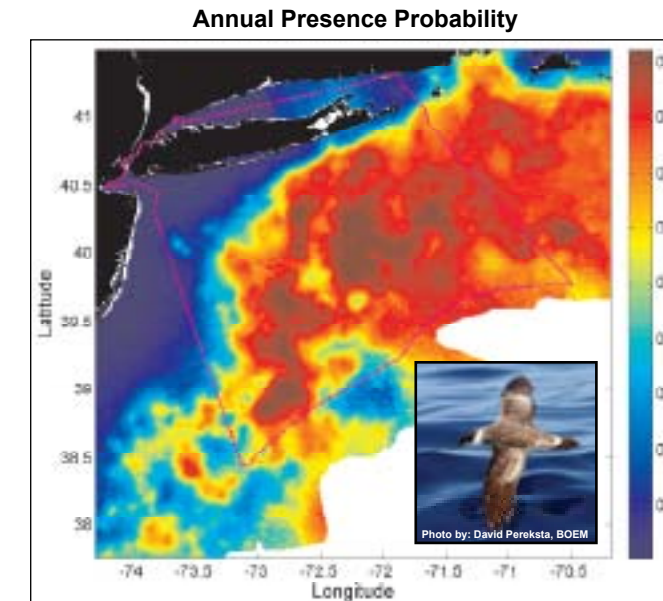
Great Shearwater

Stage I x II: Relative Abundance Predictive Model



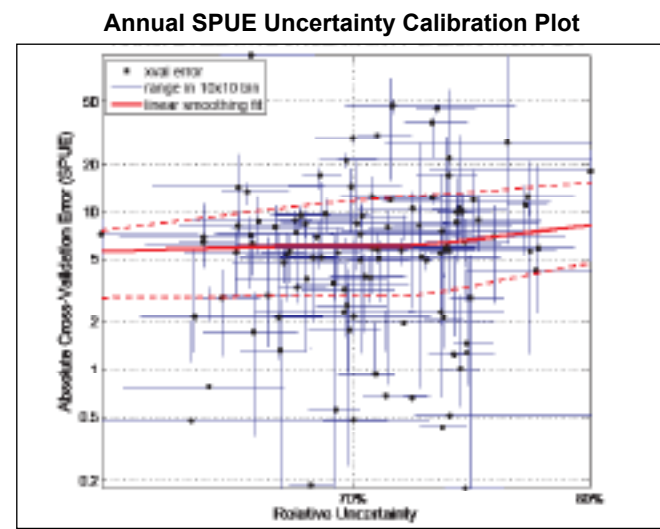
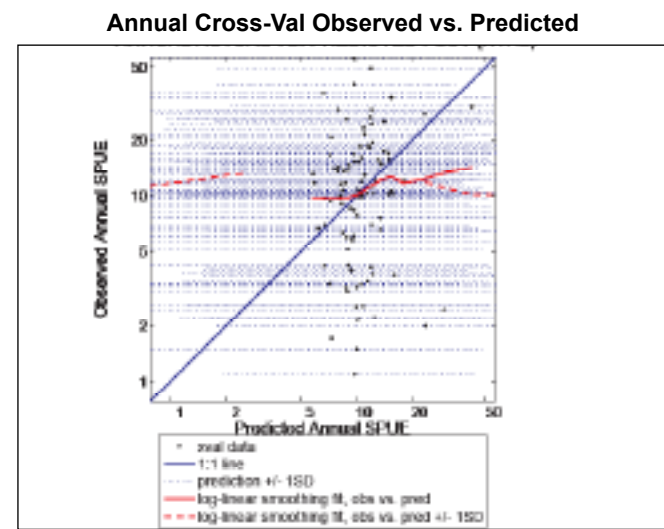
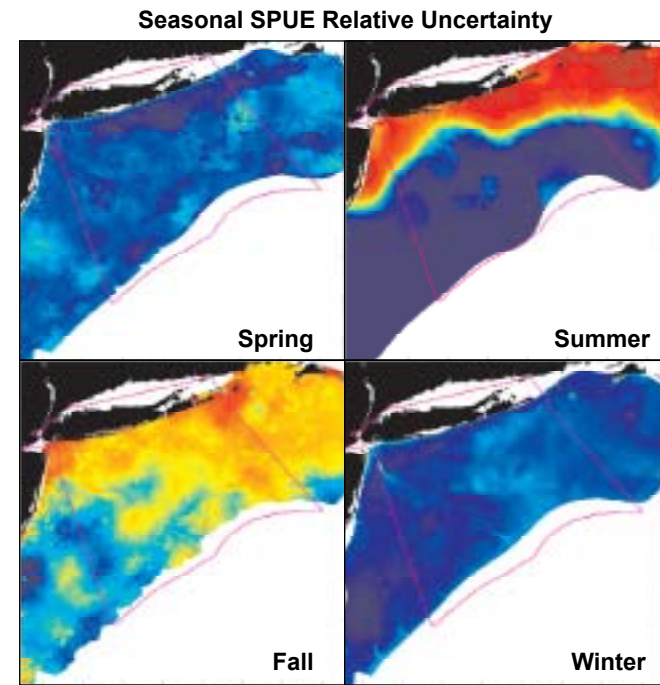
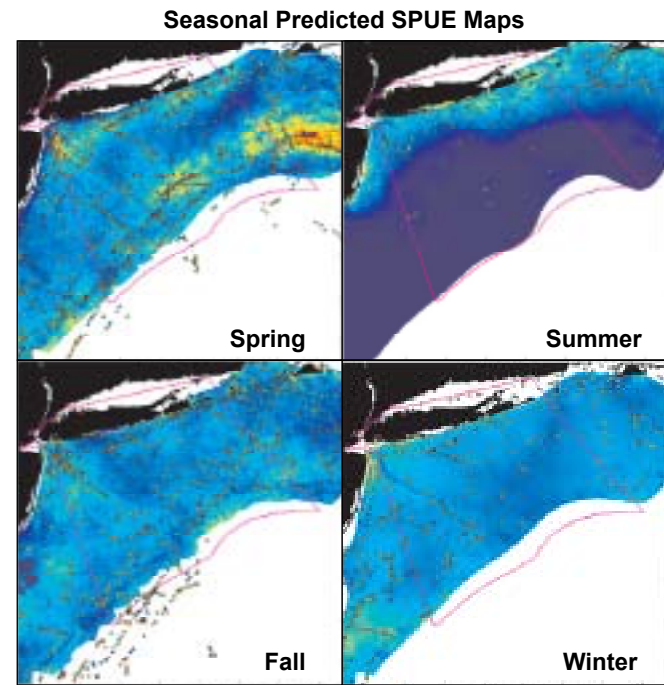
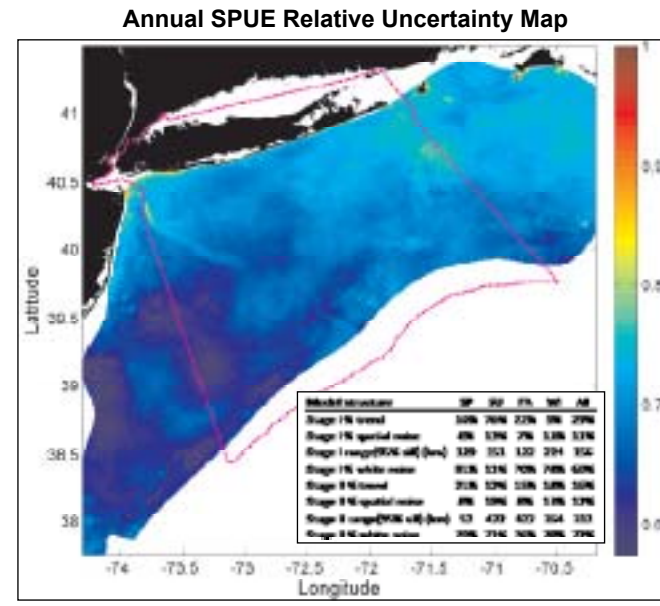
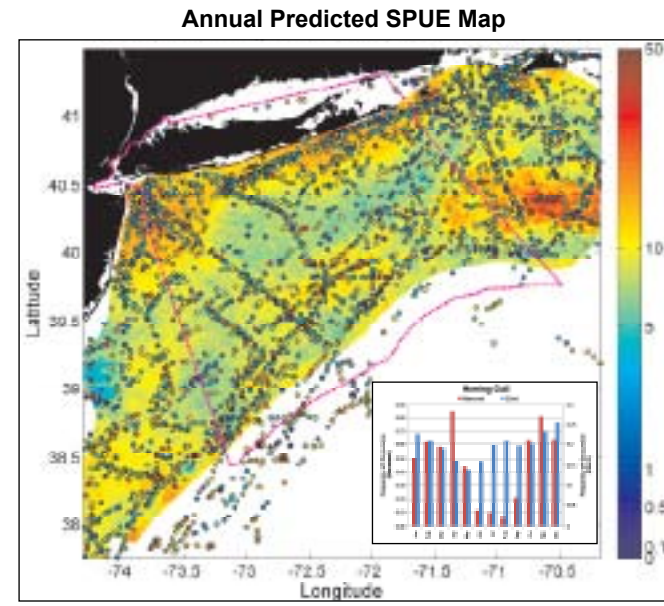
Great Shearwater

Stage I: Presence Probability Predictive Model



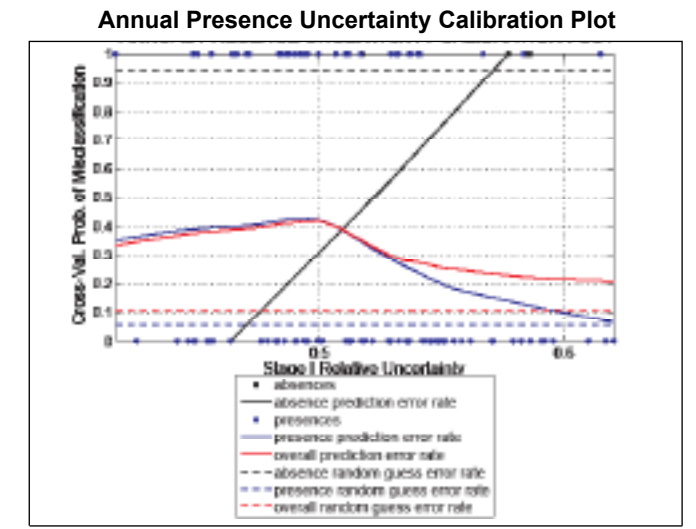
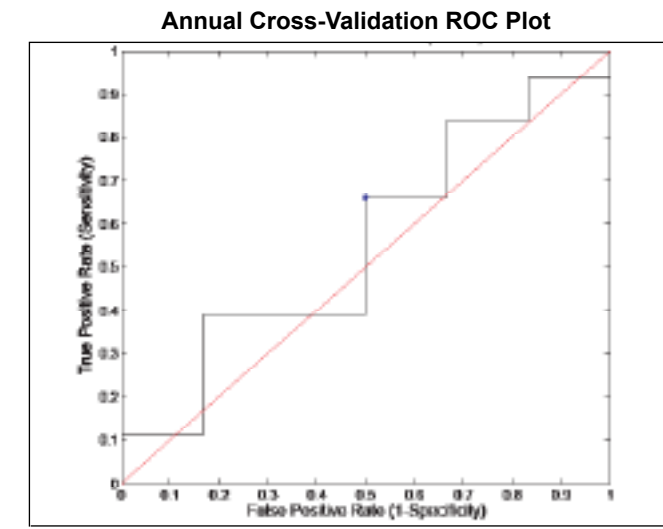
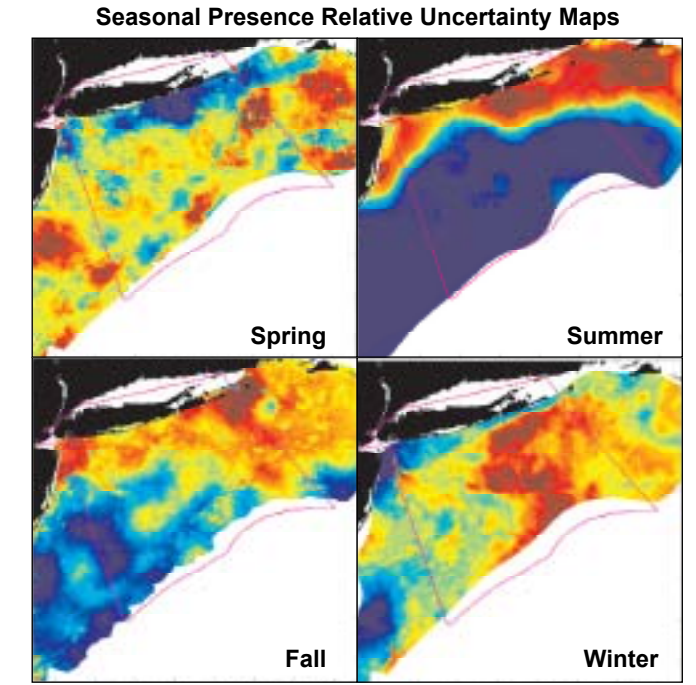
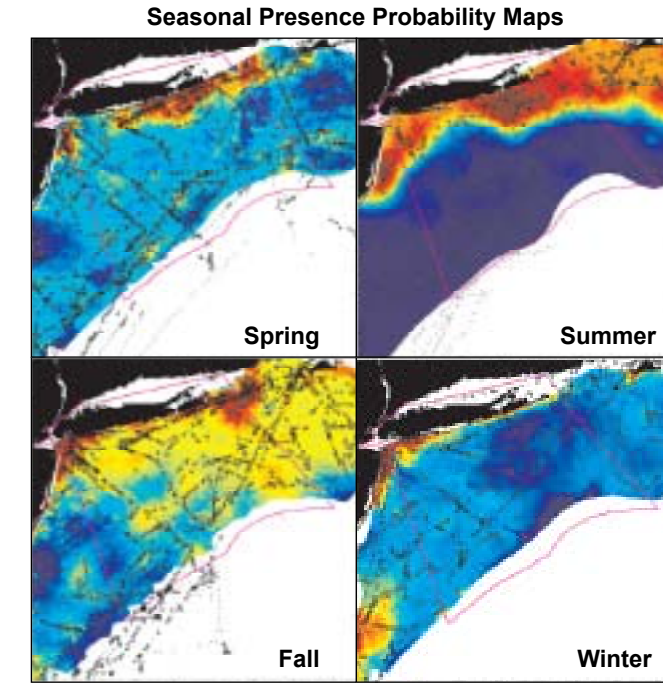
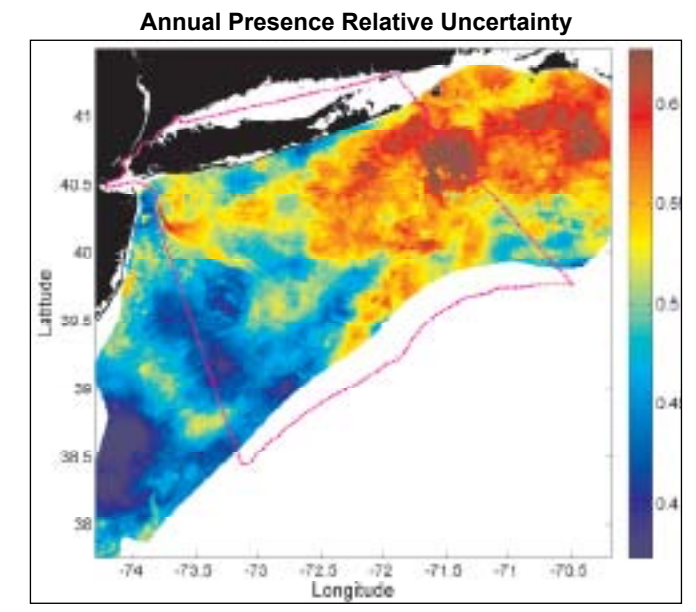
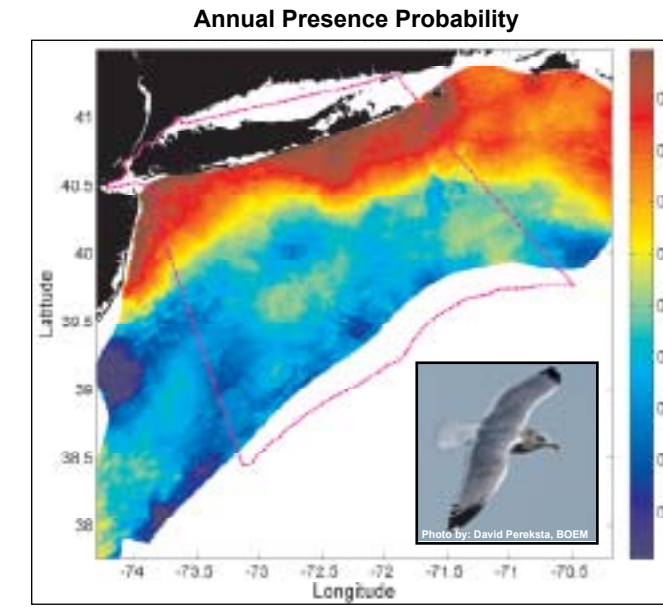
Herring Gull

Stage I x II: Relative Abundance Predictive Model



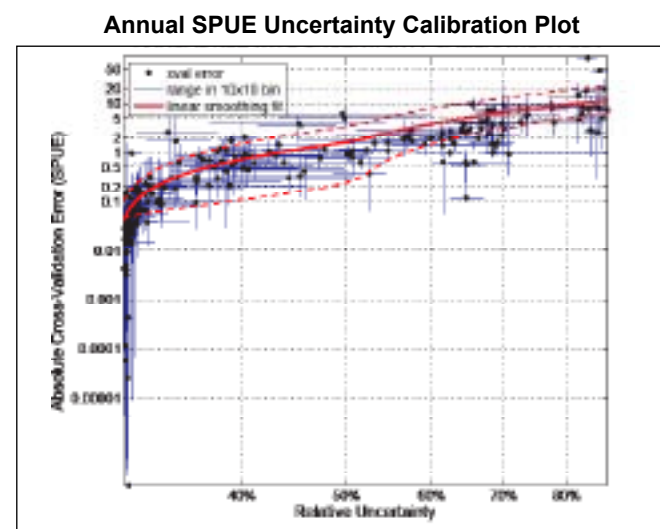
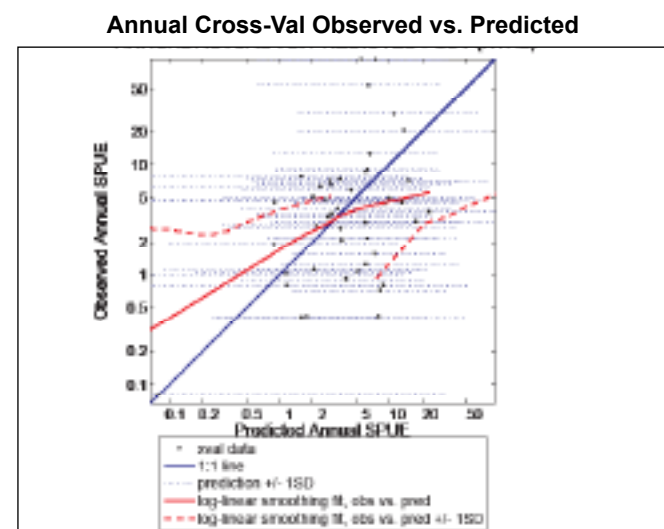
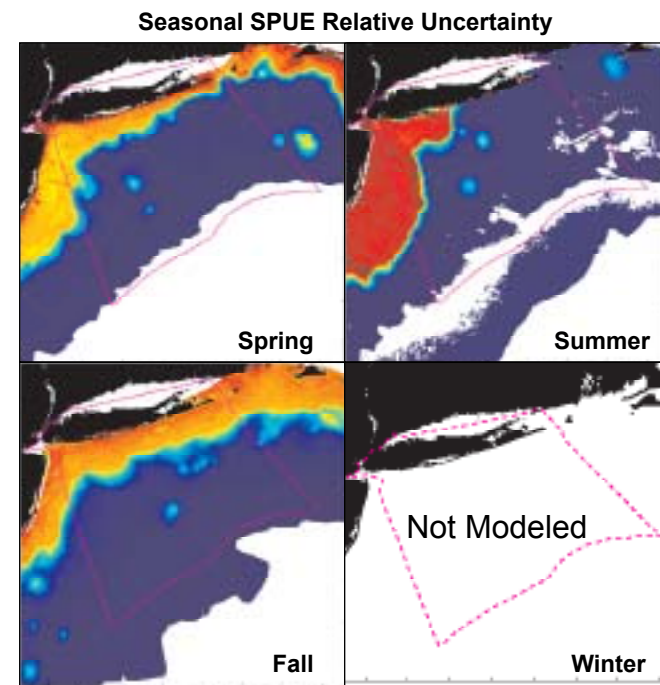
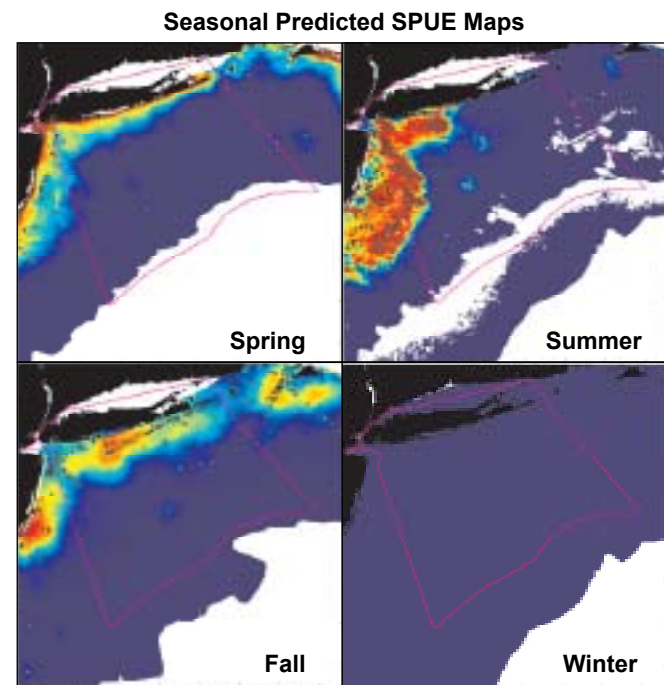
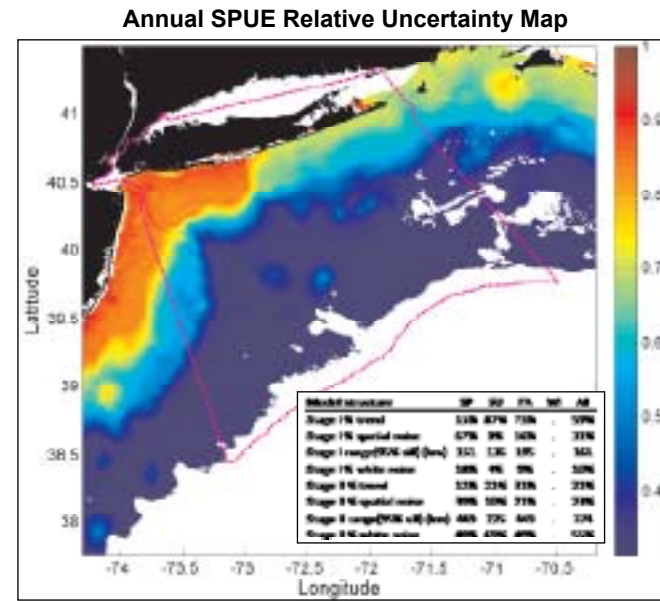
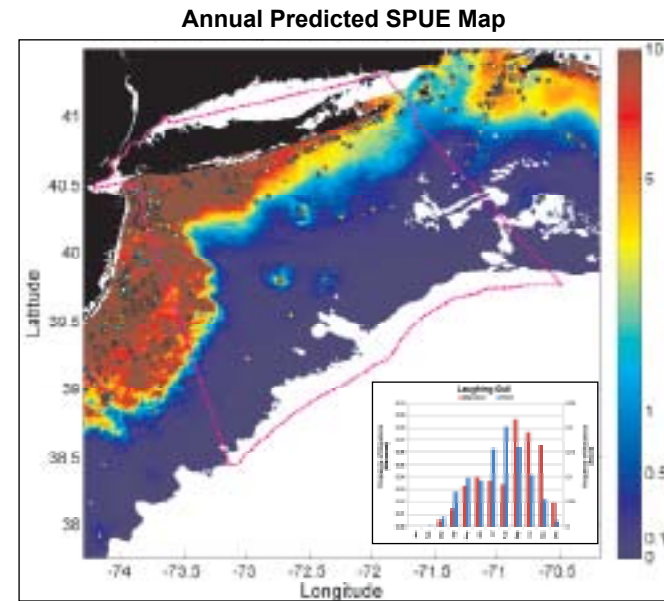
Herring Gull

Stage I: Presence Probability Predictive Model



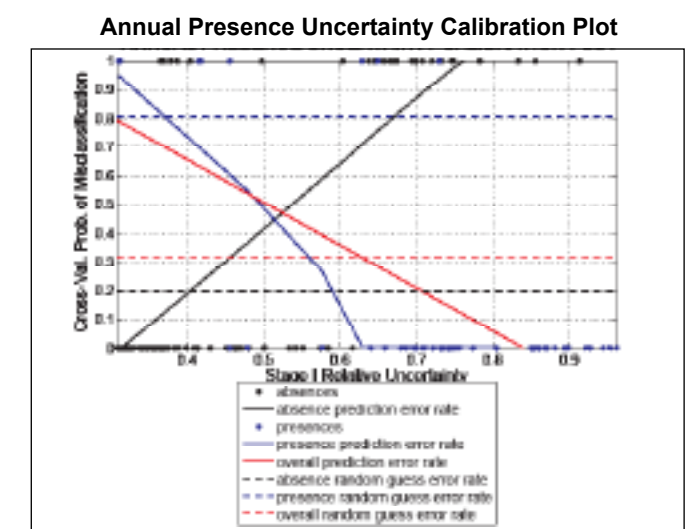
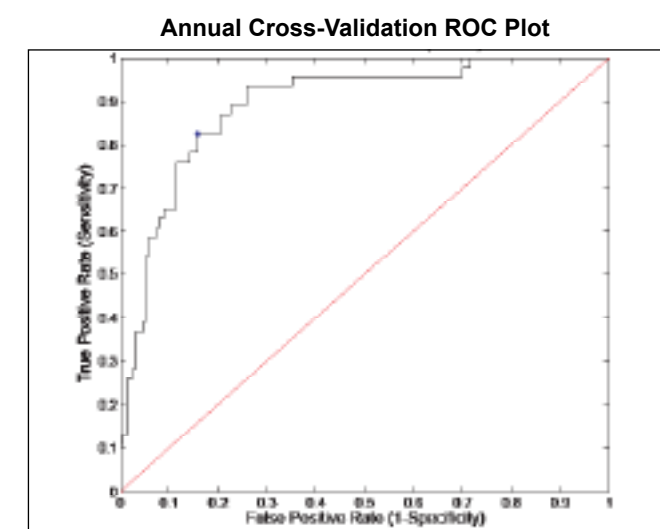
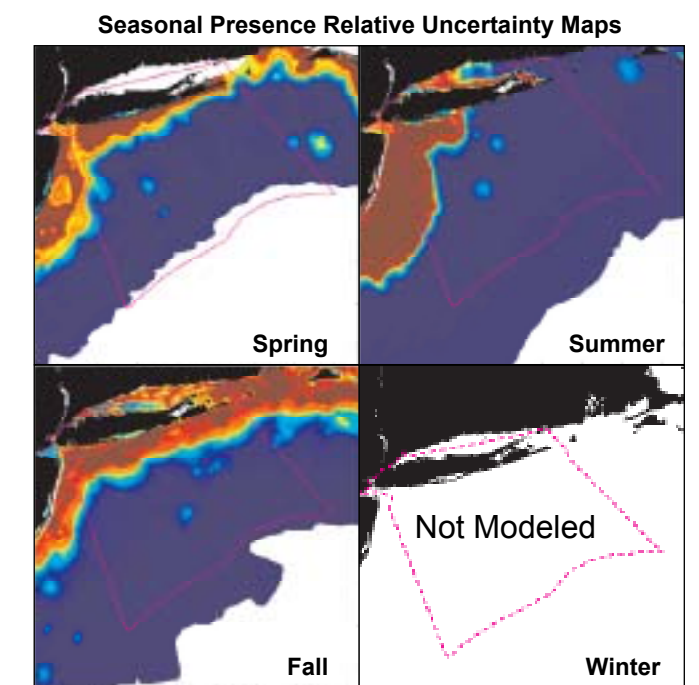
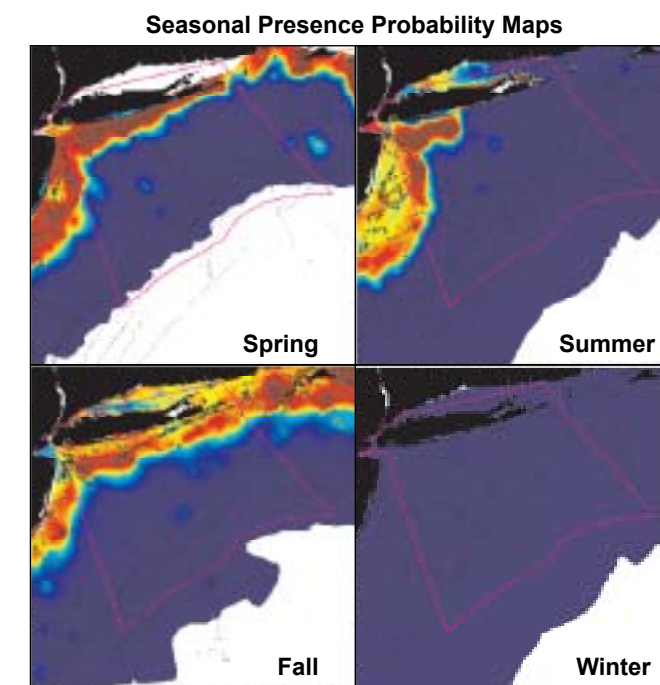
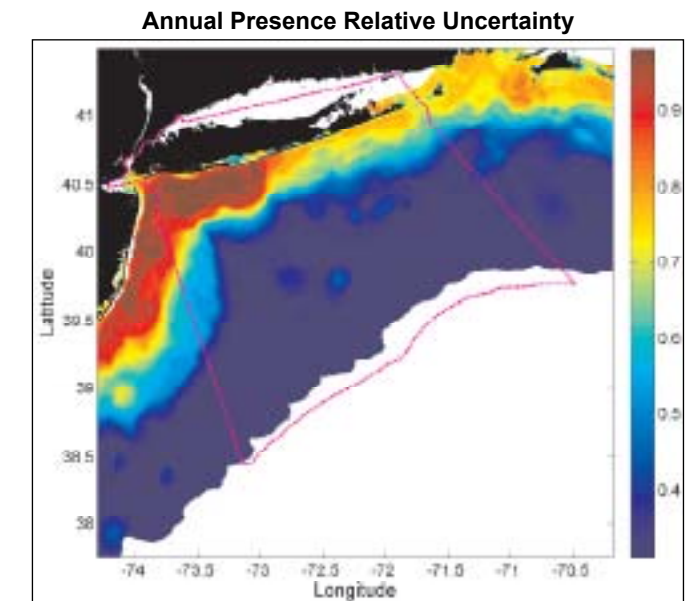
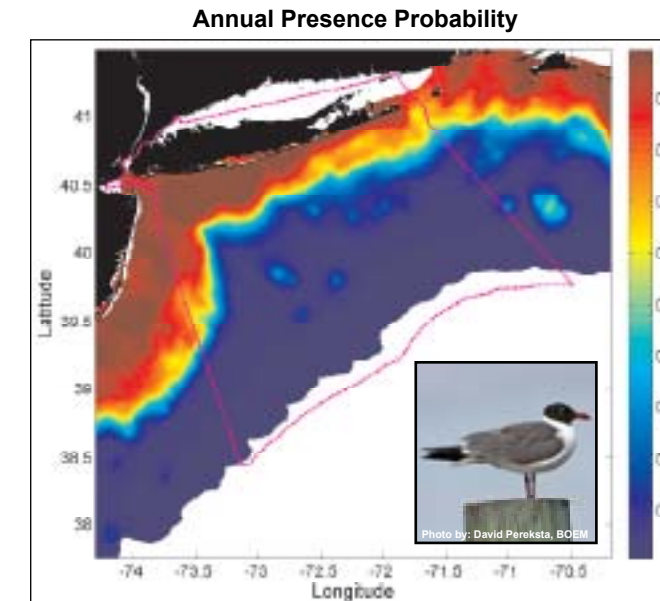
Laughing Gull

Stage I x II: Relative Abundance Predictive Model



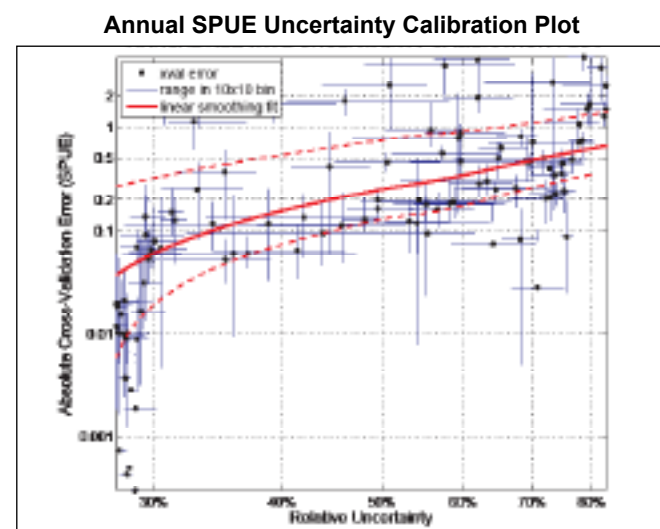
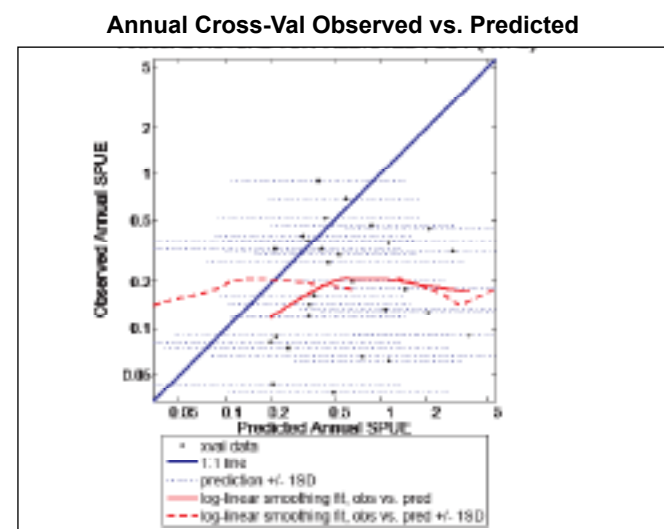
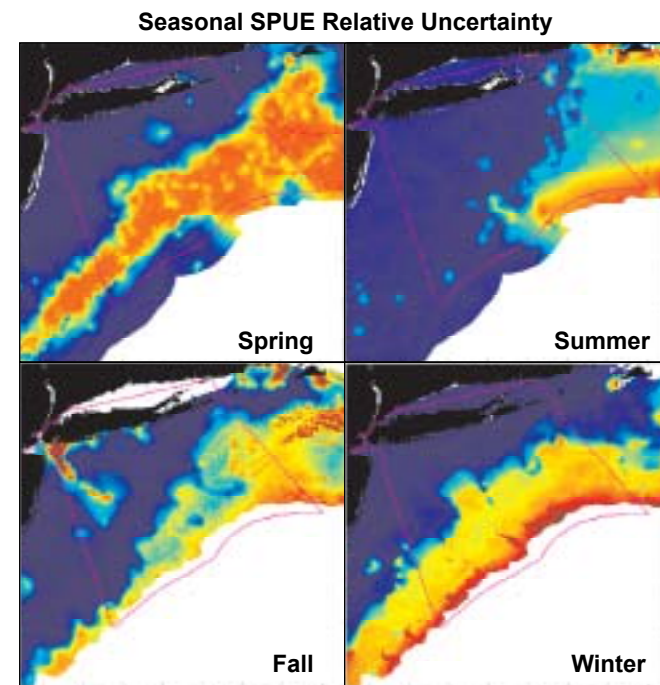
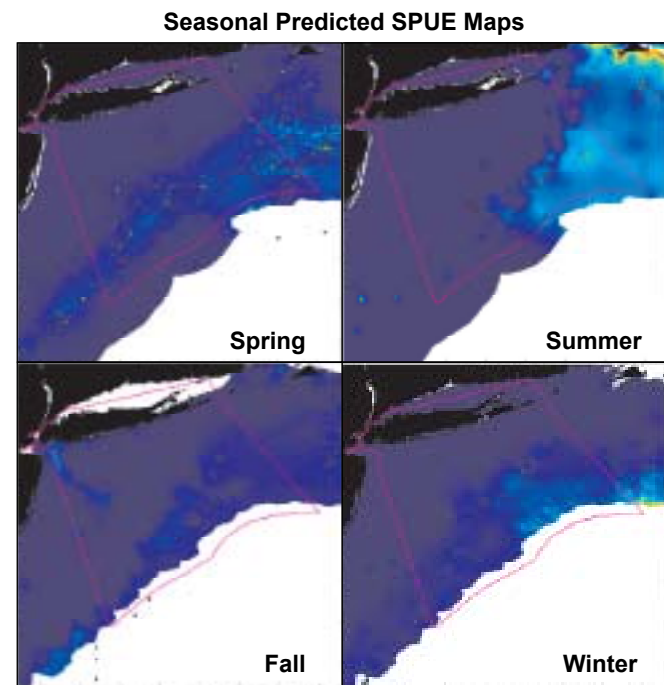
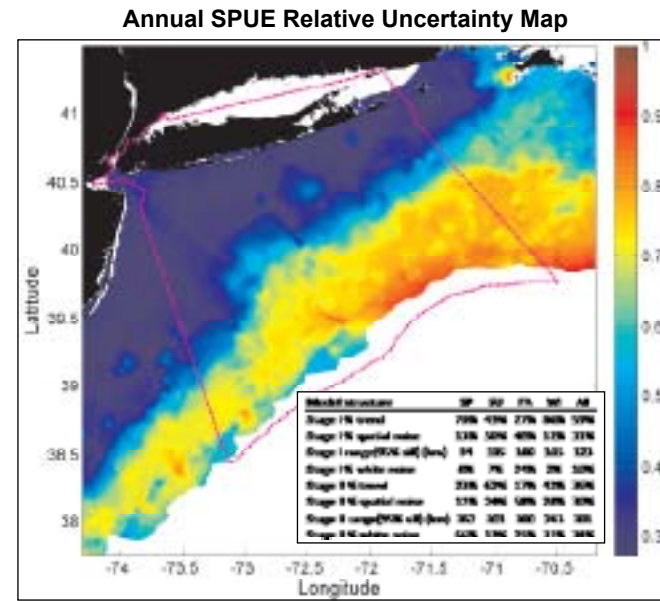
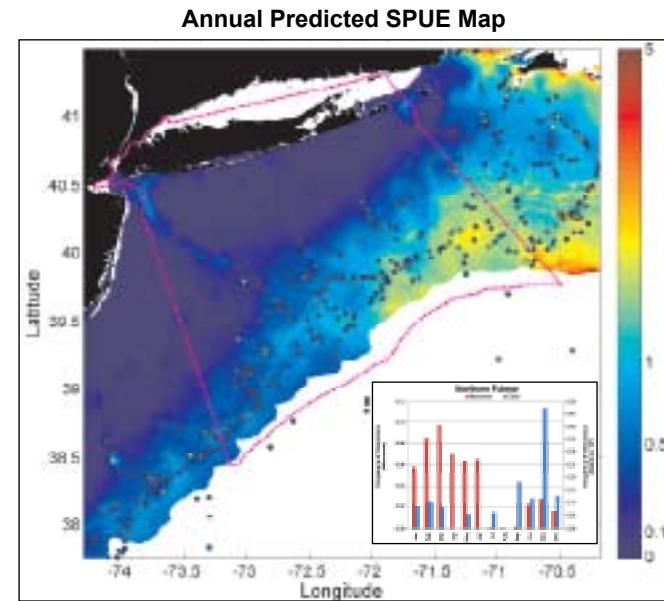
Laughing Gull

Stage I: Presence Probability Predictive Model



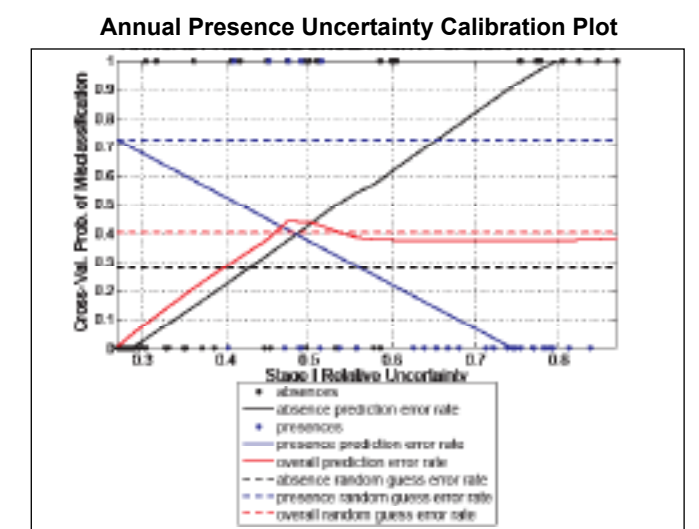
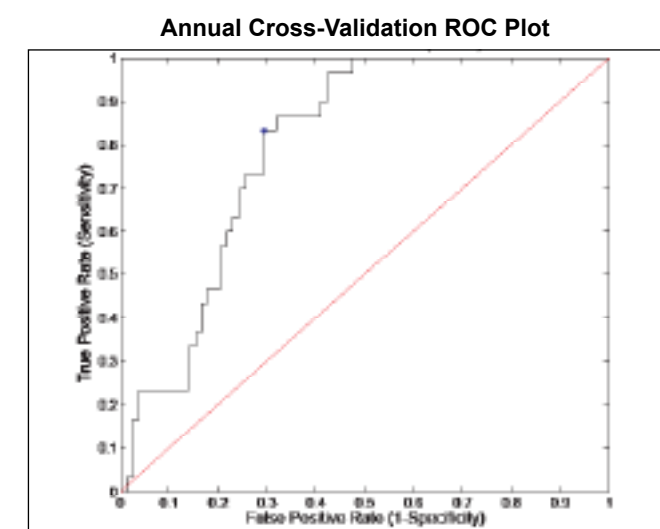
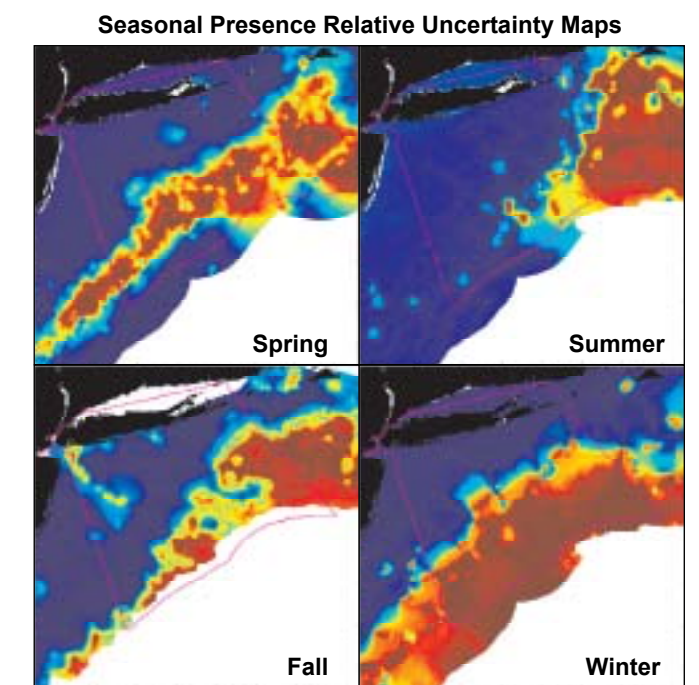
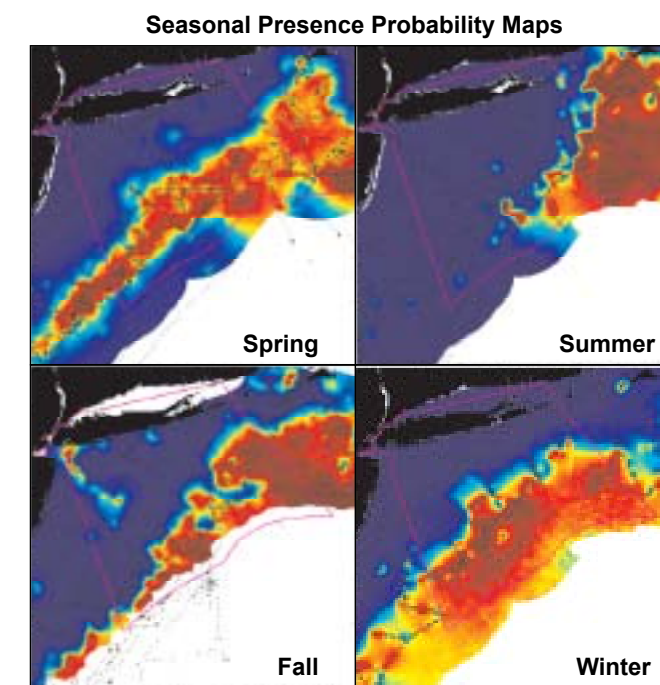
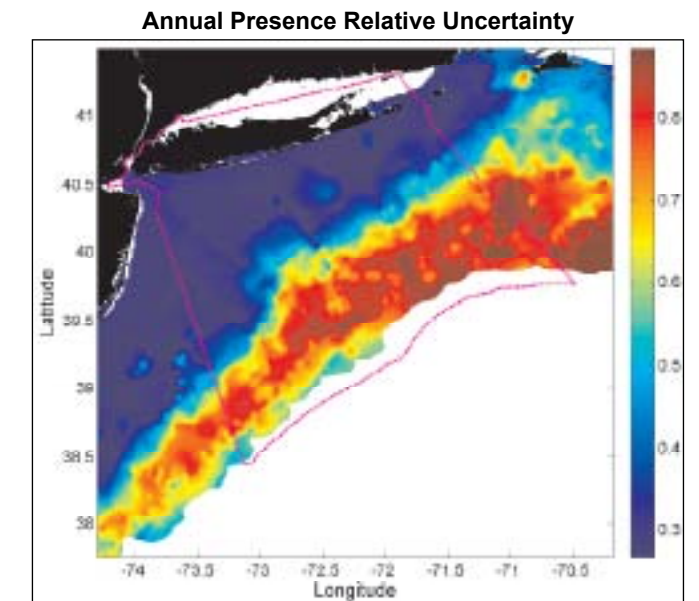
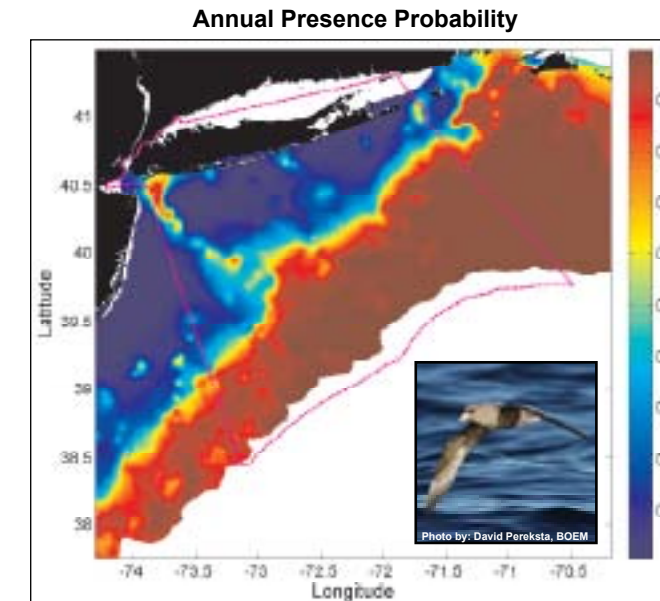
Northern Fulmar

Stage I x II: Relative Abundance Predictive Model



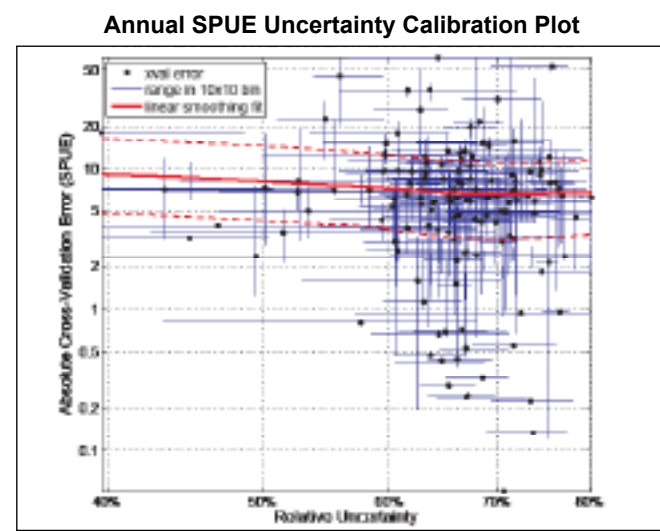
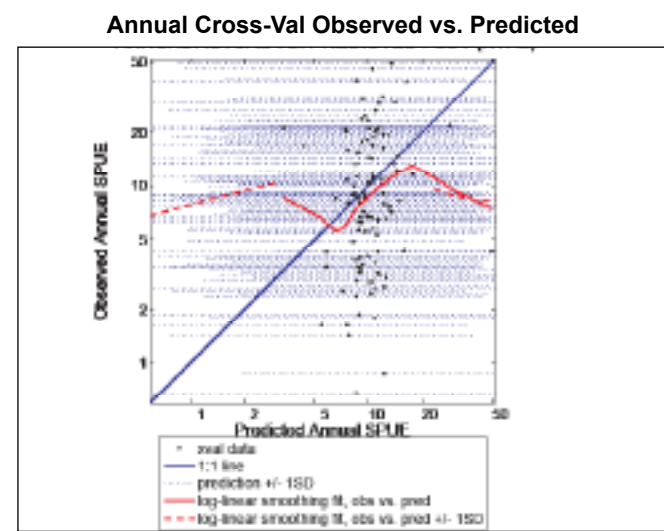
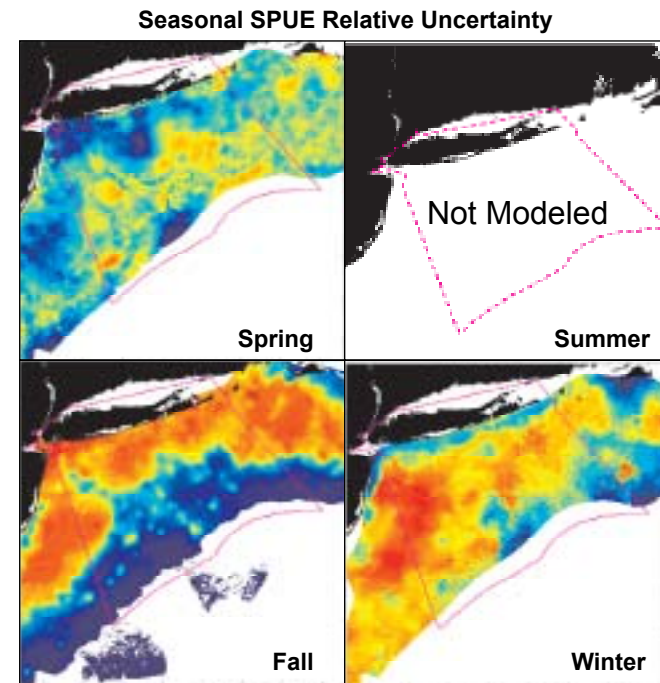
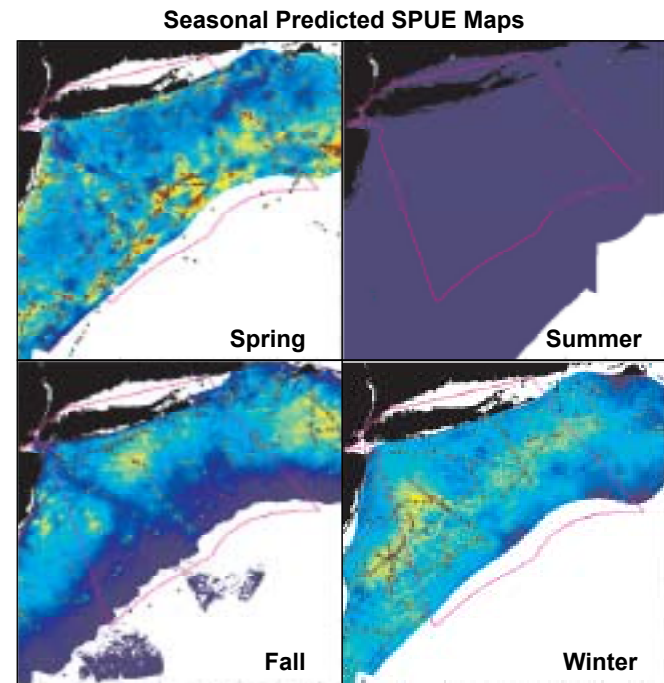
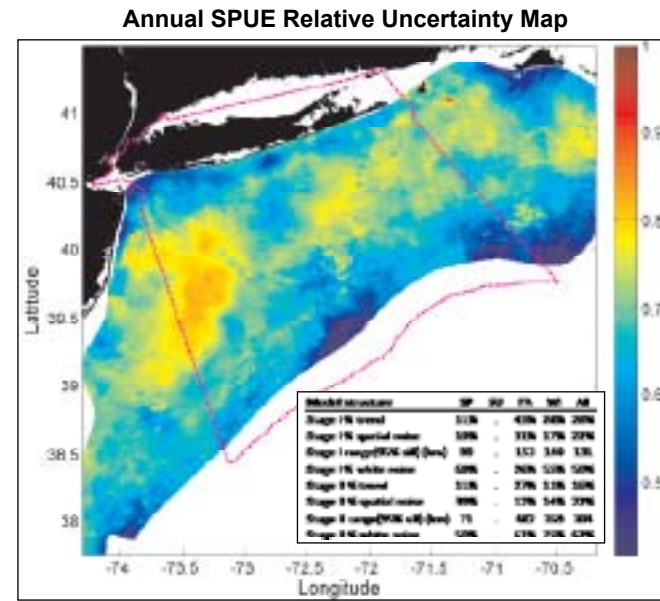
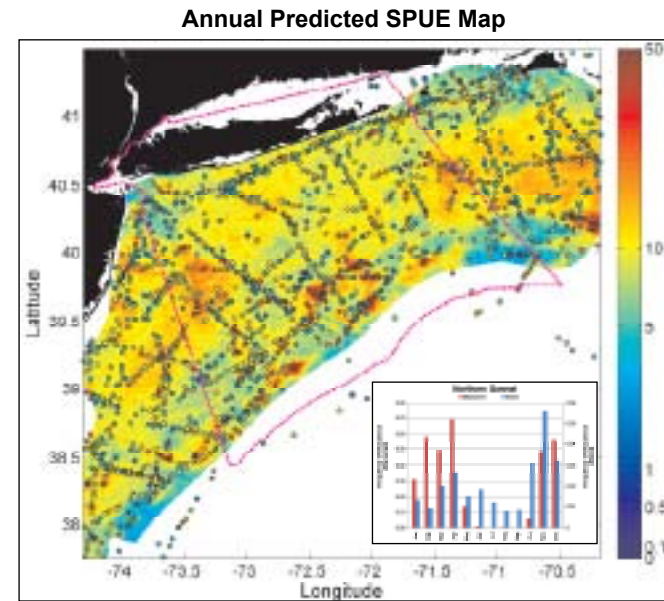
Northern Fulmar

Stage I: Presence Probability Predictive Model



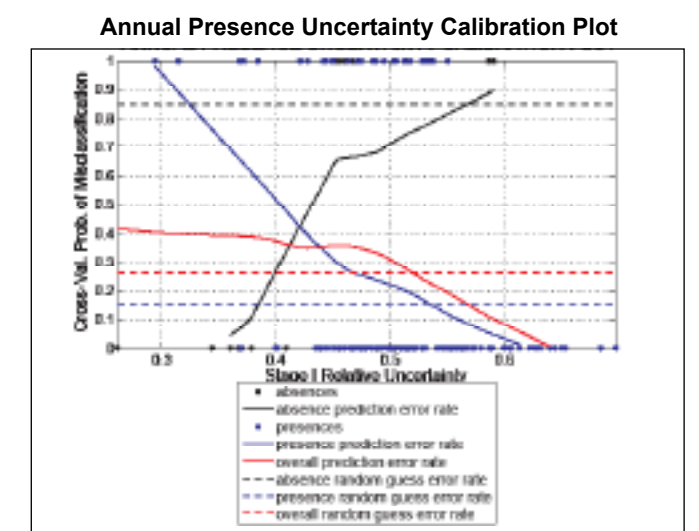
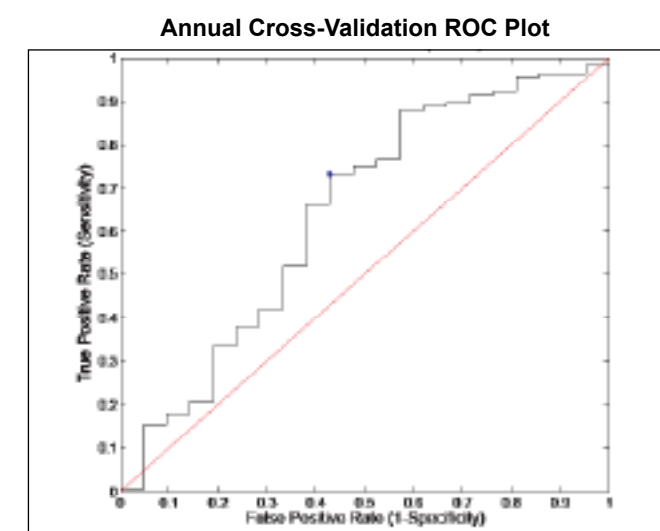
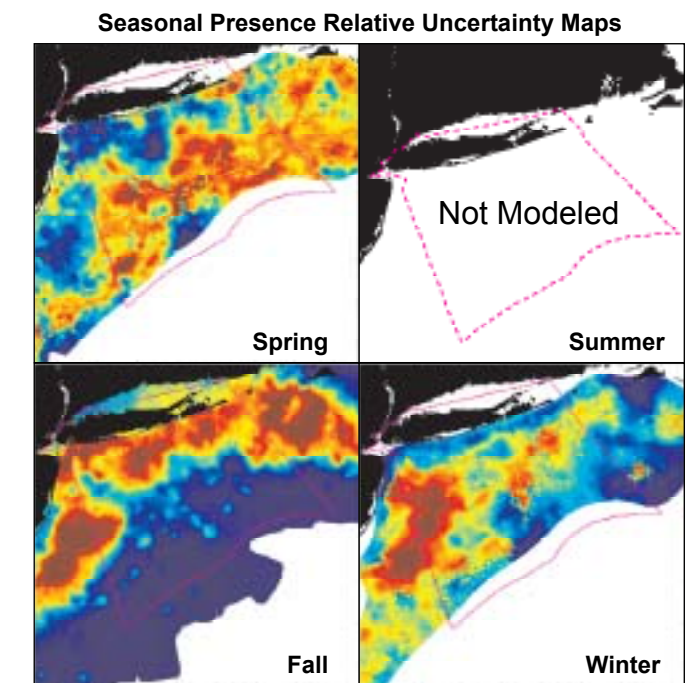
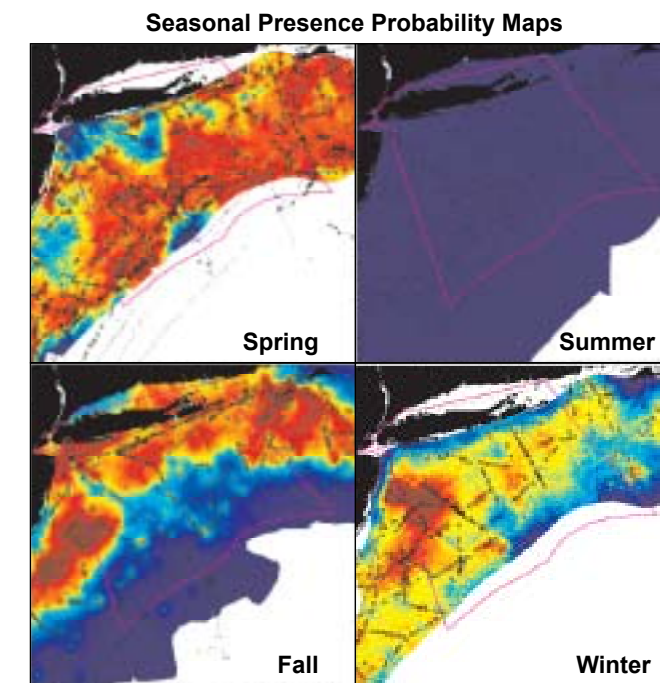
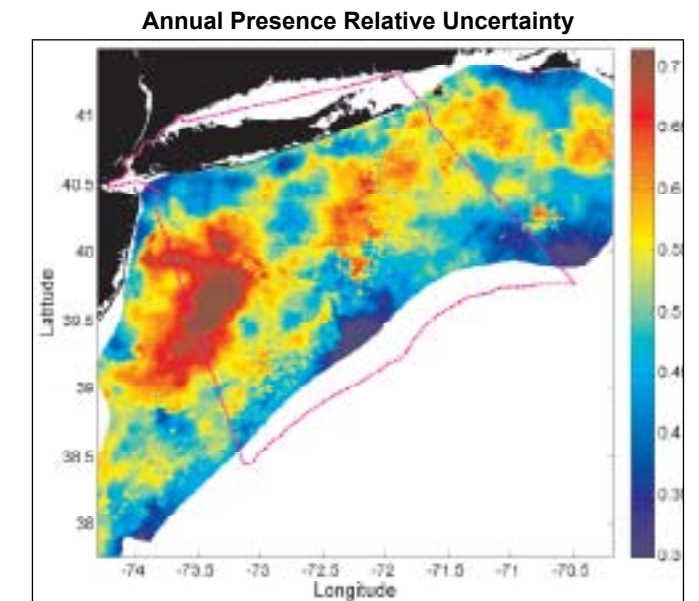
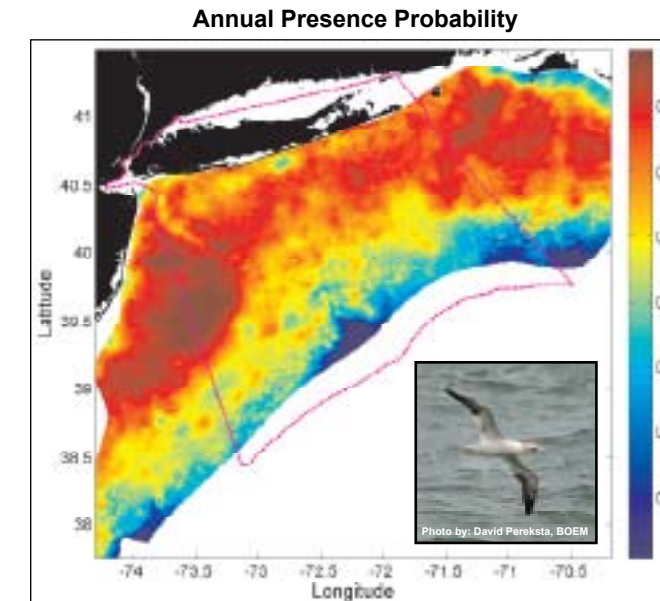
Northern Gannet

Stage I x II: Relative Abundance Predictive Model



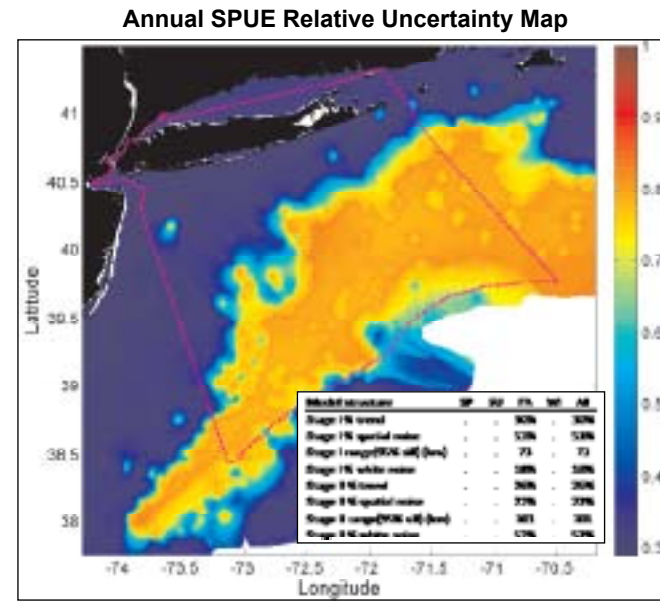
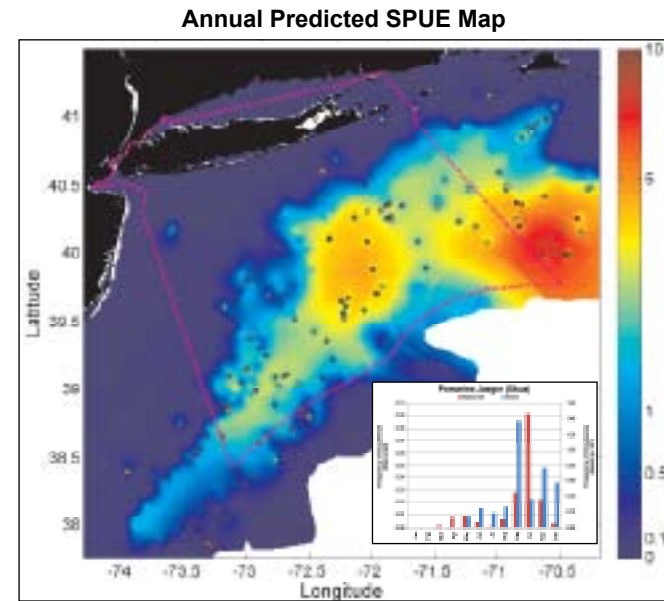
Northern Gannet

Stage I: Presence Probability Predictive Model



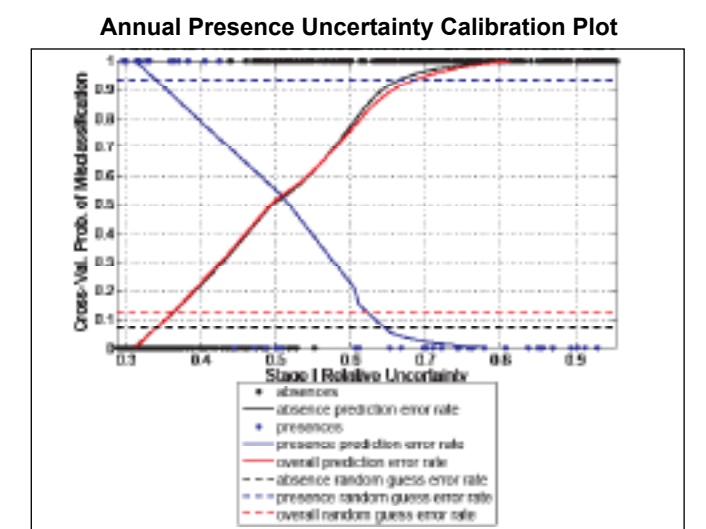
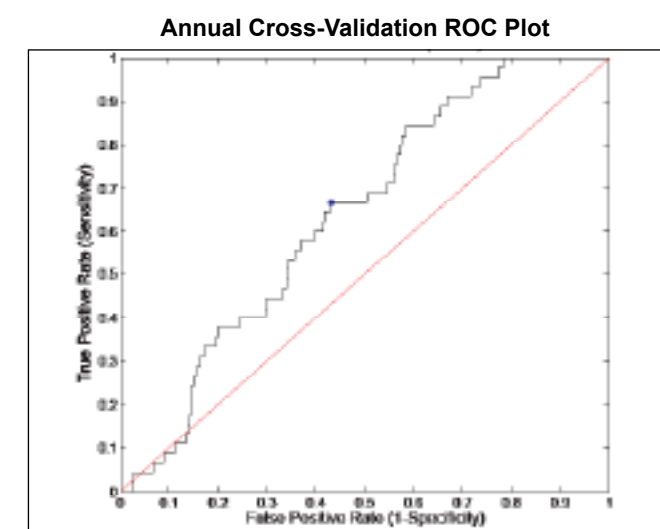
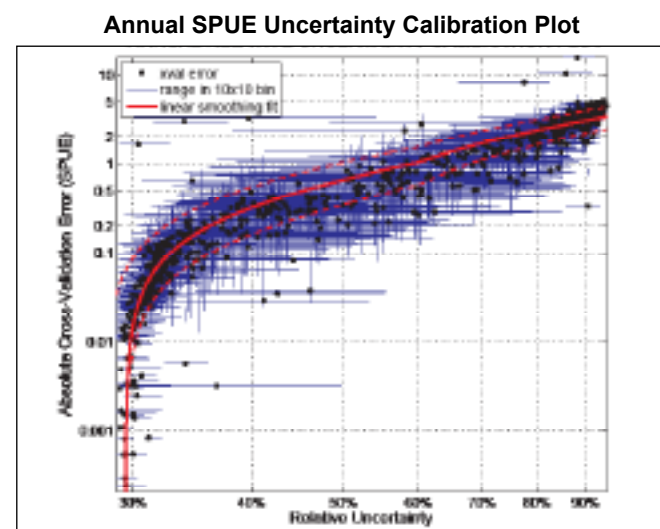
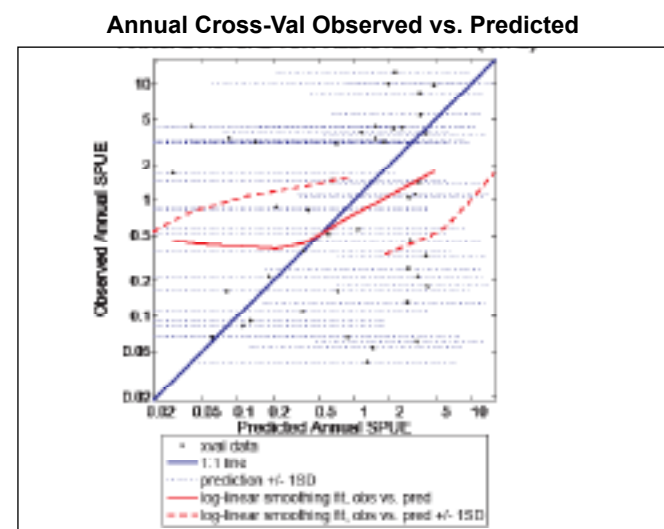
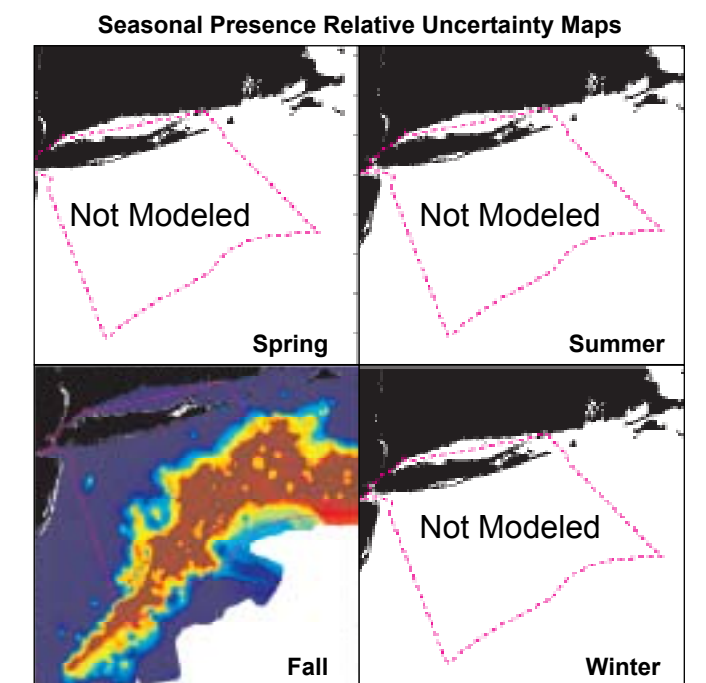
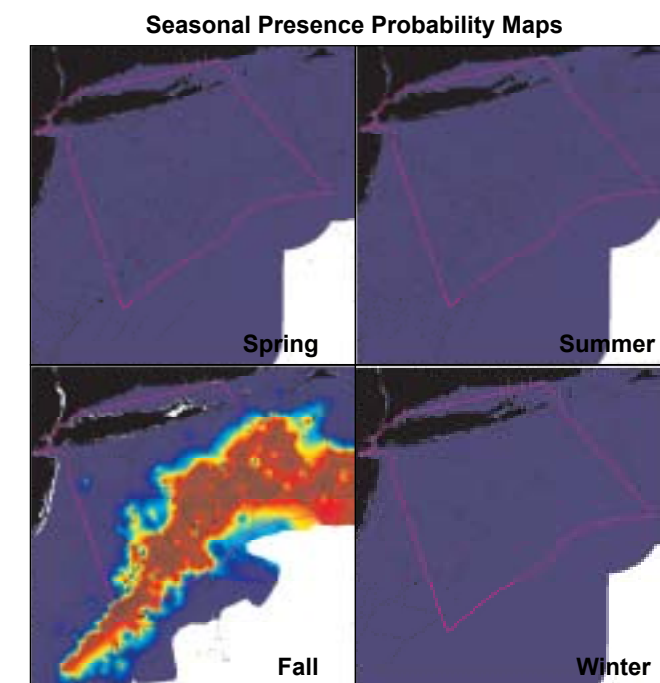
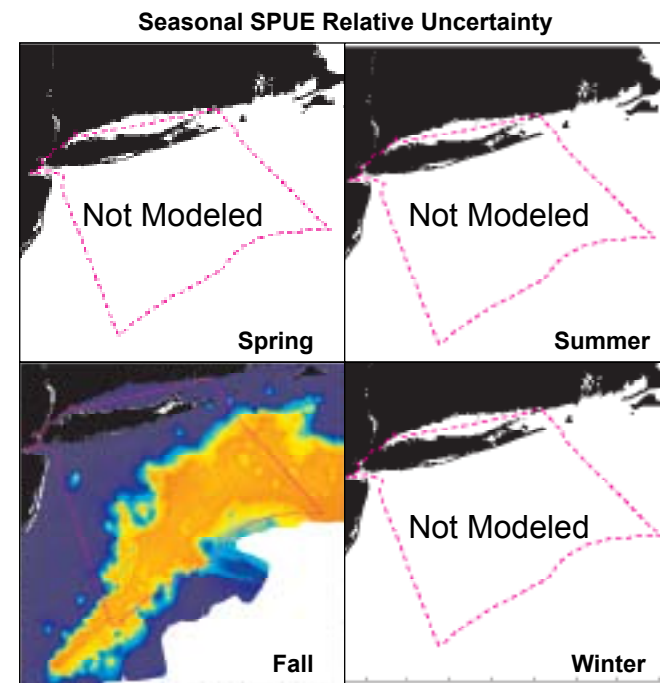
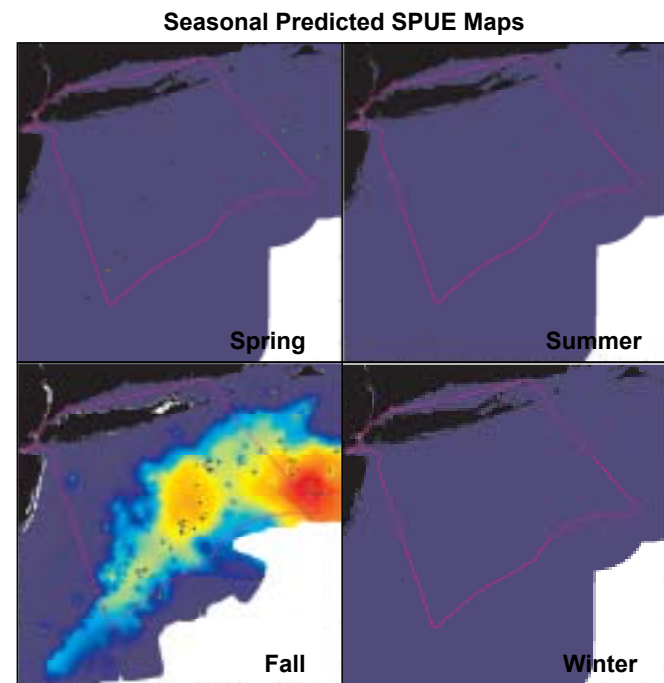
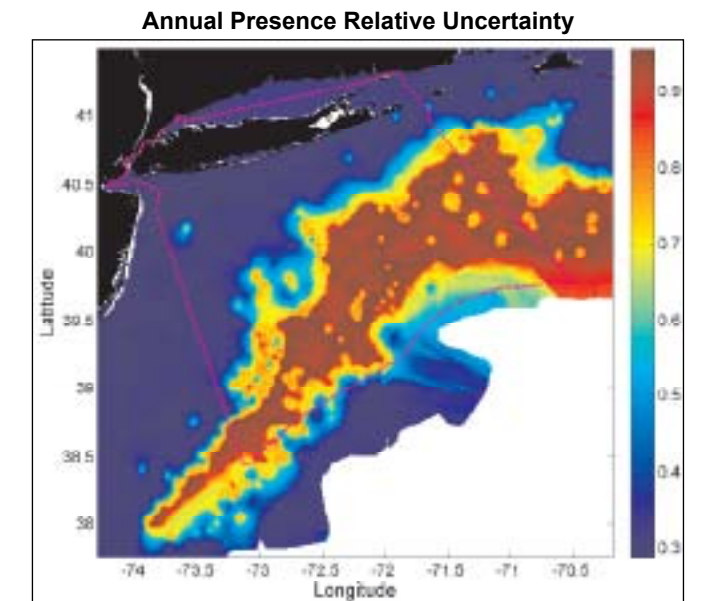
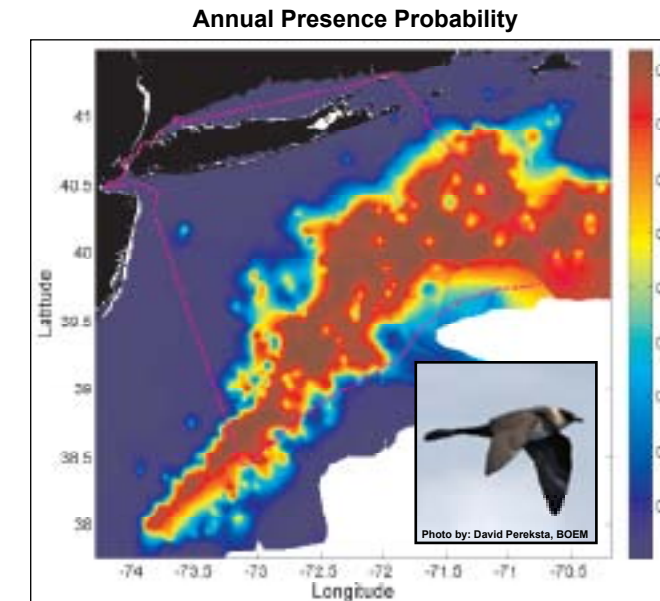
Pomarine Jaeger

Stage I x II: Relative Abundance Predictive Model



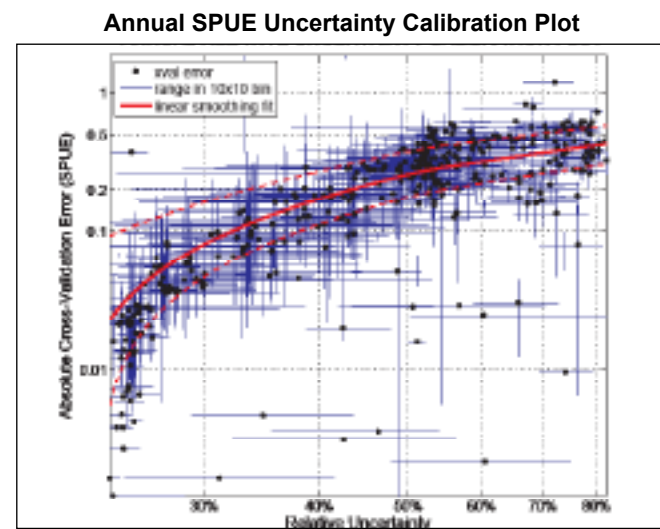
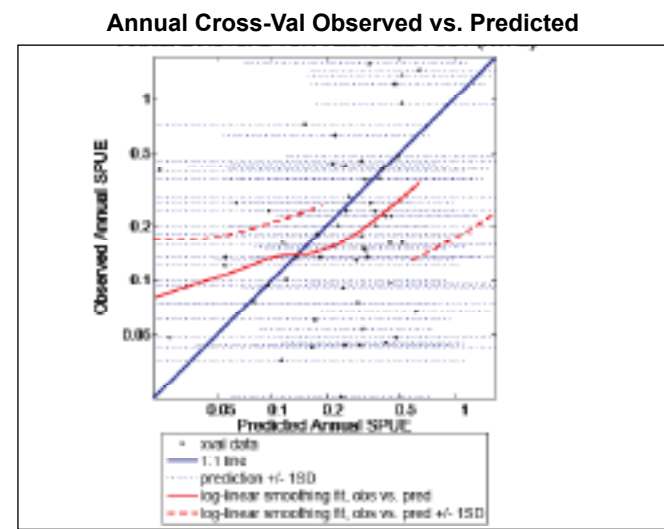
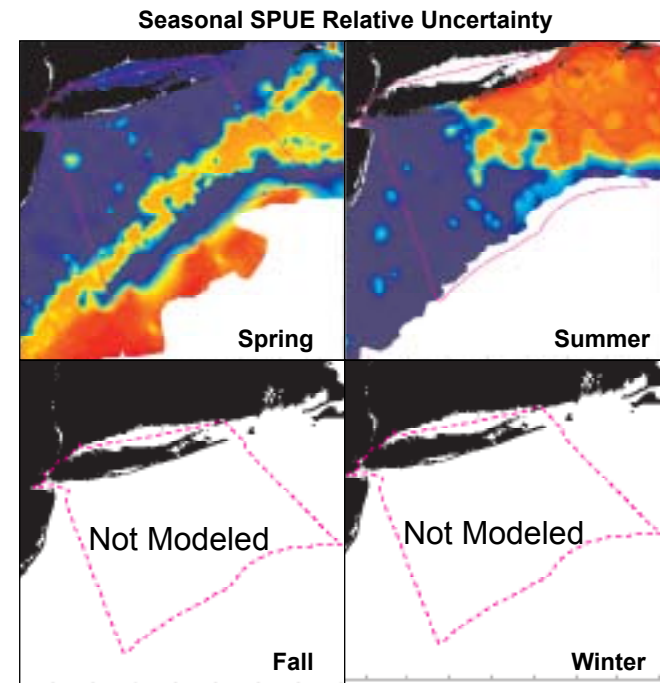
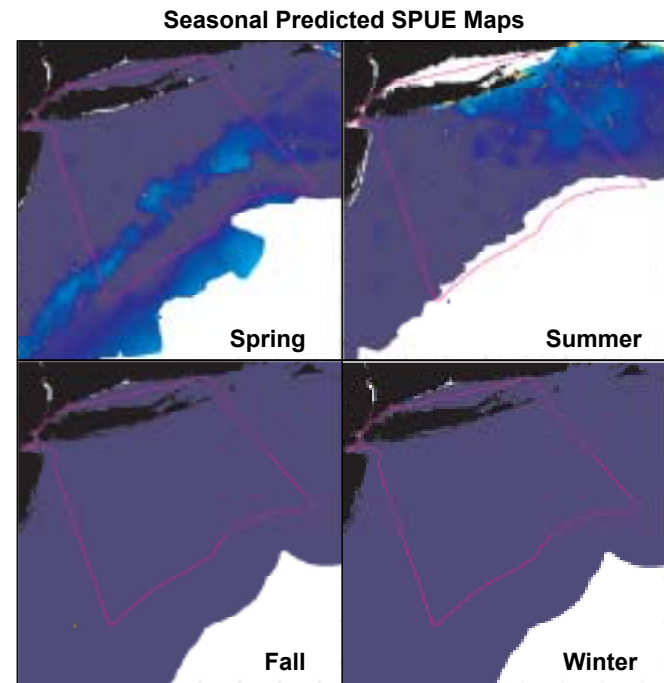
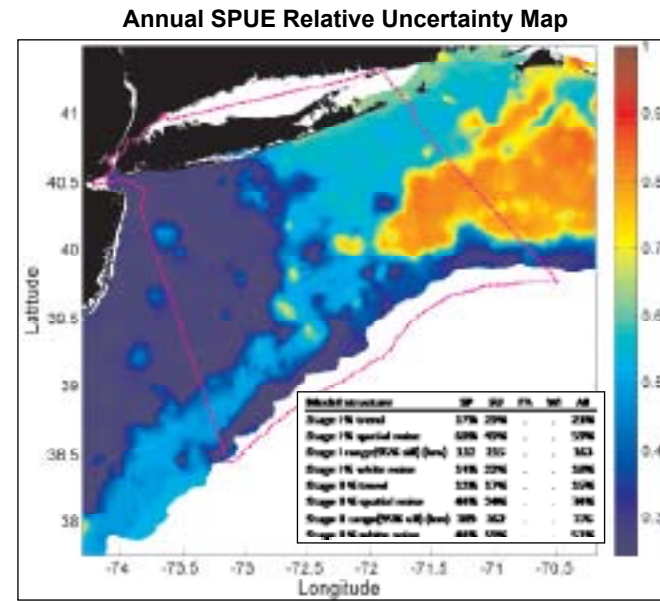
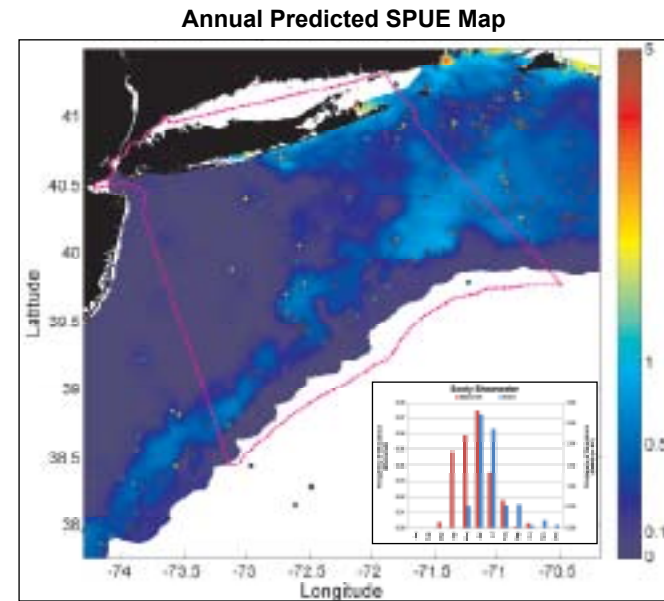
Pomarine Jaeger

Stage I: Presence Probability Predictive Model



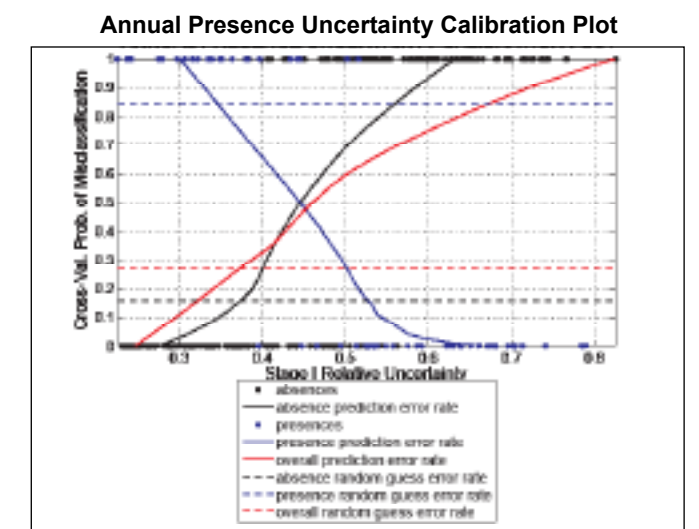
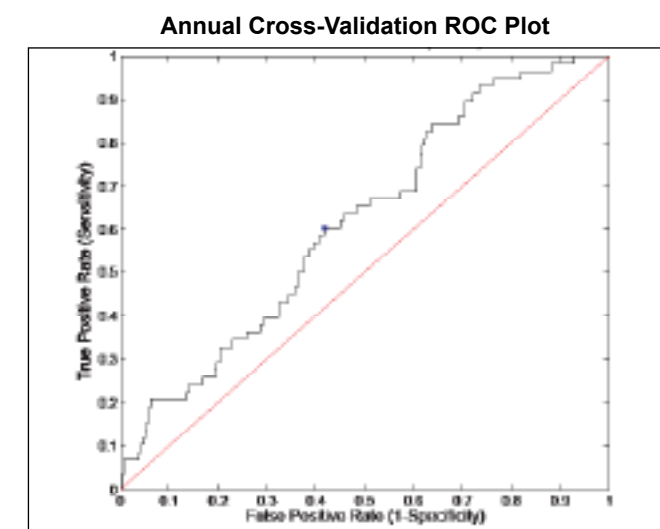
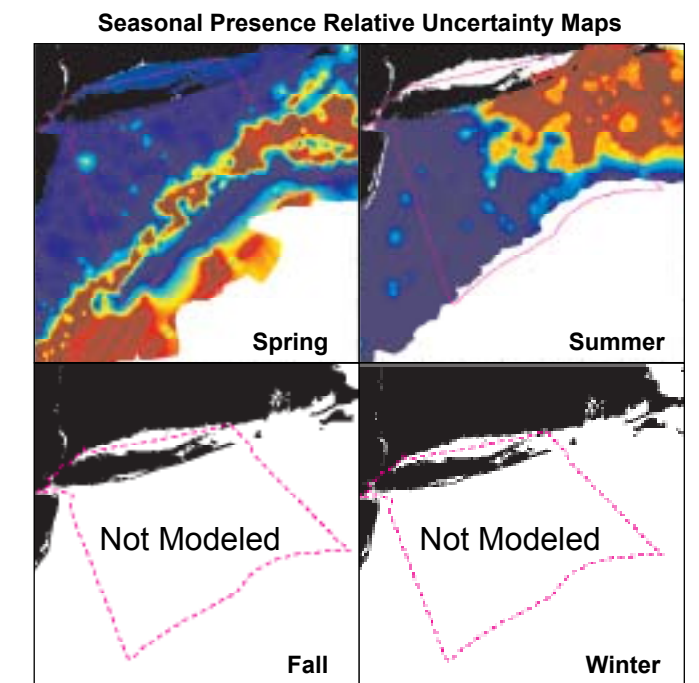
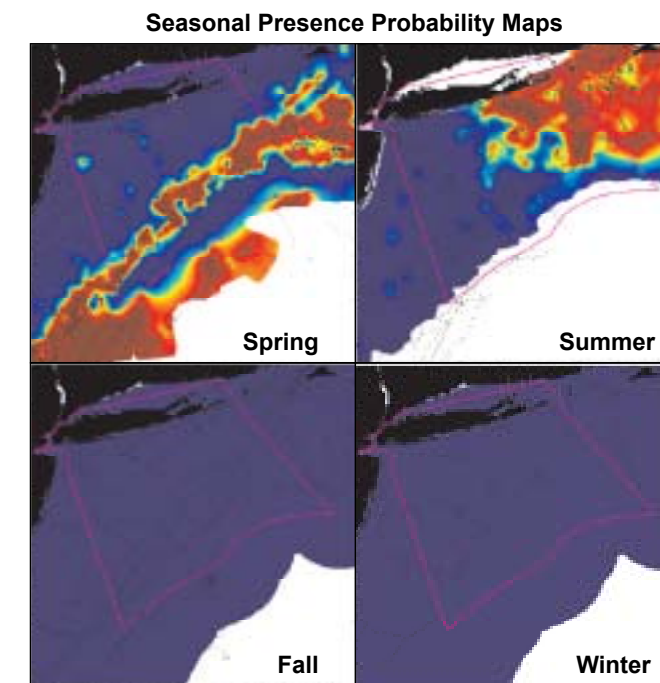
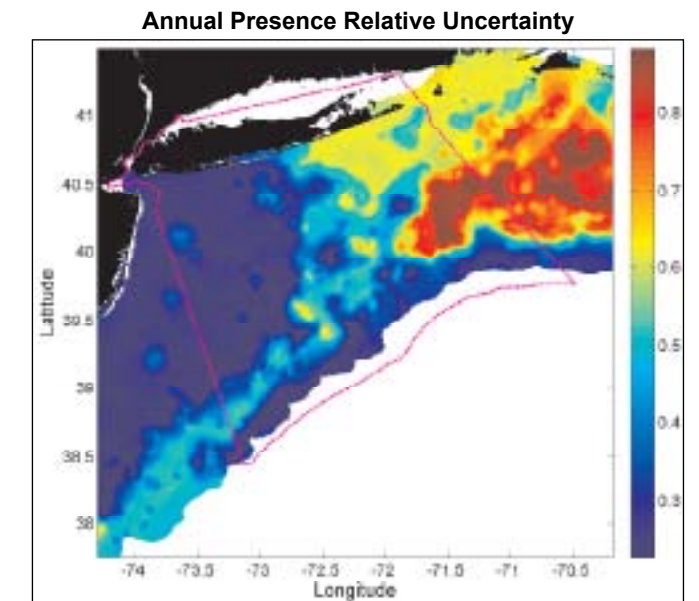
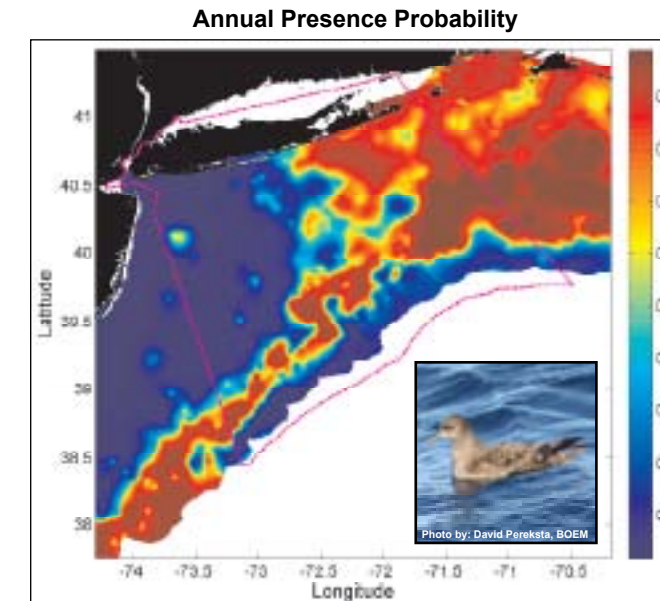
Sooty Shearwater

Stage I x II: Relative Abundance Predictive Model



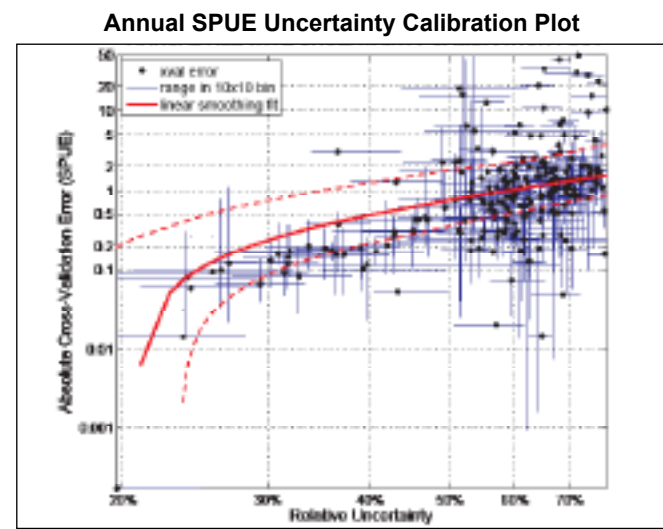
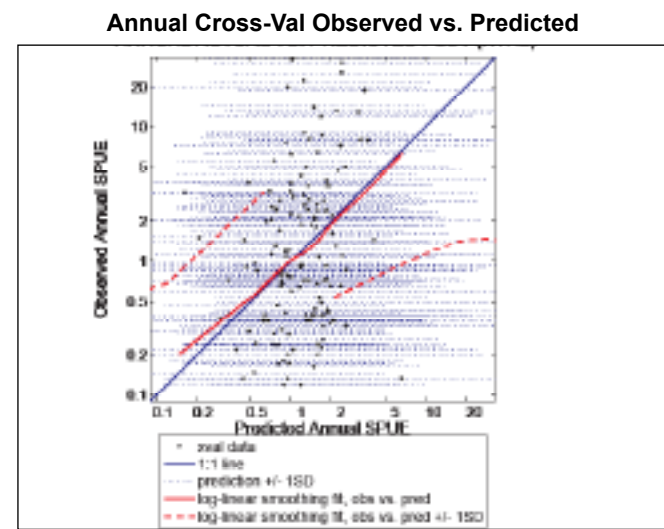
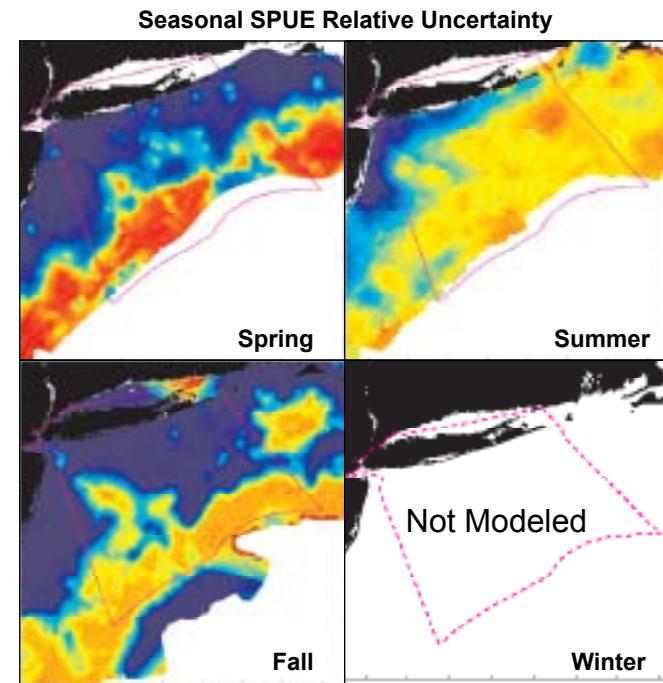
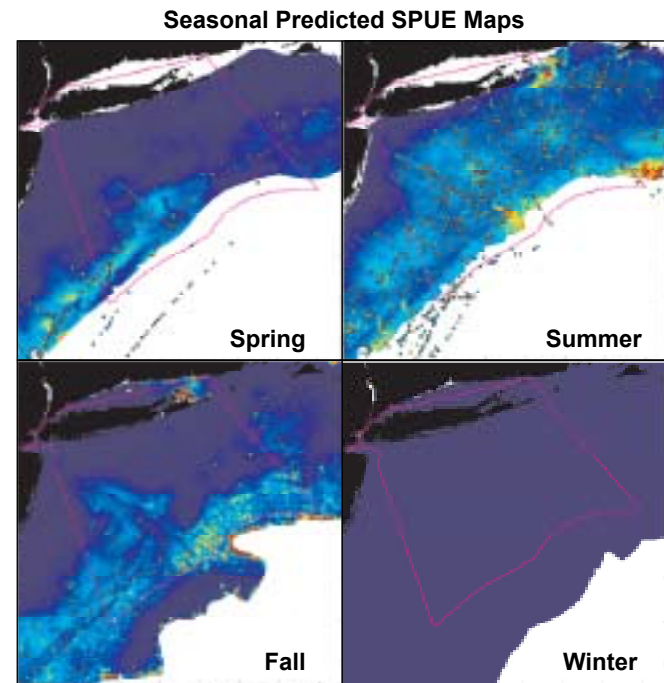
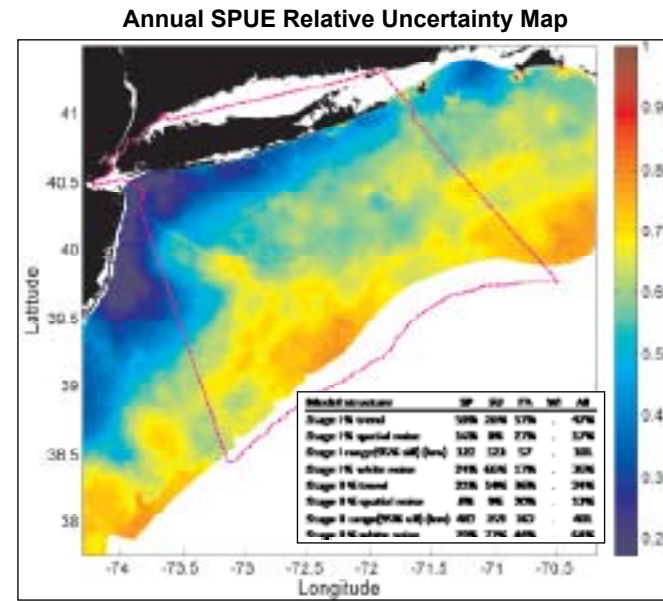
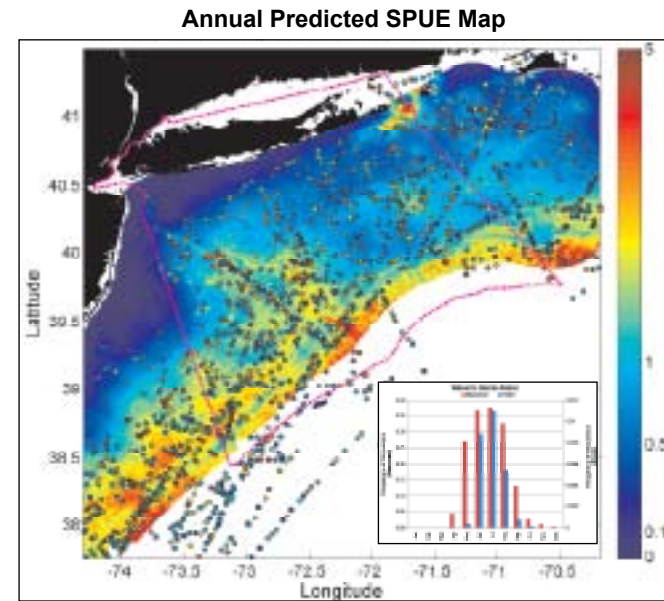
Sooty Shearwater

Stage I: Presence Probability Predictive Model



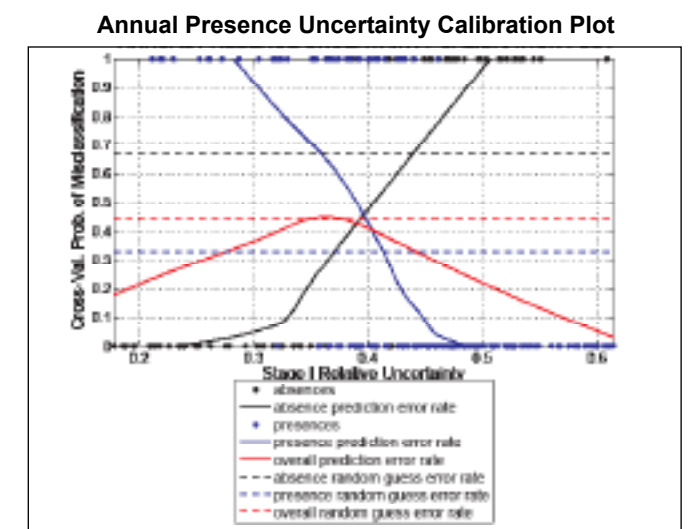
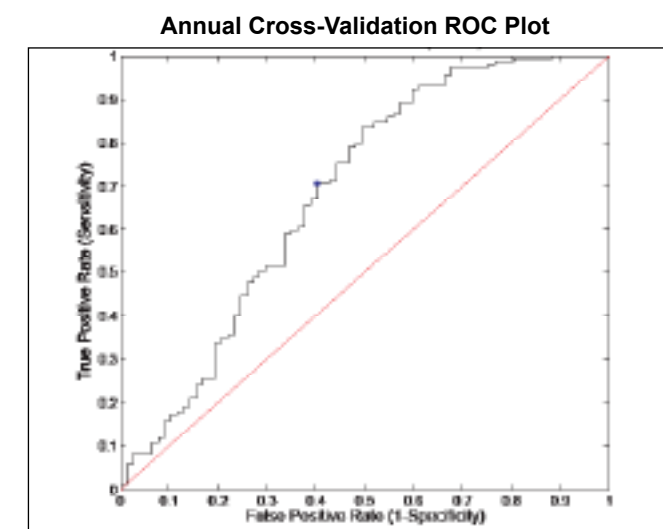
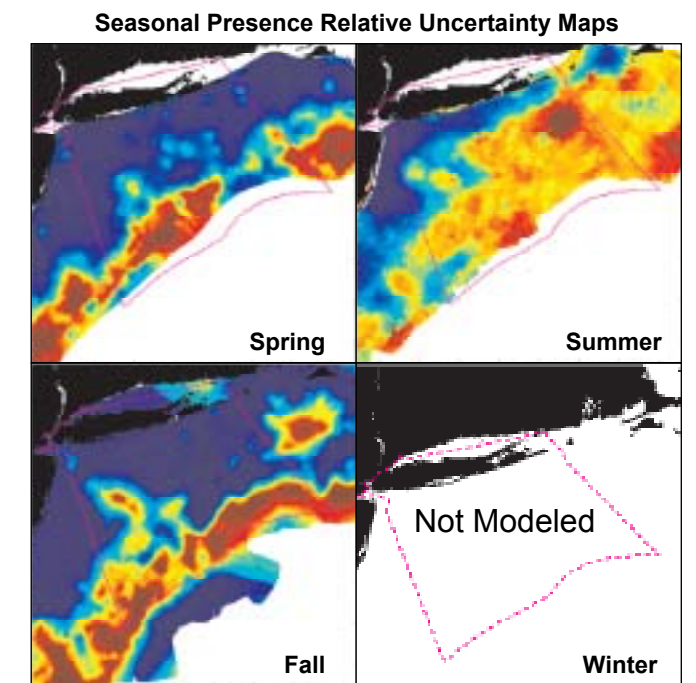
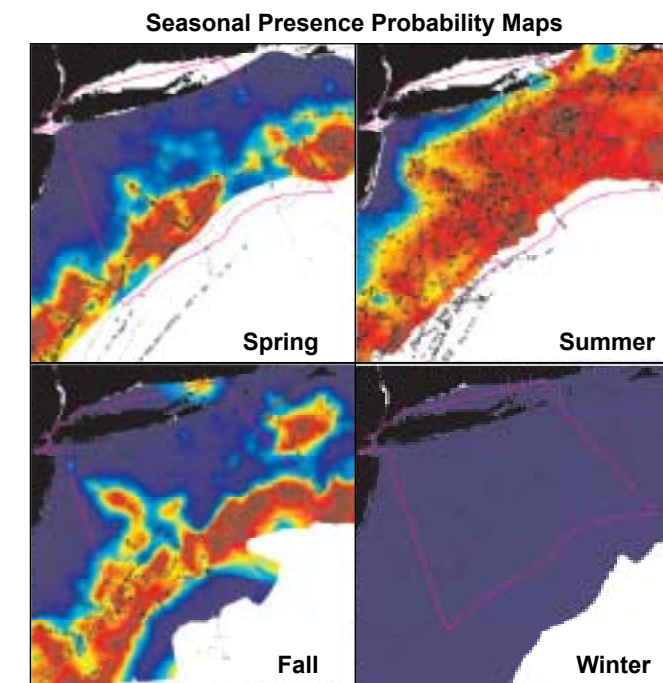
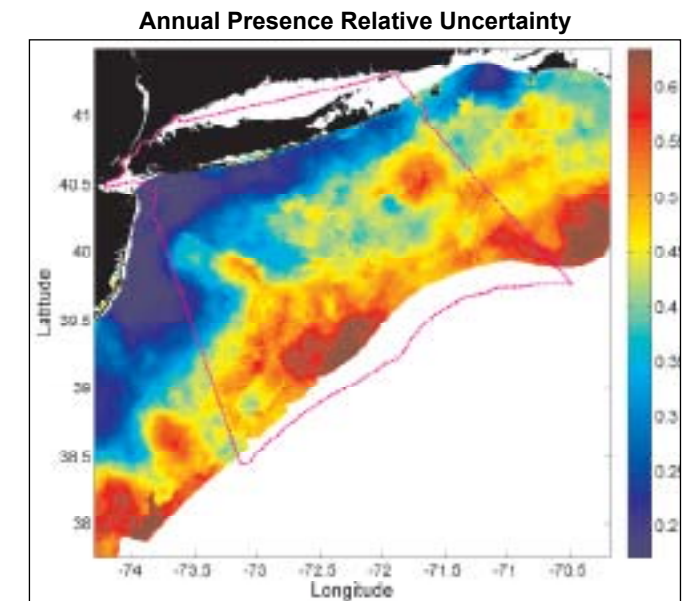
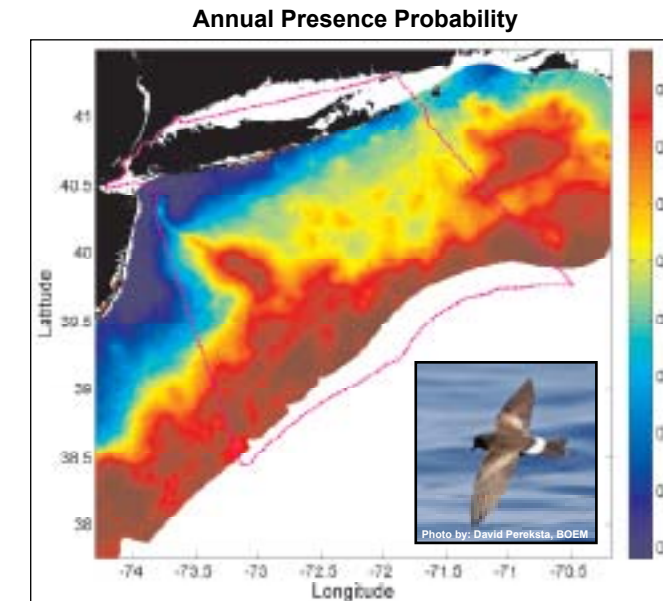
Wilson's Storm-Petrel

Stage I x II: Relative Abundance Predictive Model



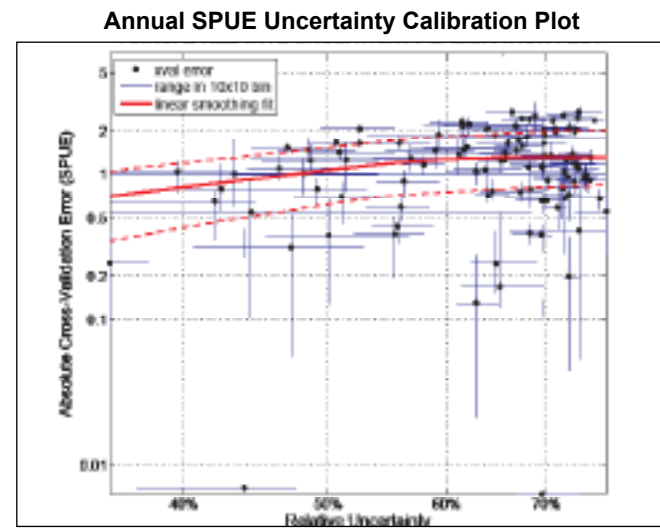
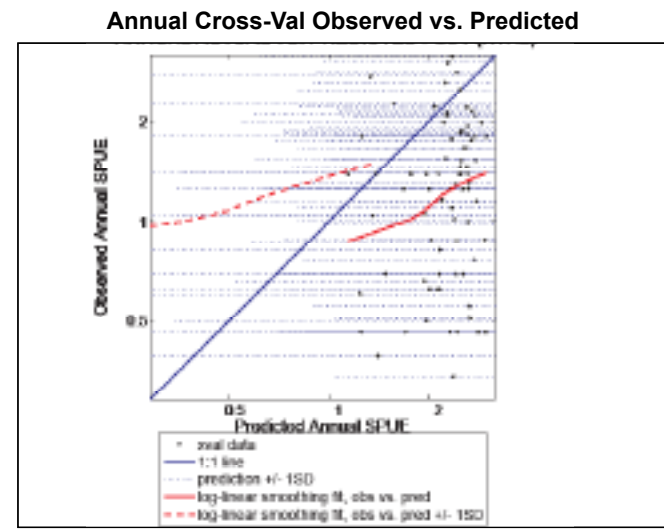
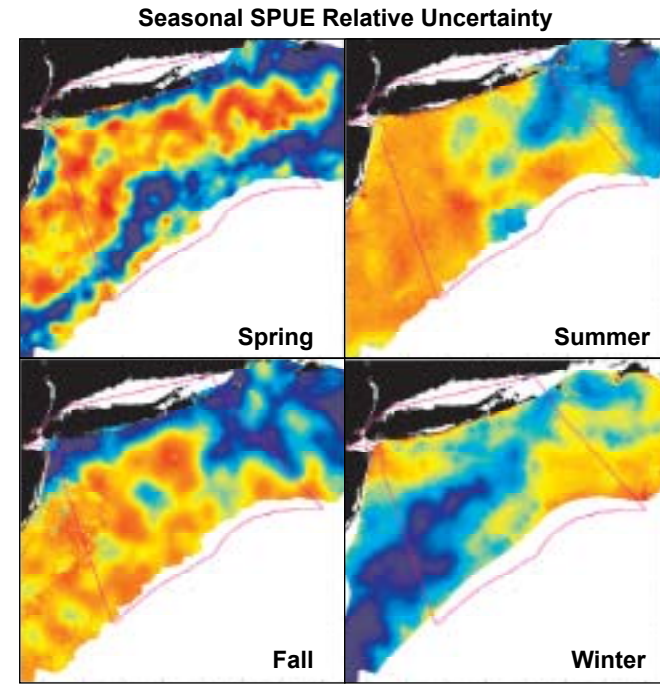
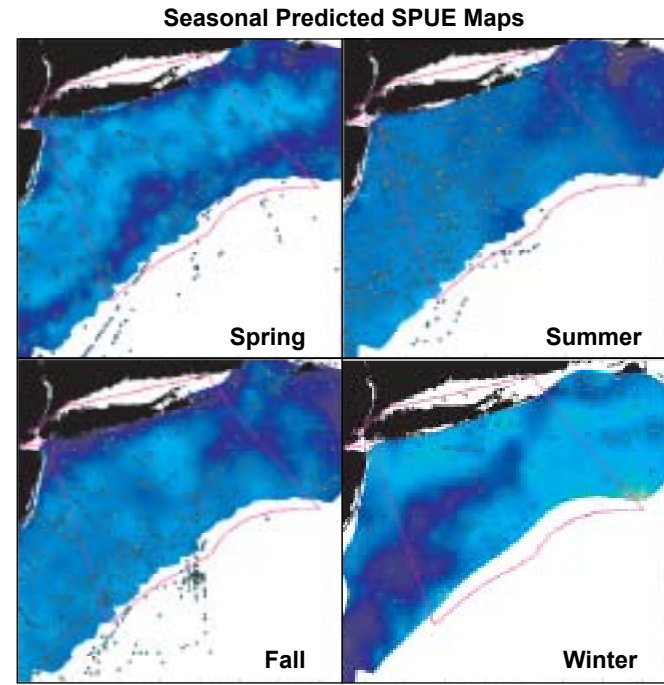
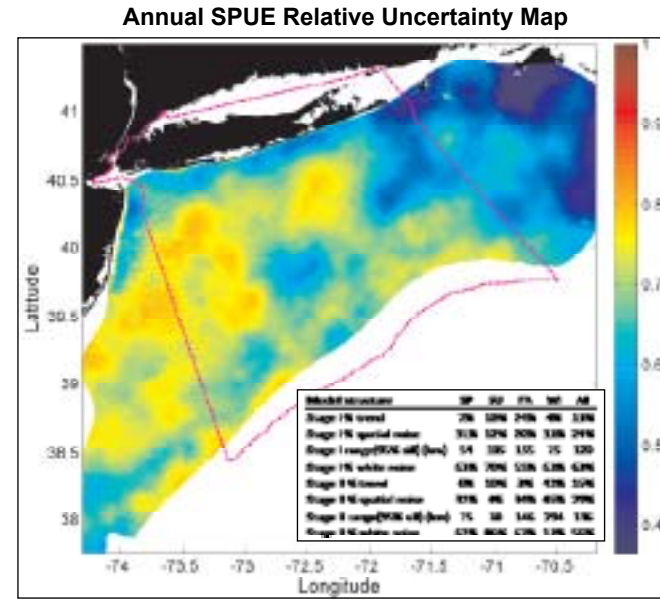
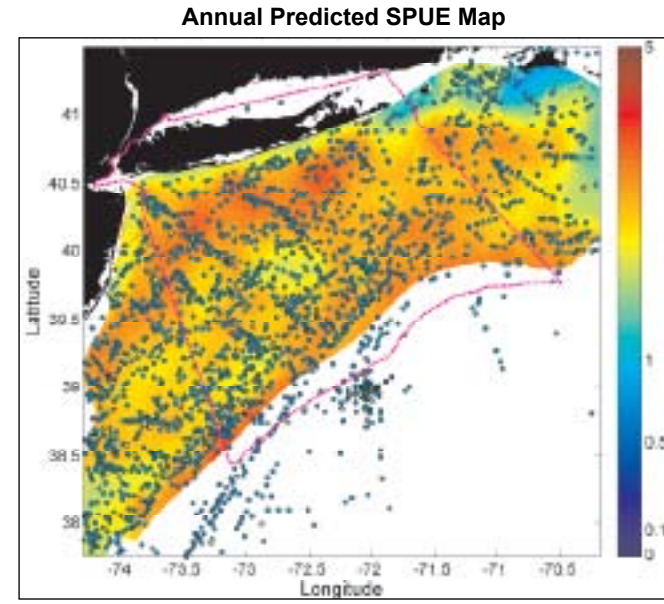
Wilson's Storm-Petrel

Stage I: Presence Probability Predictive Model



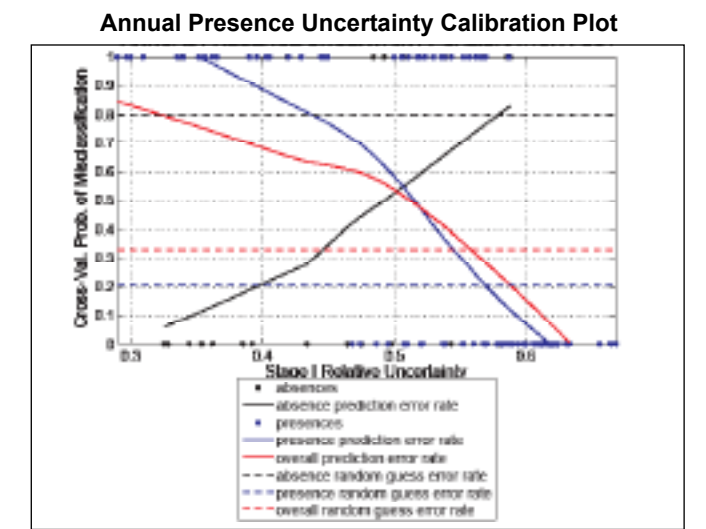
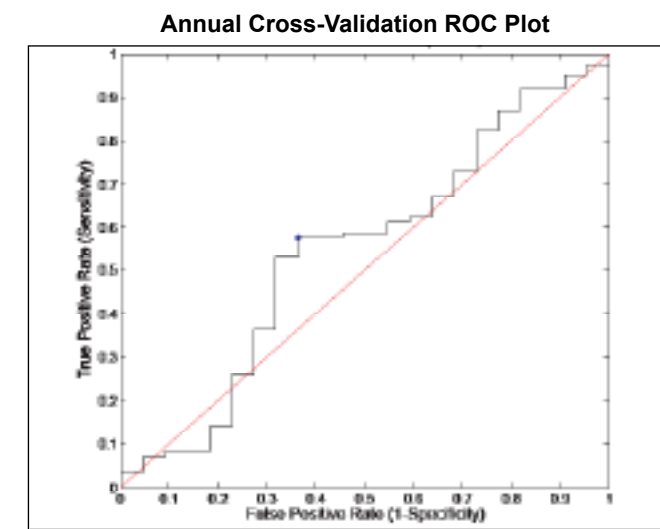
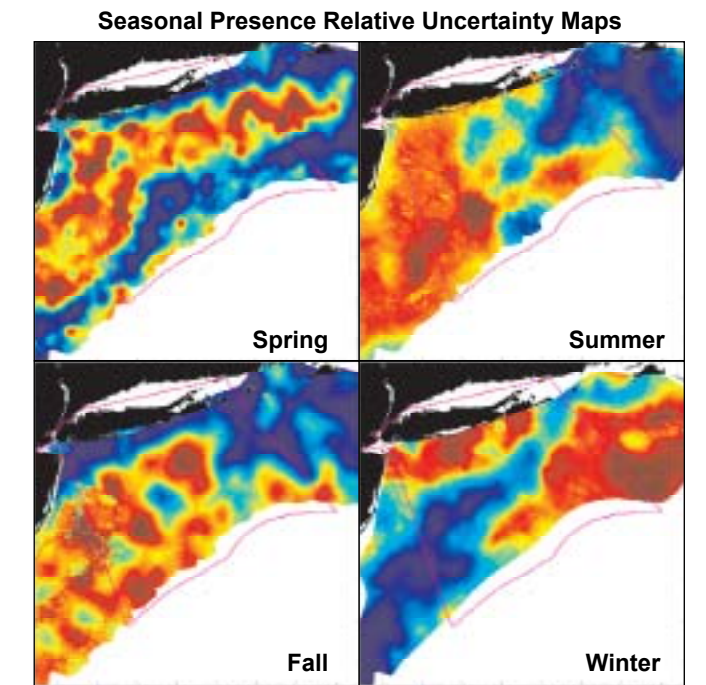
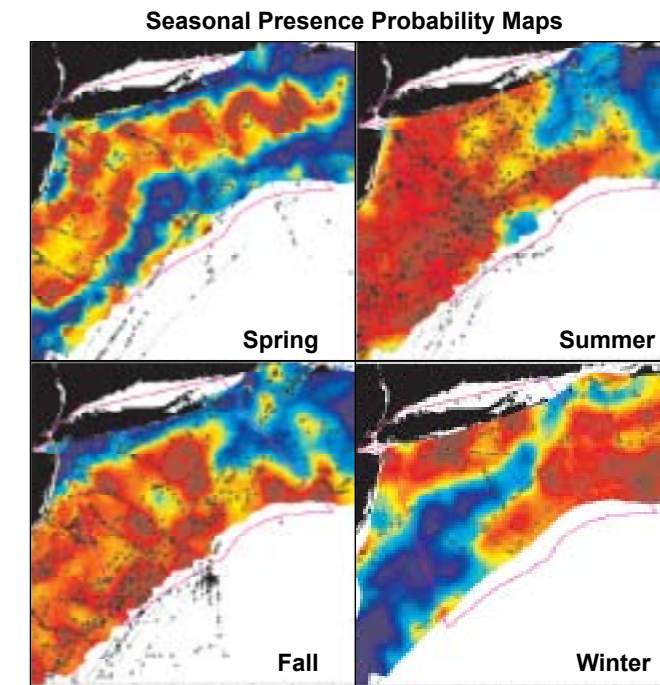
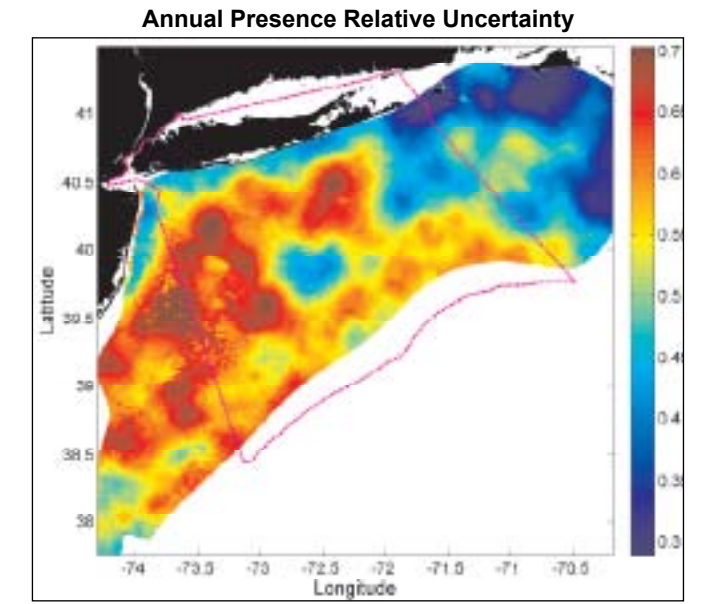
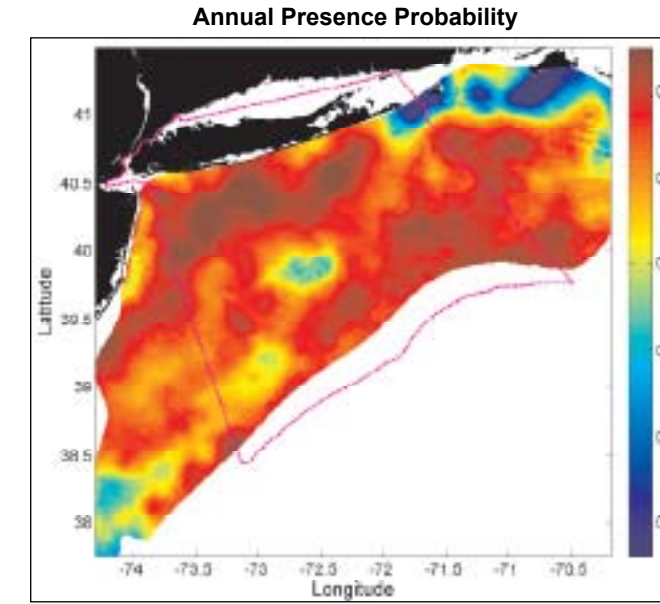
'No birds sighted'

Stage I x II: Relative Abundance Predictive Model



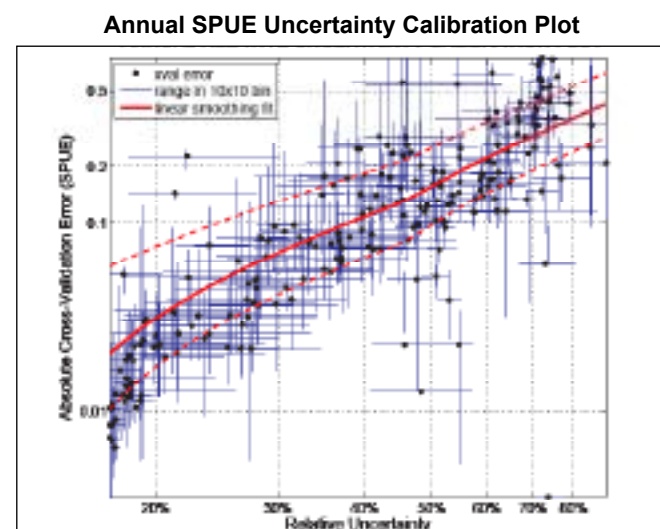
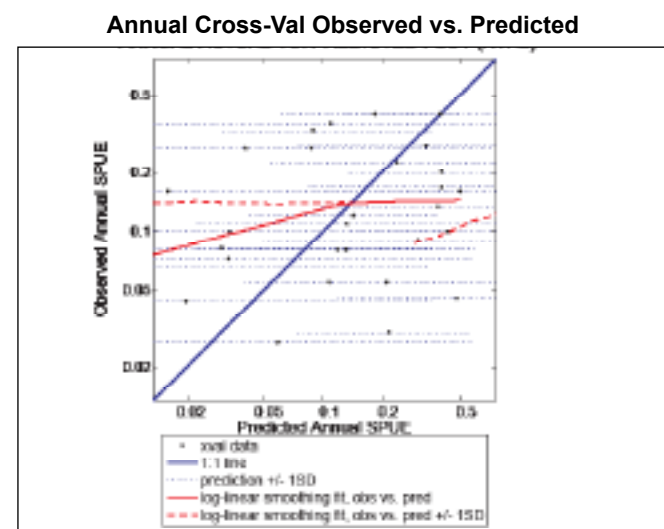
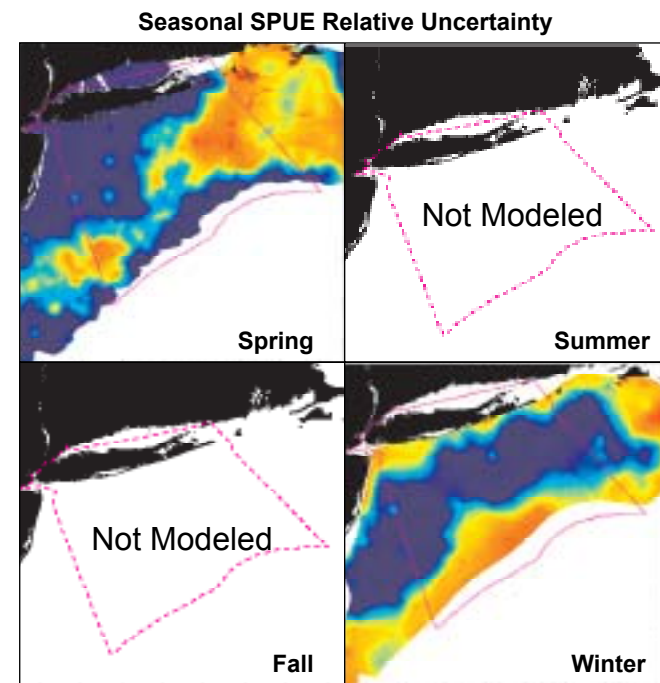
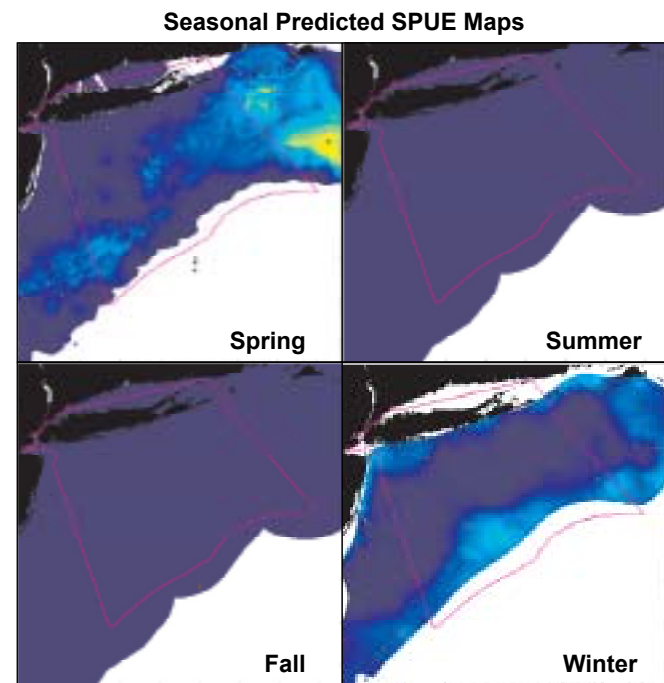
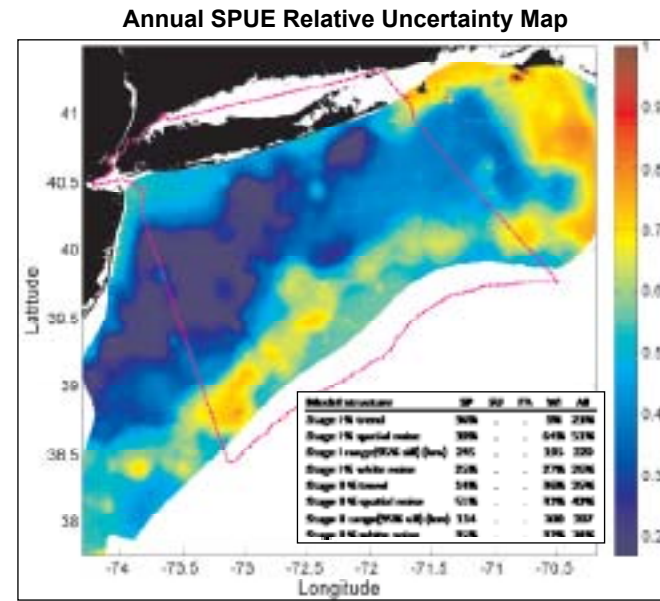
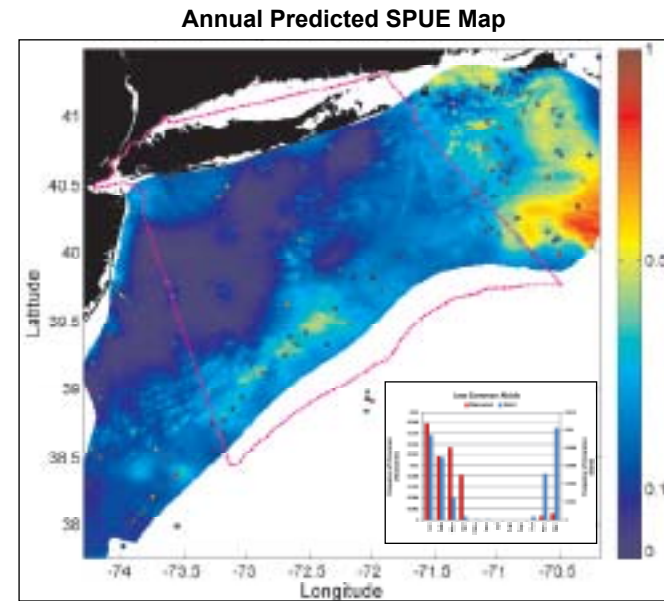
'No birds sighted'

Stage I: Presence Probability Predictive Model



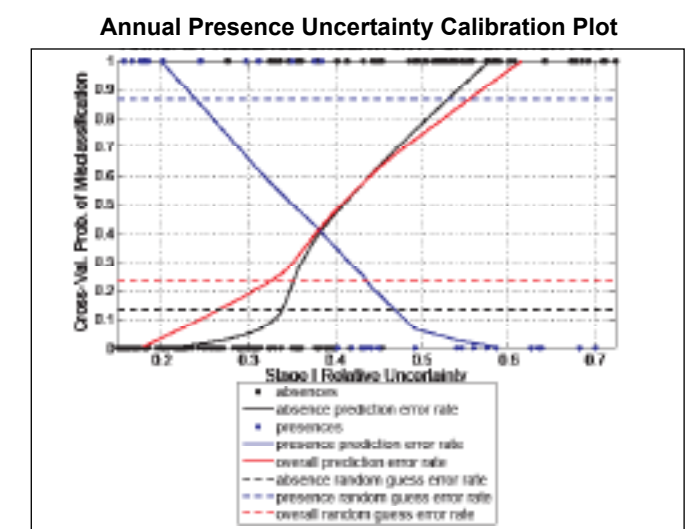
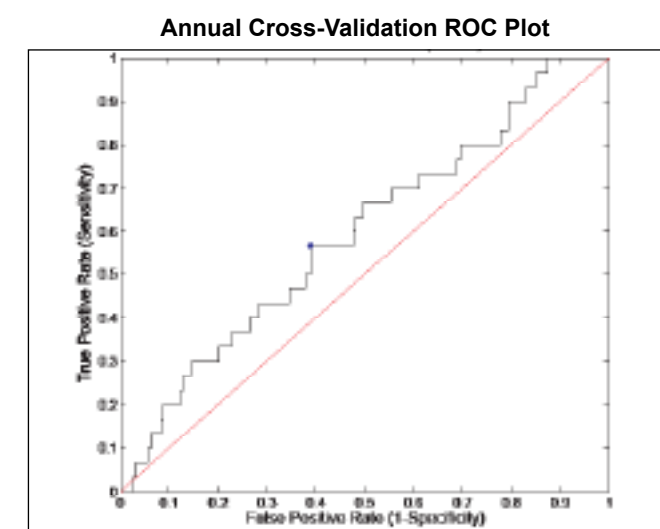
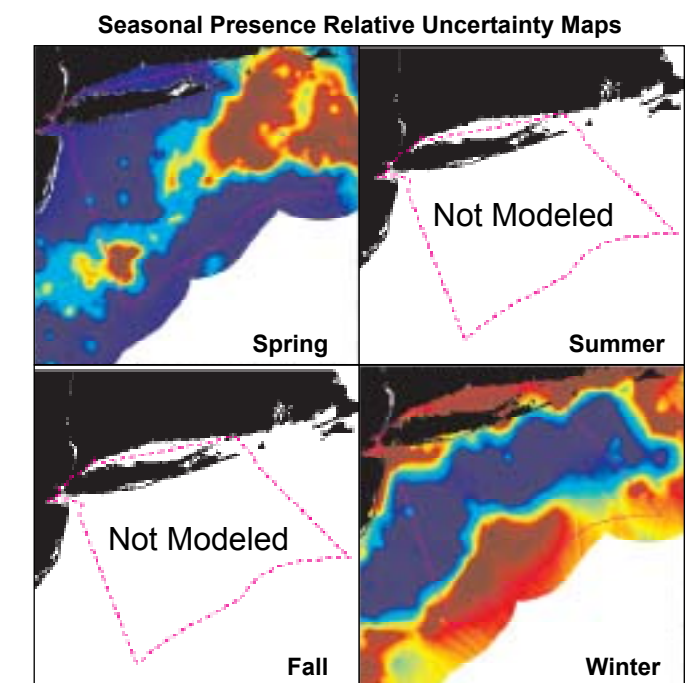
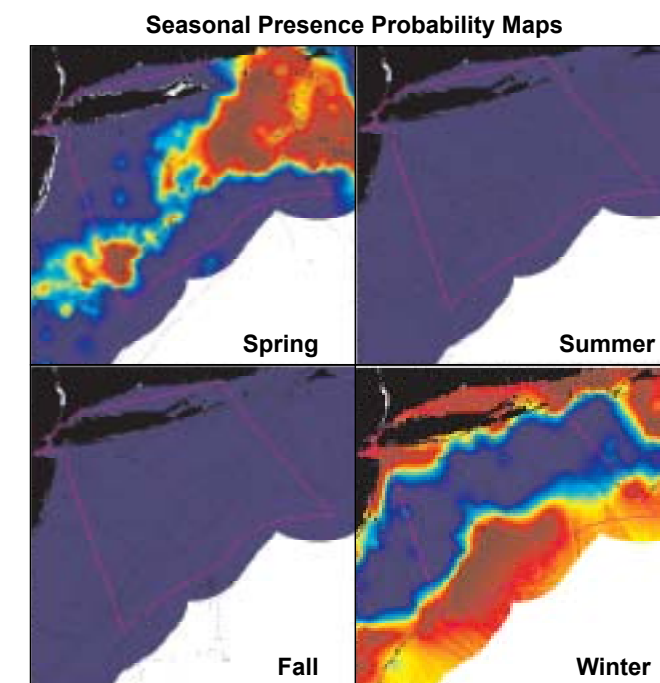
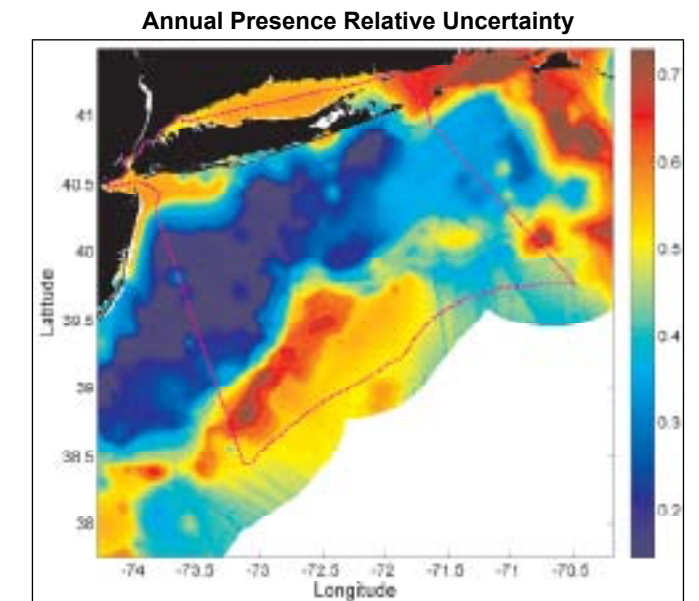
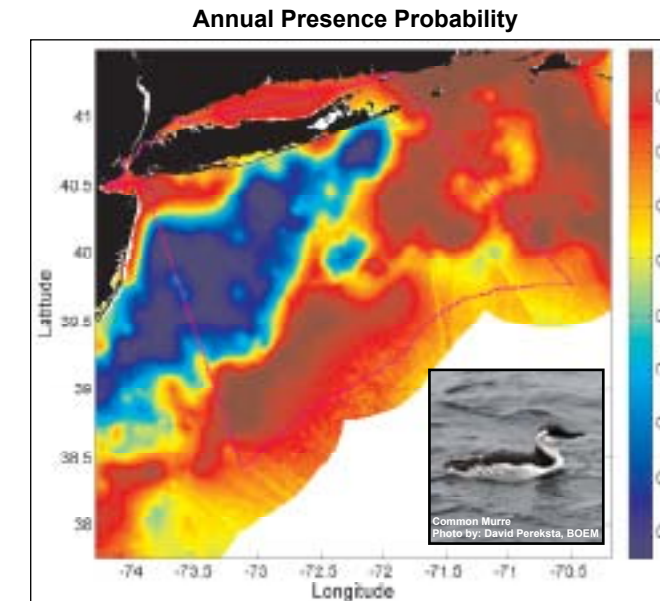
Alcids, less common

Stage I x II: Relative Abundance Predictive Model



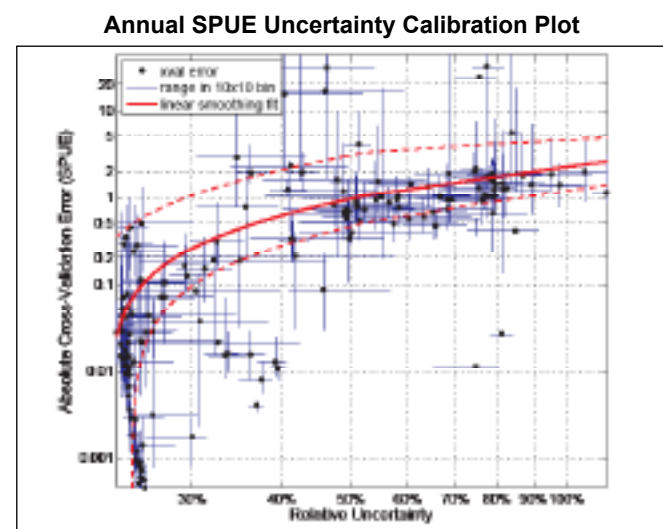
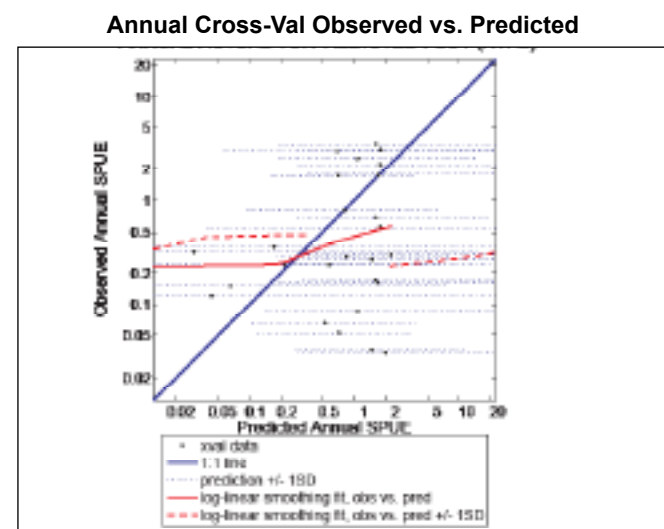
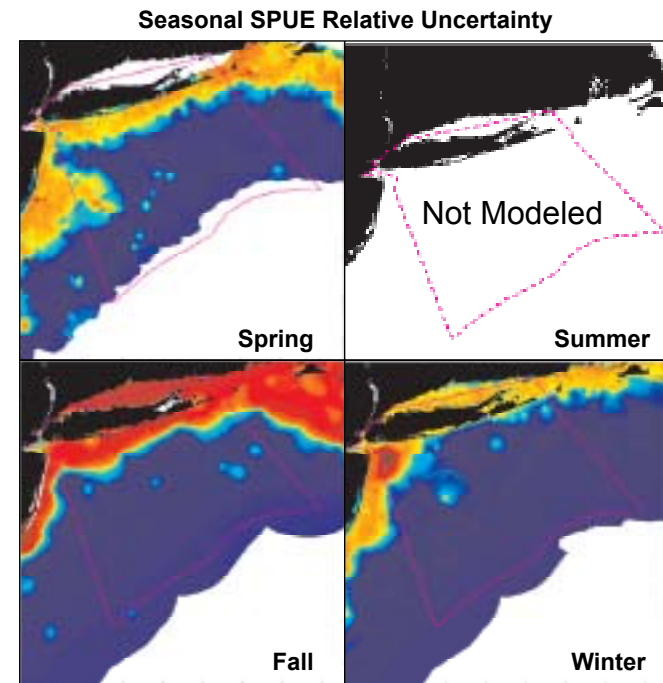
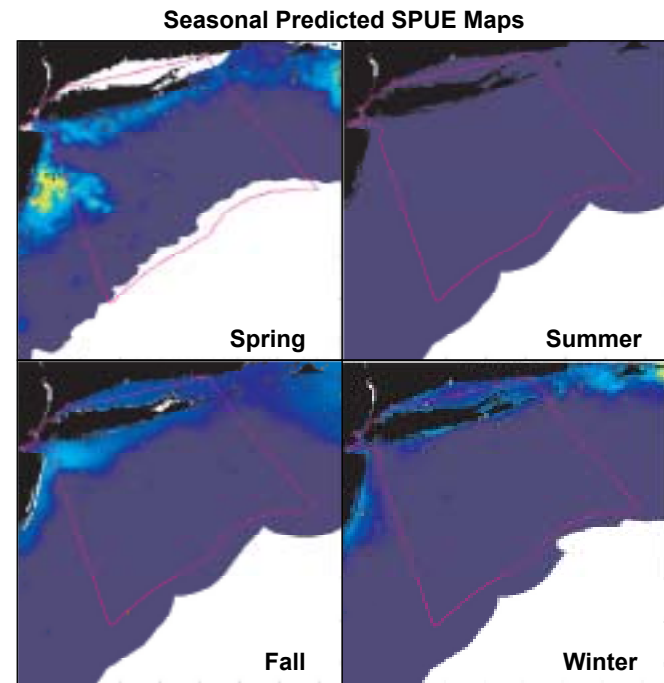
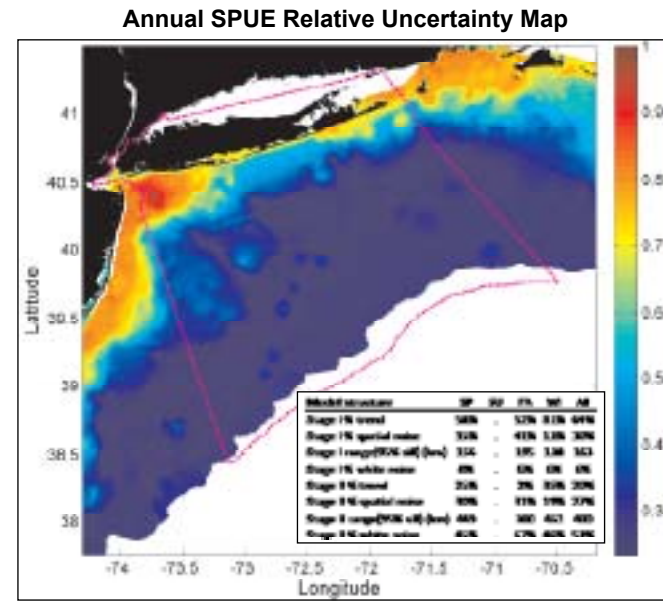
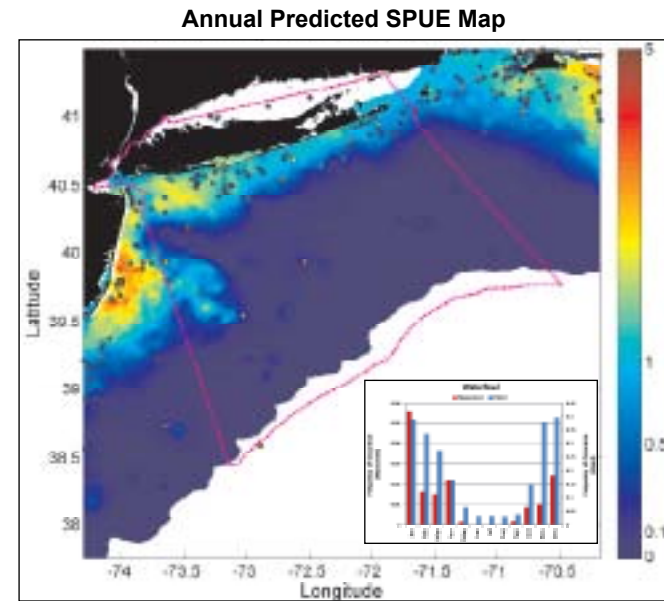
Alcids, less common

Stage I: Presence Probability Predictive Model



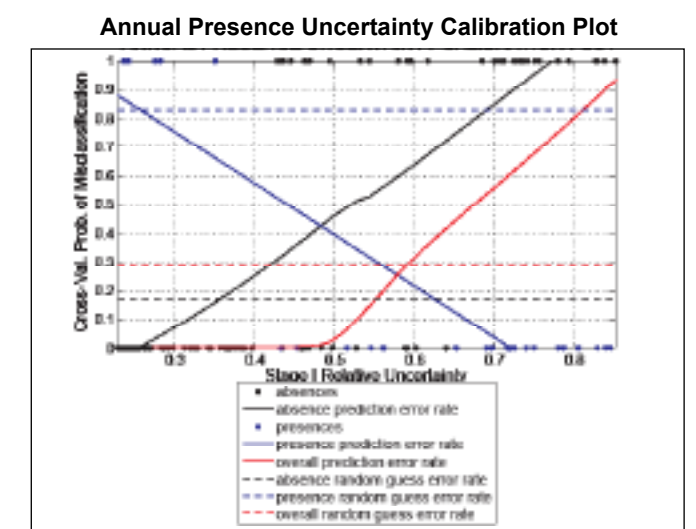
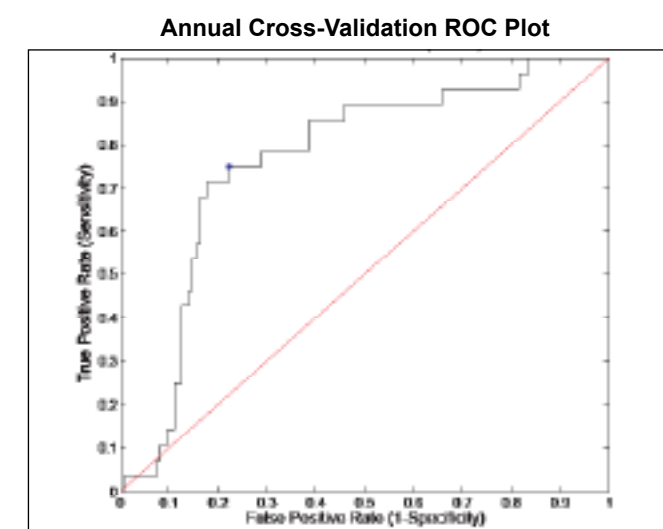
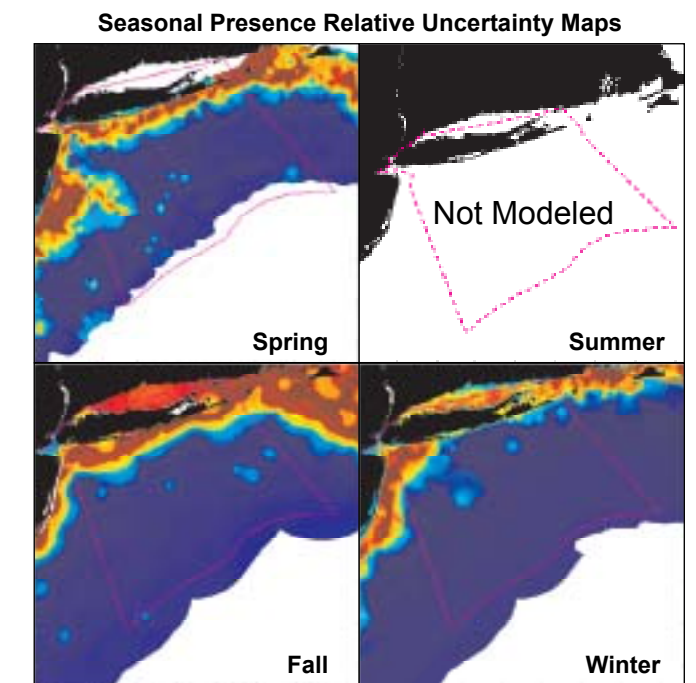
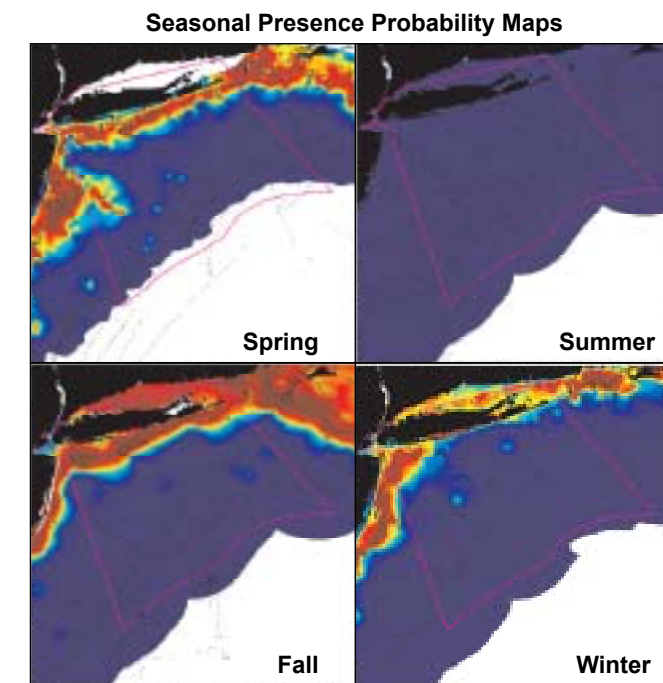
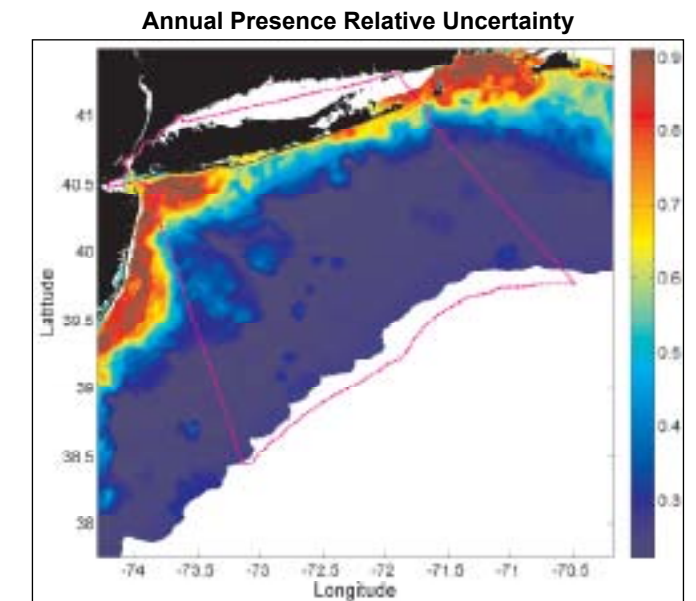
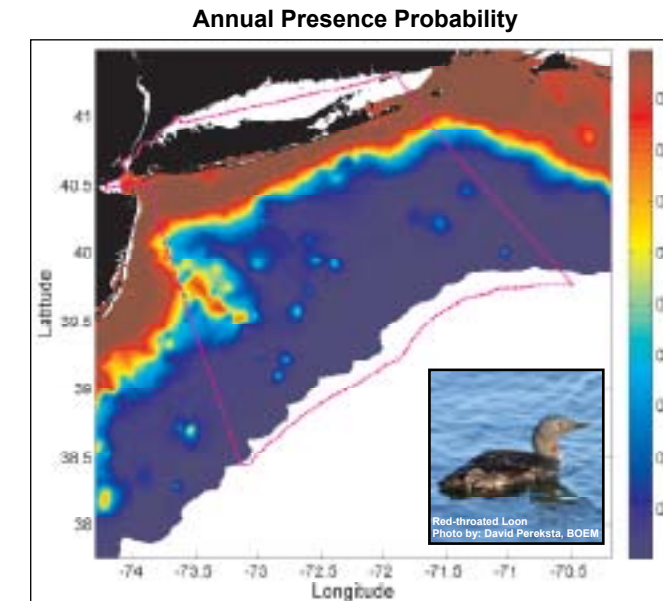
Coastal Waterfowl

Stage I x II: Relative Abundance Predictive Model



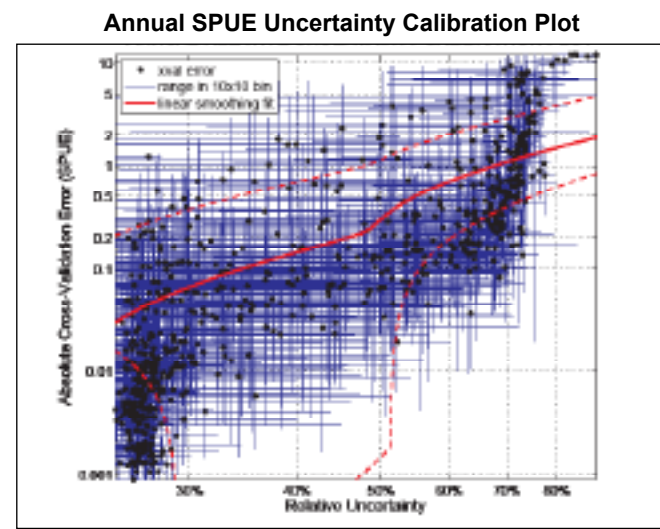
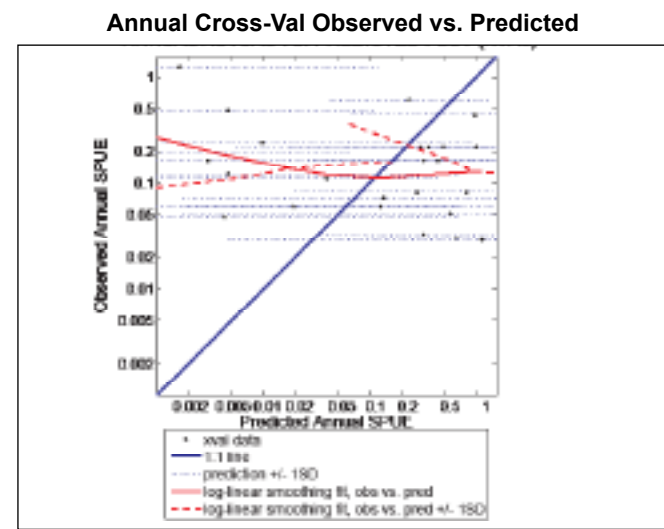
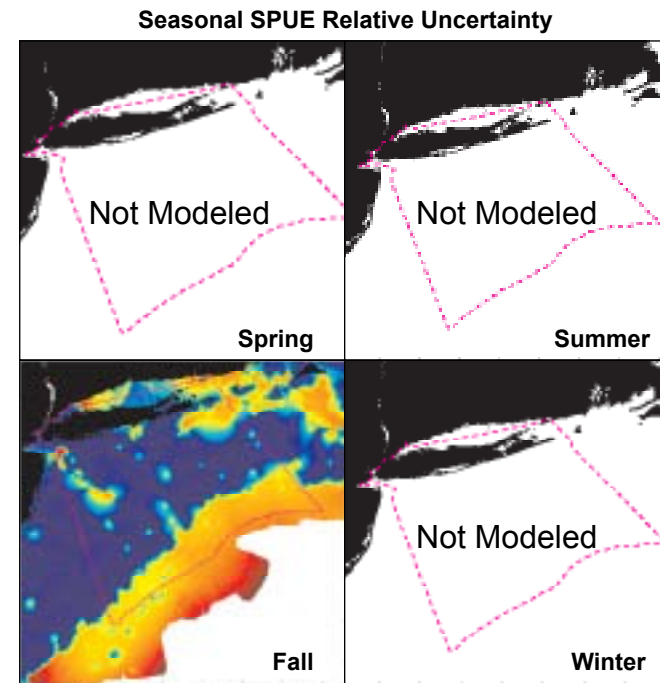
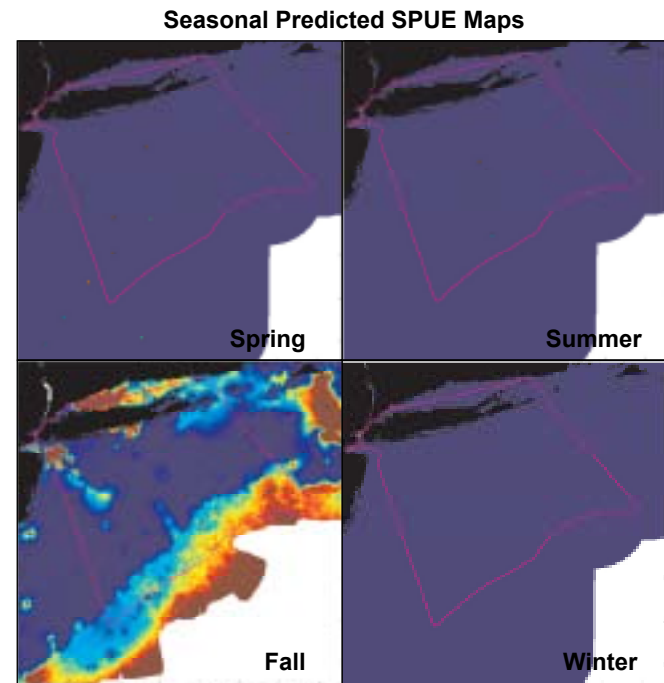
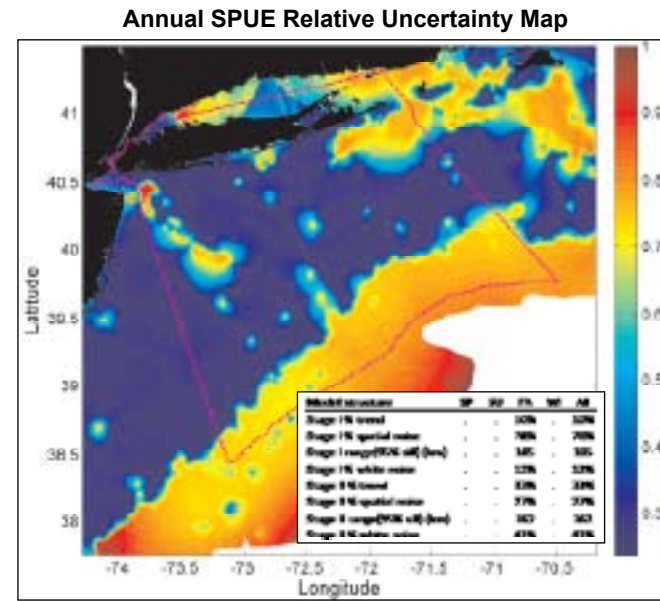
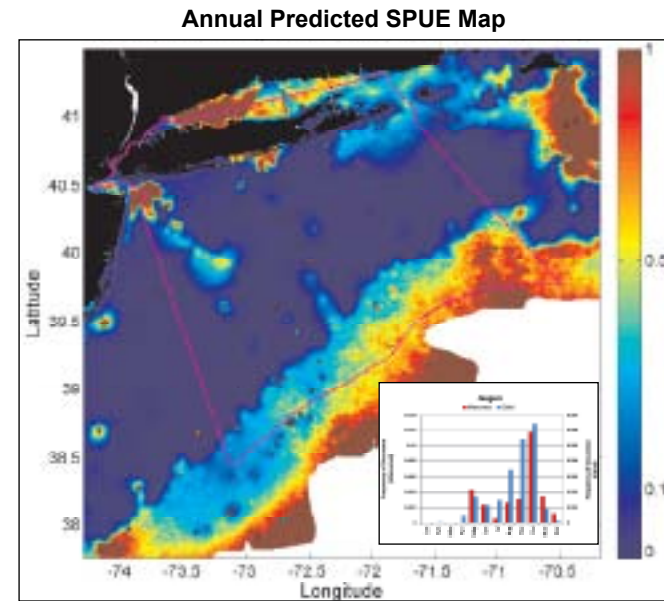
Coastal Waterfowl

Stage I: Presence Probability Predictive Model



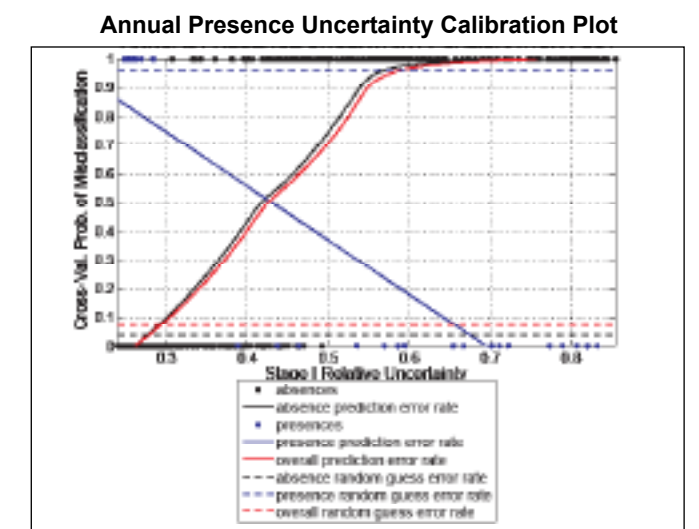
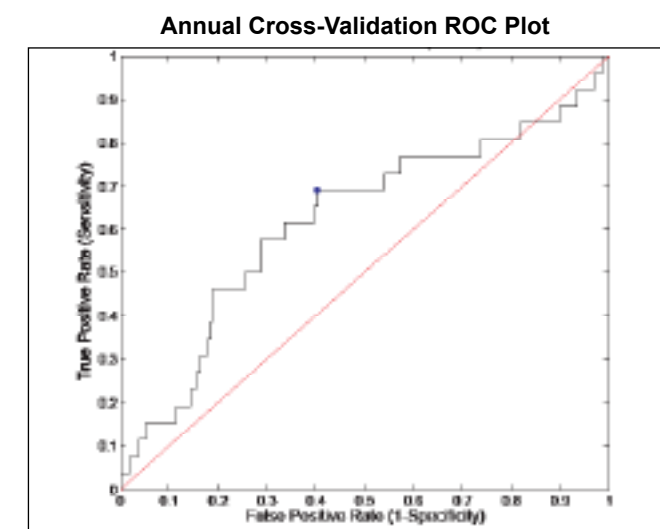
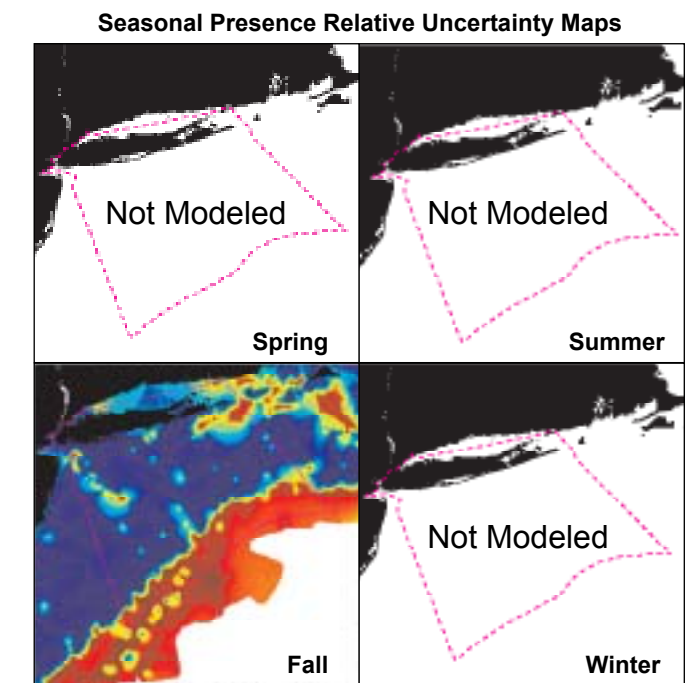
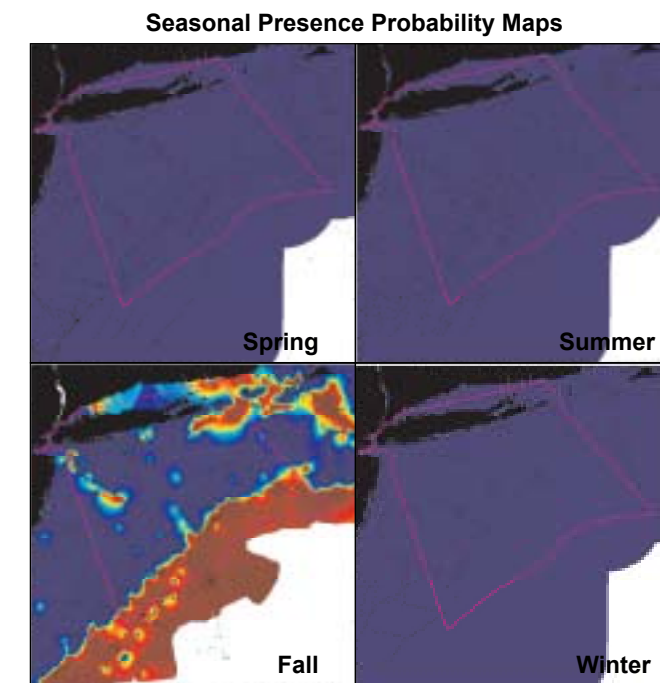
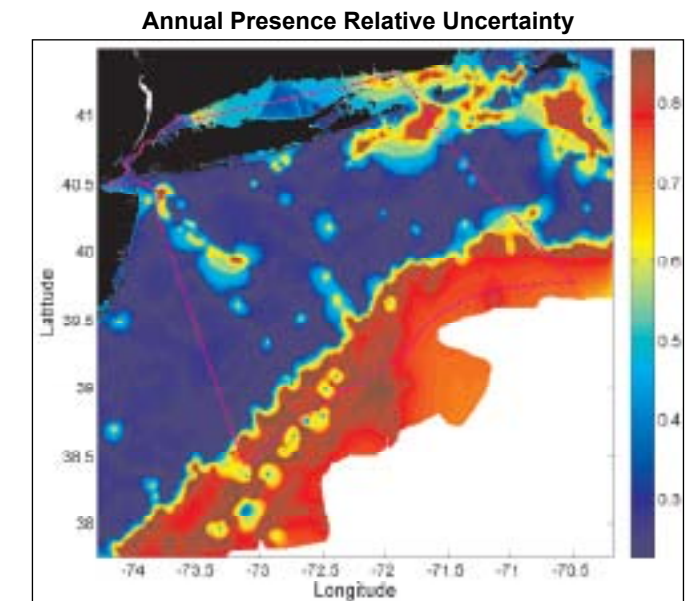
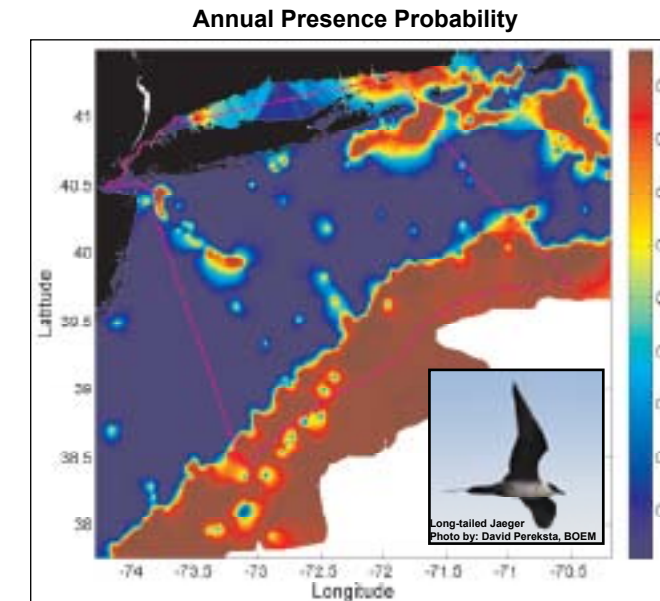
Jaegers

Stage I x II: Relative Abundance Predictive Model



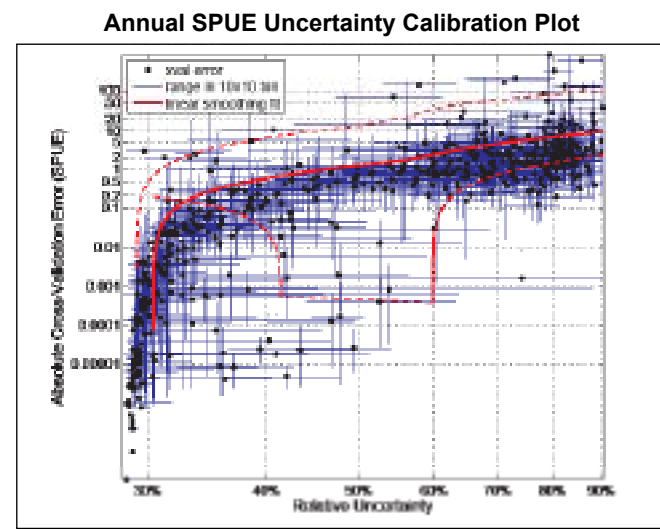
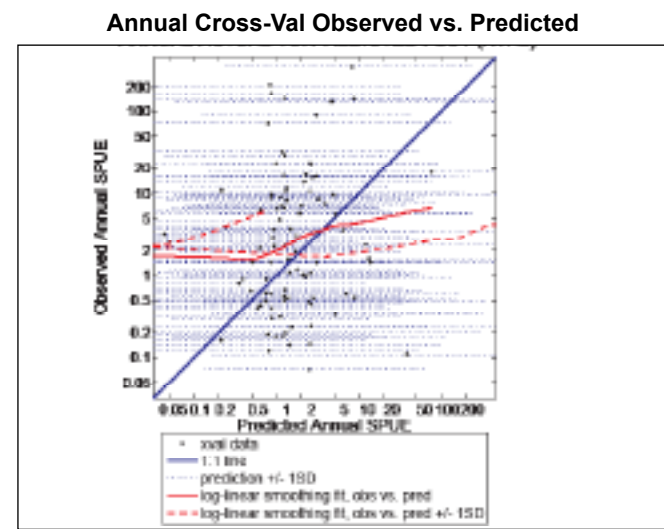
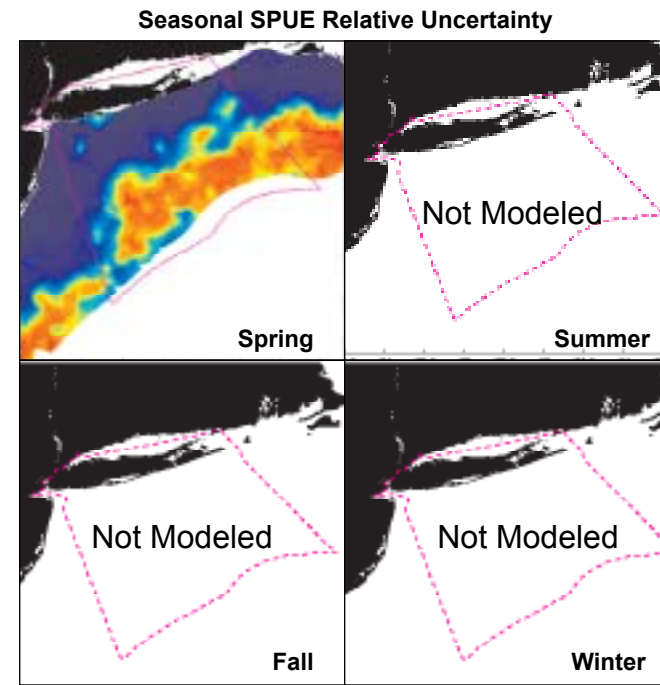
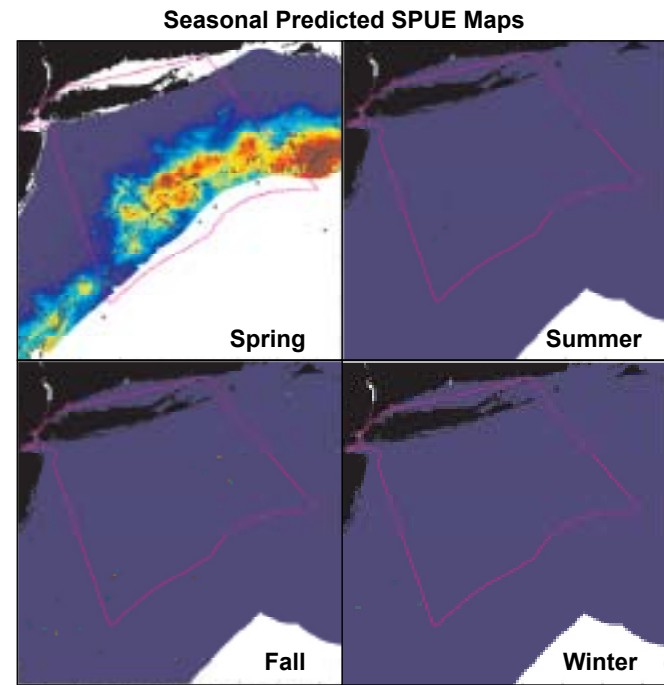
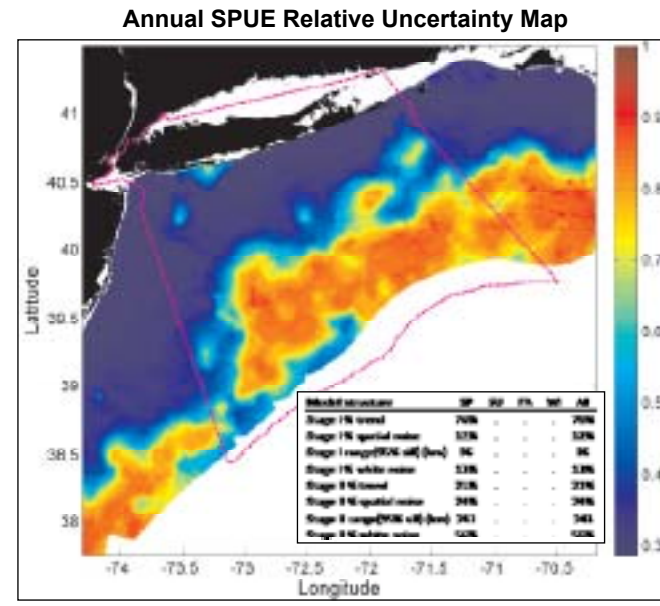
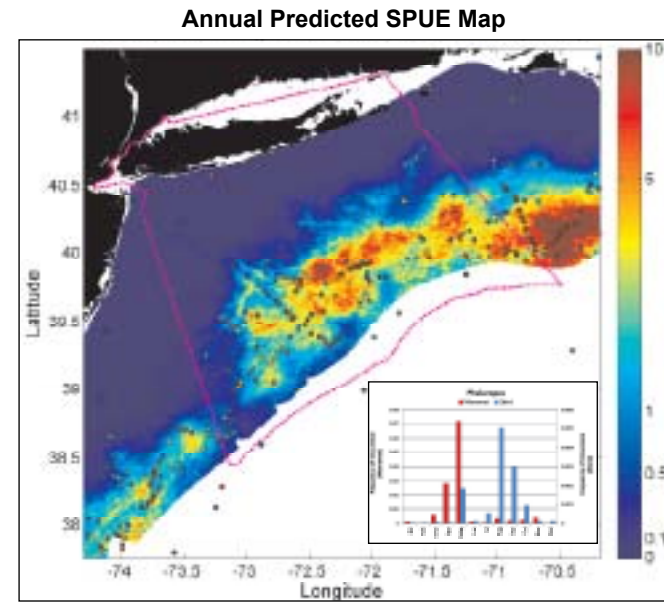
Jaegers

Stage I: Presence Probability Predictive Model



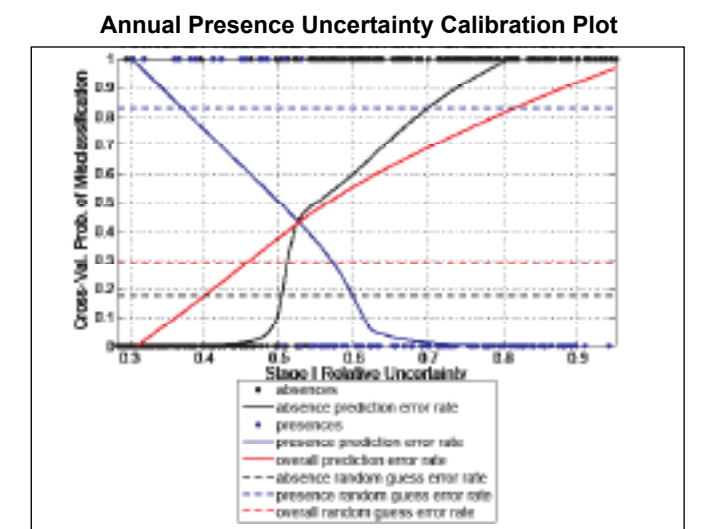
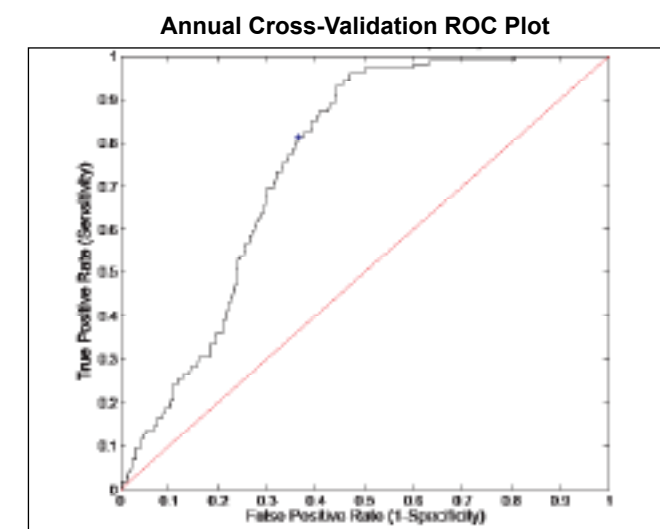
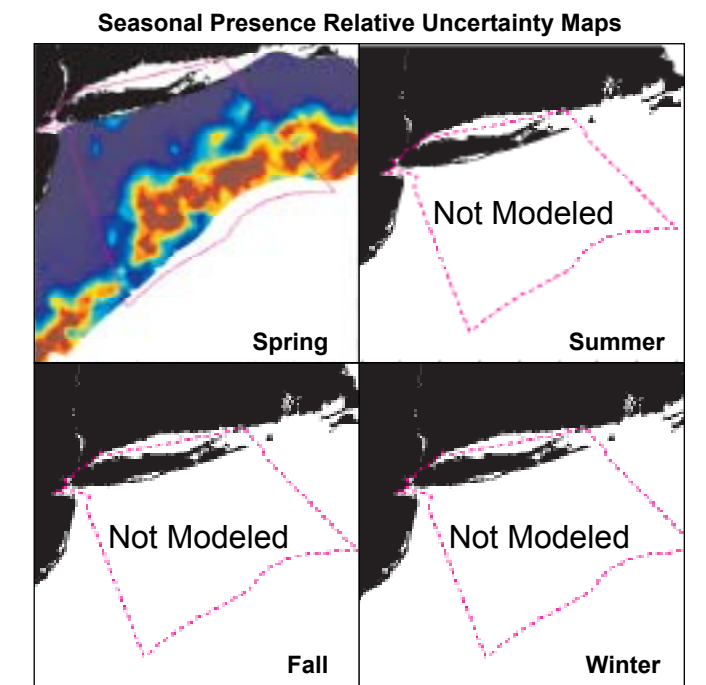
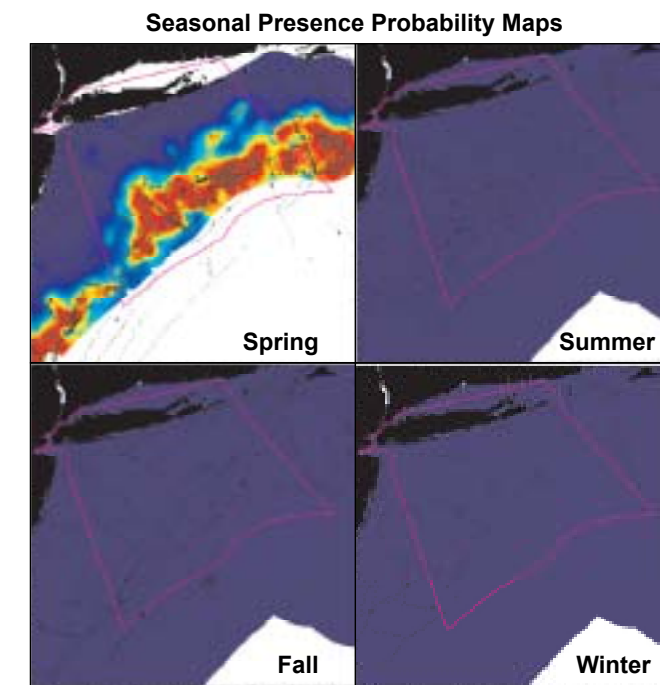
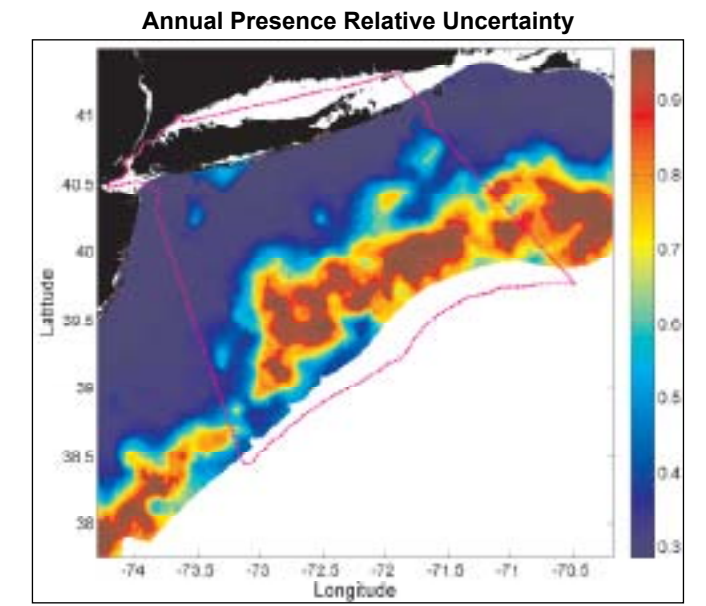
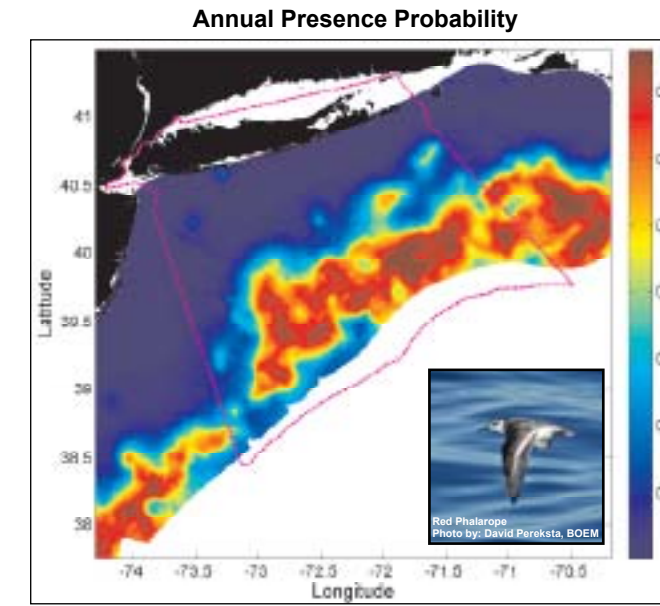
Phalaropes

Stage I x II: Relative Abundance Predictive Model



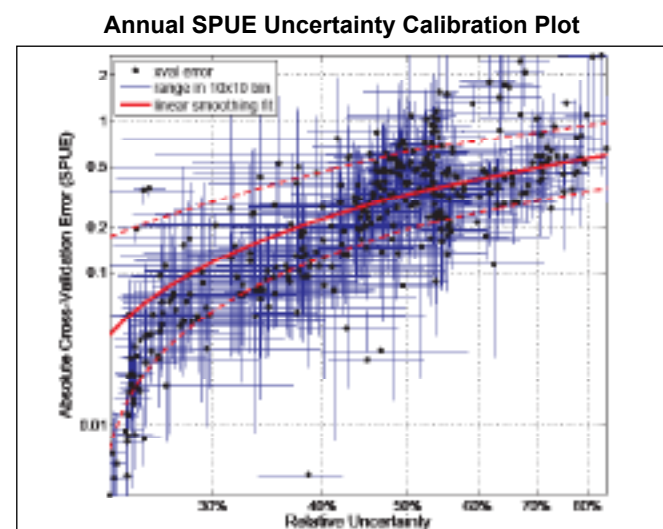
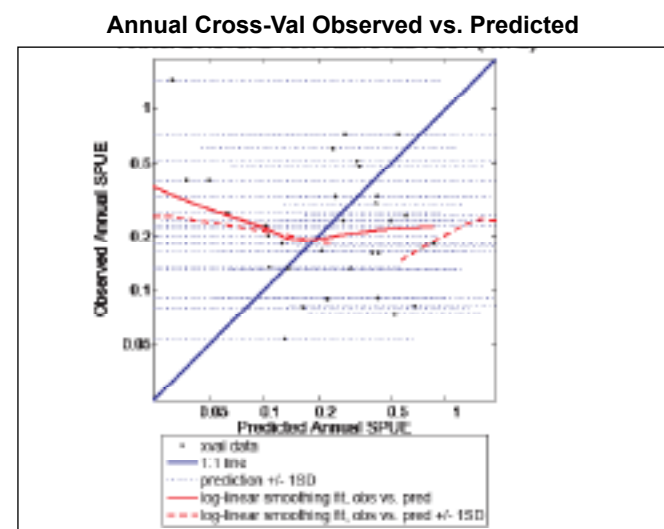
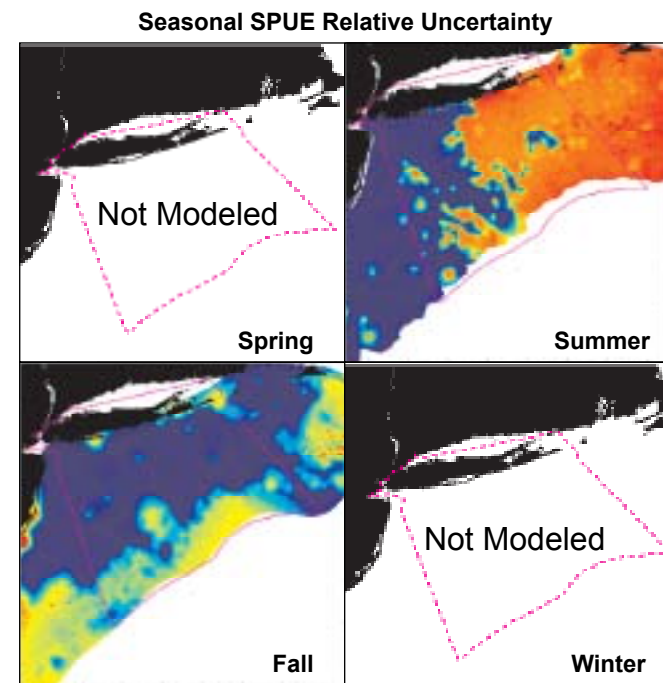
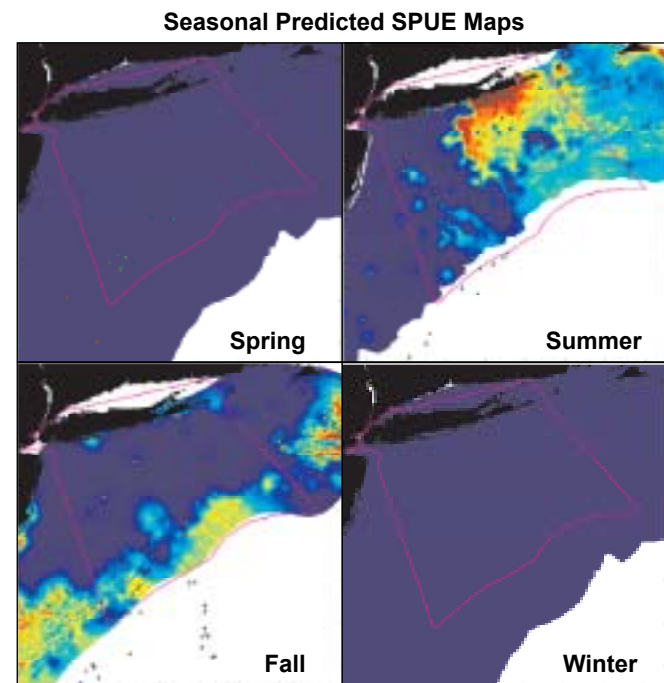
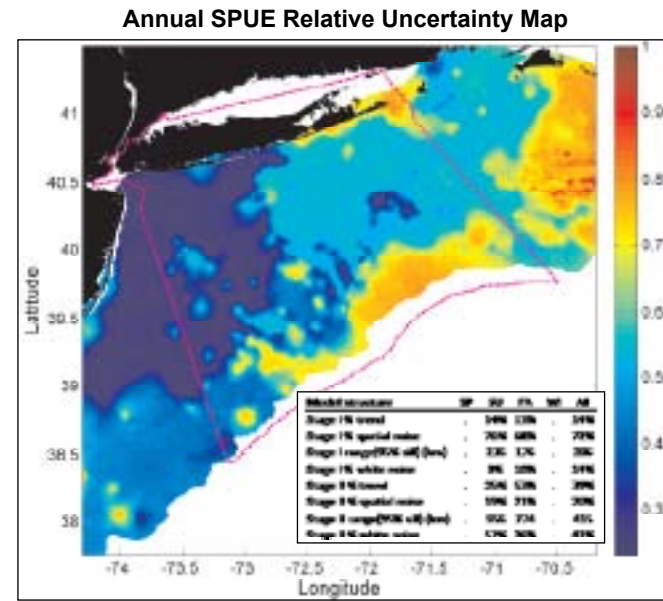
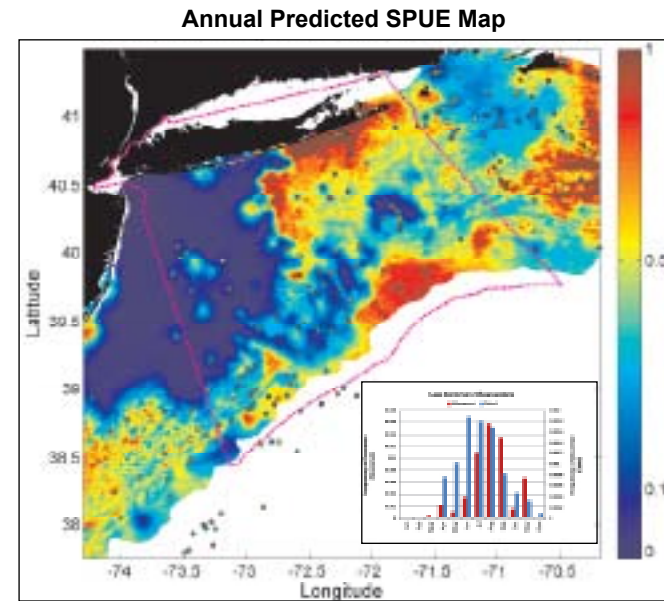
Phalaropes

Stage I: Presence Probability Predictive Model



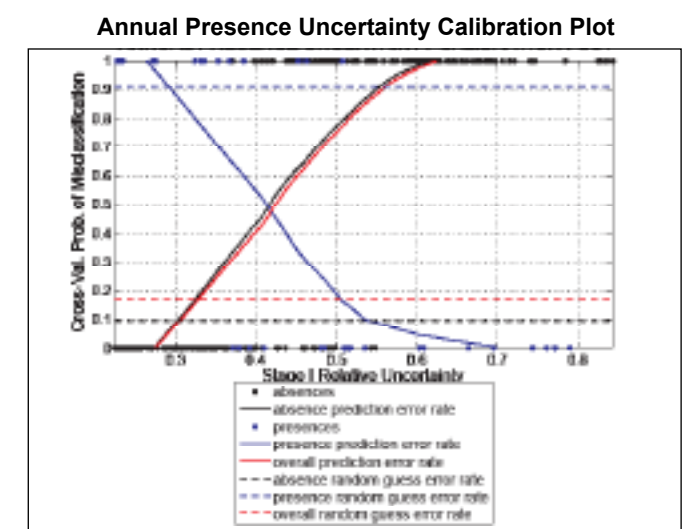
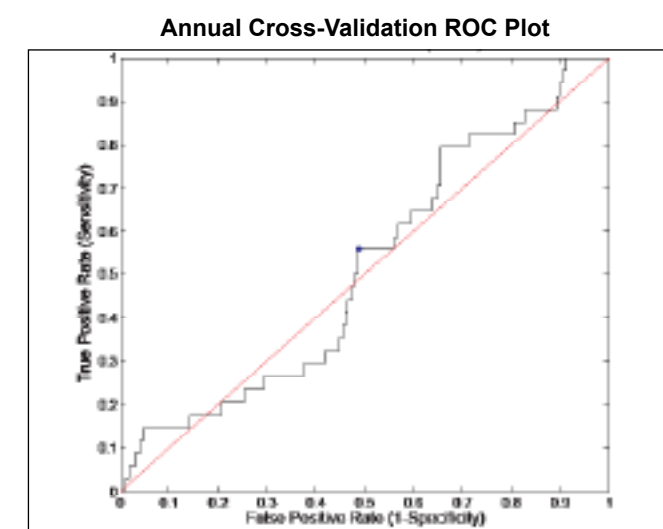
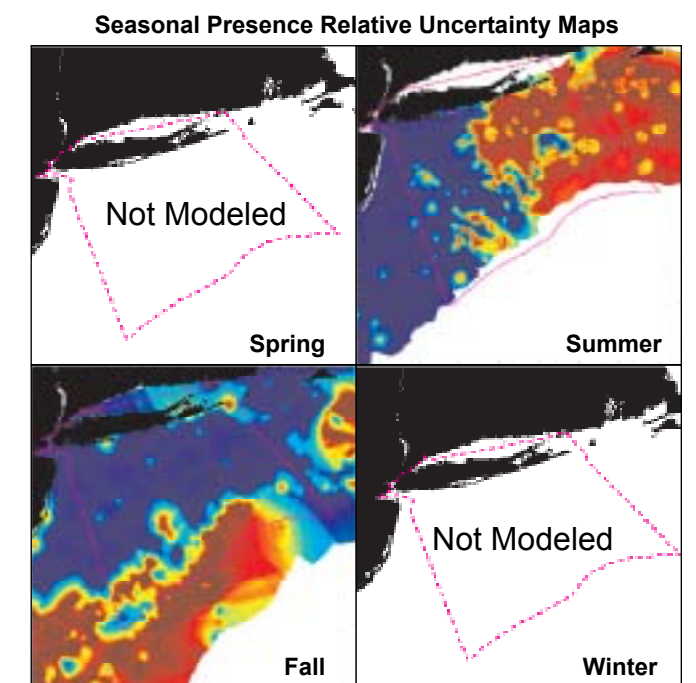
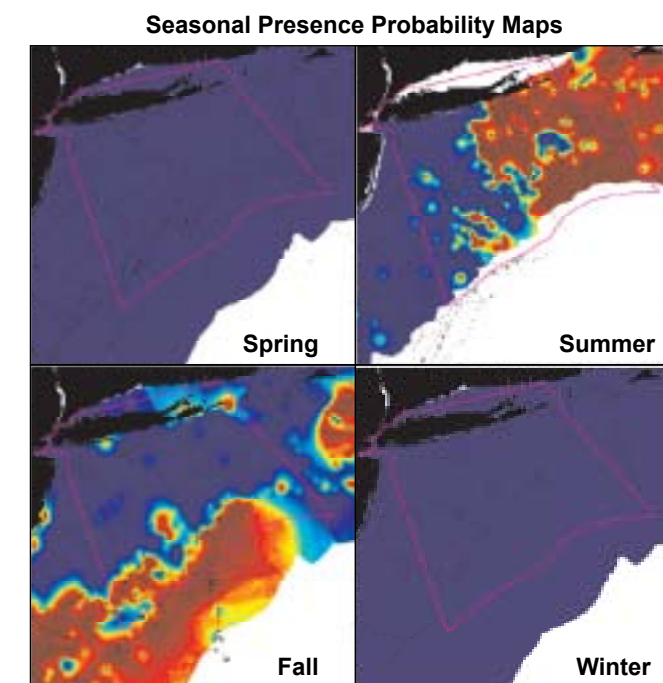
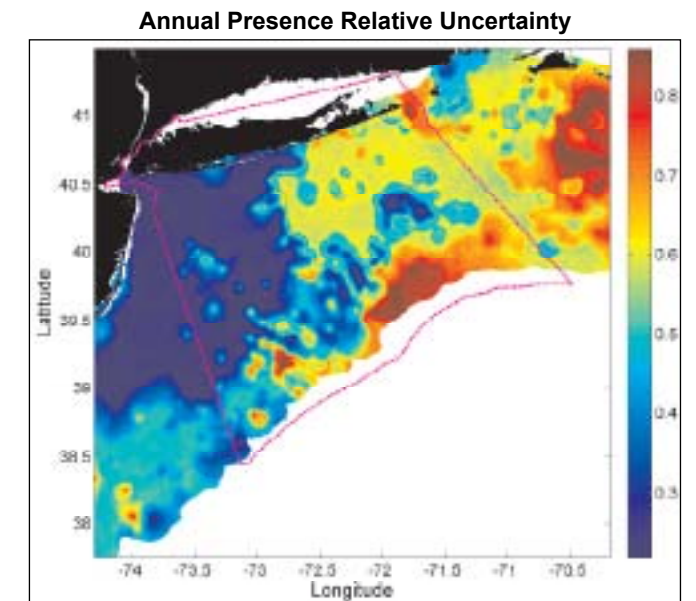
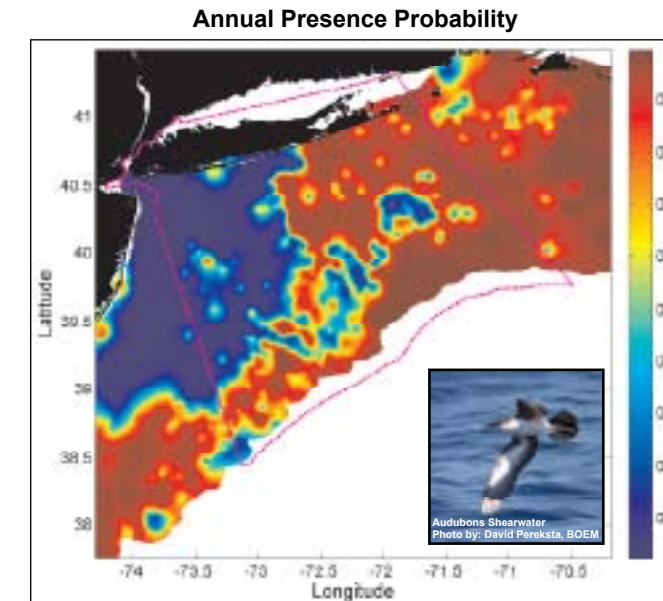
Shearwaters, less common

Stage I x II: Relative Abundance Predictive Model



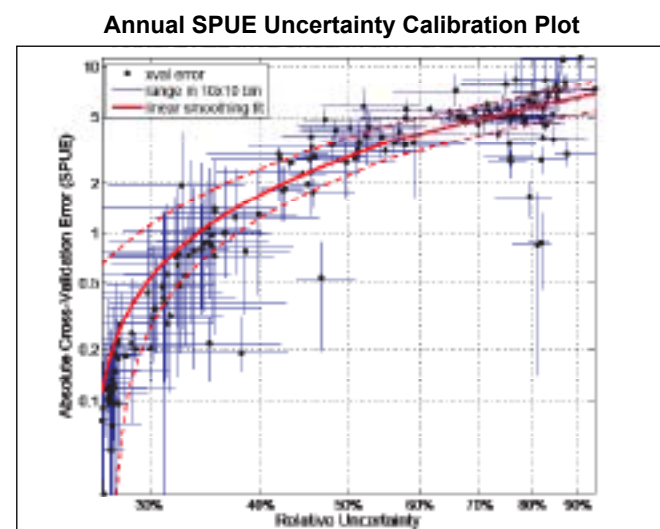
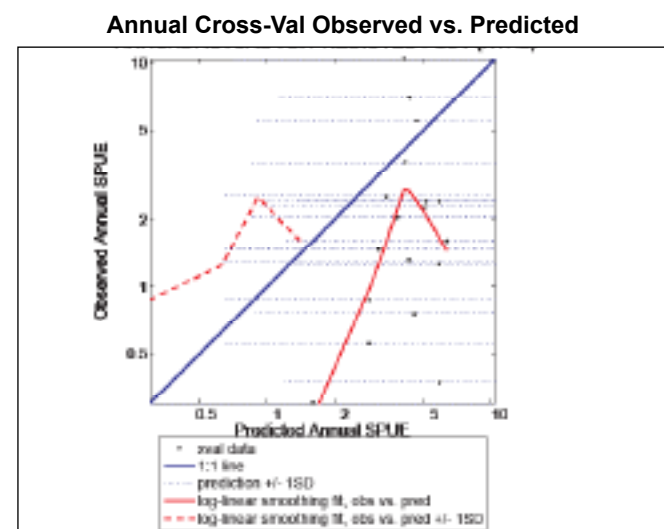
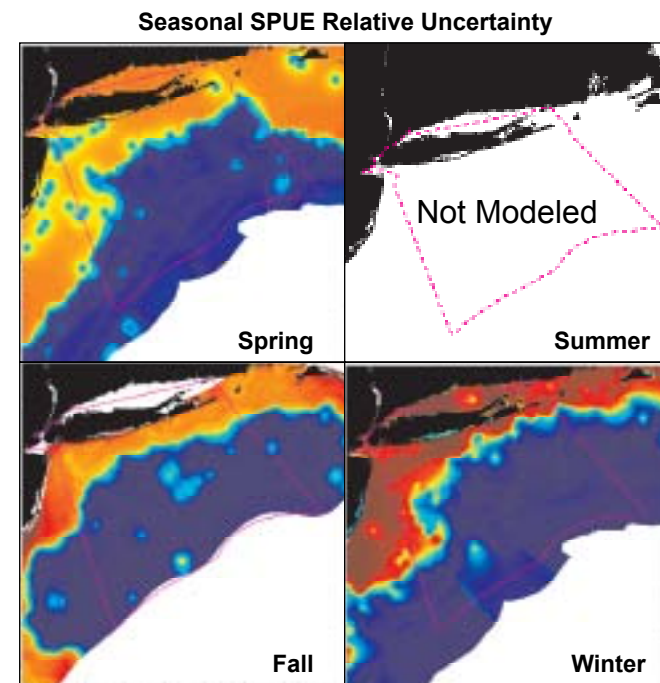
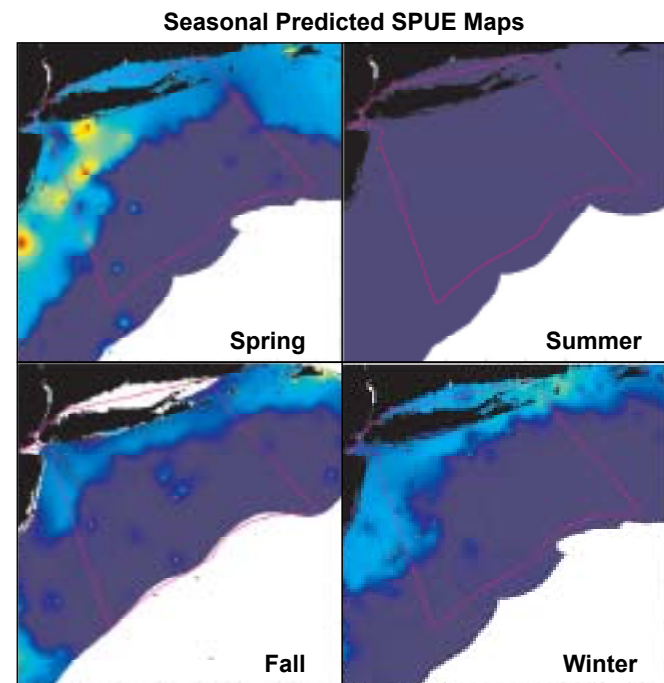
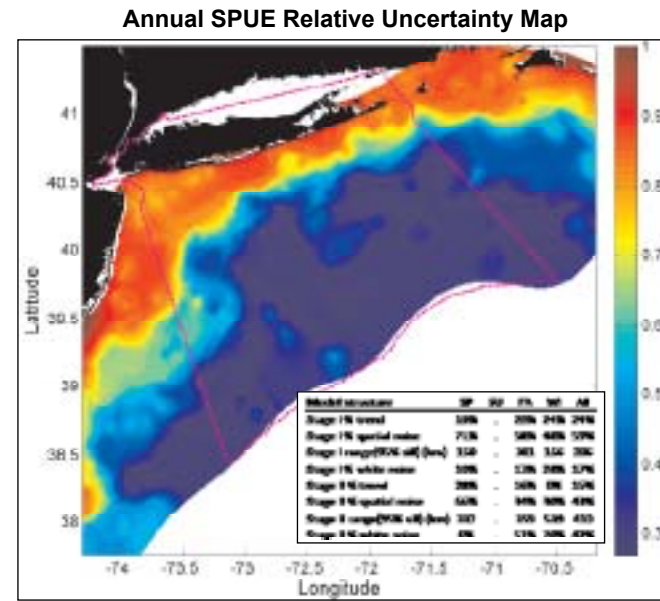
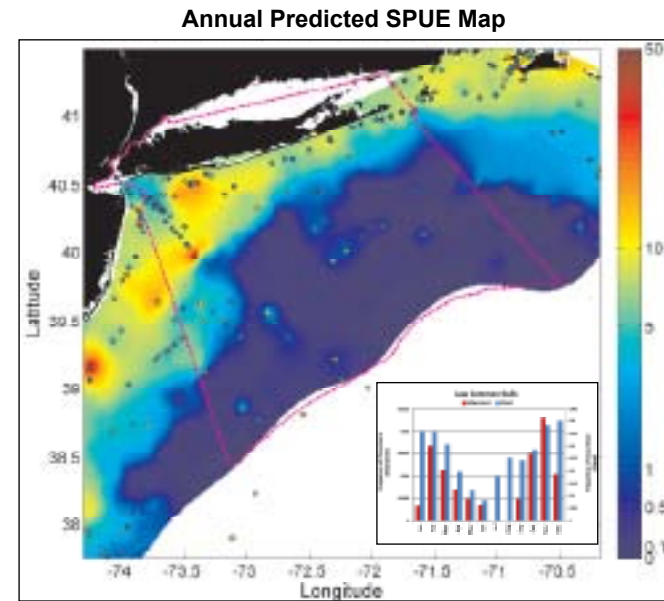
Shearwaters, less common

Stage I: Presence Probability Predictive Model



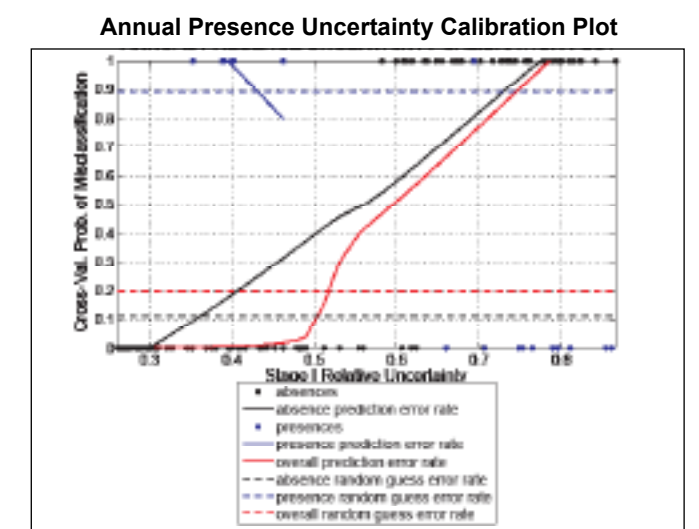
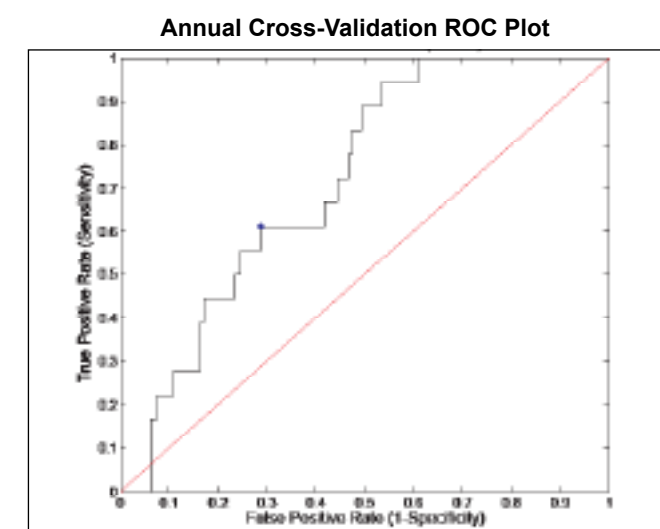
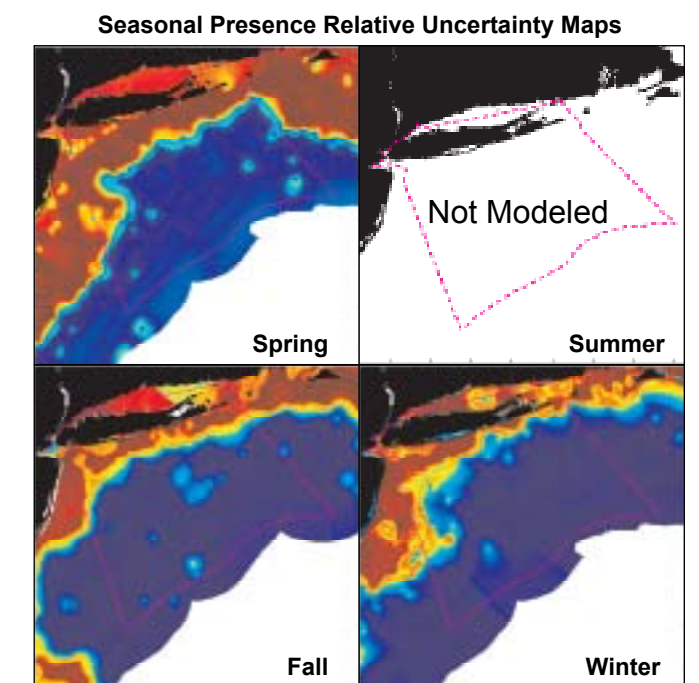
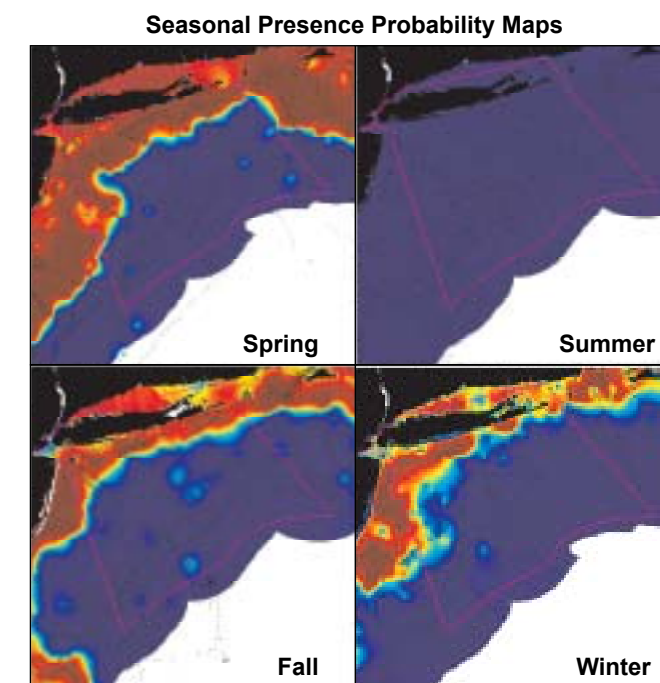
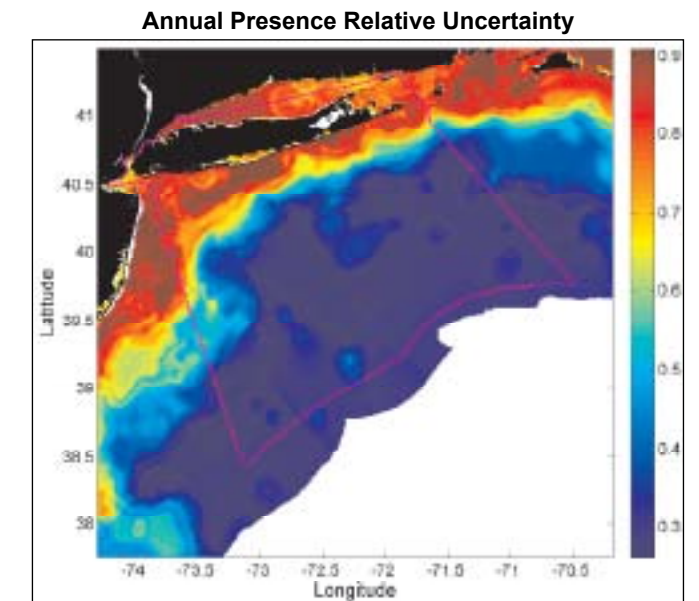
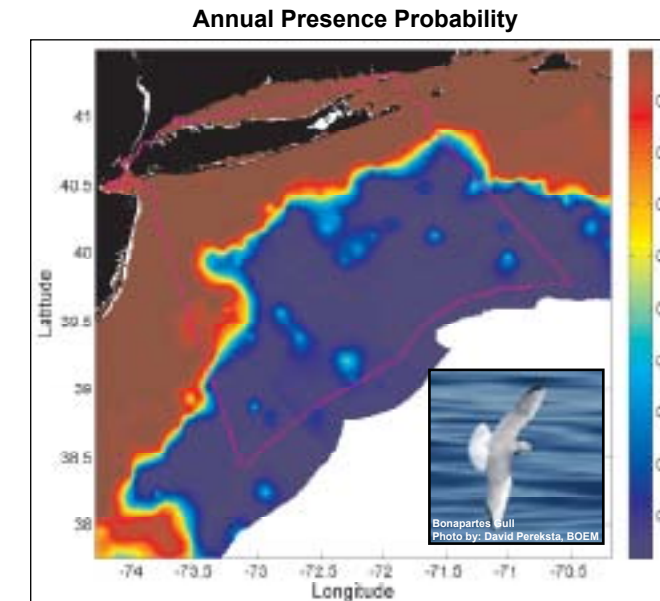
Small Gulls, less common

Stage I x II: Relative Abundance Predictive Model



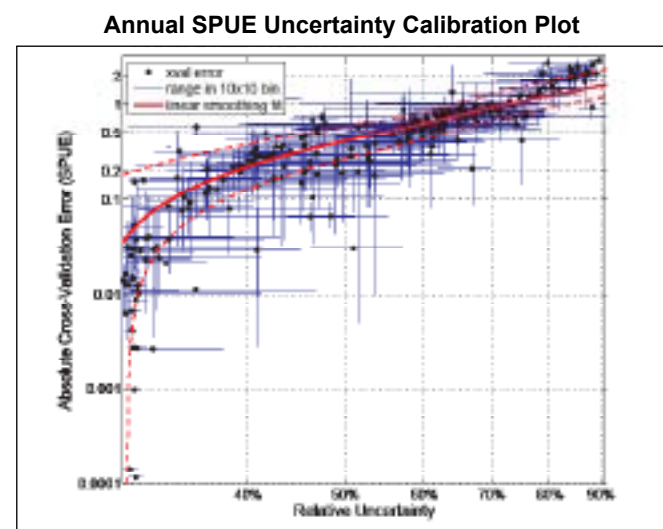
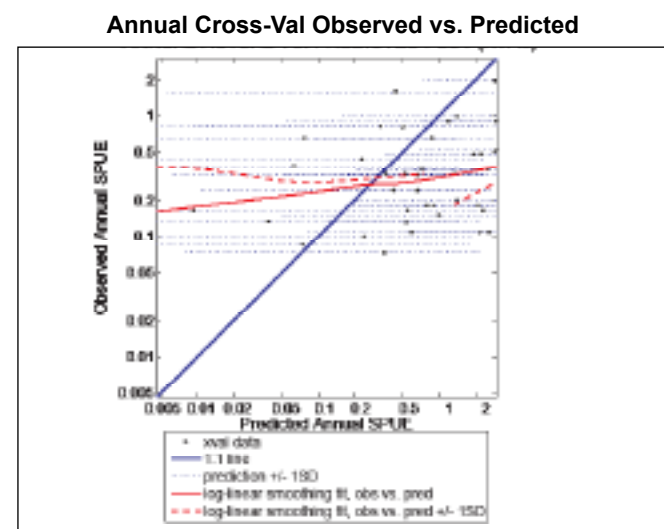
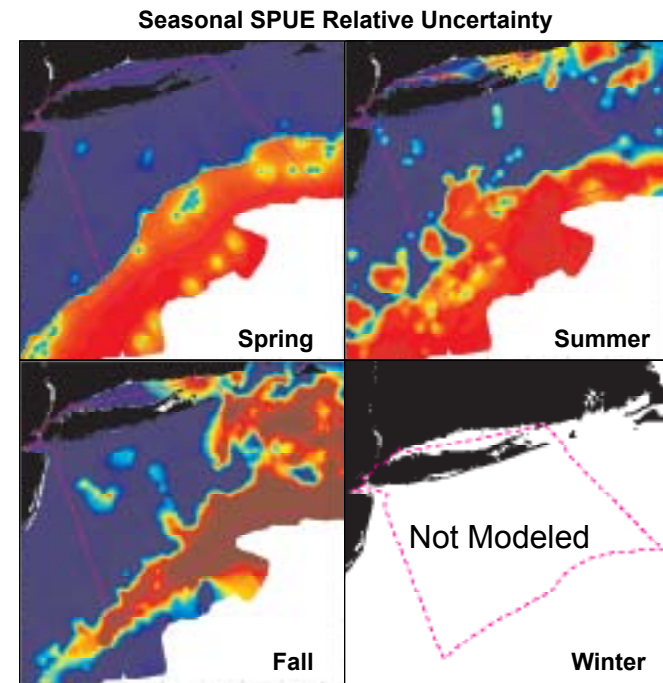
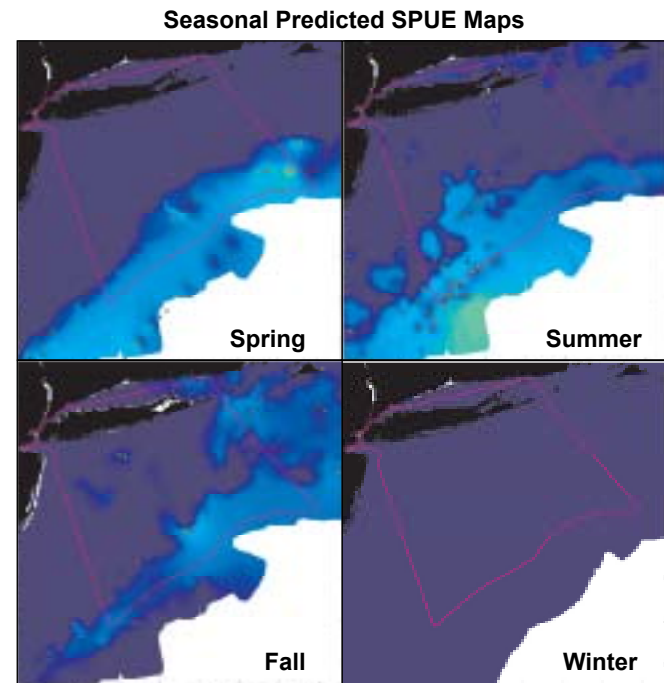
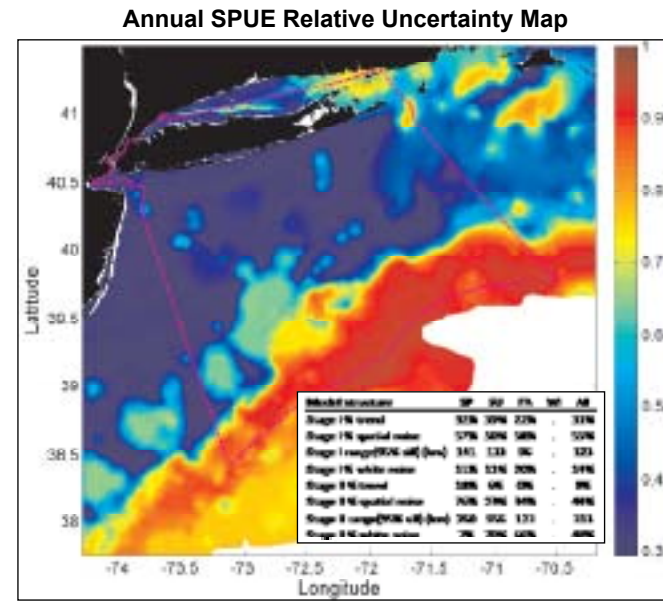
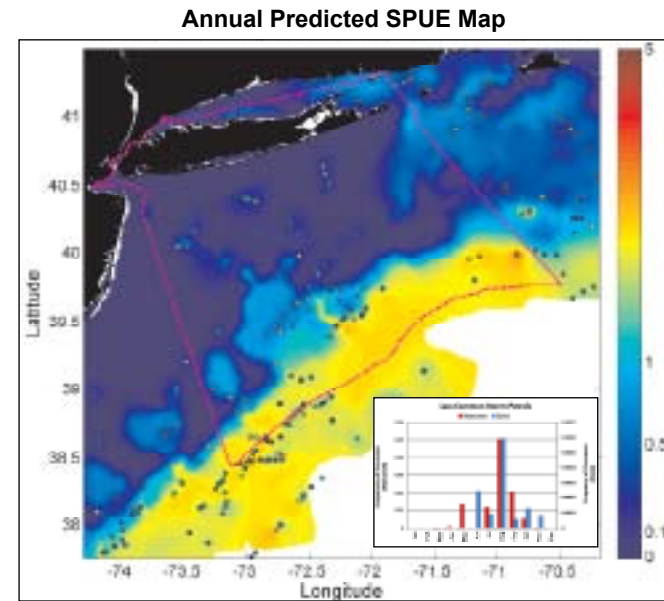
Small Gulls, less common

Stage I: Presence Probability Predictive Model



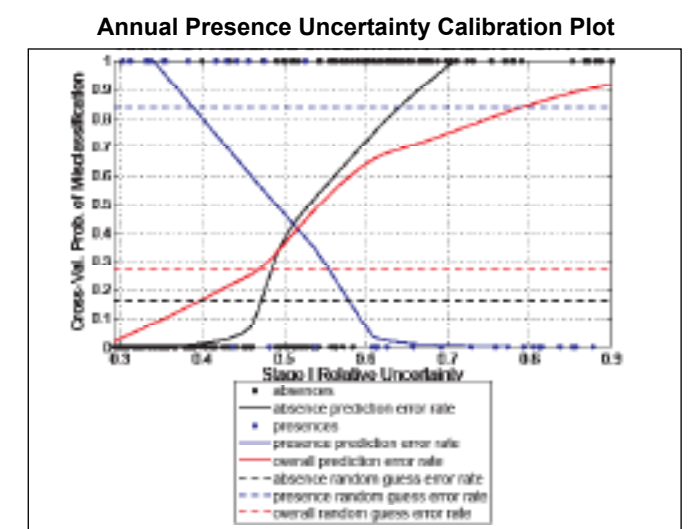
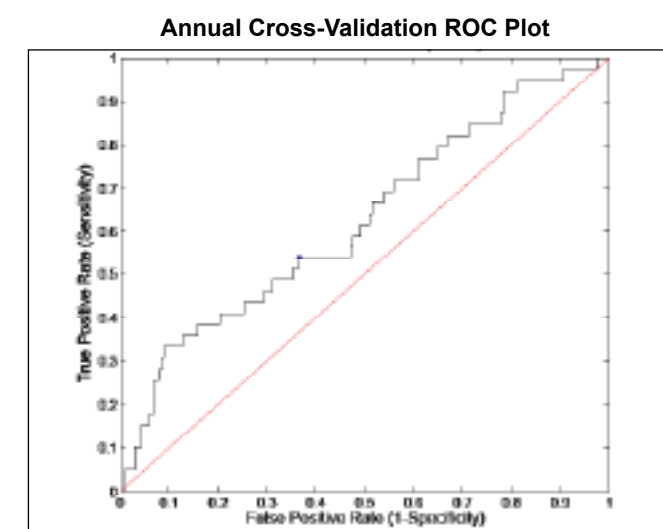
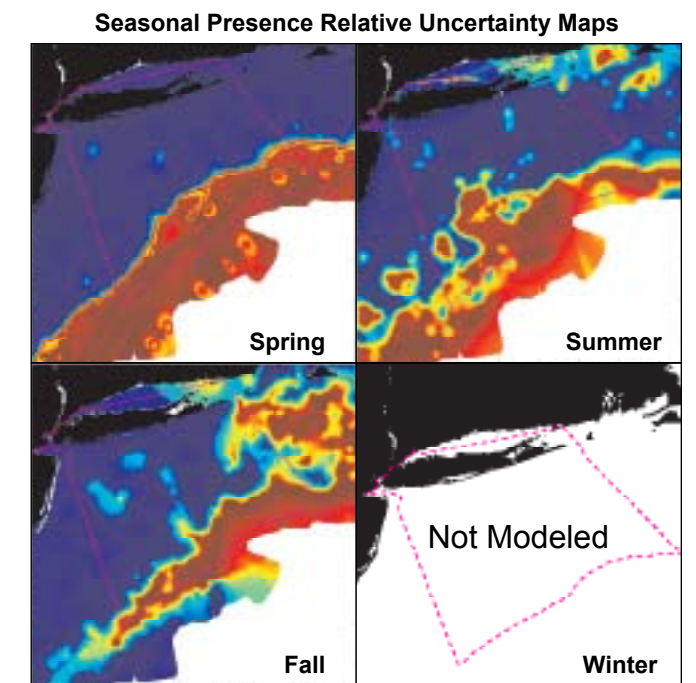
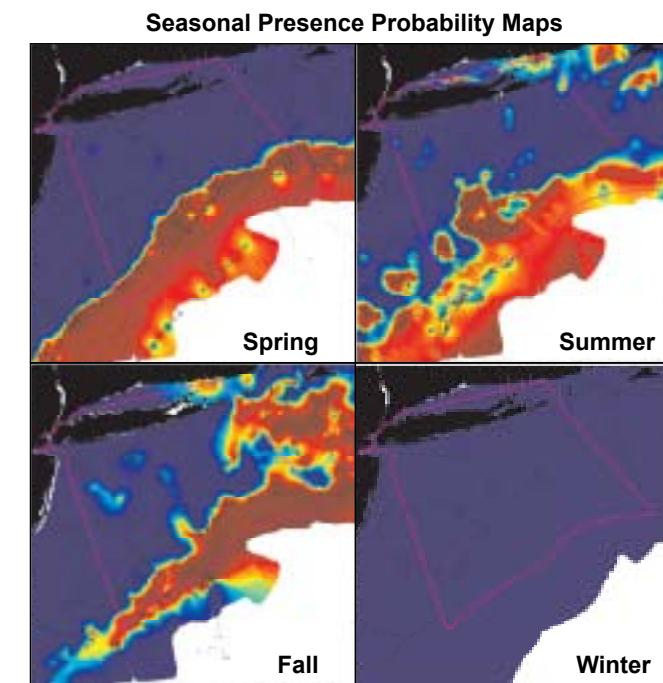
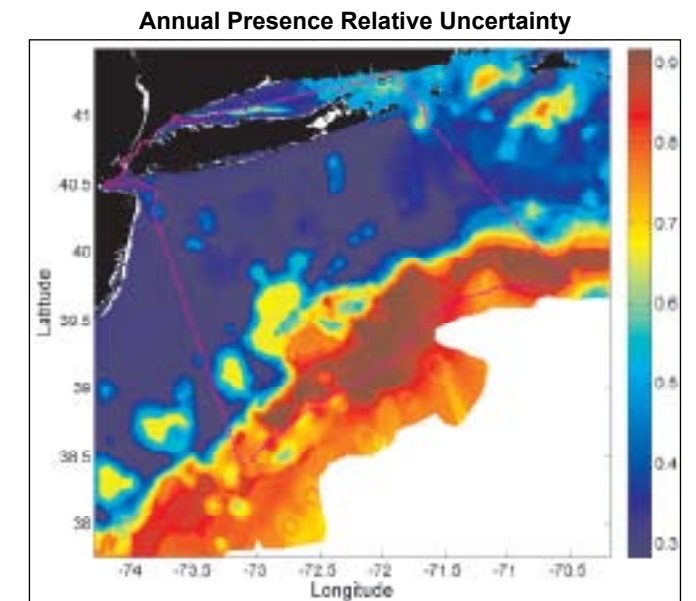
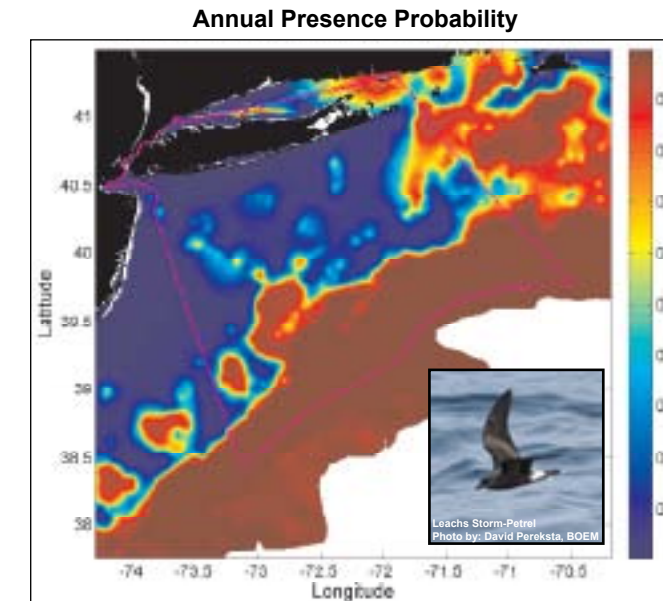
Storm-Petrels, less common

Stage I x II: Relative Abundance Predictive Model



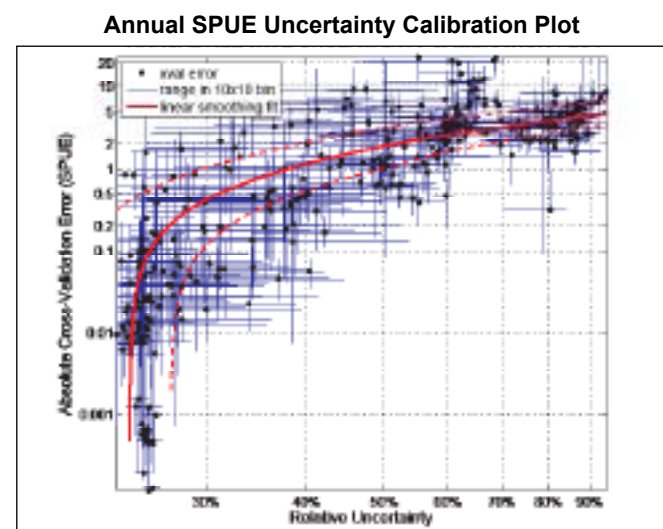
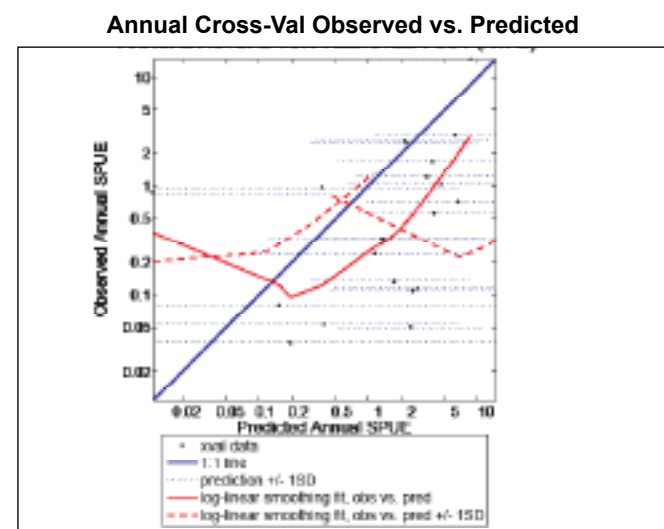
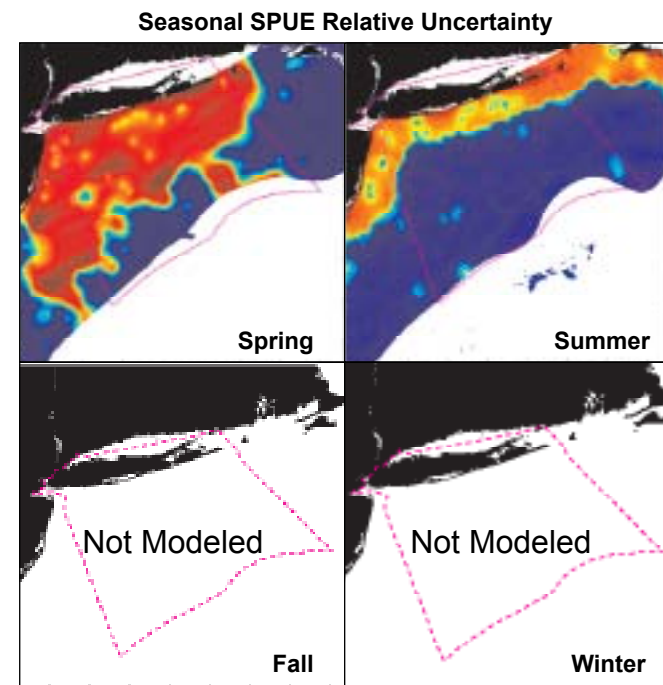
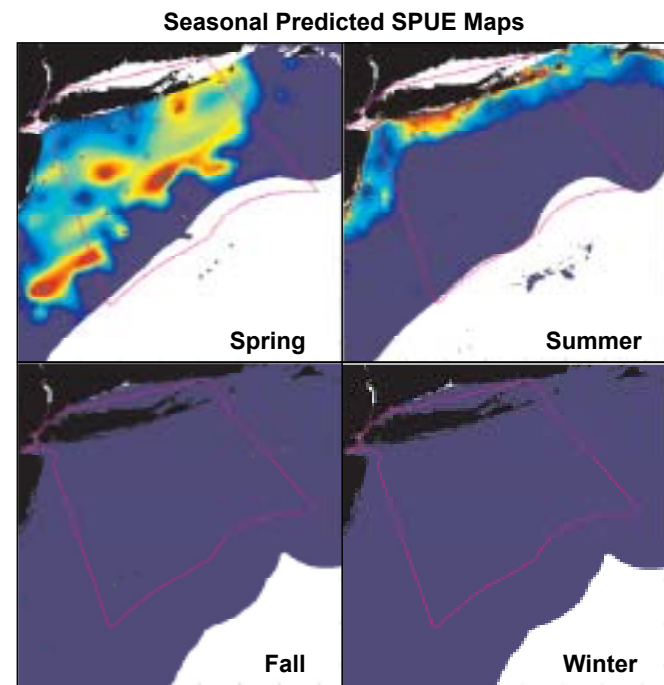
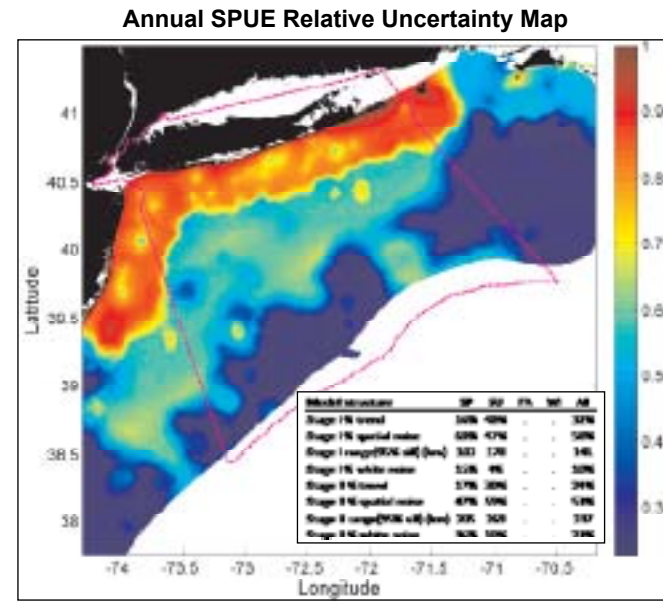
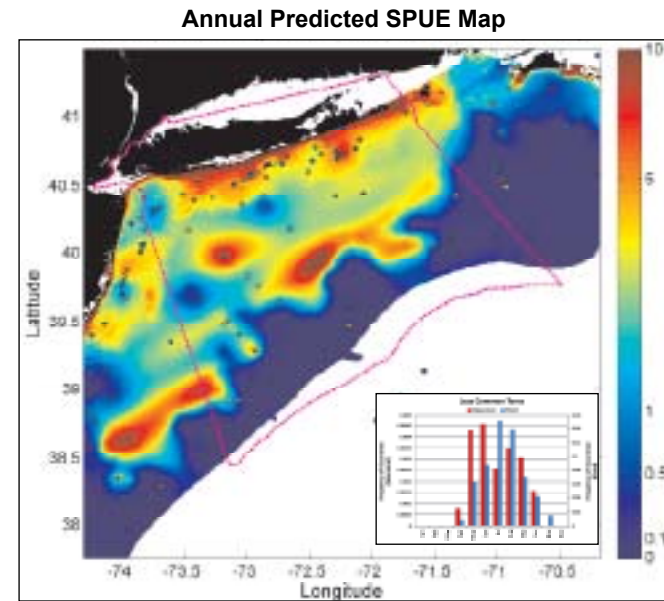
Storm-Petrels, less common

Stage I: Presence Probability Predictive Model



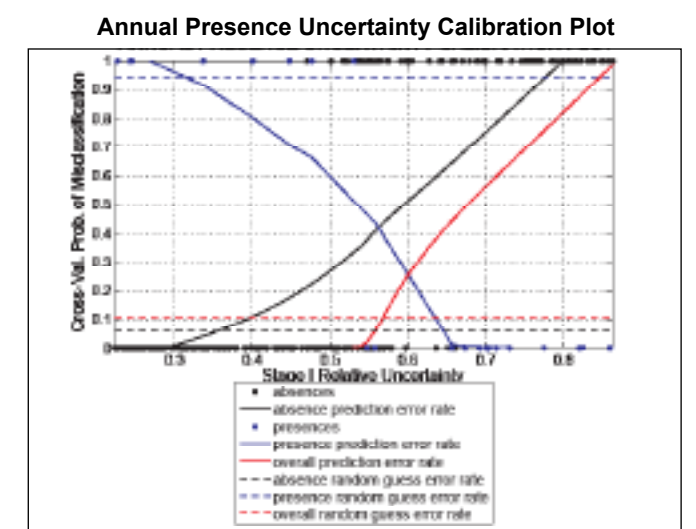
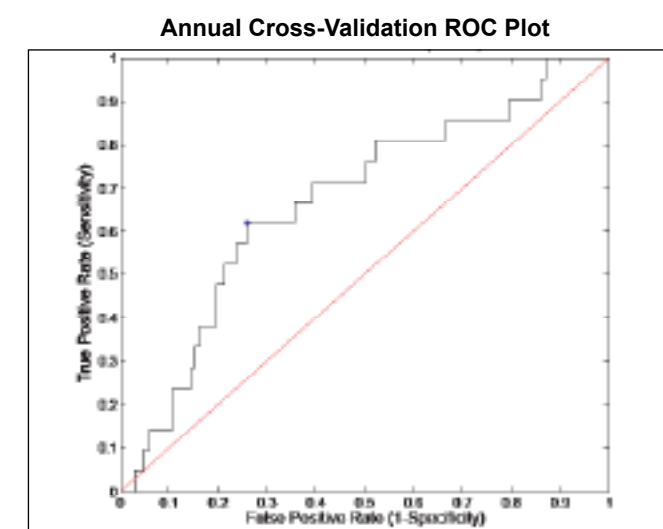
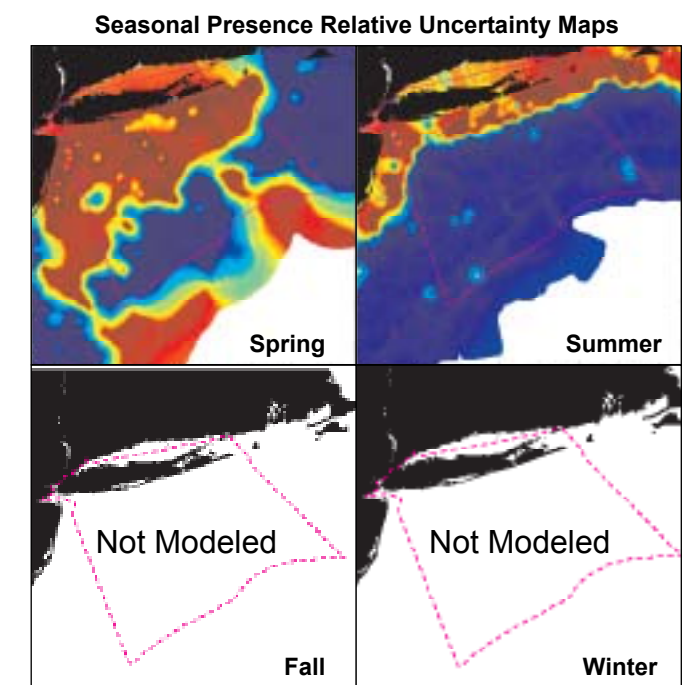
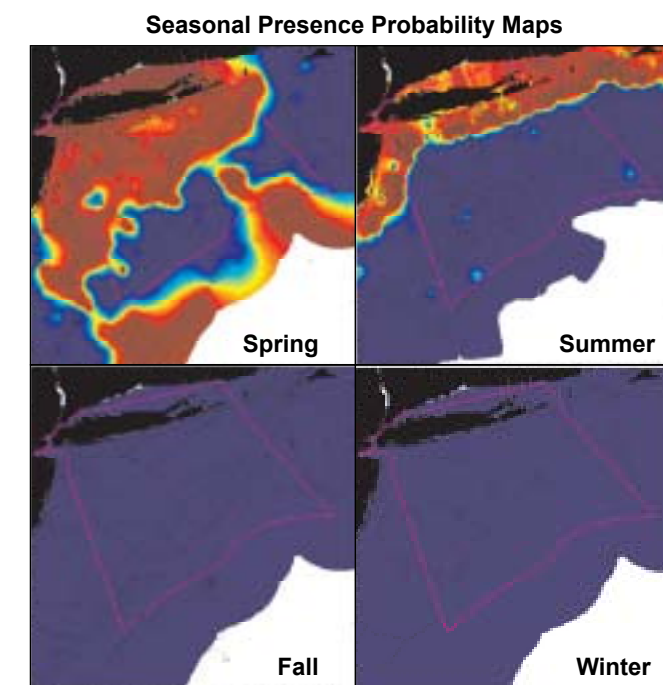
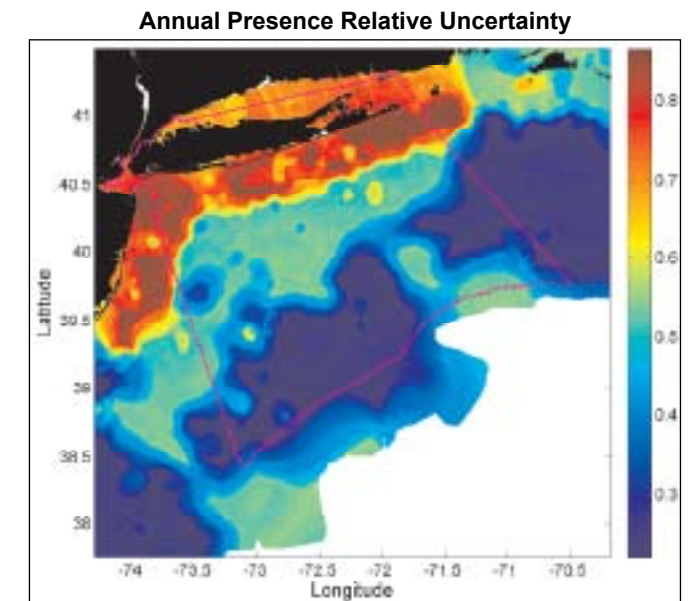
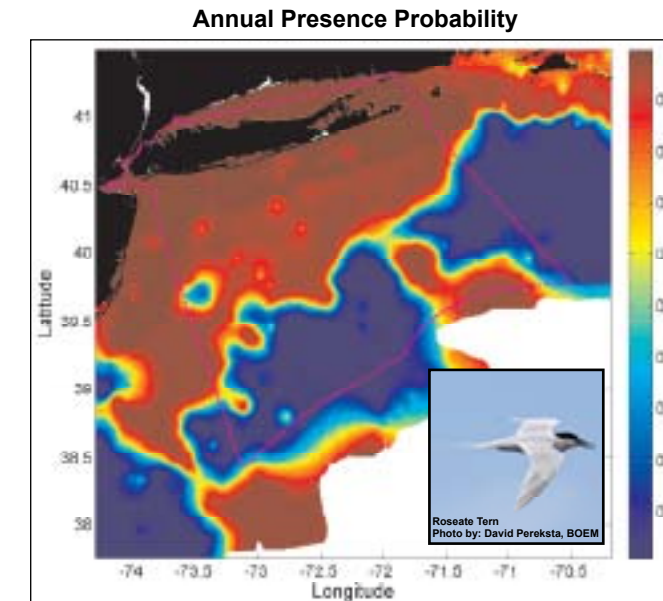
Terns, less common

Stage I x II: Relative Abundance Predictive Model



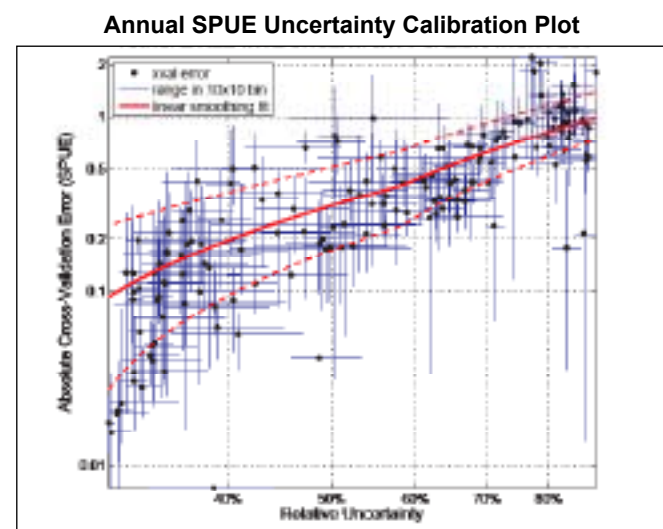
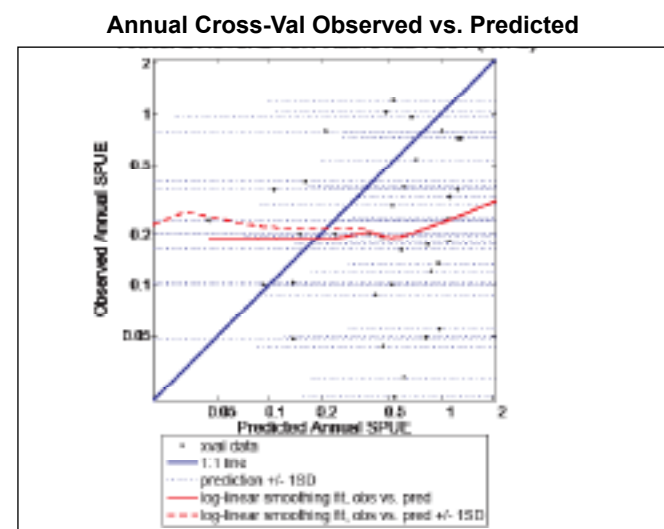
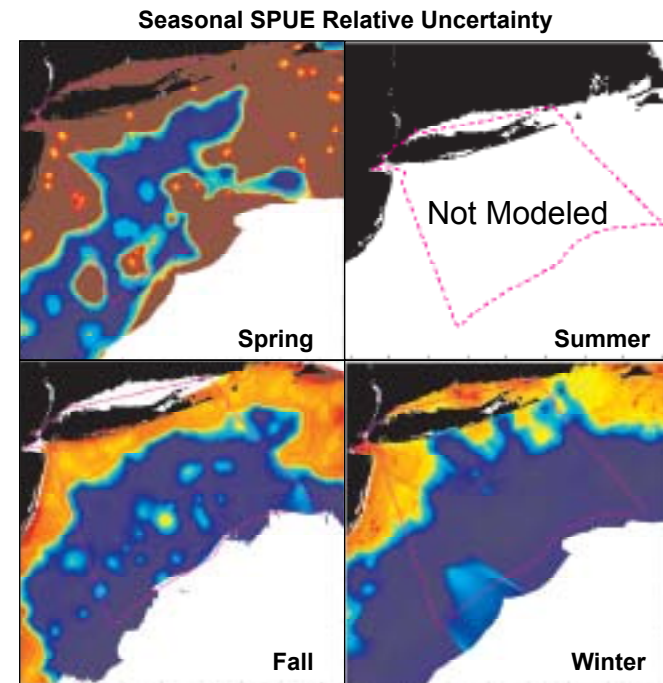
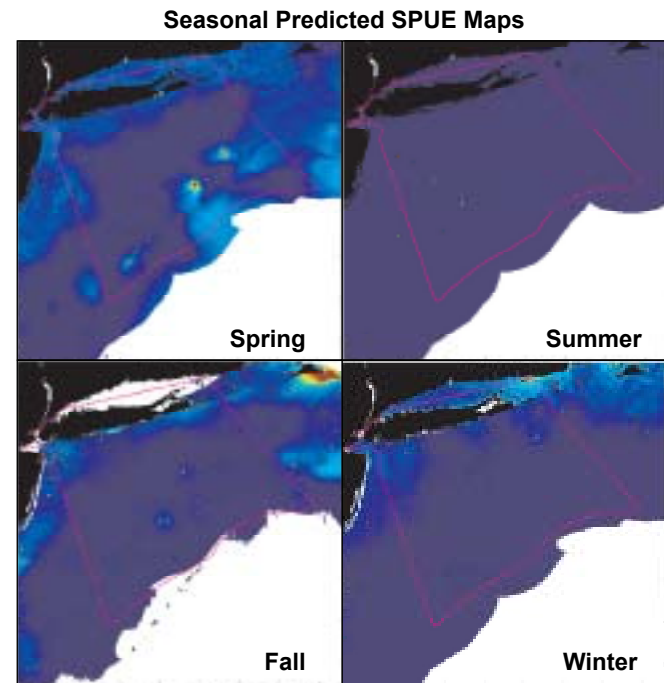
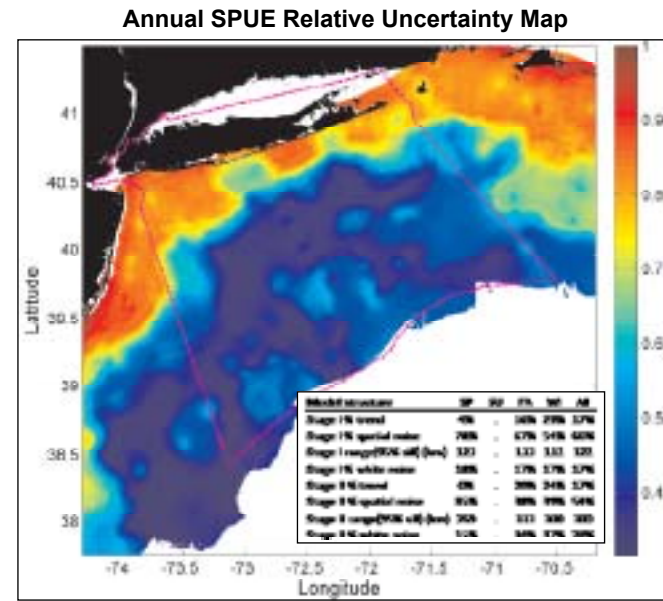
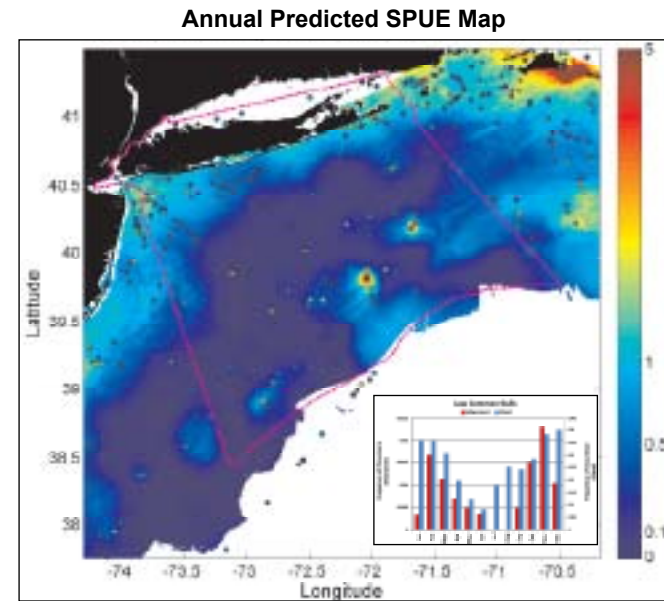
Terns, less common

Stage I: Presence Probability Predictive Model



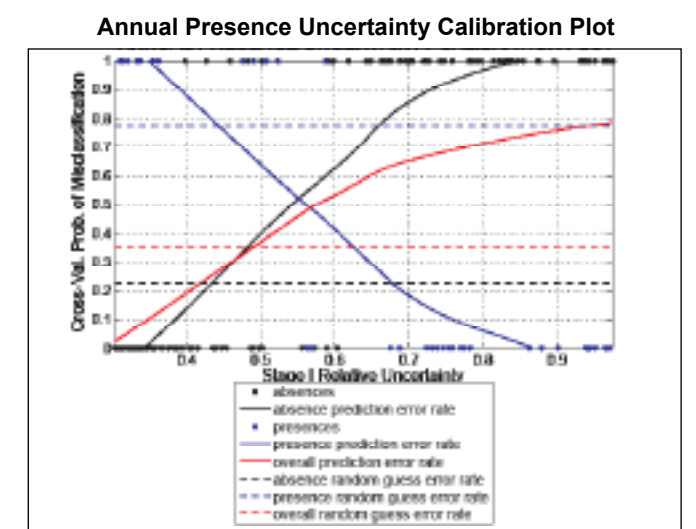
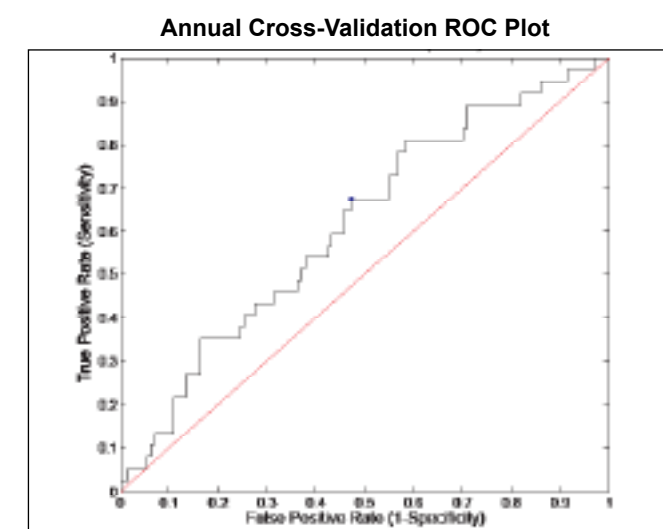
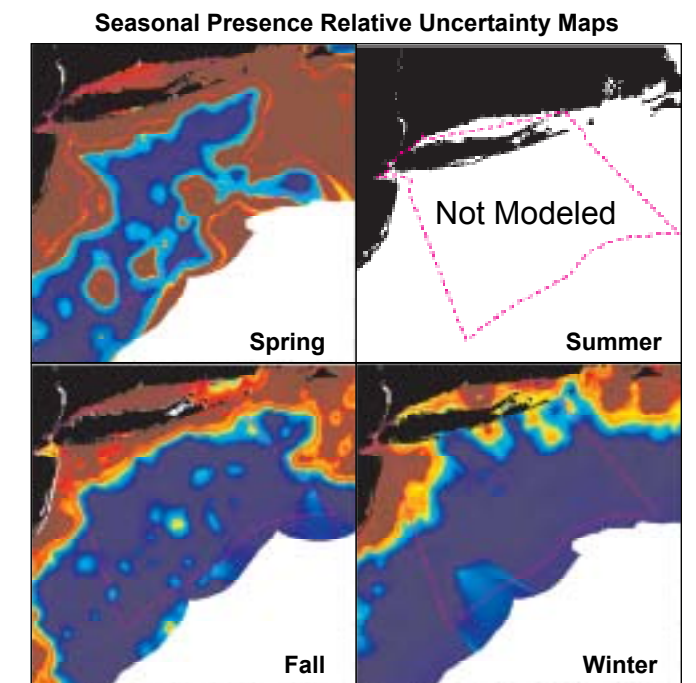
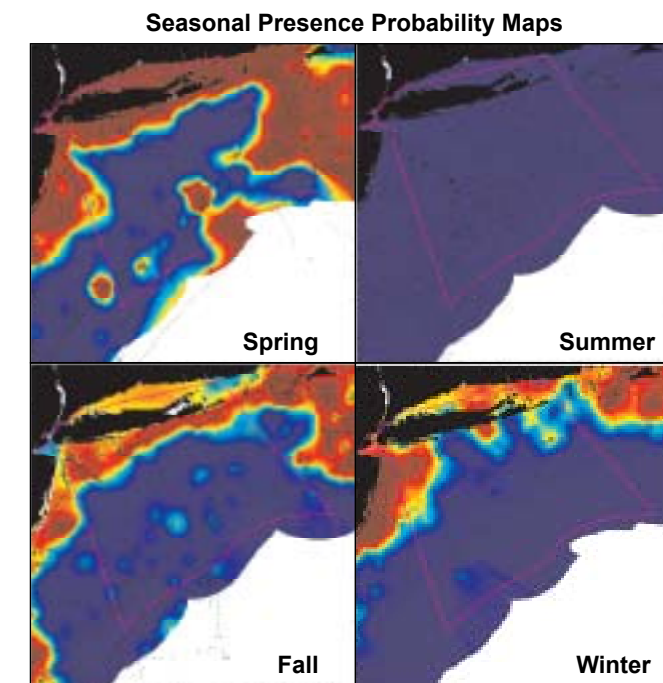
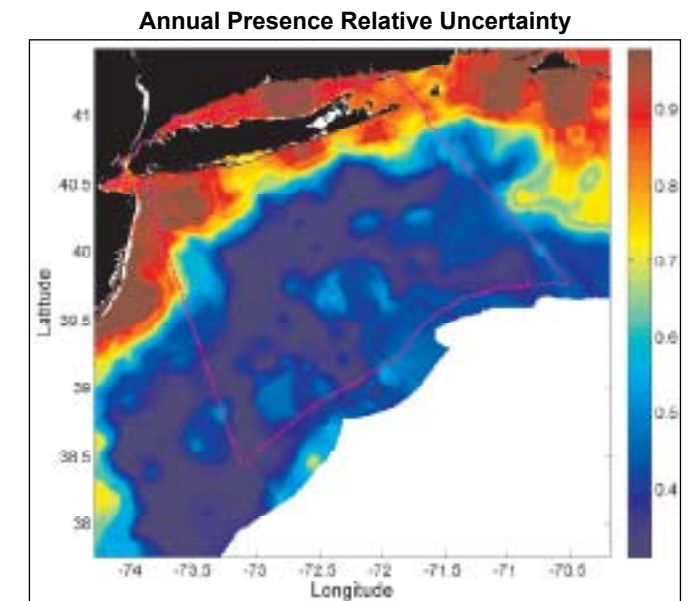
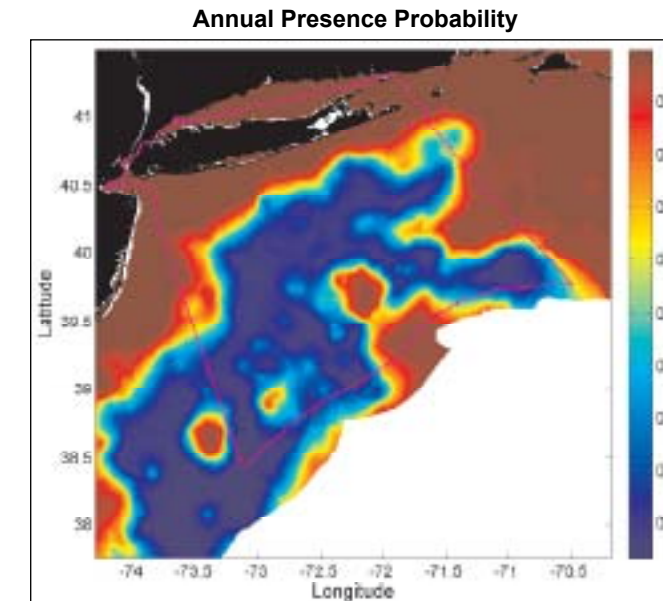
Unidentified Gulls

Stage I x II: Relative Abundance Predictive Model



Unidentified Gulls

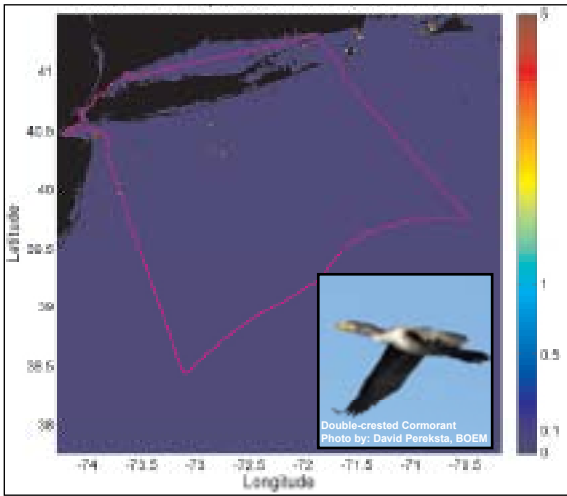
Stage I: Presence Probability Predictive Model



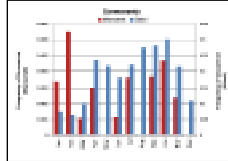
Non-modeled Groups

Cormorants (2 species)

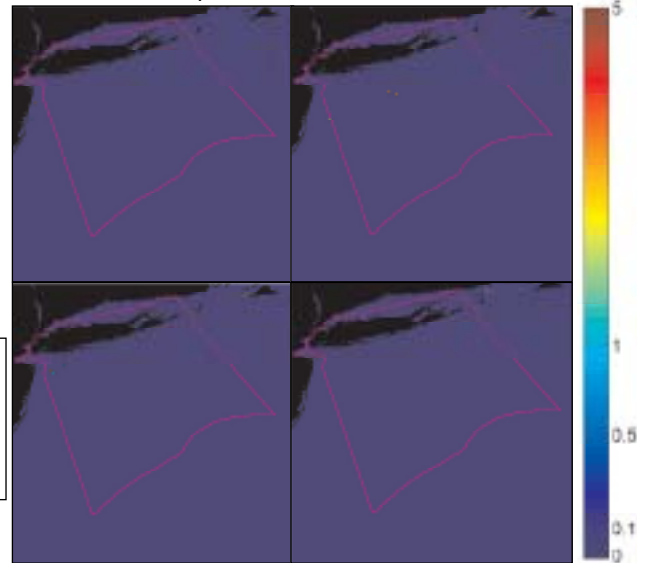
All available point observations of SPUE



Temporal histogram (Monthly pattern of occurrence)

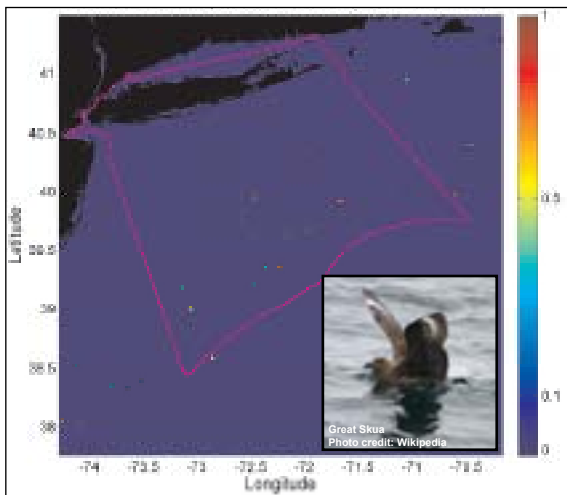


Seasonal point observations of SPUE

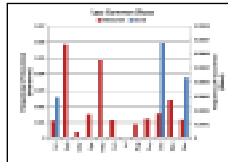


Skuas, less common (1 species)

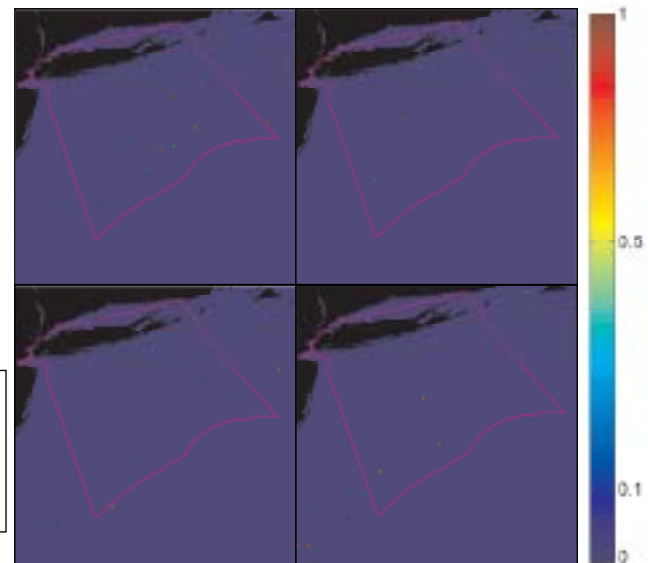
All available point observations of SPUE



Temporal histogram (Monthly pattern of occurrence)

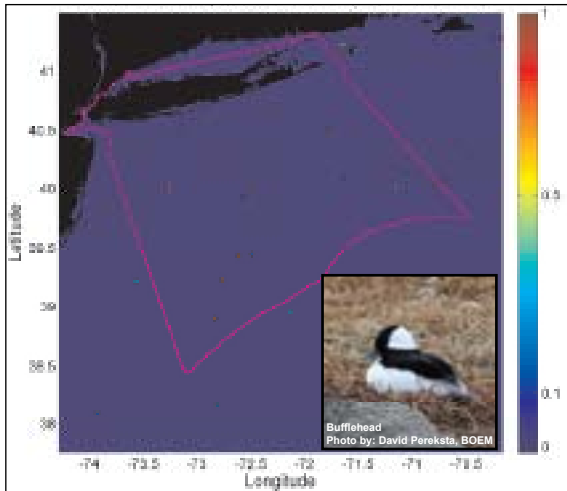


Seasonal point observations SPUE

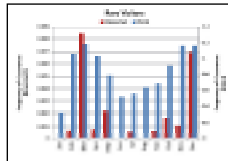


Rare Visitors (10 species)

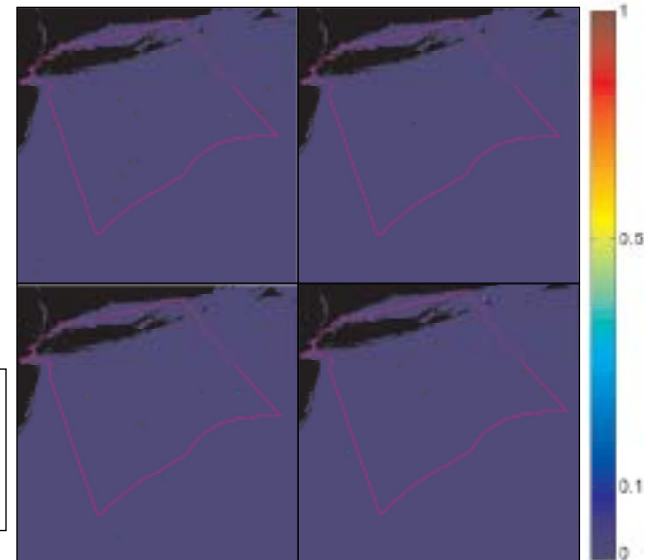
All available point observations of SPUE



Temporal histogram (Monthly pattern of occurrence)



Seasonal point observations SPUE



Appendix 6.D. Hotspot Predictive Model Profiles

6.D.1. Overview

This appendix presents detailed model profiles for the abundance, species richness, and Shannon diversity index hotspot analyses described in this chapter. The format is similar to Appendix 6.C. Annual and seasonal maps are presented, along with cross-validation observed vs. predicted plots and cross-validation relative uncertainty calibration plots. Annual cross-validation analyses were conducted in 20x20 cell (~18x18 km) bins. The larger bin size was necessary to include enough cross-validation data for all species simultaneously. Each figure in this appendix is explained in the associated caption; for detailed methods, see Appendix 6.A.

Annual hotspot relative uncertainty map

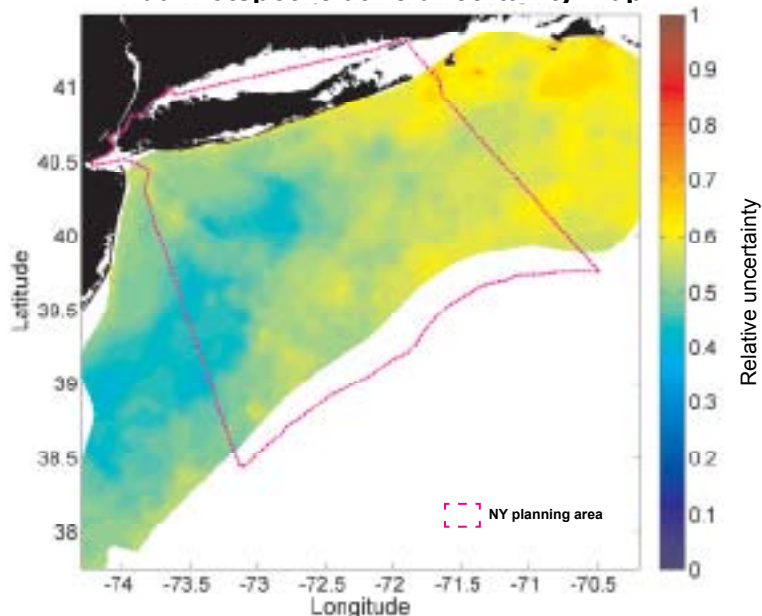


Figure 6.D.1. Annual hotspot relative uncertainty map. The relative uncertainty value is a dimensionless number scaled between 0 and 1, where values closer to 0 indicate greater certainty. The relative uncertainty value at each location is the same for all hotspot quantities (abundance, richness, and diversity index), because it is a function of the underlying trend and spatial model uncertainty for each species/group, but the relationship of the relative uncertainty value to actual prediction error varies for each of the quantities analyzed. That relationship can be seen in the uncertainty calibration plots for each predicted quantity: Figure 6.D.4 (Abundance), Figure 6.D.8 (Richness), and Figure 6.D.12 (Shannon Diversity Index).

Seasonal hotspot relative uncertainty maps

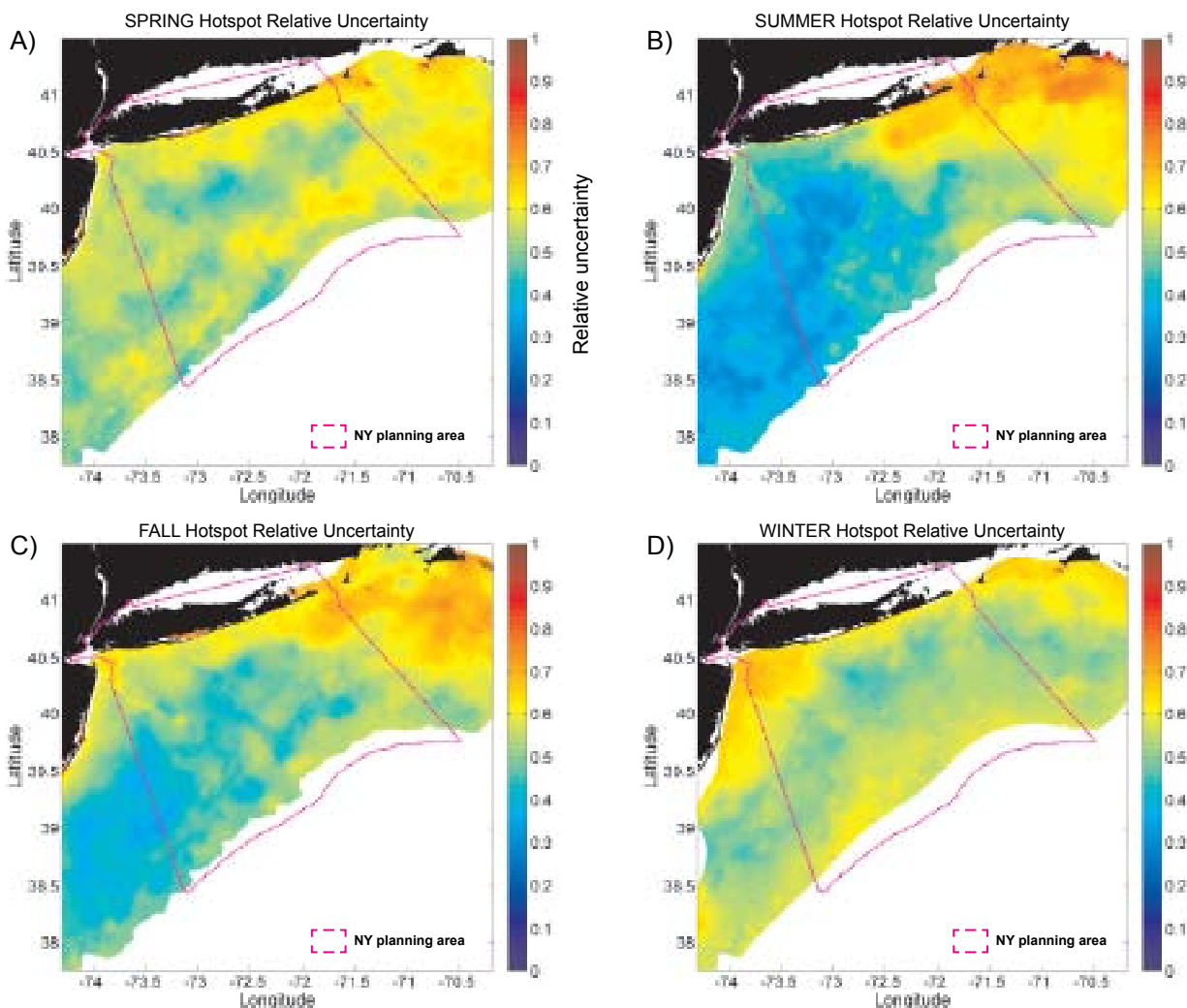


Figure 6.D.2. Seasonal hotspot relative uncertainty maps for (A)Spring, (B)Summer, (C)Fall, and (D)Winter. Explanation of relative uncertainty values is as in Figure 6.D.1.

ABUNDANCE HOTSPOTS

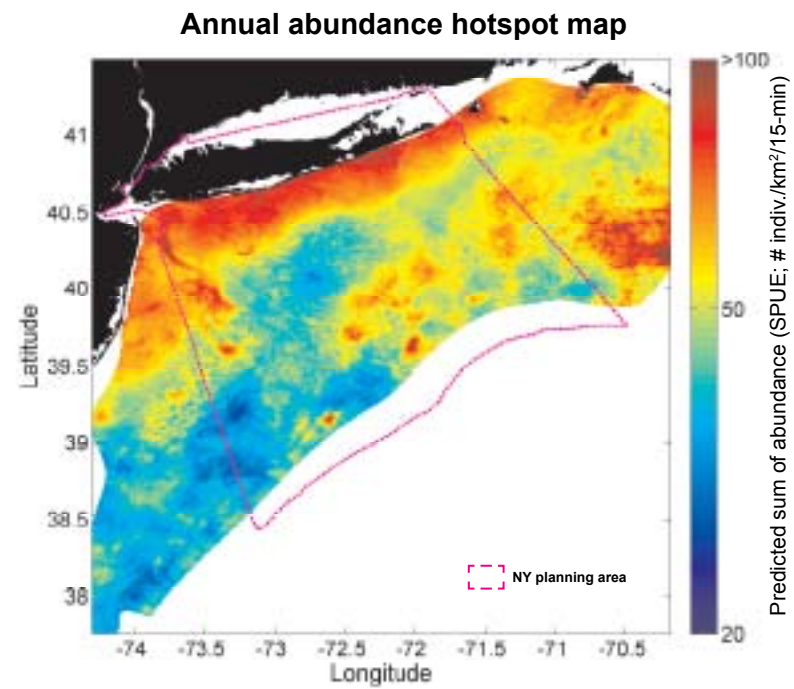


Figure 6.D.3. Annual predicted seabird relative abundance hotspot map. Shading represents the sum of the predicted relative abundance (SPUE) for all modeled species and groups over all seasons in which they were modeled ($\# \text{ indiv./km}^2/15\text{-min}$). Abundance was treated as zero for all seasons in which a species or group was not modeled. Note that this method may overestimate the abundance seen in any given 15-minute survey due to unaccounted-for correlations among species (a correction factor could be derived from the cross-validation results in Figure 6.D.5).

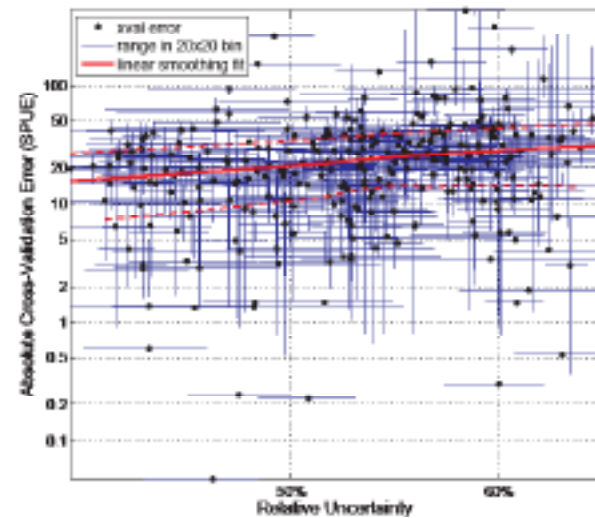
Annual Abundance Hotspots
Cross-Val. Uncertainty Calibration Plot

Figure 6.D.4. Cross-validation: relative uncertainty calibration plot for annual abundance hotspot map. The mean absolute cross-validation error calculated in 20×20 cell bins is plotted vs. the mean relative uncertainty value in the same bins; dashed lines show range of values in each bin. Red line is a robust linear loess smoothing fit (± 1 standard deviation; dashed red lines). Although the pattern is noisy, mean absolute cross validation error, measured in units of SPUE ($\# \text{ indiv./km}^2/15\text{-min}$) can be seen to decrease smoothly as relative uncertainty decreases. Note log scale on both axes.

Seasonal abundance hotspot maps

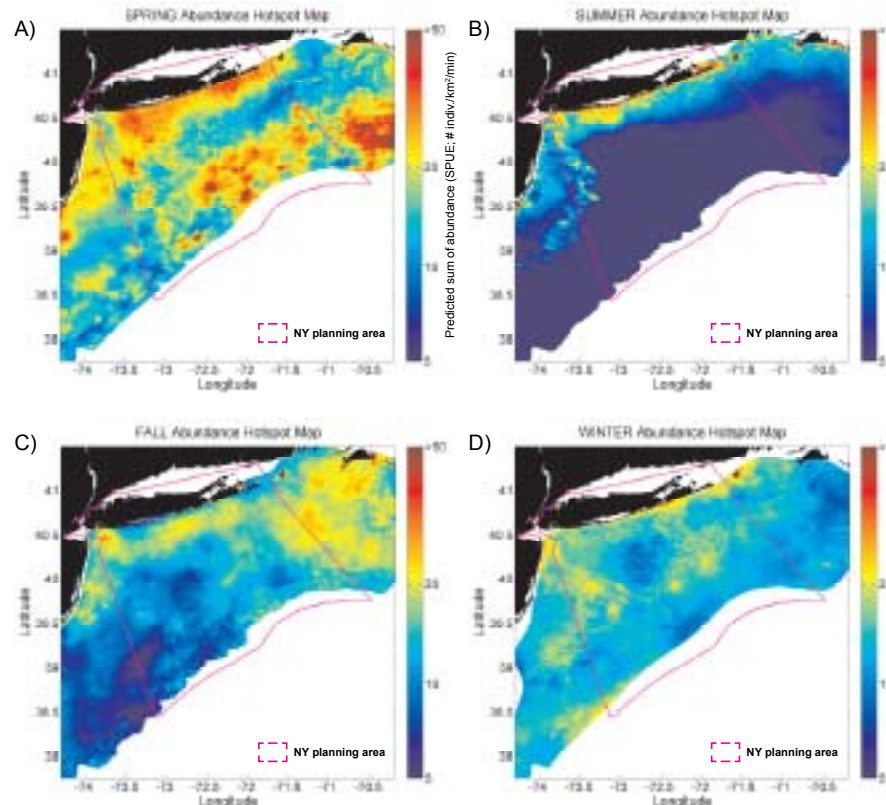


Figure 6.D.6. Seasonal predicted relative abundance hotspot maps for (A)Spring, (B)Summer, (C)Fall, and (D)Winter. Hotspots were calculated by summing predicted abundances of all modeled species and groups in the indicated season.

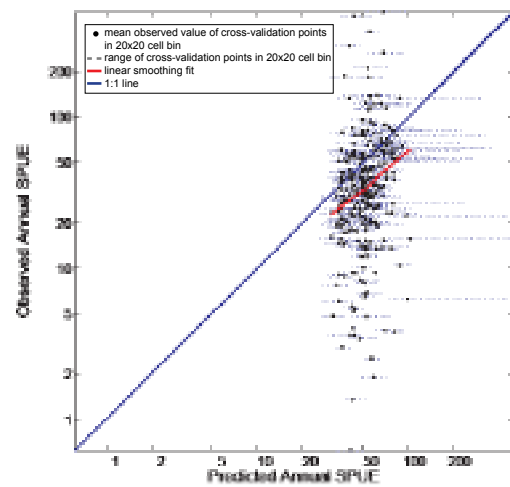
Annual Cross-Val. Observed vs.
Predicted Abundance

Figure 6.D.5. Cross-validation: observed vs. predicted values for the annual abundance hotspot map. Observations not included in the model training set were averaged in 20×20 cell bins and are plotted vs. the mean prediction value in the same bins. The 1:1 line (blue line) and a robust linear loess smoothing fit (red line) are plotted. Dashed horizontal lines show range of predictions in each bin. The x-axis is compressed compared to the y-axis for two reasons: first, the model predicts the average value expected over a long time at any given location, and individual observations vary around this average; second, many more predictions than observations are averaged to create each bin value (many of the 20×20 cell bins contain only one observation, but they contain up to 400 predictions). The loess smoothing fit suggests that predicted total abundance correlates well with observed total abundance, but that observed total abundance is systematically lower than the prediction by a factor of approximately 1.5 to 2. Note log scale on both axes.

SPECIES RICHNESS HOTSPOTS

Annual species richness hotspot map

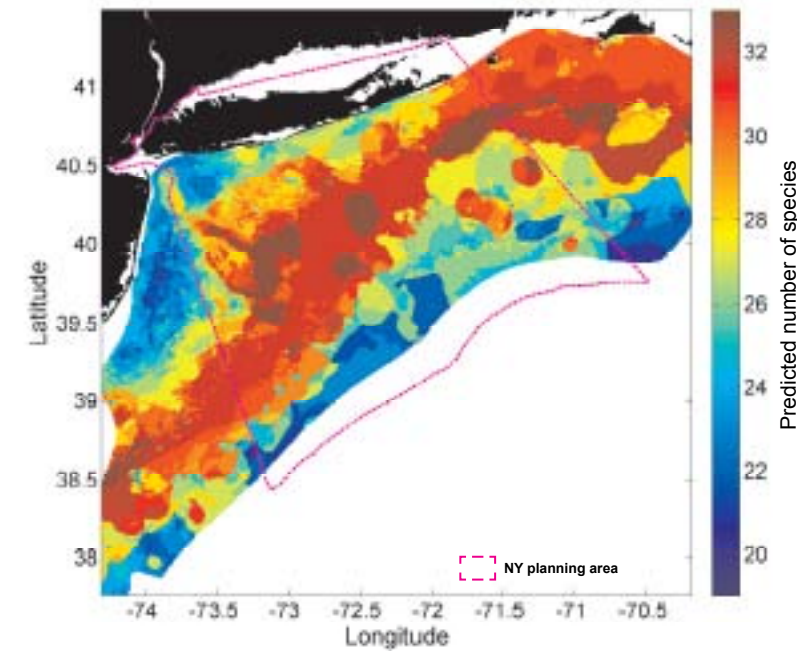


Figure 6.D.7. Annual predicted seabird species richness hotspot map. Shading represents the median of upper and lower bounds on predicted species richness at each location, obtained by summing minimum and maximum number of species that could have been present over all species and groups, treating each species or group as present if its predicted relative abundance was above a threshold. See Section 6.8.8.2 for methods. Species and groups that were not modeled in any season did not contribute to richness. Note that this estimate of richness overestimates the actual number of species that would be seen in any given 15-minute survey, both because it is unlikely that half of the species in each group will always be present, and because of unaccounted-for correlations among species (a correction factor could be derived from the cross-validation results in Figure 6.D.9).

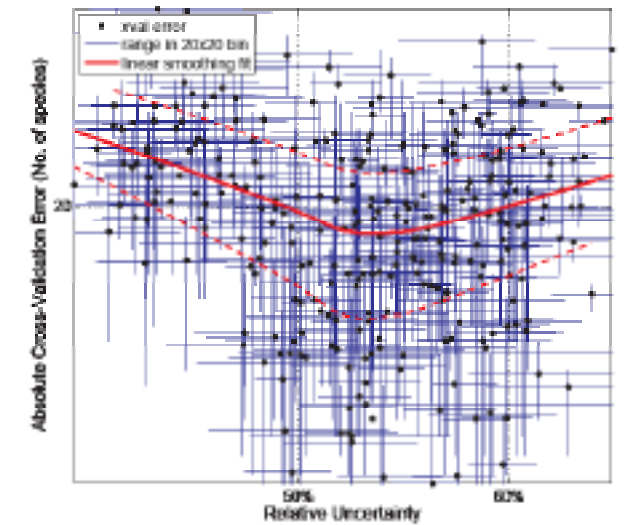
Annual Species Richness Hotspots
Cross-Val. Uncertainty Calibration Plot

Figure 6.D.8. Cross-validation: relative uncertainty calibration plot for annual richness hotspot map. The mean absolute cross-validation error calculated in 20×20 cell bins is plotted vs. the mean relative uncertainty value in the same bins; dashed lines show range of values in each bin. Red line is a robust linear loess smoothing fit (± 1 standard deviation; dashed red lines). Results indicate a very noisy and non-linear relationship between relative uncertainty and the actual observed cross-validation error in species richness; relative uncertainty values between approximately 50% and 60% correspond to the best relationship between predicted and observed values at the 20×20 cell bin scale. It is recommended that the relative uncertainty of the richness hotspot maps be interpreted with caution. Areas where relative uncertainty $< 40\%$ appear particularly unreliable. Some of this may be an artifact of the large bin size (20×20 cells) required for this cross-validation exercise. Note log scale on both axes.

Seasonal species richness hotspot maps

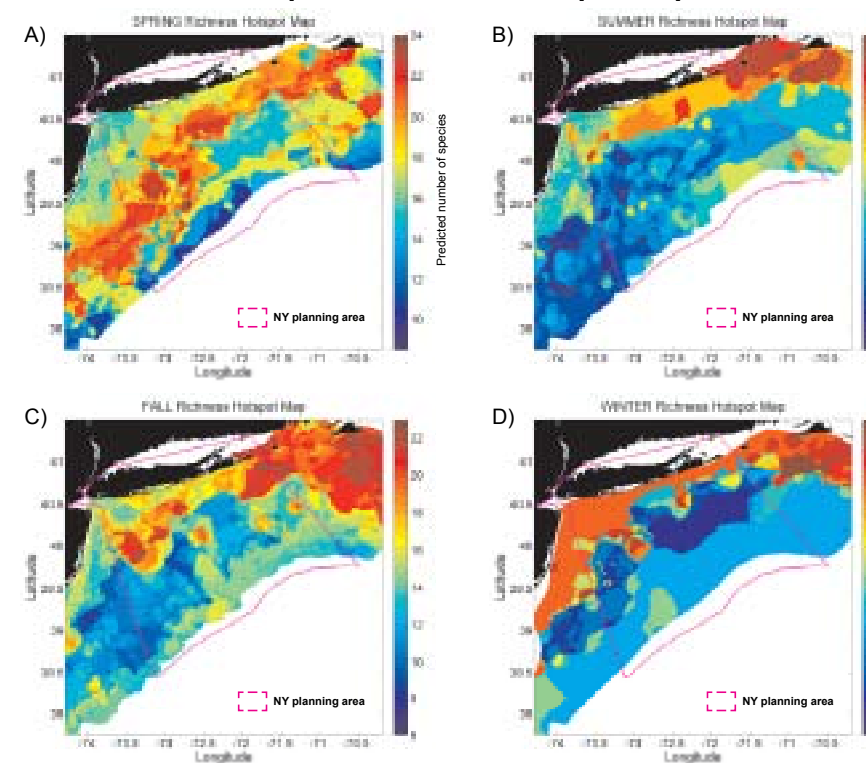


Figure 6.D.10. Seasonal predicted species richness hotspot maps for (A)Spring, (B)Summer, (C)Fall, and (D)Winter. Richness hotspots were calculated as described in Section 6.8.8.2. Species and groups not modeled in a given season did not contribute to richness for that season.

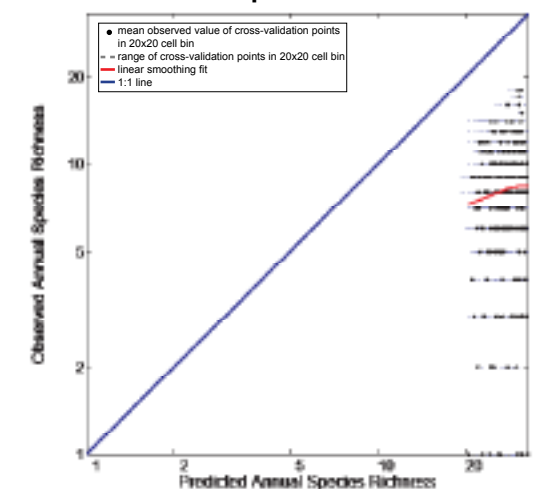
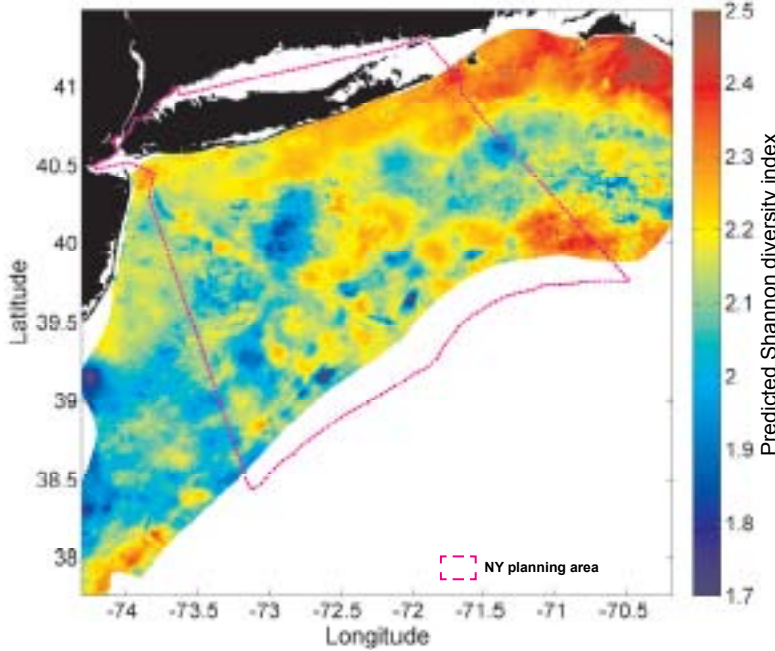
Annual Cross-Val. Observed vs.
Predicted Species Richness

Figure 6.D.9. Cross-validation: observed vs. predicted values for the annual species richness hotspot map. Observed richness at locations not included in the model training set were averaged in 20×20 cell bins and are plotted vs. the mean predicted richness in the same bins. The 1:1 line (blue line) and a robust linear loess smoothing fit (red line) are plotted. Dashed horizontal lines show range of predictions in each bin. The x-axis is compressed compared to the y-axis for the same reasons as noted in Figure 6.D.5. The loess smoothing fit suggests that predicted species richness correlates well with observed species richness, but that observed richness is systematically lower than the prediction by a factor of approximately 3 to 4. Note log scale on both axes.

SHANNON DIVERSITY INDEX HOTSPOTS

Annual diversity index hotspot map



Annual Diversity Index Hotspots
Cross-Val. Uncertainty Calibration Plot

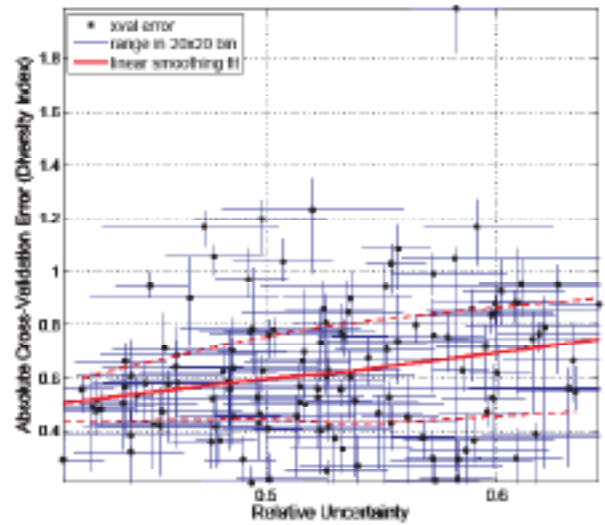


Figure 6.D.12. Cross-validation: relative uncertainty calibration plot for annual diversity index map. The mean absolute cross-validation error calculated in 20x20 cell bins is plotted vs. the mean relative uncertainty value in the same bins; dashed lines show range of values in each bin. Red line is a robust linear loess smoothing fit (+/- 1 standard deviation; dashed red lines). Although the pattern is noisy, mean absolute cross validation error, measured in units of the Shannon diversity index, can be seen to decrease smoothly as relative uncertainty decreases. Note that y-axis is linearly scaled and x-axis is log scaled.

Figure 6.D.11. Annual predicted seabird Shannon diversity index. The Shannon index incorporates both presence and relative abundance. See section 6.8.8.3 for methods. Species and groups that were not modeled in any season did not contribute to index calculation. Note that this estimate of diversity overestimates the actual value of diversity index calculated in any given 15-minute survey for the reasons noted in captions for Figures 6.D.3 and 6.D.7 (a correction factor could be derived from the cross-validation results in Figure 6.D.13).

Seasonal diversity index hotspot maps

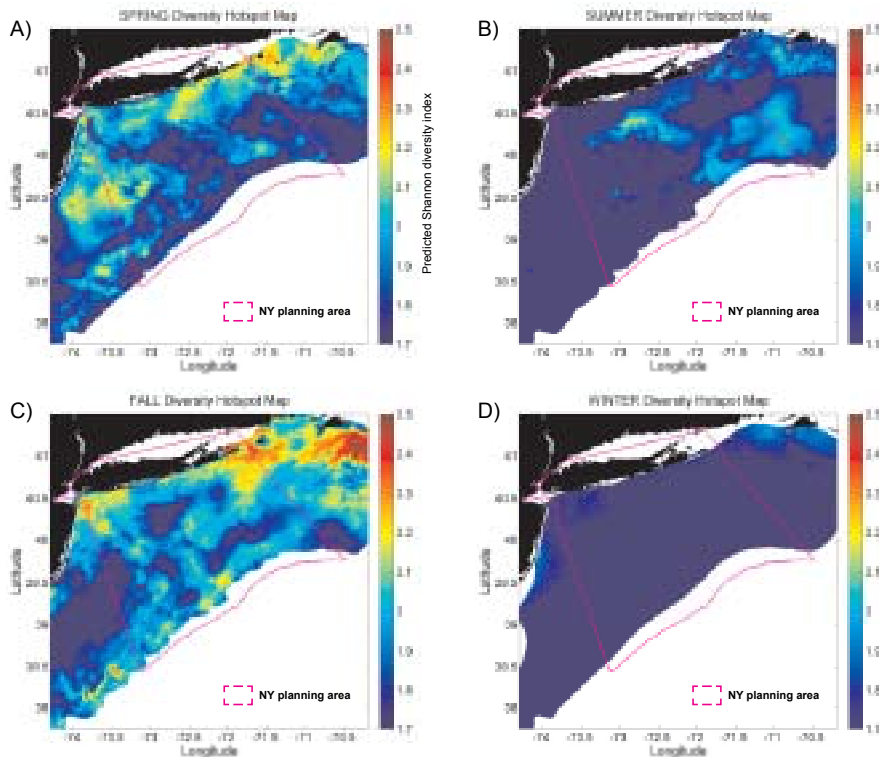


Figure 6.D.14. Seasonal predicted Shannon diversity index maps for (A)Spring, (B)Summer, (C)Fall, and (D)Winter. Diversity index values were calculated as described in Section 6.8.8.2. Species and groups not modeled in a given season did not contribute to diversity calculations for that season.

Annual Cross-Val. Observed vs. Predicted Diversity Index

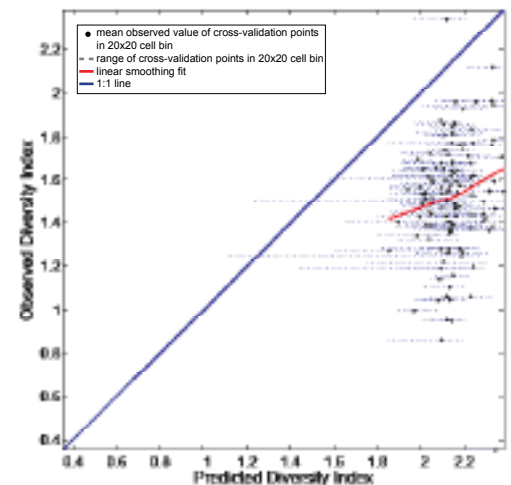


Figure 6.D.13. Cross-validation: observed vs. predicted values for the annual Shannon diversity index map. Observed Shannon diversity index at locations not included in the model training set was averaged in 20x20 cell bins and is plotted vs. the mean predicted Shannon diversity index in the same bins. The 1:1 line (blue line) and a robust linear loess smoothing fit (red line) are plotted. Dashed horizontal lines show range of predictions in each bin. The x-axis is compressed compared to the y-axis for the same reasons as noted in Figure 6.D.5. The loess smoothing fit suggests that the predicted Shannon diversity index correlates well with the observed value of the index in 20x20 cell bins, but that observed diversity is systematically lower than the prediction by a factor of approximately 1.2 to 1.4. Note that both axes are linearly scaled.



U.S. Department of Commerce

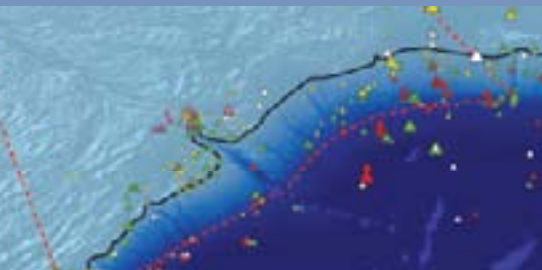
Dr. Rebecca Blank, *Acting Secretary*

National Oceanic and Atmospheric Administration

Dr. Jane Lubchenco, *Under Secretary for Oceans and Atmosphere*

National Ocean Service

David M. Kennedy, *Assistant Administrator for Ocean Service and Coastal Zone Management*



The Center for Coastal Monitoring and Assessment's mission is to assess and forecast coastal and marine ecosystem conditions through research and monitoring. CCMA conducts field observations on regional and national scales. The center provides the best available scientific information for resource managers and researchers, technical advice, and accessibility to data. For more information, visit: <http://ccma.nos.noaa.gov/>



A Biogeographic Assessment of Seabirds, Deep Sea Corals and Ocean Habitats of the New York Bight:
Science to Support Offshore Spatial Planning

NOAA TECHNICAL MEMORANDUM
NOS NCCOS 141